9-2016

Compositional Diversity in Arcs: A Record of Magmatic Processes in the Peru Coastal Batholith, Ica

Ana Maria Martinez Ardila

LOMA LINDA UNIVERSITY
School of Medicine
in conjunction with the
Faculty of Graduate Studies

Compositional Diversity in Arcs: A Record of Magmatic Processes in the Peru Coastal Batholith, Ica

by

Ana Maria Martinez Ardila

A Dissertation submitted in partial satisfaction of
the requirements for the degree
Doctor of Philosophy in Earth Sciences

September 2016

Each person whose signature appears below certifies that this dissertation in his/her opinion is adequate, in scope and quality, as a dissertation for the degree Doctor of Philosophy.

_____, Chairperson
Benjamin L. Clausen, Adjunct Associate Professor of Earth Science

_____
Ronald Nalin, Adjunct Assistant Professor of Earth Science

_____
Kevin E. Nick, Associate Professor of Earth Science

_____
Scott Paterson, Professor of Earth Science, University of Southern California

_____
Christopher C. Perry, Assistant Professor of Basic Sciences

ACKNOWLEDGEMENTS

There are many people to whom I would like to express my sincere gratitude for being part of this chapter of my life, but I would first like to express my most grateful acknowledgment to God for His love and blessings and for giving to my life meaning and purpose.

I am absolutely convinced that words would never be enough to express my gratitude to the amazing group of people who gave me the support and courage to persevere each day in the graduate student life, and of course challenged me along this way. Therefore, the path towards this dissertation, from its beginning to its completion, is thanks to…

My husband who has shown me his love and support every day of our life together. He gave me thousands of reasons to smile and to keep working hard during my most difficult days. He took my hand and walked next to me when I was feeling exhausted and overwhelmed. I am so blessed to be his wife and without his love and support this research wouldn't be successful. I would like to thank my daughter as well, she is my little one but there is so much power and strength in that little person that I couldn't imagine my life without her influence. My graduate life was challenged by her arrival and brought to my life an entirely new and fascinating world. She taught me important lessons of perseverance, patience, passion, the power of a smile from the heart, and that the little things are really the big things in this life.

To my advisor but also my friend Ben Clausen for the continuous support during my Ph.D. study and related research, for his patience, motivation, and knowledge, and immense friendship. His guidance helped me during all the time of research and writing

of this thesis. I could not have imagined having a better advisor and mentor for my Ph.D. study. He is a person that influenced my life in such a great way that I cannot describe. I truly admire him not only for his knowledge but also for his human quality. He guided me in the scientific path but also he taught me about the practice of respect and tolerance for others. I must also express my gratitude and love for his wife, a beautiful woman who welcomed me and my family in such a warm way that we felt at home with her friendship and company.

Besides my advisor, I am also thankful to Dr. Scott Paterson for his guidance, teaching, exhortation, encouragement, and the time he has invested in me during the last several years. I would like to thank the rest of my research committee: Dr. Ronald Nalin, Dr. Kevin Nick, and Dr. Christopher C. Perry for their insightful comments and encouragement to finish this research. To me, this research would not have the value that it has without the invaluable academic, educational, and human support for me as a researcher that was provided by each of them. I also want to acknowledge Dr. Vali Memeti for helpful discussions about geochemistry and for teaching me to use GCDKit.

To the Department of Earth and Biological Sciences and the Geoscience Research Institute, especially Dr. Leonard Brand, and the donors, to whom I am deeply indebted for giving me the opportunity to become a Ph. D. from a high quality institution with a philosophy of service, compassion, and love. I am grateful also to Elieze Strydom and Carol Olmo for always being extremely helpful and for the tremendous job they do for each student and researcher.

I also want to thank to Dr. Raul Esperante because he was the person who invited me to Peru and allowed me to visit there several times to collaborate with his research, introduced Dr. Leonard Brand to me, and finally put me in contact with my advisor.

I would like to thank Orlando Poma, who was always willing to work in the field and to make arrangements for me in Peru during the last six years. He worked long hours during exhausting field days and was always committed to this project. For that I am incredibly grateful.

To my LLU colleagues, Luciano Gonzalez and Lance Pompe, for your advice and feedback during our hard rock meetings and discussions, in helping me during field and lab work.

To my Spanish Sabbath School and Loma Linda University Church friends who were extremely helpful when Cesar and I moved from Colombia to this country, they made our transition to a new culture and place much easier and enjoyable.

To my friends, Emilia Belia, Robert Adorno, Elizabeth Santacruz, Claudio Japas, and Kathy Ching. They are part of this incredible journey that Cesar and I started six years ago and we have developed deep friendships that will last in our hearts and memories forever.

Last but not the least, I would like to thank my family: my mother, my brother and sister, my silly niece, and my mother and father-in-law for supporting me emotionally and spiritually throughout writing this dissertation and my life in general.

CONTENT

FIGURES

Figures Page

TABLES

Tables Page

ABSTRACT OF THE DISSERTATION

Compositional diversity in arcs: a record of magmatic processes in the Peru Coastal Batholith, Ica

by

Ana Maria Martinez Ardila

Doctor of Philosophy, Graduate Program in Earth Sciences
Loma Linda University, September 2016
Dr. Benjamin L. Clausen, Chairperson

Peruvian granitic plutons display evidence for crustal recycling and magma mixing. Evidence of physical and chemical processes operating during the formation of the Ica-Pisco complexes involves magma mixing and mingling as result of felsic and mafic interactions. Evidence of crustal recycling was identified from kilometer-scale cauldron subsidence, meter and centimeter-scale -stoping, and disaggregation. At the petrographic microscope scale, evidence for recycling and mixing between mantle and crustal magma during crystallization is found from disequilibrium features such as reaction rims, resorbed cores, and patchy zoning. Elemental and isotope geochemistry data indicate that mantle magmas have incorporated continental crust material from varying depths and sources and in increasing amounts with time. Some uranium and lead isotope single-crystal zircon analyses also indicate varying source components. The research concluded that the source of the granitic magmas making up the plutons near Ica, Peru is about half from the mantle and half from recycled crust made up of Precambrian lower crust and Phanerozoic upper crust consisting of volcanic, sedimentary, and earlier plutonic units at the emplacement level.

CHAPTER ONE

INTRODUCTION

The Coastal Batholith of Peru (PCB) forms a chain of Mesozoic plutonic bodies which are in the western foothills of the Andes. It is one of the longest plutonic belts in the Andean Cordillera having a length of approximately 1300 km from one end of the country to the other. The plutonic bodies were episodically emplaced between 131 Ma and 60 Ma into andesitic to dacitic volcanic and sedimentary rocks of generally Jurassic to Cretaceous age and largely emplaced during alternating periods of extensional and contractional tectonic settings. The extensional margin period started at least as Early Jurassic (Atherton and Petford, 1996) and then it changed to a weakly contractional setting from Late Cretaceous to present (Pitcher et al., 1985; Soler and Bonhomme, 1990).

The first large scale research project on the PCB was developed by the University of Liverpool, the British Geological Survey, and the Geological Service of Peru. The cooperative research project started in 1965. The PCB was divided into along-strike segments from northwest to southeast: Piura, Trujillo, Lima, Arequipa, and Toquepala. The division into segments was complemented with field observations and geochemistry and this approach allowed the characterization and the recognition of super-units in the PCB based on their geochemical signature.

The compositional diversity observed in the PCB presents a unique opportunity to investigate and better understand the magmatic processes that contribute to the formation of crust in continental arc settings. For this reason, a new research project was begun in

2010 in the northern Arequipa segment of the PCB to study the magmatic processes yielding the compositional diversity observed in the plutonic bodies in the Ica-Pisco area of the PCB.

Geological Setting

This research focuses on the Ica-Pisco plutons in the northern part of the Arequipa segment, a 900 km long segment of the PCB that was extensively mapped in the Rio Ica area by Moore (1979) and in the Rio Pisco area by (Agar, 1978). In this research area the plutonic rocks intrude Cretaceous volcanic and sedimentary rocks of the Quilmana Group plus early gabbroic sequences considered precursors of the PCB. The Ica-Pisco plutons include four PCB granitoids with their associated gabbro and diorite cumulate bodies. The granitoids in younging chronological order are: Linga, Pampahuasi, Tiabaya, and Incahuasi. The Linga plutons consist of several intrusions of monzogabbro, monzodiorite, monzogranite, monzonite, and granite; the Pampahuasi plutons include gabbro, diorite, tonalite, and granodiorite; the Tiabaya plutons are made up of granodiorite and granite; and the Incahuasi plutons include granodiorite and monzodiorite.

An interesting feature in this area is what appear to be mafic cumulate bodies located at the margin of some plutonic units. The dominant composition of these cumulates are gabbro and diorite. All the gabbro and diorite plutons were considered to be pre-PCB by previous authors based only on contact relationships since no ages were known. Here, based on new ages from these mafic bodies, it is suggested that the gabbro and diorite plutons in the research area may be contemporaneous with the PCB as well as preceding them.

Previous ages reported for the Arequipa segment plutons are limited and published more than 30 years ago (Beckinsale et al., 1985; Moore, 1984; Mukasa, 1986b); thus an update was necessary for the purpose of this research.

Previous Work

During the geological survey developed in 1965 by British and Peruvian geologists, several papers were published that focused on the tectonic setting and structural complexity of the PCB and the recognition of the separate rock suites and their respective characterization for the five defined segments. Below is a brief summary organized in chronological order, of the most outstanding research work done in the Arequipa segment of the Peruvian Coastal Batholith with some referring specifically to the Ica-Pisco area.

Agar (1978) mapped the geology of the Rio Pisco area. His doctoral dissertation was mainly focused on comparing the intrusives from the Lima and Arequipa segments, and their different types of mineralization. He emphasizes that the rock compositions of the batholith in the Rio Pisco area are different from those north of Lima but their emplacement modes are essentially the same. The Linga super-unit was studied in the greatest detail due to the porphyry copper mineralization, but also because monzonitic rocks were unknown in the Lima segment. He discusses the origin of both magmas and mineralization and suggests a three stage model for the petrological evolution of the Coastal Batholith.

Moore (1984) presents a detailed geologic map of the Ica-Pisco section in southern Peru and K-Ar isochron ages for the early gabbros and the Linga, Incahuasi, and

Tiabaya super-units. Moore considered the Pampahuasi super-unit to be post-gabbros and pre-Linga based on field relationships. He concluded that the batholith in the Ica-Pisco region was emplaced over a total time span of up to 26.5 my, but confined to two relatively short episodes of 107-97 Ma and 82.5-80.5 Ma. Based on the correlation of K-Ar isochron ages and mineral fabrics he associated the emplacement with periods of regional compressive tectonism which may be linked to variable rates of subduction.

Pitcher, Atherton, Cobbing, & Beckinsale (1985) published a book *Magmatism at a Plate Edge: the Peruvian Andes*, summarizing the results of research done on the granitoid batholiths of Peru into a compilation of papers. Different topics related to the emplacement of granites include: emplacement of plutons, the composite nature of the batholiths, the volcanic and plutonic interface, application of the super-unit concept and the recognition of separate rock suites in terms of geochemical signature, the discovery of segmentation in Andean batholiths, and finally the description of the Andean type of plate margin with special reference to magma sources.

Mason (1985) did a complete petrographic study from samples collected in the Tumaray and Puscao plutons of the Lima segment. Mason determined that the mineralogy and textures of these plutons generally reflect magmatic crystallizing processes and a progressive crystallization history during residence within interconnected magma chambers at ascending levels in the crust.

Mukasa (1986) presents whole rock zircon U-Pb ages determined for the super-units of the Lima, Arequipa, and Toquepala segments. For the Arequipa segment ages were estimated for the Patap super-units, Tiabaya, Pampahuasi, Linga (Pisco-Ica), and Linga (Arequipa). Mukasa divided the Linga super-unit into two parts on the basis of

high-K plutons and age differences and he adopted the names "Linga (Pisco-Ica)" (101.4 Ma.) and "Linga (Arequipa)" (66.6-70.5 Ma.). Age results confirmed that the super-units had short time spans for emplacement.

Boily, Brooks, and Ludden (1989) present a study of the chemical and isotopic evolution of the southern PCB. The research was focused on the super-units of the Arequipa and Toquepala segments. Values of major and trace element analyses revealed that each super-unit was formed by distinct suites of I-type calc-alkaline plutons. Negative εNd_i and positive εSr_i values followed by a significant decrease in $^{206}Pb/^{204}Pb$ ratios led them to classify the intrusives into three groups. Group 1 consists of intrusives with positive εNd_i (+2.4 to +0.4) and generally negative εSr_i values (-7.4 to +0.7). Group 2 consists of plutons with intermediate values of εNd_i (+0.5 to -2.2) and εSr_i (+7.1 to +55.7). Group 3 is composed of intrusives showing negative εNd_i (-4.4 to -8.0) and positive εSr_i values (+27.1 to +56.1). They suggested that several petrological models can explain the trace element, isotopic, and geographic correlations observed within the Coastal Batholith of southern Peru. However, they suggested that the parental mafic magma(s) of the plutonic suites of each super-unit must be ultimately derived from an isotopically depleted mantle wedge above the subduction zone. The gabbro-diorite-granodiorite-monzogranite association is formed via crustal assimilation and fractional crystallization (i.e., AFC) during ascent in the Andean crust.

Atherton & Aguirre (1992) present the thermal and geotectonic setting of pre-batholith Cretaceous volcanic rocks near Ica in relation to Andean crustal thinning. The authors divided the Cretaceous volcanic rocks in the Ica region into those deposited in (1) the Cañete marginal basin (north of the Lima area) developed on the Precambrian

Arequipa Massif, and (2) the volcaniclastic rocks of the Huarmey Basin (north of the Ica area), which are mantle-derived material with trace-element abundances related to subduction and/or asthenospheric components. The Cañete basin volcanoclastic rocks show very low-grade, non-deformational prehnite-pumpellyite to zeolite facies metamorphism formed under moderate thermal gradients. In contrast, the rocks of the Huarmey Basin show a high thermal gradient related to more extensive crustal splitting and/or thinning. They considered the source of the Ica volcanic rocks as old enriched mantle beneath the Precambrian Arequipa Massif, in contrast to the mantle beneath the Huarmey basin which is considered much younger and less enriched. Finally, they suggested that crustal contributions to the volcanic rocks are not important, certainly not involving the upper crust of the Arequipa Massif.

Wise (2002) provides examples of syntectonic instead of passive pluton emplacement in the Coastal Batholith of Peru. Wise presents the problem with the super-unit classification system in the Coastal Batholith and the scarcity of radiometric data to establish the relationships among plutons. He proposes that the Coastal Batholith was formed by numerous processes instead of by a single mode of emplacement. In place of the super-unit system, he suggests four new plutonic suites in the Arequipa segment. He considered these suites to be syntectonic intrusions and due to right-lateral strike-slip motion along this arc segment.

Outline for this Research Project

The primary data used to accomplish the objectives of this research project are based on 100 days of fieldwork, petrographic study of 124 thin sections, elemental

geochemistry from 124 whole rock samples, whole rock isotope analysis from 46 samples, and geochronology results from 9 samples taken from plutons in the northern Arequipa segment of the PCB. Here these data are documented, presented, interpreted, and discussed to establish the types and magnitudes of magmatic processes playing a role in developing the compositional diversity of the granitic rocks in this arc segment.

This research is divided into five chapters and five Appendices. The major topics are presented in chapters 2-4. Chapter 2 discusses the physical and chemical evidence recorded in the granitic rocks of the Ica-Pisco area to identify magma sources, processes responsible for magmatic diversification, and the scales of magma chamber processes during incremental crustal growth. Chapter 3 focuses on quantifying the extent of magmatic recycling and contamination. Physical and chemical evidence is discussed to provide qualitative and quantitative estimates of recycling. Chapter 4 presents a paper for which I am a coauthor. It has been accepted for publication in the *American Mineralogist: Journal of Earth and Planetary Materials*. This paper integrates large datasets of geochronological, geochemical, and plate kinematic data to document the Paleozoic to Mesozoic development of the Cordilleran orogen in eight transects from British Columbia to Patagonia. My contribution to this paper in chapter 4 involved gathering and organizing the data from Peru and participating in discussions for interpreting the data in the regional context. Finally, chapter 5 summarizes the conclusions of this research and presents some ideas for future studies in the research area.

CHAPTER TWO

MAGMATIC DIFFERENTIATION PROCESSES IN CONTINENTAL ARC SETTINGS: AN EXAMPLE FROM THE PERUVIAN COASTAL BATHOLITH

Introduction

The Coastal Batholith of Peru (PCB) formed as a consequence of major Mesozoic magmatic events resulted in a wide variety of rock compositions. It is an especially favorable area to integrate field observations, petrography, geochemical, and isotopic data for understanding the magma chamber processes responsible for magmatic diversification. The most well-known published papers of the PCB were the result of a major research project developed in 1965 by the University of Liverpool, the British Geological Survey, and the Geological Service of Peru. The research project focused on the recognition of the separate rock suites in the PCB based on their geochemical signature. The PCB was divided into along-strike segments (Figure 1a) from northwest to southeast: Piura, Trujillo, Lima, Arequipa, and Toquepala with each segment divided into "super-units" (Cobbing and Pitcher, 1972). Since these early stages of research, the overall geologic setting of the PCB has been widely reviewed in papers by Cobbing and Pitcher (1972); Stewart et al. (1974); Myers (1975); Bussell et al. (1976); Agar (1978); Moore (1979); Sanchez-Fernandez (1982); Mukasa (1984); Beckinsale et al. (1985); Pitcher et al. (1985); Boily et al. (1989); Soler and Rotach-Toulhoat (1990); Atherton and Aguirre (1992); Davila (1993); and most recently by Haederle and Atherton (2002); Wise (2002); Mamani et al. (2010); and Coldwell et al. (2011).

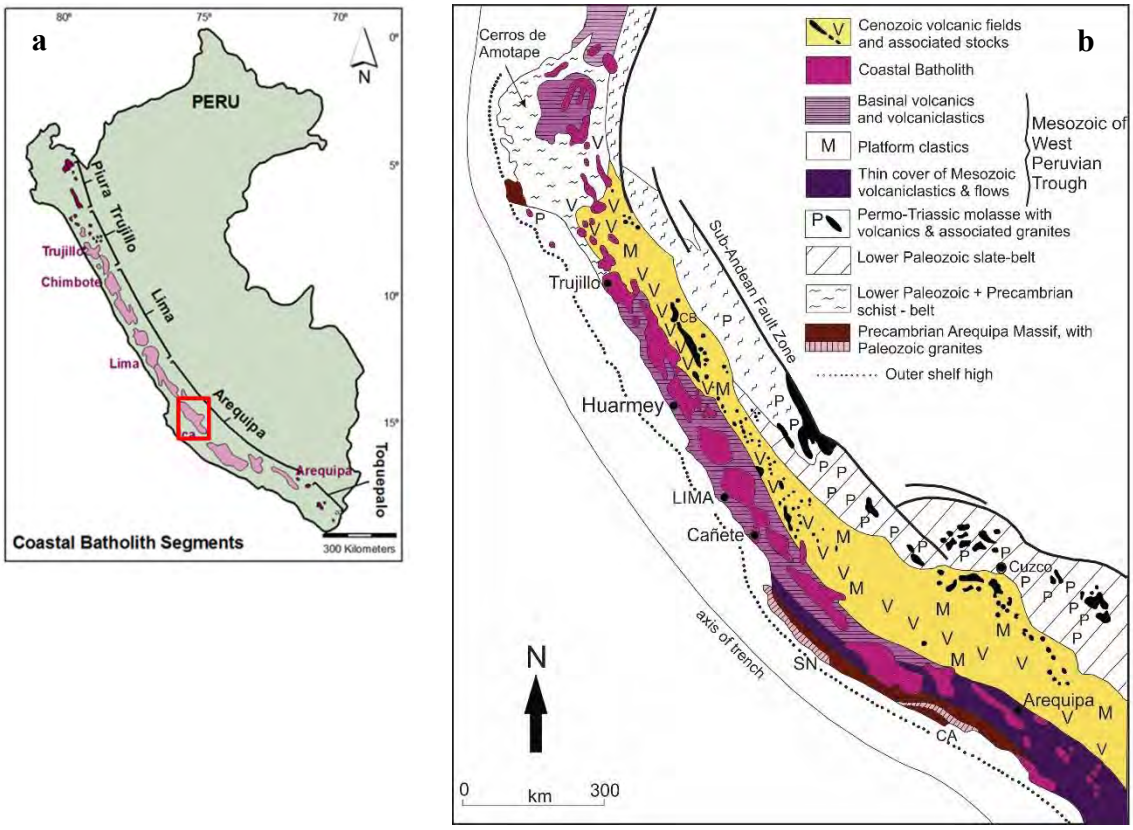

Figure 1. (a) The Coastal Batholith located in the western Cordillera of Peru includes five compositionally distinct segments. The research area is located in the northern part of the Arequipa segment of the PCB in SW Peru near the city of Ica. Modified from Cobbing et al. (1977). (b) Intrusives formed during the late Mesozoic suggest a continuous association between volcanic eruptions and plutonic intrusions. Modified from Pitcher et al. (1985).

Geologic Setting

The research area studied in this paper involves the Cretaceous plutons in the Arequipa segment of the Peruvian Coastal Batholith (PCB) located at the Rio Ica and Rio Pisco valleys. This area displays compositional diversity with a range from gabbroic to granitic rocks. These plutons preserve important evidence of magma chamber processes, particularly contamination, mixing, fractionation, and scales of various magmatic processes.

In this paper, documentation and interpretation of the preserved granitoid structures and textures, such as contact relationships, schlieren layering, cumulates, hybrid rocks, enclaves, xenoliths, mineral fabrics, and mingling-mixing microstructures are integrated with geochemical data. Our new geochemical data set comes from 124 whole rock major and trace element analyses and 40 Sr, Nd, and Pb isotopic analyses from the Cretaceous plutons, as well as Cretaceous volcaniclastic rocks and Precambrian basement. $\delta^{18}O$ analyses are also presented for six samples of the Cretaceous plutons and one from the Cretaceous volcaniclastic rocks. Interpretation of geochemical and isotopic trends is complemented with whole rock geochemistry mass balance calculations based on partial melting and fractional crystallization, and nine new U-Pb zircon ages. The data are presented to identify and discuss magma sources, processes responsible for magmatic diversification, and the scales of magma chamber processes during incremental crustal growth.

The PCB, located in the western Cordillera of Peru, forms a continuous linear belt of calc-alkaline intrusives that were assembled episodically between 103 and 37 Ma (Figure 1a), although largely during the Late Cretaceous (Pitcher et al., 1985). The PCB

formed by individual magma batches emplaced during the last part of the extensional tectonic setting and the beginning of a contractional tectonic setting. The extensional margin setting started at least as early as the Jurassic (Atherton and Petford, 1996) and changed to a weakly contractional setting from Late Cretaceous to present (Pitcher et al., 1985; Soler and Bonhomme, 1990). From 103 to 37 Ma an eastward progression of magmatism related to subduction shallowing has been proposed (Coira et al., 1982). The across arc eastward change in chemical and isotopic signatures of the PCB is related to an eastward increase in thickness of continental crust (Atherton and Petford, 1996).

Each segment of the PCB was divided across the arc into "super-units" based on geochemical affinities between plutons showing progressive evolution of both mineralogy and texture (Cobbing and Pitcher, 1972). The super-unit concept was described by Larsen (1948) and was widely used in the PCB (Agar, 1978; Atherton and Petford, 1996; Beckinsale et al., 1985; Boily et al., 1989; Haederle and Atherton, 2002; Mukasa, 1986b; Petford and Atherton, 1996; Pitcher et al., 1985). After 50 years, the super-unit concept is still being used to characterize the nature and origin of the granitic rocks in the PCB in the geological literature. Definitions of the terms used in previous research and also the preferred terms used in this research for referring to the plutonic rocks of the Ica-Pisco area are presented in Appendix A.

The Ica-Pisco Plutos in the Arequipa Segment

This research focuses on the Ica-Pisco plutons in the northern part of the Arequipa segment, a 900 km long segment of the PCB that was extensively mapped in the Rio Ica area by Moore (1979); (1984) an in the Rio Pisco area by Agar (1978); (1981). The Arequipa segment magmas have been minimally influenced by contamination with the Precambrian and Paleozoic basement in the northern part, but shows higher crustal contamination towards the south (Beckinsale et al., 1985; Boily et al., 1989). In the research area the plutonic rocks intrude Cretaceous volcanic and sedimentary rocks of the Quilmana Group plus early gabbroic sequences which were considered precursors of the PCB (Leon et al., 2007) (Figure 2).

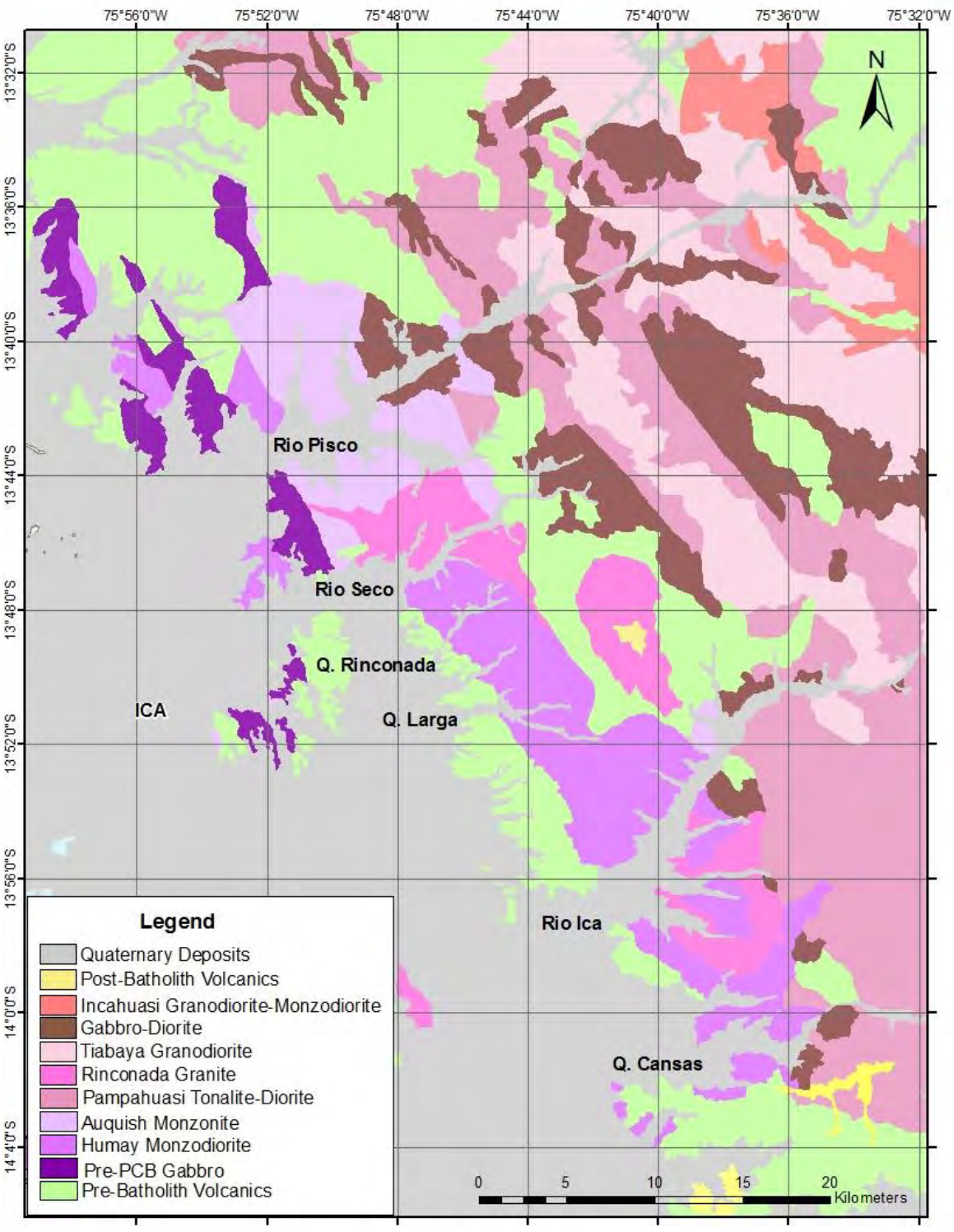

Figure 2. Simplified geologic map of the Arequipa segment near Ica showing the Ica-Pisco plutons in the northern Arequipa segment, pre- and post-batholith rocks, and the Rio Pisco and Rio Ica valleys where the main fieldwork transects are located. Modified from INGEMMET (2002).

The Ica-Pisco plutons in younging order are: the pre-PCB Gabbro, Linga, Pampahuasi, Tiabaya, Incahuasi, and associated gabbro and diorite bodies (Figure 2). The gabbro and diorite plutons without reported ages were all considered pre-PCB by previous authors on the basis of contact relationships. Here, it is suggested that some of the gabbro and diorite plutons in the research area precede, but may also be contemporaneous with the PCB. The map view shape of the plutons is tabular or rectangular to elliptical, trending NW-SE (Figure 2). The research area in this northern part of the Arequipa segment is approximately 60 km long by 40 km wide.

Previous ages reported for the Arequipa segment plutons are few and published more than 30 years ago. The Ica-Pisco pluton ages will be discussed in detail in the geochronology section. The main intrusive rocks of the batholith are listed in Table 1 in order of previous published ages.

Table 1. Units and ages of the Peruvian Coastal Batholith, Arequipa segment near the city of Ica. Previously published ages: K-Ar isochron ages determined by Moore (1984), Rb-Sr isochron ages determined by Beckinsale et al. (1985), and U-Pb ages determined by Mukasa (1986b).

UNIT	MAIN ROCK TYPES	PREVIOUS AGES (Ma)		
		K-Ar	**Rb-Sr**	**U-Pb**
Incahuasi	granodiorite	80-85	78±1	
Tiabaya	granodiorite-tonalite	77-85	81±9	78
Rinconada	granite-monzonite	94-97		
Pampahuasi	diorite-tonalite	82-96	82-93	94
Linga – Auquish	monzonite-granite	96-97	96±3	101
Linga – Humay	monzogabbro-monzodiorite		140±9	
Pre-PCB Gabbro	gabbro	<107		

Linga Intrusive Complex (LIC)

The LIC occurs along the western flank of the Arequipa segment. Near Ica, it is divided into three units: Humay, Auquish, and Rinconada (Figure 2). Humay is mostly represented by monzogabbro, monzodiorite, and small local bodies of syenite; Auquish is characterized by monzonite, monzogranite, and local bodies of syenite; and Rinconada, the youngest unit of this intrusive complex, is mostly represented by granite and less abundant monzogranite compositions. The emplacement mechanisms previously interpreted for the LIC involve cauldron collapse, formation of ring complexes, and stoping processes (Agar, 1978; Moore, 1979). The LIC has contacts with the sedimentary and volcanic envelope rocks of the Quilmana Group, and with tonalite plutons and gabbro-diorite bodies associated with the Pampahausi unit.

Pampahuasi Unit

The Pampahuasi NW-SE elongate unit is located in the central part of this segment and is the most extensive in the study area (Figure 2). The Pampahuasi unit from margins to the center includes: diorite, tonalite, and local granodiorite compositions. The Pampahuasi unit was considered to be part of the Incahuasi units by Agar (1978), but was separated out as an earlier intrusion (Moore, 1979), and eventually considered to be post-Linga (Mukasa, 1986b). The Pampahuasi unit is in contact with volcanic envelope rocks, the Auquish monzonite, the Rinconada granite, and the Tiabaya unit. It was suggested that the Pampahausi unit was dissected in its central part by a younger tonalite pluton associated with the Tiabaya plutons (Davila, 1993).

Tiabaya Plutons

The Tiabaya plutons occupy a central position in the northern part of the Arequipa segment and have a NW-SE elongated shape (Figure 2). Three major lithologic units were previously identified by Agar (1978): granodiorite, tonalite, and adamellite (quartz monzonite). However, these units have been typically mapped as a single unit called Tiabaya because internal contacts are not easily observed (Leon et al., 2007). Tiabaya granodiorite was the main lithology identified during fieldwork and it has contact relationships with pre-PCB volcanic rocks, and the Pampahuasi and Incahuasi plutons.

Incahuasi Plutons

The Incahuasi granodiorite is the youngest member of the Arequipa segment and the data supporting this are presented in the geochronology section and Appendix E. The Incahuasi unit is exposed along the eastern part of the research area (Figure 2). These plutons are dominated by granodiorite with minor amounts of tonalite and granite. Based on mineralogy, Agar (1978) described two units: Magocancha granodiorite and Huaytara granodiorite. The Magocancha granodiorite is described as fine grained, with less of K-feldspar than the Huaytara granodiorite. The Huaytara granodiorite is the more leucocratic member and rich in K-feldspar. The Incahuasi plutons are in contact with Jurassic volcanoclastic envelope rocks, as well as the Pampahuasi and Tiabaya plutons.

Field Observations

Field surveys of the plutonic rocks in the Ica-Pisco area were carried out to describe and classify the PCB units, and to collect samples for petrographic and geochemical analyses. The simplified geologic map in Figure 3 shows the field stops where data were collected. This section presents a documentation of the preserved granitoid structures and textures, such as schlieren layering, enclaves, xenoliths, mineral fabrics, and mingling-mixing microstructures. Information from field stops of contacts outside of the research area are included to provide a general geological framework.

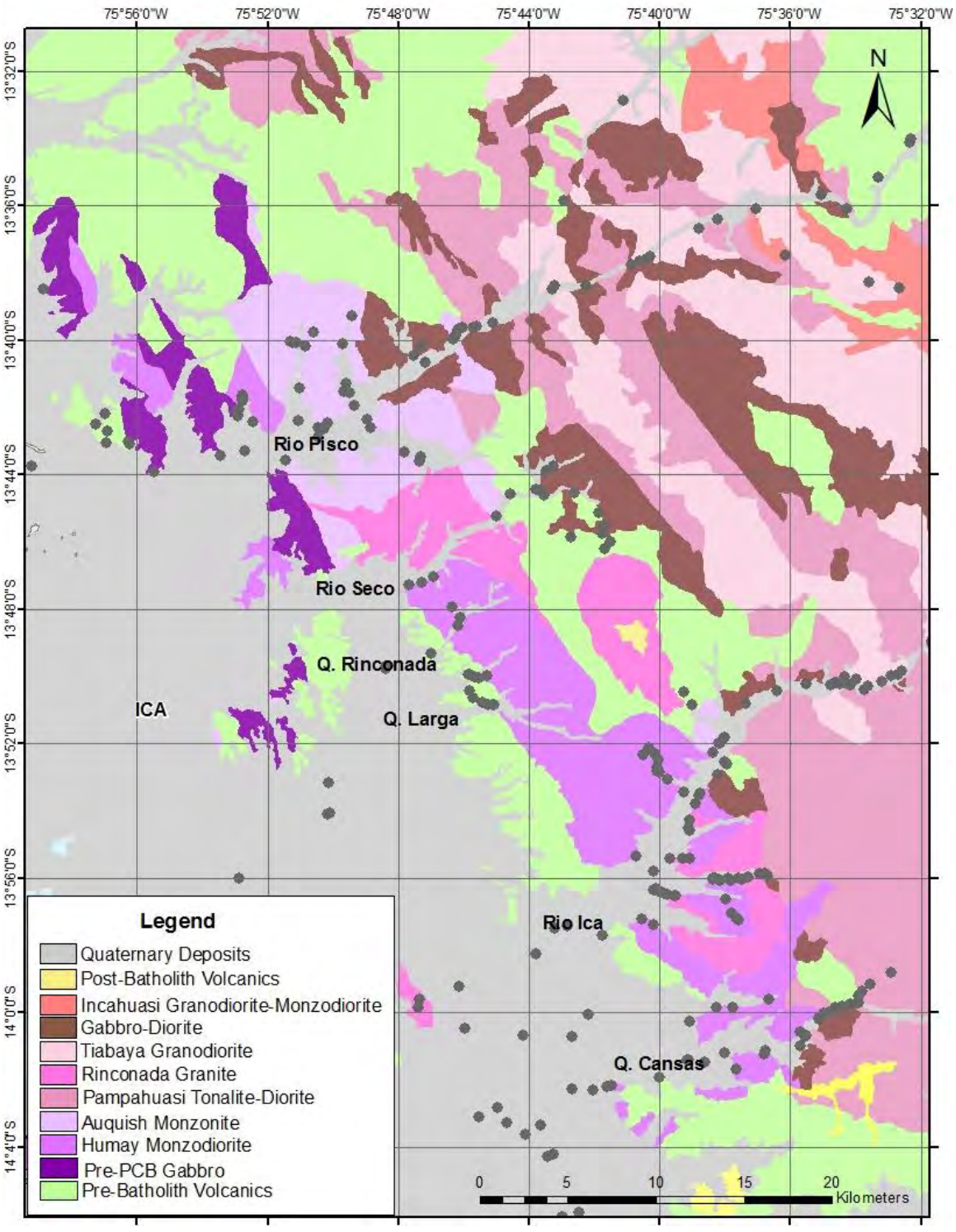

Figure 3. Simplified geologic map of the Ica-Pisco plutons in the Arequipa segment, showing the field stops. Map modified from Davila (1993). Location for each stop is presented in Appendix A.

Magmatic Structures

Field observations led to the identification of magma flow, crystal accumulation, mingling, mixing, and recycling structures that indicate the physical interactions taking place in the Ica-Pisco plutons. This section summarizes the magmatic structures identified in the Ica-Pisco plutons.

Schlieren Layers

Schlieren are local layered zones from decimeter to meter scale, typically observed in gradational contact zones, and generally associated with other magmatic structures such as xenoliths, enclaves, and mineral clusters. The internal contacts between the Humay monzodiorite and Auquish monzonite units are characterized by relatively straight local schlieren layering, and the presence of abundant mafic enclaves and xenoliths. Individual schlieren layers are from 1 cm to 10 cm wide and characterized by cumulates of mafic biotite and hornblende and felsic feldspar and quartz. The gradational contact zone between the Auquish monzonite and the Pampahuasi tonalite-diorite is characterized by a zone of stretched and partially disaggregated enclaves grading to schlieren as illustrated in Figure 4.

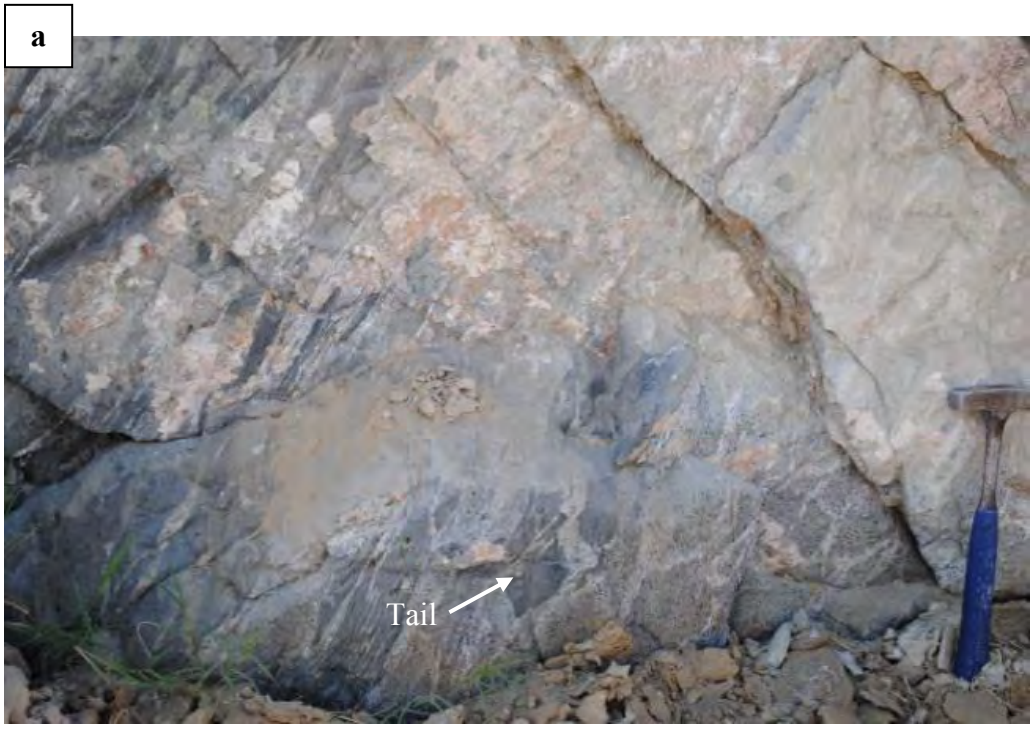

Figure 4. Gradational internal contact zone between hybrid rocks of Pampahuasi tonalite-diorite and Auquish monzonite stop 13828F. For the schlieren structures: note in particular the mafic magmatic enclaves with tails.

Xenoliths and Mafic Enclaves

Xenoliths and enclaves are commonly observed throughout the Ica-Pisco plutons. Xenoliths show a variety of morphologies and compositions. Smaller xenoliths, from centimeter to decimeter scale, generally occur in clusters throughout the pluton, do not fit together, and have rounded and subrounded shapes and digested edges. On the other hand, large meter scale xenoliths with angular to subrounded margins occur along the pluton margins close to roof and wall zones (Figure 5*Figure 5*).

Mafic enclaves are commonly observed close to the gradational contact zones and are associated with mafic dikes and local schlieren zones. Mafic enclaves are characterized by elliptical shapes in 2D, cuspate and sharp margins with the host rocks, homogeneous textures, mafic gabbro and diorite compositions, and a range of sizes from millimeter to centimeter scale. They range from ellipsoidal to highly elongate bodies in zones where magmatic foliation is developed (Figure 6). Enclave swarms were observed in areas of gradational contacts and next to mafic dikes and schlieren zones.

In the Rio Pisco transect, the gradational contact zone between the Humay monzodiorite and Auquish monzonite exhibit swarms of mafic magmatic enclaves (MME) with gabbroic and dioritic compositions, rounded shapes, and cuspate margins (Figure 7). In the same Rio Pisco transect in the central zone of the batholith, mafic undisturbed dikes and composite dikes associated with MME were identified in the Pampahuasi tonalite unit (Figure 8).

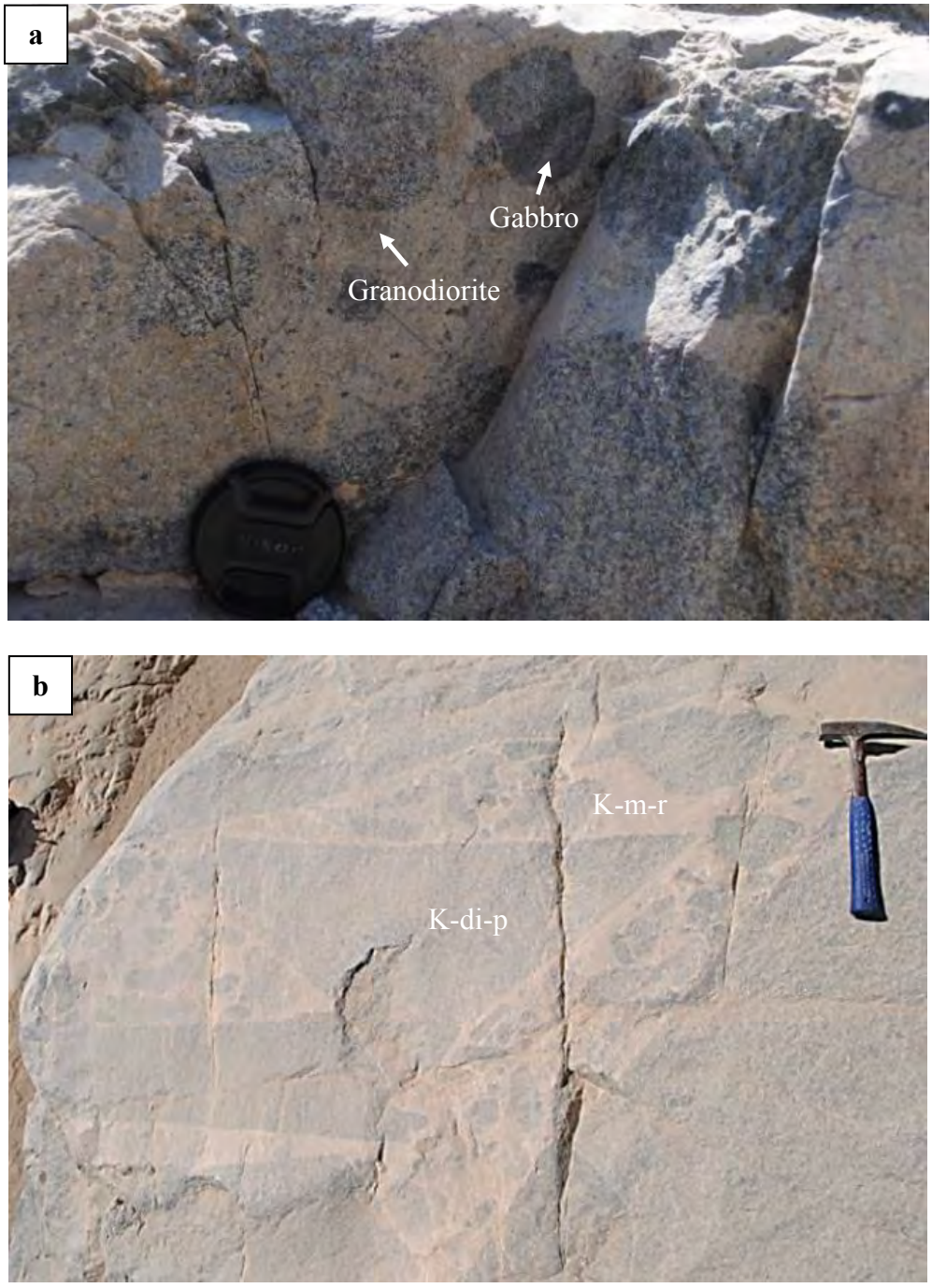

Figure 5. Stop 13902M. Internal discordant contact zone where the Pampahuasi unit (K-di-p) is intruded by Rinconada granitic dikes (K-m-r). (a) Populations of xenoliths, especially noting differences in texture and composition. (b) Granitic magma engulfing subrounded to angular xenoliths. Note that some of the angular xenoliths of Pampahuasi tonalite-diorite seem to be rotated.

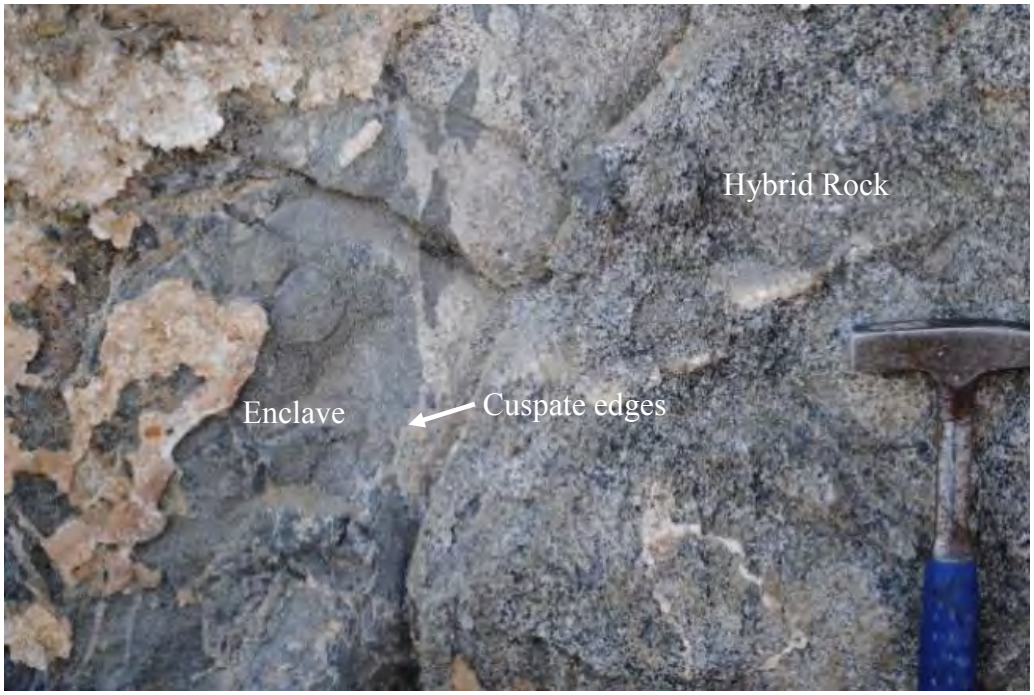

Figure 6. Stop 13828F. Gradational internal contact zone between hybrid rocks of Pampahuasi tonalite-diorite and Auquish monzonite. Note enclaves with cuspate edges. Pampahuasi rocks are the light grey colors and dark areas represent the enclaves.

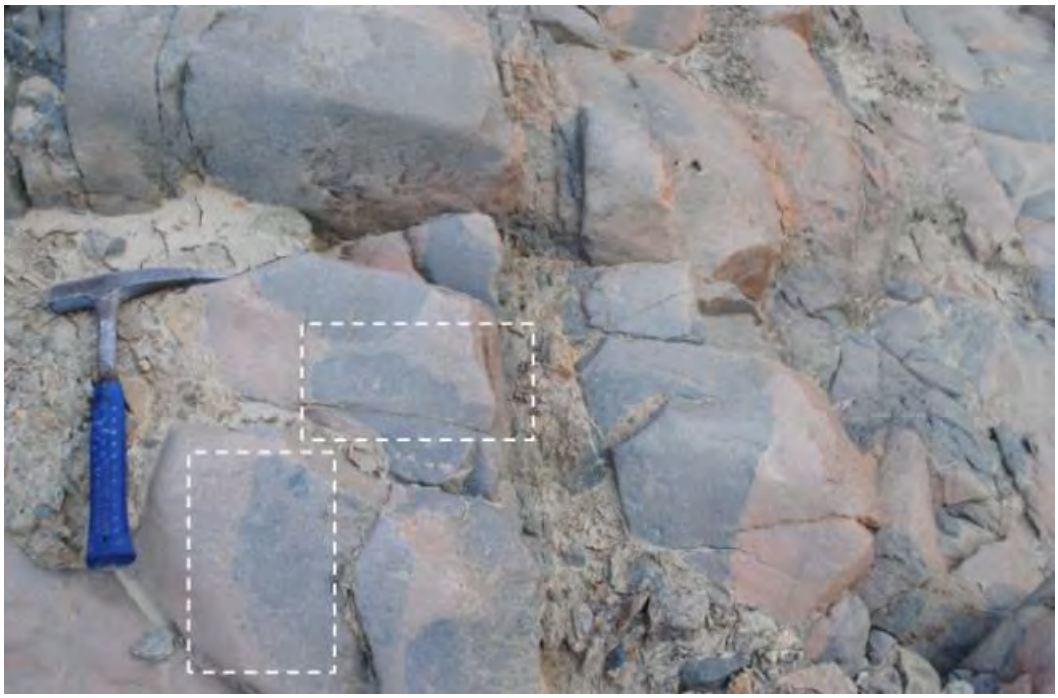

Figure 7. Stop 13820I. Auquish monzonite outcrop with MMEs showing cuspate edges due to compaction. Rectangles used to indicate where the cuspate edges are observed.

Figure 8. Pampahuasi tonalite outcrop with a swarm of MME and a mafic dike with mineral clusters. Enclaves and mafic dike show diffuse margins.

Magmatic Fabrics

Development of magmatic fabrics in the Ica-Pisco plutons varies from the western zone (WZ), where the Linga and Pampahuasi plutons display little magmatic fabric, to the central (CZ) and eastern zones (EZ), where the Tiabaya and Incahuasi plutons respectively display a moderate development of fabrics.

In some outcrops of the Pampahuasi tonalite, magmatic fabrics were associated with schlieren layers, enclaves, and around xenoliths. Magmatic mineral fabrics associated with schlieren layers were parallel to the laterally continuous contacts between mafic and felsic layers. Figure 9 shows magmatic fabrics around a xenolith of tonalite-diorite of the Pampahuasi unit, located along the contact zone between the Pampahausi and Tiabaya plutons. Magmatic fabrics are also defined by the orientation of enclaves observed in several outcrops of the Pampahausi unit and eastern plutons of Tiabaya unit (Figure 9 and 10).

Figure 9. Stop 12717D. Pampahuasi xenolith in Tiabaya granodiorite host rock. Note fabrics and chilled margins and smaller crystal size around the xenolith.

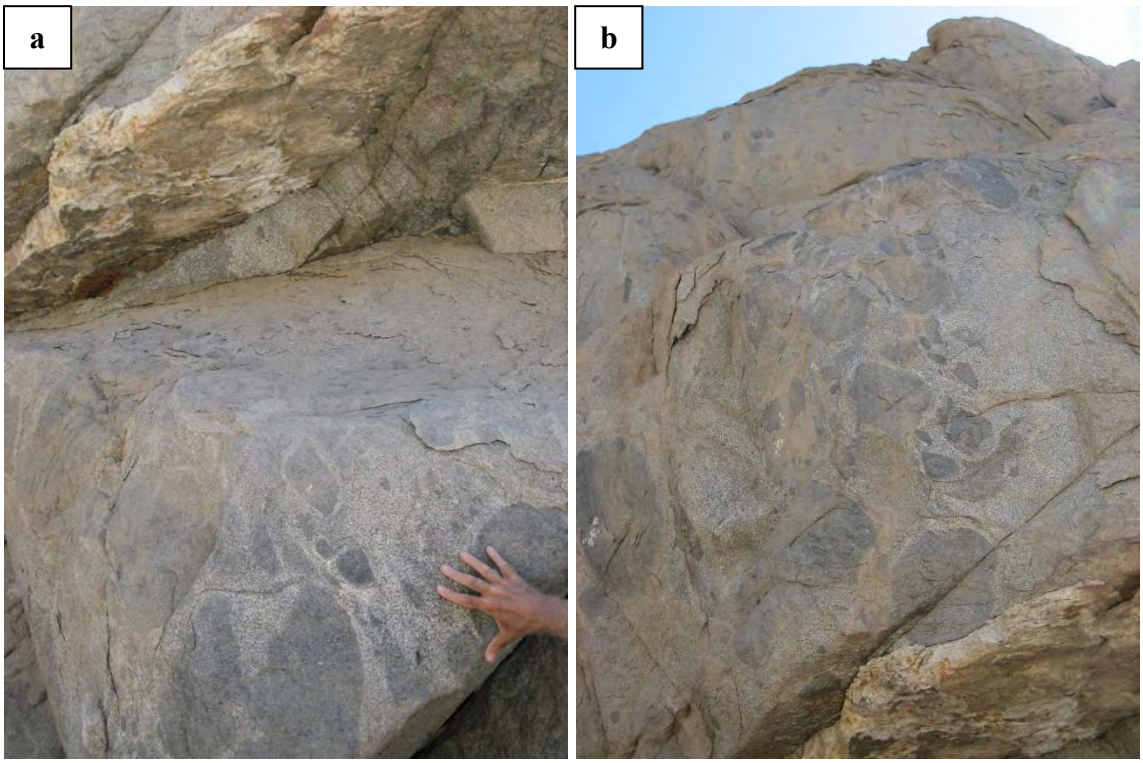

Figure 10. Stop 11828B. Magmatic fabric defined by oriented mafic enclaves in an outcrop of Tiabaya granodiorite (a) at the bottom of the outcrop and (b) at the top of the outcrop.

Mafic Dikes and Mineral Accumulations

Two types of mafic dikes formed in this area. The first type has sharp and well defined edges (Figure 11) and the second type has diffuse edges and ductile deformation (Figure 8). Dikes with sharp and well-defined edges were intruded when the pluton was completely solidified, and dikes with diffuse edges which often meander through the host rock probably intruded when the host magma retained enough interstitial melt to allow ductile deformation (Turnbull, 2009; Wiebe, 1993). The second type of dike is less frequently observed and is associated with mineral clusters of plagioclase megacrystals. Based on contact relationships it was injected contemporaneously with pluton crystallization.

Figure 11. Stop 13827F. Mafic dike with plastic deformation injected in monzonite of Auquish. Trafic signal is 2 meters.

Petrography Data

Petrographic analyses were done on 124 thin sections from samples collected in the Ica-Pisco plutons, as well as samples of the volcanic envelope rocks, gabbro-diorite bodies, some mafic enclaves, and hybrid rocks. The petrography was used to classify the rocks in terms of composition and texture and to look for features indicative of magma chamber processes. Modal analyses were performed using point counting method with 300 space points taken over each thin section. A full list of thin sections, their respective locations, modal abundances, and microstructures can be found in Appendix B.

Pre-PCB Gabbro

The gabbro bodies mapped as pre-PCB Gabbro plutons correspond to gabbro-diorite plutons which are exposed in the margins of the the Pampahuasi unit and in contact with the LIC and the Tiabaya unit. Gabbro-diorite rocks are composed of plagioclase, pyroxene, hornblende, and biotite. The most common gabbros are augite and hornblende gabbro. Mineralogy is 50-70% plagioclase, 2-26% hornblende, 2-29% pyroxene, and 0-6% biotite. The opaque minerals magnetite/ilmenite and pyrite make up less than approximately 4%. Plagioclase crystals are subhedral and tabular, and coarser than the hornblende, pyroxene, and biotite crystals (Figure 12). Some of the gabbros collected in the research area might represent gabbroic cumulates and these seem to be related to the first stages of fractionational crystallization in the associated granitic units. In this study evidence from fieldwork and petrography supports the cumulate interpretation for the gabbro-diorite bodies but the most relevant evidence comes from chemical data and it will be presented in the geochemistry section.

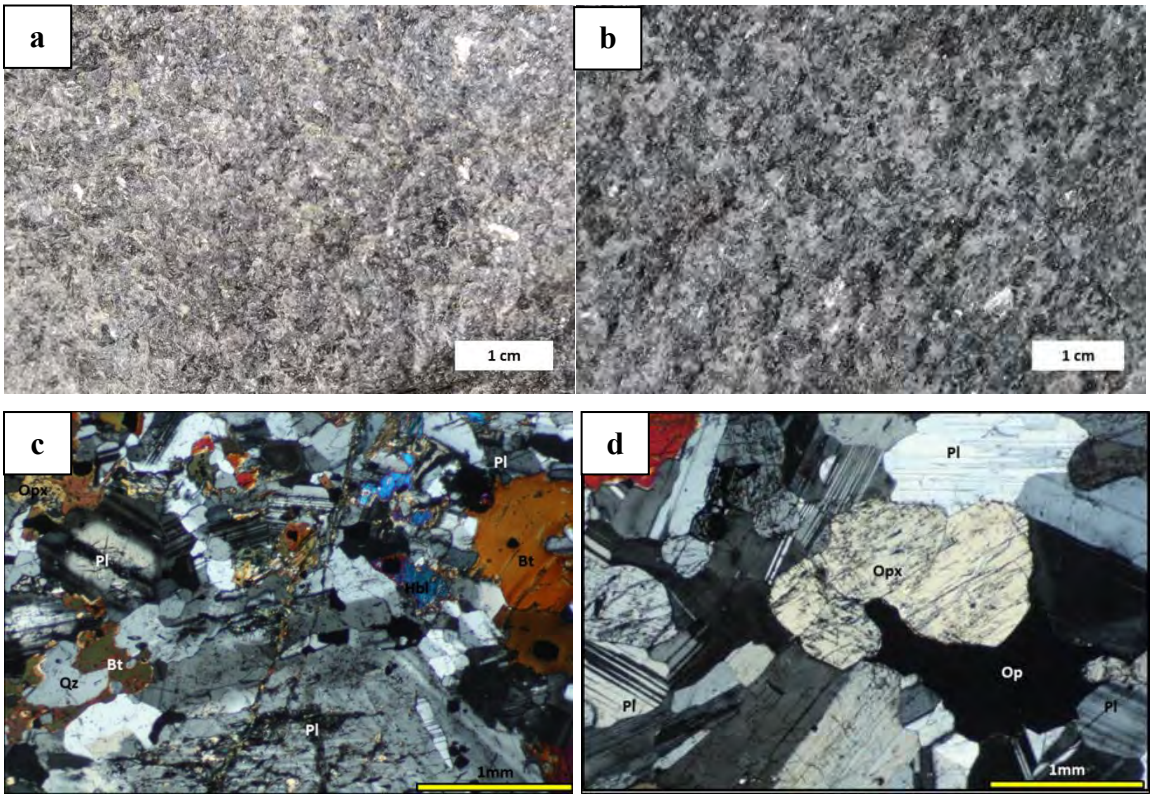

Figure 12. Typical appearance of the gabbro-diorite rocks. Hand samples: (a) medium crystal-size gabbro sample 11829C and (b) medium to coarse crystal-size gabbro sample 12722K. Microphotographs of gabbro samples in cross-polarized light: (c) gabbro sample 11825B with medium crystal size and (d) sample 11829D of gabbro with inequigranular texture and coarse to medium crystal size. Qz-quartz; Pl-plagioclase; Bt-biotite; Opx-orthopyroxene; Op-opaque.

Linga Intrusive Complex (LIC)

The LIC is divided into three major units: Humay monzogabbro, Humay monzodiorite, Auquish monzogranite-monzonite, and Rinconada granite.

Humay Monzogabbro-Monzodiorite

Humay monzogabbro plutons are located in the northwestern part of the research area and include areas of hybrid rocks. The monzogabbro is made of: 40-62% plagioclase, 4-22% pyroxene, 2-14% K-feldspar, 2-17% hornblende, 5-7%biotite, and 3-14% quartz. The monzodiorite is the largest pluton of the LIC and includes some local compositional variations from granodiorite to syenite. The mineralogy of the monzodiorite is made up of: 38-65% plagioclase, 1-20% K-feldspar, 3-23% quartz, 1-8% pyroxene, 4-15% hornblende, and 1-15% biotite. Accessory minerals of the Humay units include: titanite, apatite, zircon, and opaque minerals (magnetite-ilmenite). Equigranular and inequigranular textures were identified, and medium to coarse crystal sizes are dominant (Figure 13a-d).

Auquish Monzogranite-Monzonite

The Auquish unit located in the north part of the research area is characterized mainly by monzonites and granites (Figure 14a-b). The unit also includes a few granodiorites and monzodiorites which are possibly the result of the interaction in contact zones between Humay and Auquish that increased the mafic content in the monzonites and granites, resulting in monzodiorites and granodiorites in a mingling-mixing contact zone. The minerals in the monzogranites are: 30-40% K-feldspar, 6-20% plagioclase, 5-

25% quartz, 5-10% hornblende, and <1-5% biotite. The quartz-monzonites are made of: 30-60% K-feldspar, 15-30% plagioclase, 5-18% quartz, 5-10% hornblende, and <1-5% biotite. Accessory minerals in the range of compositions from monzonite to monzogranite include titanite, apatite, zircon, and opaque minerals (magnetite-ilmenite). Secondary minerals resulting from hydrothermal alteration are abundant in Linga Humay and Linga Auquish, and include epidote, K-feldspar, sericite, calcite, biotite and chlorite.

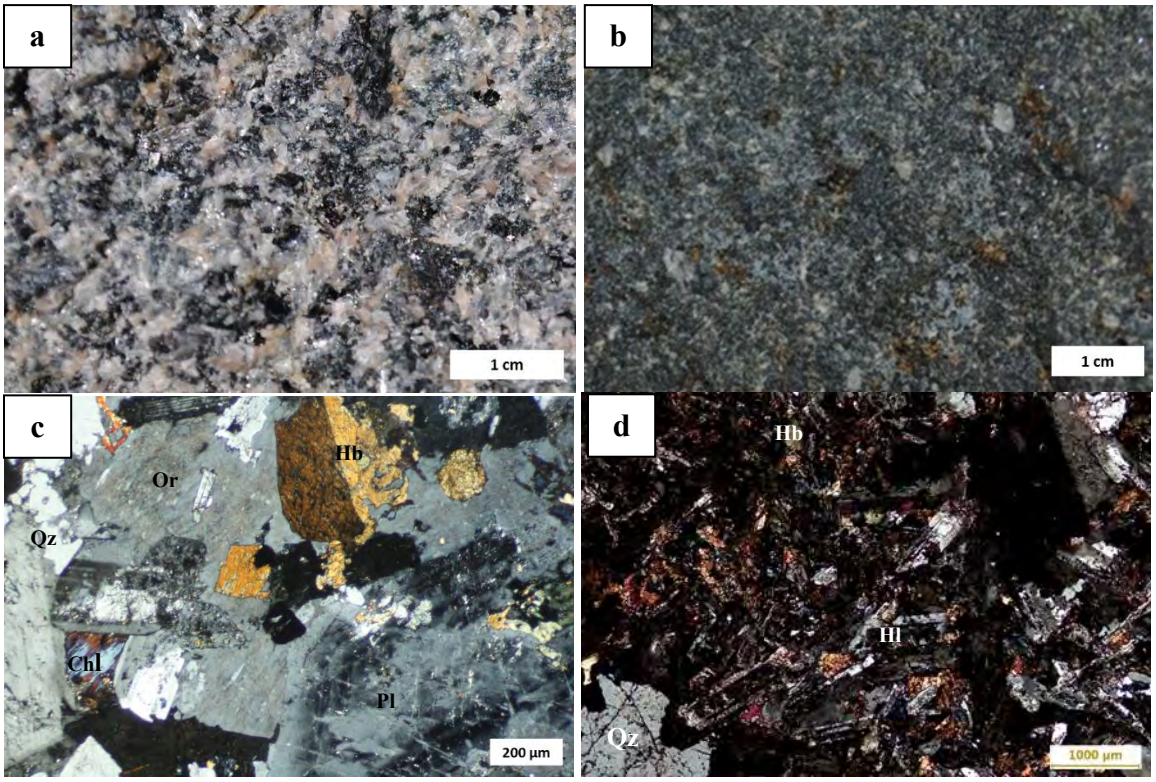

Figure 13. Typical appearance of the Linga Humay rock samples. Hand sample pictures: (a) monzodiorite sample 10714H and (b) monzogabbro sample 13820M. Microphotographs in cross-polarized light, showing inequigranular textures and medium to coarse crystal size: (c) monzodiorite sample 10721M and (d) monzogabbro sample 13820M. Qz-quartz; Pl-plagioclase; Or-orthoclase; Hb-hornblende; Chl-chlorite.

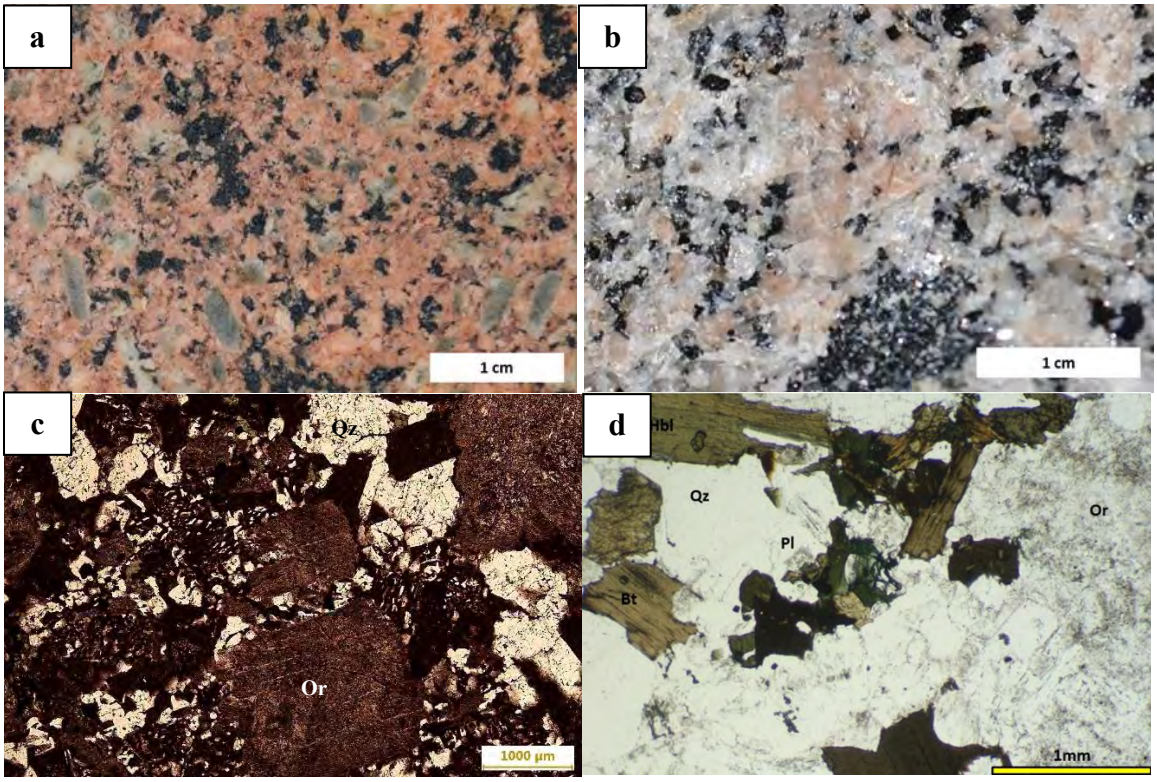

Figure 14. Typical appearance of the Linga Auquish rock samples. Hand samples: (a) syenite-monzonite 13821H and (b) monzogranite sample 10714J. Microphotographs: (c) sample 13821H Auquish monzonite with intense alteration and (d) sample 10714J monzogranite of Auquish. Qz-quartz; Pl-plagioclase; Or-orthoclase; Hb-hornblende; Chl-chlorite.

Rinconada Granite

The Rinconada unit, located at the central and southwestern part of the research area, consists primarily of granites and granodiorites. The dominant minerals are: 19-40% quartz, 10-30% K-feldspar, 10-25% plagioclase, 2-10% hornblende, and 4-11% biotite. Accessory minerals include titanite, apatite, zircon, and opaque minerals (magnetite-ilmenite). Secondary minerals resulting from hydrothermal alteration include epidote and chlorite. Textures are equigranular medium to coarse crystal size (Figure 15). Granophyric and perthitic textures are common in the K-feldspar crystals (Figure 15d).

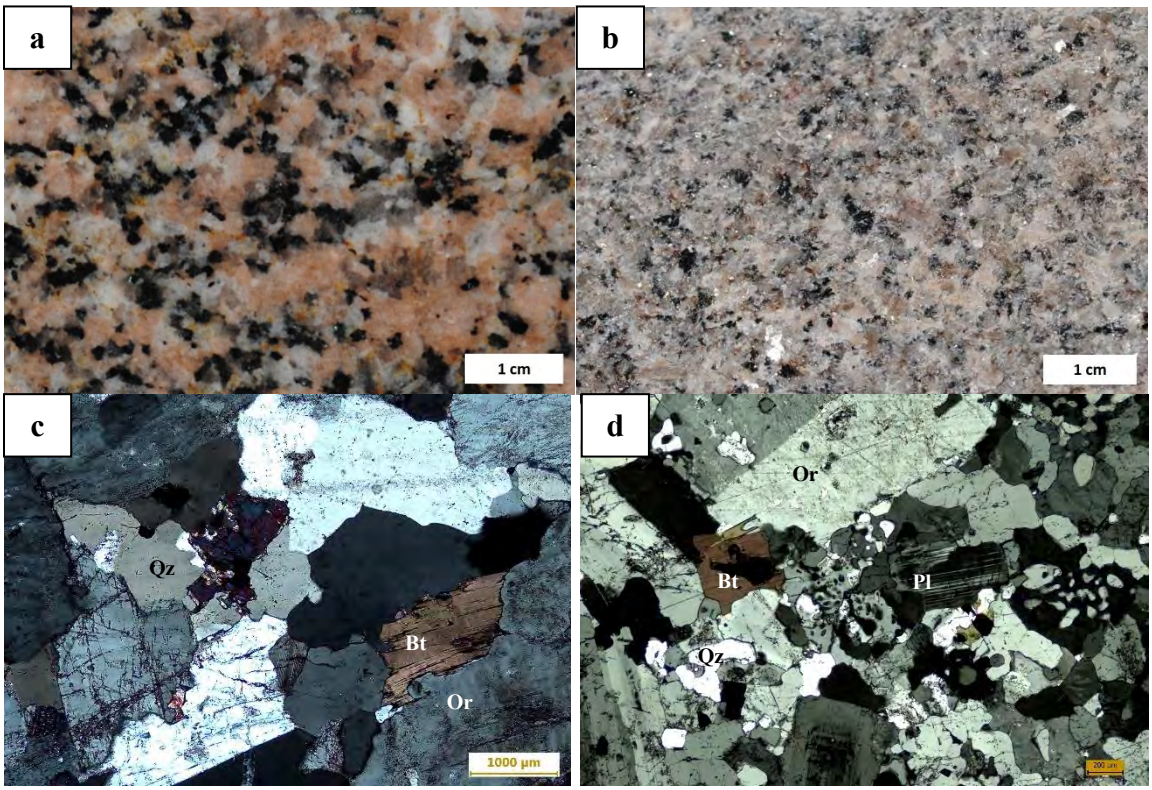

Figure 15. Typical appearance of the Linga Rinconada rock samples. Hand samples: (a) sample 13930D granite with coarse crystal size and (b) sample 12715C granite. Microphotographs in cross-polarized light: (c) sample 13830D granite, scale bar=1000 µm, and (d) sample 12715C granite with granophyric texture. Qz-quartz; Pl-plagioclase; Or-orthoclase; Bt-biotite. Scale bar=200 µm.

Pampahuasi Unit

The Pampahuasi unit, located in the central part of the research area unit, consists of diorite and tonalite plutons forming a zoned tabular body. Field observations revealed that the Pampahuasi plutons show a compositional zoning with a more mafic margins to a more felsic center. The margins contain localized gabbro-diorite bodies that may correspond to mafic cumulates and data supporting this new idea will be presented in the chemical section. In the past, these gabbro and diorite plutons were all assumed to be pre-PCB, but the field and petrographic relationships with the Pampahuasi unit might support the interpretation that these mafic plutons are part of the Pampahuasi unit.

In the previous literature, the Pampahuasi plutons were classified as mostly diorites and minor tonalites (Beckinsale et al., 1985; Leon et al., 2007; Moore, 1984; Mukasa, 1986b); however, based on the petrographic analysis from this research, the Pampahuasi plutons are zoned from the margin to the center, from gabbro-diorites to quartz-diorites to tonalites (Figure 2 and 16). The dominant minerals in the quartz-diorites are 40-60% plagioclase, 10-20% quartz, 8-13% hornblende, 5-10% biotite, 3-5% K-feldspar, and <1-4% pyroxene. The tonalites are made of: 35-50% plagioclase, 20-30% quartz, 7-12% hornblende, 5-10% biotite, <1-2% pyroxene, and 4-8% K-feldspar. The mineralogy of the granodiorites consists of: 30-55% plagioclase, 5-11% hornblende, 2-25% quartz, 1-10% biotite, and 1-9% K-feldspar. Accessory minerals include titanite, apatite, zircon, and opaque minerals (magnetite-ilmenite, pyrite, and chalcopyrite).

Local compositional variations from quartz-diorites and tonalites to granodiorites are observed close to the contact zone with the Linga Auquish plutons; the northwest margin of the Pampahuasi unit is possibly the result of mingling-mixing interactions that

could increase the K-spar content in the tonalite-diorites resulting in local granodioritic compositions. The compositional and textural features of the gabbro-diorite rocks referred as possible cumulates in the marginal zones of the Pampahuasi plutons were described in the pre-PCB Gabbro section.

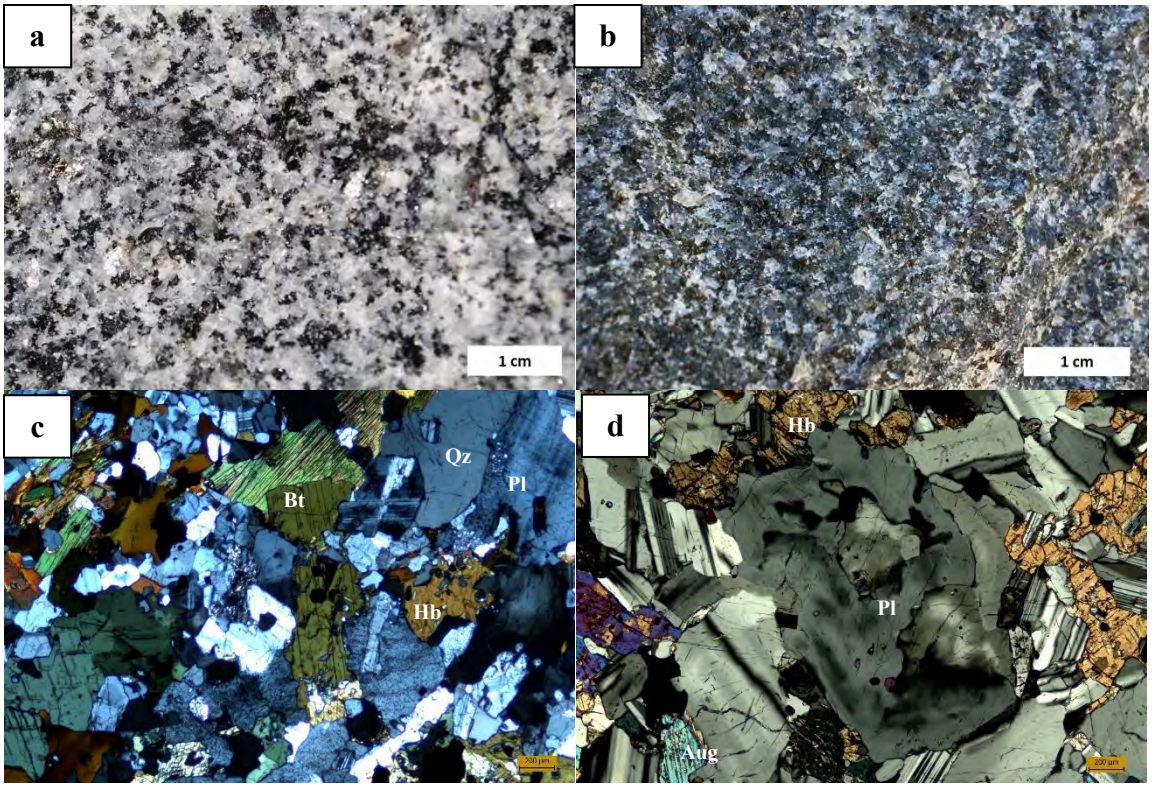

Figure 16. Typical appearance of the Pampahuasi rocks. Hand samples: (a) tonalite sample 12722E and (b) diorite sample 12717C. Microphotographs in cross-polarized light, scale bar=200 μm. (c) 12722E tonalite and (d) 12717C diorite with equigranular textures and medium to coarse crystal size. The hornblende proportion is higher than biotite. Qz-quartz; Pl-plagioclase; Bt-biotite; Hb-hornblende; Aug-augite.

Tiabaya Unit

The Tiabaya unit is characterized by large K-feldspar crystals and the euhedral habit of mafic minerals (Figure 17a). The dominant lithology is granodiorite, but tonalite and local granite lithologies are also present. The mineralogy of the granodiorites consists of: 35-50% plagioclase, 15-30% quartz, 5-12% hornblende, 4-10% biotite, and 3-10% K-feldspar. Accessory minerals include titanite, apatite, zircon, and opaque minerals (magnetite-ilmenite, chalcopyrite, and pyrite). Secondary minerals resulting from hydrothermal alteration are not commonly observed but include: epidote, calcite, and chlorite. Equigranular, inequigranular, and porphyritic textures were identified in thin sections (Figure 17b).

Incahuasi Unit

The Incahuasi plutons are dominated by granodiorites (Figure 18), but granites and monzodiorites are also present. The mineralogy of the granodiorites consists of: 35-45% plagioclase, 20-28% quartz, 15-20% K-feldspar, 4-12% biotite, 4-10% hornblende, and 1-2% pyroxene. Monzodiorites are made of: 35-50% plagioclase, 10-15% K-feldspar, 8-12% quartz, 4-10% biotite, 4-10% hornblende, and 1-2% pyroxene. Accessory minerals include titanite, apatite, zircon, and opaque minerals (magnetite-ilmenite and pyrite). Secondary minerals resulting from hydrothermal alteration include hornblende, epidote, and chlorite.

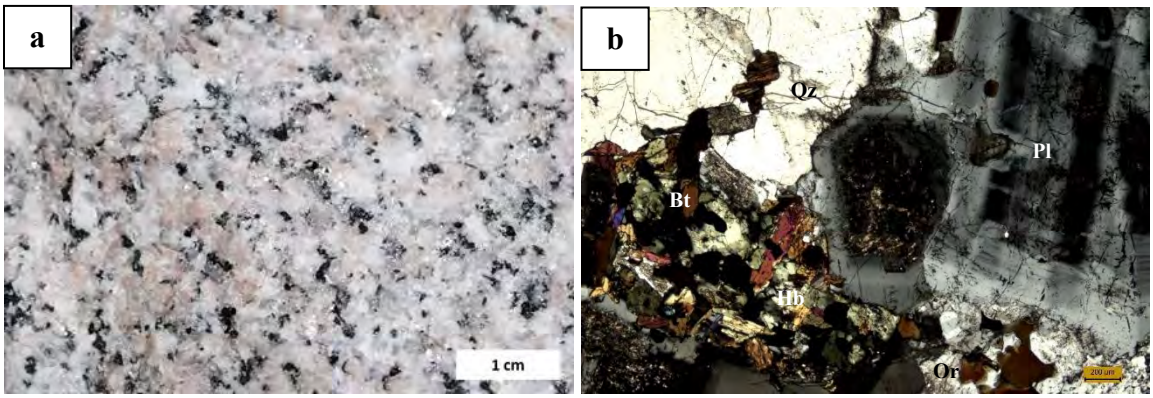

Figure 17. Typical appearance of the Tiabaya rocks. Sample 12719I (a) granodiorite hand sample and (b) microphotograph in cross-polarized light showing inequigranular texture and coarse to medium crystal size. Qz-quartz; Pl-plagioclase; Or-orthoclase; Bt-biotite, and Hb-hornblende. Scale is 200 µm in (b).

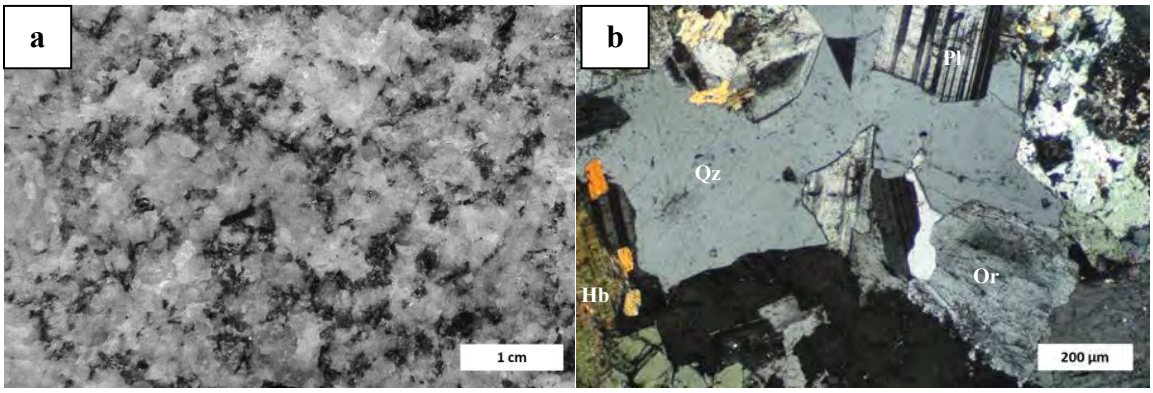

Figure 18. Typical appearance of the Incahuasi rocks. Sample 11831EE granodiorite (a) hand sample and (b) microphotograph in cross-polarized light showing inequigranular texture and coarse to medium crystal size. Scale bar=200 µm. Qz-quartz, Pl-plagioclase, Or-orthoclase, and Hb-hornblende.

Rock Types and Modal Classifications of the Ica-Pisco Plutons

A wide variety of rocks are observed in the Ica-Pisco plutons. The Linga plutons are grouped as an intrusive complex. The other plutons are: Pampahuasi, Tiabaya, and Incahuasi. The compositions of the Ica-Pisco plutons are based on modal analyses presented in Figure 19 using the classification diagram by Streckeisen (1973) suggested by the International Union of Geological Sciences (IUGS). The Linga Intrusive Complex (LIC) and the Incahuasi plutons have a monzonitic character, that is not observed either in the Pampahuasi or the Tiabaya plutons. The gabbro compositions in this plot are represented exclusively by gabbro-diorite samples collected in the pluton margins, especially associated with LIC and Pampahuasi unit. These gabbros were mapped as pre-PCB Gabbro plutons in the past, but here the samples are presented as representing possible cumulates. Average mineralogical abundances are presented for each unit in Table 2.

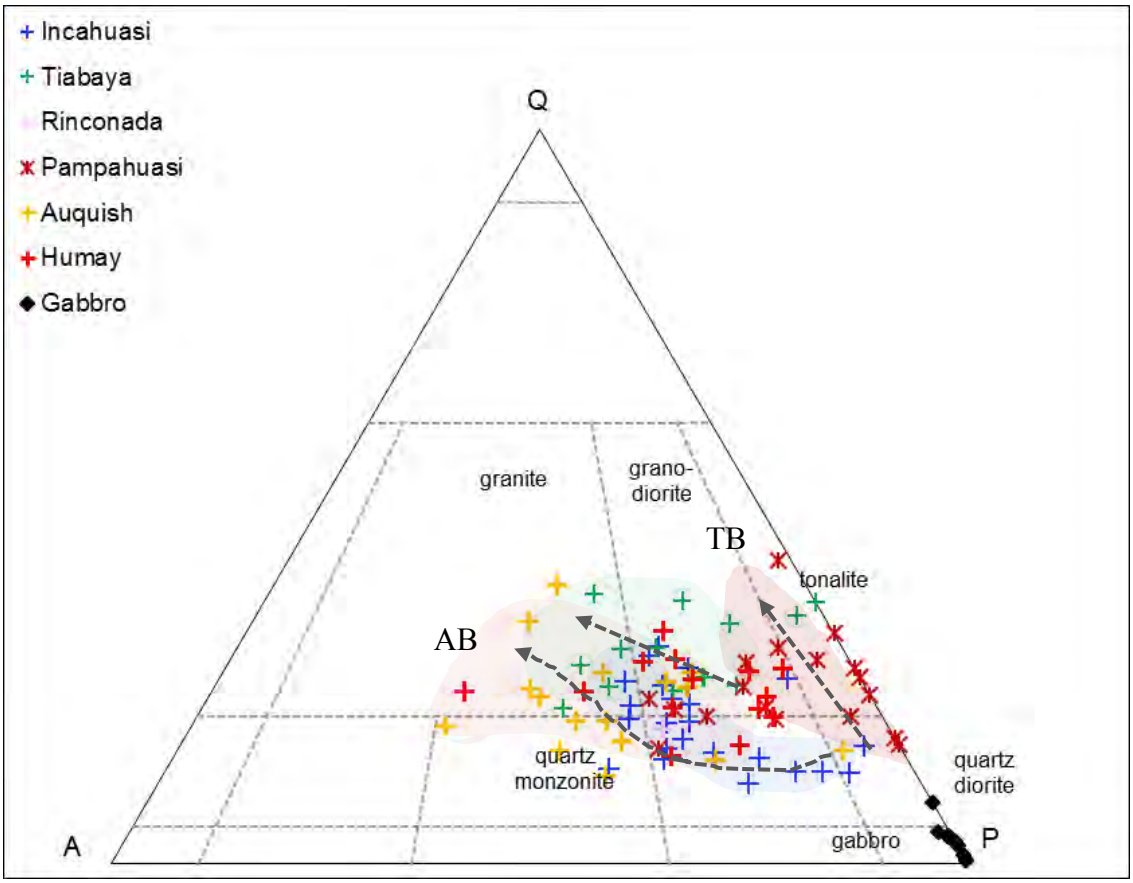

Figure 19. IUGS classification diagram (Streckeisen, 1973) based on modal analyses of collected samples from the different intrusive complexes in the Ica-Pisco area. The arrows show magmatic differentiation progression in the Ica-Pisco plutons. Tholeiite basalt (TB) and Alkaline basalt (AB) series (Lameyre and Bonin, 1991).

Table 2. Average mineralogical composition of the Ica-Pisco plutons. Mineral abbreviations are: quartz (Qz), plagioclase (Pl), K-feldspar (Kfs), biotite (Bt), hornblende (Hb), clinopyroxene (Cpx), and orthopyroxene (Opx). Sample size (N), Linga Intrusive Complex (LIC), Pampahuasi (P), Tiabaya (T), and Incahuasi (I).

Group	Plutons	Unit	N	Qz	Pl	Kfs	Bt	Hb	Cpx	Opx
LIC	Pre-PCB Gabbro	Gabbro-Diorite	10	1.4	63.6	0.4	3.6	13.2	12.5	15.6
	Humay	Monzogabbro	3	9.1	48.2	7.6	6.1	12.3	12.6	0.3
	Auquish	Monzodiorite	11	15.6	45.3	14.8	5.5	11.8	3.4	7.6
		Monzogranite	3	20.0	42.3	18.7	0.3	7.0	9.7	
		Qz-Monzonite	13	16.1	25.5	32.6	4.1	8.0	0.7	
P	Rinconada	Granite	2	19.1	45.5	9.7	4.3	12.0	7.4	0.3
	Pampahuasi	Tonalite	6	23.6	45.8	6.7	9.8	11.8	0.7	0.9
		Qz-Diorite	10	15.5	49.9	5.1	12.4	13.2	3.2	3.4
T	Tiabaya	Granodiorite	6	26.4	48.9	10.3	6.8	8.9		
		Granite	8	24.2	39.9	24.6	5.6	5.3	1.2	0.3
I	Incahuasi	Monzodiorite	19	11.5	48.8	14.5	9.8	9.8	2.7	3.2
		Granodiorite	8	25.7	43.9	18.2	9.1	5.9	1.2	1.2

Microstructures of Minerals due to Crystal/Melt Interactions

During the formation of magma bodies, mafic magmas from the mantle and felsic magmas from the crust can mingle and mix and microtextures can record the interactions occurring in the magmatic liquids from which the crystals grow. It is well known that evidence of magma chamber processes can be derived from single mineral textures (Anderson, 1984; Hattori and Sato, 1996; Hibbard, 1995; Nixon and Pearce, 1987; Troll and Schmincke, 2002; Vernon, 2004). Textures associated with magma mixing that are observed in single minerals are interpreted to be the result of injections of new magma that might incorporate old crystals that have already started forming in the magma chamber. The incorporation of old crystals into new magma batches and their resorption and overgrowth are records of these processes.

The microtextures that indicate magma mingling and mixing and recycling processes in the rocks of the Ica-Pisco plutons are: (1) truncated zoning and contact melting, (2) calcic zones, (3) corroded rims or embayments, (4) sieve texture in plagioclase crystals, (5) poikilitic textures (in quartz or K-feldspar), (6) ocellar quartz, and (7) acicular apatite. No one of these textures by itself is irrefutable evidence for magma mixing; however, they are possible indicators of local recycling processes that can be confirmed with fieldwork and elemental and isotopic analysis. The description of the following microtextures is mostly based on the work of Hibbard (1995) and Vernon (2004).

(1) Truncated zoning is characterized by an abrupt change at a "truncating boundary" from a relatively calcic to a more sodic plagioclase (Figure 20). The earlier calcic plagioclase commonly shows evidence of partial reabsorption. This microtexture

has also been interpreted as forming due to pressure reduction during the ascent of magma within the crust causing resorption of crystals (Ginibre et al., 2002; Humphreys, 2009; Humphreys et al., 2006).

(2) Calcic zones in plagioclase crystals are simply defined as abrupt (step) zoning to a more calcic plagioclase zone (Figure 21a). These abrupt changes to more calcic plagioclase are due to the mixing of more mafic magma with crystal-bearing felsic magma. Each calcic zone is possibly the result of a batch of magma from depth being fed into a pre-existing magma chamber. In general, these microtextures can be formed by multiple magma influxes or by circulation in a compositionally zoned magma reservoir.

(3) Corroded rims or embayments (Figure 21b) in plagioclase crystals are interpreted as the result of an injection of hotter, more juvenile magma into a cooling and crystallizing magma chamber that can digest some edges of the crystals.

(4) Sieve texture in plagioclase crystals is defined as a crystal of plagioclase with inclusions of other minerals (Figure 22). This feature may be formed if a plagioclase crystal is placed into a magma in which it is not in equilibrium, in which case the crystal will become corroded, and the melt will penetrate into the crystal structure.

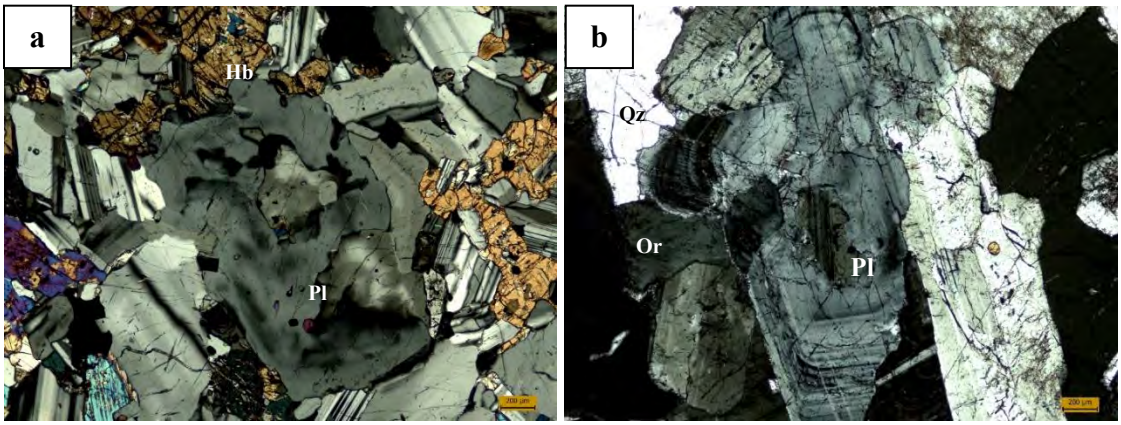

Figure 20. Microphotographs of microtextures associated with magmatic recycling as observed in plagioclase crystals (cross-polarized light, scale bar=200 μm). Truncated growth zoning textures: (a) Sample 12717C from Pampahuasi quartz-diorite. (b) Sample 12717H from Tiabaya granodiorite. Qz-quartz; Pl-plagioclase; Or-orthoclase; Hb-hornblende.

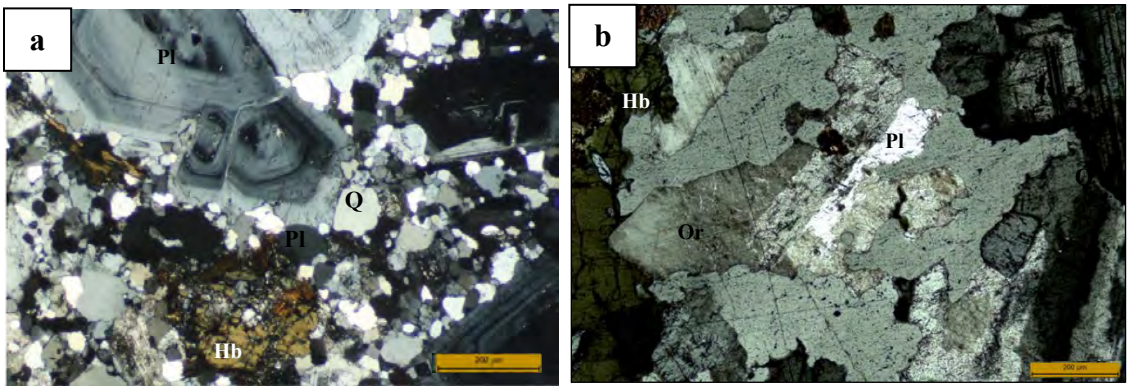

Figure 21. Microphotographs of microtextures associated with magmatic recycling observed in plagioclase crystals (cross-polarized light, scale bar=200 μm). (a) Sample 10720V from Tiabaya granodiorite showing calcic zones and normal, oscillatory zoning. (b) Granodiorite of the Rinconada unit, showing plagioclase with corroded/resorbed rims (embayments). Qz-quartz; Pl-plagioclase; Or-orthoclase; Hb-hornblende.

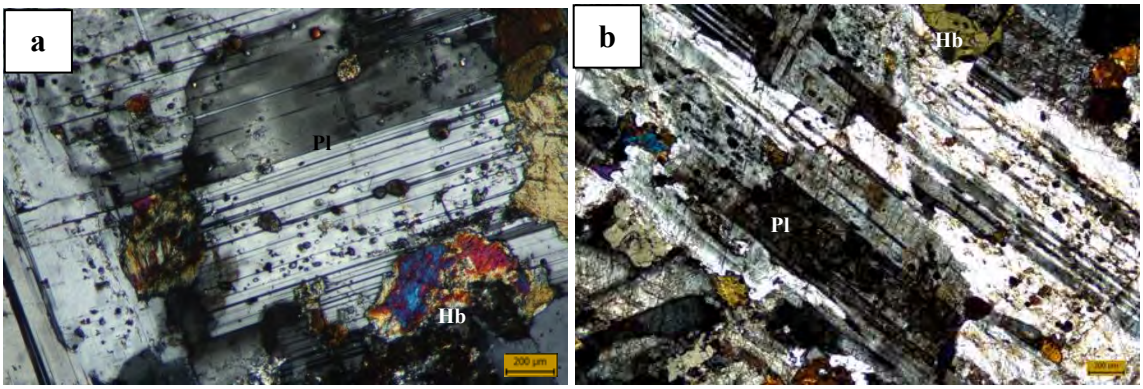

Figure 22. Microphotographs of microtextures associated with magmatic recycling observed in plagioclase crystals (cross-polarized light, scale bar=200 µm). Sieve textures in plagioclase crystals from Humay monzodiorite: (a) sample 10714H. (b) sample 12724E. Qz-quartz; Pl-plagioclase; Hb-hornblende.

(5) Poikilitic textures in quartz or K-feldspar are described as numerous crystals in random orientation which are completely enclosed within a large, optically continuous crystal of different composition. This microtexture represents a late-stage crystallization of felsic melt. Since the more felsic system is reheated, large crystals of quartz and/or K-feldspar include the earlier small crystals (Figure 23).

(6) Ocellar quartz ovoids are mantled by hornblende and/or biotite crystals. The ocellar quartz is attributed to magma mixing processes where quartz crystals are included in a mafic magma and ferromagnesian minerals crystallize upon contact with those that are at lower temperature (Figure 24a).

(7) Acicular apatite crystals are associated with rapid crystal growth in undercooled magma. In a magma-mixing hybridizing system, this results in acicular, rather than stubby, prismatic growth of the apatite (Figure 24b).

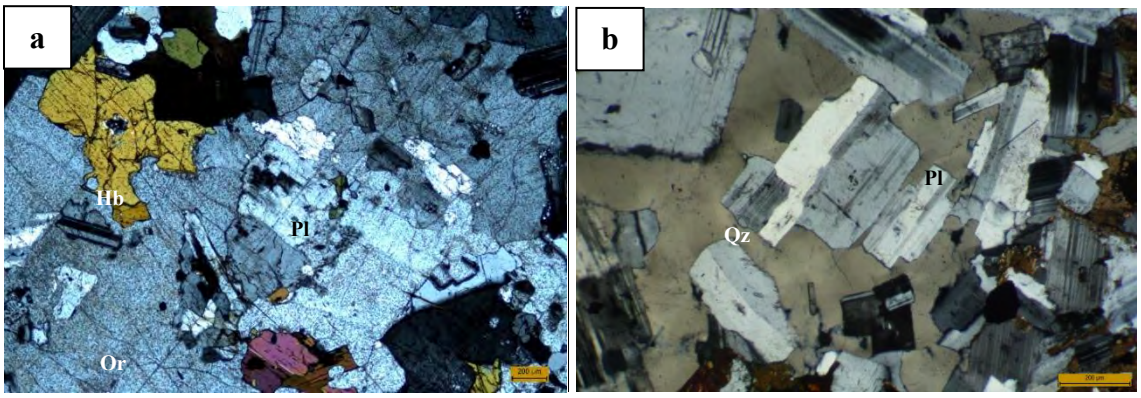

Figure 23. Microphotographs in cross-polarized light with scale bar=200 µm. Poikilitic textures in tonalite of the Pampahuasi pluton: (a) sample 12722E with poikilitic alkali feldspar texture enclosing resorbed plagioclase and hornblende crystals. (b) sample 10714P with poikilitc quartz texture. Qz-quartz; Pl-plagioclase; Or-orthoclase; Hb-hornblende.

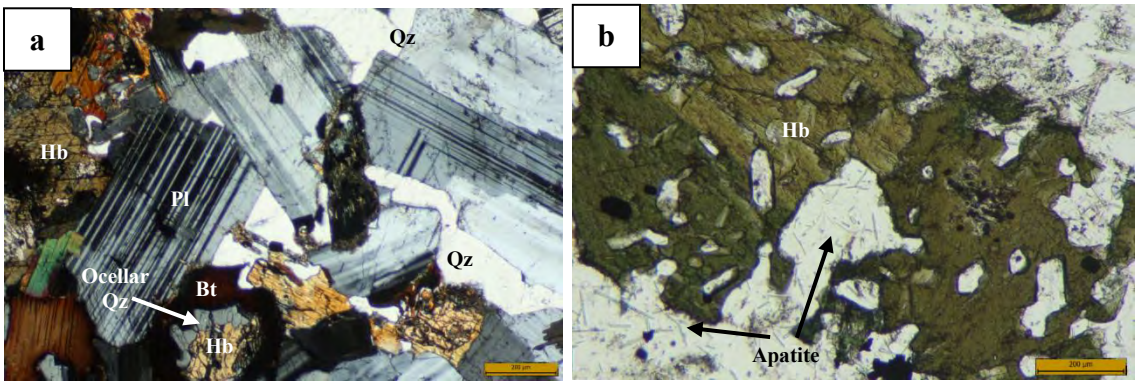

Figure 24. Microphotographs in cross-polarized light with scale bar=200 µm. (a) Sample 11828I from Incahuasi monzodiorite with ocellar texture. (b) Sample 10721D from Humay monzodiorite with apatite crystals showing acicular shape. Qz-quartz; Pl-plagioclase; Hb-hornblende; Bt-biotite.

Analytical Methods

The whole rock chemical data set of the Ica-Pisco area consists of 113 whole rock analyses from the Cretaceous plutons, as well as seven samples of Cretaceous volcanic and volcaniclastic envelop rocks, one sample of nearby Paleozoic rocks, and three samples of the Precambrian basement. Major and trace element concentrations were determined at the SGS laboratories in Canada using a Thermo Jarrell Ash Enviro II simultaneous and sequential ICP with a detection limit between 0.001 and 0.01% for major elements, 0.002 and 0.05 ppm for REE, and 0.01 to 20 ppm for other trace elements. Two instrumentation techniques were used by SGS Laboratories to get the chemical data. These are ICM90A using sodium peroxide fusion analyzed via inductively coupled plasma mass spectrometry (ICP-MS) and ICP95A using lithium metaborate fusion analyzed via inductively coupled plasma atomic emission spectroscopy (ICP-AES). The analytical major and trace element data are reported in Appendix C, which are in the Excel spread sheet that is an electronic supplement for this paper.

Isotopic analyses for 40 selected samples are presented for Sr, Nd, and Pb. Radiogenic isotopes were measured at the Geochronology and Thermochronology Lab of the University of Arizona via multicollector ICP-MS. Analyses of oxygen isotopes were conducted for nine samples at the Stable Isotope Laboratory of the California State University at Long Beach (CSULB). Oxygen isotope values were obtained for several single minerals, including: quartz, plagioclase, feldspar, biotite, hornblende, and magnetite. All the isotope data are reported in Appendix D.

The ages used to calculate Sr_i, Nd_i, and Pb_i values of the Ica-Pisco plutonic rocks are from nine new U-Pb zircon ages for Pre-PCB Gabbro, Auquish, Rinconada,

Pampahuasi, Tiabaya, and Incahuasi. The ages used for Precambrian, Cretaceous Quilmana volcaniclastic, and Humay rocks are from previously published ages.

Our new U-Pb zircon ages from multiple single zircon crystals per sample were performed at the LaserChron Center of the University of Arizona using laser-ablation at the ICP mass spectrometer (LA-ICPMS). The details of the new geochronological data for the Ica-Pisco plutons are presented in Appendix E.

Geochronology Data

U-Pb zircon ages are crucial to unraveling the chronology of magmatic events and better understanding the relations of the recycling processes observed in the Ica-Pisco plutons. Zircon features such crystal shape, zoning, and Th/U values are described for understanding better the significance of the geochronology data. Crystal shape and zoning can provide information of recycled zircons and Th/U values in zircon are commonly used to discriminate between metamorphic ($Th/U < 0.1$) and magmatic ($Th/U > 0.1$) origin for zircon overgrowths. This section will summarize the previously published geochronological data of the Ica-Pisco plutons and present the nine new ages from this research. The previous ages are presented in Table 1 and the details of the zircon crystals analyzed and the new ages are presented in Table 3.

Pre-PCB Gabbro Ages

There are no previously published ages for the pre-PCB Gabbro unit and the assumed age by Moore (1984) was Albian, which he indicated was younger than 107 Ma. A gabbro sample (15826Aa) mapped as Linga Humay monzogabbro, taken from the northwest edge of the PCB along the Rio Pisco, gave an age of 131.0±1.5 Ma (Figure 25a). The assumed age of this gabbro sample is from 23 beam spots on 7 analyzed zircons. Rb-Sr ages taken in this same area 30 years ago yielded an isochron age of about 138 Ma that was interpreted as due to magma mixing (Beckinsale et al., 1985) because it was assumed to be part of the Linga super-unit with an age of 100 Ma. Another gabbro sample (14713C) collected from this same unit gave ages with no concordia that appear to be Paleozoic inherited ages (Figure 25b). Our new age of 131.0±1.5 Ma is assumed to be an age of the pre-PCB Gabbro unit instead of representing an age of the Linga Humay unit.

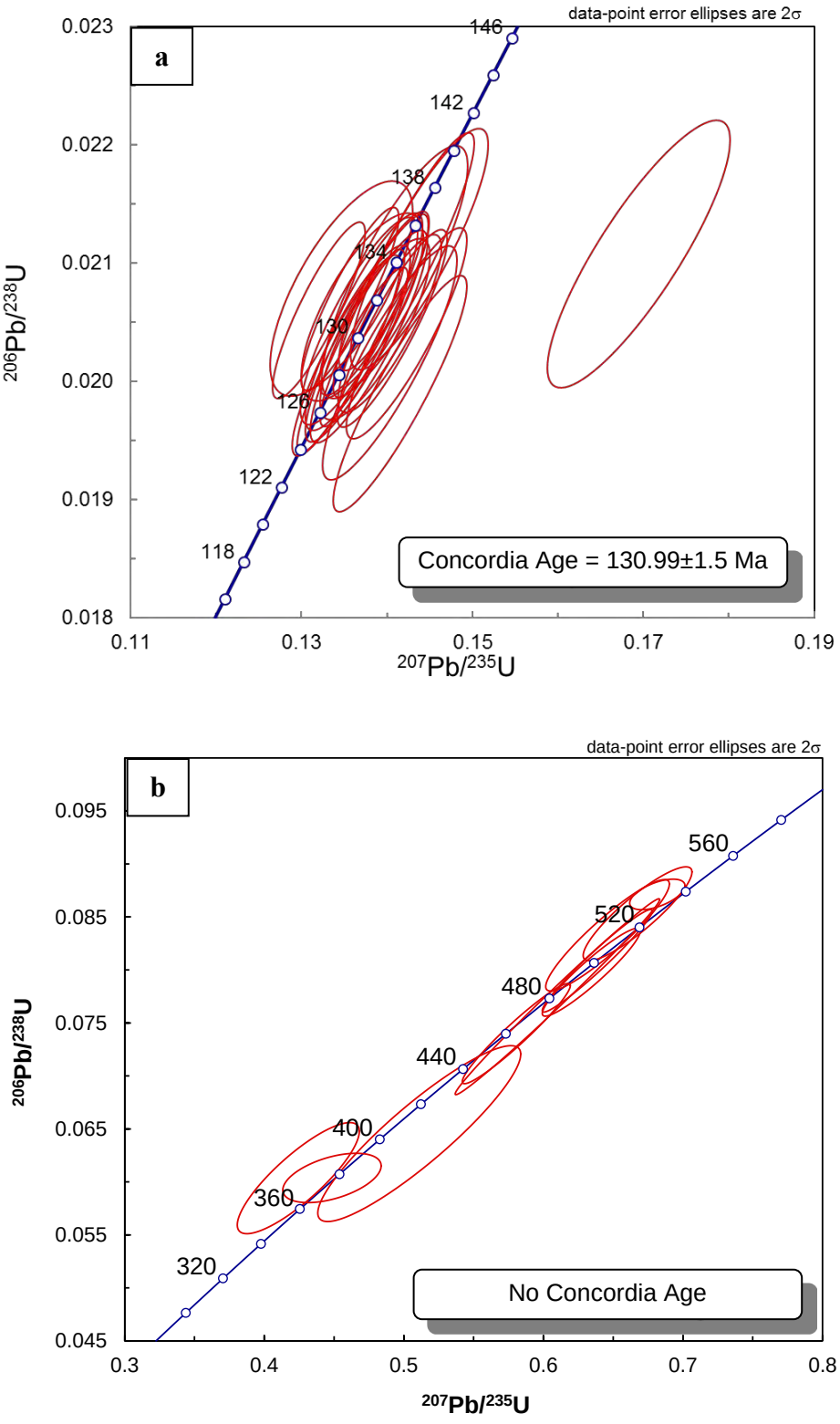

Figure 25. Zircon U–Pb concordia diagrams for samples (a) 15826Aa and (b) 14713C from the pre-PCB Gabbro unit.

LIC Ages

Published ages for the LIC in general are controversial. A K-Ar age of emplacement of 97.0 ± 3.0 Ma from a sample collected in the Rio Ica was determined by Moore (1984). However, based on samples collected from the LIC in the Rio Pisco and near the city of Arequipa, the complex was divided by Mukasa (1986a) into two distinct super-units. Mukasa (1986a) introduced "Linga Pisco-Ica" with an age of 101.4 Ma, for the unit corresponding to the research area in this study and the "Linga Arequipa" for the area located in the southern part of the segment with an age of 66.6-70.5 Ma.

For the Auquish monzonite, fourteen zircon crystals with fifteen beam spots were analyzed from sample 14721Ac (Table 3). Most of the zircons from this sample occur as subhedral crystals and have oscillatory zoning and high Th/U ratios (0.4-1.2), suggesting an igneous origin. Analyses on different zircons give relatively coherent apparent ages from 103 to 106 Ma and yield a weighted mean age of 104.84±0.4 Ma (Figure 26a), which is considered to represent the emplacement age of the Auquish pluton.

The new U-Pb zircon age for Rinconada comes from thirty-five beam spots in thirty-two zircon crystals of the granitic sample 14727U (Table 3). Most of the zircons are subhedral with oscillatory zoning, and have high Th/U ratios (1.1-4.9), expected for an igneous origin. Analyses on different zircons give relatively coherent apparent ages from 95 to 107 Ma and yield a weighted mean age of 98.31±1.92Ma (Figure 26b), which represents the emplacement age of the Rinconada pluton. Based on our fieldwork and new U-Pb zircon ages of 95-100 Ma, it is confirmed that the Rinconada pluton is part of the LIC and represents the youngest event of this intrusive complex as was suggested by previous authors (Beckinsale et al., 1985; Moore, 1984).

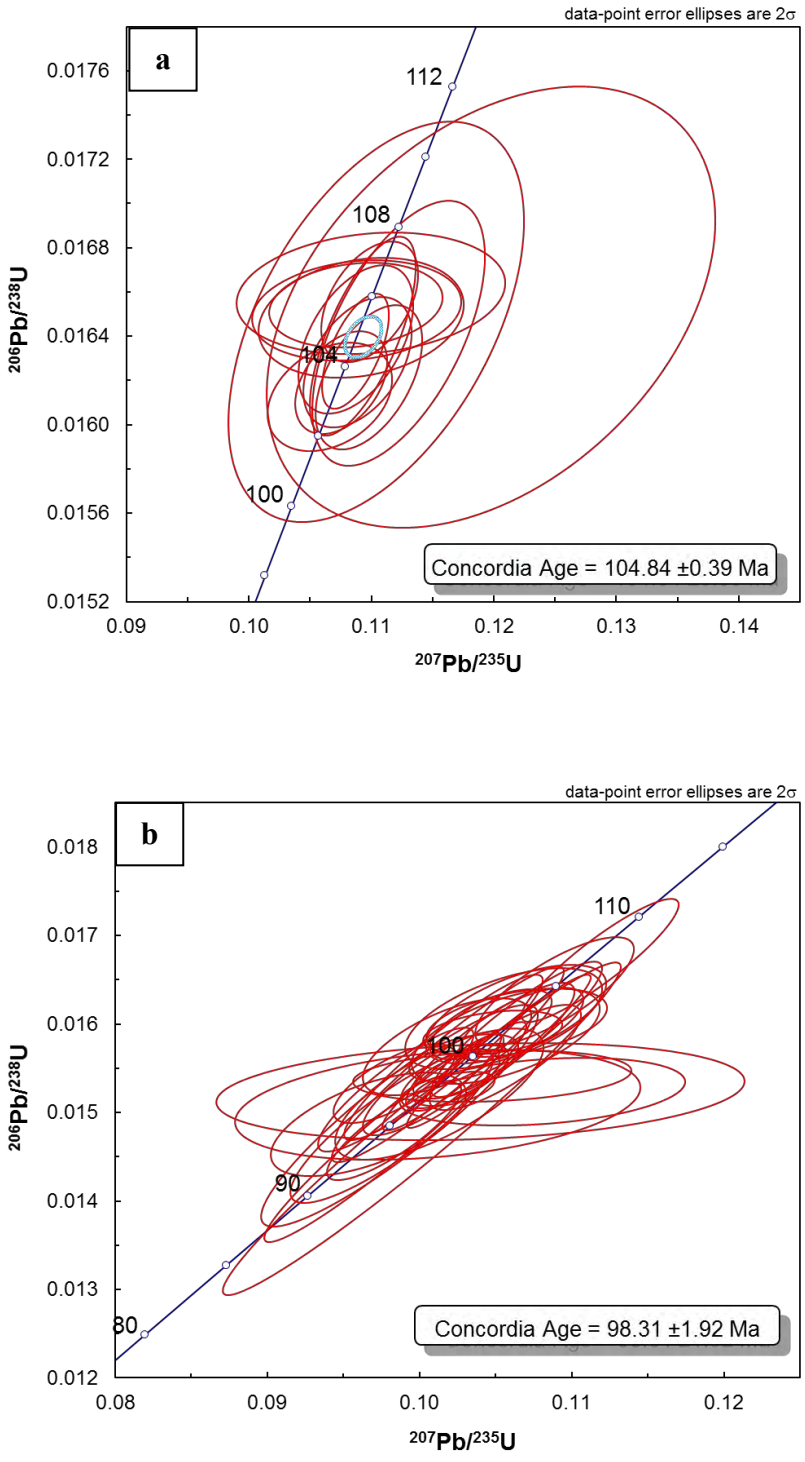

Figure 26. Zircon U–Pb concordia diagrams for sample (a) 14721Ac from the Linga Auquish and (b) 14727U from the Linga Rinconada.

Pampahuasi Unit Ages

The rocks of the Pampahuasi unit consist of tonalites and diorites and were divided into two time-separated units by previous authors (Davila, 1993). However, in this study these two units were not identified. The age of emplacement, based on radiometric dating by K-Ar is 95.9±4.2 Ma. Moore (1984) considered Pampahuasi to be post-Gabbros and possibly pre-Linga due to field relationships, but Mukasa (1986b) considered it post-Linga and adopted a U-Pb age of 93.7 ±1.4 Ma.

The two new U-Pb zircon ages in the present study were obtained from nineteen spot beams in zircons analyzed for sample 14715G and twenty-five spot beams from twenty-one zircons analyzed for sample 10714P (Table 3). Most of the zircons from these samples have euhedral and stubby prismatic shapes, oscillatory zoning, and high Th/U ratios (0.8–2.8), confirming their igneous origin. Analyses on different zircons from sample 14715G give relatively coherent concordia ages from 94 to 103 Ma and yield a weighted mean age of 97.80±0.7Ma (Figure 27a). Analyses on different zircons from sample 10714P give relatively coherent apparent $^{206}Pb/^{238}U$ ages from 90 to 96 Ma and yield a weighted mean age of 91.4±1.4 (Figure 27b). The sample 10714P, formerly mapped in the Tiabaya super-unit was collected in the Rio Ica transect and our new U-Pb zircon age of 90-91 Ma for this sample is significantly older than the 78 Ma zircon age adopted for the unit by Mukasa (1986b). If correct, the age difference between Mukasa's age and our new age could be the result of dating a Pampahuasi unit rather than a sample associated with Tiabaya plutons. Thus, the new ages reported here are considered to represent the emplacement age of the Pampahuasi unit.

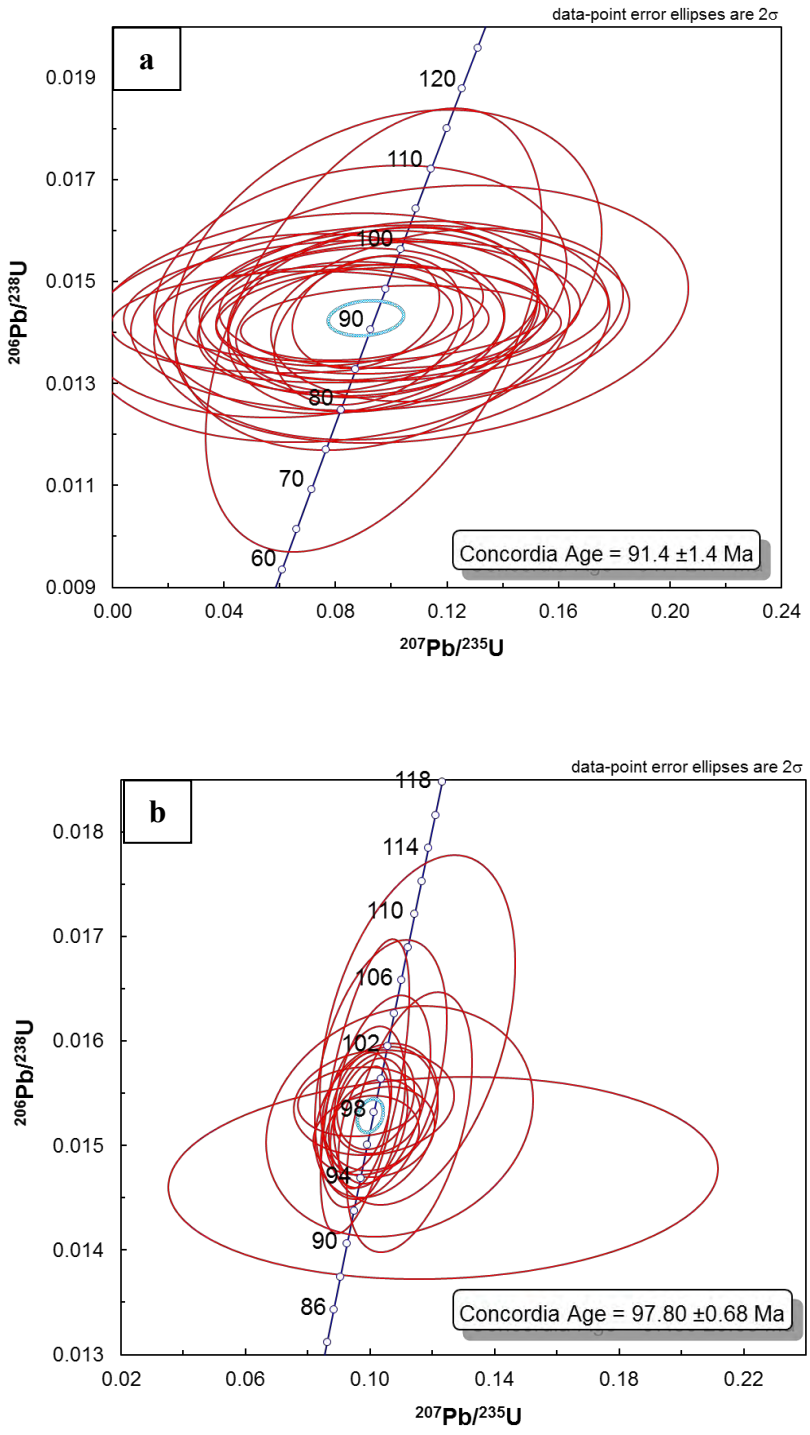

Figure 27. Zircon U–Pb concordia diagrams for the Pampahuasi samples (a) 10714P and (b) 14715G.

Tiabaya Unit Ages

This unit was suggested to be the youngest major component of the Arequipa segment in the Ica-Pisco area by Moore (1984). Three major lithologic units have been previously identified and reported for the Tiabaya: tonalite, granodiorite, and adamellite (quartz monzonite) (Agar, 1978). However, these units have been typically mapped as a single unit called Tiabaya, because internal contacts are not easily observed (Leon et al., 2007). A Rb-Sr age of 82.9±9.1 Ma in the Rio Ica from the Tiabaya super-unit was reported by Sanchez Fernandez (1982). A K-Ar isochron published by Moore (1984) provides a cooling age of 80.5±1.4 Ma for this unit. Mukasa (1986b) reported three U-Pb zircon ages of 86.4-84.4, 84.0, and 78.3 Ma.

A granodiorite sample (15826Fa) analyzed for geochronology was mapped as Incahuasi but collected very close to the Tiabaya pluton north of the Rio Pisco. Eleven spot beams in zircon crystals analyzed for this sample had subhedral crystals with oscillatory, and sector zoning, and high Th/U ratios (1.0-2.0). Analyses on different zircons give a relatively coherent apparent concordia age of 84.4±2.7 Ma (Figure 28a). The second age is from sample 15826Ca mapped as gabbro in the Rio Pisco transect, but interpreted as a Tiabaya gabbro cumulate. Thirty-five beam spots on ten zircons gave an age of 85.3±1.5 Ma (Figure 28b). The analyzed zircons showed subhedral and euhedral shapes, oscillatory zoning, and high Th/U ratios (0.1-3.2). The new ages reported here represent the emplacement age of the Tiabaya unit.

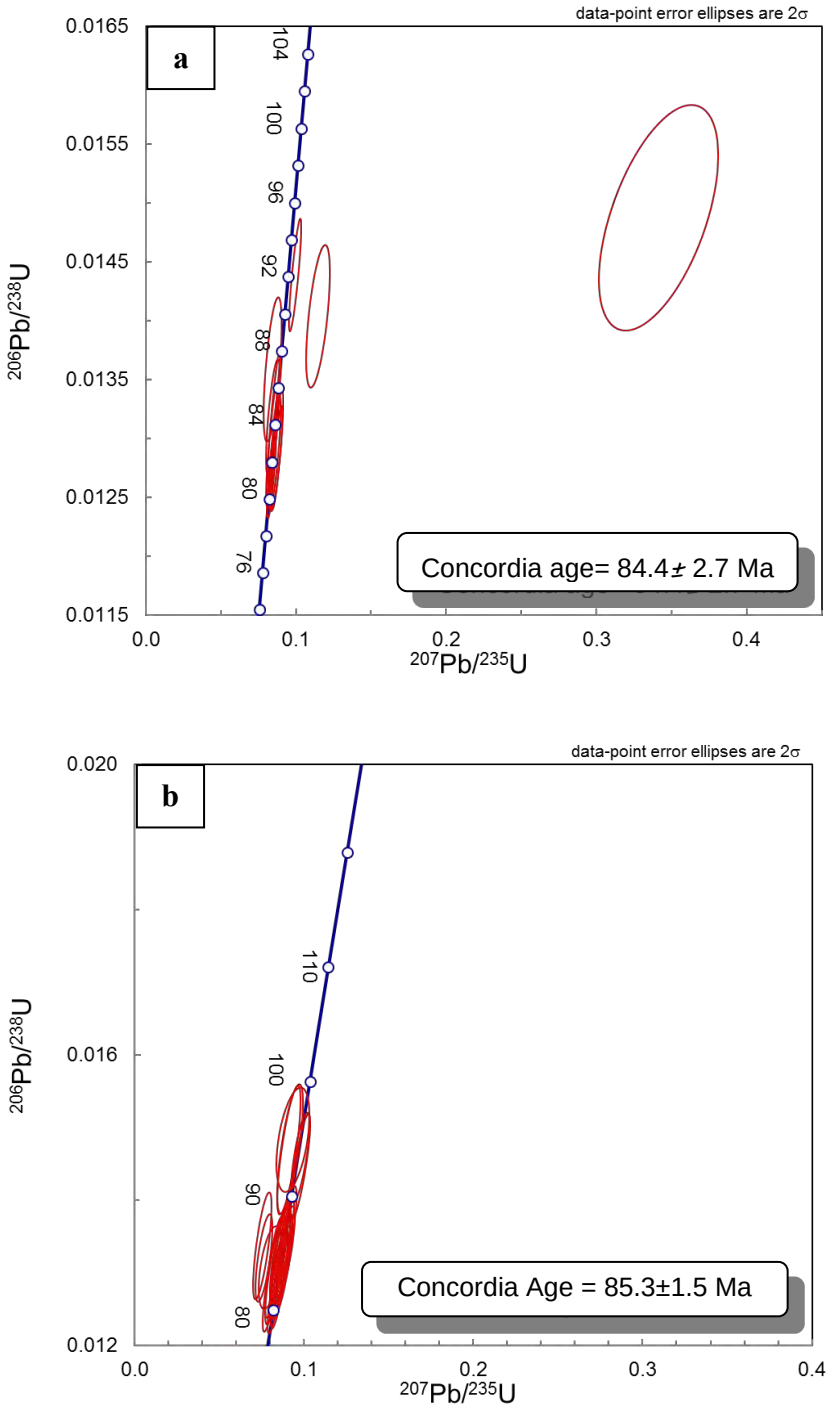

Figure 28. Zircon U–Pb concordia diagrams for the Tiabaya samples (a) 15826Fa and (b) 15826Ca.

Incahuasi Unit Ages

Different emplacement ages have been suggested for this complex. Rb-Sr ages with large errors reported by Sanchez Fernandez (1982) are: 94.7±11.7 Ma and 90.8±18.0 Ma. A K-Ar isochron cooling age of 82.5±1.4 Ma with a small uncertainty was obtained by Moore (1984). Based on these previously reported ages, plutons mapped as Incahuasi were considered part of the Ica-Pisco magmatic event and older than Tiabaya plutons.

Two new U-Pb zircon ages are presented here from samples collected in the Rio Pisco transect. The first age is from twenty zircons analyzed with twenty-five beam spots for sample 14710F and most of the zircons from this sample have euhedral to subhedral and stubby prismatic shapes, oscillatory zoning, and high Th/U ratios (1.1-1.8). Analyses on different zircons give a weighted mean age of 68.01±0.9 Ma (Figure 29a). The second analyzed sample (15826D) was mapped as Tiabaya but in the present study is considered as Incahuasi. This sample was collected north of the Rio Pisco and near the Incahuasi unit. This sample has zircons with subhedral and euhedral shapes, oscillatory and sector zoning, and high Th/U ratios (0.6-1.8). A total of 68 beam spots on zircons gave an age of 58.9±0.6 Ma (Figure 29b).

These new ages reported for the Incahuasi unit are significantly younger than the 82.5 Ma zircon age adopted by Mukasa (1986b). The difference between Mukasa's age and the new ages needs to be explored in more detail with more ages from the different lithologies grouped in the Incahuasi unit. Our new ages are considered to represent the emplacement age of the Incahuasi unit and it is suggested that the Incahuasi unit is the youngest magmatic event in the Ica-Pisco area.

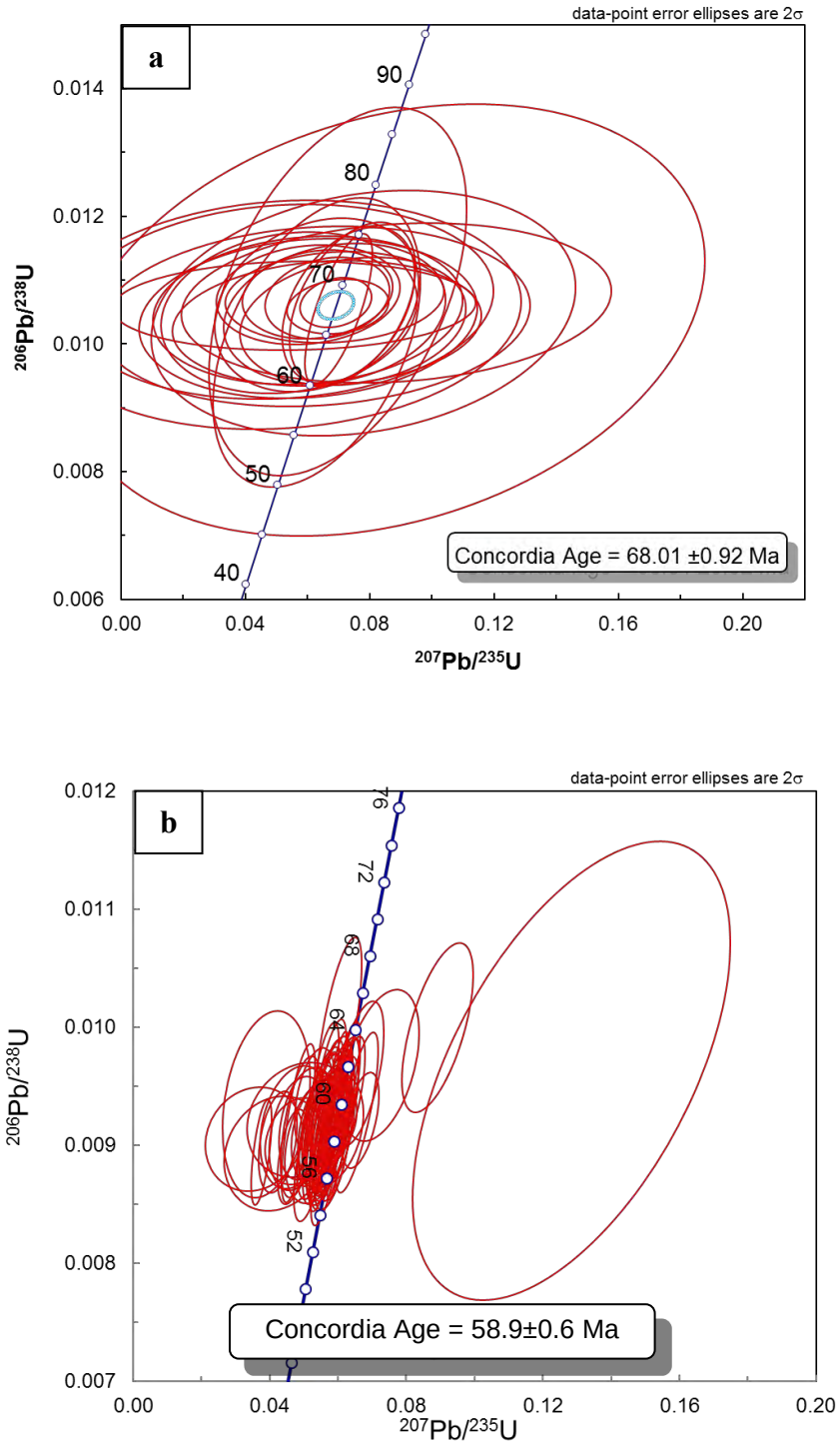

Figure 29. Zircon U–Pb concordia diagrams for the Incahuasi samples (a) 14710F and (b) 15826D.

Table 3. Details of the zircon crystals analyzed for geochronological data. The number of zircons represent the total number of zircons obtained from mineral separtation to be used during the analyses.

Sample	Pluton	Rock Type	# Zircons	# Spots	Th/U ratio	Weighted Mean $^{206}Pb/^{238}U$ Age
15826D	Incahuasi	Granodiorite	300	68	0.6-1.8	58.9±0.6
14710F	Incahuasi	Granodiorite	20	25	1.1-1.8	68.0±0.9
15826Ca	Tiabaya	Gabbro	10	35	0.1-3.2	85.3±1.3
15826Fa	Tiabaya	Granodiorite	14	11	1.0-2.0	84.4±2.7
10714P	Pampahuasi	Tonalite	21	25	13-2.8	91.4±1.4
14715G	Pampahuasi	Qz-Diorite	19	19	0.8-2.6	97.8±0.7
14727U	Rinconada	Granite	32	35	1.1-4.9	98.3±1.9
14721Ac	Auquish	Monzonite	14	15	0.4-1.2	104.8±0.4
15826Aa	Pre-PCB	Gabbro	7	23	1.0-1.4	131.0±1.5
14713C	Pre-PCB	Monzogabbro	2	10	1.2-3.0	No concordia

Geochronology Data Discussion

These new U-Pb zircon ages for samples in the Ica-Pisco area of the PCB document up to 70 m.y. (ca. 131-59 Ma) of intrusive activity with a north-eastward younging trend. The suggested age ranges for the Ica-Pisco plutons from our new U-Pb zircon data are: the pre-PCB Gabbro 131 Ma, Linga 105-98 Ma, Pampahuasi 98-92 Ma, Tiabaya 85-78 Ma, and Incahuasi 68-59 Ma. The data suggest a possibly constant state of magmatic activity from ca. 105 to 92 Ma involving the Linga and Pampahuasi units. The plutons associated with Linga and Pampahuasi might represent a single prolonged magmatic event, as their U-Pb zircon data form a continuum age. Two possible magmatic gaps can be identified between 92 and 85 Ma (between Pampahuasi and Tiabaya plutons) and the other magmatic gap between 78 and 68 Ma (between Tiabaya and Incahuasi plutons). However, the possible gaps of magmatic activity could be due to sampling bias. Therefore, under-representation of igneous bodies exposed in areas of difficult access might affect the age spectrum presented in this study.

In addition to the past understanding of gabbro bodies emplaced before the PCB (Pre-PCB gabbro), this present study provides the first U-Pb zircon age of 131 Ma for the Pre-PCB gabbro. The Tiabaya gabbro sample (15826Ca) advocates that the study area also displays gabbros emplaced contemporaneous with the PCB and this new age suggests the need for a significant revision of the gabbro bodies that had been mapped in previous studies as the Pre-PCB gabbro.

Considering the regional distribution of the PCB plutons (Figure 30) a north-eastward arc migration trend is observed for the research area. Using the spatial distribution of the granitoids and the new U-Pb zircon ages, the arc migration rate can be calculated for

this area. The results suggest that the migration rate of magmatism is approximately 1km/Ma (Figure 31).

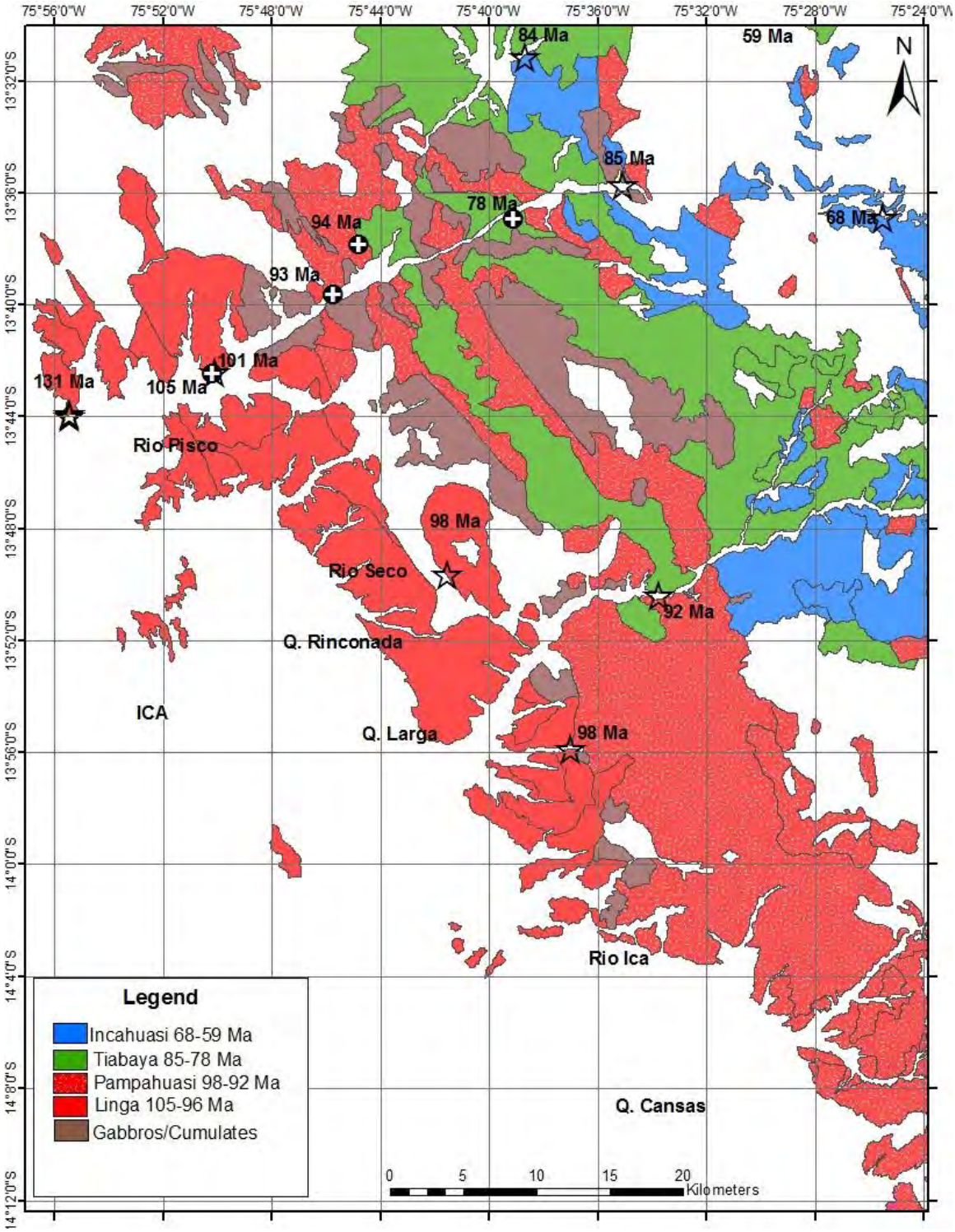

Figure 30. Ages of the Ica-Pisco plutons**.** Stars used for the new U-Pb zircon ages and circles are ages published by Mukasa (1986b).

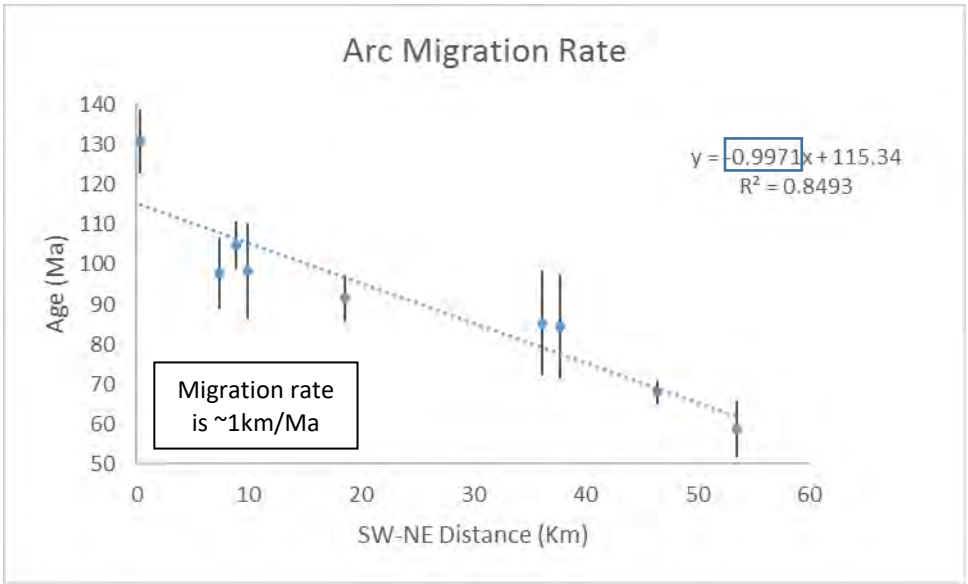

Figure 31. Estimated arc migration rate for the PCB in the Ica area. Error bars indicate total range of all measured zircons.

Geochemical Data Organization

Geochemical data will be presented based on the four gechoronological cycles defined in the previous chapter. These four cycles also correspond to lithologic groups arranged in a parallel SW-NE direction, younging towards the NE (Figure 30 and 32). Details of the sampling and calculation of the SW-NE distance are presented in Appendix B. The resulting groups are: pre-PCB Gabbro, Linga-Pampahuasi (western zone "WZ"), Tiabaya (central zone "CZ"), and Incahuasi (eastern zone "EZ").

The geochemical data sets are plotted using the Geochemical Data Toolkit (GCDkit) version 4.1. Samples from the same group age are organized in data fields in several of the plots, for ease of visualization. These fields were manually drawn to include all the samples within major clusters, excluding single outliers or samples where there is uncertainty on cycle assignments due to their sampling location at the margin between plutons of different cycles.

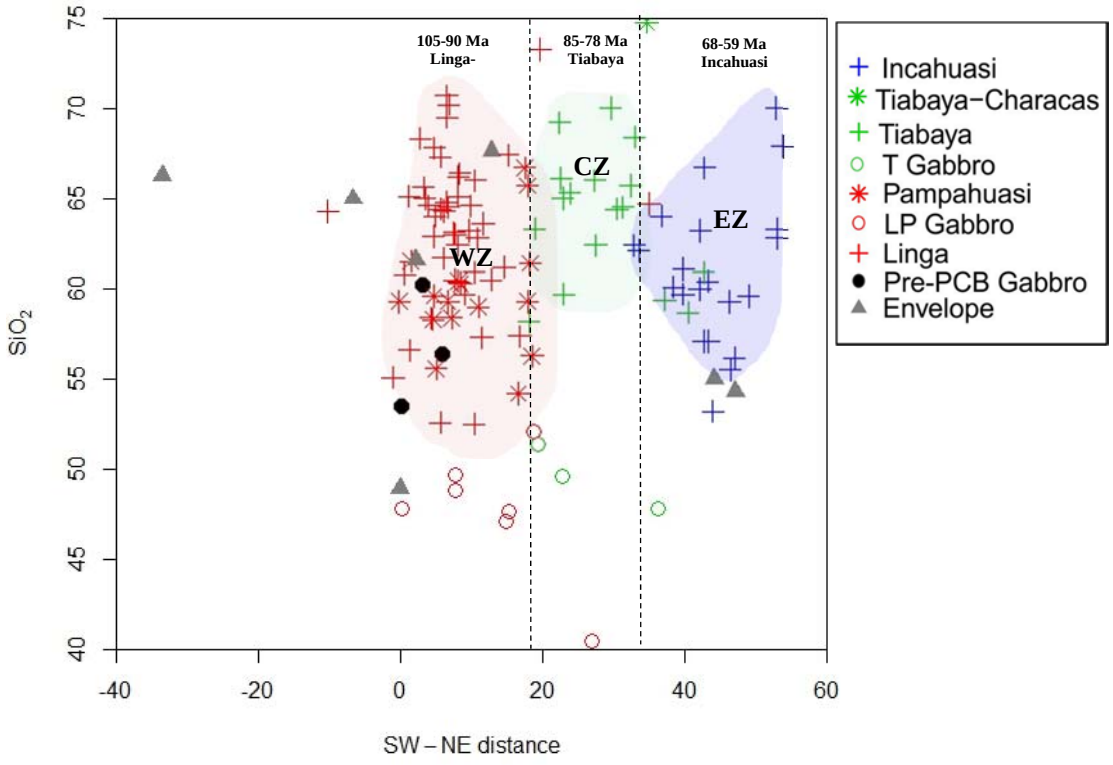

Figure 32. SW-NE distance vs. SiO2 plot showing the resulting groups for the Ica-Pisco plutons using unit and emplacement age. Red field correspond to the WZ (Linga-Pampahuasi plutons), green field correspond to the CZ (Tiabaya plutons), and blue field is the EZ (Incahuasi plutons). Pre-PCB Gabbro is located in the WZ and has an age of 131Ma. Calculation of the SW-NE distance for each sample is presented in Appendix B.

Geochemical and Isotopic Data

Major and trace element and isotopic analyses of the plutonic and related volcanic rocks plotted in Figures 33-39 show the diversity of chemical and isotopic features of the Ica-Pisco plutons in the northern part of the Arequipa segment. The plots are based on analyses reported in Appendices C and D. The plot in Figure 32 illustrates the data fields for samples collected in the western, central and eastern zones.

Major Element Chemistry

In Figure 34, Harker plots display fractionation trends in most of the plots. Two major groups are seen in the Harker plots. The older units of the WZ Linga and Pampahuasi group in the same field based on their similar chemical character. The youngest EZ rocks of the Incahuasi unit plot in the same region as the rocks of the Linga-Pampahuasi group. In contrast, the CZ rocks of Tiabaya have a different chemical signature than the other groups.

The Linga complex has more diversity than the other units with its wide range of SiO2 compositions from 52 to 73%. In the Harker plots Tiabaya exhibits higher values of Al_2O_3 and Na_2O but lower FeO_T and TiO_2 values than the other groups. The decrease from mafic to felsic rocks of the mafic major elements (e.g., FeO_T and TiO_2) might be due to an increasingly crystallizing trend in minerals that contain TiO_2 like sphene, ilmenite, or high TiO_2 biotite. The Al_2O_3 plot shows that Tiabaya rocks in general have higher alumina than the others, suggesting that this unit may have incorporated more volcaniclastic upper crustal materials.

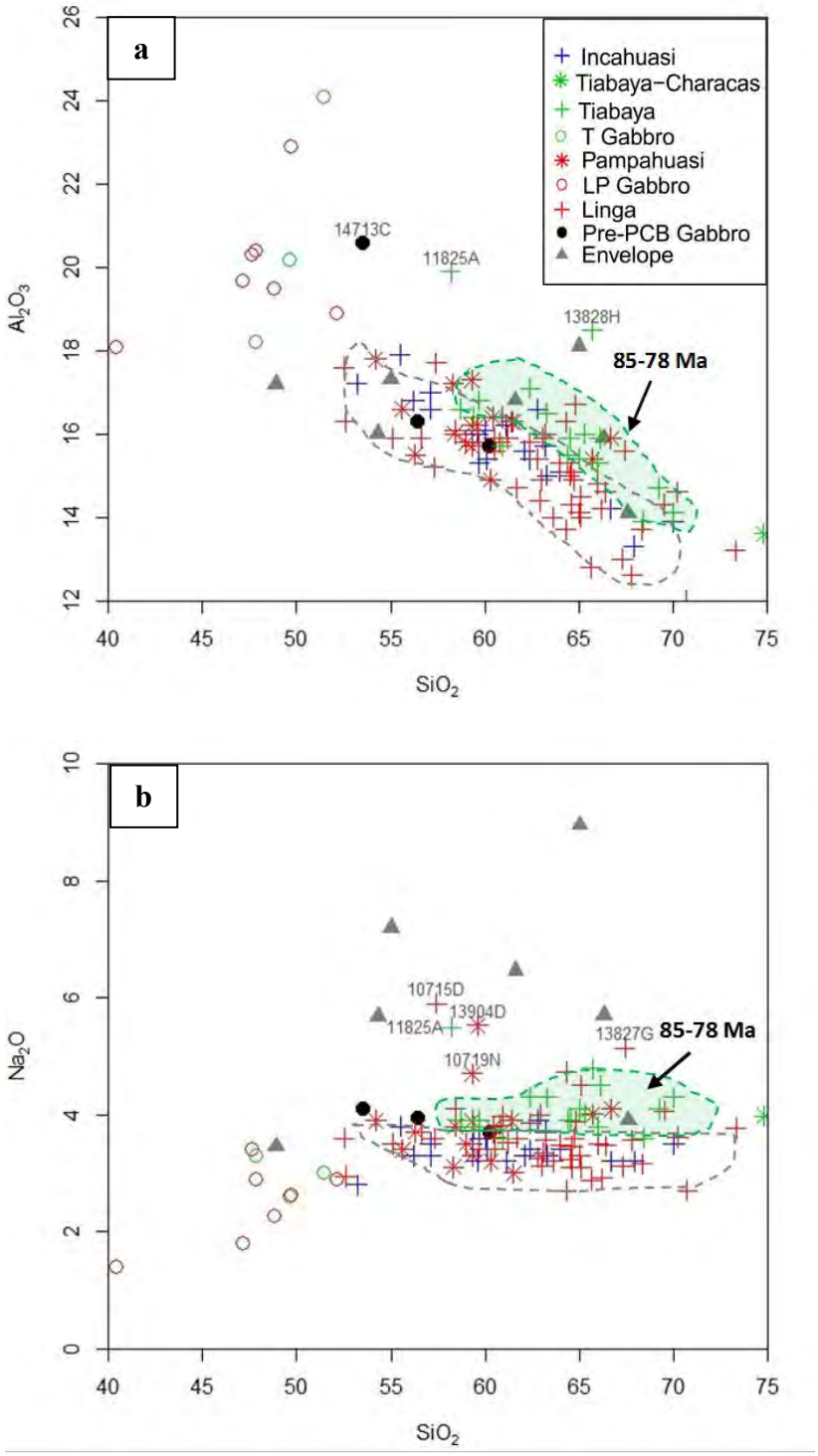

Figure 33. Harker diagrams for (a) Al_2O_3 and (b) Na_2O.

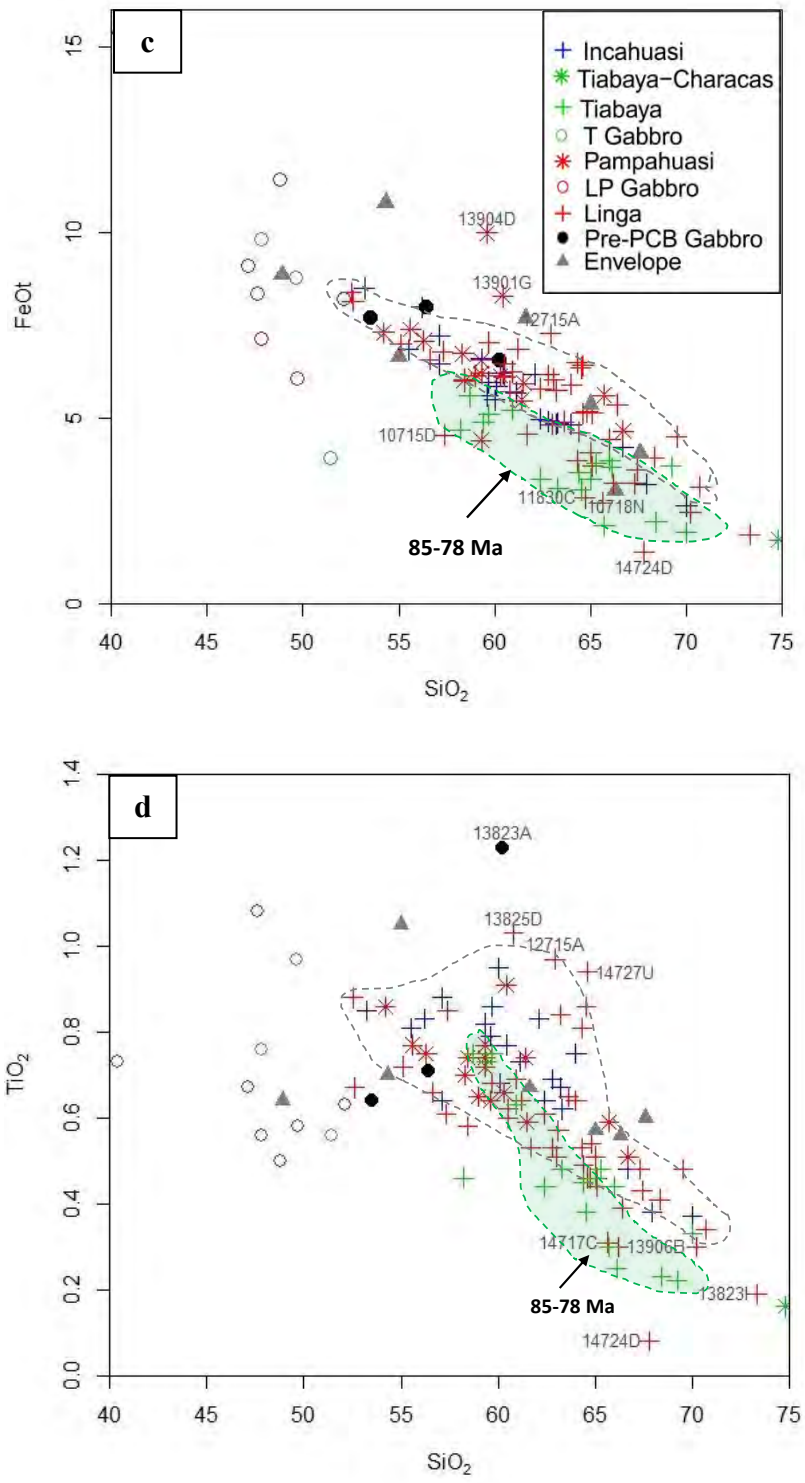

Figure 33. Harker diagrams for (c) FeOt and (d) TiO_2. Note the fractionation trends and distinctive patterns of the cumulates. Linga, Pampahuasi, and Incahuasi rocks show similar patterns but Tiabaya has a separate trend.

Based on Figure 33, gabbroic and dioritic compositions with SiO2 less than about 53% are assumed to be mafic cumulates. For this reason, they are plotted with a different symbol to distinguish them from the pre-PCB Gabbro unit. Mafic cumulates are a common feature observed in the WZ and CZ but not commonly found in the EZ.

Figure 34a uses the FeOt/MgO versus SiO2 plot by Miyashiro (1974) to define the magma series. Most of the samples from the Linga-Pampahuasi group are in the tholeiite series field. Compared to the QAP modal classification diagram, only Pampahuasi shows a tholeiitic differentiation trend, whereas Linga shows an alkaline trend. The Pampahuasi rocks might be related to a magma coming from a subducted tholeiitic (oceanic crust) protolith. On the other hand, Tiabaya and Incahuasi are in the calc-alkaline series field which is representative of subduction-related rocks.

Another very unique chemical feature of the Ica-Pisco area is the high alkalinity observed in the Linga, Pampahuasi, and Incahuasi plutons. The alkalinity is clearly seen in the K2O vs. SiO2 plot in Figure 34b. The Linga-Pampahuasi and Incahuasi plutons show high-K content, whereas the Tiabaya plutons have a lower K content.

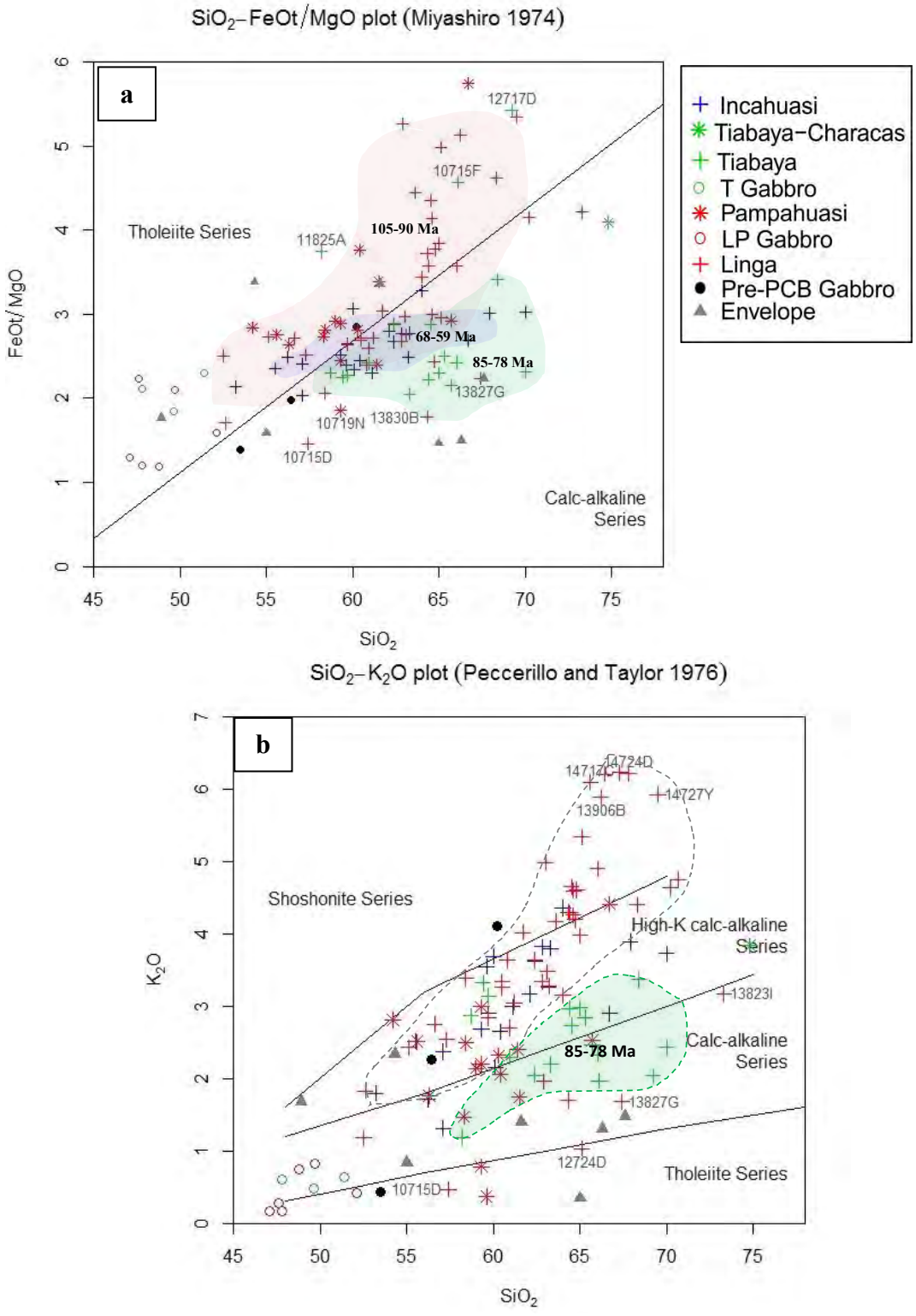

Figure 34. (a) FeO_T/MgO vs. SiO_2 diagram, after Miyashiro (1974), distinguishing tholeiitic and calc-alkaline series. (b) SiO_2 vs. K_2O diagram after Peccerillo and Taylor (1976) distinguishing High-K, calc-alkaline, and tholeiite series.

Trace Element Chemistry

The evidence for shallow vs. deep magma sources and differentiation can be observed in Figure 35 and 36 on a Sr/Y vs. Y and La/Yb vs. SW-NE distance plots, with La/Yb and Sr/Y ratios larger in the youngest Incahuasi cycle than in the older LP and Tiabaya cycles. The variation of the La/Yb ratio is displayed in a 2D contour plot in Figure 36. La/Yb ratios correlate with crustal thickness at global scales (Gromet and Silver, 1987). Incahuasi has the highest Sr/Y and La/Yb ratios. Low Sr values are the result of magma coming from a shallower source where plagioclase is stable and Sr remains in the solid. The La/Yb values are related to the garnet stability zone indicating a deeper magma source (Tulloch and Kimbrough, 2003). Profeta et al. (2015), suggested a numerical correlation between whole-rock values of Sr/Y and crustal thickness for intermediate rocks from modern subduction-related magmatic arcs. These correlations are used for inferring crustal thicknesses and tracking changes of crustal thickness through time.

Using the approach from Profeta et al. (2015) it is suggested that the Incahuasi magma came from a deeper magma source and possibly traversed more crust and assimilated more continental crust material. In contrast, the LP and Tiabaya rocks have lower Sr/Y and La/Yb ratios suggesting a shallower magma source. The median of the Sr/Y ratios suggests a Moho depth of approximately 20 km for Linga, 23 km for Pampahuasi and Tiabaya, and approximately 26 km for Incahuasi (Table 4).

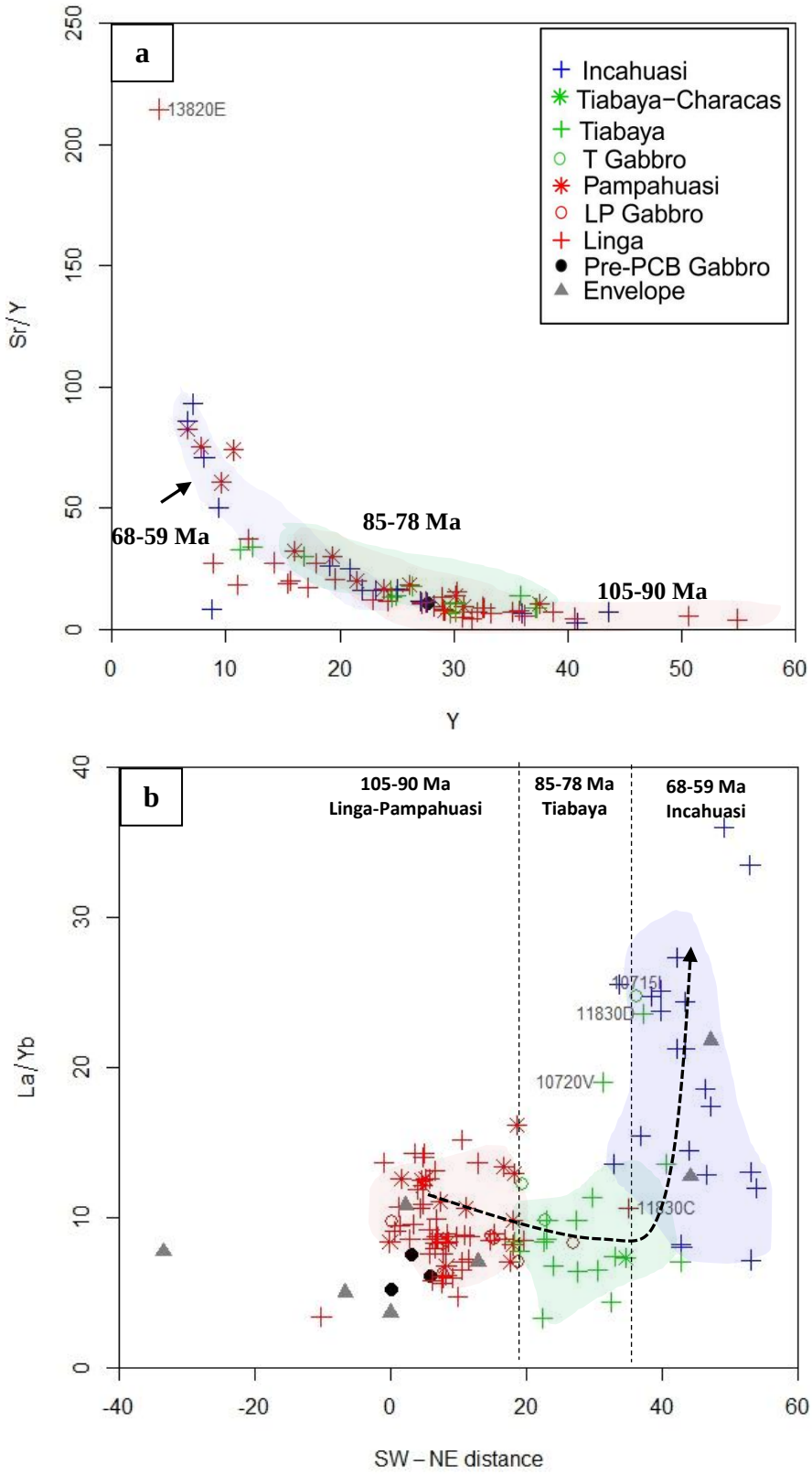

Figure 35. (a) Sr/Y vs. Y bivariate plot and (b) La/Yb vs. SW-NE distance plot Sr/Y and La/Yb ratios are interpreted as the result of different depth of magma sources.

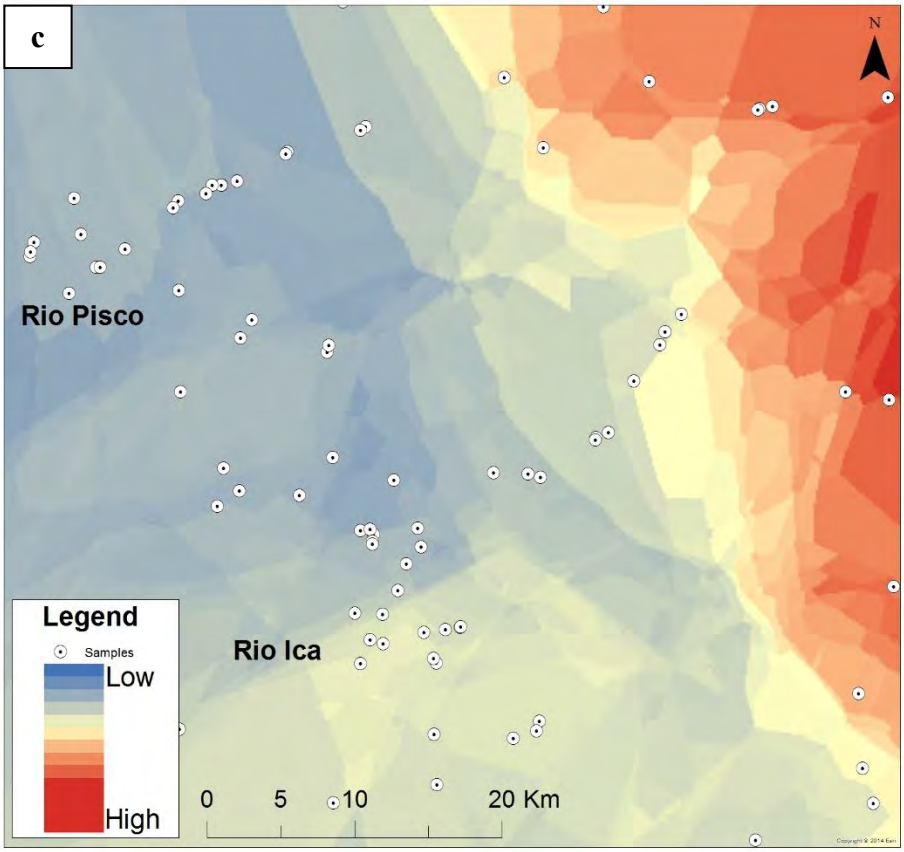

Figure 36. SW-NE variation in La/Yb displayed in a 2D contour plot created using ArcMap version 10.3.1. Sr/Y and La/Yb ratios are interpreted as the result of different depth of magma sources.

Table 4. Median values and calculated Moho depth for the Ica-Pisco plutons using the equation presented by Profeta et al. (2015).

Unit	Median Sr/Y	Moho Depth (Km)
Incahuasi	16.0	26
Tiabaya	13.5	23
Pampahuasi	13.6	23
Linga	11.0	20

Rare Earth Element Chemistry

Chondrite normalized REE patterns, based on averages of the chemical analyses results from the Ica-Pisco plutons (Table 5) are shown in Figure 37. REE patterns for the Linga, Pampahuasi, and Tiabaya plutons are quite similar. Compared with the other units, the Incahuasi has a distinctively different trend. REE patterns show a gentle slope for Linga, Pampahuasi, and Tiabaya but a steep slope for Incahuasi. The steep slope pattern is associated with Y-depleted melt from a deep source.

Linga, Pampahuasi, and Tiabaya all display a significant negative Eu anomaly (Figure 37), and are therefore interpreted as melts from a shallow crustal level affected by plagioclase fractionation. Incahuasi shows no Eu anomaly, indicating a Ca- rich melt from a deep magma source**.**

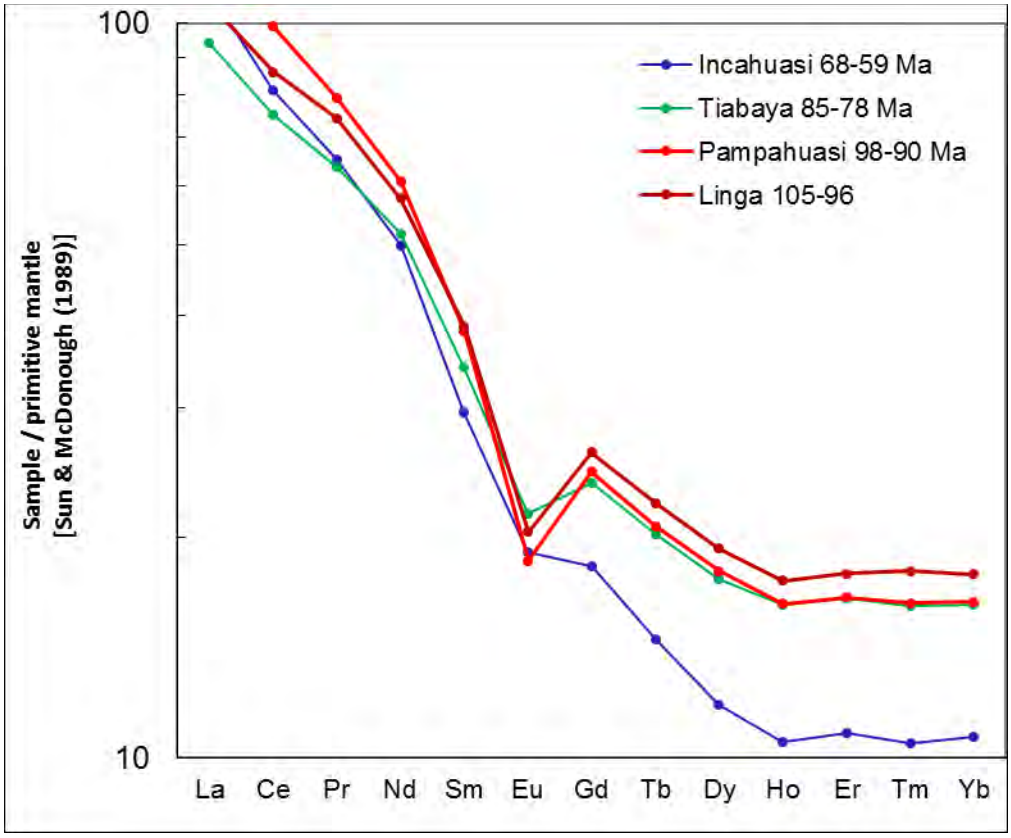

Figure 37. Rare earth element (REE) abundances from the Ica-Pisco plutons. Lines are averages of the analyzed samples.

Table 5. Normalized average REE values of the Ica-Pisco plutons. Number of samples used for calculations (N). Values used for preparing plots of REE.

	N	La	Ce	Pr	Nd	Sm	Eu	Gd	Tb	Dy	Ho	Er	Tm	Yb
Normalization - REE														
Sun and McDonough (1989)		0.237	0.613	0.093	0.457	0.148	0.056	0.199	0.036	0.246	0.055	0.16	0.025	0.161
Normalized Average														
Incahuasi 68-59 Ma	22	111.0	81.2	65.4	49.8	29.6	19.1	18.2	14.5	11.8	10.5	10.8	10.5	10.7
Tiabaya 85-78 Ma	17	94.0	75.1	63.8	51.8	34.0	21.5	23.7	20.1	17.5	16.2	16.5	16.1	16.2
Pampahuasi 98-90 Ma	15	125.8	99.2	79.2	61.0	38.1	18.5	24.6	20.7	18.0	16.2	16.5	16.3	16.3
Linga 105-96 Ma	49	106.5	85.8	74.3	57.8	38.7	20.3	26.1	22.3	19.3	17.4	17.8	18.0	17.8

Whole-Rock Isotope Analyses

Looking at the εNd vs. Sr_i plot in Figure 38, the Sr_i values for most of the intrusives are relatively low between 0.7040 to 0.7065 and εNd values are relatively high from +2 to -1. The distribution of the data fits in two groups. The first group consists of the WZ Linga-Pampahuasi units and CZ Tiabaya unit, with lower Sr_i and positive εNd values. The second group consists of the Incahuasi unit in the EZ, showing generally higher Sr_i and lower εNd values. For the Ica-Pisco plutons generally, Sr_i increases and εNd decreases from west to east. Initial $^{87}Sr/^{86}Sr$ ratios of the Ica-Pisco plutons largely overlap with those of the volcaniclastic rocks of the Quilmana Group.

The Pb data are listed in Appendix D and displayed in Figure 39. Looking at the $^{208}Pb/^{204}Pb$ vs. $^{206}Pb/^{204}Pb$ ratios, the overall values for the Ica-Pisco plutons exhibit a linear trend towards higher $^{208}Pb/^{204}Pb$ ratios values. The Tiabaya samples are grouped tightly at lower values showing a different distribution than the LP and Incahuasi samples which have a larger spread of values.

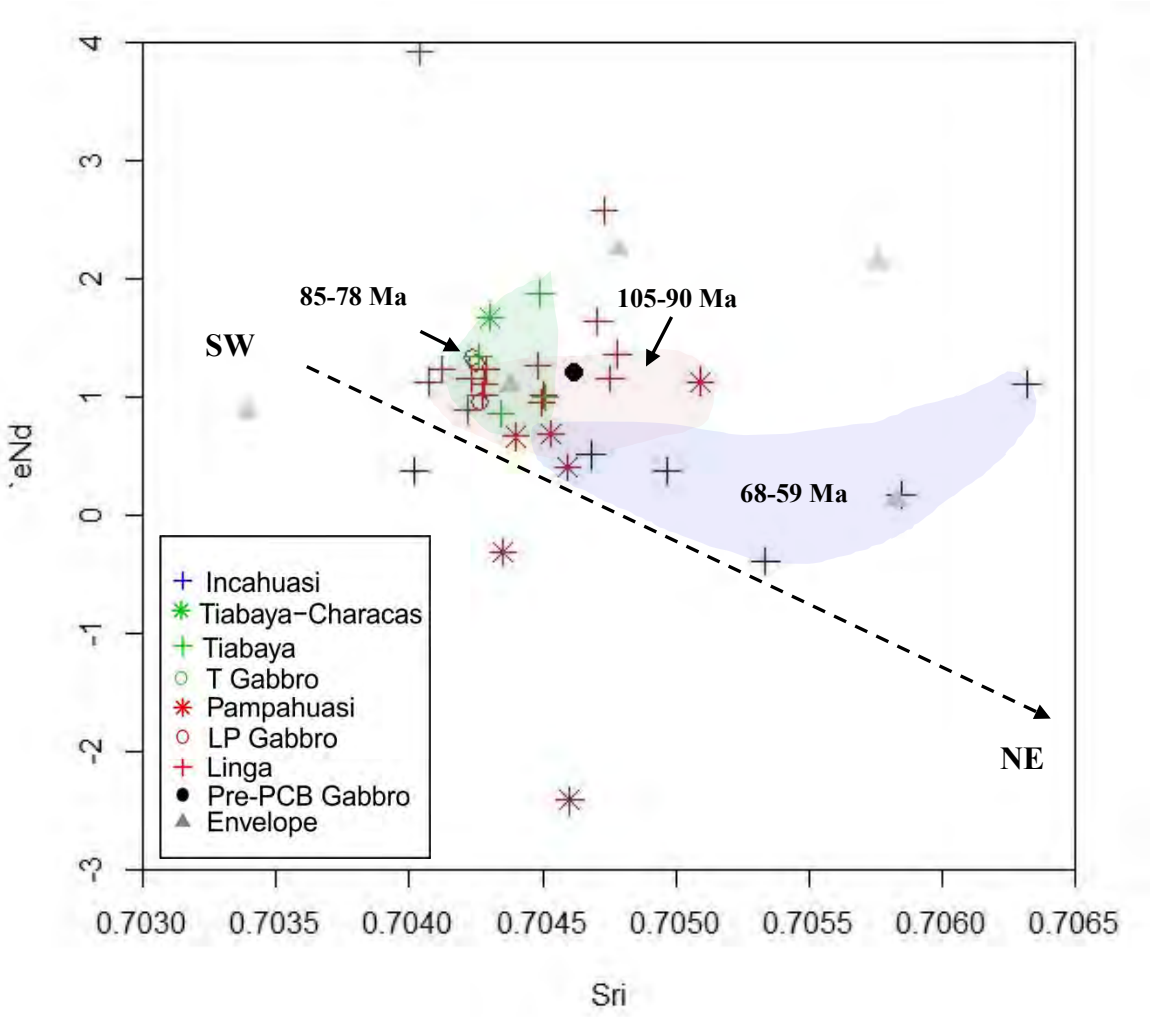

Figure 38. Isotope ratios of Nd and Sr showing an increase of Sr_i and decrease of εNd towards younger and more evolved compositions.

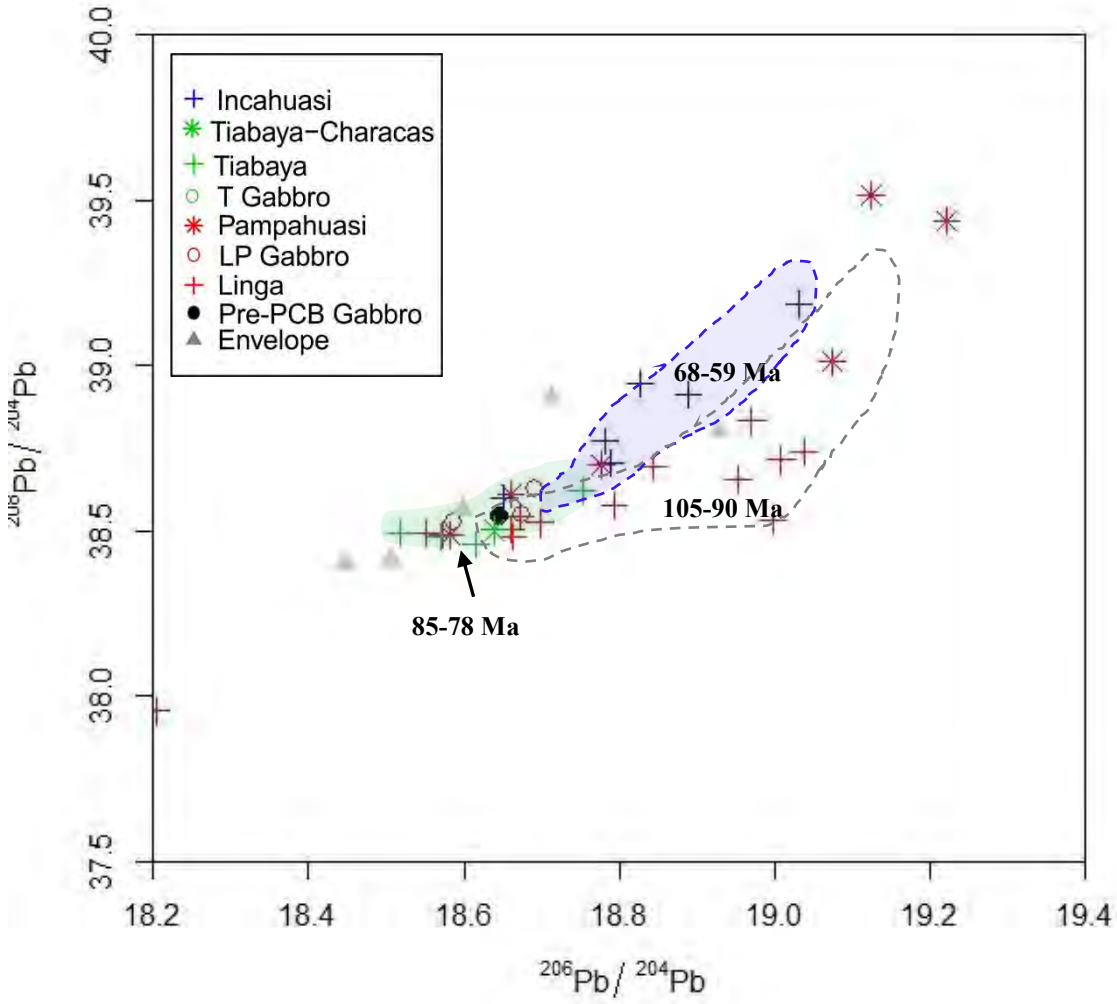

Figure 39. Variation of $^{208}Pb/^{204}Pb$ versus $^{206}Pb/^{204}Pb$.

Stable Isotope Analysis

In Figure 40, the $\delta^{18}O$ values of whole rocks from the Linga and Pampahuasi units show an increase from SW to NE. In general, the samples have very similar $\delta^{18}O$ values with one of the Pampahuasi samples showing a higher value. James (1981) suggested that it is possible to differentiate between crustal or source contamination by using a combination of Sr_i and $\delta^{18}O$ isotopes. Crustal contamination is the result of mantle-derived magmas which assimilated crustal material. On the other hand, the term source contamination is used when the contamination is the result of reflux of subducted sediments into the mantle source. In Figure 40, the distribution of the samples suggests two different groups possibly due to different sources of contamination: (1) rocks from Linga and Pampahausi plutons are located in the crustal contamination field, and (2) the Incahuasi sample is located in the source contamination field. The $\delta^{18}O$ values of the Cretaceous volcanic and sedimentary sample from the envelope exhibit similar value than the $\delta^{18}O$ value of the Incahuasi sample, a result that might be interpreted to point to the volcanic and sedimentary rocks as the major source of magmatic contamination in these plutons.

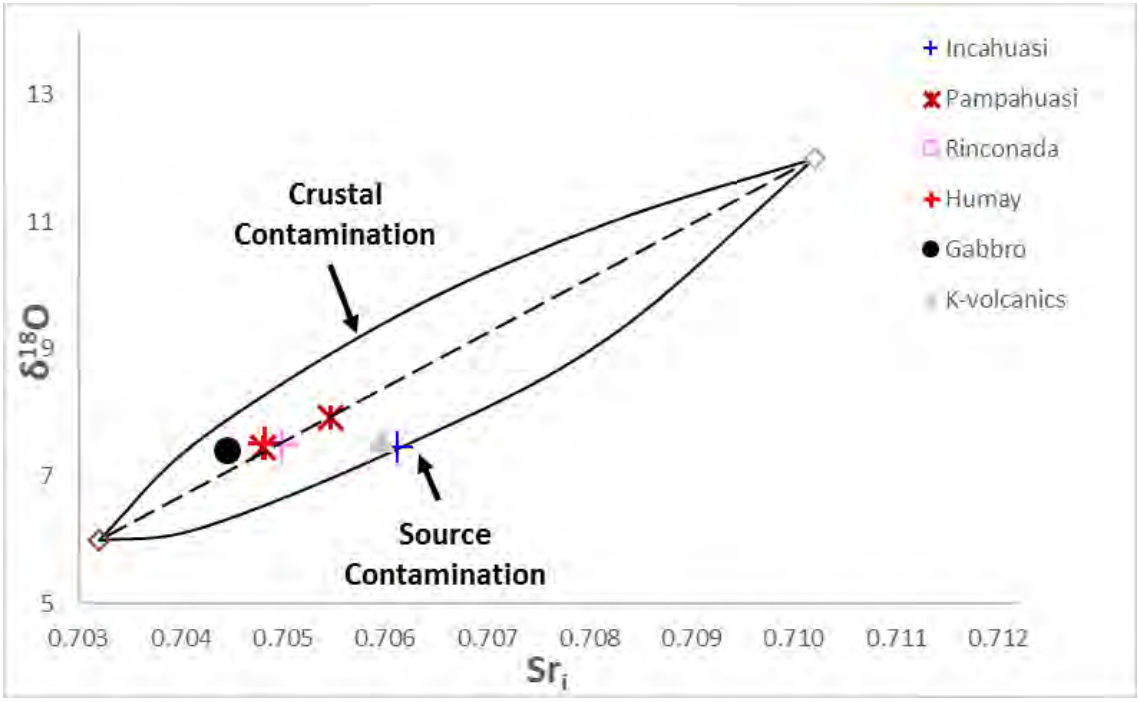

Figure 40. Diagram of two-component mixing curves for $\delta^{18}O$ vs. $^{87}Sr/^{86}Sr$ ratios. Ratio values are: for crustal contamination curve is 2:1 and for source contamination curve is 1:2. The ratios denote the proportion of Sr in crustal contaminant or in the slab-derived sedimentary fluids (After James 1981).

.

Partial Melting and Fractional Crystallization: Mass Balance Calculations

Mass balance calculations using major elements are applied to model partial melting and fractional crystallization processes for the Ica-Pisco plutons. In Figures 40 to 42 MgO Harker diagrams were used to model partial melting (PM) and fractional crystallization (FC) of the Ica-Pisco plutons. An initial lower-crust gabbro (basalt) composition of 49.5wt% SiO_2.used for the calculations is based on the average values of the Ica-Pisco gabbro samples. For all the mass-balance calculations, we used 45wt% SiO_2 as the composition of the ultramafic residue based on values from Brown and Mussett (1993).

In Figure 41, chemical data for the LP group is plotted, 10-25% partial melting of the source rock generated a magma with approximately 62wt% SiO_2, which then results in the compositional range of Linga and Pampahuasi granitoids as it fractionally crystallizes up to 70%. Fractional crystallization up to 70% plays a significant role explaining the range of compositions in most of the Linga plutons but not for the range of 55-65wt% SiO_2. These calculations revealed that partial melting and fractional crystallization may not be sufficient to explain the full range of lithologies and that magma mixing may be required to form the hybrid rocks of Linga plutons.

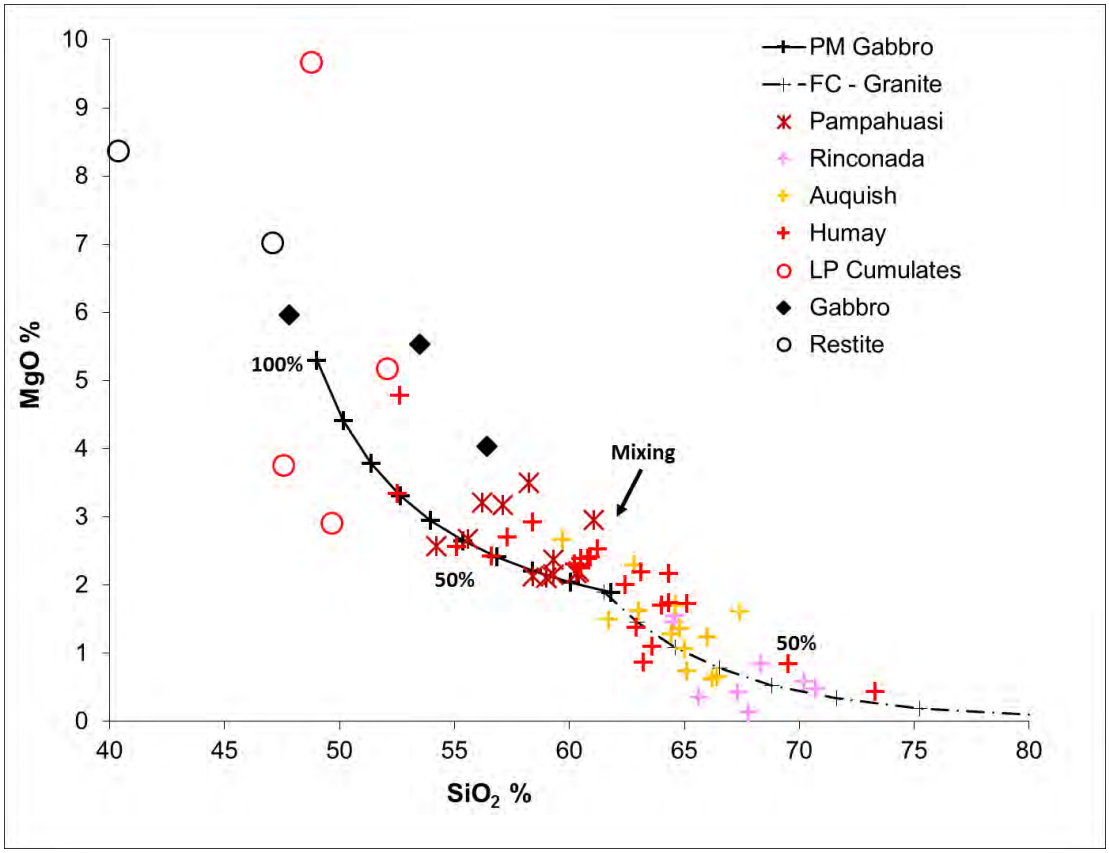

Figure 41. Evidence of magma mixing from PM and FC modeling. Magma mixing may be necessary to form the hybrid rocks of the Linga plutons.

In Figure 42 the chemical data of Tiabaya granitoids is plotted. It is assumed that 10-15% partial melting of the source rock made a magma containing approximately 63wt% SiO_2, which then produced the rock compositions identified in Tiabaya plutons as it fractionally crystallized up to 60%. Fractional crystallization plays a significant role explaining the range of compositions in the Tiabaya plutons but the spread of the samples might be the result of minor mixing processes.

Using Figure 43 for the Incahuasi calculations, 10-25% partial melting of the source rock gives a magma containing approximately 60wt% SiO_2, which then gives the range of Incahuasi granitoids as it fractionally crystallizes up to 55%. Fractional crystallization plays a significant role in explaining the range of compositions in most of the Incahuasi plutons but the spread out of the data might indicate that minor mixing processes took place.

Mass-balance calculations were performed for the Linga units to estimate the relative volume of ultramafic residue left after partial melting of lower crust gabbro. Considering an initial lower-crust basalt composition of 50wt% SiO_2, an ultramafic residue of 45wt% SiO_2, and the most differentiated granodiorite with 50wt% SiO2 the residue would have a volume of three times that of differentiated Ica-Pisco plutons. The ultramafic residue could possibly have been delaminated into the mantle.

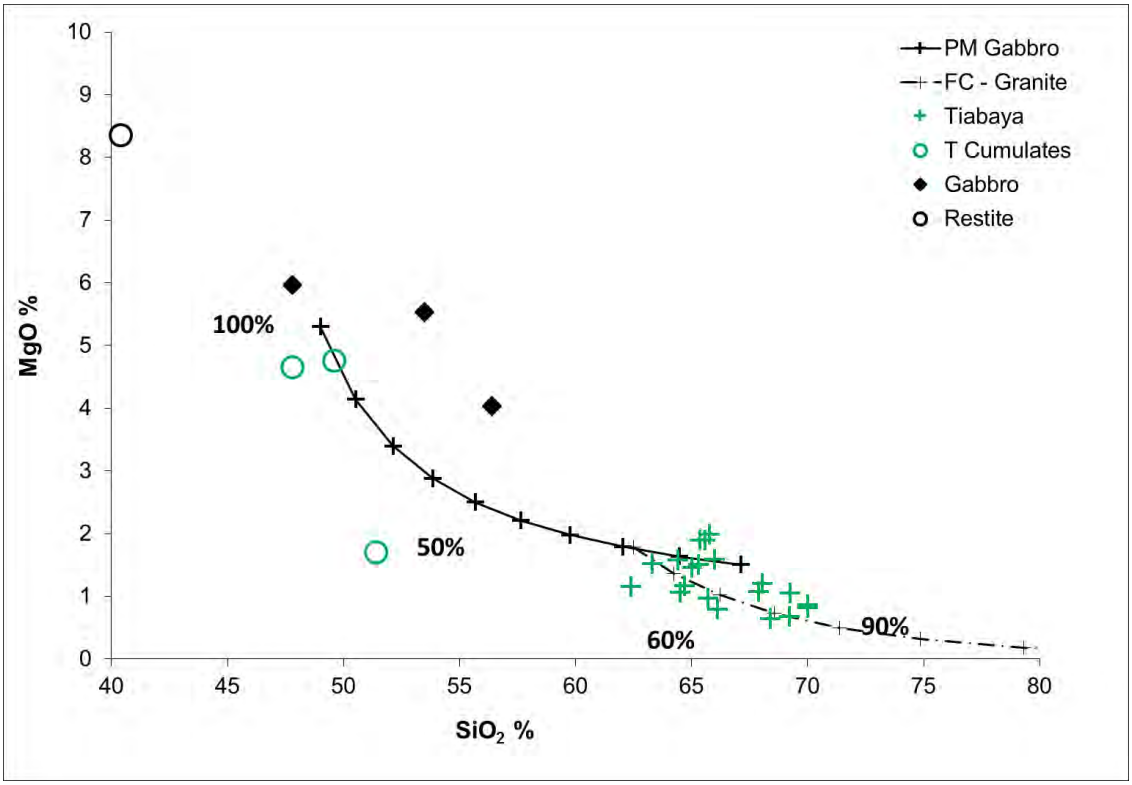

Figure 42. PM and FC modeling. FC plays the major role required to form the Tiabaya rocks.

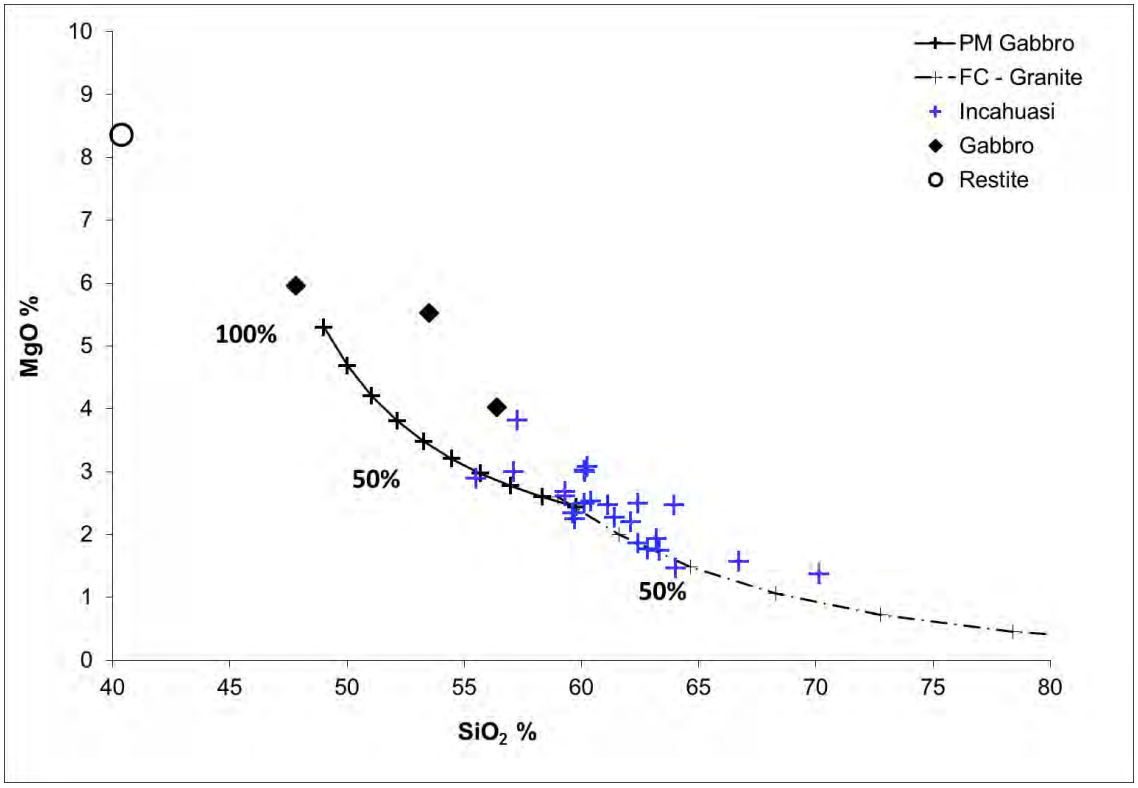

Figure 43. PM and FC modeling. FC plays the major role required to form the Incahuasi rocks.

Discussion

Magmatic structures, textures, mineralogy, and chemical characteristics of the Ica-Pisco plutons are used below to identify magma chamber processes, to evaluate the importance of the different magmatic processes in producing compositional diversity, and finally to estimate the scales of these processes during incremental crustal growth. The compositional diversity in the Ica-Pisco plutons is shown to principally reflect temporal regional changes in magma series, source depth, crustal thickness, and crustal contamination in mantle-derived magmas.

Four cycles of magmatism are suggested for the Ica-Pisco area based on the geochronology and geochemical data. These four cycles of magmatism from SW to NE across the PCB in the Ica area are: (1) Pre-PCB gabbro at 131 Ma, (2) Linga and Pampahuasi from 105 to 92 Ma, (3) Tiabaya from 85 to 78 Ma, and (4) Incahuasi from 68 to 59 Ma. This new interpretation for the four magmatic cycles in the Ica-Pisco area is supported by the geochronology data discussed previously and by the observed SW-NE geochemical trend. The geochronology data is the major criteria used to group the Linga and Pampahuasi as one cycle. The ages obtained for the Pampahuasi plutons overlap with the age of the youngest Linga Rinconada plutons which is interpreted as a single prolonged magmatic event. The geochemical features of Pampahuasi are very similar to the Linga features and it supports the interpretation of the Linga and Pampahuasi as part of the same magmatic event.

A summary of the geochemical features of the PCB Ica-Pisco plutons is presented in Table 6. Linga and Pampahuasi are independently presented to notice the similar features between them.

Table 6. Summary of the geochemical characteristics and interpretations for the Ica-Pisco plutons.

Cycle	Linga	Pampahuasi	Tiabaya	Incahuasi
Age (Ma)	105-98	98-92	85-78	68-59
Zone	Western zone	Western zone	Central zone	Eastern zone
Rock Types	Monzodiorite-Granite	Diorite-Tonalite	Granodiorite-Granite	Monzodiorite-Granite
Tectonic Regime	Extensional?	Extensional?	Extensional?	Compressional
Magma Source	Tholeiitic Basalt?	Tholeiitic Basalt	Alkaline Basalt	Alkaline Basalt
Alkalinity	High	High	Low	High
Bt+Hb %	10-15%	22%	12%	17%
FeO_T & TiO_2	High	High	Low	High
Na_2O & Al_2O_3	Low	Low	High	Low
Sr/Y and La/Yb	Low = shallow source	Low = shallow source	Low = shallow source	High = deeper source
REE	(-)Eu anomaly and gentle slope=shallow source	(-)Eu anomaly and gentle slope=shallow source	(-)Eu anomaly and gentle slope=shallow source	Steeper slope = deeper magma source
Sri	Low =0.7040-0.7046	Low =0.7044-0.7050	Low =0.7040-0.7046	Higher=0.7046-0.7063
εNd	Positive	Positive	Positive	Negative
Pb	Low-High	Low-High	Low	Low-High

The Importance of Magmatic Processes in Forming Compositional Diversity

Magmatic structures observed in the research area provide evidence of magmatic processes controlling the compositional diversity in the graniotoids. The observed magmatic structures can be interpreted to result from magma processes such as repeated injection of magma, intra-chamber flow, convection-related mass transfer within plutons, fractional crystallization, magma mingling-mixing, and magmatic recycling.

Repeated Injection of Magma and Intra-Chamber Flow

The repeated input of mafic magma into the magma chamber(s) resulted in a variety of magmatic features including enclaves, swarms of enclaves, schlieren layering, and mafic dikes. The presence of mafic dikes with varying forms and contact relationships, and injected during different stages of pluton crystallization based on field observations, is evidence for the continuous input of mafic magma into the magma chamber throughout its crystallization history. Schlieren layers are interpreted as developing along the borders of zones due to intra-chamber flow that might result in complex geochemical interrelationships (Memeti et al., 2014).

Convection-related Mass Transfer Processes

The development of magmatic fabrics provides evidence for magma flow in the magma chamber. Magmatic fabrics, enclave swarms and zones of stretched and disaggregated enclaves grading to schlieren structures were observed in the Ica-Pisco plutons. Magmatic fabrics were minimal in the WZ plutons, but more frequent in the CZ and in the EZ plutons. The isotropic character or absence of fabrics in the Linga plutons

might be evidence of a shallow intrusion and higher rate of cooling. Fabrics wrapping around xenoliths are interpreted to form during or after final chamber growth (Paterson and Miller, 1998). The fabrics defined by highly stretched enclaves can be interpreted as a result of convective flow within the surrounding magma (Turnbull, 2009). All these features suggest active zones of local convection-related mass transfer, and processes of magma intrusion with mingling and mixing taking place within active magma chamber(s).

Magma Mingling and Mixing

Mafic enclaves are another feature seen in magma chamber processes that are related to magma mingling and mixing (Barbey et al., 2008). Composition and temperature are considered to be the main factors controlling the mingling and mixing interactions between different magmas associated with the formation of enclaves (Barbarin and Didier, 1992; Chen et al., 2009; Słaby et al., 2008; Troll and Schmincke, 2002). Structures and textures can provide information about the conditions controlling the magma mingling and mixing between compositionally diverse but coeval magmas (Appleby et al., 2008; Bachmann, 2004; Griffin et al., 2002; Nixon and Pearce, 1987). Enclaves observed in the Ica-Pisco plutons with fine-grained, quenched margins indicate that the key parameter controlling the style of preserved magma interaction was temperature contrast, and that composition played a minor role. However, enclaves showing diffuse edges and gradational changes in composition are interpreted as forming under minimal temperature contrast where magma mixing and hybridization processes easily took place.

The hybridization process is explained by Huppert and Sparks (1988) in this way: (1) felsic crustal melt mixes with hot mantle derived mafic magmas; (2) through extensive and combined mechanical and chemical exchange, the mixing continues with more and more hybrid mafic magmas; (3) as time progresses, the high-temperature hybrid melts through more mixing could become homogenized hybrid magmas. Based on these ideas it is suggested that the hybrid rocks and associated enclaves observed during fieldwork and also well defined by PM and FC calculations in the Linga plutons might represent different degrees of magma mixing between felsic and mafic magmas interacting in the magma chamber where the hybridization processes were controlled by the physical properties of the magmas (Barbarin, 2005; Barbarin and Didier, 1992; Chen et al., 2009; Kocak et al., 2011).

Fractional Crystallization

Chemical data from the Ica-Pisco plutons suggest that magmatic differentiation is primarily due to fractional crystallization, although some mixing effects are also indicated by the spread of the data and by PM and FC mass balance calculations.

In previous studies, all the gabbro bodies in the Ica-Pisco area were mapped as pre-PCB Gabbro. However, the gabbro bodies identified at the marginal zones of the plutons in this research are referred as cumulate bodies. The pre-PCB Gabbro corresponds to the earliest intrusive event in the Arequipa segment and this lithology is similar to the early gabbros observed in the Linga segment. Cumulates were clearly identified from the chemical data and these provide evidence of FC processes. Our field observations, as well as petrological and geochronological data suggest that some gabbro

and diorite bodies precede the main PCB intrusion, but other bodies are cumulates contemporaneous with the PCB. Here, it is suggested that the monzogabbros of Humay are the earliest intrusive event in the Ica-Pisco area and these are defined as the pre-PCB Gabbro unit based on the geochronology data.

The decrease of FeO_T and TiO_2 in the Ica-Pisco plutons can be explained as early minerals forming cumulates in the lower portion of the magma chamber and not being preserved in the sampled pluton areas. However, another possible explanation for the decrease of TiO_2 can be that it records a change in the amount of TiO_2 in the magma sources that might be associated to dehydration melting in the mantle wedge (Gastil et al., 1990).

Magma Sources

Chemical data support the relationship between magma source depth and crustal contamination observed in the Ica-Pisco plutons. Based on Sr/Y and La/Yb ratios, we suggest that Linga-Pampahuasi "LP" and Tiabaya cycles are from a shallow source but the Incahuasi cycle is from a deeper magma source. Isotope data confirm that cycles from a shallow source have low crustal contamination and the Incahuasi cycle from a deeper source has higher contamination from lower crustal materials.

The relatively low Sr_i values in the WZ and CZ may indicate minimal contamination from Precambrian cratonic crust during the early magmatic events, but contamination with Precambrian crust seems to be slightly higher in the last magmatic events. It is also important to consider as another explanation for the increase in Sr_i and the more negative εNd values the influence of different mantle sources. The Sr_i values

within the Ica-Pisco plutons could represent complex mixtures of heterogeneous mantle with highly variable crustal material and may not be due just to little crustal contamination (Hildebrand and Whalen, 2014).

Using Pb isotope data, Mukasa (1986a) invoked the addition of Pacific sediments to explain an "enriched" mantle source of the PCB. Mukasa developed his idea by comparing isotopic data of the Nazca plate basalts and Pacific sediments from data published by Tilton and Barreiro (1980), Barreiro and Stern (1982), Unruh and Tatsumoto (1976), Reynolds and Dash (1971) and Dash (1981), and suggested that the contamination resulted from the pervasive invasion of metasomatic fluids produced by the dehydration of sedimentary materials. This idea differs from the interpretations presented here, because higher water content is not associated with the more contaminated Incahuasi plutons. In the present study, the Incahuasi rocks appear to have a lower water content based on mineralogy, i.e., lower biotite and hornblende hydrous minerals and this evidence disagrees with the idea of invoking contamination as result of interaction with metasomatoc fluids.

The idea of an "enriched" mantle source for the Ica-Pisco plutons can still be valid, but through an alternative enrichment mechanism due to the influence of subcontinental lithospheric mantle (SCLM). This model involving the influence of the SCLM is described for Cenozoic mafic rocks from southern Peru (Carlier et al., 2005). The isotopic compositions, especially the $\delta^{18}O$ data support the model of different contamination source regions or complex mixing processes. The $\delta^{18}O$ isotopes seem to suggest several different sources of contamination affecting the Ica-Pisco plutons. The first group is defined by Pre-PCB Gabbro, Linga, and Pampahuasi samples and the

second group is defined by the Incahuasi sample. The sources of contamination might be: (1) the Precambrian and Paleozoic rocks, (2) the volcaniclastic rocks, and (3) subducted sediments.

Magmatic Recycling

Field observations and chemical evidence supports the idea that the Ica-Pisco plutons are the result of widespread magmatic recycling of older volcanic and plutonic rocks into younger plutons. From fieldwork, magmatic recycling is identified from kilometer-scale cauldron subsidence to meter-scale stoping of xenoliths, and centimeter-scale disaggregation of xenoliths. The scales of magmatic recycling are associated with the stages of the recycling process. Large kilometer- and meter-scale angular xenoliths with minimal evidence of transport and assimilation or digested edges are formed by cauldron subsidence. Small centimeter-scale and rounded xenoliths with digested edges display more transport and/or partial melting and the adding of chemical contamination to the magma. Based on these scales, recycling can be characterized by a sequence of events from breaking off of large blocks, incorporation and transport of xenoliths, and assimilation and contamination at the chemical level.

Magma Source and Alkalinity

The LIC, Pampahuasi, and Incahuasi rocks have high-K content but Tiabaya rocks exhibit low-K content. The variation in alkalinity may be controlled by: source depth (Kuno 1959), water content from the slab (Hawkesworth et al., 1984), extent of partial melting, and contamination from a high-K source. The high-K content in the Ica-

Pisco plutons can be explained by using a combination of results from petrographic and chemical analysis and mass balance calculations.

The first potential variable for explaining the high-K is source depth. The Sr/Y and La/Yb ratios and REE plot indicate that Linga, Pampahuasi, and Tiabaya melts came from a shallow source but Incahuasi came from a deeper magma source. For this reason, the depth argument cannot explain the high-K content for the LP and Tiabaya rocks, but it can be used to explain the high-K of Incahuasi rocks.

Based on the quantity of biotite and hornblende presented in Table 7, it is possible to suggest that the amount of slab fluids might be a significant factor contributing to the high-K content of the Linga Humay and Pampahuasi plutons. Specifically, Pampahuasi rocks have higher amounts of these minerals than the other plutons, indicating higher water interaction with the magma. The high content of hydrous minerals suggests that these magmas were wet and possibly led to the high-K content. On the other hand, the Linga Auquish rocks have lower percentages of biotite and hornblende compared with the Linga Humay and Pampahuasi, and the high-K content requires another explanation than high water content. The extent of partial melting seems to provide a better explanation for the discussed changes in alkalinity in the Linga units. Based on the relative higher average of the silica composition for Linga Auquish (65wt% SiO_2) compared with Linga Humay (60wt% SiO_2), it is suggested that lower percent partial melting in the Linga Auquish led to higher-K content. The high-K content in Rinconada unit is explained as due to extreme fractional crystallization.

For Tiabaya rocks, the low-K content might be the result of low water content, since the previous Linga and Pampahuasi magmas incorporated fluids during the intense

dehydration melting process and no more water was available to transport potassium at the time of Tiabaya magmatic event.

Finally, continuing with the sequence of events at the time of melt generation, the reappearance of high-K content in the Incahuasi melt may be explained as related to source depth, since geochemical evidence supports a deeper magma source for this cycle. Contamination of a parental high-K source can also explain the high-K content for Incahuasi because it is the only unit showing slightly higher Sr_i values interpreted as the result of crustal contamination. The contamination effect was suggested previously as the major explanation for the high-K content of the Linga super-unit (Agar, 1978; Atherton and Aguirre, 1992). However, the isotopic data do not support the contamination argument for the Linga plutons.

Table 7. Details of the biotite and hornblende percentages of the Ica-Pisco plutons.

UNIT	Bt+Hb %
Incahuasi	17
Tiabaya	12
Rinconada	12
Pampahuasi	22
Auquish	10
Humay	15

Scales of Various Procesess During Incremental Growth

The LP and Tiabaya cycles of the WZ and CZ respectively display primitive Sr_i ratios that suggest a limited interval between melt extraction from the mantle and crystallization resulting in a limited continental crust component. The fractional

crystallization of the LP rocks can possibly be explained by a short time scale for fractionation, but the mixing forming hybrid rocks of the Linga plutons required longer time scales. The Incahuasi cycle in the EZ has slightly more elevated Sr_i ratios and it is interpreted as due to magma from a distinct source and involving some degree of continental crustal contamination.

U-Pb dating of the nine samples from the Ica-Pisco plutons supports the interpretations that the sequence shows a NE younging direction and that the LP intrusive complex represent a system of large magma chamber(s) active between approximately 105 and 92 Ma. On the other hand, the Tiabaya unit represents a large magma chamber that was probably active during a period of time between approximately 85 and 78 Ma. The Incahuasi unit may represents a possibly smaller magma chamber compared with the exposed area of the Pampahuasi and Tiabaya plutons that was active between approximately 68 and 59 Ma. Large magma chambers with longer active residence times could experience greater degrees of magma mixing.

Finally, the estimate of arc migration rate based on U-Pb zircon ages and SW-NE spatial distribution of the Ica-Pisco plutons suggest that the migration rate of magmatism in the northern part of the Arequipa segment was on the order of 1km/Ma.

Conclusions

SW-NE geochemical trends are observed for the Ica-Pisco plutons of the northern Arequipa segment. These trends are based on changes in magma source depth, crustal contamination, magma series, and alkalinity. The Ica-Pisco plutons represent four cycles of magmatism from SW to NE across the PCB: (1) pre-PCB Gabbro at ~131 Ma, (2)

Linga-Pampahuasi intrusive complex at 105-92 Ma, (3) Tiabaya plutons at 85-78 Ma, and (4) Incahuasi plutons at 68-59 Ma.

Shallow magma sources for the first three cycles are explained as due to a shallow subducting Nazca plate and only the Incahuasi cycle magma came from a deeper magma source probably associated with a thicker crustal segment. The effects of a thicker crustal segment are reflected in an increase of the isotopic signature of crustal contamination in the Incahuasi plutons.

The alkalinity content changes from west to east showing high values in the WZ, low values in the CZ, and then increasing again in the EZ. High-K values in the WZ are due to dehydration melting; the low-K content in the CZ is attributed to fluids exhaustion; high-K content in the EZ is related to a great source depth and not to a high volume of fluids.

References

Agar, R. (1978) The Peruvian Coastal Batholith: Its monzonitic rocks and their related mineralization. The geology of the rio Pisco, a sector of the Arequipa segment of the Coastal Batholith. Geology, Doctor of Philosophy, p. 293. University of Liverpool, Liverpool.

-. (1981) Copper mineralization and magmatic hydrothermal brines in the Rio Pisco Section of the Peruvian Coastal Batholith. Economic Geology, 76, 677-693.

Anderson, A.T. (1984) Probable relations between plagioclase zoning and magma dynamics, Fuego Volcano, Guatemala. American Mineralogist, 69, 660-676.

Atherton, and Aguirre. (1992) Thermal and geotectonic setting of Cretaceous volcanic rocks near Ica, Peru, in relation to

Andean crustal thinning. Journal of South American Earth Sciences, 5(1), 47-69.

Atherton, and Petford. (1996) Plutonism and the growth of Andean Crust at 9'S from 100 to 3 Ma. Journal of South American Earth Sciences, 9, 1-9.

Barbarin, B. (2005) Mafic magmatic enclaves and mafic rocks associated with some granitoids of the central Sierra Nevada batholith, California: nature, origin, and relations with the hosts. Lithos, 80(1-4), 155-177.

Barbarin, B., and Didier, J. (1992) Genesis and evolution of mafic microgranular enclaves through various types of interaction between coexisting felsic and mafic magmas. Earth and Environmental Science Transactions of the Royal Society of Edinburgh, 83(1-2), 145-153.

Barbey, P., Gasquet, D., Pin, C., and Bourgeix, A.L. (2008) Igneous banding, schlieren and mafic enclaves in calc-alkaline granites: The Budduso pluton (Sardinia). Lithos, 104(1-4), 147-163.

Beckinsale, R.D., Sanchez-Fernandez, A.W., Brook, M., Cobbing, E.J., Taylor, W.P., and Moore, N.D. (1985) Rb-Sr whole-rock isochrons and K-Ar age determinations for the Coastal Batholith of Peru. Blackie, Glasgow.

Boily, M., Brooks, C., and Ludden, J.N. (1989) Chemical and isotopic evolution of the Coastal Batholith of southern Peru. Journal of Geophysical Research, 94(89), 12483-12489.

Brown, G.C., and Mussett, A.E. (1993) The Innaccessible Earth. An integrated view to its structure and composition. Chapman & Hall.

Bussell, M.A., Pitcher, W.S., and Wilson, P.A. (1976) Ring complexes of the Peruvian Coastal Batholith: a long-standing subvolcanic regime. Canadian Journal of Earth Sciences, 13(8), 1020-1030.

Chen, B., Chen, Z.C., and Jahn, B.M. (2009) Origin of mafic enclaves from the Taihang Mesozoic orogen, north China craton. Lithos, 110(1–4), 343-358.

Cobbing, E.J., Ozard, J.M., and Snelling, N.J. (1977) Reconnaissance geochronology of the crystalline basement rocks of the Coastal Cordillera of southern Peru. Geological Society of America Bulletin, 88(2), 241-246.

Cobbing, E.J., and Pitcher, W.S. (1972) The Coastal Batholith of central Peru. Journal of the Geological Society, 128(5), 421-454.

Coira, B., Davidson, J.P., Mpodozis, C., and Ramos, V. (1982) Tectonic and magmatic evolution of the Andes of northern Argentina and Chile. Earth Science Reviews, 18, 303-332.

Coldwell, B., Clemens, J., and Petford, N. (2011) Deep crustal melting in the Peruvian Andes: Felsic magma generation during delamination and uplift. Lithos, 125(1-2), 272-286.

Davila, M.F. (1993) Geología de los cuadrángulos de Pisco, Guadalupe, Punta Grande, Ica y Córdova. Instituto Geológico Minero y Metalúrgico del Perú "INGEMMET", 47, 78.

Gastil, G., Diamond, J., Knaack, C., Walawender, M., Marshall, M., Boyles, C., Chadwick, B., and Erskine, B. (1990) Chapter 2: The problem of the magnetite/ilmenite boundary in southern and Baja California California. Geological Society of America Memoirs, 174, 19-32.

Ginibre, C., Kronz, A., and Worner, G. (2002) High-resolution quantitative imaging of plagioclase composition using accumulated backscattered electron images: new constraints on oscillatory zoning. Contributions to Mineralogy and Petrology, 142, 436-448.

Gromet, P., and Silver, L.T. (1987) REE Variations Across the Peninsular Ranges Batholith: Implications for Batholithic Petrogenesis and Crustal Growth in Magmatic Arcs. Journal of Petrology, 28(1), 75-125.

Haederle, M., and Atherton, M.P. (2002) Shape and intrusion style of the Coastal Batholith, Peru. Tectonophysics, 345, 17-28.

Hattori, K., and Sato, H. (1996) Magma evolution recorded in plagioclase zoning in 1991Pinatubo eruption products. American Mineralogist, 81, 982-994.

Hawkesworth, C.J., Rogers, N.W., van Calsteren, P.W.C., and Menzies, M.A. (1984) Mantle enrichment processes. Nature, 311(5984), 331-335.

Hibbard, M.J. (1995) Petrography to petrogenesis. 242-260 p. Prentice-Hall, Englewood Cliffs, New Jersey.

Hildebrand, R.S., and Whalen, J.B. (2014) Arc and slab-failure magmatism in Cordilleran batholiths II—The Cretaceous Peninsular Ranges batholith of Southern and Baja California: Paul Hoffman Volume: . Geoscience Canada, 41, 339-458.

Humphreys, M.C.S. (2009) Chemical Evolution of Intercumulus Liquid, as Recorded in Plagioclase Overgrowth Rims from the Skaergaard Intrusion. Journal of Petrology, 50(1), 127-145.

Humphreys, M.C.S., Blundy, J.D., and Sparks, R.S.J. (2006) Magma Evolution and Open-System Processes at Shiveluch Volcano: Insights from Phenocryst Zoning. Journal of Petrology, 47(12), 2303-2334.

Huppert, H.E., and Sparks, R.S.J. (1988) The Generation of Granitic Magmas by Intrusion of Basalt into Continental Crust. Journal of Petrology, 29(3), 599-624.

Kocak, K., Zedef, V., and Kansun, G. (2011) Magma mixing/mingling in the Eocene Horoz (Nigde) granitoids, Central southern Turkey: evidence from mafic microgranular enclaves. Mineralogy and Petrology, 103(1-4), 149-167.

Lameyre, J., and Bonin, B. (1991) Granites in the main plutonic series. Elsevier.

Larsen, E.S. (1948) Batholith and associated rocks of Corona, Elsinore, and San Luis Rey Quadrangles, Southern California. Geological Society of America Memoirs, 29, 182.

Leon, W., Aleman, A., Torres, V., Rosell, W., and De La Cruz, O. (2007) Estratigrafía, sedimentología, y evolución tectónica de la cuenca de Pisco oriental. In S.E.y. Minas, Ed. serie D, Nº27. INGEMMET, Lima-Peru.

Mamani, M., Wörner, G., and Sempere, T. (2010) Geochemical variations in igneous rocks of the Central Andean orocline (13°S to 18°S): Tracing crustal thickening and magma generation through time and space. Geological Society of America Bulletin, 122(1-2), 162-182.

Memeti, V., Paterson, S., and Mundil, R. (2014) Day 4: Magmatic evolution of the Tuolumne Intrusive Complex. Field Guides, 34, 43-74.

Miyashiro, A. (1974) Volcanic rock series in island arcs and active continental margins. American Journal of Science, 274, 321-355.

Moore, N.D. (1979) The Geology and Geochronology of the Arequipa Segment of the Coastal Batholith of Peru. , Doctor of Philosophy, p. 549. Liverpool, London.

-. (1984) Potassium-Argon ages from the Arequipa Segment of the Coastal Batholith of Peru and their correlation with regional tectonic events. Journal of the Geological Society, 141(3), 511-519.

Mukasa, S.B. (1984) Comparative Lead Isotope Systematics and Zircon Uranium-Lead Geochronology for the Coastal, San Nicolas and Cordillera Blanca Batholiths, Peru. Geology. University of California, Santa Barbara.

Mukasa, S.B. (1986a) Common Pb isotopic compositions of the tima, Arequipa and Toquepala segments in the Coastal batholith, Peru: Implications for magmagenesis. Geochimica Et Cosmochimica Acta, 50, 771-782.

Mukasa, S.B. (1986b) Zircon U-Pb ages of super-units in the Coastal batholith, Peru: Implications for magmatic and tectonic processes. Geological Society of America Bulletin, 97(2), 241.

Myers, J.D. (1975) Cauldron subsidence and fluidization: mechanisms of intrusion of the Coastal Batholith of Peru into its own volcanic ejecta. Geological Society of America, 86, 1209-1220.

Nixon, G.T., and Pearce, T.H. (1987) Laser-interferometry study of oscillatory zoning in plagioclase: The record of magma mixing and phenocryst recycling in calc-alkaline magma chambers, Iztaccihuatl volcano, Mexico. American Mineralogist, 72, 1144-1162.

Paterson, S.R., and Miller, R.B. (1998) Stoped blocks in plutons: paleo-plumb bobs, viscometers, or chronometers? Journal of Structural Geology, 20(9–10), 1261-1272.

Peccerillo, A., and Taylor, S.R. (1976) Geochemistry of eocene calc-alkaline volcanic rocks from the Kastamonu area, Northern Turkey. Contributions to Mineralogy and Petrology, 58(1), 63-81.

Petford, N., and Atherton, M. (1996) Na-rich Partial Melts from Newly Underplated Basaltic Crust: the Cordillera Blanca Batholith, Peru. Journal of Petrology, 37(6), 1491-1521.

Pitcher, W.S., Atherton, M.P., Cobbing, E.J., and Beckinsale, R.D. (1985) Magmatism at a plate edge: the Peruvian Andes. Wiley.

Profeta, L., Ducea, M.N., Chapman, J.B., Paterson, S.R., Henriquez, S.M., Kirsch, M., Petrescu, L., and DeCelles, P.G. (2015) Quantifying crustal thickness over time in magmatic arcs. Scientific Reports, 5(17786), 7.

Sanchez-Fernandez, A.W. (1982) Edades Rb-Sr en los segmentos Arequipa-Toquepala del Batolito de la costa del Peru. Quinto Congreso Latinoamericano de Geologia, p. 487-504, Argentina.

Soler, P., and Bonhomme, M.G. (1990) Relation of magmatic activìty to plate dynamics in central Peru from Late Cretaceous to present. Geological Society of America, 173-192.

Soler, P., and Rotach-Toulhoat, N. (1990) Sr-Nd Isotope Compositions of Cenozoic Granitoids along a Traverse of the Central Peruvian Andes. Geological Journal, 25, 351-358.

Stewart, J.W., Evernden, J.F., and Snelling, N.J. (1974) Age Determinations from Andean Peru: A Reconnaissance Survey. Geological Society of America Bulletin, 85(7), 1107-1116.

Streckeisen, A.L. (1973) Classification and nomenclature recommended by the IUGS subcommission on the systematics of igneous rocks. Geotimes, 10, 26-31.

Troll, V.R., and Schmincke, H.-U. (2002) Magma Mixing and Crustal Recycling Recorded in Ternary Feldspar from Compositionally Zoned Peralkaline Ignimbrite 'A', Gran Canaria, Canary Islands. Journal of Petrology, 43(2), 243-270.

Turnbull, R.E. (2009) Mafic-felsic interaction in a high level magma chamber – the Halfmoon pluton, Stewart island, New Zealand: implications for understanding arc magmatism. 1-280.

Vernon, R.H. (2004) A practical guide to rock microstructure. 594 p. Cambridge University Press, New York.

Wiebe, R.A. (1993) Basaltic injections into floored silicic magma chambers. Eos, Transactions American Geophysical Union, 74(1), 1-3.

Wise, J. (2002) Examples of syntectonic emplacement instead of passive pluton emplacement in the Coastal Batholith of Peru and implications for Late Creataceous Nazca plate motions. Boletin de la Sociedad Geologica del Peru, 94, 99-106.

CHAPTER THREE

MAGMATIC RECYCLING DURING CONSTRUCTION OF A BATHOLITH: AN EXAMPLE FROM THE PERUVIAN COASTAL BATHOLITH

Introduction

Magmatic recycling is the result of physical and chemical processes when new magma batches incorporate and reuse older material that has been either completely solidified or not yet fully solidified. Recycling in magma chambers involves processes such as magmatic erosion (physical assimilation), transport of materials, and partial or complete chemical assimilation of older host rock or magma mush. Magmatic erosion can be defined as the breaking off of other units through physical assimilation (mechanical fragmentation). The mechanical fragmentation involves: thermal stress fracturing, release of stored elastic strain energy, explosive release of volatiles, melt-induced cracking, and anatectic disaggregation (Farris and Paterson, 2007).The process of fragmentation can contribute to magma contamination, and if it is continuous, might produce abundant xenocrysts. The chemical assimilation can be defined as the process of breaking old bonds and creating new chemical bonds in foreign minerals. The chemical assimilation can occur by melting or partial melting (contamination) of the xenolith, if the temperature of the magma is above that of the xenolith solidus and the overall bulk-composition of the magma is altered toward that of the xenolith. However, if the magma does not have the required physical or chemical properties to assimilate xenoliths, they will persist as unequilibrated relics.

Recycling during magma chamber construction is important because it can affect the evolving petrology of arc systems, their emplacement and thermal history, and estimates of magma addition rates when discussing "arc tempos" (Clarke, 2007; Lackey et al., 2008; Marsh, 1982a; Paterson et al., 2011). An important consequence is that host-rock fragments are incorporated into a magma chamber and, assimilation can occur by partial melting of the xenolith, thus affecting the composition of the magma (Bolhar et al., 2008; Clarke, 2007; Clarke et al., 1998; Dallai et al., 2003; Daly, 1903; DePaolo, 1981; Farris and Paterson, 2007; Furlong and Myers, 1985; Marsh, 1982b; Pignotta and Paterson, 2007).Through stoping, the xenoliths may increase the size of the pluton over the volume of magma introduced (Clarke et al., 1998). Similarly, if younger magma batches removed older material and recycle them into the younger magma, it would reduce the apparent volume of older batches. Thus, quantification of the true magmatic volumes must consider the amount of magmatically eroded and recycled materials involved in the evolution of the arc.

The evidence for recycling – that younger batches are not all new material added from the mantle – must be taken into account when calculating crustal growth curves and mass addition rates during arc construction. Stoping of host-rock fragments into the magma does facilitate magma ascent by vertical mass exchange and should be considered as one of a number of host rock displacement processes and an important mechanism for pluton emplacement (Burchardt et al., 2012; Dumond et al., 2005; Farris and Paterson, 2007; Furlong and Myers, 1985; Gagnevin et al., 2008; Marsh, 1982a; Miller and Miller, 2002; Paterson and Miller, 1998; Paterson et al., 2008; Pignotta and Paterson, 2007).

Thermal effects can be expected as the result of the incorporation of "cold" material (rock fragments) into the magma chamber.

The Peruvian Coastal Batholith (PCB), with its classic examples of multi-scale stoping and contamination represents an exceptional place to study magmatic recycling processes and their implications. Particularly, the Arequipa segment near the city of Ica provides a wide range of evidence for recycling of "host rock" in all the different units of the PCB (west to east) from the whole extent of each unit (north to south), and from the different parts of each magma chamber (top to bottom and edge to center). In the research area the plutons have mostly incorporated slightly older volcanic and plutonic materials. Therefore, the term "host rock" in this paper is used to refer to both older solid pre-emplacement host rock and earlier parts of the magmatic system that may or may not be completely crystallized.

The most important features that support recycling of rock materials are: (1) discordant and stepped contacts with no evidence of faulting, (2) truncation and missing portions of the wall rock along discordant intrusion margins, (3) large stoped blocks near contacts and smaller stoped blocks within plutons, (4) disturbance of magmatic fabrics by xenoliths, (5) mineral textures and compositional zoning in crystals due to transport and interaction of compositionally distinct magma batches by magma mixing, and (6) geochemical evidence of magma contamination (mixing-mingling) due to assimilation of xenoliths. In this paper, the evidence for magma mixing and recycling processes is used to establish their types and magnitudes in plutons from the Arequipa segment of the Peruvian Coastal Batholith (PCB) during magmatic events with ages ranging from 131 to 78 Ma.

Field Data

The northern area of the Arequipa segment displays evidence for widespread magmatic recycling of older volcanic and plutonic units into younger magmatic pulses and mingling with mafic magma injections as well. Evidence for magmatic recycling is identified from kilometer-scale cauldron subsidence to meter-scale stoping of xenoliths resulting in blocks of host rock in younger plutonic phases and disaggregation of xenoliths. Based on these scales, recycling can be characterized by a sequence of events from breaking off of large blocks, incorporation and transport of xenoliths and assimilation and contamination at the elemental level. The geochemical mixing/contamination will be described in a later section. The following section qualitatively describes the stages of magmatic recycling, summarizes the distribution of these recycling features in the Ica area, and estimates the amount of magmatic recycling.

Qualitative Description of Recycling Evidence

Large kilometer and meter scale angular xenoliths with minimal evidence of transport and assimilation or digested edges are formed by cauldron subsidence. Small centimeter scale and rounded xenoliths with digested edges display more transport and/or partial melting and the adding of chemical contamination to the magma. Figure 44 provides a map showing the location of the major recycling features. Fieldwork observations seem to suggest that general recycling trends and the stages of magmatic recycling are associated. The evidence is categorized as (1) major with 16-70% density of xenoliths, (2) intermediate with 4-16% density, (3) minor with 1-4%, and (4) none

with less than 1%. In the next section the major localities and general recycling trends are described and displayed in pictures and diagrams.

Pluton roofs with stepped margins and large blocks enclosed by younger plutonic phases suggest major recycling due to cauldron subsidence. Spectacular examples can be seen at the mouth of Quebrada Larga (Figure 45), the mouth of Quebrada La Mina along the Rio Ica (Figure 46), and in the La Esquina area along the Rio Pisco (Figure 47).

In the Quebrada Larga area Humay monzodiorite magma has been intruded into the volcanic host rock forming sharp stepped contacts at the roof on a scale of tens to hundreds of meters (Figure 45). The volcanic host rock layering dips toward the pluton suggesting the complete separation of host rock into the magma chamber, rather than host rock uplift. In a few locations at the roof, concordant sill and discordant dike geometries are observed (Figure 48).

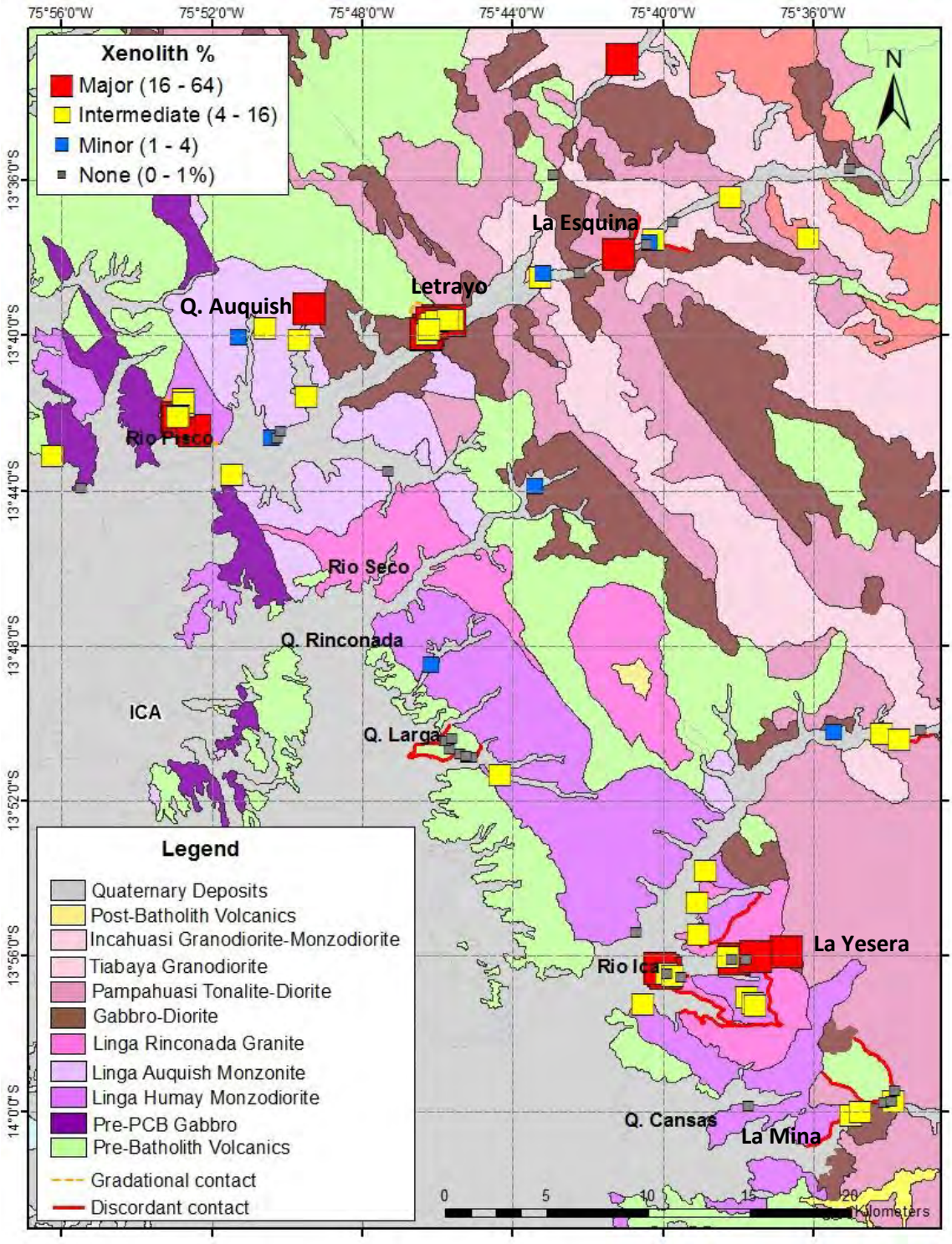

Figure 44. Map of recycling features showing the density and distribution of xenoliths.

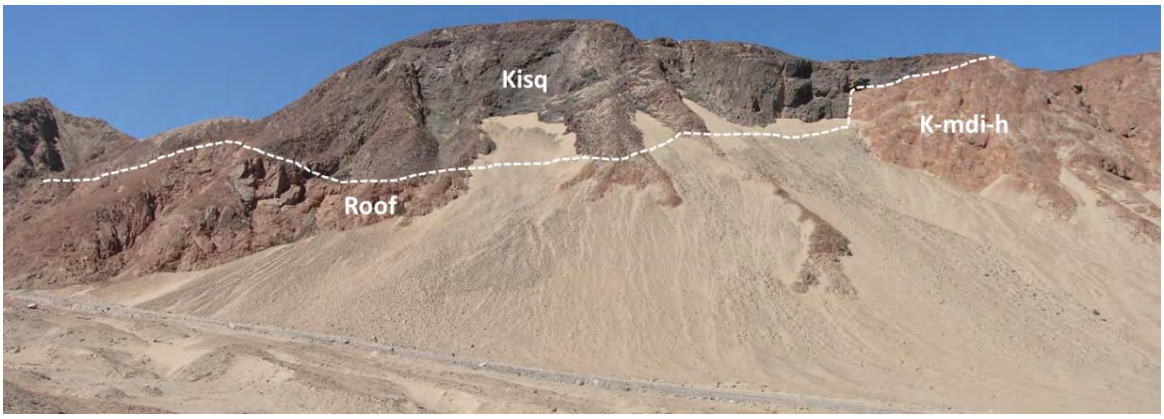

Figure 45. Stop 13903F. Sharp contact of the plutonic rocks with the volcanic host rock characterized by subhorizontal roof contacts, sharp corners, and steep walls. Linga Humay monzodiorite (K-mdi-h) and Quilmana volcaniclastic (Kisq).

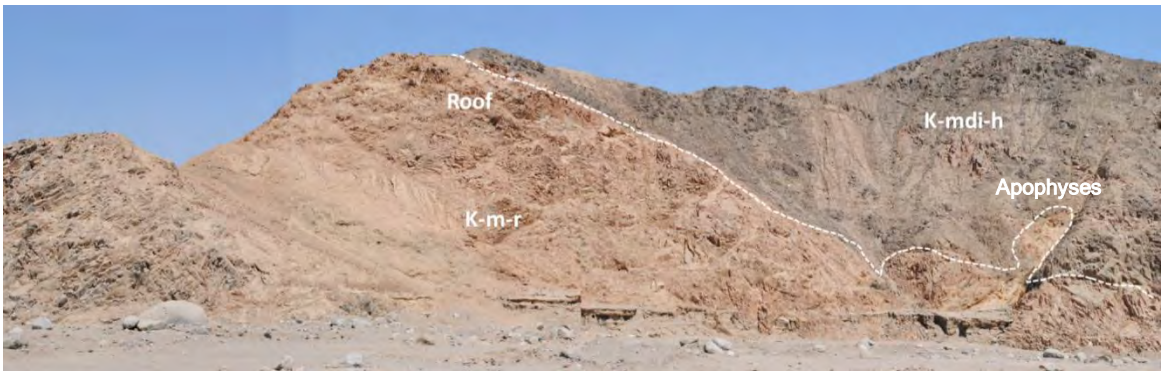

Figure 46. Stop 13830D. Pluton roof characterized by sharp and steep contacts. Rinconada monzonite (K-m-r) and Humay monzodiorite (K-mdi-h).

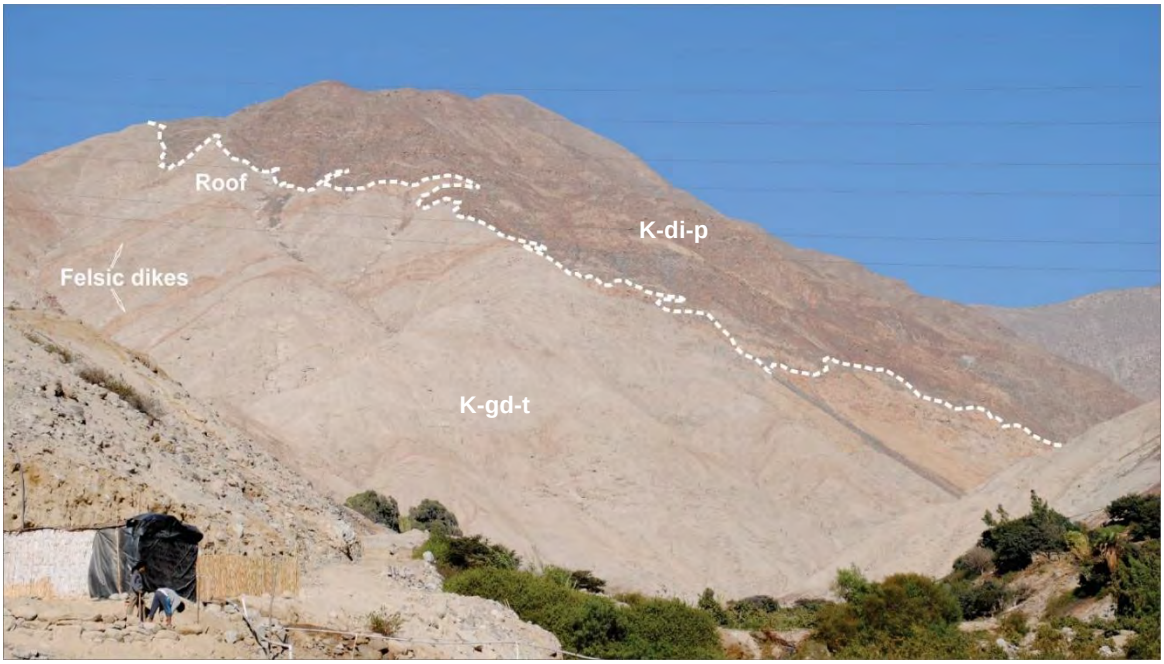

Figure 47. Stop 12717H. View from Rio Pisco canyon toward the western part of the Tiabaya pluton exposed in the La Esquina area. The exposed thickness of the pluton in this section is around 400 m. The contact is characterized by a sub-horizontal roof, steps, apophyses, cuspate indentations, dikes, and stoped blocks. Mafic rocks correspond to the Pampahuasi pluton.

Figure 48. Stop 13903C. Sharp contact between Humay monzodiorite (K-mdi-h) and Quilmana volcaniclastics (Kisq). Injections of monzodiorite into the volcanic roof rocks are a combination of sill and dike geometries.

Cauldron Subsidence and Stoping

Near the mouth of Rio Ica towards the east end of the Quebrada La Mina the roof of the Rinconada granite appears to be in contact with the Humay mozodiorite. This area is characterized by vertical ring dikes of the Rinconada granite, tabular plutons of the Humay monzodiorite, and abundant stoping with subangular and subrounded xenoliths of monzodiorite, gabbro and porphyritic andesite. The steep walls and spatial association of the ring dikes and tabular plutons suggest that the plutons in this area were emplaced mainly by the mechanism of cauldron subsidence where stoping and recycling mechanisms can be expected.

In the La Esquina area along the Rio Pisco, the Tiabaya granodiorite intrudes the Pampahuasi pluton forming a roof grading laterally into a wall chamber (Figure 49a). In roof zones of this pluton, large meter to centimeter scale subangular xenoliths surrounded by a network of granodioritic veins and dikes associated with intrusion of the Tiabaya granodiorite are observed at several places (Figure 49b).

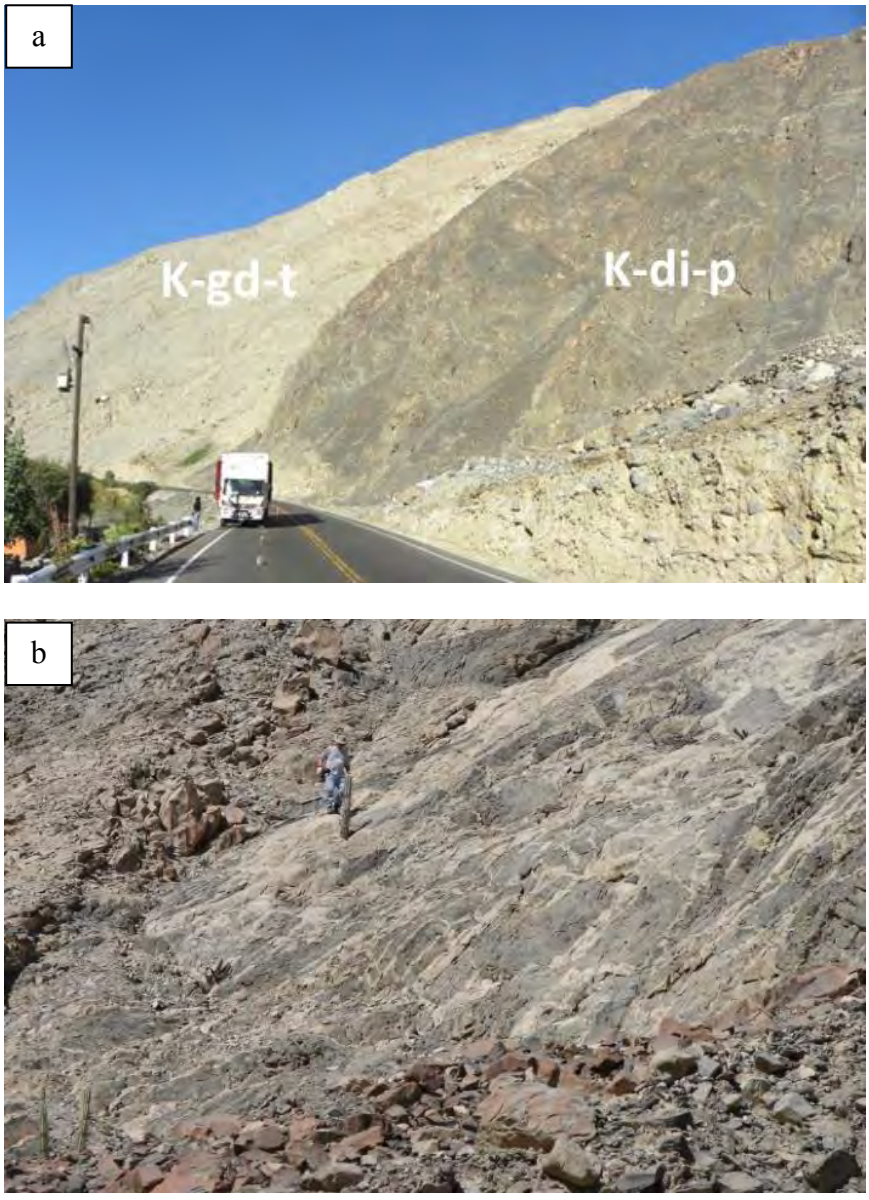

Figure 49. (a) Stop 12717F. Pluton roof and wall zone between Pampahausi diorite (K-di-p) and Tiabaya granodiorite (K-gd-t). (b) Stop 14711B. Sharp internal contacts characterized by a network of granodioritic veins of Tiabaya and large stoped blocks of Pampahuasi quartz-diorite with very angular shapes.

Discordant subhorizontal contacts and stepped margins, weak metamorphic aureoles, and the lack of distortion and ductile deformation in the host rocks are compatible with the removal of host blocks into the magma chamber (Figure 48).

Xenolith Distribution

Figure 44 shows the distribution and density of volcaniclastic and plutonic xenoliths in the Ica area. Areas with a high density of xenoliths are associated with the initial stage of breakdown of country rock and display minimal transport near roof/wall zones of pluton. An intermediate to low density of xenoliths with more subrounded and rounded shapes suggesting more transport and assimilation of the recycled materials are observed within the plutons.

Many localities with a high density of volcanic xenoliths are not horizontally close to volcanic outcrops, suggesting that they must be vertically close to volcanic country rock above the magma chamber. High densities of volcanic xenoliths are found in the Monte Sierpe area, at the north end of the Quebrada Auquish, and at Letrayo along the Rio Pisco. In the Monte Sierpe area ubiquitous volcanic xenoliths with centimeter scale and subrounded to subangular shapes in the Humay monzodiorite are common recycling features. At the north end of Quebrada Auquish, one can drive a vertical kilometer from the Auquish monzonite into the overlying Quilmana volcanics from fairly homogeneous Auquish to ubiquitous volcanic xenoliths that are smaller and more rounded with increasing distance from the roof. At the Letrayo area large and subangular to subrounded volcanic xenoliths are observed in the Pampahuasi pluton. These three described localities display the complex interplay of plutonic intrusion and volcanic host

rock near the roof and the resulting movement and accumulation of xenoliths into the magma chamber beneath.

Localities with high densities of gabbro and older PCB plutonic xenoliths are commonly found along the edge of plutons in the El Encanto area along the Rio Pisco and in the Quebrada la Mina and Quebrada la Yesera along the Rio Ica. In the El Encanto area as described previously large scale of stoping associated with intense diking near the pluton roof and wall zone was observed (Figure 49b). In the Quebrada la Mina subangular to rounded xenoliths of volcanics, gabbros, and Humay mozodiorite are stoped into the Rinconada granite and the stoping in this area is mainly controlled by the cauldron subsidence mechanism. In Quebrada La Yesera angular to subangular xenoliths of Pampahuasi diorite and rounded to subrounded xenoliths of Linga Humay monzodiorite and gabbro are stoped into Linga Rinconada dikes/conduits (Figure 50). In this area several populations of xenoliths are distinguished suggesting magmatic recycling from several plutons.

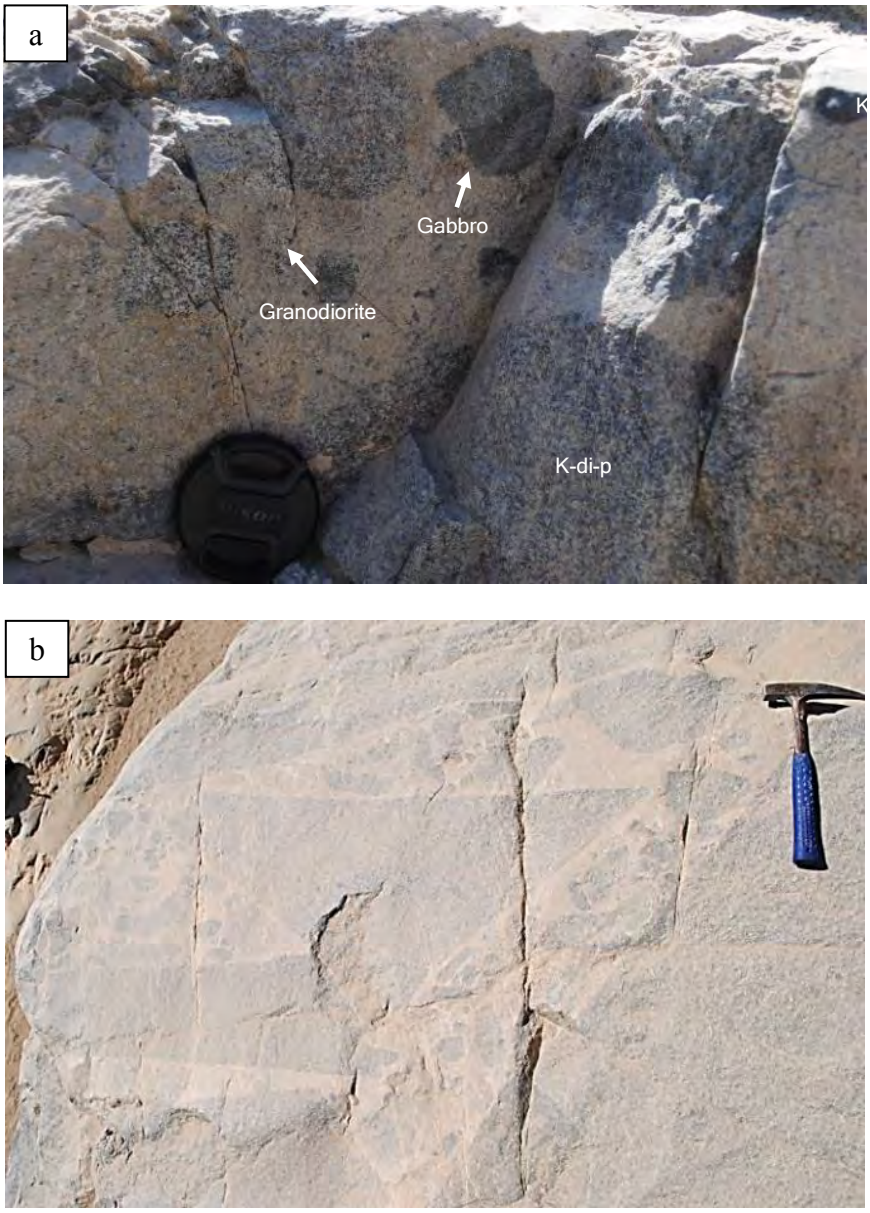

Figure 50. Internal discordant contact zone. Pampahuasi quartz-diorite (K-di-p) is intruded by Linga Rinconada granitic dikes (K-m-r). (a) Populations of xenoliths, especially noting changes in texture and composition. (b) Granitic magma engulfing subrounded to angular xenoliths. Note that some of the angular xenoliths of Pampahuasi quartz-diorite seem to be rotated.

The density of xenoliths in the research area suggest that a trend is observed in the distribution where large subangular centimeter to meter-scale host-rock xenoliths occur near pluton roof/wall zones and centimeter-scale rounded to subrounded xenoliths are observed mainly within plutons (Figure 44). Therefore, the distribution and preservation of the xenoliths in the plutons seems to be mainly controlled by the distance from pluton margins (roof/walls).

Xenolith Formation Models

Fieldwork data for xenolith distribution and morphologies as well as diking is presented to identify the model for xenolith formation in the Ica area. The El Encanto and Quebrada la Yesera areas are the two prime localities near roof contact zones that are presented as examples to discuss the evidence for xenolith formation.

In the El Encanto area along the Rio Pisco major diking can be seen at the walls and roof of the plutons and spectacular diking and stoping is observed (Figure 49b and 52). Granodioritic dikes associated with the Tiabaya pluton intruded and broke apart meter-scale rock fragments of Pampahuasi diorite-tonalite resulting in various sizes and orientations with no evidence of ductile deformation. The angular to subangular xenoliths are rotated within the felsic magma. Several xenoliths near the pluton roof have been preserved at various stages of separation from the host-rock walls indicating complete separation from the walls as well (Figure 512a-b). A detailed examination of these pieces could allow one to reassemble the xenoliths using matching boundary features. The breaking off and movement of xenoliths possibly began during magma injection and thermal expansion cracking at shallow levels (Roy et al., 2012).

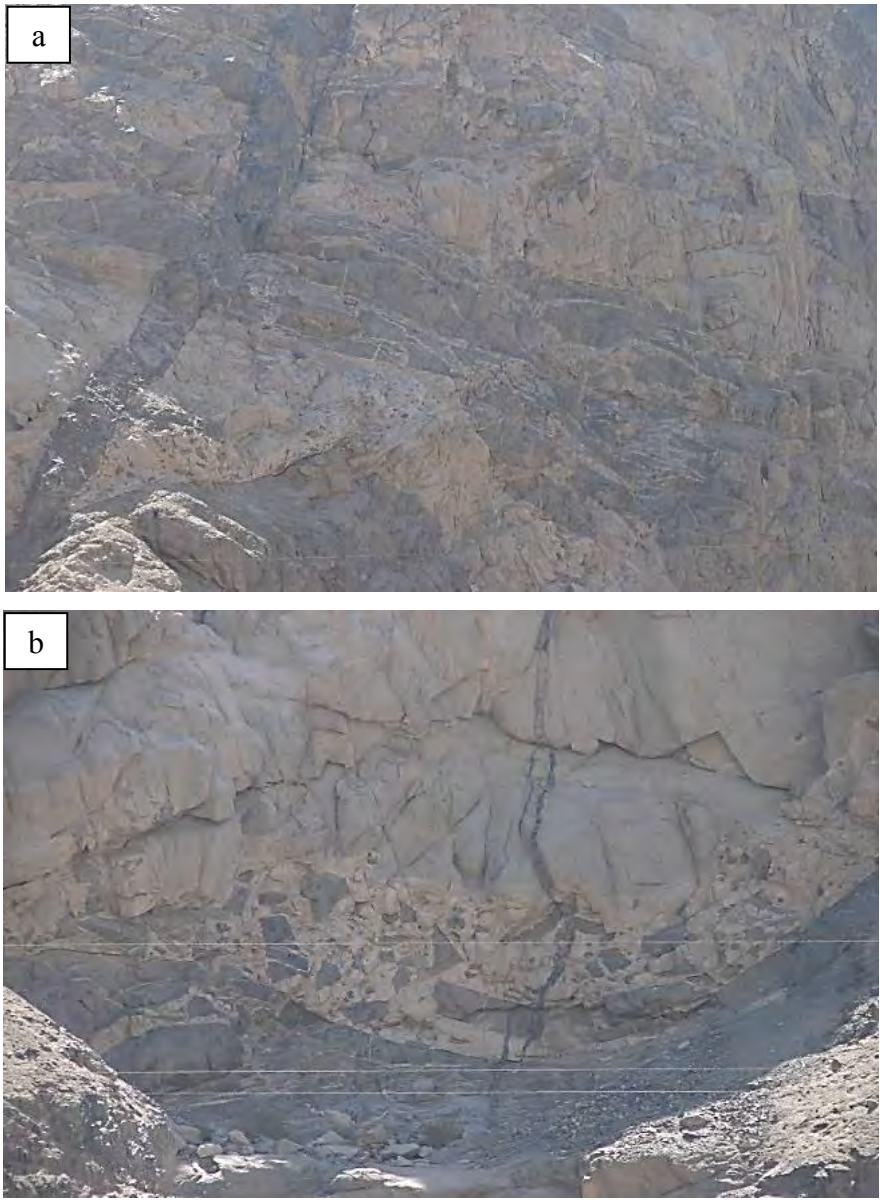

Figure 51. Tiabaya intrusive event in Pampahuasi. Close to pluton roof, large stoped blocks at different stages and mafic dikes. Tiabaya diking results in fragmentation and transport of large stoped blocks from Pampahuasi quartz-diorite. Mafic dikes and xenoliths with triangular and rectangular shapes are observed in pictures (a) and (b).

In the Quebrada la Yesera area dikes of Rinconada granite intruded Pampahuasi tonalite pluton. The diking provides evidence of ductile deformation and rectangular and triangular rock fragments of the Pampahuasi tonalite that intruded into the Rinconada granite can be fit together if rotated into the right orientation (Figure 51b). The mechanism that could produce the breaking off of blocks in this situation is possibly cracking and melt intrusion by channelized magma flow suggested by Paterson et al. (2012). This model suggests the production of (1) fine-grained veins with diffuse margins and tips which dissipate into the host rock and (2) multiple magma pulses intruding into a rectangular and/or triangular network of cracks. However, that model is more appropriate for deeper crustal level processes and it is necessary to explore with more detail the complexity in this outcrop since there is evidence for the two models presented.

Most of the diking and resulting xenoliths observed in the research area can be explained by the mechanism of thermal expansion cracking. However, the model of cracking and melt intrusion by channelized magma flow model plays a part, although not a major role in forming xenoliths.

Xenolith Disaggregation and Magma Mixing

Xenolith compositions, size, shape, and type of margins in the research area provide information about magmatic recycling processes. These recycling features can be the result of magma transport and mixing processes that affected the xenoliths in the magma chamber.

The morphology and size of the xenoliths seems to be linked to their settling in specific areas in the magma chamber. Smaller xenoliths from centimeter to decimeter

scales generally occur in clusters throughout the pluton, do not fit together, have rounded and subrounded shapes and digested edges. On the other hand, large meter scale xenoliths with angular to subrounded margins occur along the pluton margins close to roof and wall zones. The smaller xenoliths have a range of compositions and orientations that provide evidence that the xenoliths after forming have been rotated and transported by magma flow for some distance in the magmatic host. The rounded shape of centimeter scale xenoliths might be the result of abrasion during transport and/or partial melting. A different situation is represented by large xenoliths that could be reassembled using matching boundaries and these are interpreted as involving breakdown and little rotation or transport.

In terms of margin types, either sharp or digested, some clues can be inferred for understanding the recycling processes. Diffuse digested margins on some xenolith contacts indicate that at least parts of the xenolith have been totally digested and removed by chemical mixing. On the other hand, xenoliths with sharp margins suggest that mingling has occurred, but that recycling to the level of chemical mixing is minimal.

Quantification of Recycling

To estimate volume percent of xenoliths at the outcrop-scale, field observations in notes and pictures were surveyed. Where outcrop-scale contamination material was observed, it is made up of volcanic and plutonic xenoliths. Therefore, the quantification of the contamination presented in this section is biased by the natural predominance of outcrop exposures observed.

Pre-PCB volcanic xenoliths make up almost 20% of the Auquish monzonite unit and the other units contain about 10% or less. PCB plutonic xenoliths make up almost 20% of the Rinconada granite unit and the other units contain about 5%. Based on field observations we estimate that where recycled material was observed it made up 20-40% of the rock with the greatest percentage in the Auquish, Rinconada, and Tiabaya plutons. Although, perhaps three-fourths of the plutons were not observed due to poor exposures or difficult access, half of the remainder contained recycled material and the other half was fairly homogeneous. The homogeneity observed in the outcrops could mean either no recycling or a very efficient mixing and assimilation process of the recycled materials. If recycling percentages are obtained from map features like the ring complex area at the mouth of Rio Ica and compared to the fieldwork observations, the amount of recycling suggested seems to agree in general. Thus over the entire Linga and Tiabaya plutons we estimate that 10-20% is recycled material and this material in general was located close to the walls and roof of these plutons.

Petrographic Data

Information about magmatic recycling processes comes from the petrographic analysis of 124 thin sections from the PCB units that display contact relationships, textural and compositional features from xenoliths and their respective contact relationships with the granitic host magma, and plutonic host rock single mineral textures. Recycling/mixing features discussed in this section are: xenoliths, crystal capture during injections of magma batches, reaction rims and resorbed mineral cores due to disequilibrium conditions.

Xenoliths

Petrographic analysis of xenoliths indicate that they are porphyritic andesitic basalt from the Quilmana volcanics, clinopyroxene-hornblende gabbro and diorite from the Gabbro plutons, and monzodiorite from the Humay unit (Figure 52). Thin sections of the xenoliths and the rock units were compared in order to accurately classify the rock unit.

Felsic reaction rims dominated by quartz crystals were observed at the boundary of some volcanic xenoliths in the Auquish monzonite and in the Humay monzodiorite. The presence of reaction rims for the xenoliths might imply that locally the process of xenolith-magma interaction involved partial melting of the xenoliths resulting in chemical mixing. Large temperature gradient between xenolith and magma and longer residence time would result in more mechanical abrasion due to transport and more partial melting in the magma chamber. This would affect the intensity of mingling and mixing between the xenolith and host rock.

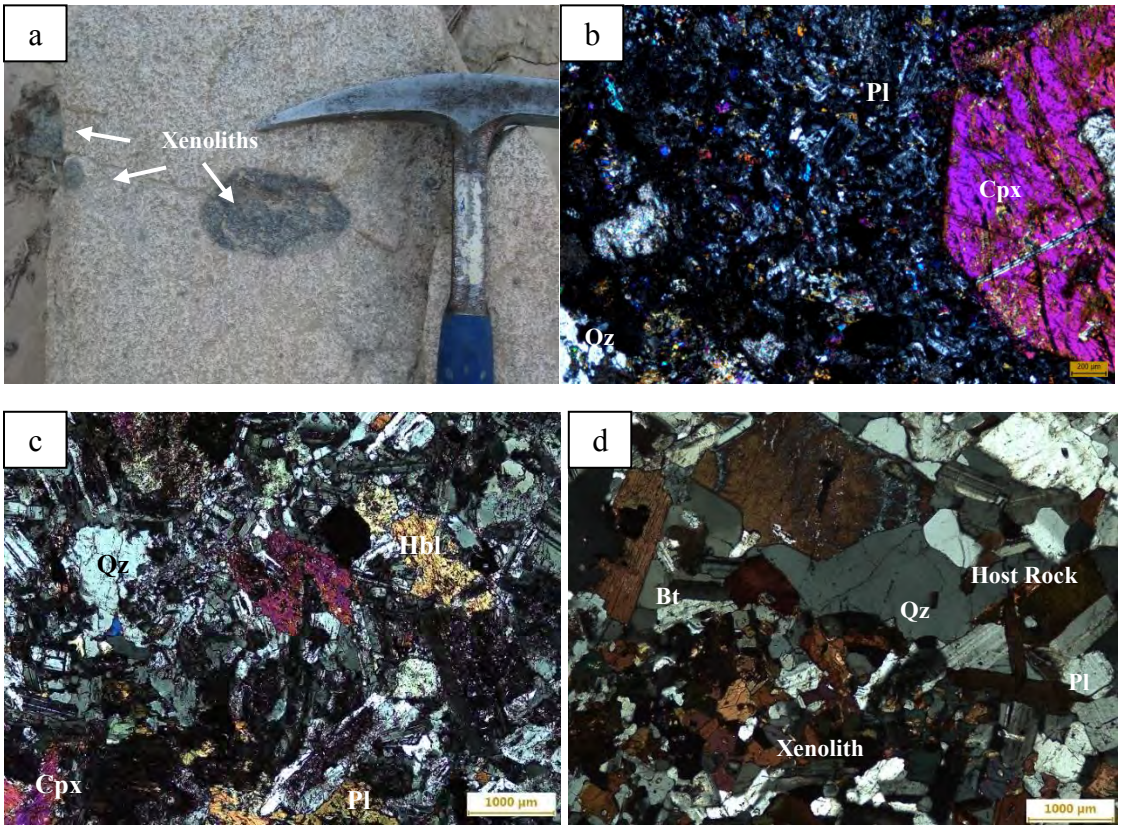

Figure 52. Xenolith types. (a) Volcaninc xenoliths in Humay monzodiorite with sevaral sizes. (b) Quilmana volcanic porphyritic xenolith with abundant plagioclase and clinopyroxene crystals in Humay monzodiorite. (c) Gabbro xenolith in Auquish monzonite. (d) Humay monzodiorite xenolith (bottom) in Rinconada granite host rock (top). Qz-quartz; Pl-plagioclase; Hbl-hornblende; Bt-biotite; Cpx-clinopyroxene.

Mineral Textures of Plutonic Host Rocks

Evidence of magma chamber processes, including magma recycling and contamination events, can be derived from single mineral textures (Anderson, 1984; Hattori and Sato, 1996; Hibbard, 1995; Nixon and Pearce, 1987; Troll and Schmincke, 2002; Vernon, 2004). Magma mixing textures in single minerals are interpreted as the result of injections of new magma that recycle crystals that have already started forming in the magma chamber or crystals that are the result of assimilation and partial melting of recycled xenoliths. The exchange of crystals and their resorption and overgrowth are records of the recycling process.

A good example of a texture that records changes in the magma chamber is the zoning pattern observed in plagioclase crystals. The zoning represents the chemical composition of the crystal, and thus the record of the crystallization history of the plutonic rock. Plagioclase is the most abundant crystal in samples collected from the PCB units and with a wide range of zoning textures from simple to complex. Simple normal zoning goes from Ca-rich plagioclase core to Na-rich plagioclase rim and simple reverse zoning goes in the opposite trend. The complex zoning is used in this paper to refers to a pattern that is characterized by a combination of oscillatory and truncated/patchy zoning (Phemister, 1934). Oscillatory zoning in plagioclase crystals is attributed to disequilibrium processes related to growth-induced compositional gradients in melt adjacent to a crystal interface, whereas major compositional hiatuses require sudden large changes in physical conditions (Nixon and Pearce, 1987). Truncated/patchy zoning is characterized by major compositional hiatuses, i.e., an abrupt change at a "truncating boundary" from a relatively calcic to a more sodic plagioclase (Figure 53a). This

microtexture has also been interpreted to form as the result of pressure reduction associated with the ascent of magma within the crust causing resorption of crystals. Calcic zones in plagioclase crystals are shown in Figure 53b. A calcic zone is defined as abrupt (step) zoning to a more calcic plagioclase zone due to the mixing of more mafic magma with crystal-bearing felsic magma. Each calcic zone is possibly the result of a new batch of magma from depth being fed into a pre-existing magma chamber.

The quantification of the types of zoning in the plagioclase crystals in thin section was performed by point counting. Crystals with simple normal zoning are dominant in the older units but crystal with complex zoning are abundant in younger units (Figure 54). In the older plutons simple normal zoning ranges from 70% to 50% and from 40% to 30% in the younger plutons. On the other hand, complex zoning goes from 60% to 30% in the older plutons and from 70% to 60% in the younger plutons.

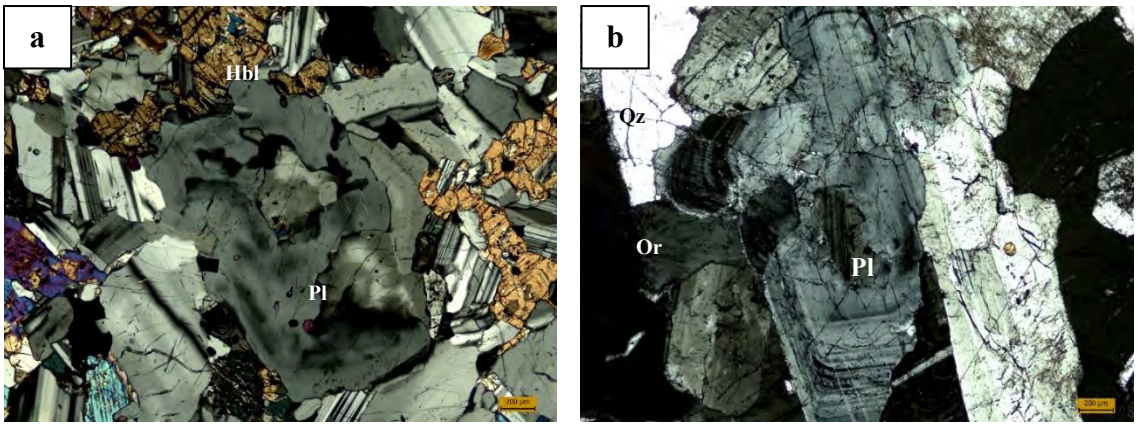

Figure 53. Microphotographs of microtextures that could be associated with magmatic recycling events as observed in plagioclase crystals (cross-polarized light, scale bar=200 μm). Truncated growth zoning textures: (a) Sample 12717C from Pampahuasi quartz-diorite. (b) Sample 12717H from Tiabaya granodiorite. Qz-quartz; Pl-plagioclase; Or-orthoclase; Hbl-hornblende.

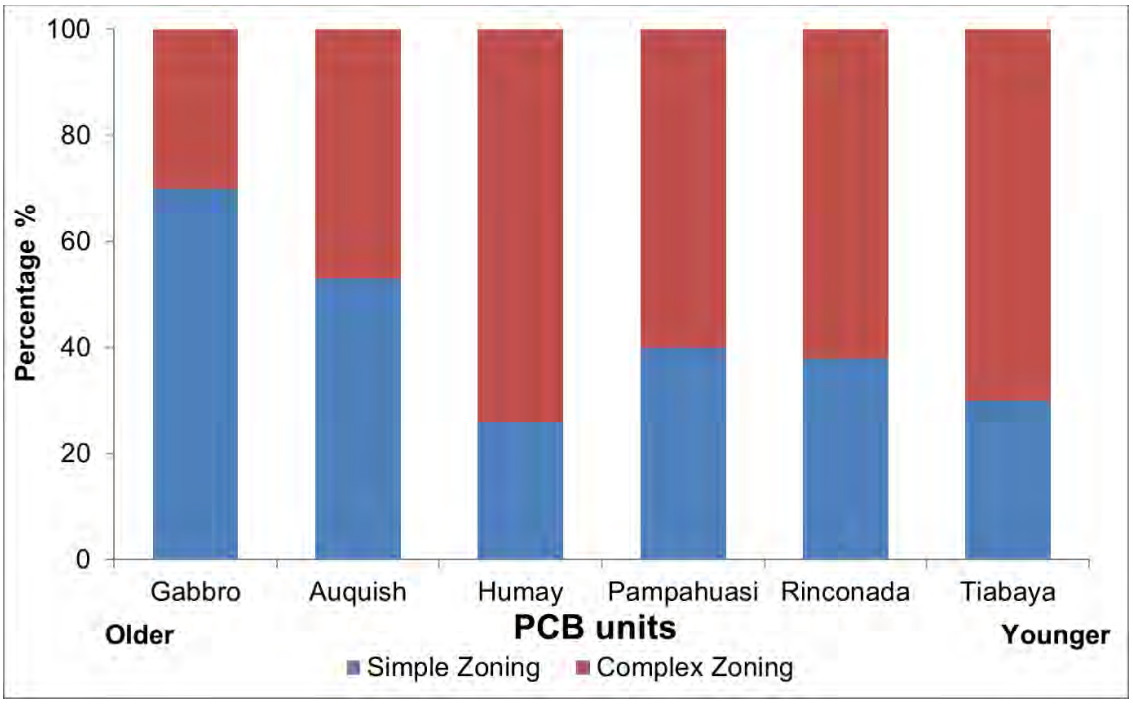

Figure 54. Histogram for Ica-Pisco plutons in which plagioclase textures are found. Note the trend of increasing complexity as units get younger. The gabbro samples do not include those associated with the Pampahuasi plutons and the gabbro refers to the Pre PCB gabbro plutons.

The interpretation is that the intensity of the plagioclase complex zoning is consistent with the intensity of the magmatic recycling/mixing process. Pre-PCB gabbros have the lowest density of plagioclase with 30% of complex zoning and Tiabaya granites and Humay monzogabbros and monzodiorites have the highest density with ≥ 70% of complex zoning density in. If Humay is considered a special case, it seems to be a trend in the density of mixing/recycling textures for increasing in the younger magmatic events (Figure 54). The high complex zoning in the Humay monzogabbros and monzodiorite is interpreted as a result of magmatic hybridization by intense interaction between mafic and felsic injections.

Other internal textural features observed in plagioclase crystals indicative of recycling/mixing processes are corroded rims and sieve textures. Corroded or resorbed rims in plagioclase crystals are illustrated in Figure 55a and are considered to be the result of an injection of hotter, more juvenile magma into a cooling and crystallizing magma chamber (Winter, 2010). Sieve texture in plagioclase crystals as illustrated in Figure 55b is defined as a crystal of plagioclase with inclusions of other minerals. It may be formed if a plagioclase crystal is injected into a magma where it is not in equilibrium. Then the crystal will become corroded, and the melt will penetrate into the crystal structure. Many sieve textures and internal zones of patchy extinction can be explained as the result of dissolution processes as well (Nixon and Pearce, 1987).

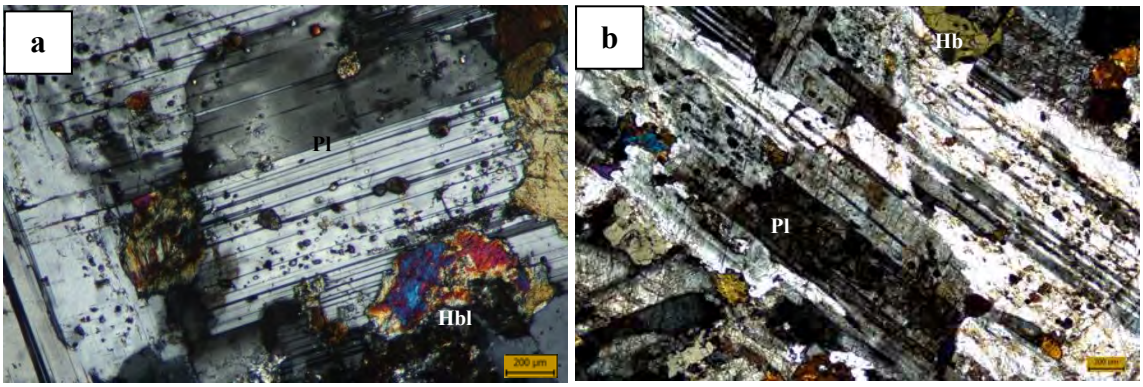

Figure 55. Microphotographs of microtextures associated with magmatic recycling observed in plagioclase crystals (cross-polarized light, scale bar=200 μm). Sieve textures in plagioclase crystals from Humay monzodiorite: (a) Sample 10714H. (b) Sample 12724E. Qz-quartz; Pl-plagioclase; Hbl-hornblende.

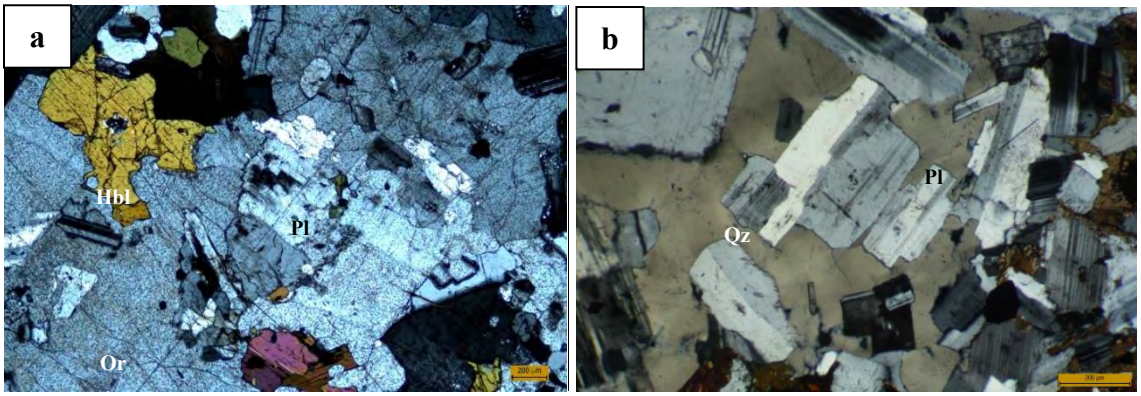

Figure 56. Poikilitic textures in tonalites of the Pampahuasi plutons: (a) Sample 12722E with poikilitic alkali feldspar texture enclosing resorbed plagioclase and hornblende crystals. (b) Sample 10714P with poikilitc quartz texture. Qz-quartz; Pl-plagioclase; Or-orthoclase; Hbl-hornblende.

Microtextures associated with disequilibrium processes in other minerals are poikilitic textures in quartz or K-feldspar, ocellar quartz ovoids mantled by hornblende and/or biotite crystals, and acicular apatite crystals. Poikilitic textures in quartz or K-feldspar are described as numerous randomly oriented crystals which are completely enclosed within a large, optically continuous crystal of a different composition. This microtexture represents a late-stage crystallization of felsic melt after crystallization. Since the more felsic system is reheated, large crystals of quartz and/or K-feldspar include the earlier small crystals (Figure 56).

Recycling and Mixing

Textural features discussed in this section could be explained by magmatic recycling and mixing processes. Some of these microtextures could be explained either as evidence for mafic and felsic recharge or magmatic recycling in the magma chamber(s). The evidence from plagioclase microtextures specially the zoning patterns might indicate a complex history of recycling due to multiple magma influxes and evidence of magmatic circulation in a compositionally zoned magma reservoir (Anderson, 1984; Troll and Schmincke, 2002).

Geochemical Data

A large new whole rock geochemical data set of major and trace elements from 113 samples and Sr, Nd, and Pb isotopes from 40 samples of the PCB, Cretaceous volcanic cover, and basement rocks are presented in this section. Nine new U-Pb zircon ages from PCB plutons are included as well.

Major and Trace Element Data

In Figures 57 Harker plots are characterized by a strong negative correlation of SiO_2 with compatible elements such CaO and MgO, kink and break patterns observed especially in the TiO_2 plot, and a large spread in the data. Since the data are spread out, it is not clear whether these patterns are mostly fractionation (normally curved trends) or mixing (normally straighter trends). The Harker diagrams seem to indicate that the fractionation trends have been spread out by mechanical and chemical transfer between magmas of different compositions. The combination of scatter and linear data trends is in agreement with magma mixing and contamination.

The alumina plot in Figure 57c and the alumina saturation index diagram in Figure 58 shows that Tiabaya in general has higher alumina and molecular A/CNK ratios than the other units suggesting that the granodiorites incorporated more sediments and volcaniclastic cover than the other units. The molecular A/CNK ratios are in the range 0.70 - 1.0 which is characteristic of hybrid continental-arc granitoids (Barbarin, 1990).

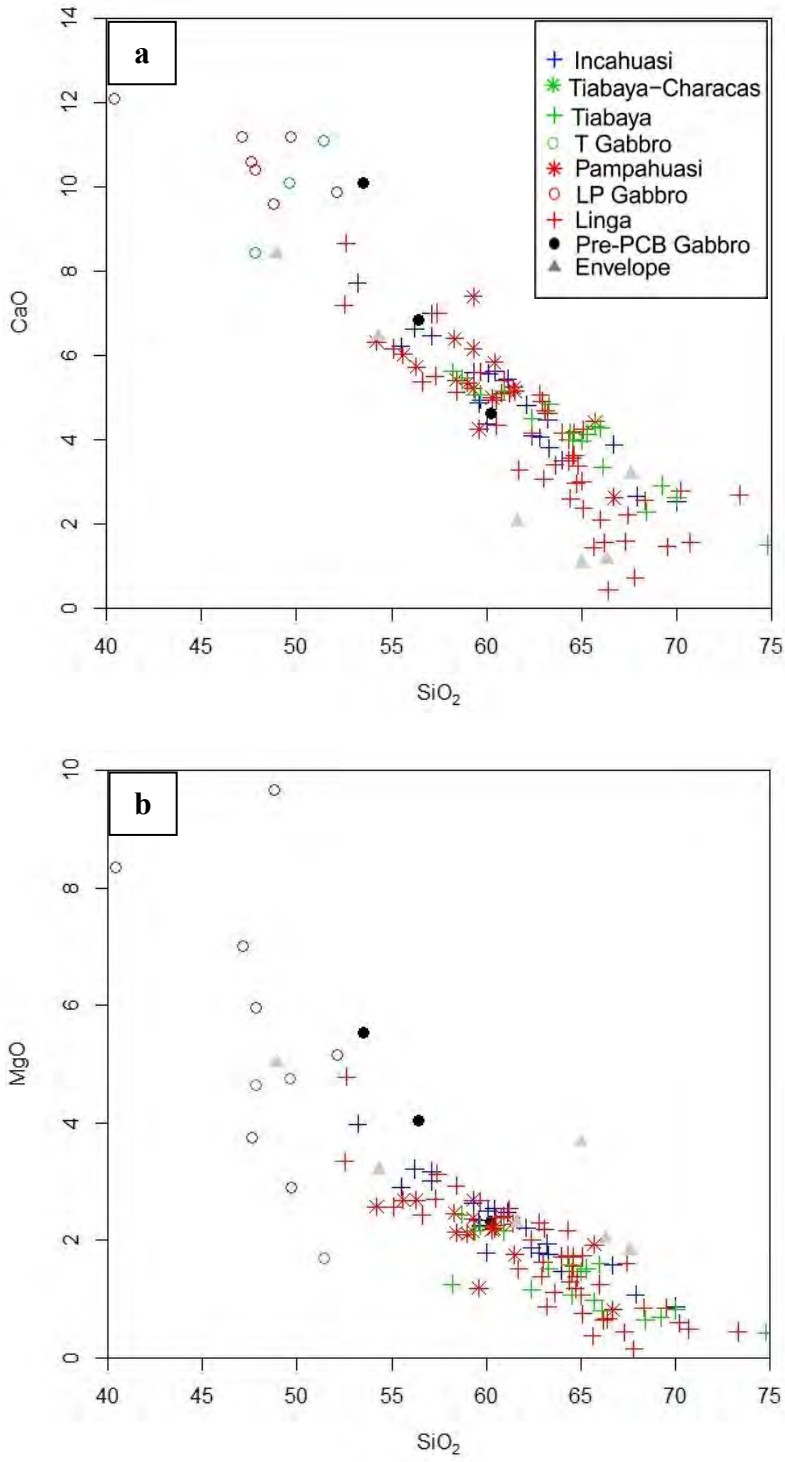

Figure 57. Harker diagrams of selected major elements for the granitic rocks. Note in (a) CaO vs. SiO2 wt% and (b) MgO vs. SiO2wt% the straight line patterns. Straight line patterns are produced by mixing in oxide-oxide bivariate plots using compatible (CaO and MgO) vs. incompatible (SiO_2) elements.

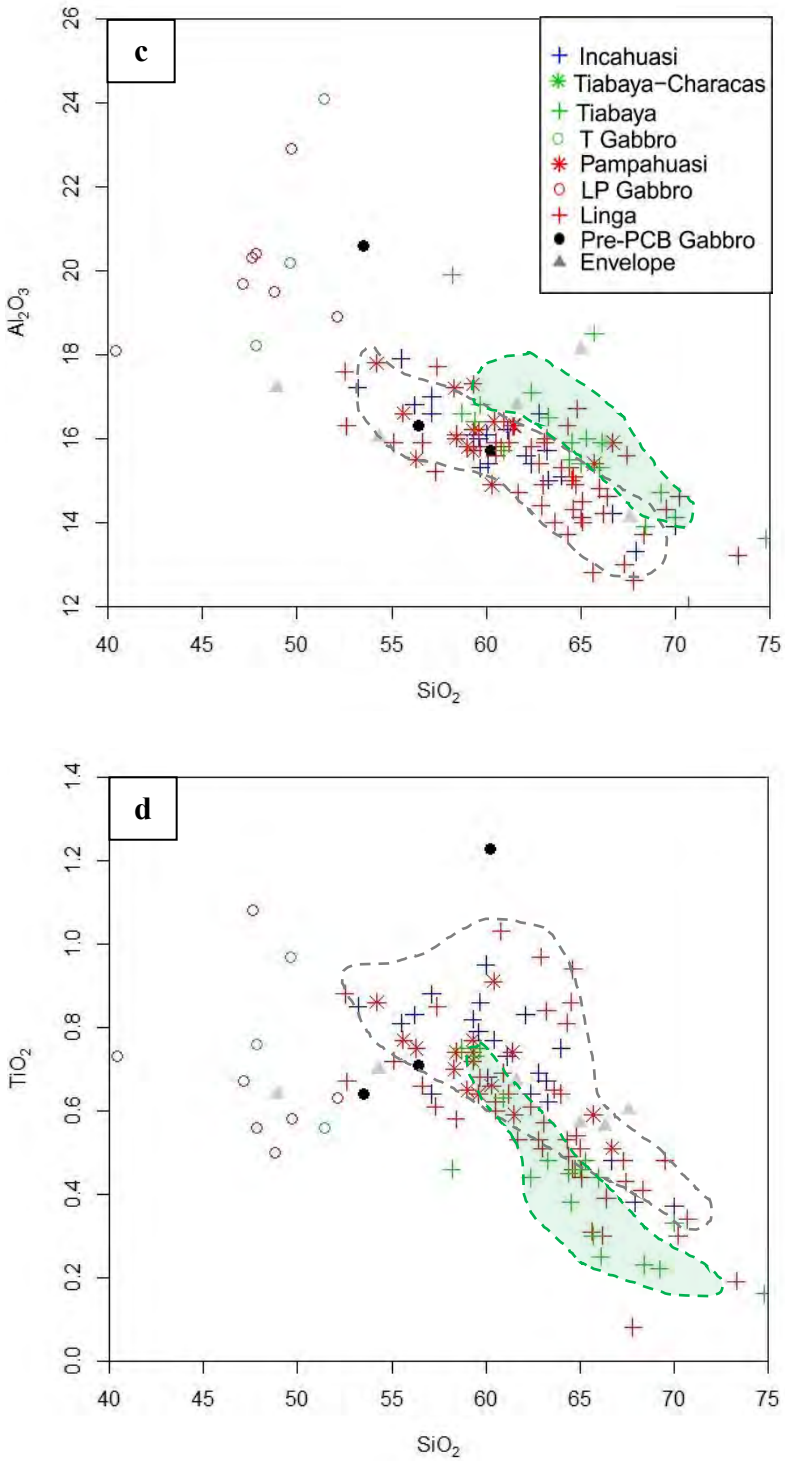

Figure 57. Harker diagrams of selected major elements for the granitic rocks. Note in (c) and (d) that Linga, Pampahuasi, and Incahuasi rocks show similar patterns but Tiabaya has a separate trend.

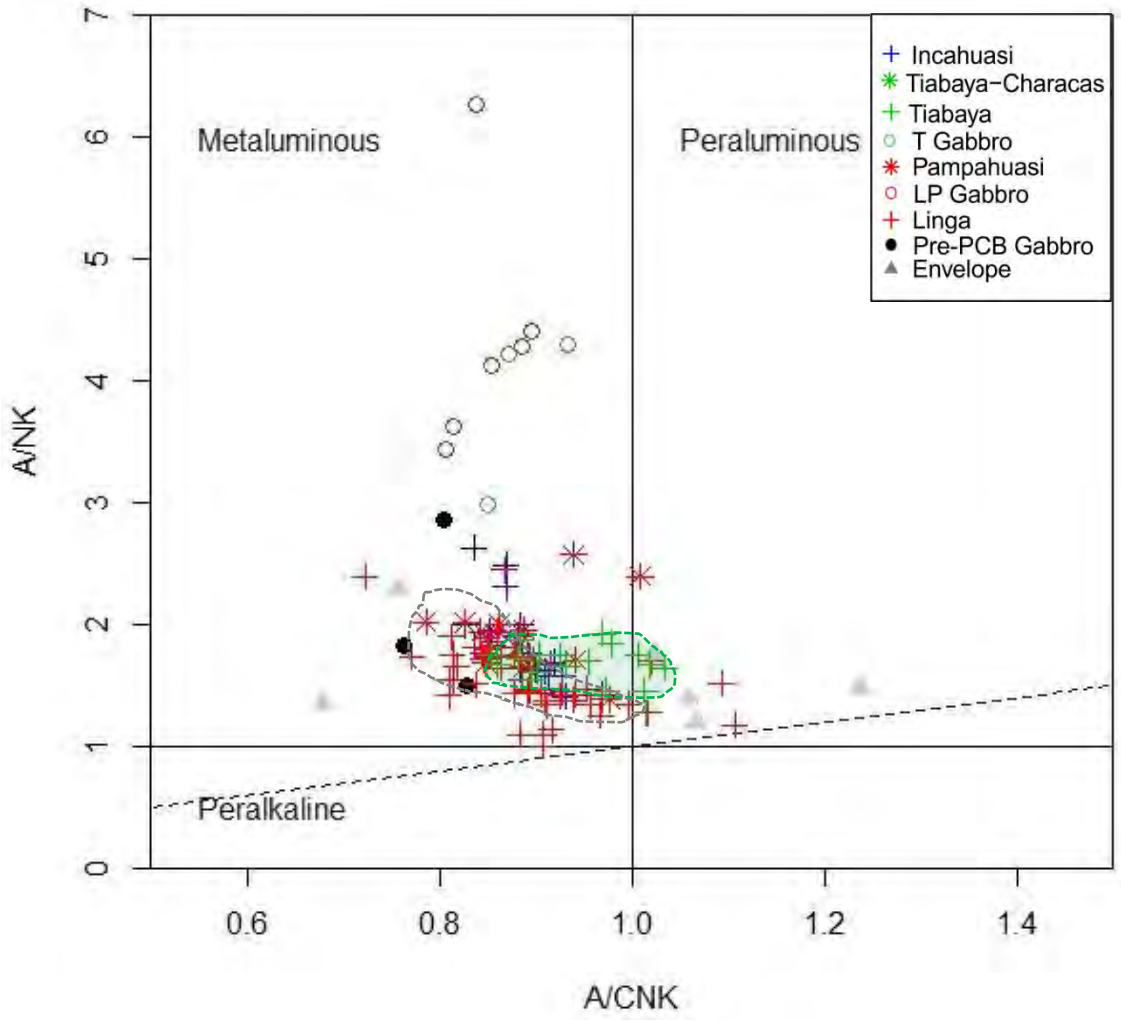

Figure 58. Alumina saturation index diagram (Shand, 1943). Some samples are in the peraluminous field, especially some Tiabaya samples suggesting that the magma is contaminated by volcaniclastic material from the volcanic cover. In general, A/CNK ratios are < 1.1 and this is a typical signature of hybrid continental (mixed mantle and crust sources) arc magmatism (Barbarin, 1990).

The Sr/Y plot in Figure 59 indicates that Incahuasi has a higher Sr/Y ratio and seems to suggest a different (deeper) magma source (Tulloch and Kimbrough, 2003). Thus the Incahuasi magma probably traversed more crust and could assimilate more continental lower crust material. In contrast, the Linga, Pampahuasi, and Tiabaya plutons have a lower Sr/Y ratio suggesting a shallower magma source and minor influence from the lower crust.

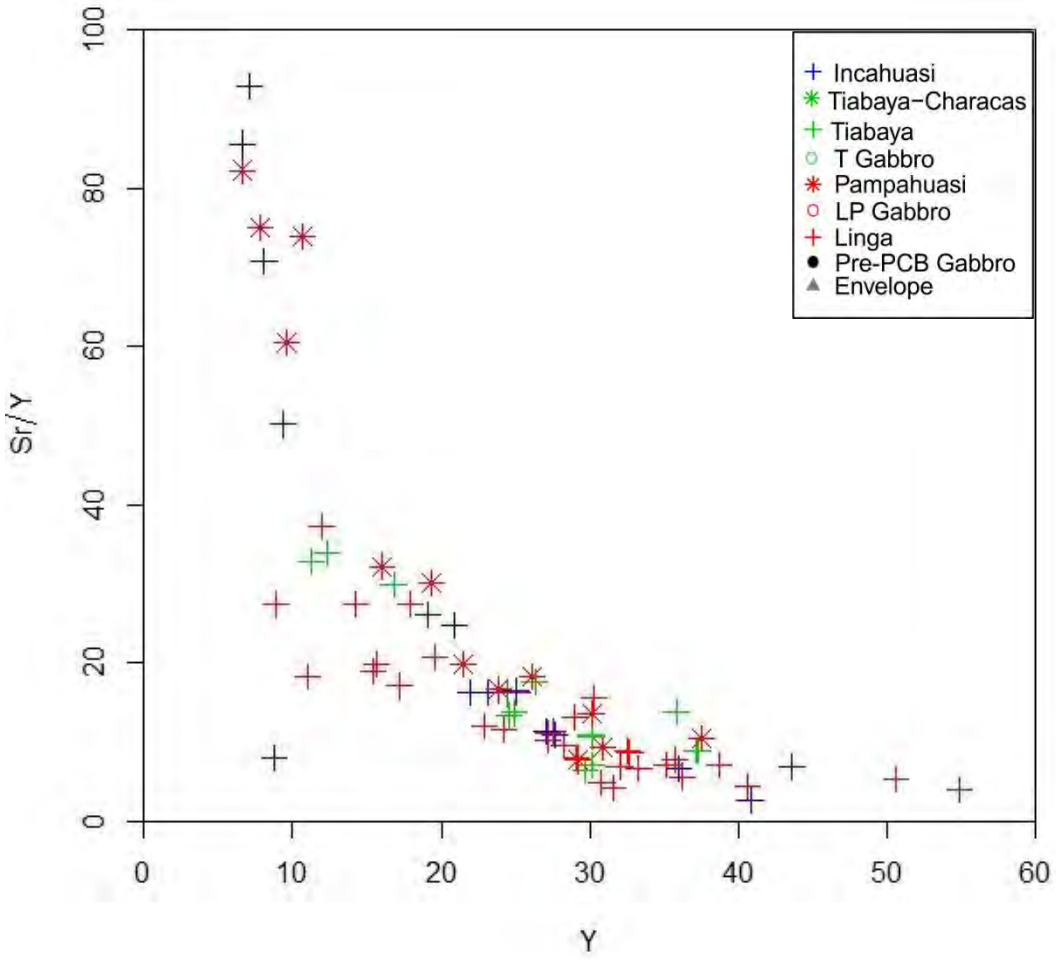

Figure 59. Sr/Y vs. Y bivariate plot ratios are interpreted as the result of different depth magma sources and variable amounts of crustal contamination.

Isotope Geochemistry

Looking at the εNd vs. Sr_i plot in Figure 60, the Sr_i values for most of the intrusives are relatively low between 0.704 and 0.705 and εNd values are relatively high of approximately +1. The distribution of the data seems to fit in two major trends: the first one with higher εNd values and the second one with lower εNd values. Specifically, the first trend is defined by the Linga plutons, where the Sr_i increases from western Humay to eastern Auquish and then Rinconada and several Humay monzogabbro-monzodiorite samples have higher εNd values. The second trend includes Tiabaya and Pampahuasi rocks that exhibit variation in Sr_i and lower εNd values. The data observed in the Linga and Tiabaya rocks tends to be more widely spread, whereas the Pampahuasi data is more tightly grouped. For the intrusive complexes generally, Sr_i increases and εNd decreases from Linga to Tiabaya to Pampahuasi plutons. Comparing the distribution of the data to the gabbro and volcanic samples, the gabbro data fits in the field of both the Linga and Tiabaya and the volcanic Sr_i values includes that for the intrusives, but has a much wider spread.

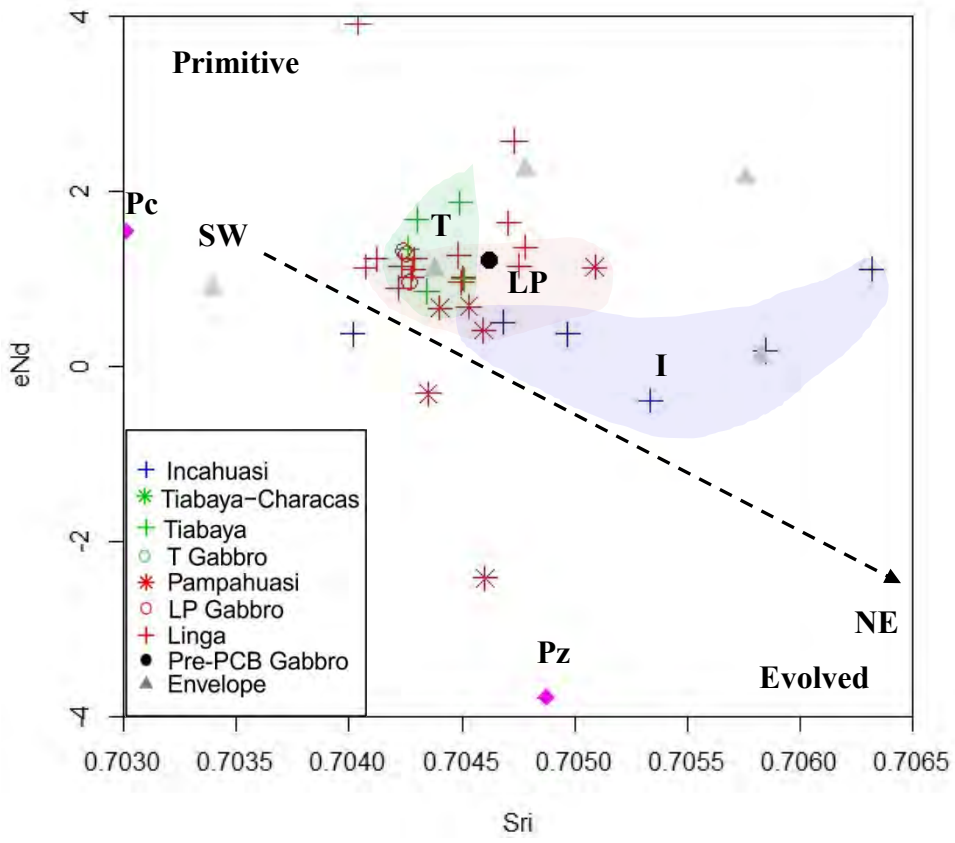

Figure 60. Isotope ratios of Nd and Sr. Plutons have a range of Sri and εNd values. Slightly increase of Sri towards younger and more evolved compositions. Intrusive complexes fields are for: Linga and Pampahuasi (LP), Tiabaya (T), and Incahuasi (I). Precambrian (Pc) and Paleozoic (Pz) samples plotted for comparisons.

The Pb data are illustrated in Figure 61. Looking at the $^{208}Pb/^{204}Pb$ vs. $^{206}Pb/^{204}Pb$ ratios, the overall values for the Incahuasi and LP rocks together display higher Pb values than Tiabaya rocks. The Tiabaya values are grouped tightly at lower$^{208}Pb/^{204}Pb$ and $^{206}Pb/^{204}Pb$ values showing a different behavior than the LP and Incahuasi samples which have a larger spread of values. For the LP rocks, the data have a larger spread in Pb values. The volcanics generally follow the same trend and spread as the intrusive rocks.

Oxygen isotopes from whole rock define two distinct groups: (1) $\delta^{18}O$ average value of 7.6 ‰ for Quilmana volcanics and Incahuasi rocks with slightly higher Sr_i values and (2) $\delta^{18}O$ range values of 7.4–7.9 ‰ represented by Pre-PCB gabbro and LP rocks. In Figure 62 these values are plotted in the diagram presented by James (1981) to identify the possible sources of contamination.

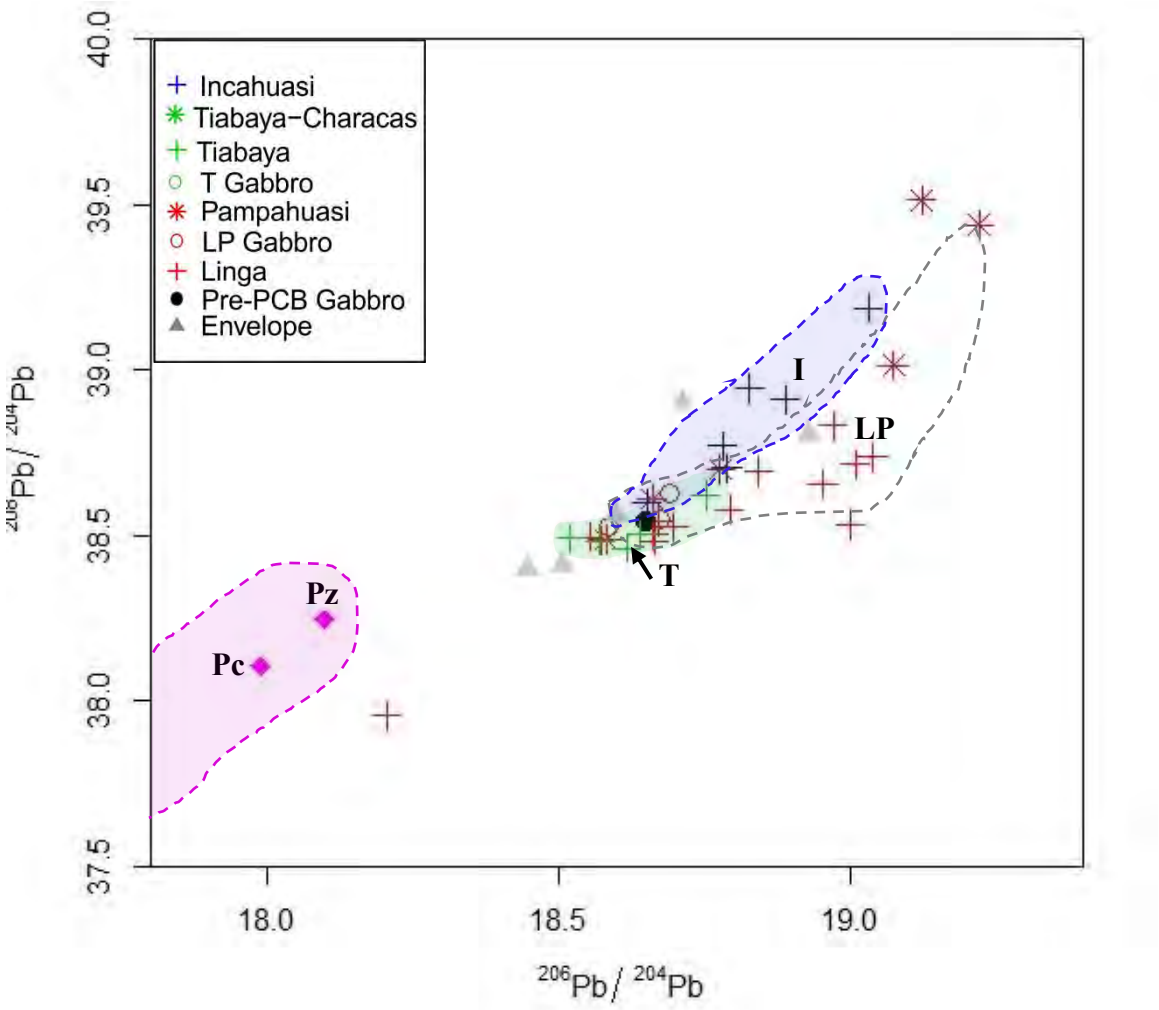

Figure 61. Magma sources and variation of $^{208}Pb/^{204}Pb$ versus $^{206}Pb/^{204}Pb$. Isotope ratios of the principal magma sources and Ica plutons. For comparisons the old cratonic continental rocks (Pc and Pz) are included.

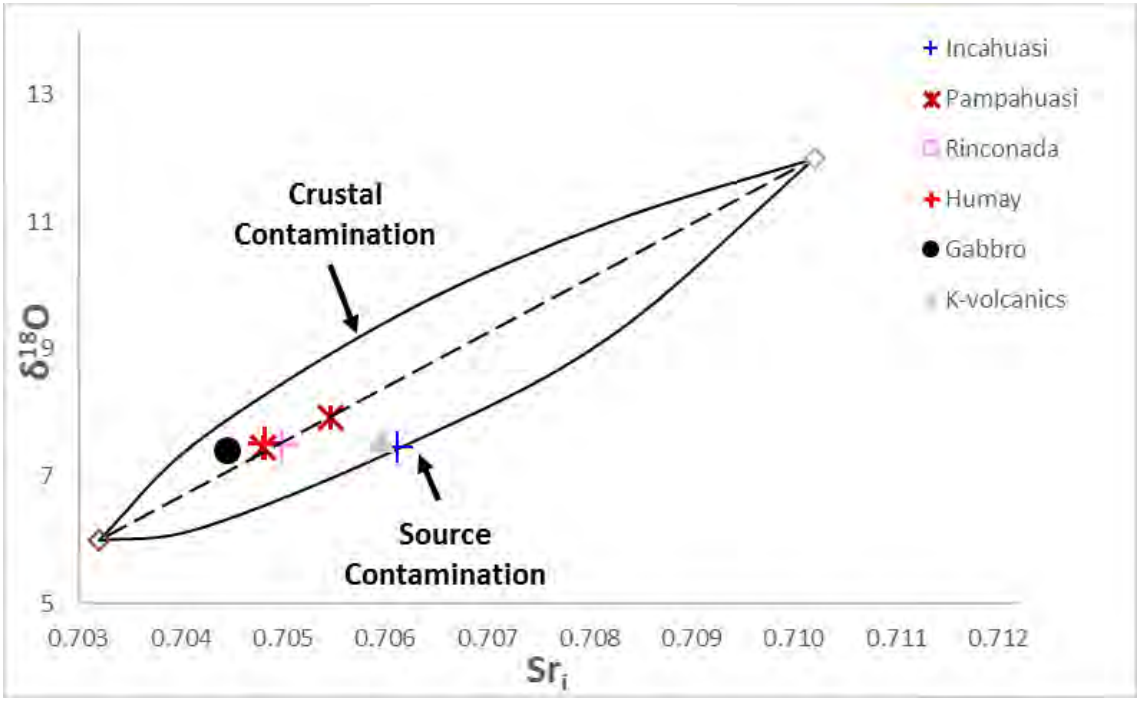

Figure 62. Diagram of two-component mixing curves for $\delta^{18}O$ vs. $^{87}Sr/^{86}Sr$ ratios. Ratio values are: for crustal contamination curve is 2:1 and for source contamination curve is 1:2. The ratios denote the proportion of Sr in crustal contaminant or in the slab-derived sedimentary fluids (After James 1981).

Isotopic Data Interpretations

The minimal change in εNd values is not clearly understood but it seems to be associated with time, as an age dependent variable (Barnes et al., 1992). Thus, the relatively constant values observed in the LP rocks might be due to the similar ages of the cogenetic magmas (Humay monzodiorite, Auquish monzonite, Rinconada granite, and Pampahuasi diorite-tonalite).

Most of the rocks exhibit low Sr_i values, but these may not indicate minimal crustal contamination and may suggest only that crustal contamination comes from primitive rock sources. The relatively low Sr_i trend within the PCB has been explained as representing complex mixtures of heterogeneous mantle with highly variable crustal material (Hildebrand and Whalen, 2014; Mukasa, 1986a). The LP and Tiabaya exhibits a more primitive character with Sr_i values that reflect a heterogeneous mantle source and Pb isotope values interpreted as resulting from minor contamination with ancient crustal materials. On the other hand, Incahuasi plutons have a more evolved character, having higher Sr_i values. Tiabaya samples have a trend towards the ancient crust suggesting higher assimilation of lower crustal material but also having contamination from the upper crust.

The isotope data are consistent with the idea that the granitoids represent a combination of variable amounts of mantle and crustal components. Integrating the all the isotopic data, the possible major sources of recycling/contamination for the granitic rocks proposed are: Precambrian and Paleozoic lower crust, Jurassic and Cretaceous basin fill sediments that include sedimentary and volcanic rocks, and slightly older plutonic rocks.

Similarities of isotope data between the volcanic, gabbro, and granitic samples suggest that they might share a common magma source. The Pre-PCB gabbro melt represents the precursor of granitic plutons. The possible source of the gabbro might be a combination of depleted mantle basalts and felsic melts from the lower crust. The volcanic samples fit in general in the same trend as the plutonic rocks with a similar range of Sr_i values.

Geochronology and Inherited Zircon Crystals

U-Pb zircon ages are crucial to unravelling the chronology of magmatic events and better understanding the relations of the recycling processes observed in the PCB. Previous ages reported for the Arequipa segment plutons are few and published 30 years ago: K-Ar ages presented by Moore (1984), Rb-Sr isochron ages by Beckinsale et al (1985), and U-Pb zircon ages by Mukasa (1986b). Thus, U-Pb zircon ages from multiple zircon crystals per sample were determined at the LaserChron Center of the University of Arizona using laser-ablation on the ICP mass spectrometer (LA-ICPMS). Coherent weighted mean LA-ICPMS ages range from 104.8 ± 1.1 for the Auquish monzonite to 58.9±0.6 for the Incahuasi granodiorite. The ages of the main plutonic and some pre and post-batholith rocks are reported in Appendix E and listed in Table 8.

Table 8. New ages for the plutons of the Peruvian Coastal Batholith, Arequipa segment near the city of Ica. Previously published Ages: K-Ar isochron ages assigned by Moore (1984), Rb-Sr isochron ages assigned by Beckinsale et al. (1985), U-Pb ages assigned by Mukasa (1986b), and the new ages from this research.

Sample	Pluton	Rock Type	Weighted Mean $^{206}Pb/^{238}U$ Age
15826D	Incahuasi	Granodiorite	58.9±0.6
14710F	Incahuasi	Granodiorite	68.0±0.9
15826Ca	Tiabaya	Gabbro	85.3±1.3
15826Fa	Tiabaya	Granodiorite	84.4±2.7
10714P	Pampahuasi	Tonalite	91.4±1.4
14715G	Pampahuasi	Qz-Diorite	97.8±0.7
14727U	Rinconada	Granite	98.3±1.9
14721Ac	Auquish	Monzonite	104.8±0.4
15826Aa	Pre-PCB	Gabbro	131.0±1.5
14713C	Pre-PCB	Monzogabbro	No concordia
14710A	Quilmana	Andesite	No concordia

Data from some zircon crystals indicated a much older and apparently inherited xenocrystic cores in several crystals from the Quilmana volcanic sample and in one crystal from the unit mapped as Humay monzogabbro but considered in this research as Pre-PCB gabbro. The sample classified as a basaltic andesite of the Quilmana volcanics was characterized by unusually small subrounded zircons that average 60 μm in length (Figure 63a). From this sample, U-Pb ages ranging from 540 Ma up to 2600 Ma were determined. Internal zircon features were difficult to identify due to the small size of the crystals, but these very old ages indicate that the crystals are xenocrysts. When it was possible to observe internal features of the crystals, it was noted that cores were separated from rims by irregular boundaries which truncate internal zoning. The majority of the zircon crystals from these samples are xenocrysts with a record of Precambrian and Paleozoic magmatic rocks that suggest evidence of material recycled by the Quilmana volcanic event. Even though the Quilmana volcanics are not the focus of this research, we consider the evidence of recycling in pre-plutonic rocks in our research area to be important.

The other interesting age came from a zircon xenocyrst of the Pre-PCB gabbro with a subrounded shape and displayed a dark inner core mantled by two newly grown zones characterized by lighter color (Figure 63b). The shape and the boundaries between two core zones suggest that this zircon was assimilated into younger magma batches. Based on the 403-540 Ma ages obtained from this zircon, the source of this xenocryst might be the San Nicolas Paleozoic basement.

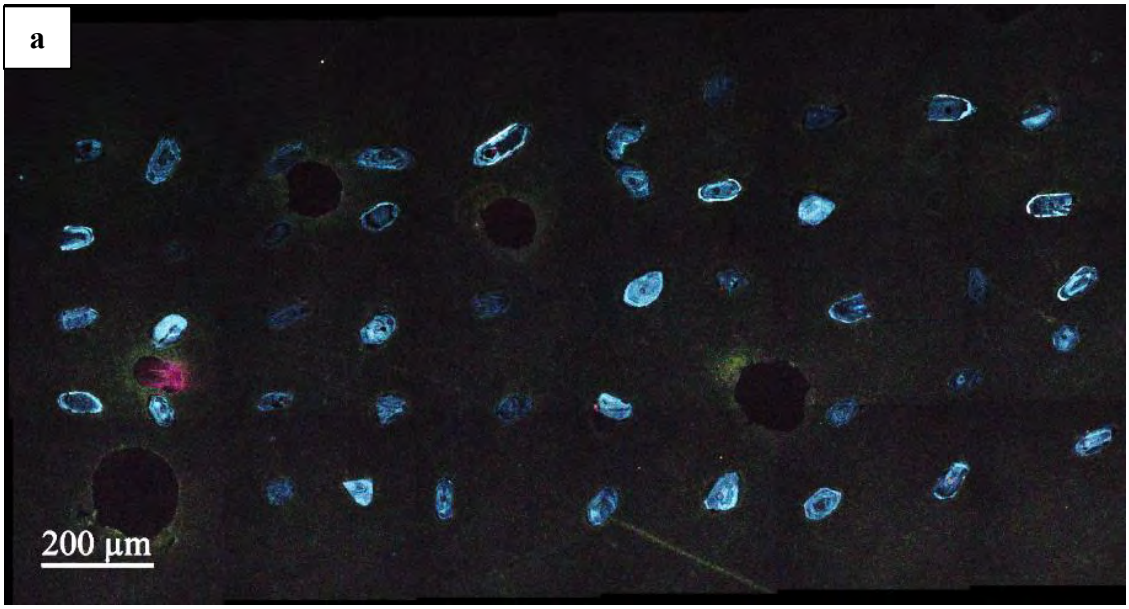

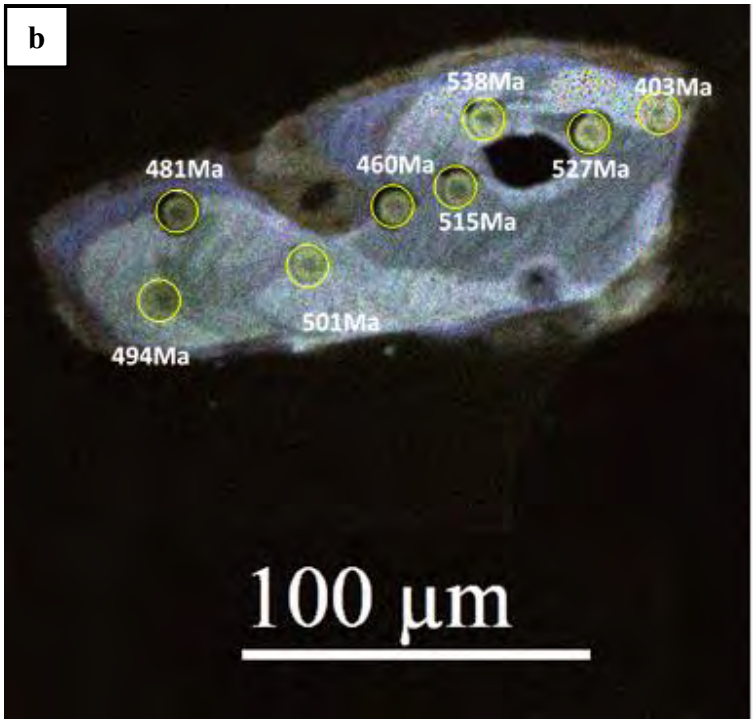

Figure 63. (a) CL image of the zircons from a sample of basaltic andesite of Quilmana volcanics. Zircon crystals with subrounded morphologies and complex internal zoning. (b) Cathodoluminescence (CL) image of a zircon xenocryst. Complex growth zoning with local resorption in zircon from Pre-PCB gabbro shows an age range of 403-540Ma.

Mass Balance Calculations

Partial Melting and Fractional Crystallization

A MgO Harker diagram (Figure 64) was used to model partial melting (PM) and fractional crystallization (FC) of the Linga rocks with important evidence for mafic and felsic magmatic interaction. For the mass balance calculations involving the Linga rocks, we suggest an initial lower-crust gabbro (basalt) composition of 49.5% SiO_2, an ultramafic residue composition of 45% SiO_2, a cumulate from fractional crystallization of the felsic magmas with 61.7% SiO_2, 10% to 25% partial melting, and up to 70% fractional crystallization before the crystals were locked in. Mass balance calculations suggest that a volume three times that of differentiated Linga melt is a feasible estimate of the ultramafic residue left after partial melting of lower crust gabbro (basalt). At least part of this may have delaminated back into the mantle. These calculations revealed that partial melting and fractional crystallization are not sufficient to explain the 50-65% SiO_2 range and that magma mixing appears to be required to form the hybrid rocks of the Linga plutons.

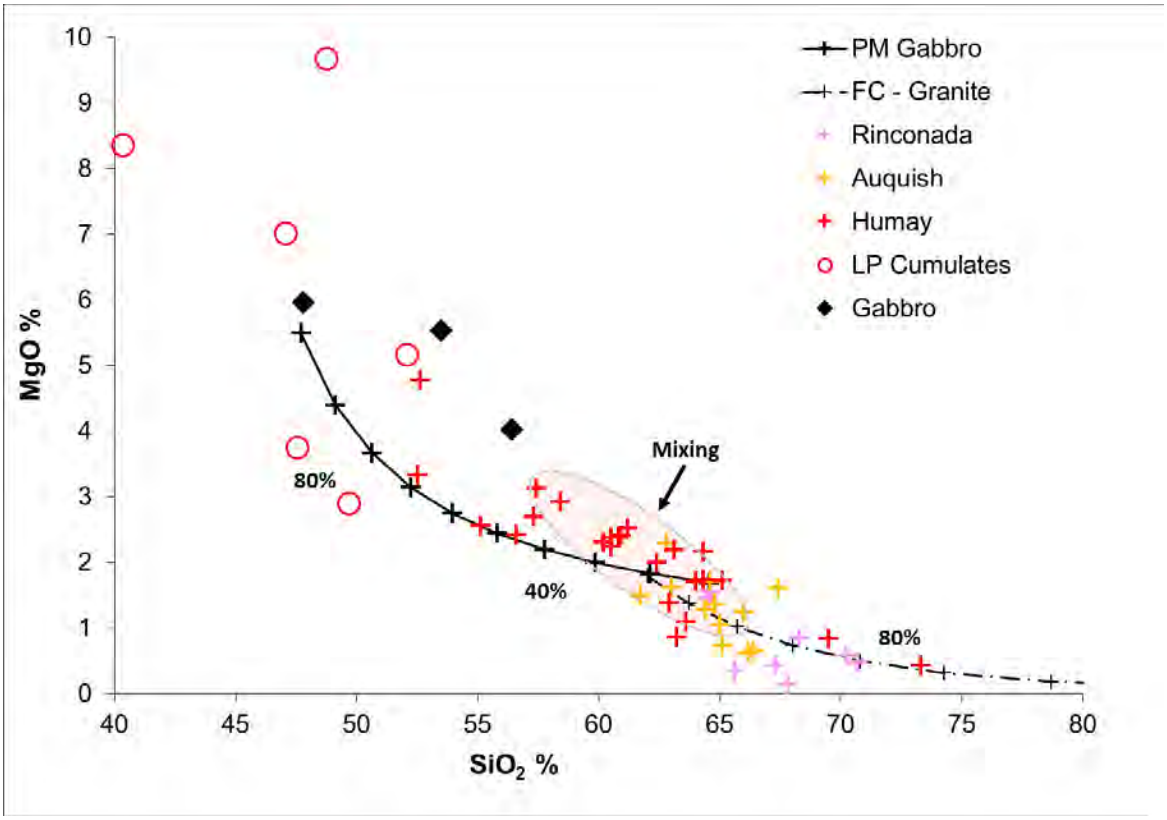

Figure 64. Evidence of magma mixing from PM and FC modeling. Magma mixing seems to be required to form the hybrid rocks of the Linga plutons.

Combined Assimilation and Fractional Crystallization (AFC) Calculations

Assimilation and fractional crystallization (AFC) modeling using trace elements is a useful tool to estimate the amounts of assimilated crustal material and to identify the possible end members involved in the magmatic evolution of plutonic rocks. In this study we have considered a simple model using the methodology presented by DePaolo (1981). A continuous calc-alkaline trend of 50-70% SiO_2 is seen for a majority of the Ica-Pisco plutons. The Pre-PCB gabbros fit well on almost all elemental trends and are considered to be the parental composition for AFC modeling. The other end members assumed for this modeling and the representative sources for crustal contamination through which the magmas ascended is the ancient continental crust and the volcanic envelop.

For the first case, using the least evolved Pre-PCB gabbro as the average parental composition and the ancient continental crust as the contaminant, and AFC calculations using a variety of elements (Rb-Sr and Co-Ba). The majority of the samples lie on a common trend defined by the ratio (r) of assimilation rate to crystallization rate having a value of 0.3 and are thus interpreted as the result of a combination of mostly fractionation with some mixing effects (Figure 65a and c). Few samples lie on a trend defined by r=0 which represents pure fractional crystallization from the Pre-PCB gabbros to some granodiorite rocks (shown mainly by Tiabaya granodiorites). Very few samples lie on the trend of pure mixing (r=infinite) between the gabbros and the Precambrian rocks. It seems that the Pampahausi diorite-tonalite and Linga Humay monzodiorite are the units slightly higher affected by assimilation of ancient crust than Tiabaya and Incahuasi units.

For the second case, using the least evolved gabbros as the average parental composition and the pre-PCB volcaniclastic rocks as the contaminant. The AFC

modeling worked for Rb-Sr plot but it didn't work for the Ba-Co plot using the volcaniclastic rocks as a contaminant. The AFC modeling is described only for the Rb-Sr plot. The majority of the samples lie on a common trend defined by the ratio (r) of assimilation rate to crystallization rate having a value of 0.3 and are thus interpreted as the result of a combination of mostly fractionation with some mixing effects (Figure 65b). Another group of samples lie on a trend defined by r=0 which represents pure fractional crystallization from the Pre-PCB gabbros to some granodiorite rocks (shown mainly by some samples from Tiabaya and Incahuasi plutons). Very few samples lie on the trend of pure mixing (r=infinite) between the gabbros and the volcaniclastic rocks. It seems that the samples exhibit a distribution resulting from the fractional crystallization trends affected by assimilation of volcaniclastic rocks.

Based on the graphical results, we suggest that the elemental variations resulted from the interaction of two major distinct components: (1) a basic parental depleted magma generated in the mantle, above the subduction zone and (2) lower crustal melts. The observed spread of some samples in the graphical modeling may account for other potential sources of contamination such as Precambrian and Paleozoic basement, Mesozoic sedimentary, volcanic, and plutonic continental crust such as exposed in the study area. Thus, AFC calculations using Rb-Sr and Co-Ba plots indicate 15-30% assimilation of crustal materials into the Ica-Pisco plutons.

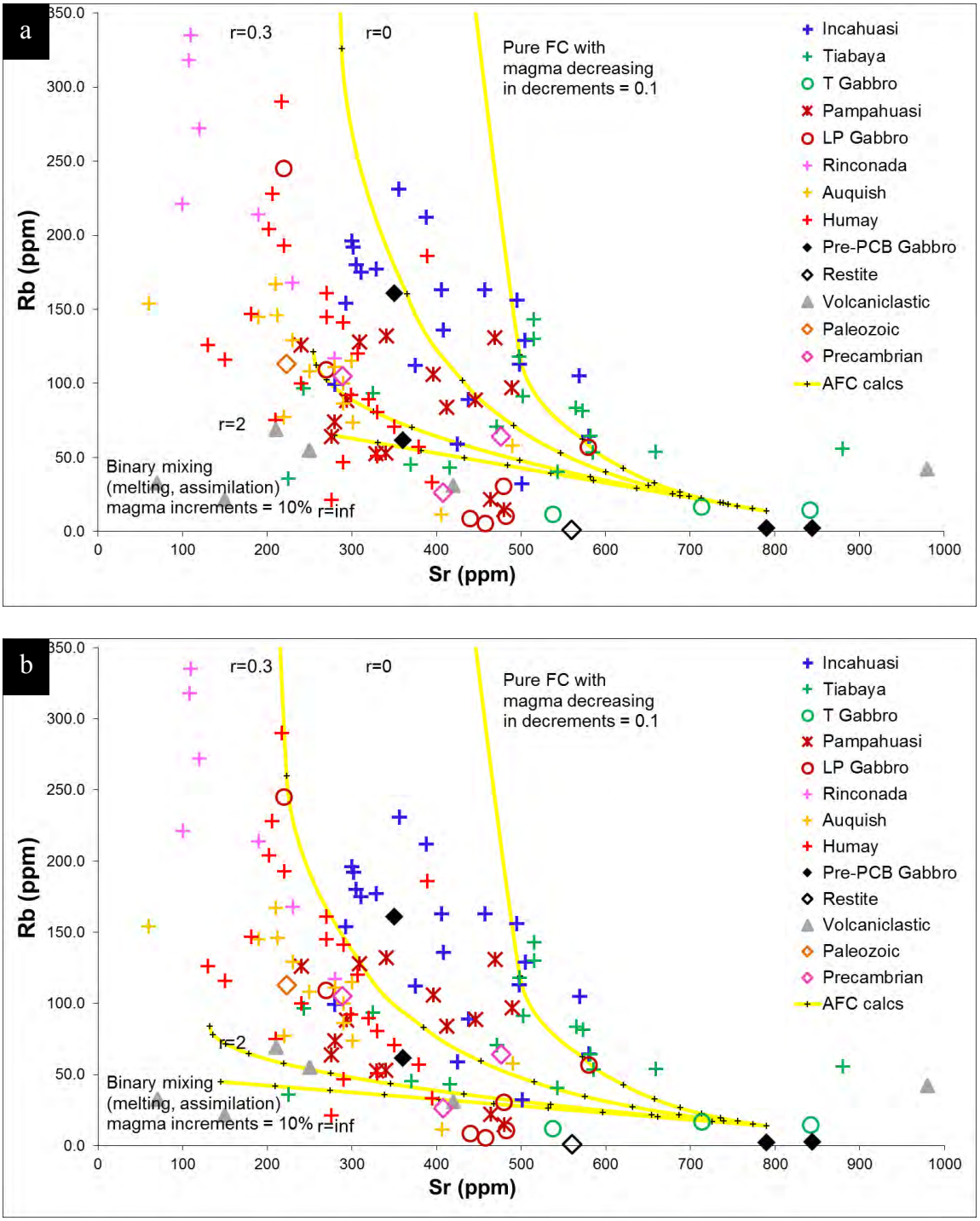

Figure 65. AFC modeling for the PCB. (a)Rb vs. Sr plot using the ancient crust as one of end members. (b)Rb vs. Sr plot using the volcanic rocks as one end member. Note that F values (mass of magma/initial mass of magma, parental magma) starts at F= 1.0 at the origin and decreases by 0.1 with each increment away from the origin. The AFC model suggests assimilation percentages of 15-30%.

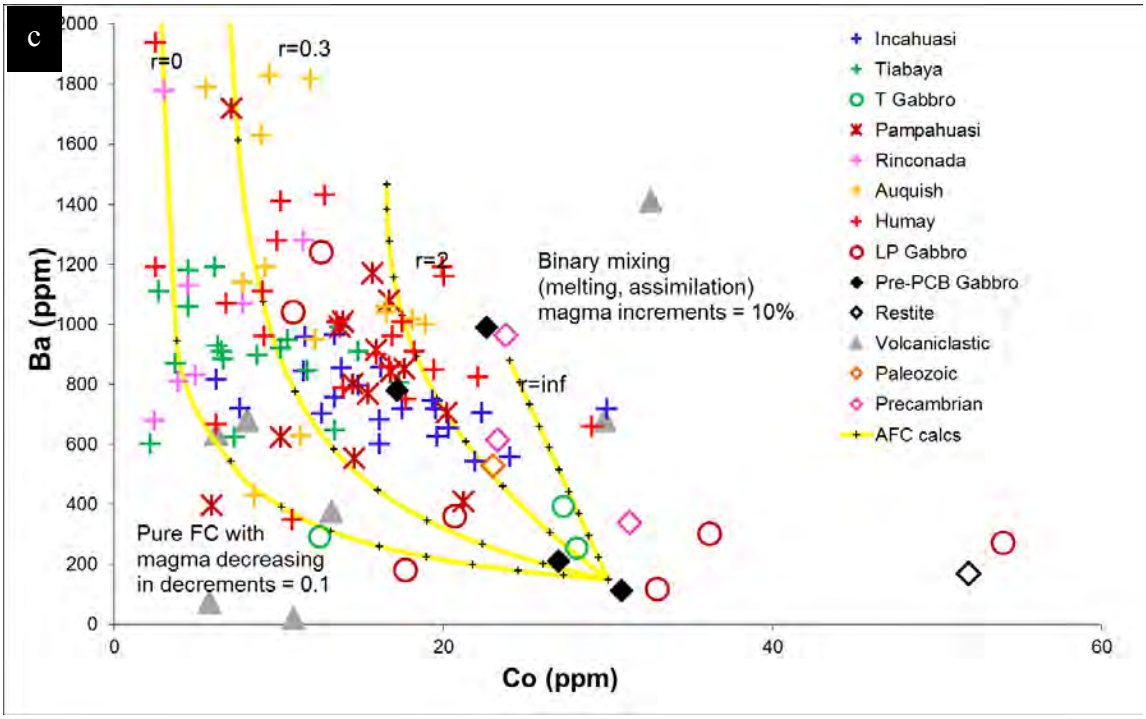

Figure 65. AFC modeling for the PCB. (c) Ba vs. Co plot using the ancient crust as one of end members. Note that F values (mass of magma/initial mass of magma, parental magma) starts at F= 1.0 at the origin and decreases by 0.1 with each increment away from the origin. The AFC model suggests assimilation percentages of 15-30%.

Discussion and Conclusions

Based on field observations, the Ica-Pisco area plutons records evidence of contamination and widespread recycling of older volcanic and plutonic units into younger plutons ranging from kilometer to centimeter scale. Quantification of these features suggest that perhaps 20% of the pre-PCB envelop is recycled into the Ica-Pisco plutons and 10% of early PCB units may be recycled into later PCB units. The distribution and quantification of well-preserved recycled materials along the edge of plutons seems to suggest that the northern part of the Arequipa Segment has been an active magmatic zone for recycling processes taking place during batholith construction.

Microtextural features in microphotographs are explained by magma mixing and recycling processes. The evidence from plagioclase microtextures specially the zoning patterns indicate a complex history of magmatic contamination. Complex compositional zoning in plagioclase crystals might be interpreted as crystals originating in an older or just slightly older magmatic host rock that were transported and then disaggregated and mingled into younger magma pulses. Based on these features, it is suggested that at least 10% of pre-PCB envelop and early PCB units may be recycled into later PCB units. However, at this scale we cannot discriminate between the different sources and single mineral chemical analysis is required.

Elemental chemistry and qualitative estimates suggest: (1) combined processes of fractional crystallization and magma mixing/contamination should be considered to explain the full range of lithologies; (2) alumina plots indicate that the Tiabaya plutons may have assimilated more sedimentary materials than the other units; (3) Sr/Y ratios

indicate that Incahuasi plutons may be derived from a deeper source than the other units and/or the magma may have traversed thicker crust making more assimilation possible.

Variation of the isotope ratios of Nd, Sr, and Pb seems to suggest that crustal contamination is involved in defining the compositional variation of the Ica-Pisco plutons and are used to characterize the magma reservoirs. Isotopic compositions suggest that the LP and Tiabaya plutons represent early magmas emplaced into a thin crust segment that experienced minimal contamination from ancient crustal materials but probably higher contamination with Pre-PCB volcaniclastic rocks. On the other hand, Incahuasi plutons represent magmas emplaced into thick crust segment with more involvement of ancient crustal materials.

Quantitative estimates of the magnitude of recycling using assimilation and fractional crystallization (AFC) calculations indicate that the Ica-Pisco plutons are a combination of fractionation (being the dominant process) and mixing effects.

Integration of the field, petrographic, and geochemical evidence suggests that the magma composition of the Ica-Pisco plutons is made up of basalts from the depleted mantle, recycled Precambrian and Paleozoic lower crust, and recycled upper crust volcanics and older plutonic units. All this is consistent with the idea that the recycling process potentially has a dramatic effect on magmatic systems during arc construction. Finally, it is suggested that chemical contamination and magma mingling and mixing structures and textures from outcrop to thin section scale vary throughout the magma chamber(s) indicating that magmatic recycling processes varied in intensity and relative importance through time in the plutons of the Arequipa segment in the PCB.

References

Agar, R. (1978) The Peruvian Coastal Batholith: Its monzonitic rocks and their related mineralization. The geology of the rio Pisco, a sector of the Arequipa segment of the Coastal Batholith. Geology, Doctor of Philosophy, p. 293. University of Liverpool, Liverpool.

-. (1981) Copper mineralization and magmatic hydrothermal brines in the Rio Pisco Section of the Peruvian Coastal Batholith. Economic Geology, 76, 677-693.

Anderson, A.T. (1984) Probable relations between plagioclase zoning and magma dynamics, Fuego Volcano, Guatemala. American Mineralogist, 69, 660-676.

Atherton, and Aguirre. (1992) Thermal and geotectonic setting of Cretaceous volcanic rocks near Ica, Peru, in relation to

Andean crustal thinning. Journal of South American Earth Sciences, 5(1), 47-69.

Atherton, and Petford. (1996) Plutonism and the growth of Andean Crust at 9'S from 100 to 3 Ma. Journal of South American Earth Sciences, 9, 1-9.

Barbarin, B. (1990) Granitoids: Main petrogenetic classifications in relation to origin and tectonic setting. Geological Journal, 25(3-4), 227-238.

-. (2005) Mafic magmatic enclaves and mafic rocks associated with some granitoids of the central Sierra Nevada batholith, California: nature, origin, and relations with the hosts. Lithos, 80(1-4), 155-177.

Barbarin, B., and Didier, J. (1992) Genesis and evolution of mafic microgranular enclaves through various types of interaction between coexisting felsic and mafic magmas. Earth and Environmental Science Transactions of the Royal Society of Edinburgh, 83(1-2), 145-153.

Barbey, P., Gasquet, D., Pin, C., and Bourgeix, A.L. (2008) Igneous banding, schlieren and mafic enclaves in calc-alkaline granites: The Budduso pluton (Sardinia). Lithos, 104(1-4), 147-163.

Barnes, C.G., Petersen, S.W., Kistler, R.W., Prestvik, T., and Sundvoll, B. (1992) Tectonic implications of isotopic variation among Jurassic and Early Cretaceous plutons, Klamath Mountains. Geological Society of America Bulletin, 104(1), 117-126.

Beckinsale, R.D., Sanchez-Fernandez, A.W., Brook, M., Cobbing, E.J., Taylor, W.P., and Moore, N.D. (1985) Rb-Sr whole-rock isochrons and K-Ar age determinations for the Coastal Batholith of Peru. Blackie, Glasgow.

Boily, M., Brooks, C., and Ludden, J.N. (1989) Chemical and isotopic evolution of the Coastal Batholith of southern Peru. Journal of Geophysical Research, 94(89), 12483-12489.

Bolhar, R., Weaver, S.D., Whitehouse, M.J., Palin, J.M., Woodhead, J.D., and Cole, J.W. (2008) Sources and evolution of arc magmas inferred from coupled O and Hf isotope systematics of plutonic zircons from the Cretaceous Separation Point Suite (New Zealand). Earth and Planetary Science Letters, 268(3-4), 312-324.

Brown, G.C., and Mussett, A.E. (1993) The Innaccessible Earth. An integrated view to its structure and composition. Chapman & Hall.

Burchardt, S., Tanner, D., and Krumbholz, M. (2012) The Slaufrudalur pluton, southeast Iceland—An example of shallow magma emplacement by coupled cauldron subsidence and magmatic stoping. Geological Society of America Bulletin, 124(1-2), 213-227.

Bussell, M.A., Pitcher, W.S., and Wilson, P.A. (1976) Ring complexes of the Peruvian Coastal Batholith: a long-standing subvolcanic regime. Canadian Journal of Earth Sciences, 13(8), 1020-1030.

Chen, B., Chen, Z.C., and Jahn, B.M. (2009) Origin of mafic enclaves from the Taihang Mesozoic orogen, north China craton. Lithos, 110(1–4), 343-358.

Clarke, D.B. (2007) Assimilation of xenocrysts in granitic magmas: principles, processes, proxies, and problems. The Canadian Mineralogist, 45(1), 5-30.

Clarke, D.B., Henry, A.S., and White, M.A. (1998) Exploding xenoliths and the absence of “elephants’ graveyards” in granite batholiths. Journal of Structural Geology, 20, 1325–1343

Cobbing, E.J., Ozard, J.M., and Snelling, N.J. (1977) Reconnaissance geochronology of the crystalline basement rocks of the Coastal Cordillera of southern Peru. Geological Society of America Bulletin, 88(2), 241-246.

Cobbing, E.J., and Pitcher, W.S. (1972) The Coastal Batholith of central Peru. Journal of the Geological Society, 128(5), 421-454.

Coira, B., Davidson, J.P., Mpodozis, C., and Ramos, V. (1982) Tectonic and magmatic evolution of the Andes of northern Argentina and Chile. Earth Science Reviews, 18, 303-332.

Coldwell, B., Clemens, J., and Petford, N. (2011) Deep crustal melting in the Peruvian Andes: Felsic magma generation during delamination and uplift. Lithos, 125(1-2), 272-286.

Dallai, L., Ghezzo, C., and Sharp, Z.D. (2003) Oxygen isotope evidence for crustal assimilation and magma mixing in the Granite Harbour Intrusives, Northern Victoria Land, Antarctica. Lithos, 67(1-2), 135-151.

Daly, R.A. (1903) The mechanics of igneous intrusion. American Journal of Science, 15, 269–298.

Davila, M.F. (1993) Geología de los cuadrángulos de Pisco, Guadalupe, Punta Grande, Ica y Córdova. Instituto Geológico Minero y Metalúrgico del Perú "INGEMMET", 47, 78.

DePaolo, D.J. (1981) Trace element and isotopic effects of combined wallrock assimilation and fractional crystallization. Earth and Planetary Science Letters, 53(2), 189-202.

Dumond, G., Yoshinobu, A.S., and Barnes, C.G. (2005) Midcrustal emplacement of the Sausfjellet pluton, central Norway: Ductile flow, stoping, and in situ assimilation. Geological Society of America Bulletin, 117(3-4), 383-395.

Farris, D.W., and Paterson, S.R. (2007) Contamination of silicic magmas and fractal fragmentation of xenoliths in Paleocene plutons on Kodiak island, Alaska. The Canadian Mineralogist, 45(1), 107-129.

Furlong, K.P., and Myers, J.D. (1985) Thermal-mechanical modeling of the role of thermal stresses and stoping in magma contamination. Journal of Volcanology and Geothermal Research, 24(1–2), 179-191.

Gagnevin, D., Daly, J.S., and Poli, G. (2008) Insights into granite petrogenesis from quantitative assessment of the field distribution of enclaves, xenoliths and K-feldspar megacrysts in the Monte Capanne pluton, Italy. Mineralogical Magazine, 72(4), 925-940.

Gastil, G., Diamond, J., Knaack, C., Walawender, M., Marshall, M., Boyles, C., Chadwick, B., and Erskine, B. (1990) Chapter 2: The problem of the magnetite/ilmenite boundary in southern and Baja California California. Geological Society of America Memoirs, 174, 19-32.

Ginibre, C., Kronz, A., and Worner, G. (2002) High-resolution quantitative imaging of plagioclase composition using accumulated backscattered electron images: new constraints on oscillatory zoning. Contributions to Mineralogy and Petrology, 142, 436-448.

Gromet, P., and Silver, L.T. (1987) REE Variations Across the Peninsular Ranges Batholith: Implications for Batholithic Petrogenesis and Crustal Growth in Magmatic Arcs. Journal of Petrology, 28(1), 75-125.

Haederle, M., and Atherton, M.P. (2002) Shape and intrusion style of the Coastal Batholith, Peru. Tectonophysics, 345, 17-28.

Hattori, K., and Sato, H. (1996) Magma evolution recorded in plagioclase zoning in 1991Pinatubo eruption products. American Mineralogist, 81, 982-994.

Hawkesworth, C.J., Rogers, N.W., van Calsteren, P.W.C., and Menzies, M.A. (1984) Mantle enrichment processes. Nature, 311(5984), 331-335.

Hibbard, M.J. (1995) Petrography to petrogenesis. 242-260 p. Prentice-Hall, Englewood Cliffs, New Jersey.

Hildebrand, R.S., and Whalen, J.B. (2014) Arc and slab-failure magmatism in Cordilleran batholiths II—The Cretaceous Peninsular Ranges batholith of Southern and Baja California: Paul Hoffman Volume: . Geoscience Canada, 41, 339-458.

Humphreys, M.C.S. (2009) Chemical Evolution of Intercumulus Liquid, as Recorded in Plagioclase Overgrowth Rims from the Skaergaard Intrusion. Journal of Petrology, 50(1), 127-145.

Humphreys, M.C.S., Blundy, J.D., and Sparks, R.S.J. (2006) Magma Evolution and Open-System Processes at Shiveluch Volcano: Insights from Phenocryst Zoning. Journal of Petrology, 47(12), 2303-2334.

Huppert, H.E., and Sparks, R.S.J. (1988) The Generation of Granitic Magmas by Intrusion of Basalt into Continental Crust. Journal of Petrology, 29(3), 599-624.

Kocak, K., Zedef, V., and Kansun, G. (2011) Magma mixing/mingling in the Eocene Horoz (Nigde) granitoids, Central southern Turkey: evidence from mafic microgranular enclaves. Mineralogy and Petrology, 103(1-4), 149-167.

Lackey, J.S., Valley, J.W., Chen, J.H., and Stockli, D.F. (2008) Dynamic Magma Systems, Crustal Recycling, and Alteration in the Central Sierra Nevada Batholith: the Oxygen Isotope Record. Journal of Petrology, 49(7), 1397-1426.

Lameyre, J., and Bonin, B. (1991) Granites in the main plutonic series. Elsevier.

Larsen, E.S. (1948) Batholith and associated rocks of Corona, Elsinore, and San Luis Rey Quadrangles, Southern California. Geological Society of America Memoirs, 29, 182.

Leon, W., Aleman, A., Torres, V., Rosell, W., and De La Cruz, O. (2007) Estratigrafía, sedimentología, y evolución tectónica de la cuenca de Pisco oriental. In S.E.y. Minas, Ed. serie D, Nº27. INGEMMET, Lima-Peru.

Mamani, M., Wörner, G., and Sempere, T. (2010) Geochemical variations in igneous rocks of the Central Andean orocline (13°S to 18°S): Tracing crustal thickening and magma generation through time and space. Geological Society of America Bulletin, 122(1-2), 162-182.

Marsh, B.D. (1982a) On the mechanics of igneous diapirism, stoping and zone melting. American Journal of Science, 282, 87.

Marsh, B.D. (1982b) On the mechanics of igneous diapirism, stoping, and zone melting. American Journal of Science, 282, 808-855.

Memeti, V., Paterson, S., and Mundil, R. (2014) Day 4: Magmatic evolution of the Tuolumne Intrusive Complex. Field Guides, 34, 43-74.

Miller, C.F., and Miller, J.S. (2002) Contrasting stratified plutons exposed in tilt blocks, Eldorado Mountains, Colorado River Rift, NV, USA. Lithos, 61(3–4), 209-224.

Miyashiro, A. (1974) Volcanic rock series in island arcs and active continental margins. American Journal of Science, 274, 321-355.

Moore, N.D. (1979) The Geology and Geochronology of the Arequipa Segment of the Coastal Batholith of Peru. , Doctor of Philosophy, p. 549. Liverpool, London.

-. (1984) Potassium-Argon ages from the Arequipa Segment of the Coastal Batholith of Peru and their correlation with regional tectonic events. Journal of the Geological Society, 141(3), 511-519.

Mukasa, S.B. (1984) Comparative Lead Isotope Systematics and Zircon Uranium-Lead Geochronology for the Coastal, San Nicolas and Cordillera Blanca Batholiths, Peru. Geology. University of California, Santa Barbara.

Mukasa, S.B. (1986a) Common Pb isotopic compositions of the tima, Arequipa and Toquepala segments in the Coastal batholith, Peru: Implications for magmagenesis. Geochimica Et Cosmochimica Acta, 50, 771-782.

Mukasa, S.B. (1986b) Zircon U-Pb ages of super-units in the Coastal batholith, Peru: Implications for magmatic and tectonic processes. Geological Society of America Bulletin, 97(2), 241.

Myers, J.D. (1975) Cauldron subsidence and fluidization: mechanisms of intrusion of the Coastal Batholith of Peru into its own volcanic ejecta. Geological Society of America, 86, 1209-1220.

Nixon, G.T., and Pearce, T.H. (1987) Laser-interferometry study of oscillatory zoning in plagioclase: The record of magma mixing and phenocryst recycling in calc-alkaline magma chambers, Iztaccihuatl volcano, Mexico. American Mineralogist, 72, 1144-1162.

Paterson, S.R., Memeti, V., Pignotta, G., Erdmann, S., Žák, J., Chambers, J., and Ianno, A. (2012) Formation and transfer of stoped blocks into magma chambers: The high-temperature interplay between focused porous flow, cracking, channel flow, host-rock anisotropy, and regional deformation. Geosphere, 8(2), 443-469.

Paterson, S.R., and Miller, R.B. (1998) Stoped blocks in plutons: paleo-plumb bobs, viscometers, or chronometers? Journal of Structural Geology, 20(9–10), 1261-1272.

Paterson, S.R., Okaya, D., Memeti, V., Economos, R., and Miller, R.B. (2011) Magma addition and flux calculations of incrementally constructed magma chambers in continental margin arcs: Combined field, geochronologic, and thermal modeling studies. Geosphere, 7(6), 1439-1468.

Paterson, S.R., Žák, J., and Janoušek, V. (2008) Growth of complex sheeted zones during recycling of older magmatic units into younger: Sawmill Canyon area, Tuolumne batholith, Sierra Nevada, California. Journal of Volcanology and Geothermal Research, 177(2), 457-484.

Peccerillo, A., and Taylor, S.R. (1976) Geochemistry of eocene calc-alkaline volcanic rocks from the Kastamonu area, Northern Turkey. Contributions to Mineralogy and Petrology, 58(1), 63-81.

Petford, N., and Atherton, M. (1996) Na-rich Partial Melts from Newly Underplated Basaltic Crust: the Cordillera Blanca Batholith, Peru. Journal of Petrology, 37(6), 1491-1521.

Phemister, J. (1934) Zoning in Plagioclase Feldspar.

Pignotta, G.S., and Paterson, S.R. (2007) Voluminous stoping in the Mitchell Peak Granodiorite, Sierra Nevada Batholith, Californa, USA. The Canadian Mineralogist, 35, 87-106.

Pitcher, W.S., Atherton, M.P., Cobbing, E.J., and Beckinsale, R.D. (1985) Magmatism at a plate edge: the Peruvian Andes. Wiley.

Profeta, L., Ducea, M.N., Chapman, J.B., Paterson, S.R., Henriquez, S.M., Kirsch, M., Petrescu, L., and DeCelles, P.G. (2015) Quantifying crustal thickness over time in magmatic arcs. Scientific Reports, 5(17786), 7.

Roy, S.G., Johnson, S.E., and Koons, P.O. (2012) Fractal analysis and thermal-elastic modeling of a subvolcanic magmatic breccia: The role of post-fragmentation partial melting and thermal fracture in clast size distributions. Geochemistry, Geophysics, Geosystems, 13(5), 23.

Sanchez-Fernandez, A.W. (1982) Edades Rb-Sr en los segmentos Arequipa-Toquepala del Batolito de la costa del Peru. Quinto Congreso Latinoamericano de Geologia, p. 487-504, Argentina.

Shand, S.J. (1943) The Eruptive Rocks. 444 p. John Wiley, New York.

Soler, P., and Bonhomme, M.G. (1990) Relation of magmatic activìty to plate dynamics in central Peru from Late Cretaceous to present. Geological Society of America, 173-192.

Soler, P., and Rotach-Toulhoat, N. (1990) Sr-Nd Isotope Compositions of Cenozoic Granitoids along a Traverse of the Central Peruvian Andes. Geological Journal, 25, 351-358.

Stewart, J.W., Evernden, J.F., and Snelling, N.J. (1974) Age Determinations from Andean Peru: A Reconnaissance Survey. Geological Society of America Bulletin, 85(7), 1107-1116.

Streckeisen, A.L. (1973) Classification and nomenclature recommended by the IUGS subcommission on the systematics of igneous rocks. Geotimes, 10, 26-31.

Troll, V.R., and Schmincke, H.-U. (2002) Magma Mixing and Crustal Recycling Recorded in Ternary Feldspar from Compositionally Zoned Peralkaline Ignimbrite 'A', Gran Canaria, Canary Islands. Journal of Petrology, 43(2), 243-270.

Tulloch, A., and Kimbrough, D. (2003) Paired plutonic belts inconvergent margins and the development of high Sr/Y magmatism: Peninsular Ranges batholith of Baja-California and Median batholith of New Zealand. Geological Society of America(374), 275-295.

Turnbull, R.E. (2009) Mafic-felsic interaction in a high level magma chamber – The Halfmoon pluton, Stewart island, New Zealand: implications for understanding arc magmatism. 1-280.

Vernon, R.H. (2004) A practical guide to rock microstructure. 594 p. Cambridge University Press, New York.

Wiebe, R.A. (1993) Basaltic injections into floored silicic magma chambers. Eos, Transactions American Geophysical Union, 74(1), 1-3.

Winter, J.D. (2010) An introduction to igneous and metamorphic petrology. 697 p. Prentice-Hall, New Jersey.

Wise, J. (2002) Examples of syntectonic emplacement instead of passive pluton emplacement in the Coastal Batholith of Peru and implications for Late Creataceous Nazca plate motions. Boletin de la Sociedad Geologica del Peru, 94, 99-106.

CHAPTER FOUR

TEMPORAL HISTORIES OF CORDILLERAN ARC MAGMATISM

Introduction

Convergent continental margins, where oceanic lithosphere is subducted beneath continental lithosphere, are areas of intense magmatism, and important sites of crustal growth (e.g., Crisp 1984; Rudnick 1995; Tatsumi 2005; Davidson and Arculus 2006). Assessing crustal production rates and understanding the mechanisms controlling magmatic addition in continental arcs are two issues that are of key importance in tectonic studies. The Cordilleran orogenic system is particularly well suited for addressing these aspects, as it features a spatially extensive (>15,000 km), nearly continuous mountain belt that is the expression of subduction of oceanic lithosphere beneath a continental margin. Subduction-related activity in the Cordilleran orogen initiated in the Early Paleozoic along some parts of the arc (e.g., Bahlburg and Hervé 1997; Ramos 2009) and is still on-going today, thus providing an exceptionally long continental magmatic arc record. Based on the relative abundance of igneous rocks with known ages, a non-steady state behavior of magmatic arc activity, characterized by periods of magmatic quiescence alternating with magmatic flare-ups, has been documented in several Cordilleran arc segments including the Coastal Ranges, British Columbia (e.g., Armstrong 1988; Ducea and Barton 2007; Gehrels et al. 2009), the Cascade Mountains, Washington (R. B. Miller et al. 2009), the Sierra Nevada, California (Bateman and Shervais 1992; Ducea 2001; DeCelles et al. 2009; Paterson et al. 2014), the Transverse Ranges, California (Barth et al. 1997; 2008), the Sierra Madre Occidental and

Trans-Mexican Volcanic Belt, Mexico (Ferrari et al. 1999), and the central Andes (Haschke 2002; Haschke et al. 2006; Trumbull et al. 2006). Existing models to explain the non-steady state magmatic activity of continental arcs either invoke (i) external forcing by plate tectonic processes (Pilger 1984; Hughes and Mahood 2008), (ii) intra-arc cyclic processes largely independent of plate motions (Kay and Mahlburg Kay 1993; Ducea and Barton 2007; DeCelles et al. 2009; C. A. Lee et al. 2013) or (iii) a crustal modulation of mantle energy input (de Silva and Gosnold 2007; de Silva 2008; de Silva et al. 2015). Most of these models are based on a temporally and spatially limited record. In order to test the validity of the proposed models, large datasets are needed.

This paper uses an ever-growing database of U-Pb bedrock and detrital zircon age data between 400 and 80 Ma for the American Cordilleras from British Columbia in the north to Patagonia in the south as a means to evaluate the timing and relative strength of continental arc magmatic activity. As the proposed mechanisms for magmatic arc activity operate over distinct temporal and spatial scales, evaluating the scale of repeated age patterns provides a means to test these proposals. Furthermore, by examining 15,000 km of arc length, we are able to evaluate if the proposed mechanisms invoked for a small segment of an arc are representative for entire arc systems, which exhibit variable basement characteristics and subducting plate parameters.

A fundamental question concerns the role of external factors (e.g. plate motions and mantle power) vs. internal factors (e.g. feedback processes in the upper plate) in controlling continental arc magmatic activity. To assess the relative importance of these respective factors, this study evaluates the relationship between magmatic accretion rate and (i) plate kinematic parameters such as plate convergence rate that control magma

production in the mantle wedge (e.g., Cagnioncle et al. 2007), as well as (ii) arc magma composition, which is primarily governed by processes during the transfer of magma from the mantle wedge to the upper crust, i.e. depends on thickness, composition, and state of stress of the upper plate (e.g., Leeman 1983; Mantle and Collins 2008; Chiaradia 2015).

Geological Setting

The Cordilleran orogen, extending along the western edge of the American continents, forms a long (ca. 15,000 km), nearly continuous belt of magmatic arc assemblages generated by the persistent convergence and interaction between lower oceanic and upper continental plates (Dewey and Bird 1970; e.g., Dickinson 1970; Armstrong 1974). Following the break-up of Rodinia, subduction along the North American Cordilleran margin initiated in the Middle–Late Devonian (Burchfield and Davis 1972; 1975; Monger and Price 2002; Dickinson 2004; 2009), whereas the western margin of South America preserves a record of almost continuous subduction since the Cambrian, with the inception of the Terra Australis orogen (Rapela et al. 1998a; 1998b; Pankhurst et al. 2000; Ramos and Aleman 2000; Cawood 2005; Chew et al. 2007; Collo et al. 2009). Despite having formed under one geodynamic regime, the Cordilleran orogen is segmented, i.e. features along-strike tectonic, structural, and morphological variations (Sempere et al. 2008; Ramos 2009). For the sake of the analysis in this paper, the Cordilleran margin is divided into 8 sectors, including from north (British Columbia) to south (Patagonia): (1) the Coast Ranges, (2) the Sierra Nevada, (3) the Peninsular Ranges to Mojave, (4) southeastern Mexico and Central America, (5) the northern Andes,

(6) the Peruvian Andes, (7) the south-central Andes, and (8) the southern Andes. In some cases, the boundaries of these sectors coincide with the spatial limits of tectono-magmatic provinces, in other cases the division is arbitrary and simply a compromise of choosing sectors large enough to incorporate a statistically meaningful amount of data, and small enough to account for local differences in the geological evolution. In the following, the tectonic and magmatic history of the individual Cordilleran arc sectors is briefly summarized. Age compilations and analyses of arc processes presented in this paper are limited to a timeframe between 400 and 80 Ma, hence these summaries focus on the Paleozoic and Mesozoic geological history, with particular emphasis on subduction initiation and evolution.

Coast Range (55–43°N)

This sector is herein defined as the region between 55 and 43° northern latitude. The pre-Cretaceous geological history of this region includes the accretion of several oceanic arc terranes, such as the Swakane and Triassic Chelan Mountains terrane (Tabor et al. 1989; R. B. Miller et al. 1994; Matzel et al. 2004). Subsequent continental arc magmatism in this region is preserved in the ca. 1500 km long Coast Plutonic Complex (e.g., Monger et al. 1982; Tabor et al. 1989), which records continental magmatic arc activity between ca. 170 and ca. 50 Ma with flare-ups at 160–140 Ma, 120–78 Ma, and 55–48 Ma (Gehrels et al. 2009). Magmatism was accompanied by crustal extension until the mid-Cretaceous, when the accretion of the Alexander-Wrangellia terrane to the western margin of Laurentia caused local compression, crustal thickening and thrusting (Gehrels et al. 2009). The Late Cretaceous to Early Tertiary marks a transition to dextral

transpressional tectonics in the Coast Mountains sector, attributed to changing plate kinematics, which resulted in a dramatic reduction of magmatic production (Gehrels et al. 2009). During the Late Cretaceous to Early Tertiary, arc magmatism in the Coast Mountains Batholith migrated eastward. After ca. 48 Ma, plate convergence ceased along this portion of the Cordilleran orogen.

Sierra Nevada (43–32°N)

The Sierra Nevada section of the Cordilleran magmatic arc is located in western California, USA, limited to the north by the Mendocino triple junction at ca. 43°N and to the south by the Garlock fault at ca. 32°N. After the breakup of Rodinia in the Late Neoproterozoic, this part of the Cordilleran margin remained passive until the middle to late Devonian, when an intraoceanic arc complex formed in the eastern Klamath and northern Sierra terranes (Bradley 2008; Dickinson 2009; Colpron and Nelson 2011). These subduction complexes subsequently collided with the Pacific margin in the Late Devonian to Early Mississippian Antler orogeny, which involved the thrusting of oceanic strata of the Golconda Allochthon onto the Paleozoic miogeocline. Subsequently, arc magmatism ceased with the beginning of Late Devonian to Early Carboniferous extensional tectonics that gave rise to a marginal ocean basin, the Slide Mountain Ocean Basin (Nokleberg et al. 2000; Nelson et al. 2006). This ocean basin closed in the Middle Permian as a consequence of a subduction zone jump and polarity reversal, which led to the accretion of additional fringing oceanic island arc complexes onto the Laurentian platform during the Late Permian–Early Triassic Sonoma orogeny (Dickinson 2009). The Early Triassic marks the inception of a continental magmatic arc along (not only) the

Sierran sector of the Cordilleran orogen (Barth and Wooden 2006; Paterson et al. 2014). Continued subduction of Pacific lithosphere culminated in the construction of the voluminous Sierra Nevada batholith, which records episodic magmatic activity between ca. 250 and ca. 80 Ma with peaks occurring in Triassic (ca. 230–210 Ma), Middle to Late Jurassic (ca. 180–160 Ma), and mid-Cretaceous (ca. 115–95 Ma) time (T. W. Stern et al. 1981; Ducea and Barton 2007; Ducea 2011; Paterson et al. 2014). Latest Cretaceous pluton crystallization ages become progressively younger towards the east, which has been associated with gradual slab flattening (Chen and Moore 1982; Silver and Chappell 1988). The ensuing episode of flat-slab subduction is commonly linked with the Laramide orogeny (Dickinson and Snyder 1978; E. L. Miller et al. 1992), and eventually led to the cessation of magmatism in the Sierras at ca. 85 Ma (Chen and Moore 1982; Lipman 1992).

Peninsular and Transverse Ranges, Mojave, and Northern Mexico (35–20°N)

This sector extends from the southern limit of the Sierra Nevada at ca. 35°N to about 20°N, and includes the morphotectonic domains of the Peninsular Ranges, Transverse Ranges, and the Mojave Desert in the US, and Baja California and the Cordillera Occidental in Mexico. The plutonic record of this region includes overlapping continental arc segments of Permian to Cretaceous age (Barth et al. 2008). Mesozoic (Triassic to Cretaceous) plutonic suites are distributed in this region along three NNW-trending belts (Barth et al. 1997; Kistler et al. 2014). Early to Late Cretaceous magmatism is manifested by the numerous plutons of the ca. 128–86 Ma Peninsular Ranges Batholith that records a west to east progression of subduction transitioning from

an oceanic to a continental arc setting (Hildebrand and Whalen 2014; Morton et al. 2014).

Southeastern Mexico and Central America (25–15°N)

Southeastern Mexico and Central America are composed of several fault-bounded crustal blocks with different geological histories that were juxtaposed in the course of Pangea amalgamation and dispersal during the Paleozoic and Mesozoic (Campa and Coney 1983; Sedlock et al. 1993; Dickinson and Lawton 2001; J. D. Keppie 2004). Processes attributed to the subduction of (Paleo-)Pacific oceanic lithosphere have affected the region at least since the Carboniferous (Proenza et al. 2004; J. D. Keppie et al. 2008; 2010; 2012; Galaz et al. 2013). Continental arc magmatism was particularly abundant during the Carboniferous–Permian, as manifested by the detrital zircon record and isolated outcrops of igneous rocks in the Mixteca and Oaxaquia terranes (Torres et al. 1999; Kirsch et al. 2012; Ortega-Obregón et al. 2014) as well as the Chiapas Massif of the Maya block (Schaaf et al. 2002; Weber et al. 2007; Solari et al. 2009). In the Acatlán Complex, which forms the Paleozoic basement of the Mixteca terrane, basin formation and the intrusion of calc-alkaline plutons was associated with local intra-arc extension, interpreted as a result of oblique, east dipping Pacific subduction (Ramos-Arias et al. 2008; J. D. Keppie et al. 2012; Kirsch et al. 2013). The Middle–Late Triassic history of southeastern Mexico is characterized by subdued magmatic arc activity and local compression and uplift, which have been attributed to transient flat-slab subduction (Kirsch et al. 2014). Magmatic arc activity was re-established by the Early–Middle Jurassic and continued into the Cretaceous (e.g., Barboza-Gudiño et al. 2004; Campa-Uranda et al. 2004; Fastovsky et al. 2005; Barboza-Gudiño et al. 2008; Zavala-Monsiváis

et al. 2009; Godínez-Urban et al. 2011; Zavala-Monsiváis et al. 2012). During the Late Triassic to Early Jurassic, peripheral (back-arc?) ocean basins formed at the western margin of continental Mexico (Centeno-García et al. 1993; Martini et al. 2010), accompanied by the deposition of siliciclastic rocks with a passive margin signature (Silva-Romo et al. 2000; Centeno-García 2005) and the intrusion of mafic rocks with a back-arc geochemical signature (Grajales-Nishimura et al. 1999; Valencia-Moreno et al. 2001; J. D. Keppie et al. 2006; Helbig et al. 2012a; 2012b). These basins were subsequently closed in the Early Cretaceous, when a Middle Jurassic–Lower Cretaceous arc assemblage known as the Guerrero Composite Terrane accreted to mainland Mexico (Martini et al. 2011; 2013; Palacios-García and Martini 2014).

Northern Andes (12°N–5°S)

The sector referred to as the Northern Andes comprises the western margin of South America between 12° N and 5° S latitude (present coordinates), i.e. Colombia and Ecuador, and western Venezuela. The southern boundary of this sector coincides with the Huancabanga deflection, which marks a change in strike orientation of the Andean orogen. Due to this region's paleogeographical location close to the Ouachita-Marathon suture, the Paleozoic to Mesozoic tectonic and magmatic history of this region, recently summarized by (Spikings et al. 2014), is to a large part influenced by processes related to Pangea assembly and break-up. Moreover, the accretion of the Caribbean Large Igneous Province in the late Mesozoic has had an impact on the geological record of the northern Andes (Spikings et al. 2014). The earliest evidence of a continental arc in the northern Andes includes arc-derived Ordovician schists and gneisses in the Eastern Cordillera of Ecuador and the Central Cordillera of Colombia (Litherland et al. 1994; Carmona and

Pimentel 2002; Chew et al. 2007). Magmatic rocks between 290–240 Ma occur in the Santa Marta Massif and the Guajira Peninsula, as well as the Cordillera Central in Colombia (Litherland et al. 1994; Cardona et al. 2010; Villagómez et al. 2011; Laya and Tucker 2012; Van der Lelij et al. 2015) and are interpreted to have formed above an east dipping Pacific subduction zone during the final stages of Pangea formation. Based on plate reconstructions (Elías-Herrera and Ortega-Gutiérrez 2002; Weber et al. 2007) and the occurrence of similarly aged arc-related igneous rocks, the basement terranes of southern Mexico and Central America are interpreted to have formed the conjugate margin to NW South America (Cochrane et al. 2014). Crustal anatectites and juvenile mafic suites with ages between 240–216 Ma are considered to record the oblique rifting of these Mexican terranes from the NW South American margin. The ensuing passive margin stage was superseded by renewed active margin magmatism that initiated diachronously along the North Andean margin between 213 and 185 Ma (Cochrane et al. 2014; Van der Lelij et al. 2015) and continued into the Cretaceous (Villagómez et al. 2011; Boekhout et al. 2012; Reitsma 2012; Villagómez and Spikings 2013; Cochrane et al. 2014). A period of back-arc extension marks the period of 145–114 Ma, which led to the emplacement of juvenile igneous rocks in the Cordillera Real, Cordillera Central and the Santander Massif (Litherland et al. 1994; Romeuf et al. 1995; Bustamante et al. 2010; Cochrane et al. 2014; Van der Lelij et al. 2015) and may have resulted in the detachment of continental slivers (Chaucha and Tahamí terranes, Spikings et al. 2014 and references therein). These slivers are inferred to have been accreted back to the margin during a switch to compressional tectonics at ca. 115 Ma (Ruiz et al. 2007; Villagómez et al. 2011). Arc magmatism is scarce between ca. 115 Ma and 100 Ma due to highly oblique

convergence between the newly formed Caribbean plate and the South American plate (Pindell and Kennan 2009). The origin of acidic magmatism between 100–75 Ma, e.g. represented by the 95–85 Ma Antioquia batholith (Villagómez et al. 2011; Villagómez and Spikings 2013), is currently debated (Pindell and Kennan 2009; Spikings et al. 2014). Mafic igneous rocks occurring in the Western Cordillera of Ecuador and Colombia that have ages between ca. 100 and 85 Ma belong to the Carribean Large Igneous Province, parts of which amalgamated to northwestern South America between 75–70 Ma (Spikings et al. 2001; Kerr et al. 2002; Vallejo et al. 2006; Spikings et al. 2010; Villagómez and Spikings 2013).

Peruvian Andes (6–18°S)

In the Peruvian Andes, located between 6° S (the Huancabamba deflection) and 18° S (the Arica deflection, or Bolivian orocline), continental arc magmatism initiated in the Ordovician along the northern and central Peruvian Eastern Cordillera as part of the Famatinian orogenic cycle (Mukasa and Henry 1990; Gosen and Prozzi 1998; Pankhurst et al. 2000; Cawood 2005; Vaughan and Pankhurst 2008; Bahlburg et al. 2009). The Silurian and Devonian mark a hiatus in the magmatic arc record (Chew et al. 2007; Bahlburg et al. 2009), possibly due to changing plate kinematics of the detachment of a segment of the Arequipa-Antofalla block, which is a Precambrian basement block that underlies much of the coastal region of southern Peru (Loewy et al. 2004). Magmatic activity resumed in the Early Mississippian (ca. 345 Ma: Chew et al. 2007; Mišković et al. 2009) and was followed by Late Permian to Late Triassic lithospheric thinning, accompanied by metamorphism and deformation, as well as the emplacement of partially

migmatized granitoids at 285–223 Ma (Mišković et al. 2009 and references therein). Easterly subduction of Pacific lithosphere and associated calc-alkaline magmatism in the Western Peruvian Cordillera was re-established by the Late Triassic (Boekhout et al. 2012; Demouy et al. 2012), but was interrupted by a period of back-arc extension and bimodal igneous activity in the Jurassic (Ramos and Aleman 2000; Sempere et al. 2002; Boekhout et al. 2012; Demouy et al. 2012), which is attributed to a global change in plate kinematics (Ramos 2010).

South-Central Andes (18–40°S)

The Cordilleran sector defined here as the south-central Andes includes the Andean Range of Bolivia, northern Chile and west-central Argentina from the Arica deflection, at 18°S in the north, to 40°S latitude in the south (present coordinates) that corresponds to the Chilenia–Patagonia terrane boundary. The basement of the south-central Andes is characterized by a number of parautochthonous and allochthonous crustal fragments, namely the Pampia, Famatina, Antofalla, Cuyania, and Chilenia terranes that accreted to the South American margin at various times throughout the Late Neoproterozoic and Early Paleozoic (Ramos 2009 and references therein). Evidence for early magmatic activity in the south-central Andes is found in the Famatinian orogen, a continental magmatic arc active between ca. 505 Ma and 420 Ma (Bahlburg et al. 2009). The Devonian is marked by magmatic and tectonic quiescence along the south-central Andean margin (Bahlburg and Hervé 1997; Chew et al. 2007; Bahlburg et al. 2009; Cardona et al. 2009), but locally, such as in the Sierras Pampeanas in NW Argentina, Middle–Late Devonian A-type granitoids occur (Dahlquist et al. 2013). Continental arc

magmatism was widespread during the Late Paleozoic to Early Mesozoic, for example represented by the Chilean Frontal Cordillera Batholith that shows magmatic pulses during the Mississippian, Early Permian, Late Permian–Middle Triassic, and Upper Triassic (Hervé et al. 2014; Maksaev et al. 2014). After another gap in arc magmatic activity during the Late Permian to Late Triassic, subduction was re-established and persisted into the present day in what is referred to as the Andean cycle (Ramos and Aleman 2000; Haschke et al. 2006). During the Jurassic to Early Cretaceous, extensional tectonics characterized the south-central Andean margin, which led to the development of a magmatic arc located along the present-day coastal Cordillera, and a series of back-arc basins to the east (e.g., Oliveros et al. 2012; Rossel et al. 2013).

Southern Andes (39–55°S)

The southern Andean sector coincides with the tectonic province known as Patagonia, which extends from about 39°S to 55°S latitude. The Paleozoic geological history of Patagonia is not agreed upon in every aspect, but is generally interpreted to have involved the collision of an (para-)autochthonous northern block, and an allochthonous southern block in the Carboniferous (Pankhurst et al. 2006; Ramos 2008; Rapalini et al. 2010; Ramos and Naipauer 2014). Subduction-related magmatic rocks of Early Devonian to Carboniferous age occurring in the North Patagonian Massif are interpreted to reflect the destruction of the ocean basin between these blocks (e.g., Hervé et al. 2013). In the southern block, east-dipping subduction may have commenced at ca. 390 Ma and continued into the Mesozoic (Kato et al. 2008; Chernicoff et al. 2013). Voluminous and regionally extensive Mesozoic to Cenozoic continental magmatic arc

activity in the southern Andes is evidenced by the Patagonian batholith that is subdivided into a Late Cretaceous to Late Miocene northern part (Pankhurst et al. 1999), a Late Triassic central part (Rapela and Pankhurst 1992; Zaffarana et al. 2014), and a Late Jurassic to Neogene southern part (Rolando et al. 2002; Hervé et al. 2007).

Methods

Age Compilations

Age spectra between 400 and 80 Ma were constructed on the basis of ca. 1,300 (bulk) U/Pb crystallization ages of igneous rocks, and 15,575 detrital zircon U/Pb ages from published and unpublished sources (see Appendix F for complete list of references). The compilation contains U-Pb analyses only, because Rb/Sr, K/Ar and $^{40}Ar/^{39}Ar$ analyses may yield erroneous ages due to daughter isotope loss, low-grade metamorphism and/or hydrothermal activity post-dating volcanic and plutonic rock emplacement, even in young volcanic rocks (e.g., Montecinos et al. 2008). The age compilation combines TIMS (thermal ionization mass spectrometry), LA-ICP-MS (laser ablation inductively coupled plasma mass spectrometer), SHRIMP (sensitive high-resolution ion microprobe), and SIMS (secondary ion mass spectrometry) analyses. Coordinates were extracted for each bedrock and detrital zircon sample to enable the division of age data into predefined sectors along the Cordilleran arc. To constrain data collection and analyses, we focused on age data between 400 Ma and 80 Ma only. These limits are arbitrary, but were chosen because (i) magmatic arc activity started in the Early Paleozoic in many places along the Cordilleran orogen and terminated at around 80 Ma in the Sierran sector, (ii) the number of available Cenozoic igneous and detrital U/Pb ages is

inadequate due to the fact that young igneous arcs are commonly dated with the $^{40}Ar/^{39}Ar$ method and there are few detrital zircon studies of Cenozoic deposits.

Each bedrock age represents a multiple or bulk zircon age of analyses from three or more single zircon grains (or domains therein) that were calculated by the original author. This does not apply for the Sierran sector, for which single zircon bedrock ages have been compiled. The dated rocks summarized as "bedrock ages" comprise chiefly plutonic rocks with a predominantly felsic to intermediate composition and only a few volcanic rocks.

Detrital zircon samples of different depositional age were included in the compilation to sample the maximum number of sources exposed at various times in the geological past. The detrital zircons are interpreted to represent magmatic ages. Zircon ages identified to have a metamorphic origin (mostly based on U/Th ratios) by the original investigators are excluded from the compilation. The concordance of each zircon grain was calculated from $^{206}Pb/^{238}U$ and $^{207}Pb/^{235}U$ ages to ensure that only concordant grains, i.e. with < 10 % normal and < 5 % reverse discordance, were included in the age compilation.

For igneous and detrital zircon data, respectively, age data (Figure 67) are plotted as (i) histograms with a 10 Ma bin width, and (ii) kernel density estimates (KDE's; Vermeesch 2012), which are overlain on the histograms. The histograms allow visual evaluation of the number of samples forming age peaks and enables inter-sample comparison, but are constructed using a constant bin size, which may not be appropriate for zircon age distributions, which are neither smooth nor unimodal (e.g., Vermeesch 2012). The calculated KDEs, on the other hand, are based on adaptive kernel density

estimation, in which the bandwidth is varied according to the local density. As a smooth and continuous alternative to the discrete and discontinuous histogram, KDEs facilitate the automatic extraction of peaks and other time series parameters and allows normalization and thus the combination of bedrock and detrital zircon age data.

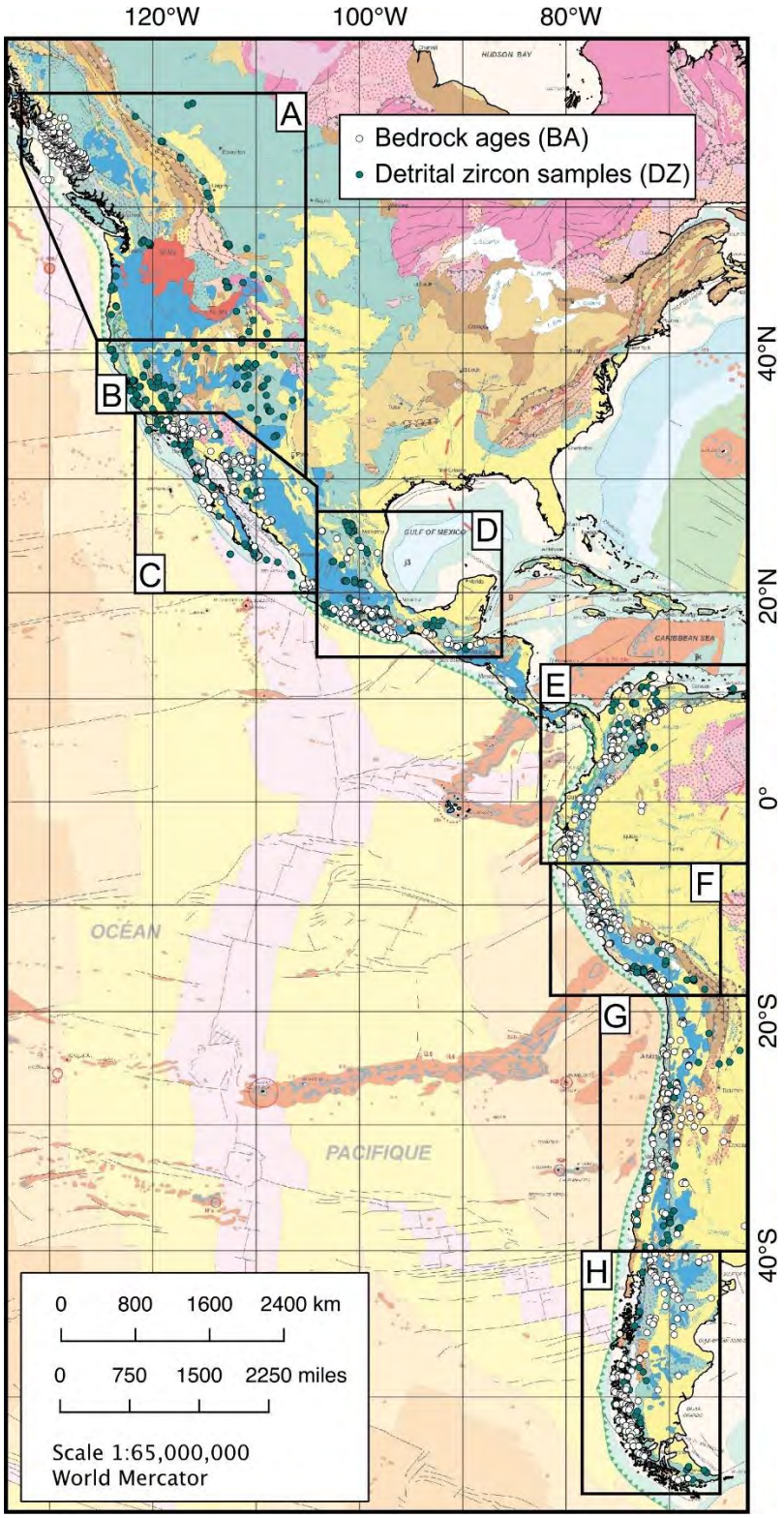

Figure 66. Map showing the extent of defined arc sectors, and sample locations of the igneous and detrital zircon U-Pb data a. Geological map data from Bouysse et al. (n.d.).

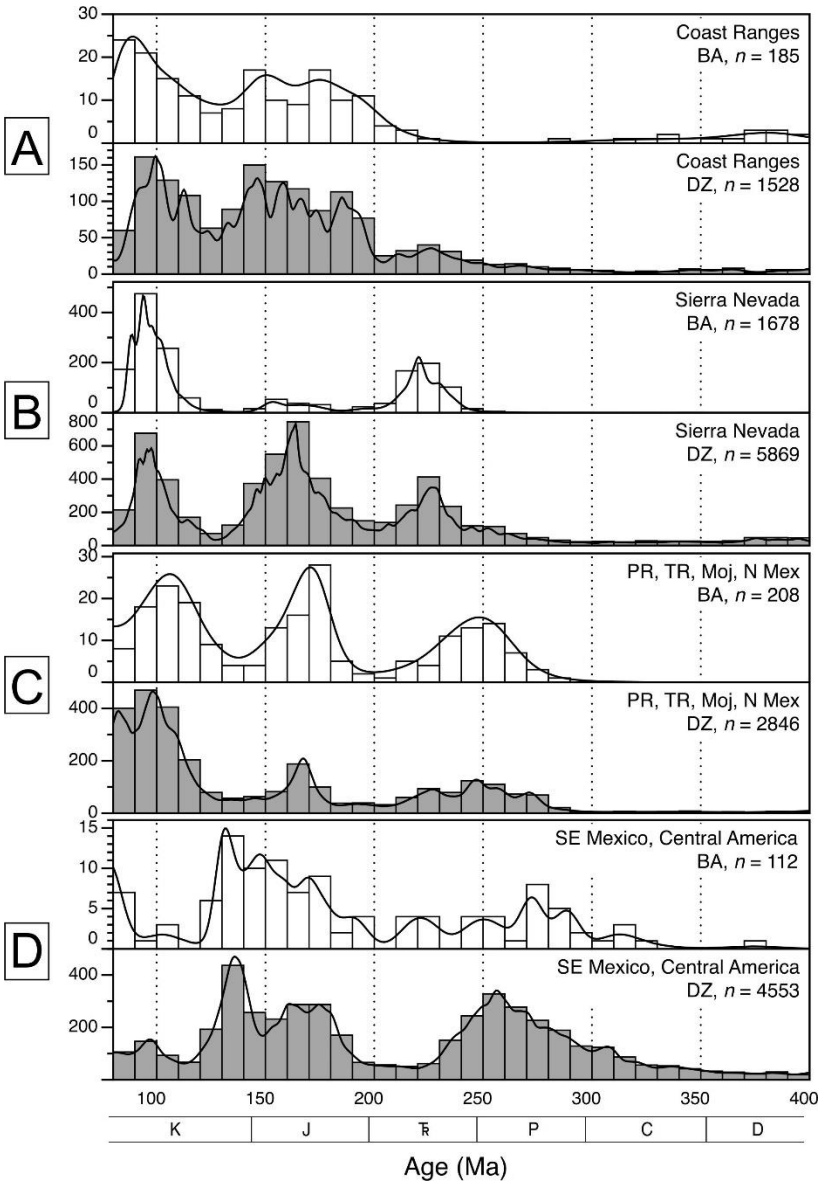

Figure 67. Igneous and detrital zircon U-Pb age spectra providing a temporal record of Cordilleran arc magmatism between 400 and 80 Ma. Individual diagrams include TIMS, LA-ICP-MS, SHRIMP, and SIMS age data presented as histograms with a 10 Ma bin width and adaptive Kernel Density Estimator (KDE) functions (see text for details). For igneous rocks (IGN), the number of analyses (*n*) given in each plot represents the number of crystallization ages, which are composite ages calculated from three or more single zircons. Exception: igneous ages from the Sierra Nevada represent single zircon ages. In detrital zircon spectra (DZ), *n* refers to ages of single zircon grains (or a domain therein). Abbreviations in the age plots are as follows: PR—Peninsular Ranges, TR—Transverse Ranges, Moj—Mojave Desert, N Mex—Northern Mexico, SE Mexico—Southeastern Mexico. See Appendix F for data sources.

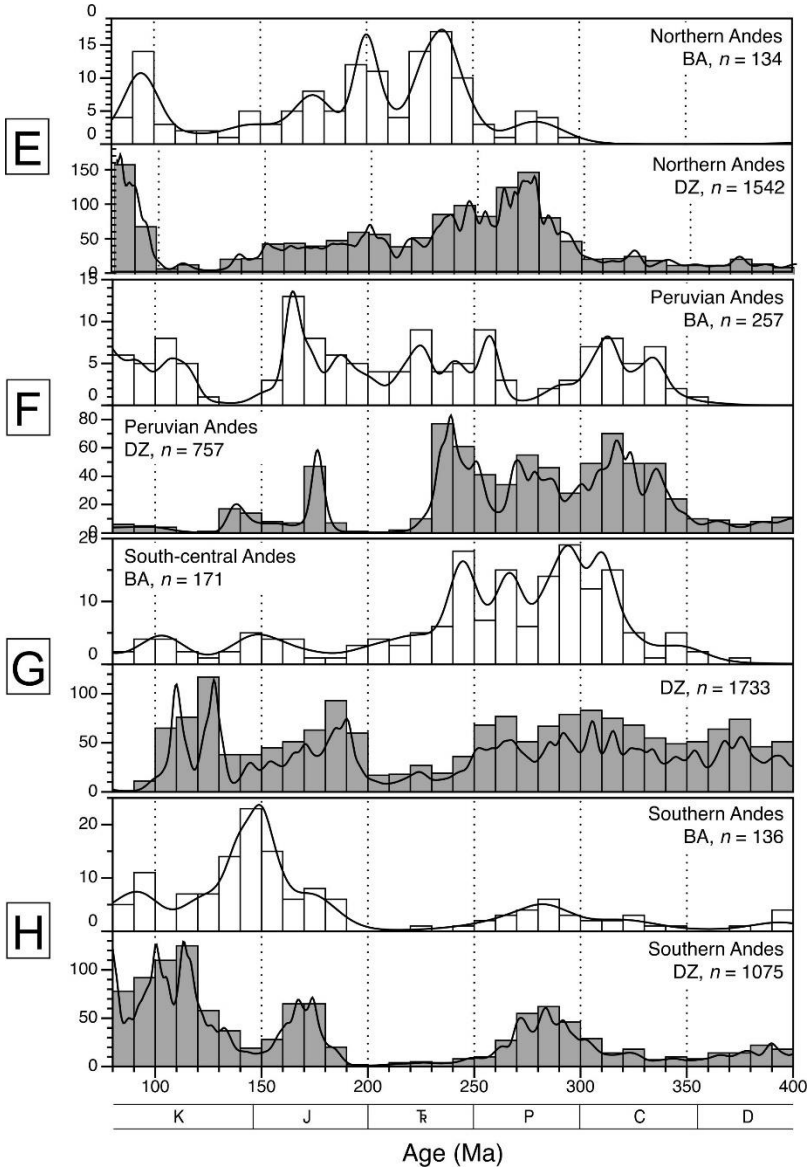

Figure 67. Continued. Igneous and detrital zircon U-Pb age spectra providing a temporal record of Cordilleran arc magmatism between 400 and 80 Ma. Individual diagrams include TIMS, LA-ICP-MS, SHRIMP, and SIMS age data presented as histograms with a 10 Ma bin width and adaptive Kernel Density Estimator (KDE) functions (see text for details). For igneous rocks (IGN), the number of analyses (*n*) given in each plot represents the number of crystallization ages, which are composite ages calculated from three or more single zircons. Exception: igneous ages from the Sierra Nevada represent single zircon ages. In detrital zircon spectra (DZ), *n* refers to ages of single zircon grains (or a domain therein). Abbreviations in the age plots are as follows: PR—Peninsular Ranges, TR—Transverse Ranges, Moj—Mojave Desert, N Mex—Northern Mexico, SE Mexico—Southeastern Mexico. See Appendix F for data sources.

KDEs were chosen as a statistical technique to visualize age populations rather than probability density plots (PDPs) because KDEs are considered statistically more robust than the mostly used PDP, especially when data quantity and/or precision is high (Vermeesch 2012). Furthermore, because the kernel density estimate does not take into account analytical uncertainties, the different levels of precision of the compiled TIMS, LA-ICP-MS, SHRIMP, and SIMS age data have no effect on the shape of the KDEs. KDE calculation was accomplished using an open-source Java application developed by Peter Vermeesch (Density Plotter, http://www.ucl.ac.uk/~ucfbpve/densityplotter/). Composite KDE functions, in which bedrock and detrital age spectra are combined by summing the respective normalized KDE values for each age interval, are plotted in a space-contour plot (Figure 68a) to visualize along-arc variation in magmatic activity. Using Gauss fitting, statistical parameters such as peak location, height, prominence, width, and skewness were calculated from these composite KDE functions. Furthermore, a time-series spectral analysis was performed using the Lomb-Scargle method (Lomb 1976; Scargle 1982) to establish whether or not the zircon age spectra exhibit cyclic behavior. The term "cyclic" is in this paper used synonymously with "periodic", and is defined as a repetition of an event or a sequence of events at regular time intervals. The terms "episode" and "episodic", on the other hand, refer to unique or randomly repeated events. The Lomb-Scargle method is based on a fast Fourier transform, in which the individual composite KDE functions (containing both bedrock and detrital zircon ages from each Cordilleran sector) are decomposed into a combination of sinusoids of different frequencies, amplitudes, and phases. Magnitudes in the resulting Lomb-Scargle periodogram (Figure 68b) represent the contribution of a frequency or period to the

original time series. A periodic event or cycle in the data will create a distinct spike in the periodogram. Frequencies or periods with a high spectral magnitude can be attributed to a periodic event, but only if the sampling interval supports at least 3 periods of that frequency (e.g., Telgársky 2013). Hence, only periods up to 100 Ma are considered.

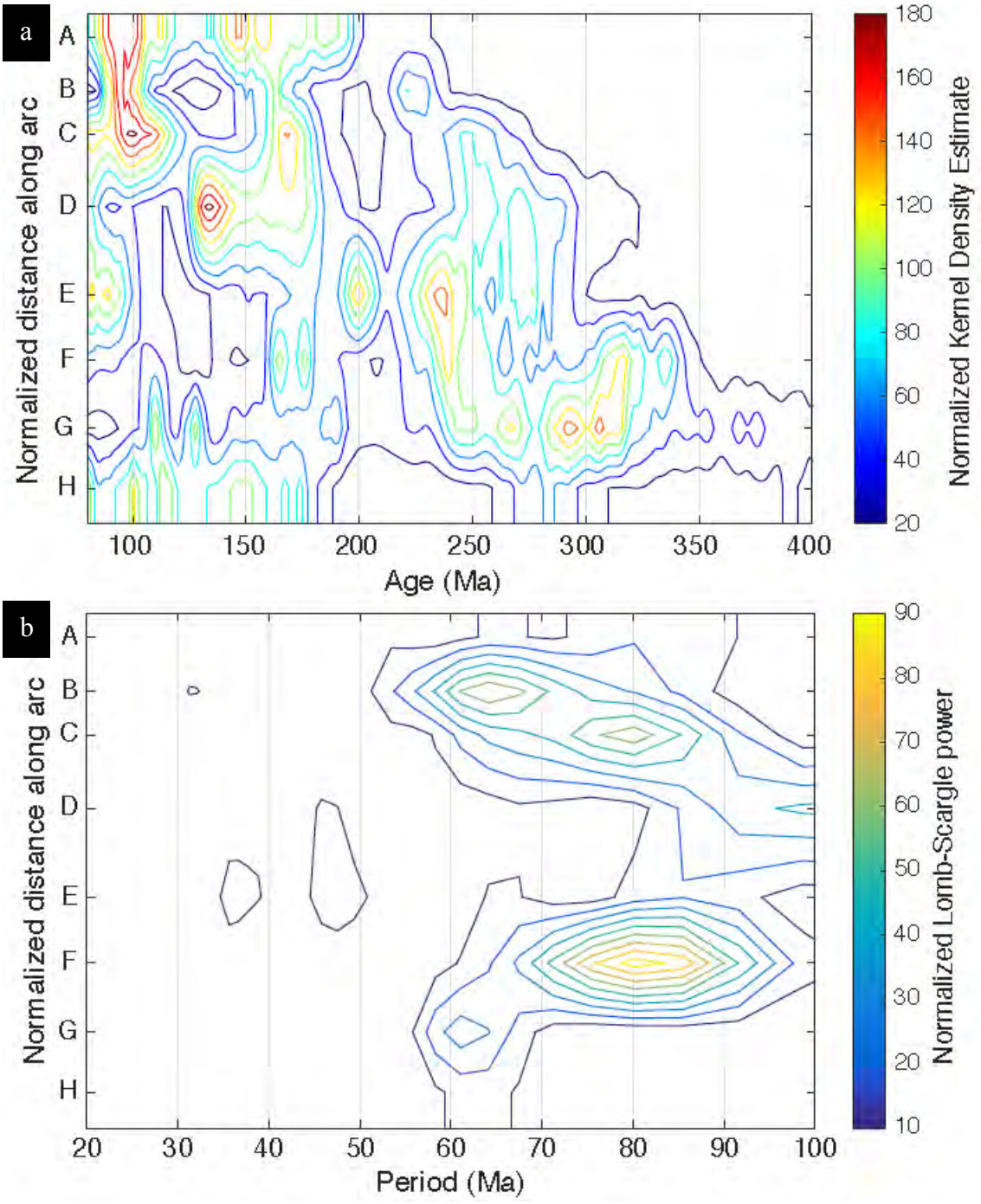

Figure 68. (a) Color contour plot of composite KDE functions, highlighting the spatial and temporal distribution of age populations (i.e., magmatic arc activity) along the Cordilleran arc. Labels of y-axis indicate the latitudinal centers of each Cordilleran arc sector along an along-arc profile. Letters A–H refer to arc sectors as defined in Figure 67. (b) Color contour plot showing results of a Fast Fourier Transform (FFT) based time series analysis to evaluate periods of dominant frequencies in Cordilleran arc age data.

Geochemical Data

In order to investigate how changes in geochemical composition of arc-related igneous rocks correlate with magmatic arc activity, geochemical data are currently being compiled by the authors for all eight arc domains. In this paper, three of these datasets, i.e. from (i) the Sierra Nevada, (ii) the Peninsular Ranges, Transverse Ranges, Mojave, and northern Mexico, and (iii) southeastern Mexico and Central America are presented. Flare-up events, identified on composite KDE functions of the individual arc sector by visual gauging of peak distribution, width, and height, were used as a reference for description of trends in geochemical data. The geochemical proxies include SiO_2 to evaluate extent of differentiation, εNd_i and $^{87}Sr/^{86}Sr_i$ to assess the relative roles of crustal and mantle components in arc magmas (e.g., DePaolo and Wasserburg 1979; DePaolo 1981a), and Sr/Y and $(Sm/Yb)_n$ for a measure of magma source depth and crustal thickness (e.g., Mamani et al. 2010; Chiaradia 2015; Profeta et al. 2015). Due to the scarcity of available geochemical data with U/Pb zircon ages in the Peninsular Ranges and the southern Mexican sector, respectively, U-Pb-zircon constrained data were supplemented by geochemical data with ages constrained by other means, including $^{40}Ar/^{39}Ar$, K/Ar, Rb-Sr, and Sm-Nd geochronology, and ages estimated using (bio-)stratigraphic evidence. Apart from the data points, median values ± one standard deviation were plotted for a moving 10 Ma average to allow a better evaluation of trends and degree of scatter (Figure 69). In the case of Sr/Y and $(Sm/Yb)_n$, only rocks with < 70 wt.% SiO_2 are plotted to exclude the effect of plagioclase fractionation, affecting Sr/Y, and to exclude garnet bearing granites (e.g., Zhang et al. 2012), affecting both Sr/Y and $(Sm/Yb)_n$.

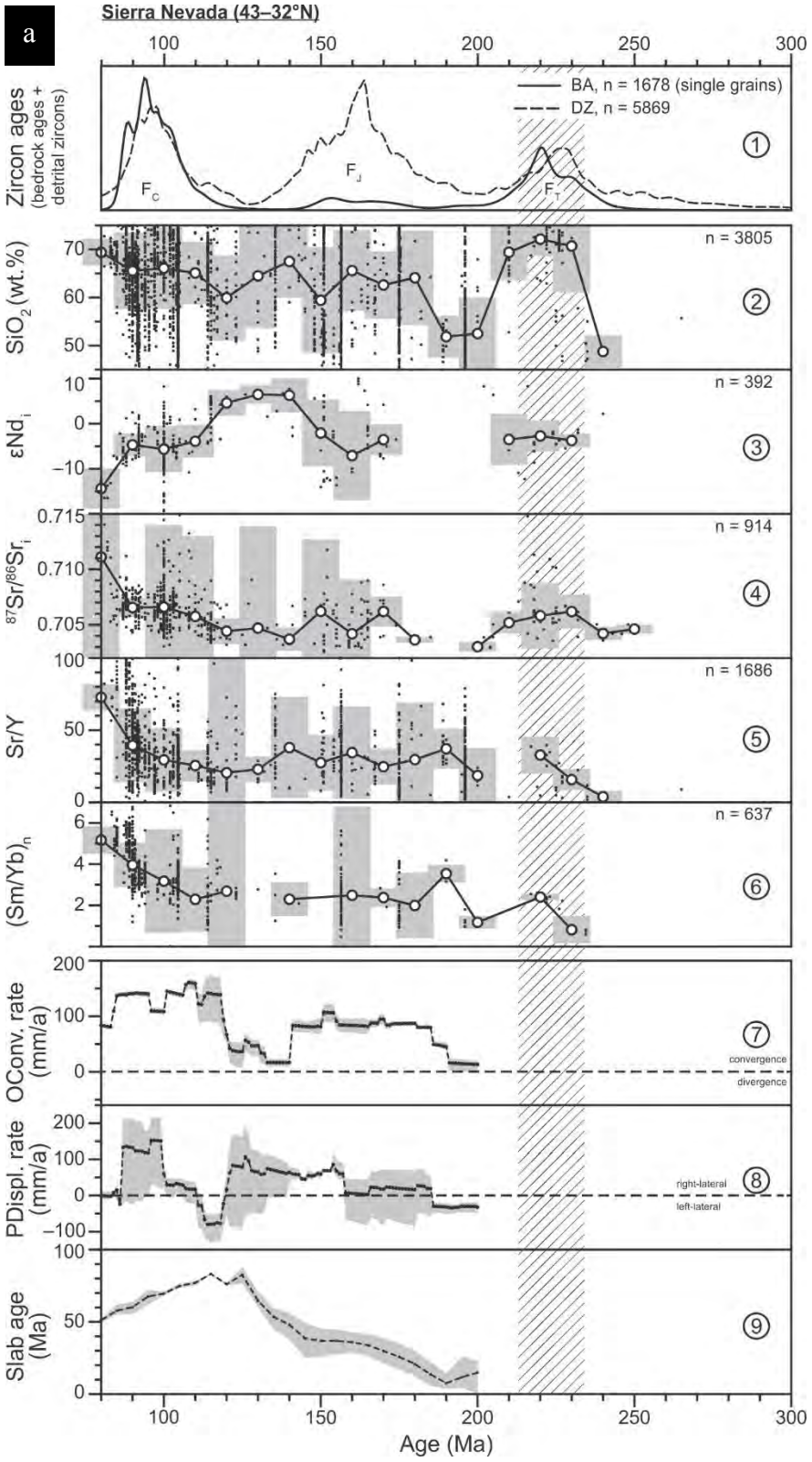
a
Sierra Nevada (43–32°N)
100
150
200
250
300
Zircon ages
(bedrock ages + detrital zircons)
BA, n = 1678 (single grains)
DZ, n = 5869
F_C
F_J
F_T
①
SiO2 (wt.%)
70
60
50
n = 3805
②
εNdi
10
0
−10
n = 392
③
87Sr/86Sri
0.715
0.710
0.705
n = 914
④
Sr/Y
100
50
0
n = 1686
⑤
(Sm/Yb)n
6
4
2
n = 637
⑥
OConv. rate (mm/a)
200
100
0
⑦
convergence
divergence
PDispl. rate (mm/a)
200
100
0
−100
⑧
right-lateral
left-lateral
Slab age (Ma)
100
50
0
⑨
Age (Ma)

Figure 69. (a) Comparison of geochronological (panel 1), geochemical (panels 2–6), and kinematic data (panels 7–9) for arc-related igneous rocks in the sector of the Sierra Nevada. Diagonally hatched bands mark magmatic flare-up events, visually delineated on the basis of peaks in the age spectra. For geochemical data, individual data points are plotted (dots), along with median values ± 1σ (circles and grey bars) for a moving 10 Ma average. For kinematic data, black dots are average values, grey envelopes represent minimum–maximum ranges from a set of three values extracted per arc domain. Abbreviations: BA—bedrock ages, DZ—detrital zircons, OConv.—orthogonal convergence rate, PDispl.—parallel displacement rate. For data sources see Appendix F.

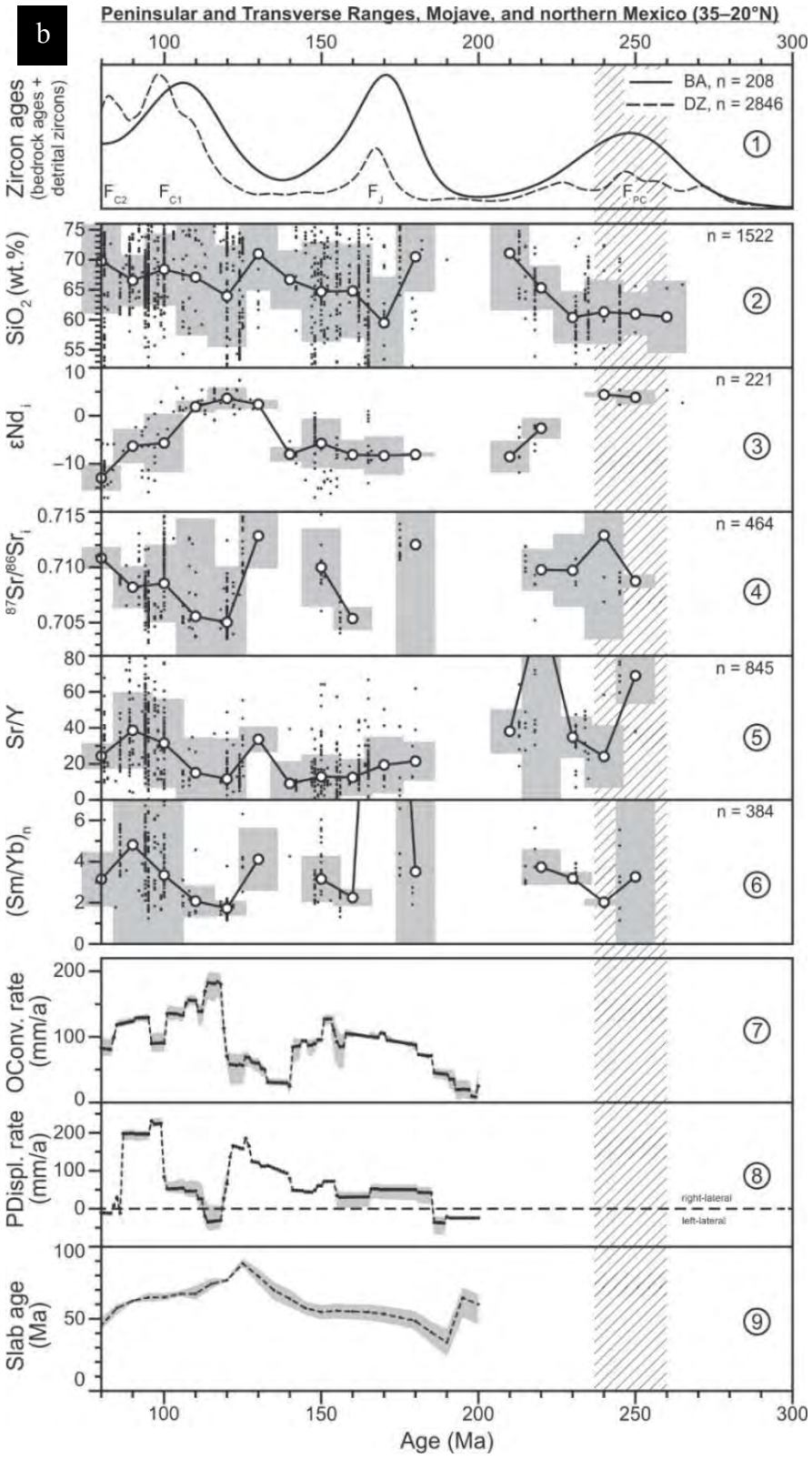
b
Peninsular and Transverse Ranges, Mojave, and northern Mexico (35–20°N)
Zircon ages (bedrock ages + detrital zircons)
BA, n = 208
DZ, n = 2846
F_C2
F_C1
F_J
F_PC
SiO2 (wt.%)
n = 1522
εNdi
n = 221
87Sr/86Sri
n = 464
Sr/Y
n = 845
(Sm/Yb)n
n = 384
OConv. rate (mm/a)
PDispl. rate (mm/a)
right-lateral
left-lateral
Slab age (Ma)
Age (Ma)

Figure 69. (b) Comparison of geochronological (panel 1), geochemical (panels 2–6), and kinematic data (panels 7–9) for arc-related igneous rocks in the sector of the Peninsular and Transverse Ranges, Mojave, and northern Mexico. Diagonally hatched bands mark magmatic flare-up events, visually delineated on the basis of peaks in the age spectra. For geochemical data, individual data points are plotted (dots), along with median values ± 1σ (circles and grey bars) for a moving 10 Ma average. For kinematic data, black dots are average values, grey envelopes represent minimum–maximum ranges from a set of three values extracted per arc domain. Abbreviations: BA—bedrock ages, DZ—detrital zircons, OConv.—orthogonal convergence rate, PDispl.—parallel displacement rate. For data sources see Appendix F.

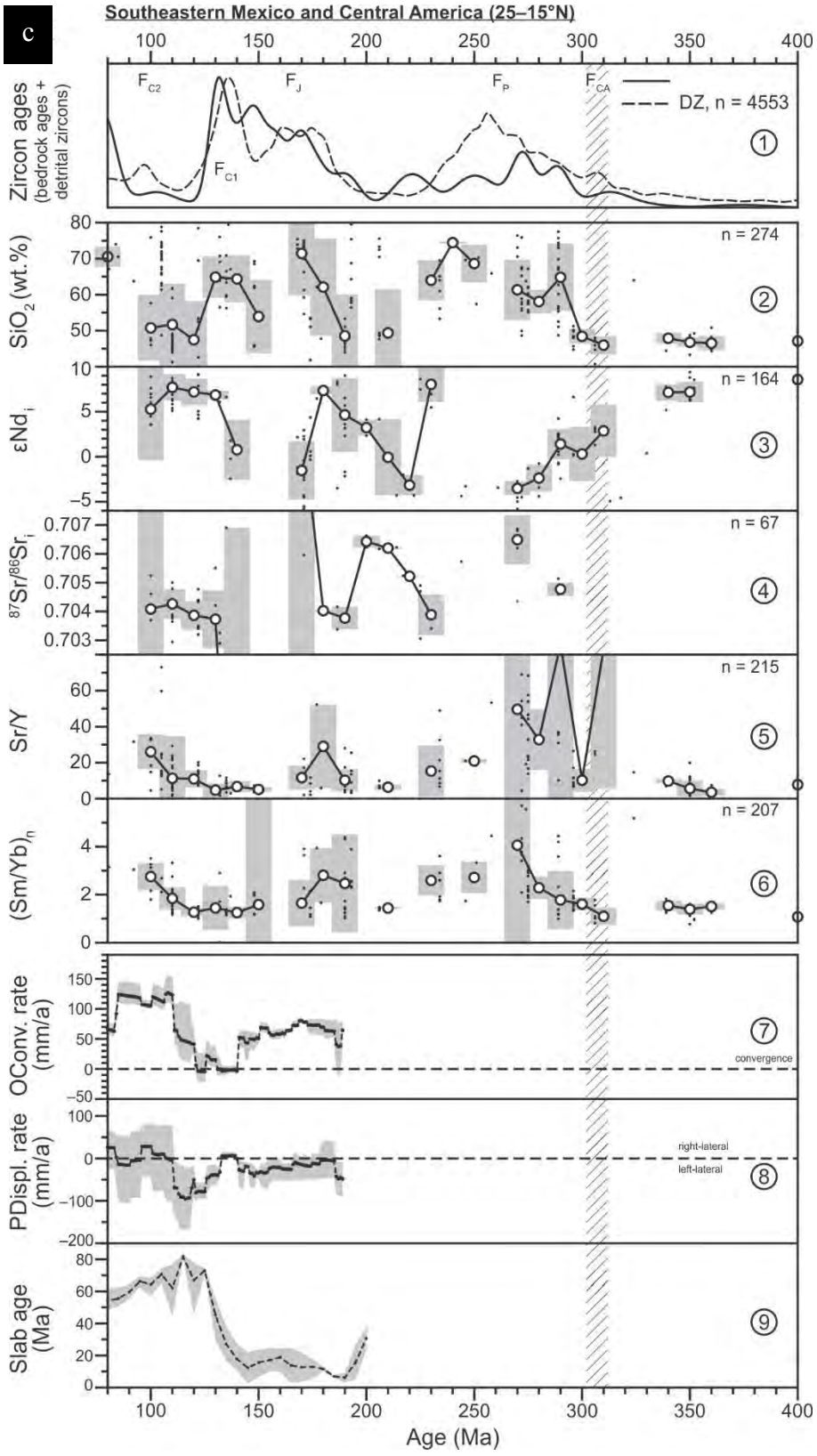
c
Southeastern Mexico and Central America (25–15°N)
Zircon ages (bedrock ages + detrital zircons)
F_C2
F_C1
F_J
F_P
F_CA
DZ, n = 4553
SiO2 (wt.%)
n = 274
εNdi
n = 164
87Sr/86Sri
n = 67
Sr/Y
n = 215
(Sm/Yb)n
n = 207
OConv. rate (mm/a)
convergence
PDispl. rate (mm/a)
right-lateral
left-lateral
Slab age (Ma)
Age (Ma)

Figure 69. (c) Comparison of geochronological (panel 1), geochemical (panels 2–6), and kinematic data (panels 7–9) for arc-related igneous rocks in the sector of southeastern Mexico and Central America. Diagonally hatched bands mark magmatic flare-up events, visually delineated on the basis of peaks in the age spectra. For geochemical data, individual data points are plotted (dots), along with median values ± 1σ (circles and grey bars) for a moving 10 Ma average. For kinematic data, black dots are average values, grey envelopes represent minimum–maximum ranges from a set of three values extracted per arc domain. Note differing age range in (c) compared with the other sectors. Abbreviations: BA—bedrock ages, DZ—detrital zircons, OConv.—orthogonal convergence rate, PDispl.—parallel displacement rate. For data sources see Appendix F.

Kinematic Data

In order to investigate the relationship between continental magmatic arc activity and plate kinematics, rates of (i) trench-orthogonal convergence and (ii) trench-parallel displacement between down-going oceanic and upper continental plates, as well as (iii) slab age were compared.

We obtained relative plate motion from a recent plate kinematic model for the interval of 200–0 Ma (Shephard et al. 2013) by using the Python script convergence.py written by Nathaniel Butterworth, EarthByte Group, School of Geosciences, University of Sydney, and based on the pyGPlates application programming interface for GPlates[1] (Boyden et al. 2011). The relative movement of the upper plate was sampled at 24 selected locations (three per arc domain) in vicinity to the subduction zone vertices in 1 Ma intervals using GMT[2]. To account for changes in plate motion rate within individual arc domains, these three sets of plate motion values per arc domain were used to calculate and plot average values together with minimum and maximum values (Figure 70 and 76). The slab age, i.e., the age of the plate entering the trench, was extracted for 200–0 Ma in 5 m.y. intervals from paleo-age grids used by Seton et al. (2012) and released in Müller et al. (2013) applying the same procedure as described above.

To statistically evaluate the link kinematic parameters and magmatic activity, the Pearson product moment correlation coefficient, which reflects the extent of a linear relationship, was calculated for each parameter pair after reducing the variables to evenly spaced values (Figure 71). Age spectra for arc sectors D–H were extended to 50 Ma to

1 http://www.gplates.org/

2 http://gmt.soest.hawaii.edu/

allow for a more rigorous evaluation of patterns.

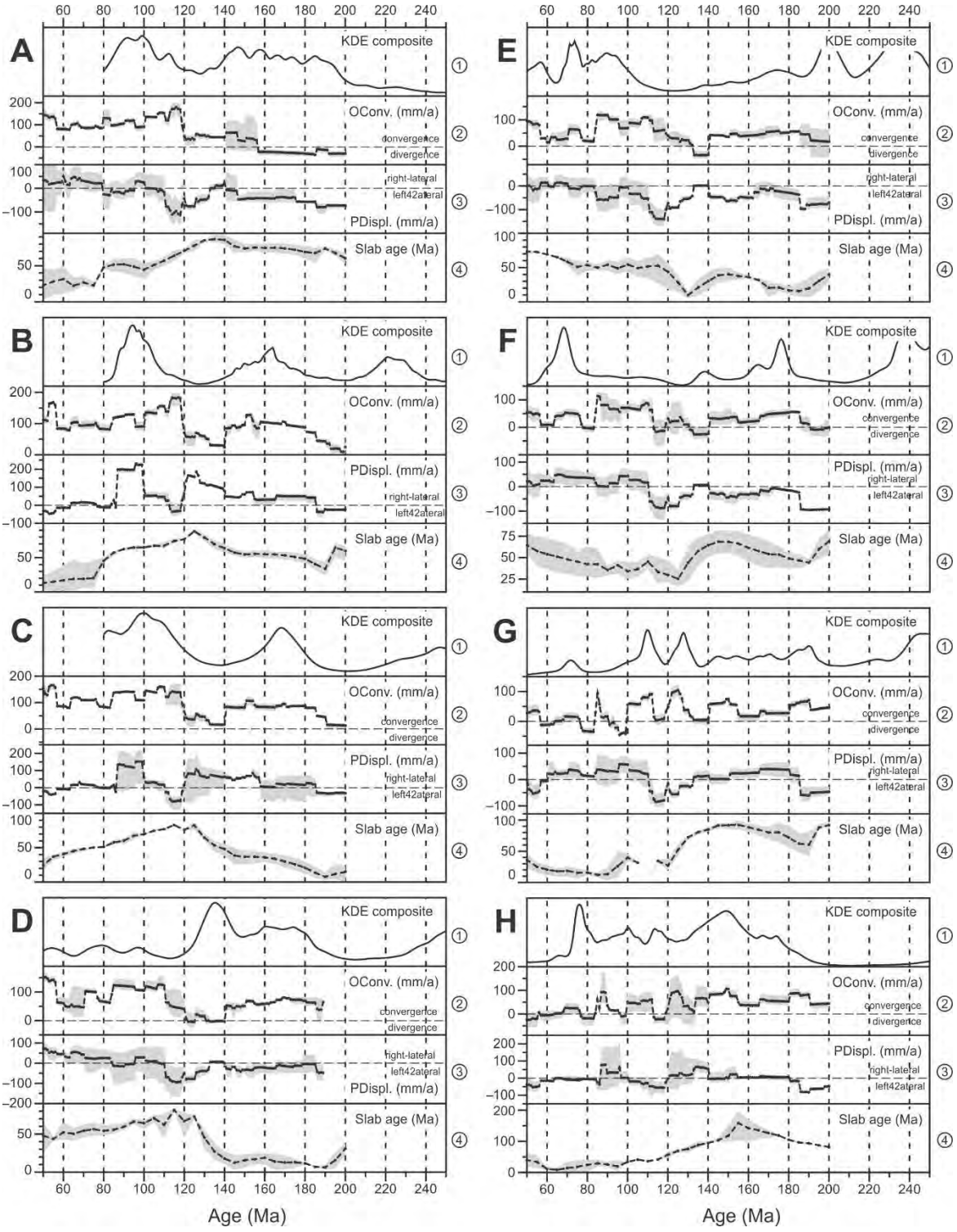
A
B
C
D
E
F
G
H
KDE composite
OConv. (mm/a)
convergence
divergence
PDispl. (mm/a)
right-lateral
left42ateral
Slab age (Ma)
Age (Ma)

Figure 70. Compilation of kinematic data for the Cordilleran orogen for the time between 200 and 50 Ma. Letters A–H refer to arc sectors as defined in Figure 67. Each diagram contains (1) kernel density estimates of combined bedrock and detrital zircon age data, (2) trench-orthogonal convergence rates and (3) trench-parallel displacement rates between down-going oceanic and upper continental plates, and (4) slab age. Black dots in 2–4 are average values, grey envelopes represent minimum–maximum ranges from a set of three values extracted per arc domain.

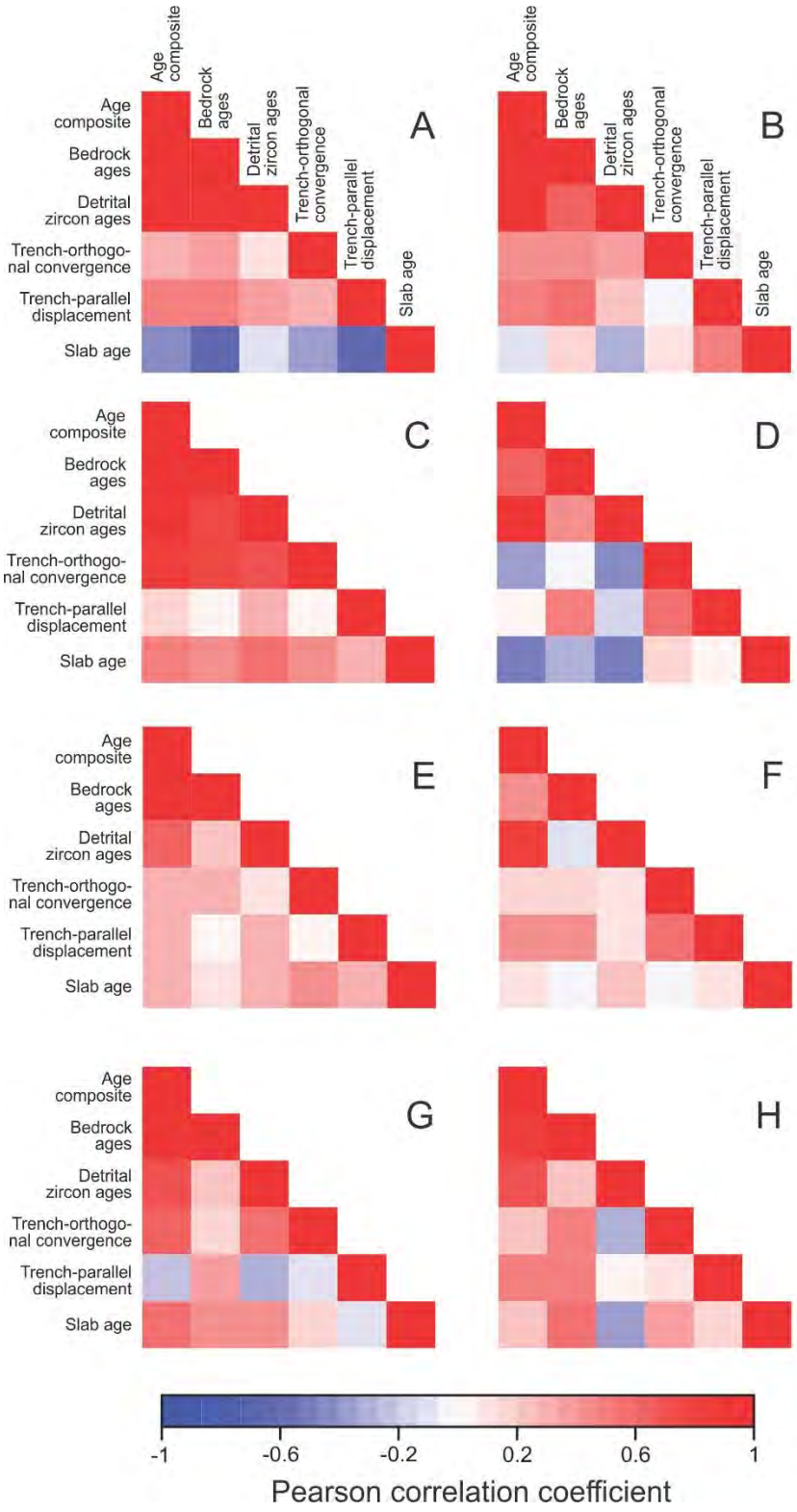

Figure 71. Covariance matrix showing Pearson correlation coefficients for parameters of magmatism and plate kinematics. Letters A–H refer to arc sectors as defined in Figure 66. Red is strong positive correlation; blue is strong negative correlation.

Results

Age Compilation

The number of age data for each Cordilleran arc sector varies between a minimum of 112 (SE Mexico and Central America) to a maximum of 257 composite (Peruvian Andes) or 1678 single zircon bedrock ages (Sierra Nevada), and between 757 (Peruvian Andes) and 5869 (Sierra Nevada) detrital zircon ages. Detrital zircon age spectra are mostly complex, exhibiting many peaks (between 10–Sierra Nevada and 29–Northern Andes), whereas the igneous spectra are characterized by fewer peaks (3–Sierra Nevada to 11–SE Mexico and Central America) of comparatively larger wavelength. KDEs based on bedrock and detrital zircon ages, respectively, generally show a similar distribution of peaks, but these peaks may have different relative amplitudes (Figure 68). In a few cases, maxima in the bedrock age data coincide with minima in the detrital zircon data and vice versa (e.g., at ca. 130 Ma and 275 Ma in F, and at ca. 150 Ma in H). The Pearson product moment correlation coefficient, evaluating the similarity between bedrock and detrital age KDE functions, ranges between 0.14 (Peruvian Andes), and 0.87 (Coast Ranges). Correlation coefficients show a bimodal distribution—high values (0.62–0.87) correspond to the North American sectors, whereas the Andean sectors are characterized by low values (0.14–0.42).

The spatial and temporal distribution of maxima and minima of composite KDEs along the Cordilleran arc, displayed in the color contour plot of Figure 68a, shows both bull's-eye-features reflecting high-amplitude variations of zircon age populations of limited spatial and temporal extent (e.g., ca. 130 Ma minimum in B-C; 134 Ma maximum in D; 200 Ma maximum in E), as well as subtle, along-arc striking linear features of

variable length, such as a 105–90 Ma band of high values along A-B-C, a 280–265 Ma band of high values along D-E-F-G-H, and a 175–165 Ma band of high values and 220–210 Ma band of low values along the entire Cordilleran orogen. The Lomb-Scargle periodogram shows relatively high power values at periods of ca. 60–80 m.y. across most of the Cordilleran orogen. In the Coast Ranges, the Peninsular Ranges and the Peruvian Andes, a periodic signal of 80–85 m.y. is particularly pronounced, and periods of ca. 62–68 Ma have the highest magnitudes in the Sierra Nevada, the South-central and Southern Andes. Smaller, 44–46 m.y. periods are identified in the Coast Ranges, the southeastern Mexican sector and the northern Andes. Other, subordinate, peaks occur at periods of ca. 31 m.y. (Sierra Nevada), 52 m.y. (Peninsular Ranges), 39 m.y. (southeastern Mexico), and 36 m.y. (Northern Andes).

Other statistical parameters derived from the composite KDE time series show a high variability, but with increasing age, peak height and prominence decreases, and peak width normalized to peak height increases for most of the datasets, as a result of a decrease in analytical precision with increasing age inherent to the geochronological datasets. Peak symmetry also varies within any given arc sector, but is predominantly positively skewed (i.e., has a longer right tail) in the Sierra Nevada, and negatively skewed in the Peninsular Ranges sector.

Geochemical Data

Sierra Nevada (sector B).

For Cordilleran sector B, flare-up events (F) occur during the Triassic at ca. 234–213 Ma (F_T), during the Jurassic, at ca. 170–150 Ma (F_J), and during the Cretaceous, at ca. 103–88 Ma (F_C). These flare-up events are separated by periods of low zircon

production, i.e. magmatic lulls. Overall, the number of available age-constrained geochemical data in the Sierra Nevada sector is high, ranging between 392 samples (εNd_i) to 3808 samples (SiO_2). The following trends can be observed (Figure 69a): SiO_2 exhibits higher median values during F_T than during lulls prior and following F_T. From ca. 180 Ma to 90 Ma, median SiO_2 values fluctuate between 60 and 70 wt.%, independent of age relative to a flare-up or lull. SiO_2 increases further from ca. 90 Ma to the end of the observation period. εNd_i exhibits similar median values of ca. -3 during F_T and F_J.

Between these two flare-up events, there is a data gap. Subsequent to F_J, εNd_i increases to median values of up to +5, and then decreases back to values around -5 during F_C, and keeps decreasing after F_C. The inverse trend of that for εNd_i is observed for $^{87}Sr/^{86}Sr_i$, i.e., relatively high values during flare-ups, and low values during lulls. $^{87}Sr/^{86}Sr_i$ data density and scatter are generally lower during lulls than during flare-ups. There is an increase in $^{87}Sr/^{86}Sr_i$ above average values during the last 10 Ma of the observation period. Sr/Y and $(Sm/Yb)_n$ show almost identical patterns, with highly variable values during flare-ups, but with lower median values than during lulls. At the end of F_C to 80 Ma, both proxies increase to median values above average.

Peninsular Ranges, Transverse Ranges, Mojave, and northern Mexico (sector C).

The number of compiled age-constrained geochemical data in Cordilleran sector D ranges between 221 samples (εNd_i) and 1522 (SiO_2). Flare-up events are recognized within the following approximate limits (Figure 69b): (F_{PC}) 260–237 Ma, (F_J) 175–160 Ma, (F_{C1}) 110–94 Ma, and (F_{C2}) 86–80 Ma. Median SiO_2 values are lower during F_{PC} and F_J than during periods following these respective flare-up events. From about 120 Ma onwards, SiO_2 fluctuates only slightly around a median value of ca. 67 wt.%. In terms of

εNd_i, data density is low for ages up to 180 Ma, but εNd_i seems to decrease from a median of ca. +5 during F_{PC} to a median of ca. -7 in the following lull. Median values form a "plateau" between ages of 180 and 140 Ma. Halfway through the lull between F_J and F_{C1}, εNd_i increases, before decreasing steadily through F_{C1} and F_{C2} until the end of the observation period. There is little $^{87}Sr/^{86}Sr_i$ data for the time up to ca. 130 Ma, but median $^{87}Sr/^{86}Sr_i$ values are relatively high at the end of F_{PC} and shortly prior to F_J. Following F_J, median $^{87}Sr/^{86}Sr_i$ increases from values around 0.705, to about 0.713 halfway through the following lull, before it drops back to 0.705 at the beginning of F_{C1}, and then increases steadily until 80 Ma.

Thus, from ca. 130 Ma onward, the $^{87}Sr/^{86}Sr_i$ signal is approximately inverse to the εNd_i signal. Data density is low for Sr/Y for the prior to 180 Ma. Median Sr/Y values either decrease (F_{PC}, F_J, F_{C2}) or increase (F_{C1}) during flare-up events. Short-lived excursions of median Sr/Y values towards higher values are observed during magmatic lulls. The peak at ca. 220 Ma up to median Sr/Y values of ca. 100 is particularly pronounced. $(Sm/Yb)_n$ shows a similar trend as Sr/Y, with a decrease (F_{PC}, F_J, F_{C2}) or increase (F_{C1}) in median values through flare-up events, and short-lived excursions to higher values during lulls. The peak in $(Sm/Yb)_n$ during F_J is only based on four values. Data scatter is high during F_{C1} and the following lull.

SE Mexico and Central America (sector D).

The oldest flare-up event that can be identified in the Cordilleran arc sector D is a Carboniferous, ca. 312–302 Ma event (F_{CA}), which is followed by a Permian, ca. 272–250 Ma event (F_P), a Jurassic, ca. 177–155 Ma event (F_J) and two Cretaceous events at ca. 141–128 Ma (F_{C1}) and 102–94 Ma (F_{C2}), respectively (Figure 69c). Within an

observation period of 400–80 Ma, the amount of age-constrained geochemical data for southeastern Mexico is only a fraction of that available for sector B and C, i.e., ranges between only 67 samples ($^{87}Sr/^{86}Sr_i$) to 274 samples (SiO_2). Despite overall low data density and occasional data gaps, the following trends are discernable: SiO_2 increases more or less steadily from values around 50 wt.% to values of 70 wt.% that are reached shortly after the end of F_P. The Triassic lull marks a drop in SiO_2 values, before peaking again during F_J. This pattern, of low SiO_2 during lulls, and high SiO_2 during flare-up events, is maintained throughout the next two sets of flare-ups and lulls. During F_{C2}, SiO_2 remains low, but increases towards the end of the observation period. εNd_i decreases up to F_P and then oscillates two times between median values of ca. +7 and -2 prior to F_J. Data density is low in the following period, but the lull between F_{C1} and F_{C2} seems to be dominated by high εNd_i, whereas the subsequent flare-up event is accompanied by a decrease in εNd_i values. There is little $^{87}Sr/^{86}Sr_i$ data in the period prior to ca. 230 Ma, but the data suggest that there is an increase in $^{87}Sr/^{86}Sr_i$ values in the period leading up to F_P.

During the Triassic lull, $^{87}Sr/^{86}Sr_i$ fluctuates inversely to the εNd_i pattern, reaching extremely high median values at the beginning of F_J. Data is missing during the following lull. The lull between F_{C1} and F_{C2} marks an increase in $^{87}Sr/^{86}Sr_i$ from low to moderately high values. Both Sr/Y and $(Sm/Yb)_n$ patterns are similarly displaying an increase up toward F_P, a fluctuation about low values through most of the Mesozoic (with intermittent data gaps), and finally an increase in the period leading up to F_{C2}.

Kinematic Data

Trench- orthogonal convergence rates vary in a non-steady state manner. They are predominantly positive for all Cordilleran arc sectors (Figure 71), i.e., associated with advancing slabs, but small negative values are present during the intervals 200–160 Ma in sector A, 140–130 Ma in sector E, 140–110 Ma in sector F, 98–58 Ma in sector G, and 120–50 Ma in sector H indicating minor episodes of slab retreat.

The variation of orthogonal convergence rates within an individual arc sector is usually < 50 mm/a. Higher variation is exhibited by (i) sector A at 160–140 Ma due to the accretion of the Wrangellia Superterrane and associated closure of the Cache Creek Ocean (Shephard et al. 2013), (ii) sector D at 120–110 Ma and 72–65 Ma as a result of changes in the position of the trench leading to a ca. 2000 km offset of the points from the active subduction trench, and (iii) sector E at 200–185 Ma that is due to a combination of the geometry of the subduction zone of the northern Andean sector and highly oblique (sinistral) convergence, leading to positive convergence in the north, and negative convergence in the southern part. The Pearson product moment correlation coefficient (r), providing a statistical means of evaluating the likeness of the composite zircon age spectra and trench-orthogonal plate convergence velocities, shows values between -0.38 (sector D) to 0.62 (sector G) (Figure 70).

Trench-parallel displacement rates fluctuate between positive (right-lateral) and negative (left-lateral) values in most arc sectors (Figure 71). Sectors B and C predominantly exhibit right-lateral tectonics throughout the observation period, whereas mainly left-lateral movement is observed in the northern Andean domain. The variation of lateral displacement within an individual arc sector is generally < 80 mm/a. Larger

variations are observed in certain intervals due to points getting caught on the other side of trenches as a result of changes in the shape and position of the subduction zones as defined in the plate models. Composite zircon age spectra and trench-parallel displacement rates exhibit r values between -0.24 and 0.52 (Figure 70).

Slab age data exhibit large wavelength fluctuations that are poorly correlated with the composite KDE age spectra (r = -0.53–0.54). Up to 50 Ma variations of slab ages within individual arc sectors can be explained by the different temporal resolution of the kinematic data sets (1 Ma for plate polygon data, 5 Ma for age grids). Larger variations occur in certain intervals of sectors B, F, and H as a result of two different oceanic plates subducting beneath the same arc domain, i.e. Farallon–Kula in B, Farallon–Phoenix/Chasca in F, and Antarctica–Phoenix in H.

Discussion

Limits, Biases, Uncertainties, and Artifacts

Age Compilations Preservation bias: The underlying premise of this study is that the observed distributions of U-Pb ages reflect relative changes in the vigor of subduction-related magmatic activity in the Cordilleran arc. However, rather than measuring additions of new crustal material, peaks in zircon age spectra have been argued to reflect times of reduced destruction (Condie et al. 2009; Hawkesworth et al. 2009; Belousova et al. 2010; Hawkesworth et al. 2010; Condie et al. 2011; Cawood et al. 2012; Hawkesworth et al. 2013). We use a combination of bedrock ages and detrital zircon ages (from samples with different depositional age) to compensate for the fragmentary preservation record of arc magmatism. Hence, although the igneous suite of a certain age may no longer be preserved in situ due to recycling processes occurring at subduction zones, such as subduction erosion (Clift and Vannucchi 2004; Hawkesworth et al. 2009; Scholl and Huene 2009), detrital zircons from sediments in arc-flanking basins may provide a record of the magmatic activity represented by the obliterated crust. Intrinsic factors, such as erodibility and zircon content of the source rock, as well as extrinsic factors, such as erosion (climate, relief, etc.) and transport processes (wind and drainage patterns, distance of source to sink, etc.) determine to what degree an igneous source is represented in the detrital zircon record (Cawood et al. 2012). These factors and the issue of preservation likely bias the observed abundance relative to the true abundance in the source area. Hence, the age spectra cannot be used to quantitatively evaluate the mass balance of igneous rocks, but can only be used as a general, qualitative indicator of magmatic arc activity.

Sampling bias: Igneous rocks that are only exposed in remote or logistically challenging areas will be under-represented in the bedrock age spectrum, whereas intense sampling of igneous rocks from small geographic areas can bias the relative significance of a peak in the age spectrum. Furthermore, arc-parallel drainage systems or wind trajectories may potentially introduce zircons from adjacent sectors, yielding extraneous peaks in the detrital zircon spectra of a certain arc domain. Trench-parallel displacements of crustal blocks along strike-slip faults may be another way of introducing external material to any given arc sector. Since the boundaries of the eight arc domains are based on present day geographic location, trench-parallel displacements of crustal fragments, either during or subsequent to the 400–80 Ma observation period, such as those documented in southern California (Luyendyk et al. 1980; J. Jackson and Molnar 1990; Nicholson et al. 1994), southern Mexico (e.g., Dickinson and Lawton 2001; Elías-Herrera and Ortega-Gutiérrez 2002; Pindell et al. 2012), the south-central Andes (Brown et al. 1993; Taylor et al. 1998), and the southern Andes (Cembrano et al. 2002; Rosenau et al. 2006), may distort age spectra of these or adjacent arc domains. Considering that along-arc translations of the mentioned crustal blocks are usually in the range of a few hundred kilometers at the most, and that the geographic limits of individual arc domains mostly coincide with tectonic boundaries, the effects on age spectra imposed by lateral displacements of crustal fragments should be relatively minor.

Tectonic setting bias: Our study is concerned with continental arc magmatism, so we want to compare rocks from the same tectonic setting. The compiled zircon ages, both igneous and detrital, are believed to represent magmatic ages, as zircon ages identified as metamorphic ages by the original investigators, have been excluded. However, apart from

being produced in continental arc magmas, igneous zircon can also be generated due to continental collision, or rifting (e.g., Hawkesworth et al. 2009). Collisional processes associated with plate reorganizations during Pangea assembly particularly influence the Northern and Peruvian Andean sectors between 300–230 Ma (Mišković et al. 2009; Spikings et al. 2014), whereas notable episodes of extensional tectonics are documented in sector D at 215–185 (Centeno-García et al. 1993; Martini et al. 2010), in sector E at 240–216 Ma (Spikings et al. 2014), in sector F in the Jurassic (Ramos 2010) and in sector G at 200–140 Ma. However, magma volumes generated as a result of continental collision are typically low, and igneous rocks associated with extensional tectonics are predominantly mafic (Storey 1995), and are thus not expected to yield large amounts of zircon (Cawood et al. 2012). Island arcs, which after their formation have collided with the continental margin, potentially represent additional sources of magmatic zircon, and can lead to spurious peaks in the zircon age spectra. Oceanic terranes and island arcs with ages between 400 and 80 Ma are documented in (i) the Coast Ranges, i.e. the Triassic Chelan Mountains terrane (Tabor et al. 1989; Matzel et al. 2008), (ii) the Sierra Nevada, i.e. Early Paleozoic and Jurassic intraoceanic arc complexes in the eastern Klamath and northern Sierra terranes (Colpron and Nelson 2009; Dickinson 2009; Colpron and Nelson 2011) and the Late Paleozoic Golconda Allochthon (Riley et al. 2000), (iii) northern Mexico, i.e. the Early Cretaceous Alisitos arc terrane (Busby 2004), and (iv) southeastern Mexico, i.e. the Middle Jurassic–Lower Cretaceous Guerrero Composite Terrane (Martini et al. 2011; 2013; Palacios-García and Martini 2014).

Accumulating evidence indicates that both the Alisitos and the Guerrero Composite Terrane are not far-travelled island arc terranes, but peripheral arc systems

that formed due to subduction-related extension at the Mexican continental margin (Busby 2004; Centeno-García et al. 2011 and references therein). In that sense, magmatism relating to these respective terranes is not exotic with respect to the continental arc to which these terranes subsequently accreted, but a result of "accordion" tectonics characteristic of convergent continental margins (e.g., Collins 2002). Nevertheless, because the Alisitos and Guerrero fringing arc terranes are not underlain by continental crust, but by transitional to oceanic crust (Busby 2004; Centeno-García et al. 2011), compositional data derived from these domains have to be interpreted with care, as there can a bias towards more juvenile compositions. The contribution of Devonian-aged island arc-derived zircons in the Sierra Nevada arc domain seems to be only minor, as apparent from the age compilation (Figure 67).

Methodological bias: Plutons in continental arcs are often assembled incrementally (e.g., Barboni et al. 2013; Klemetti and Clynne 2014). The longevity of silicic magmatic systems can lead to complex growth of zircon, which may impart a positive age bias. Furthermore, age analyses acquired by techniques in which zircons are not treated by chemical abrasion may be affected by lead loss (e.g., Crowley et al. 2014; Schaltegger et al. 2015), possibly imparting a negative age bias. For the compilation of bedrock ages, which are multi-zircon ages (except for Sierra Nevada bedrock ages) we blindly accept the interpretation of the original authors that these represent the true crystallization age of the igneous rock. For detrital zircon data, the statistical adequacy, i.e., to what degree the observed age abundance matches the corresponding abundance in the sediment, is influenced by the number of grains analyzed and by the sample preparation procedure, as artificial biases introduced during sample preparation, and an

insufficient number of zircons analysed per sample may cause certain age populations to go undetected, or result in spurious peaks in the age spectra (e.g., Dodson et al. 1988; Sircombe 2000; Vermeesch 2004; Andersen 2005).

As with the bedrock data, we have compiled detrital zircon data with no regard to the statistical robustness of the individual datasets, thus accepting the methodological choices made by the original investigators. An additional factor that may influence the distribution of peaks in the age spectra concerns the representation of age frequency data. For histograms of this study, a constant bin size of 10 Ma, which corresponds to the average value of "ideal" bin widths as calculated for every dataset using Sturge's or Rice's rule, was chosen to allow a comparison between datasets. However, because zircon age distributions are neither smooth nor unimodal, choosing a constant band- or bin width to visualize age frequency data may not be appropriate (e.g., Vermeesch 2012). Hence, in addition to histograms, kernel density estimates (KDEs) are used for statistical analyses of the age data. For the calculation of KDEs, bandwidths are varied according to local density, i.e., where data density is low, a large bandwidth is used resulting in a smoothed distribution, and in parts with abundant data, a narrower bandwidth is used providing a higher resolution (Vermeesch 2012). The resulting KDEs of the detrital zircon datasets, each based on 757 data points and more, locally exhibit frequency variations in the order of ca. 3–5 Ma, whereas generally low data density in bedrock data results in relatively large-scale variations in the KDE at a resolution of ca. 20–40 Ma. Hence, the temporal resolution of bedrock data only allows the identification of large-scale variations in arc-magmatism.

Geochemical Data Preservation bias: Geochemical data may be biased by the ages of the material preserved and sampled, so they underlie the same biases and uncertainties that apply for the age compilations. Sampling bias: The Alisitos and Guerrero fringing arc terranes of Triassic to Jurassic age, which cover a substantial area in arc domains C and D, respectively, are not underlain by continental crust, but by transitional to oceanic crust (Busby 2004; Centeno-García et al. 2011), which causes a bias towards more juvenile compositions in this age interval. Hence, caution should be used in interpretations concerning crustal vs. mantle components in arc magmas as well as estimates of crustal thickness. Slab window formation, slab tearing or cracking, and slab detachment may cause upwelling of hotter asthenospheric mantle and associated adakite-type igneous activity in certain arc segments (e.g., Yogodzinski et al. 2001). Compositional data may furthermore be affected by inboard or outboard migration of the continental arc due to changes in the angle of the subducting slab, episodes of subduction erosion, or accretion of terranes. Spatial migration of the arc may shift the focus of magmatism to areas where the crust exhibits differing thermal or compositional properties, potentially introducing artifacts into the compositional data. The location of continental arcs may be traced by the distribution of currently exposed igneous rocks, and to a lesser degree by the distribution of detrital zircon populations. In southeastern Mexico and Central America, for example, the Carboniferous–Permian arc seems to spatially coincide with the Jurassic (Nazas) arc, whereas the Cretaceous arc is located further outboard, due to the accretion of the Guerrero Composite Terrane in the Early Cretaceous (Figure 72). Tectonic setting bias: In this paper, we intend to only compare the compositions of igneous rocks that are a product of continental arc magmatism only. Whereas excluding data associated with

other tectonic settings is difficult for zircon age data, compositional data can be filtered using suitable proxies and threshold values. For instance, according to Pearce et al. (1984), Yb+Ta values allow an effective separation of igneous rocks of volcanic arcs (Yb+Ta < 6) from those of within plate settings and ocean ridges (Yb+Ta > 6). Applying this constraint to the data results in a reduction in the number of samples by up to 80 % (e.g., SiO_2 values in the Sierra Nevada sector), caused mostly by a dearth of trace elements data, but overall yields negligible changes in the general pattern of the compositional data. Hence, in Figure 69, unfiltered datasets are presented.

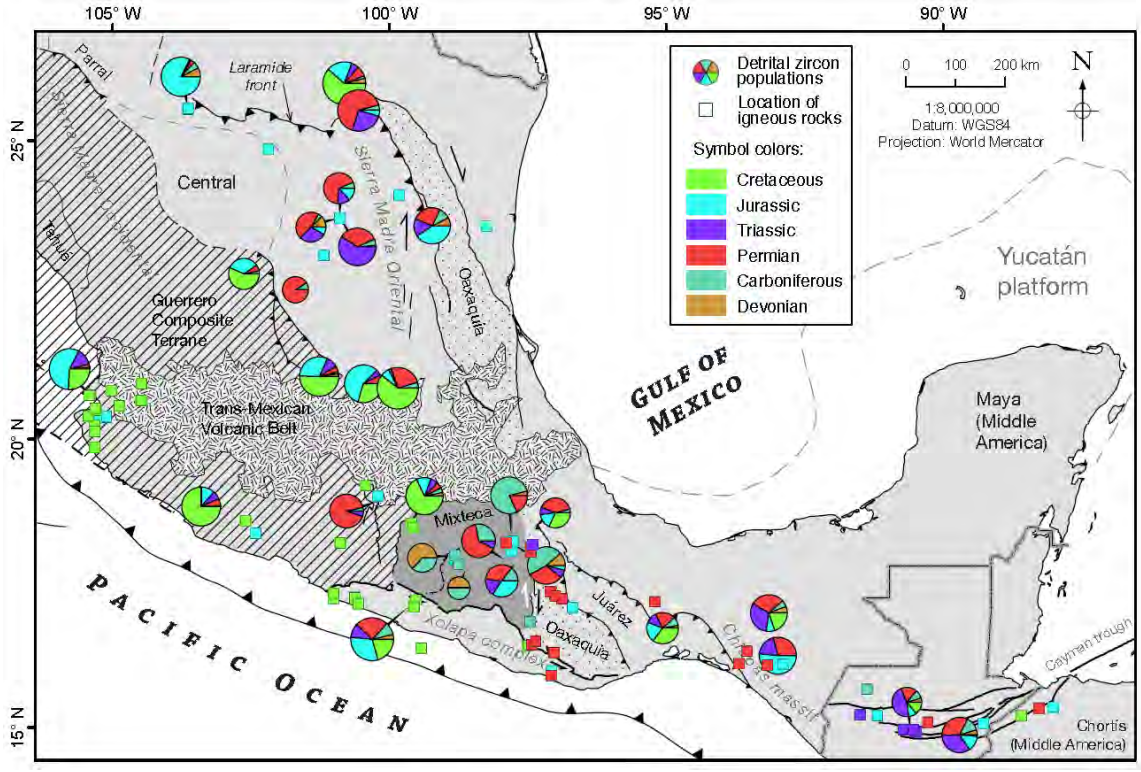

Figure 72. Tectonic map showing the principal geologic features of southeastern Mexico and Central America (J. D. Keppie 2004; Dowe et al. 2005; Helbig et al. 2012b). Colored squares indicate the location and age of igneous rocks. Pie-charts show detrital zircon age populations between 400 and 80 Ma.

Methodological bias: Mafic rocks are notoriously difficult to date by U-Pb zircon methods, hence, mafic rocks may be underrepresented in the geochemical dataset. However, U-Pb-zircon constrained data were supplemented by geochemical data with ages constrained by other means, including $^{40}Ar/^{39}Ar$, K/Ar, Rb-Sr, and Sm-Nd geochronology, and ages estimated using (bio-)stratigraphic evidence. These dating techniques should not be greatly affected by magma chemistry. A problem with $^{40}Ar/^{39}Ar$, K/Ar, Rb-Sr, and Sm-Nd geochronology, however, is an increased risk of daughter isotope loss brought about by low-grade metamorphism and/or hydrothermal activity post-dating volcanic and plutonic rock emplacement, which may result in erroneous ages, i.e. affect the position of data points along the x(time)-axis, and in case of Nd and Sr isotopic data, also along the y-axis, as ages are used to calculate the initial strontium and neodymium compositions. Plotting median values ± one standard deviation for a moving 10 Ma average allows for a fast evaluation of trends and degree of scatter. However, the median and σ-values of the compositional data are strongly influenced by the size of bins. A bin size of 10 Ma has been chosen for all geochemical proxies of this study (independent of sample size, to allow comparison between datasets), as this seems appropriate for an analysis on this temporal scale, but this precludes the recognition of smaller-scale compositional variations.

Uncertainties concerning magma source: Continental arc magmas reflect variable contributions from mantle, crustal and subducted reservoirs (e.g., Hildreth and Moorbath 1988; Hawkesworth et al. 1993; Jones et al. 2015). The geochemical proxies Sr/Y and Sm/Yb are in this paper primarily used to estimate magma source depth and crustal thickness (e.g., Mamani et al. 2010; Chiaradia 2015; Profeta et al. 2015). Magmas of

thicker arcs evolve at deeper average levels, stabilizing amphibole ± garnet at the expense of plagioclase in the mineral assemblage of residual magmas and partial melts (e.g., Kay 1978; Defant and Drummond 1990; Mahlburg Kay and Mpodozis 2001). Given the marked affinity of Yb for garnet, Y for garnet and amphibole, and Sr for plagioclase, higher Sr/Y and Sm/Yb values arguably indicate amphibole and garnet-dominated melts sources (either lower crustal residue or deep mantle), and thus, a thicker crust. However, there are several processes that can upset the Sr/Y ratio, such as (i) a contribution of slab melts (e.g., Defant and Kepezhinskas 2001; König et al. 2006; Chiaradia 2015), (ii) plagioclase fractionation, and (iii) crustal anatexis producing garnet-bearing granites (e.g., Zhang et al. 2012). While adakitic rocks derived from slab melts are relatively rare in continental arcs, only rocks with < 70 wt.% SiO_2 are plotted for Sr/Y and $(Sm/Yb)_n$ to exclude the effect of plagioclase fractionation, and to exclude highly felsic garnet-bearing granites.

Kinematic Data

Our analysis implicitly accepts the respective plate motion models and the geodynamic concepts upon which these are based. However, due to the progressive destruction of oceanic lithosphere by subduction, uncertainties associated with paleogeographic reconstructions increase with age. For example, the link between South America and the subducting Farallon Plate must be determined indirectly by a series of intermediate rotations, called plate circuits, because subduction has consumed most of Panthalassa's oceanic plates (e.g., Seton et al. 2012). The Farallon-South America plate circuit involves five "hops" via the Farallon, Pacific, West and East Antarctic, African,

and finally, South American Plates. The link through the Pacific Plate is only possible for times since the Late Cretaceous, when seafloor spreading between the Pacific and West Antarctic Plates was established (e.g., Eagles et al. 2004; Wobbe et al. 2012). For the time prior to the Late Cretaceous, a hotspot reference system must be used for the Pacific Plate (Seton et al. 2012). The Early Cretaceous separation of Patagonia from Africa involved substantial intracontinental extension, which led to misfits in the South Atlantic plate reconstruction. Several models have been proposed to minimize uncertainties in the block rotation between Patagonia and South America (e.g., Eagles 2007; Torsvik et al. 2009; Heine et al. 2013), but they show large discrepancies. Similar problems exist for other portions of the Cordilleran margin. Plate kinematic parameters used in this paper must thus be considered with care and applied to first-order processes only.

Testing of Models

There are two schools of thought on what governs the episodic behavior of arc systems. One set of models invokes events outside the arc, such as plate reconfigurations and changes in mantle flow as the ultimate driver of magmatic activity in arcs (e.g., Armstrong 1988; Hughes and Mahood 2008; Zellmer 2008; de Silva et al. 2015), whereas another set of models is based on arc-internal feedback processes involving magmatic/tectonic crustal thickening, crustal melting, and delamination (K. E. Karlstrom et al. 1993; Ducea 2001; DeCelles et al. 2009; L. Karlstrom et al. 2014; Chin et al. 2015; DeCelles et al. 2015). These sets of models predict differences in terms of the spatial distribution and the temporal scale of magmatic activity as well as the relationship between magmatic activity and magma composition, and kinematic parameters,

respectively. More specifically, if arc systems were externally controlled, i.e. governed by parameters of the downgoing plate, such as convergence rate, age, and subduction angle, flare-ups and lulls in magmatic activity would likely be widely distributed along the arc and occur as distinct (random) events that may coincide with periods of global plate reorganization. In contrast, models invoking an internal forcing should be independent of plate parameters, and are often characterized by cyclic behavior, i.e. events recurring at regular intervals. Flare-ups and lulls would also be spatially limited, because, depending on the crustal architecture of the arc sector, different parts may be at different stages in the cycle at any given time. Furthermore, arc-internal processes, such as crustal thickening, delamination, etc., predict changes in arc chemistry that should correspond to variations in magmatic activity, whereas no such correlation is expected in case of an external forcing.

Spatial and Temporal Pattern.

The distribution of U/Pb bedrock and detrital zircon ages, used as a proxy for the timing of magmatic accretion, shows a great variability in the spatial scales of Cordilleran magmatic arc activity (Figure 69). Some minima and maxima are nearly synchronous for thousands of km along the arc, other peaks and troughs, although the period length may be the same, are "shifted" by up to 30 Ma from one sector to the next (e.g. Permo-Triassic flare-up and lull in sector B and C). On one hand, these features suggest an external, i.e. plate tectonic influence on Cordilleran arc magmatism; on the other they highlight the importance of internal feedback processes operating independently in different sectors due to distinct crustal properties.

Previous studies in Cordilleran magmatic arcs suggest that flare-up events occur with a periodicity of 25–45 Ma in the Central Andes (Haschke et al. 2006), and 20–50 Ma in the North American Cordilleras (Barton 1996; Ducea 2001; Gehrels et al. 2009; Mahoney et al. 2009; Paterson et al. 2011; Barth et al. 2013; DeCelles et al. 2015). Our analysis shows that while periods between 20 and 50 m.y. are present in the dataset, a period of ca. 60 to 80 m.y. is more prominent in the Cordilleran orogen, although the relative magnitude of this periodicity is highly variable for different sectors. In models advocating internal feedback processes in the upper plate as a control of arc magmatism, the periodicity signal is often attributed to a cyclic development and subsequent removal of a crustal arc root (e.g., Ducea 2001; DeCelles et al. 2009; L. Karlstrom et al. 2014; Chin et al. 2015; DeCelles et al. 2015). According to a recent numerical model (C.-T. A. Lee and Anderson 2015), these processes have a period length of 10–30 million years. The presence or absence of a periodic component in itself may be diagnostic of either an internal or an external control on arc magmatism, respectively. Although supercontinent formation, too, has been suggested to be cyclic (Nance et al. 2014 and references therein), it exhibits a period of 250–320 m.y. and hence it is not directly apparent in the lifetime of Cordilleran arcs. However, processes associated with the fragmentation and assembly of supercontinents may register as distinct events in the record of magmatic activity that may be superimposed on any cyclicity, or even cause cycles to become interrupted or (re-) initiated. The observed variability in period length and magnitude are likely a consequence of a superposition of different processes, both cyclic and random.

Relationship with Magma Chemistry

Annen et al. (2006) state that although melt production in the lower crust strongly depends on emplacement rate of mantle-derived basalt, crustal melting is limited by the availability of fertile crust that can be partially melted. In the model by DeCelles et al. (2009; 2015) the availability of fertile crustal material is the driving force of magmatic episodicity. According to these authors, periods of high arc magma production in the continental arc are fuelled by underthrusting of forearc and/or retroarc lithosphere, which may also be brought about by increased plate convergence. Hence, the correlation between convergence rates and continental arc magmatism apparent in our data can also be interpreted to reflect a relationship between convergence rates and the rate at which melt-fertile continental lithosphere is fed into the zone of high heat flux and melting (DeCelles et al. 2015). In terms of arc magma geochemistry, DeCelles et al.'s crustal thickening model predicts SiO_2, $^{87}Sr/^{86}Sr_i$, Sr/Y, $(Sm/Yb)_n$ to be proportional, and εNd_i inversely proportional to arc magma production (DeCelles et al. 2009). The presented geochemical data in this paper generally shows a good correlation between geochemistry and arc magma production, but with notable limitations: (i) In the Sierra Nevada, the expected increase in $^{87}Sr/^{86}Sr_i$, Sr/Y, $(Sm/Yb)_n$ during flare-ups and relative decrease is not as pronounced for the Triassic and Jurassic flare-up event as for the Cretaceous event.

Accordingly, numerical modelling (Cao et al. 2016) suggests that crustal thickening was not as pronounced for the pre-Cretaceous flare-up events. Furthermore, the Early Cretaceous marks a period of high variation in Sr/Y and $(Sm/Yb)_n$ ratios that finds no expression in the age spectrum. (ii) The Peninsular Ranges and northern Mexico sector shows an anti-correlation between SiO_2 and zircon age density estimates for the

time prior to ca. 130 Ma. Moreover, there are short periods of elevated Sr/Y and $(Sm/Yb)_n$ ratios during magmatic lulls. (iii) Southeastern Mexico and Central America exhibit relatively low SiO_2, high εNd_i, and low $(Sm/Yb)_n$ during the Carboniferous flare-up event. In addition, the Triassic lull is characterized by low εNd_i and high $^{87}Sr/^{86}Sr_i$.

Even if age and geochemical patterns show the correlation predicted by crustal thickening and ensuing delamination of arc roots, these mechanisms may not be the only explanation. Instead, an increase in SiO_2, $^{87}Sr/^{86}Sr_i$, Sr/Y, $(Sm/Yb)_n$, and a decrease in εNd_i may be a reflection of a migration of the arc through crust with different properties. In the Peninsular Ranges Batholith, where the Cretaceous flare-up event is marked by an east-west progression from an oceanic arc to a continental arc setting (e.g., Morton et al. 2014), overall chemical changes within this corridor (Figure 69b) are likely the result of an associated increased proportion of assimilated continental material. Hence, the flare-up event may not have been triggered by crustal thickening, but by an increase in mantle input. These observations suggest that not every flare-up event may be associated with crustal thickening, and that other factors may be important in governing the rates of magma production in continental arcs.

Relationship with Plate Parameters

The source region for arc magmas is located in the mantle beneath the arc, where melts are generated as a result of fluid release from the subducted slab (e.g., Gill 1981; Arculus 1994; Tatsumi and Eggins 1995) and mantle decompression caused by subduction-induced corner-flow (e.g., Elkins Tanton et al. 2001; England and Katz 2010). Next to lithospheric thickness of the overriding plate, which may determine the length of

the melting column in the mantle wedge (e.g., England et al. 2004; L. Karlstrom et al. 2014; Chin et al. 2015), subduction parameters such as convergence rate or slab age have also been proposed to have an influence the wedge thermal structure and extent of melting beneath arcs (Peacock 1990; Iwamori 1998; Hebert et al. 2009; England and Katz 2010; Turner and Langmuir 2015a; 2015b). Generally, it is assumed that higher convergence rates (i) lead to more vigorous hydration of the mantle wedge causing increased melting (e.g., Cagnioncle et al. 2007; Plank et al. 2009), and/or (ii) increase the flux of hot mantle into the wedge corner, raising the temperature and causing increased melt formation beneath the arc (England and Wilkins 2004; England and Katz 2010; Turner and Langmuir 2015a; 2015b). In terms of the age of the ocean floor, two competing processes may influence magma formation in the mantle: fluid fluxing (proportional to age; e.g., Leeman 1996; Hebert et al. 2009), and thermal gradient (inversely proportional with age; e.g., England et al. 2004).

Igneous rocks with mafic–ultramafic composition that are in equilibrium with the mantle wedge are scarce in exposed portions of continental arcs due to density filtering and internal modification processes of ascending magmas in the continental crust, mainly by a combination of fractional crystallization of primary magmas, and partial melting and/or assimilation of crustal material (DePaolo 1981b; Hildreth and Moorbath 1988; Tatsumi and R. J. Stern 2006). The majority of models for the generation of intermediate melts characteristic of continental arcs invokes processes occurring at lower crustal depth, such as underplating, or the intrusion of mafic magma in form of sills and/or dykes (Huppert and Sparks 1988; Bergantz 1989; Petford and Gallagher 2001; Annen and Sparks 2002; M. D. Jackson et al. 2003; Annen et al. 2006; Otamendi et al. 2009; Jagoutz

2010; Otamendi et al. 2012). The extent to which magma production in the mantle influences the rate at which magmas migrate to upper crustal levels is an issue of much controversy (e.g., de Silva et al. 2015). Numerical models show that, to a first order, a higher basalt emplacement rate into the lower crust leads to an increase in the production of residual melts (due to crystallization of basalt) and partial melts (Bergantz 1989; Barboza et al. 1999; Barboza and Bergantz 2000; Dufek and Bergantz 2005; Annen et al. 2006), although it is known that magma transfer rates through the crust are also dependent on other, second order, factors, such as the initial geotherm as well as crustal thickness, stress state, density, and composition (e.g., Lima et al. 2012; Chaussard and Amelung 2014).

If convergence rates and plate ages governed melt production in the mantle wedge, and if the magma transferred to the middle and upper crust was proportional to the magma advected from the mantle wedge (e.g., Zellmer and Annen 2008), there should be a correlation between plate parameters and magmatic arc activity. Although some studies (e.g., Armstrong 1988; Hughes and Mahood 2008; Zellmer 2008) provide evidence of such a correlation, others (e.g., Ducea 2001; DeCelles et al. 2009; 2015; Cao et al. 2016) have negated such a link, because flare-up events in some parts of the Cordillera are seemingly out of sync with peaks in convergence rates. However, the latter studies are based on spatially and temporally limited geochronological and plate motion data (e.g., Engebretson et al. 1985; Pardo Casas and Molnar 1987; Somoza 1998; Sdrolias and Müller 2006). Our compilation of geochronological data and plate parameters extracted from a modern global plate motion model (Seton et al. 2012) that extends back to 200 Ma allows us to re-evaluate the strength of this relationship on a

broader scale. The data show that the degree of correlation between orthogonal convergence rates and age spectra is generally poor, but highly variable from one Cordilleran arc sector to the next. However, if variable lag times (up to 16 Ma) are introduced to account for an incubation period or thermal lag as the system adapts to a new configuration between magmatic episodes (e.g., Annen et al. 2006; de Silva et al. 2006; Mamani et al. 2010; Paterson and Ducea 2015), it leads to a notable increase (up to 2.8 times) in the correlation coefficient for several sectors, resulting in a moderate ($0.3 < r < 0.5$) to high ($0.5 < r < 1.0$) degree of correlation for all sectors but the southeastern Mexican (Figure 72).

For pre-Jurassic times, no plate parameters can be extracted due to the lack of a reliable plate model, but certain maxima and minima in the along-arc age correlation chart (Figure 69) coincide with known tectonic events along the Pacific margin of Pangea, such as (i) the onset of the pan-Pacific Gondwanide orogeny at ca. 300 Ma (e.g., Cawood 2005; Cawood and Buchan 2007), (ii) the closure of the Panthalassan Gondwana suture at ca. 250 Ma (Scotese 1997; Cocks and Torsvik 2002; Stampfli and Borel 2002; Murphy and Nance 2008), and (iii) the opening of the central Atlantic and dispersal of Gondwana at ca. 200 Ma (Nance et al. 2012; Seton et al. 2012; D. F. Keppie 2015), events which are associated with global plate kinematic reorganization, affecting the direction and speed of plate convergence along the Cordilleran orogen. A major plate reorganization event also occurred at ca. 100 Ma (Matthews et al. 2012), which may have triggered the Cretaceous flare-up events in the Northern Cordilleran sectors (Figure 69). Together, these data suggest that a possible link between arc-external events and magmatic episodicity should be re-evaluated and once again explored as larger and more

precise geochronological and plate kinematic datasets become available.

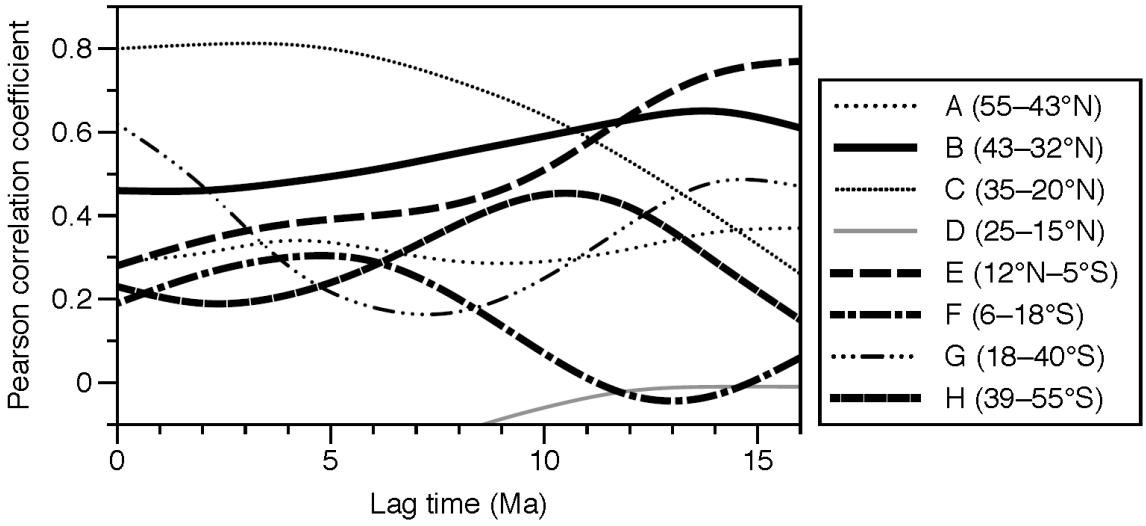

Figure 73. Effect of lag time on Pearson correlation coefficients between age composite and orthogonal convergence rate. Letters A–H refer to arc sectors as defined in Figure 66. Arc sectors represented by bold lines show an increase in correlation coefficients with variable lag times.

Future Research

The geochronological, geochemical, and plate kinematic database that form the foundation of this study are a work in progress. Increasing the sample size as more data become available, adding more geochemical/isotopic proxies, and amplifying the temporal and spatial range will allow more rigorous interpretations of these large datasets in terms of characterizing episodic arc magmatism and testing model predictions. To minimize the sampling bias, time dependent magma addition rates need to be determined from retro-deformed surface areas of magmatic rocks and geobarometric data (Matzel et al. 2006; Paterson et al. 2011; Memeti et al. 2014; Paterson and Ducea 2015).

Lithospheric stress state is a crucial parameter in models of arc magmatism (e.g., DeCelles et al. 2009; 2015) and a controlling factor for magma ascent; hence establishing structural databases is essential in order to estimate rates of tectonic shortening. Another critical aspect concerns the temporal record of island arc magmatism. Lacking the density filter of thick continental crust, oceanic arcs can provide a simpler, more direct way of studying cause and effect, so obtaining large temporal records for island arcs would be desirable. However, this is a difficult task, because island arcs are often short-lived, mostly poorly preserved, and predominantly mafic, the latter of which makes them harder to date by zircon geochronology. Preliminary age records from the Talkeetna, Aleutian, and Kohistan island arcs (Paterson and Ducea 2015), however, show a certain degree of episodicity, suggesting that plate parameters and the availability of mantle melts play a big part in governing arc magmatism, irrespective of the thickness and composition of the upper plate. Oceanic arcs can also be used to estimate the background magma production rate of continental arcs. Recent studies have shown that magma production rates in

intraoceanic arcs are comparable to the volumes of magma produced during flare-ups in continental arcs (Jicha and Jagoutz 2015). This means that instead of finding a process to explain increased magma production during flare-ups, a mechanism is needed to temporarily suppress magma production in continental arcs, such as flat slab subduction (e.g., McGeary et al. 1985; Gutscher et al. 2000; C. R. Stern 2004).

Implications

We examine large geochronological, geochemical and kinematic data sets for the Cordilleran orogen as a means to test existing models for episodic magmatism in continental arcs. Bedrock and detrital U-Pb zircon age distributions, which have been shown to be qualitative indicators of magmatic activity within the arc, show a clear non-steady state pattern of variable temporal and spatial scales. Whereas most flare-up events are discrete in time and space, some are synchronous many thousand kilometers along arc-strike, and a moderate periodicity between 60 and 80 million years is apparent in certain portions of the Cordilleran orogen. Covariations between arc magma chemistry and magmatic arc activity suggest crustal thickening during flare-up events, but arc migration poses a challenge, as it can produce similar geochemical patterns. Kinematic data based on recent global plate reconstructions provide a means of evaluating mantle heat input.

The correlation between orthogonal convergence rate and Cordilleran arc activity as well as the coincidence between certain flare-up events and lulls with global events of plate tectonic reorganization demonstrates that an external control of continental arc magmatism should be reevaluated. Our results suggest that driving mechanisms for flare-

ups/lulls vary along this Mesozoic arc and that second order effects vary between flare-ups and arc segments.

References

Andersen, T. (2005) Detrital zircons as tracers of sedimentary provenance: limiting conditions from statistics and numerical simulation. Chemical Geology, 216, 249–270.

Annen, C., and Sparks, R.S.J. (2002) Effects of repetitive emplacement of basaltic intrusions on thermal evolution and melt generation in the crust. Earth and Planetary Science Letters, 203, 937–955.

Annen, C., Blundy, J.D., and Sparks, R.S.J. (2006) The genesis of intermediate and silicic magmas in deep crustal hot zones. Journal of Petrology, 47, 505–539.

Arculus, R.J. (1994) Aspects of magma genesis in arcs. Lithos, 33, 189–208.

Armstrong, R.L. (1974) Magmatism, orogenic timing, and orogenic diachronism in the Cordillera from Mexico to Canada. Nature, 247, 348–351.

Armstrong, R.L. (1988) Mesozoic and early Cenozoic magmatic evolution of the Canadian Cordillera. In S.P. Clark Jr., B.C. Burchfiel, and J. Suppe, Eds., Processes in continental lithospheric deformation. Geological Society of America Special Paper 218 pp. 55–92.

Bahlburg, H., and Hervé, F. (1997) Geodynamic evolution and tectonostratigraphic terranes of northwestern Argentina and northern Chile. Geological Society of America Bulletin, 109, 869–884.

Bahlburg, H., Vervoort, J.D., Frane, Du, S.A., Bock, B., Augustsson, C., and Reimann, C. (2009) Timing of crust formation and recycling in accretionary orogens: Insights learned from the western margin of South America. Earth-Science Reviews, 97, 215–241.

Barboni, M., Schoene, B., Ovtcharova, M., Bussy, F., Schaltegger, U., and Gerdes, A. (2013) Timing of incremental pluton construction and magmatic activity in a back-arc setting revealed by ID-TIMS U/Pb and Hf isotopes on complex zircon grains. Chemical Geology, 342, 1–18.

Barboza, S.A., and Bergantz, G.W. (2000) Metamorphism and anatexis in the Mafic Complex contact aureole, Ivrea Zone, northern Italy. Journal of Petrology, 41, 1307–1327.

Barboza, S.A., Bergantz, G.W., and Brown, M. (1999) Regional granulite facies metamorphism in the Ivrea zone: Is the Mafic Complex the smoking gun or a red herring? Geology, 27, 447.

Barboza-Gudiño, J.R., Hoppe, M., Gómez-Anguiano, M., and Martínez-Macías, P.R. (2004) Aportaciones para la interpretación estratigráfica y estructural de la porción noroccidental de la Sierra de Catorce, San Luis Potosí, México. Revista Mexicana de

Ciencias Geológicas, 21, 299–319.

Barboza-Gudiño, J.R., Orozco-Esquivel, M.T., Gómez-Anguiano, M., and Zavala-Monsiváis, A. (2008) The Early Mesozoic volcanic arc of western North America in northeastern Mexico. Journal of South American Earth Sciences, 25, 49–63.

Barth, A.P., and Wooden, J.L. (2006) Timing of magmatism following initial convergence at a passive margin, southwestern U.S. Cordillera, and ages of lower crustal magma sources. Journal of Geology, 114, 231–245.

Barth, A.P., Tosdal, R.M., Wooden, J.L., and Howard, K.A. (1997) Triassic plutonism in Southern California; southward younging of arc initiation along a truncated continental margin. Tectonics, 6, 290–304.

Barth, A.P., Wooden, J.L., Howard, K.A., and Richards, J.L. (2008) Late Jurassic plutonism in the southwest U.S. Cordillera. In J.E. Wright and J.W. Shervais, Eds., Ophiolites, Arcs, and Batholiths A Tribute to Cliff Hopson. Geological Society of America Special Paper 438, pp. 379–396.

Barth, A.P., Wooden, J.L., Jacobson, C.E., and Economos, R.C. (2013) Detrital zircon as a proxy for tracking the magmatic arc system: The California arc example. Geology, 41, 223–226.

Barton, M.D. (1996) Granitic magmatism and metallogeny of southwestern North America. Earth and Environmental Science Transactions of the Royal Society of Edinburgh, 87, 261–280.

Bateman, P.C., and Shervais, J.W. (1992) Plutonism in the central part of the Sierra Nevada batholith, California p. 572. Boulder, Colorado.

Belousova, E.A., Kostitsyn, Y.A., Griffin, W.L., and Begg, G.C. (2010) The growth of the continental crust: constraints from zircon Hf-isotope data. Lithos, 119, 457–466.

Bergantz, G.W. (1989) Underplating and Partial Melting: Implications for Melt Generation and Extraction. Science, 245, 1093–1095.

Boekhout, F., Spikings, R., Sempere, T., Chiaradia, M., Ulianov, A., and Schaltegger, U. (2012) Mesozoic arc magmatism along the southern Peruvian margin during Gondwana breakup and dispersal. Lithos, 146-147, 48–64.

Bouysse et al. (2010), Geological map of the world at 1:50,000,000 (3rd ed.), 2 sheets, Commission for the Geological Map of the World, UNESCO, Paris.

Boyden, J.A., Müller, R.D., and Gurnis, M. (2011) Next-generation plate-tectonic reconstructions using GPlates. Cyberinfrastructure for the Solid Earth Sciences, 95–114.

Bradley, D.C. (2008) Passive margins through earth history. Earth-Science Reviews, 91,

1–26.

Brown, M., Díaz, F., and Grocott, J. (1993) Displacement history of the Atacama fault system 25° 00′ S-27° 00′ S, northern Chile. Geological Society of America ….

Burchfield, B.C., and Davis, G.A. (1972) Structural framework and evolution of the southern part of the Cordilleran orogen, western United States. American Journal of Science, 272, 97–118.

Burchfield, B.C., and Davis, G.A. (1975) Nature and controls of Cordilleran orogenesis, western United States: Extensions of an earlier synthesis. American Journal of Science, 275A, 363–396.

Busby, C. (2004) Continental growth at convergent margins facing large ocean basins: a case study from Mesozoic convergent-margin basins of Baja California, Mexico. Tectonophysics, 392, 241–277.

Bustamante, C., Cardona, A., Bayona, G., Mora, A., Valencia, V., Gehrels, G., and Vervoort, J. (2010) U-Pb LA-ICP-MS geochronology and regional correlation of Middle Jurassic intrusive rocks from the Garzon Massif, Upper Magdalena Valley and Central Cordillera, southern Colombia. Boletín de Geología, 32, 1–17.

Cagnioncle, A.-M., Parmentier, E.M., and Elkins-Tanton, L.T. (2007) Effect of solid flow above a subducting slab on water distribution and melting at convergent plate boundaries. Journal of Geophysical Research, 112, B09402.

Campa, M.F., and Coney, P.J. (1983) Tectono-stratigraphic terranes and mineral resource distributions in Mexico. Canadian Journal of Earth Sciences, 20, 1040–1051.

Campa-Uranda, M.F., García Díaz, J.L., and Iriondo, A. (2004) El arco sedimentario del Jurásico Medio (Grupo Tecocoyunca y Las Lluvias) de Olinalá. GEOS Unión Geofísica Mexicana, 24, 174.

Cao, W., Paterson, S., Saleeby, J., and Zalunardo, S. (2016) Bulk arc strain, crustal thickening, magma emplacement, and mass balances in the Mesozoic Sierra Nevada arc. Journal of Structural Geology, 84 IS -, 14–30.

Cardona, A., Cordani, U.G., Ruiz, J., Valencia, V.A., Armstrong, R., Chew, D., Nutman, A., and Sanchez, A.W. (2009) U-Pb zircon geochronology and Nd isotopic signatures of the pre-Mesozoic metamorphic basement of the eastern Peruvian Andes: growth and provenance of a Late Neoproterozoic to Carboniferous accretionary orogen on the northwest margin of Gondwana. The Journal of Geology, 117, 285–305.

Cardona, A., Valencia, V., Garzón, A., Montes, C., Ojeda, G., Ruiz, J., and Weber, M. (2010) Permian to Triassic I to S-type magmatic switch in the northeast Sierra Nevada de Santa Marta and adjacent regions, Colombian Caribbean: Tectonic setting and implications within Pangea paleogeography. Journal of South American Earth Sciences, 29, 772–783.

Carmona, O.O., and Pimentel, M.M. (2002) Rb–Sr and Sm–Nd isotopic study of the Puquí complex, Colombian Andes. Journal of South American Earth Sciences, 15, 173–182.

Cawood, P.A. (2005) Terra Australis Orogen: Rodinia breakup and development of the Pacific and Iapetus margins of Gondwana during the Neoproterozoic and Paleozoic. Earth-Science Reviews, 69, 249–279.

Cawood, P.A., and Buchan, C. (2007) Linking accretionary orogenesis with supercontinent assembly. Earth-Science Reviews, 82, 217–256.

Cawood, P.A., Hawkesworth, C.J., and Dhuime, B. (2012) Detrital zircon record and tectonic setting. Geology, 40, 875–878.

Cembrano, J., Lavenu, A., Reynolds, P., and Arancibia, G. (2002) Late Cenozoic transpressional ductile deformation north of the Nazca–South America–Antarctica triple junction. Tectonophysics, 354, 289–314.

Centeno-García, E. (2005) Review of Upper Paleozoic and Lower Mesozoic stratigraphy and depositional environments of central and west Mexico: Constraints on terrane analysis and paleogeography. In T.H. Anderson, J.A. Nourse, J.W. McKee, and M.B. Steiner, Eds., The Mojave-Sonora megashear hypothesis Development, assessment, and alternatives. Geological Society of America Special Paper 393 pp. 233–258.

Centeno-García, E., Busby, C., Busby, M., and Gehrels, G. (2011) Evolution of the Guerrero composite terrane along the Mexican margin, from extensional fringing arc to contractional continental arc. Geological Society of America Bulletin, 123, 1776–1797.

Centeno-García, E., Ruiz, J., Coney, P.J., Patchett, P.J., and Ortega-Gutiérrez, F. (1993) Guerrero terrane of Mexico: Its role in the Southern Cordillera from new geochemical data. Geology, 21, 419–422.

Chaussard, E., and Amelung, F. (2014) Regional controls on magma ascent and storage in volcanic arcs. Geochemistry, Geophysics, Geosystems, 15, 1407–1418.

Chen, J.H., and Moore, J.G. (1982) Uranium-lead isotopic ages from the Sierra Nevada Batholith, California. Journal of Geophysical Research, 87, 4761–4784.

Chernicoff, C.J., Zappettini, E.O., Santos, J.O., McNaughton, N.J., and Belousova, E. (2013) Combined U-Pb SHRIMP and Hf isotope study of the Late Paleozoic Yaminué Complex, Rio Negro Province, Argentina: Implications for the origin and evolution of the Patagonia composite terrane. Geoscience Frontiers, 4, 37–56.

Chew, D.M., Schaltegger, U., Košler, J., Whitehouse, M.J., Gutjahr, M., Spikings, R.A., and Miskovic, A. (2007) U-Pb geochronologic evidence for the evolution of the Gondwanan margin of the north-central Andes. Geological Society of America Bulletin, 119, 697–711.

Chiaradia, M. (2015) Crustal thickness control on Sr/Y signatures of recent arc magmas: an Earth scale perspective. Scientific Reports, 5, 8115.

Chin, E.J., Lee, C.-T.A., and Blichert-Toft, J. (2015) Growth of upper plate lithosphere controls tempo of arc magmatism: Constraints from Al-diffusion kineticsand coupled Lu-Hf and Sm-Nd chronology. Geochemical Perspectives Letters, 1, 20–32.

Clift, P., and Vannucchi, P. Controls on tectonic accretion versus erosion in subduction zones: Implications for the origin and recycling of the continental crust., 42 Reviews of Geophysics RG2001 (2004).

Cochrane, R., Spikings, R., Gerdes, A., Ulianov, A., Mora, A., Villagómez, D., Putlitz, B., and Chiaradia, M. (2014) Permo-Triassic anatexis, continental rifting and the disassembly of western Pangaea. Lithos, 190-191, 383–402.

Cocks, L.R.M., and Torsvik, T.H. (2002) Earth geography from 500 to 400 million years ago : a faunal and palaeomagnetic review. Journal of the Geological Society, London, 159, 631–644.

Collins, W.J. (2002) Hot orogens, tectonic switching, and creation of continental crust. Geology, 30, 535–538.

Collo, G., Astini, R.A., Cawood, P.A., Buchan, C., and Pimentel, M. (2009) U–Pb detrital zircon ages and Sm–Nd isotopic features in low-grade metasedimentary rocks of the Famatina belt: implications for late Neoproterozoic–early Palaeozoic evolution of the proto-Andean margin of Gondwana. Journal of the Geological Society, 166, 303–319.

Colpron, M., and Nelson, J.L. (2011) A Palaeozoic NW passage and the Timanian, Caledonian and Uralian connections of some exotic terranes in the North American Cordillera. In A.M. Spencer, A.F. Embry, D.L. Gautier, A.V. Stoupakova, and K. Sørensen, Eds., Arctic Petroleum Geology: Geological Society, London, Memoirs Vol. 35, pp. 463–484.

Colpron, M., and Nelson, J.L. (2009) A Palaeozoic Northwest Passage: incursion of Caledonian, Baltican and Siberian terranes into eastern Panthalassa, and the early evolution of the North American Cordillera. In P.A. Cawood and A. Kröner, Eds., Earth accretionary systems in space and time. Geological Society, London, Special Publications Vol. 318, pp. 273–307.

Condie, K.C., Belousova, E., Griffin, W.L., and Sircombe, K.N. (2009) Granitoid events in space and time: Constraints from igneous and detrital zircon age spectra. Gondwana Research, 15, 228–242.

Condie, K.C., Bickford, M.E., Aster, R.C., Belousova, E., and Scholl, D.W. (2011) Episodic zircon ages, Hf isotopic composition, and the preservation rate of continental crust. Geological Society of America Bulletin, 123, 951–957.

Crisp, J.A. (1984) Rates of magma emplacement and volcanic output. Journal of Volcanology and Geothermal Research, 20, 177–211.

Crowley, Q.G., Key, R., and Noble, S.R. (2014) High-precision U–Pb dating of complex zircon from the Lewisian Gneiss Complex of Scotland using an incremental CA-ID-TIMS approach. Gondwana Research, 1–11.

Dahlquist, J.A., Alasino, P.H., and Bello, C. (2013) Devonian F-rich peraluminous A-type magmatism in the proto-Andean foreland (Sierras Pampeanas, Argentina): geochemical constraints and petrogenesis from the western-central region of the Achala batholith. Mineralogy and Petrology, 108, 391–417.

Davidson, J.P., and Arculus, R. (2006) The significance of Phanerozoic arc magmatism in generating continental crust. In M. Brown and T. Rushmer, Eds., Evolution and Differentiation of the Continental Crust.

de Silva, S. (2008) Arc magmatism, calderas, and supervolcanoes. Geology, 36, 671.

de Silva, S., Zandt, G., Trumbull, R., Viramonte, J.G., Salas, G., and Jimenez, N. (2006) Large ignimbrite eruptions and volcano-tectonic depressions in the Central Andes: a thermomechanical perspective. Geological Society, London, Special Publications, 269, 47–63.

de Silva, S.L., and Gosnold, W.D. (2007) Episodic construction of batholiths: Insights from the spatiotemporal development of an ignimbrite flare-up. Journal of Volcanology and Geothermal Research, 167, 320–335.

de Silva, S.L., Riggs, N.R., and Barth, A.P. (2015) Quickening the Pulse:Fractal Tempos in Continental Arc Magmatism. Elements, 11, 113–118.

DeCelles, P.G., Ducea, M.N., Kapp, P., and Zandt, G. (2009) Cyclicity in Cordilleran orogenic systems. Nature Geoscience, 2, 251–257.

DeCelles, P.G., Zandt, G., Beck, S.L., Currie, C.A., Ducea, M.N., Kapp, P., Gehrels, G.E., Carrapa, B., and Quade, J. (2015) *Cyclical orogenic processes in the Cenozoic central Andes*. In P.G. DeCelles, M.N. Ducea, B. Carrapa, and P.A. Kapp, Eds., Geodynamics of a Cordilleran Orogenic System: The Central Andes of Argentina and Northern Chile. Geological Society of America Memoir 212, pp. 459–490.

Defant, M.J., and Drummond, M.S. (1990) Derivation of some modern arc magmas by melting of young subducted lithosphere. Nature, 347, 662–665.

Defant, M.J., and Kepezhinskas, P. (2001) Evidence suggests slab melting in arc magmas. Eos Transactions, American Geophysical Union, 82, 65–69.

Demouy, S., Paquette, J.-L., de Saint Blanquat, M., Benoit, M., Belousova, E.A., O'Reilly, S.Y., García, F., Tejada, L.C., Gallegos, R., and Sempere, T. (2012) Spatial and temporal evolution of Liassic to Paleocene arc activity in southern Peru

unraveled by zircon U–Pb and Hf in-situ data on plutonic rocks. Lithos, 155, 183–200.

DePaolo, D.J. (1981a) A neodymium and strontium isotopic study of the mesozoic calc-alkaline granitic batholiths of the sierra Nevada and Peninsular Ranges, California. Journal of Geophysical Research, 86, 470–488.

DePaolo, D.J. (1981b) Trace element and isotopic effects of combined wallrock assimilation and fractional crystallization. Earth and Planetary Science Letters, 53, 189–202.

DePaolo, D.J., and Wasserburg, G.J. (1979) Petrogenetic mixing models and Nd-Sr isotopic patterns. Geochimica et Cosmochimica Acta, 43, 615–627.

Dewey, J.F., and Bird, J.M. (1970) Mountain belts and the new global tectonics. Journal of Geophysical Research, 75, 2625–2647.

Dickinson, W.R. (1970) Global Tectonics. Science, 168, 1250–1258.

Dickinson, W.R. (2004) Evolution of the North American Cordillera. Annual Review of Earth and Planetary Science Letters, 32, 13–45.

Dickinson, W.R. Anatomy and global context of the North American Cordillera. (S. Mahlburg Kay, V.A. Ramos, & W.R. Dickinson, Eds.), 204 Backbone of the Americas: Shallow Subduction, Plateau Uplift, and Ridge and Terrane Collision 1–29 (2009). Geological Society of America.

Dickinson, W.R., and Lawton, T.F. (2001) Carboniferous to Cretaceous assembly and fragmentation of Mexico. Geological Society of America Bulletin, 113, 1142–1160.

Dickinson, W.R., and Snyder, W.S. (1978) Plate tectonics of the Laramide orogeny. Geological Society of America Memoirs, 151, 355–366.

Dodson, M.H., Compston, W., Williams, I.S., and Wilson, J.F. (1988) A search for ancient detrital zircons in Zimbabwean sediments. Journal of the Geological Society, 145, 977–983.

Dowe, D.S., Nance, R.D., Keppie, J.D., Cameron, K.L., Ortega-Rivera, A., Ortega-Gutiérrez, F., and Lee, J.W.K. (2005) Deformational history of the Granjeno Schist, Ciudad Victoria, Mexico: Constraints on the closure of the Rheic Ocean? International Geology Review, 47, 920–937.

Ducea, M. (2001) The California arc: Thick granitic batholiths, eclogitic residues, lithospheric-scale thrusting, and magmatic flare-ups. GSA Today, 11, 4–10.

Ducea, M.N. (2011) Fingerprinting orogenic delamination. Geology, 39, 191–192.

Ducea, M.N., and Barton, M.D. (2007) Igniting flare-up events in Cordilleran arcs.

Geology, 35, 1047.

Dufek, J., and Bergantz, G.W. (2005) Lower Crustal Magma Genesis and Preservation: a Stochastic Framework for the Evaluation of Basalt-Crust Interaction. Journal of Petrology, 46, 2167–2195.

Eagles, G. (2007) New angles on South Atlantic opening. Geophysical Journal International, 168, 353–361.

Eagles, G., Gohl, K., and Larter, R.D. (2004) High-resolution animated tectonic reconstruction of the South Pacific and West Antarctic Margin. Geochemistry, Geophysics, Geosystems, 5, n/a–n/a.

Elías-Herrera, M., and Ortega-Gutiérrez, F. (2002) Caltepec fault zone: An Early Permian dextral transpressional boundary between the Proterozoic Oaxacan and Paleozoic Acatlán complexes, southern Mexico, and regional tectonic implications. Tectonics, 21, 1–19.

Elkins Tanton, L., Grove, T.L., and Donnelly-Nolan, J. (2001) Hot, shallow mantle melting under the Cascades volcanic arc. Geology, 29, 631.

Engebretson, D.C., Cox, A., and Gordon, R.G. (1985) Relative Motions Between Oceanic and Continental Plates in the Pacific Basin. Geological Society of America Special Papers, 206, 1–60.

England, P., and Wilkins, C. (2004) A simple analytical approximation to the temperature structure in subduction zones. Geophysical Journal International, 159, 1138–1154.

England, P., Engdahl, R., and Thatcher, W. (2004) Systematic variation in the depths of slabs beneath arc volcanoes. Geophysical Journal International, 156, 377–408.

England, P.C., and Katz, R.F. (2010) Melting above the anhydrous solidus controls the location of volcanic arcs. Nature, 467, 700–703.

Fastovsky, D.E., Hermes, O.D., Strater, N.H., Bowring, S.A., Clark, J.M., Montellano, M., and Rene, H.R. (2005) Pre–Late Jurassic, fossil-bearing volcanic and sedimentary red beds of Huizachal Canyon, Tamaulipas, Mexico. In T.H. Anderson, J.A. Nourse, J.W. McKee, and M.B. Steiner, Eds., The Mojave-Sonora Megashear hypothesis: development, assessment, and alternatives. Geological Society of America Special Paper 393, pp. 401–426..

Ferrari, L., López-Martínez, M., Aguirre-Díaz, G., and Carrasco-Núñez, G. (1999) Space-time patterns of Cenozoic arc volcanism in central Mexico: from the Sierra Madre Occidental to the Mexican Volcanic Belt. Geology, 27, 303–306.

Galaz, G., Keppie, J.D., Lee, J.K.W., and Ortega-Rivera, A. (2013) A high-pressure folded klippe at Tehuitzingo on the western margin of an extrusion zone, Acatlán Complex, southern México. Gondwana Research, 23, 641–660.

Gehrels, G., Rusmore, M., Woodsworth, G., Crawford, M., Andronicos, C., Hollister, L., Patchett, J., Ducea, M., Butler, R., Klepeis, K., and others (2009) U-Th-Pb geochronology of the Coast Mountains batholith in north-coastal British Columbia: Constraints on age and tectonic evolution. Geological Society of America Bulletin, 121, 1341–1361.

Gill, J.B. (1981) Orogenic andesites and plate tectonics, 1 p. Heidelberg, Springer, Berlin.

Godínez-Urban, A., Lawton, T.F., Molina-Garza, R.S., Iriondo, A., Weber, B., and López-Martínez, M. (2011) Jurassic volcanic and sedimentary rocks of the La Silla and Todos Santos Formations, Chiapas: Record of Nazas arc magmatism and rift-basin formation prior to opening of the Gulf of Mexico. Geosphere, 7, 121–144.

Gosen, Von, W., and Prozzi, C. (1998) Structural evolution of the Sierra de San Luis (Eastern Sierras Pampeanas, Argentina): implications for the Proto-Andean Margin of Gondwana. Geological Society, London, Special Publications, 142, 235–258.

Grajales-Nishimura, J.M., Centeno-García, E., Keppie, J.D., and Dostal, J. (1999) Geochemistry of Paleozoic basalts from the Juchatengo complex of southern Mexico: tectonic implications. Journal of South American Earth Sciences, 12, 537–544.

Gutscher, M., Spakman, W., Bijwaard, H., and Engdahl, E. (2000) Geodynamics of flat subduction: seismicity and tomographic constraints from the Andean margin. Tectonics, 19, 814–833.

Haschke, M. (2002) Repeated crustal thickening and recycling during the Andean orogeny in north Chile (21°–26°S). Journal of Geophysical Research, 107, 2019.

Haschke, M., Günther, A., Melnick, D., Echtler, H., Reutter, K.-J., Scheuber, E., and Oncken, O. (2006) Central and Southern Andean Tectonic Evolution Inferred from Arc Magmatism. In O. Oncken, Ed., The Andes: Active Subduction Orogeny pp. 337–353. Springer.

Hawkesworth, C., Cawood, P., and Dhuime, B. (2013) Continental growth and the crustal record. Tectonophysics, 609, 651–660.

Hawkesworth, C., Cawood, P., Kemp, T., Storey, C., and Dhuime, B. (2009) A Matter of Preservation. Science, 323, 49–50.

Hawkesworth, C.J., Dhuime, B., Pietranik, A.B., Cawood, P.A., Kemp, A.I.S., and Storey, C.D. (2010) The generation and evolution of the continental crust. Journal of the Geological Society, London, 167, 229–248.

Hawkesworth, C.J., Gallagher, K., Hergt, J.M., and McDermott, F. (1993) Mantle and slab contributions in arc magmas. Annual Review of Earth and Planetary Science Letters, 21, 175–204.

Hebert, L.B., Antoshechkina, P., and Asimow, P. (2009) Emergence of a low-viscosity

channel in subduction zones through the coupling of mantle flow and thermodynamics. Earth and Planetary Science Letters, 278, 243–256.

Heine, C., Zoethout, J., and Müller, R.D. (2013) Kinematics of the South Atlantic rift. Solid Earth Discussions, 5, 41–116.

Helbig, M., Keppie, J.D., Murphy, J.B., and Solari, L.A. (2012a) Exotic rifted passive margin of a back-arc basin off western Pangea: geochemical evidence from the Early Mesozoic Ayú Complex, southern Mexico. International Geology Review, 1–19.

Helbig, M., Keppie, J.D., Murphy, J.B., and Solari, L.A. (2012b) U-Pb geochronological constraints on the Triassic–Jurassic Ayú Complex, southern Mexico: Derivation from the western margin of Pangea-A. Gondwana Research, 22, 910–927.

Hervé, F., Calderón, M., Fanning, C.M., and Pankhurst, R.J. (2013) Provenance variations in the Late Paleozoic accretionary complex of central Chile as indicated by detrital zircons. Gondwana Research, 23, 1122–1135.

Hervé, F., FANNING, C.M., Calderón, M., and Mpodozis, C. (2014) Early Permian to Late Triassic batholiths of the Chilean Frontal Cordillera (28°–31°S): SHRIMP U–Pb zircon ages and Lu–Hf and O isotope systematics. Lithos, 184-187, 436–446.

Hervé, F., Pankhurst, R.J., Fanning, C.M., Calderón, M., and Yaxley, G.M. (2007) The South Patagonian batholith: 150 my of granite magmatism on a plate margin. Lithos, 97, 373–394.

Hildebrand, R.S., and Whalen, J.B. (2014) Arc and Slab Failure Magmatism in Cordilleran Batholiths II–The Cretaceous Peninsular Ranges Batholith of Southern and Baja California. Geoscience Canada.

Hildreth, W., and Moorbath, S. (1988) Crustal contributions to arc magmatism in the Andes of Central Chile. Contributions to Mineralogy and Petrology, 98, 455–489.

Hughes, G.R., and Mahood, G.A. (2008) Tectonic controls on the nature of large silicic calderas in volcanic arcs. Geology, 36, 627.

Huppert, H.E., and Sparks, R.S.J. (1988) The Generation of Granitic Magmas by Intrusion of Basalt into Continental Crust. Journal of Petrology, 29, 599–624.

Iwamori, H. (1998) Transportation of H_2O and melting in subduction zones. Earth and Planetary Science Letters, 160, 65–80.

Jackson, J., and Molnar, P. (1990) Active faulting and block rotations in the western Transverse ranges, California. Journal of Geophysical Research, 95, 22073–22022.

Jackson, M.D., Cheadle, M.J., and Atherton, M.P. (2003) Quantitative modeling of granitic melt generation and segregation in the continental crust. Journal of Geophysical Research, 108, 2332.

Jagoutz, O.E. (2010) Construction of the granitoid crust of an island arc. Part II: a quantitative petrogenetic model. Contributions to Mineralogy and Petrology, 160, 359–381.

Jicha, B.R., and Jagoutz, O. (2015) Magma Production Rates for Intraoceanic Arcs. Elements, 11, 99–105.

Jones, R.E., Kirstein, L.A., Kasemann, S.A., and Dhuime, B. (2015) Geodynamic controls on the contamination of Cenozoic arc magmas in the southern Central Andes: Insights from the O and Hf isotopic composition of zircon. Geochimica et Cosmochimica Acta, 164, 386–402.

Karlstrom, K.E., Miler, C.F., Kingsbury, J.A., and Wooden, J.L. (1993) Pluton emplacement along an active ductile thrust zone, Piute Mountains, southeastern California: Interaction between deformational and solidifcation processes. Geological Society of America Bulletin, 105, 213–230.

Karlstrom, L., Lee, C.A., and Manga, M. (2014) The role of magmatically driven lithospheric thickening on arc front migration. Geochemistry, Geophysics, Geosystems, 15, 2655–2675.

Kato, T.T., Sharp, W.D., and Godoy, E. (2008) Inception of a Devonian subduction zone along the southwestern Gondwana margin: 40Ar– 39Ar dating of eclogite–amphibolite assemblages in blueschist boulders from the Coastal Range of Chile (41°S). Can. J. Earth Sci., 45, 337–351.

Kay, R.W. (1978) Aleutian magnesian andesites: melts from subducted Pacific Ocean crust. Journal of Volcanology and Geothermal Research, 4, 117–132.

Kay, R.W., and Mahlburg Kay, S. (1993) Delamination and delamination magmatism. Tectonophysics, 219, 177–189.

Keppie, D.F. (2015) How the closure of paleo-Tethys and Tethys oceans controlled the early breakup of Pangaea. Geology, 43, 335–338.

Keppie, J.D. (2004) Terranes of Mexico revisited: A 1.3 billion year odyssey. International Geology Review, 46, 765–794.

Keppie, J.D., Dostal, J., Miller, B.V., Ortega-Rivera, A., Roldán-Quintana, J., and Lee, J.W.K. (2006) Geochronology and geochemistry of the Francisco Gneiss: Triassic continental rift tholeiites on the Mexican margin of Pangea metamorphosed and exhumed in a Tertiary core complex. International Geology Review, 48, 1–16.

Keppie, J.D., Dostal, J., Murphy, J.B., and Galaz-Escanilla, G. (2012) High pressure rocks of the Acatlán Complex, southern Mexico: Large-scale subducted Ordovician rifted passive margin extruded into the upper plate during the Devonian–Carboniferous. Tectonophysics, 560-561, 1–21.

Keppie, J.D., Dostal, J., Murphy, J.B., and Nance, R.D. (2008) Synthesis and tectonic interpretation of the westernmost Paleozoic Variscan orogen in southern Mexico: From rifted Rheic margin to active Pacific margin. Tectonophysics, 461, 277–290.

Keppie, J.D., Nance, R.D., Ramos-Arias, M.A., Lee, J.K.W., Dostal, J., Ortega-Rivera, A., and Murphy, J.B. (2010) Late Paleozoic subduction and exhumation of Cambro-Ordovician passive margin and arc rocks in the northern Acatlán Complex, southern Mexico: Geochronological constraints. Tectonophysics, 495, 213–229.

Kerr, A.C., Aspden, J.A., Tarney, J., and Pilatasig, L.F. (2002) The nature and provenance of accreted oceanic terranes in western Ecuador: geochemical and tectonic constraints. Journal of the Geological Society, 159, 577–594.

Kirsch, M., Helbig, M., Keppie, J.D., Murphy, J.B., Lee, J.K.W., and Solari, L.A. (2014) A Late Triassic tectonothermal event in the eastern Acatlan Complex, southern Mexico, synchronous with a magmatic arc hiatus: The result of flat-slab subduction? Lithosphere, 6, 63–79.

Kirsch, M., Keppie, J.D., Murphy, J.B., and Lee, J.K.W. (2013) Arc plutonism in a transtensional regime: the late Palaeozoic Totoltepec pluton, Acatlán Complex, southern Mexico. International Geology Review, 55, 263–286.

Kirsch, M., Keppie, J.D., Murphy, J.B., and Solari, L.A. (2012) Permian–Carboniferous arc magmatism and basin evolution along the western margin of Pangea: geochemical and geochronological evidence from the eastern Acatlán Complex, southern Mexico. Geological Society of America Bulletin, 124, 1607–1628.

Kistler, R.W., Wooden, J.L., Premo, W.R., and Morton, D.M. (2014) Pb-Sr-Nd-O isotopic characterization of Mesozoic rocks throughout the northern end of the Peninsular Ranges batholith: Isotopic evidence for the magmatic evolution of oceanic arc–continental margin accretion during the Late Cretaceous of southern California. Geological Society of America Memoirs, 211, 263–316.

Klemetti, E.W., and Clynne, M.A. (2014) Localized Rejuvenation of a Crystal Mush Recorded in Zircon Temporal and Compositional Variation at the Lassen Volcanic Center, Northern California. PLoS ONE, 9, e113157.

König, S., Schuth, S., Münker, C., and Qopoto, C. (2006) The role of slab melting in the petrogenesis of high-Mg andesites: evidence from Simbo Volcano, Solomon Islands. Contributions to Mineralogy and Petrology, 153, 85–103.

Laya, J.C., and Tucker, M.E. (2012) Facies analysis and depositional environments of Permian carbonates of the Venezuelan Andes: Palaeogeographic implications for Northern Gondwana. Palaeogeography, Palaeoclimatology, Palaeoecology, 331-332, 1–26.

Lee, C.-T.A., and Anderson, D.L. (2015) Continental crust formation at arcs, the arclogite “delamination” cycle, and one origin for fertile melting anomalies in the

mantle. Science Bulletin, 1–16.

Lee, C.A., Shen, B., Slotnick, B.S., Liao, K., Dickens, G.R., Yokoyama, Y., Lenardic, A., Dasgupta, R., Jellinek, M., Lackey, J.S., and others (2013) Continental arc-island arc fluctuations, growth of crustal carbonates, and long-term climate change. Geosphere, 9, 21–36.

Leeman, W.P. (1983) The influence of crustal structure on compositions of subduction-related magmas. Journal of Volcanology and Geothermal Research, 18, 561–588.

Leeman, W.P. (1996) Boron and Other Fluid-mobile Elements in Volcanic Arc Lavas: Implications for Subduction Processes. In Subduction Top to Bottom pp. 269–276. American Geophysical Union, Washington, D. C.

Lima, S.M., Corfu, F., Neiva, A.M.R., and Ramos, J.M.F. (2012) Dissecting Complex Magmatic Processes: an in-depth U-Pb Study of the Pavia Pluton, Ossa-Morena Zone, Portugal. Journal of Petrology, 53, 1887–1911.

Lipman, P.W. (1992) Magmatism in the Cordilleran United States; progress and problems. In The Cordilleran orogen : conterminous U.S pp. 481–514. Geological Society of America, Boulder, Colorado.

Litherland, M., Aspden, J.A., and Jemielita, R.A. (1994) The metamorphic belts of Ecuador, British Geological Survey, Overseas Memoir 11. British Geological Survey.

Loewy, S.L., Connelly, J.N., and Dalziel, I.W.D. (2004) An orphaned basement block: The Arequipa-Antofalla Basement of the central Andean margin of South America. Geological Society of America Bulletin, 116, 171.

Lomb, N.R. (1976) Least-squares frequency analysis of unequally spaced data. Astrophysics and Space Science, 39, 447–462.

Luyendyk, B.P., Kamerling, M.J., and Terres, R. (1980) Geometric model for Neogene crustal rotations in southern California. Geological Society of America Bulletin, 91, 211.

Mahlburg Kay, S., and Mpodozis, C. (2001) Central Andean ore deposits linked to evolving shallow subduction systems and thickening crust. GSA Today, 11, 4–9.

Mahoney, J.B., Gordee, S.M., Haggart, J.W., Friedman, R.M., Diakow, L.J., and Woodsworth, G.J. (2009) Magmatic evolution of the eastern Coast Plutonic Complex, Bella Coola region, west-central British Columbia. Geological Society of America Bulletin, 121, 1362–1380.

Maksaev, V., Munizaga, F., and Tassinari, C. (2014) Timing of the magmatism of the paleo-Pacific border of Gondwana: U-Pb geochronology of Late Paleozoic to Early Mesozoic igneous rocks of the north Chilean Andes between 20° and 31°S. Andean

Geology, 41, 447–506–506.

Mamani, M., Wörner, G., and Sempere, T. (2010) Geochemical variations in igneous rocks of the Central Andean orocline (13 S to 18 S): Tracing crustal thickening and magma generation through time and space. Geological Society of America Bulletin, 122, 162–182.

Mantle, G.W., and Collins, W.J. (2008) Quantifying crustal thickness variations in evolving orogens: Correlation between arc basalt composition and Moho depth. Geology, 36, 87.

Martini, M., Ferrari, L., López-Martínez, M., and Valencia, V. (2010) Stratigraphic redefinition of the Zihuatanejo area, southwestern Mexico. Revista Mexicana de Ciencias Geológicas, 27, 412–430.

Martini, M., Mori, L., Solari, L., and Centeno-García, E. (2011) Sandstone provenance of the Arperos Basin (Sierra de Guanajuato, central Mexico): Late Jurassic–Early Cretaceous back-Arc spreading as the foundation of the Guerrero Terrane. The Journal of Geology, 119, 597–617.

Martini, M., Solari, L., and Camprubí, A. (2013) Kinematics of the Guerrero terrane accretion in the Sierra de Guanajuato, central Mexico: new insights for the structural evolution of arc–continent collisional zones. International Geology Review, 55, 574–589.

Matthews, K.J., Seton, M., and Müller, R.D. (2012) A global-scale plate reorganization event at 105− 100Ma. Earth and Planetary Science Letters, 355-356, 283–298.

Matzel, J.E.P., Bowring, S.A., and Miller, R.B. (2006) Time scales of pluton construction at differing crustal levels: Examples from the Mount Stuart and Tenpeak intrusions, North Cascades, Washington. Geological Society of America Bulletin, 118, 1412–1430.

Matzel, J.E.P., Bowring, S.A., and Miller, R.B. (2004) Protolith age of the Swakane Gneiss, North Cascades, Washington: Evidence of rapid underthrusting of sediments beneath an arc. Tectonics, 23.

Matzel, J.E.P., Bowring, S.A., and Miller, R.B. (2008) Spatial and temporal variations in Nd isotopic signatures across the crystalline core of the North Cascades, Washington. Geological Society of America Special Papers, 438, 499–516.

McGeary, S., Nur, A., and Ben-Avraham, Z. (1985) Spatial gaps in arc volcanism: The effect of collision or subduction of oceanic plateaus. Tectonophysics, 119, 195–221.

Memeti, V., Paterson, S.R., and Putirka, K.D. (2014) Formation of the Sierra Nevada Batholith: Magmatic and tectonic processes and their tempos. (V. Memeti, S.R. Paterson, & K.D. Putirka, Eds.). Geological Society of America.

Miller, E.L., Miller, M.M., Stevens, C.H., Wright, J.E., and Madrid, R.J. (1992) Late Paleozoic paleogeographic and tectonic evolution of the western U.S. Cordillera. In The Cordilleran orogen : conterminous U.S pp. 57–106. Geological Society of America, Boulder, Colorado.

Miller, R.B., Haugerud, R.A., Murphy, F., and Nicholson, L.S. (1994) Tectonostratigraphic framework of the northeastern Cascades. Washington Division of Geology and Earth Resources Bulletin, 80, 73–92.

Miller, R.B., Paterson, S.R., and Matzel, J.P. (2009) Plutonism at different crustal levels: Insights from the ~5–40 km (paleodepth) North Cascades crustal section, Washington. Geological Society of America Special Papers, 456, 125–149.

Mišković, A., Spikings, R.A., Chew, D.M., Košler, J., Ulianov, A., and Schaltegger, U. (2009) Tectonomagmatic evolution of Western Amazonia: Geochemical characterization and zircon U-Pb geochronologic constraints from the Peruvian Eastern Cordilleran granitoids. Geological Society of America Bulletin, 121, 1298–1324.

Monger, J., and Price, R. (2002) The Canadian Cordillera: Geology and tectonic evolution. CSEG Recorder, 17, 17–36.

Monger, J.W.H., Price, R.A., and Tempelman-Kluit, D.J. (1982) Tectonic accretion and the origin of the two major metamorphic and plutonic welts in the Canadian Cordillera. Geology, 10, 70.

Montecinos, P., Schärer, U., Vergara, M., and Aguirre, L. (2008) Lithospheric Origin of Oligocene-Miocene Magmatism in Central Chile: U-Pb Ages and Sr-Pb-Hf Isotope Composition of Minerals. Journal of Petrology, 49, 555–580.

Morton, D.M., Miller, F.K., Kistler, R.W., Premo, W.R., Lee, C.A., Langenheim, V.E., Wooden, J.L., Snee, L.W., Clausen, B.L., and Cossette, P. (2014) Framework and petrogenesis of the northern Peninsular Ranges batholith, southern California. In Peninsular Ranges Batholith, Baja California and Southern California Vol. 211, pp. 61–143. Geological Society of America.

Mukasa, S.B., and Henry, D.J. (1990) The San Nicolas batholith of coastal Peru: early Palaeozoic continental arc or continental rift magmatism? Journal of the Geological Society, London, 147, 27–39.

Murphy, J.B., and Nance, R.D. (2008) The Pangea conundrum. Geology, 36, 703–706.

Müller, R.D., Dutkiewicz, A., Seton, M., and Gaina, C. (2013) Seawater chemistry driven by supercontinent assembly, breakup, and dispersal. Geology.

Nance, R.D., Gutierrez-Alonso, G., Keppie, J.D., Linnemann, U., Murphy, J.B., Quesada, C., Strachan, R.A., and Woodcock, N.H. (2012) A brief history of the Rheic Ocean. Geoscience Frontiers, 3, 125–135.

Nance, R.D., Murphy, J.B., and Santosh, M. (2014) The supercontinent cycle: A retrospective essay. Gondwana Research, 25, 4–29.

Nelson, J.L., Colpron, M., Piercey, S.J., Dusel-Bacon, C., Murphy, D.C., and Roots, C.F. (2006) Paleozoic tectonic and metallogenetic evolution of pericratonic terranes in Yukon, northern British Columbia and eastern Alaska. In M. Colpron and J.L. Nelson, Eds., Paleozoic Evolution and Metallogeny of Pericratonic Terranes at the Ancient Pacific Margin of North America Vol. 45, pp. 323–360.

Nicholson, C., Sorlien, C.C., Atwater, T., Crowell, J.C., and Luyendyk, B.P. (1994) Microplate capture, rotation of the western Transverse Ranges, and initiation of the San Andreas transform as a low-angle fault system. Geology, 22, 491–495.

Nokleberg, W.J., Parfenov, L.M., Monger, J.W.H., Norton, I.O., Khanchuk, A.I., Stone, D.B., Scotese, C.R., Scholl, D.W., and Fujita, K. (2000) Phanerozoic tectonic evolution of the Circum-North Pacific. US Geological Survey Professional Paper, 1–102.

Oliveros, V., Labbé, M., Rossel, P., and Charrier, R. (2012) Late Jurassic paleogeographic evolution of the Andean back-arc basin: New constrains from the Lagunillas Formation, northern Chile (27° 30′–28° 30′S). Journal of South American Earth Sciences, 37, 25–40.

Ortega-Obregón, C., Solari, L., Gómez-Tuena, A., Elías-Herrera, M., Ortega-Gutiérrez, F., and Macías-Romo, C. (2014) Permian–Carboniferous arc magmatism in southern Mexico: U–Pb dating, trace element and Hf isotopic evidence on zircons of earliest subduction beneath the western margin of Gondwana. International Journal of Earth Sciences, 103, 1287–1300.

Otamendi, J.E., Ducea, M.N., and Bergantz, G.W. (2012) Geological, Petrological and Geochemical Evidence for Progressive Construction of an Arc Crustal Section, Sierra de Valle Fertil, Famatinian Arc, Argentina. Journal of Petrology, 53, 761–800.

Otamendi, J.E., Ducea, M.N., Tibaldi, A.M., Bergantz, G.W., la Rosa, de, J.D., and Vujovich, G.I. (2009) Generation of tonalitic and dioritic magmas by coupled partial melting of gabbroic and metasedimentary rocks within the deep crust of the Famatinian magmatic arc, Argentina. Journal of Petrology, 50, 841–873.

Palacios-García, N.B., and Martini, M. (2014) From back-arc rifting to arc accretion: the Late Jurassic–Early Cretaceous evolution of the Guerrero terrane recorded by a major provenance change in sandstones from the Sierra de los Cuarzos area, central Mexico. International Geology Review, 56, 1377–1394.

Pankhurst, R.J., Rapela, C.W., and Fanning, C.M. (2000) Age and origin of coeval TTG, I- and S-type granites in the Famatinian belt of NW Argentina. Transactions of the Royal Society of Edinburgh: Earth Sciences, 91, 151–168.

Pankhurst, R.J., Rapela, C.W., Fanning, C.M., and Márquez, M. (2006) Gondwanide

continental collision and the origin of Patagonia. Earth-Science Reviews, 76, 235–257.

Pankhurst, R.J., Weaver, S.D., Hervé, F., and Larrondo, P. (1999) Mesozoic-Cenozoic evolution of the North Patagonian batholith in Aysen, southern Chile. Journal of the Geological Society, London, 156, 673–694.

Pardo Casas, F., and Molnar, P. (1987) Relative motion of the Nazca (Farallon) and South American Plates since Late Cretaceous time. Tectonics, 6, 233–248.

Paterson, S.R., and Ducea, M.N. (2015) Arc Magmatic Tempos: Gathering the Evidence. Elements, 11, 91–98.

Paterson, S.R., Memeti, V., Anderson, L., Cao, W., Lackey, J.S., Putirka, K.D., Miller, R.B., Miller, J.S., and Mundil, R. (2014) Overview of arc processes and tempos. In V. Memeti, S.R. Paterson, and K.D. Putirka, Eds., Formation of the Sierra Nevada Batholith: Magmatic and tectonic processes and their tempos pp. 87–116. Geological Society of America.

Paterson, S.R., Okaya, D., Memeti, V., Economos, R., and Miller, R.B. (2011) Magma addition and flux calculations of incrementally constructed magma chambers in continental margin arcs: Combined field, geochronologic, and thermal modeling studies. Geosphere, 7, 1439–1468.

Peacock, S.M. (1990) Fluid processes in subduction zones. Science, 248, 329–337.

Pearce, J.A., Harris, N.B.W., and Tindle, A.G. (1984) Trace element discrimination diagrams for the tectonic interpretation of granitic rocks. Journal of Petrology, 25, 956–983.

Petford, N., and Gallagher, K. (2001) Partial melting of mafic (amphibolitic) lower crust by periodic influx of basaltic magma. Earth and Planetary Science Letters, 193, 483–499.

Pilger, R.H., Jr (1984) Cenozoic plate kinematics, subduction and magmatism: South American Andes. Journal of the Geological Society, 141, 793–802.

Pindell, J., Maresch, W.V., Martens, U., and Stanek, K. (2012) The Greater Antillean Arc: Early Cretaceous origin and proposed relationship to Central American subduction mélanges: implications for models of Caribbean evolution. International Geology Review, 54, 131–143.

Pindell, J.L., and Kennan, L. (2009) Tectonic evolution of the Gulf of Mexico, Caribbean and northern South America in the mantle reference frame: an update. Geological Society, London, Special Publications, 328, 1–55.

Plank, T., Cooper, L.B., and Manning, C.E. (2009) emerging geothermometers for estimating slabsurface temperatures. Nature Geoscience, 2, 611–615.

Proenza, J.A., Ortega-Gutiérrez, F., Camprubi, A., Trilla, J., Elías-Herrera, M., and Reyes-Salas, M. (2004) Paleozoic serpentinite-enclosed chromitites from Tehuitzingo (Acatlán Complex, southern Mexico): a petrological and mineralogical study. Journal of South American Earth Sciences, 16, 649–666.

Profeta, L., Ducea, M.N., Chapman, J.B., Paterson, S.R., Gonzales, S.M.H., Kirsch, M., Petrescu, L., and DeCelles, P.G. (2015) Quantifying crustal thickness overtime in magmatic arcs. Scientific Reports, 1–7.

Ramos, V.A. (2009) Anatomy and global context of the Andes: Main geologic features and the Andean orogenic cycle. Geological Society of America Memoirs, 204, 31–65.

Ramos, V.A. (2008) Patagonia: A paleozoic continent adrift? Journal of South American Earth Sciences, 26, 235–251.

Ramos, V.A. (2010) The Grenville-age basement of the Andes. Journal of South American Earth Sciences, 29, 77–91.

Ramos, V.A., and Aleman, A. (2000) Tectonic Evolution of the Andes. In Tectonic Evolution of South America pp. 635–685. Rio de Janeiro.

Ramos, V.A., and Naipauer, M. (2014) Patagonia: where does it come from? Journal of Iberian Geology, 40, 1–13.

Ramos-Arias, M.A., Keppie, J.D., Ortega-Rivera, A., and Lee, J.W.K. (2008) Extensional Late Paleozoic deformation on the western margin of Pangea, Patlanoaya area, Acatlán Complex, southern Mexico. Tectonophysics, 448, 60–76.

Rapalini, A.E., de Luchi, M., Dopico, C.M., and Klinger, F. (2010) Did Patagonia collide with Gondwana in the Late Paleozoic? Some insights from a multidisciplinary study of magmatic units of the North Patagonian Massif. Geologica Acta, 8, 349–371.

Rapela, C.W., and Pankhurst, R.J. (1992) The granites of northern Patagonia and the Gastre Fault System in relation to the break-up of Gondwana. Geological Society, London, Special Publications, 68, 209–220.

Rapela, C.W., Pankhurst, R.J., Casquet, C., and Baldo, E. (1998a) Early evolution of the Proto-Andean margin of South America. Geology, 26, 707.

Rapela, C.W., Pankhurst, R.J., Casquet, C., Baldo, E., Saavedra, J., Galindo, C., and Fanning, C.M. (1998b) The Pampean Orogeny of the southern proto-Andes: Cambrian continental collision in the Sierras de Córdoba. Geological Society, London, Special Publications, 142, 181–217.

Reitsma, M.J. (2012) Reconstructing the Late Paleozoic - Early Mesozoic plutonic and sedimentary record of south-east Peru: Orphaned back-arcs along the western margin of Gondwana. (U. Schaltegger & R. Spikings, Eds.). Université de Genève, Genève.

Riley, B.C.D., Snyder, W.S., and Gehrels, G.E. (2000) U-Pb detrital zircon geochronology of the Golconda allochthon, Nevada. Geological Society of America Special Papers, 347, 65–75.

Rolando, A.P., Hartmann, L.A., Santos, J., Fernandez, R.R., Etcheverry, R.O., Schalamuk, I.A., and McNaughton, N.J. (2002) SHRIMP zircon U–Pb evidence for extended Mesozoic magmatism in the Patagonian Batholith and assimilation of Archean crustal components. Journal of South American Earth Sciences, 15, 267–283.

Romeuf, N., Aguirre, L., Soler, P., Feraud, G., Jaillard, E., and Ruffet, G. (1995) Middle Jurassic volcanism in the northern and central Andes. Andean Geology, 22, 245–259.

Rosenau, M., Melnick, D., and Echtler, H. (2006) Kinematic constraints on intra-arc shear and strain partitioning in the southern Andes between 38°S and 42°S latitude. Tectonics, 25, n/a–n/a.

Rossel, P., Oliveros, V., Ducea, M.N., Charrier, R., Scaillet, S., Retamal, L., and Figueroa, O. (2013) The Early Andean subduction system as an analog to island arcs: Evidence from across-arc geochemical variations in northern Chile. Lithos, 179, 211–230.

Rudnick, R.L. (1995) Making continental crust. Nature, 378, 1–8.

Ruiz, G.M.H., Seward, D., and Winkler, W. (2007) Evolution of the Amazon Basin in Ecuador with Special Reference to Hinterland Tectonics: Data from Zircon Fission-Track and Heavy Mineral Analysis. In Heavy Minerals in Use Vol. 58, pp. 907–934. Elsevier.

Scargle, J.D. (1982) Studies in astronomical time series analysis. II – statistical aspects of spectral analysis of unevenly spaced data. Astrophysical Journal, 263, 835–853.

Schaaf, P., Weber, B., Weis, P., Gross, A., Ortega-Gutiérrez, F., and Köhler, H. (2002) The Chiapas Massif (Mexico) revised: New geologic and isotopic data for basement characteristics. Neues Jahrbuch für Geologie und Paläontologie - Abhandlungen, 225, 1–23.

Schaltegger, U., Schmitt, A.K., and Horstwood, M. (2015) U–Th–Pb zircon geochronology by ID-TIMS, SIMS, and laser ablation ICP-MS: recipes, interpretations, and opportunities. Chemical Geology, 402, 89–110.

Scholl, D.W., and Huene, von, R. (2009) Implications of estimated magmatic additions and recycling losses at the subduction zones of accretionary (non-collisional) and collisional (suturing) orogens. Geological Society, London, Special Publications, 318, 105–125.

Scotese, C.R. (1997) The PALEOMAP Project: Paleogeographic atlas and plate tectonic software: Paleogeographic atlas and plate tectonic software.

Sdrolias, M., and Müller, R.D. (2006) Controls on back-arc basin formation. Geochemistry, Geophysics, Geosystems, 7, n/a–n/a.

Sedlock, R.L., Ortega-Gutiérrez, F., and Speed, R.C. (1993) Tectonostratigraphic Terranes and Tectonic Evolution of Mexico, 153 p. Vol. 278, pp. 1–153. Geological Society of America Special Paper 278.

Sempere, T., Carlier, G., Soler, P., Fornari, M., Carlotto, V., Jacay, J., Arispe, O., Néraudeau, D., Cárdenas, J., and Rosas, S. (2002) Late Permian–Middle Jurassic lithospheric thinning in Peru and Bolivia, and its bearing on Andean-age tectonics. Tectonophysics, 345, 153–181.

Sempere, T., Folguera, A., and Gerbault, M. (2008) New insights into Andean evolution: An introduction to contributions from the 6th ISAG symposium (Barcelona, 2005). Tectonophysics, 459, 1–13.

Seton, M., Müller, R.D., Zahirovic, S., Gaina, C., Torsvik, T., Shephard, G., Talsma, A., Gurnis, M., Turner, M., Maus, S., and others (2012) Global continental and ocean basin reconstructions since 200Ma. Earth-Science Reviews, 113, 212–270.

Shephard, G.E., Müller, R.D., and Seton, M. (2013) Earth-Science Reviews. Earth-Science Reviews, 124, 1–36.

Silva-Romo, G., Arellano-Gil, J., Mendoza-Rosales, C., and Nieto-Obregón, J. (2000) A submarine fan in the Mesa Central, Mexico. Journal of South American Earth Sciences, 13, 429–442.

Silver, L.T., and Chappell, B.W. (1988) The Peninsular Ranges Batholith: an insight into the evolution of the Cordilleran batholiths of southwestern North America. Transactions of the Royal Society of Edinburgh: Earth Sciences, 79, 105–121.

Sircombe, K.N. (2000) Quantitative comparison of large sets of geochronological data using multivariate analysis: a provenance study example from Australia. Geochimica et Cosmochimica Acta.

Solari, L.A., Ortega-Gutiérrez, F., Elías-Herrera, M., Schaaf, P., Norman, M., Torres de León, R., Ortega-Obregón, C., Chiquin, M., and Morán-Ical, S. U-Pb zircon geochronology of Paleozoic units in Western and Central Guatemala: insights into the tectonic evolution of Middle America. (K.H. James, M.A. Lorente, & J. and Pindell, Eds.), 328 Origin and Evolution of the Caribbean Plate 293–311 (2009). Geological Society of London.

Somoza, R. (1998) Updated Nazca (Farallon)—South America relative motions during the last 40 My: implications for mountain building in the central Andean region. Journal of South American Earth Sciences, 11, 211–215.

Spikings, R., Cochrane, R., Villagómez, D., Van der Lelij, R., Vallejo, C., Winkler, W., and Beate, B. (2014) The geological history of northwestern South America: from

Pangaea to the early collision of the Caribbean Large Igneous Province (290–75 Ma). Gondwana Research, 1–120.

Spikings, R.A., Crowhurst, P.V., Winkler, W., and Villagómez, D. (2010) Syn- and post-accretionary cooling history of the Ecuadorian Andes constrained by their in-situ and detrital thermochronometric record. Journal of South American Earth Sciences, 30, 121–133.

Spikings, R.A., Winkler, W., Seward, D., and Handler, R. (2001) Along-strike variations in the thermal and tectonic response of the continental Ecuadorian Andes to the collision with heterogeneous oceanic crust. Earth and Planetary Science Letters, 186, 57–73.

Stampfli, G.M., and Borel, G.D. (2002) A plate tectonic model for the Paleozoic and Mesozoic constrained by dynamic plate boundaries and restored synthetic oceanic isochrons. Earth and Planetary Science Letters, 196, 17–33.

Stern, C.R. (2004) Active Andean volcanism: its geologic and tectonic setting. Revista geológica de Chile, 31, 161–206.

Stern, T.W., Bateman, P.C., Morgan, B.A., Newell, M.F., and Peck, D.L. (1981) Isotopic U-Pb ages of zircon from the granitoids of the central Sierra Nevada, California. Professional Paper VL .

Storey, B.C. (1995) The role of mantle plumes in continental breakup: case histories from Gondwanaland. Nature, 377, 301–308.

Tabor, R.W., Haugerud, R.A., Brown, E.H., Babcock, R.S., and Miller, R.B. (1989) Accreted Terranes of the North Cascades Range, Washington: Spokane to Seattle, Washington, July 21–29, 1989. American Geophysical Union, Washington, D. C.

Tatsumi, Y. (2005) The subduction factory: How it operates in the evolving Earth. GSA Today, 15, 4–10.

Tatsumi, Y., and Eggins, S. (1995) Subduction zone magmatism, 1 p. Blackwell, Boston.

Tatsumi, Y., and Stern, R.J. (2006) The subduction factory. Oceanic and continental lithosphere: Similarities and differences, 19, 1–9.

Taylor, G.K., Grocott, J., Pope, A., and Randall, D.E. (1998) Mesozoic fault systems, deformation and fault block rotation in the Andean forearc: a crustal scale strike-slip duplex in the Coastal Cordillera of northern Chile. Tectonophysics, 299, 93–109.

Telgársky, R. (2013) Dominant Frequency Extraction. A Computing Research Repository, 1–12.

Torres, R., Ruiz, J., Patchett, P.J., and Grajales-Nishimura, J.M. (1999) Permo-Triassic continental arc in eastern Mexico; tectonic implications for reconstructions of

southern North America. In C. Bartolini, J.L. Wilson, and T.F. Lawton, Eds., Mesozoic sedimentary and tectonic history of north-central Mexico. Geological Society of America Special Paper 340, pp. 191–196.

Torsvik, T.H., Rousse, S., Labails, C., and Smethurst, M.A. (2009) A new scheme for the opening of the South Atlantic Ocean and the dissection of an Aptian salt basin. Geophysical Journal International, 177, 1315–1333.

Trumbull, R.B., Riller, U., Oncken, O., Scheuber, E., Munier, K., and Hongn, F. (2006) The Time-Space Distribution of Cenozoic Volcanism in the South-Central Andes: a New Data Compilation and Some Tectonic Implications. In O. Oncken, G. Chong, G. Franz, P. Giese, H.-J. Götze, V.A. Ramos, M.R. Strecker, and P. Wigger, Eds., The Andes pp. 29–43. Springer Berlin Heidelberg.

Turner, S.J., and Langmuir, C.H. (2015a) The global chemical systematics of arc front stratovolcanoes: Evaluating the role of crustal processes. Earth and Planetary Science Letters, 422, 182–193.

Turner, S.J., and Langmuir, C.H. (2015b) What processes control the chemical compositions of arc front stratovolcanoes? Geochemistry, Geophysics, Geosystems, 16, 1865–1893.

Valencia-Moreno, M., Ruiz, J., Barton, M.D., Patchett, P.J., Zürcher, L., Hodkinson, D.G., and Roldán-Quintana, J. (2001) A chemical and isotopic study of the Laramide granitic belt of northwestern Mexico: Identification of the southern edge of the North American Precambrian basement. Geological Society of America Bulletin, 113, 1409–1422.

Vallejo, C., Spikings, R.A., Luzieux, L., Winkler, W., Chew, D., and Page, L. (2006) The early interaction between the Caribbean Plateau and the NW South American Plate. Terra Nova, 18, 264–269.

Van der Lelij, R., Spikings, R., Ulianov, A., and Chiaradia, M. (2015) Palaeozoic to Early Jurassic history of the northwestern corner of Gondwana, and implications for the evolution of the Iapetus, Rheic and Pacific Oceans. Gondwana Research.

Vaughan, A.P.M., and Pankhurst, R.J. (2008) Tectonic overview of the West Gondwana margin. Gondwana Research, 13, 150–162.

Vermeesch, P. (2004) How many grains are needed for a provenance study? Earth and Planetary Science Letters, 224, 441–451.

Vermeesch, P. (2012) On the visualisation of detrital age distributions. Chemical Geology, 312-313, 190–194.

Villagómez, D., and Spikings, R. (2013) Thermochronology and tectonics of the Central and Western Cordilleras of Colombia: Early Cretaceous–Tertiary evolution of the Northern Andes. Lithos, 160-161, 228–249.

Villagómez, D., Spikings, R., Magna, T., Kammer, A., Winkler, W., and Beltrán, A. (2011) Geochronology, geochemistry and tectonic evolution of the Western and Central cordilleras of Colombia. Lithos, 125, 875–896.

Weber, B., Iriondo, A., Premo, W.R., Hecht, L., and Schaaf, P. (2007) New insights into the history and origin of the southern Maya block, SE México: U-Pb-SHRIMP zircon geochronology from metamorphic rocks of the Chiapas massif. International Journal of Earth Sciences, 96, 253–269.

Wobbe, F., Gohl, K., Chambord, A., and Sutherland, R. (2012) Structure and breakup history of the rifted margin of West Antarctica in relation to Cretaceous separation from Zealandia and Bellingshausen plate motion. Geochemistry, Geophysics, Geosystems, 13, Q04W12.

Yogodzinski, G.M., Lees, J.M., Churikova, T.G., and Dorendorf, F. (2001) Geochemical evidence for the melting of subducting oceanic lithosphere at plate edges. Nature.

Zaffarana, C., Tommasi, A., Vauchez, A., and Gregoire, M. (2014) Microstructures and seismic properties of south Patagonian mantle xenoliths (Gobernador Gregores and Pali Aike). Tectonophysics, 621, 175–197.

Zavala-Monsiváis, A., Barboza-Gudiño, J.R., Valencia, V.A., Rodríguez-Hernández, S.E., and García-Arreola, M.E. (2009) Las sucesiónes volcánicas pre-Cretácicas en el noreste de México. GEOS Unión Geofísica Mexicana, 29, 53.

Zavala-Monsiváis, A., Barboza-Gudiño, J.R., Velasco-Tapia, F., and García-Arreola, M.E. (2012) Sucesión volcánica Jurásica en el área de Charcas, San Luis Potosí: Contribución al entendimiento del Arco Nazas en el noreste de México. Boletín de la Sociedad Geológica Mexicana, 64, 277–293.

Zellmer, G.F. (2008) Some first-order observations on magma transfer from mantle wedge to upper crust at volcanic arcs. Geological Society, London, Special Publications, 304, 15–31.

Zellmer, G.F., and Annen, C. (2008) An introduction to magma dynamics. Geological Society, London, Special Publications, 304, 1–13.

Zhang, J., Ma, C., and She, Z. (2012) An Early Cretaceous garnet-bearing metaluminous A-type granite intrusion in the East Qinling Orogen, central China: Petrological, mineralogical and geochemical constraints. Geoscience Frontiers, 3, 635–646.

CHAPTER FIVE

CONCLUSIONS

This research project has used physical and chemical data to identify magma chamber processes that control compositional diversity in the Ica-Pisco plutons. The processes controlling magmatic diversification are repeated injection of magma and intra-chamber flow, convection-related mass transfer processes, magmatic recycling, and fractional crystallization.

The mingling and mixing features observed in the plutons during field work complemented by petrographic and chemical evidence for mixing might suggest mafic replenishment events that interacted with felsic magmas and formed sheets, enclave swarms, and hybrid compositional zones. Thus, it is suggested that the Ica-Pisco plutons formed as a result of episodic mafic magma recharge into the magma chamber(s) and that the processes varied throughout the chamber(s) and through time. Quantification of these mingling and mixing features suggest that perhaps 20% of the pre-PCB envelop is recycled into the Ica PCB and 10% of early PCB units may be recycled into later PCB units.

Magmatic diversity in this area is well defined by SW-NE geochemical trends. These trends are based on changes in magma source depth, crustal contamination, magma series, and alkalinity. The Ica-Pisco plutons can be grouped into four cycles of magmatism from SW to NE across the PCB and these cycles are: (1) Old gabbros at ~131 Ma, (2) Linga-Pampahuasi intrusive complex at ~105-90 Ma, (3) Tiabaya plutons at ~85-78 Ma, and (4) Incahuasi plutons at ~68-59 Ma. The first three cycles are explained as due magma from a shallow source related to a subducting Nazca plate; the last Incahuasi

magma cycle came from a deeper magma source probably associated with a thicker crustal segment showing an increase of crustal contamination. The alkalinity content has been noted as a very distinctive feature of the PCB. The alkalinity observed in the Ica-Pisco area is high in the WZ, low in the CZ, and then increasing again in the EZ. High-K values in the WZ are suggested to be due to dehydration melting; the low-K content in the CZ is because the fluids have been exhausted; and then the EZ has high-K again, but due to a great source depth rather than due to fluids.

Finally, it is suggested that the integration of field observations, petrography, geochronology, and geochemistry data is a good approach to identify magma sources and magmatic processes in the Ica-Pisco plutons and this methodology provides a more complete picture of the petrogenetic history of this area and can be applied to other areas for understanding changes in compositional diversity of the plutonic rocks.

Future work

A next possible step to develop the research in Peru is to move from the regional scale to a more detailed scale at selected areas such as magmatic lobe zones of the LIC. It would involve detailed fieldwork complemented with advanced analytical techniques for single minerals. Lobes are in general petrologically less complicated than the main body, because they preserve snapshots at different stages of batholith construction. Taking advantage of analytical methods developed for single minerals might provide new insights into short-timescale magmatic processes. Analytical techniques applied to feldspars and especially zircons from other plutons around the world provide abundant evidence for crystal recycling from previous magmatic events. Chemical zoning patterns

observed in single minerals can be used to identify mingling and mixing of magmas and also to estimate time scales for these processes. Working towards more single mineral analysis using advanced techniques would help to quantify the rates of magma generation, differentiation, and emplacement and finally to better constrain the timescales of the processes in order to present more quantitative models for magmatic events.

Another suggested area for future research is the presence and distribution of the gabbro-diorite plutonic bodies in this arc segment, since they are observed over the entire length of the PCB. In the past all the gabbro bodies were considered Pre-PCB events. However, preliminary evidence from this research suggests that some may be due to magmatic processes taking place during the evolution of the Ica-Pisco plutons. Some of these gabbro-diorite bodies are the result of Pre-PCB events, but others appear to be cumulate bodies associated with PCB magmatic processes. Chemical analysis can be used to identify and characterize these cumulate bodies and for understanding the type(s) of tectonic settings that these mafic rocks represent.

APPENDIX A

DEFINITIONS AND METHODOLOGY

In 1965 an exciting research project was developed by the University of Liverpool, the British Geological Survey, and the Geological Service of Peru. The research project focused on the recognition of the separate rock suites in the Peruvian Coastal Batholith (PCB) based on their geochemical signature. The super-unit concept (defined below) was used to characterize the different segments. The PCB was divided into along-strike segments from northwest to southeast: Piura, Trujillo, Lima, Arequipa, and Toquepala (Figure 74) with each segment divided into "super-units" (Cobbing and Pitcher, 1972). The super-unit concept was described by Larsen (1948) and was widely used in the PCB (Agar, 1978; Atherton and Petford, 1996; Beckinsale et al., 1985; Boily et al., 1989; Haederle and Atherton, 2002; Mukasa, 1986b; Petford and Atherton, 1996; Pitcher et al., 1985).

After 50 years, the super-unit concept is still being used to characterize the nature and origin of the granitic rocks in the PCB in the geological literature. In 2010 a new research project was started in the Arequipa segment to better understand the age and petrogenesis of the PCB. During this new research project, the difficulty of applying the term super-unit was recognized: I thus consider it important to discuss the validity of the super-unit concept based on the new petrological and geochronological evidence. The term "intrusive complex" (defined below) is preferred in this research because the super-unit term is increasingly difficult to apply to both the temporal and geochemical complexity now recognized in these plutons and in similarly complex bodies such as the Tuolumne and Guadalupe complexes in California, and the Sierra Valle Fertil complex in

Argentina (Memeti et al., 2010; Paterson et al., 2011; Putirka et al., 2014; Walker et al., 2015).

Figure 74. Segments of the Peruvian Coastal batholith. Modified from Pitcher & Cobbing (1985).

To foster a better understanding of previous and new research done in the Arequipa segment of the PCB, this appendix defines the most important concepts used to characterize the Ica-Pisco plutons of the PCB and presents the methodology used during the field sampling.

Definitions

Igneous Unit. An igneous unit is defined as rocks within the same linear batholith with the same relative age based on cross-cutting contact relationships, the same modal variation, the same texture and fabric, similar xenolith content and character, and the same relationship to any associated dike swarms (Larsen, 1948).

Superunit. The term super-unit was introduced to refer to a number of igneous units that appear to be consanguineous (i.e. related both petrographically, spatially, geochemically and temporally), or that formed a linked sequence in the sense used by Bateman & Dodge (1970). Therefore, if several genetically associated igneous units occur in close temporal and spatial association the consanguineous rock suite is referred to as a super-unit (Pitcher et al., 1985).

Igneous Complex. An igneous complex is used to refer to an assemblage of intimately associated and roughly contemporaneous igneous rocks differing in form or in petrographic type and characterized by irregularly mixed lithology or by highly complicated structural relations; the assemblage may consist of plutonic rocks, volcanic rocks, or both (Bates and Jackson, 1980). This term has evolved and today is used to include the temporal and spatial history of incrementally constructed igneous units that do not necessarily require units to be genetically linked.

Magma Mingling and Mixing. The term magma mingling is used to describe the physical interaction of two magmas where they retain most of their textural and compositional identity and do not have significant chemical exchange, such as the case of basalt mingling with a granitic magma to produce mafic enclaves (Barbarin, 2005; Barbarin and Didier, 1992; Chappell, 1996; Kocak et al., 2011). In this dissertation the term "mingling" will be used to indicate that homogeneity was not attained and that the components, for whatever reason (insufficient stirring, differences in viscosities or temperatures of crystallization), remain distinguishable in the final rock. On the other hand, the term magma mixing refers to chemical exchange between two or more magmas resulting in partial or complete hybridization of the two magmas and either the conversion of any pre-existing crystals to minerals stable in the hybrid melt, or their armoring by stable mineral compositions (Vernon, 2004). The extent of mixing between magmas of contrasting composition is controlled mostly by the composition, density, and viscosity contrasts of the two interacting magmas. Therefore, complete hybridization of melts may occur, but it is more difficult to reach with magmas (a combination of melts, crystal, $\pm$ volatiles) and it is thus considered a rare occurrence.

Crustal Assimilation and Contamination. Since the composition of the crust is generally different from the composition of magmas that pass through, there is often geochemically noticeable exchange between the crust and the magma. If crustal material is incorporated into the magma and melted to become part of the magma, the process is referred to as assimilation. If the magma physically incorporates part of the rock through which it passes, then this process is called contamination because the magma has become contaminated by the crustal materials. Clarke (2007) presents a definition of the

contamination as “changes in the bulk composition of the magma” and refers to assimilation as the process of eliminating the physical evidence of contamination. The implication of this definition is that once a foreign material is chemically “fully assimilated” there is no longer any direct physical or chemical evidence of the contaminant. Thus, there are different implications in using the term assimilation depending on the intensity of the process (physical and/or chemical exchange). In general, it is expected that both contamination and assimilation would produce a change in the chemical composition of the magma unless the material being added has the same chemical composition as the magma. Therefore, in this dissertation if physical evidence of foreign material is identified in the granitic rocks term contamination will be used, but if there is no physical evidence of foreign material incorporated into the magma and the bulk composition of the magma has changed it will be called assimilation.

Magmatic Recycling. Magmatic recycling is the result of physical and chemical processes causing new magma batches to incorporate and reuse any pre-existing igneous material that has been either partially or completely solidified. Recycling in magma chambers involves processes such as magmatic erosion (physical assimilation), transport of materials, and partial or complete chemical assimilation of older igneous material or magma mush. The magnitude of recycling during magma chamber construction is important because it can affect the evolving petrology of arc systems, their emplacement and thermal history, and estimates of magma addition rates when discussing “arc tempos” (Clarke, 2007; Lackey et al., 2008; Marsh, 1982a; Paterson et al., in press).

Xenoliths. The term xenolith refers to inclusions of foreign rocks, not related to the magmatic system, that have been broken off the walls of rising magma batches and

incorporated into the same or a later magma body. Individual grains or minerals acquired from the country rock during ascent and emplacement of the magma are called xenocrysts (Clarke, 2007).

Magmatic Enclaves. The word enclave is defined as a globule of magma mingled with the enclosing host magma. The term "magmatic" emphasizes the crystallization of these enclaves from magmas, and their typical igneous texture (Barbarin, 2005). Enclaves with mafic compositions are the most common, but there are also enclaves with felsic compositions and consequently having a different origin (Didier, 1973).

Mafic Magmatic Enclaves. Mafic magmatic enclaves are invariably darker-colored than the enclosing granitoid. and produced by injection of mafic magma into granitoid magma at different stages of crystallization of the latter. These are also known as mafic microgranular enclaves (Barbarin and Didier, 1992) or microgranitoid enclaves (Vernon et al., 1988). However, descriptions of enclaves from calcalkaline granitoid plutons throughout the world indicate and finer grained than the enclosing granitoids, but not necessarily microgranular or microgranitoid (Barbarin, 2005).

Cognate Inclusions. The term cognate inclusion refers to recycled pieces of early-precipitating aggregates formed near the margins of the pluton. In other words, the inclusion is always genetically related to its surrounding matrix. A typical example is of early forming phases near the margins of the pluton that get recycled as cognate inclusions into the younger, central units of the magmatic system.

Restite. The term restite is defined as refractory residual grains and aggregates that underwent anatexis, which may be carried in the magma from the source area, but may be difficult to detect (Clarke, 2007; Vernon, 2004).

Fieldwork and Sampling Methodology

Field surveys of the plutonic rocks in the Ica-Pisco area described and classified the PCB units. Samples were collected for petrographic and geochemical analyses from 2010 to 2015 during a total of about 100 days of fieldwork. The simplified geologic map in Figure 75 shows the field stops where data were collected. Information from field stops and sampling outside the research area provided a general geological framework. Sampling transects along main rivers and roads and also some areas with difficult accessibility were done with the main goals of sampling for petrographic and geochemical purposes and documenting structures and textures, such as contact relationships, hybrid rocks, roof pendants, schlieren layering, enclaves, xenoliths, mineral fabrics, and mingling/mixing microstructures, as evidence of magma chamber processes taking place during the construction of the batholith.

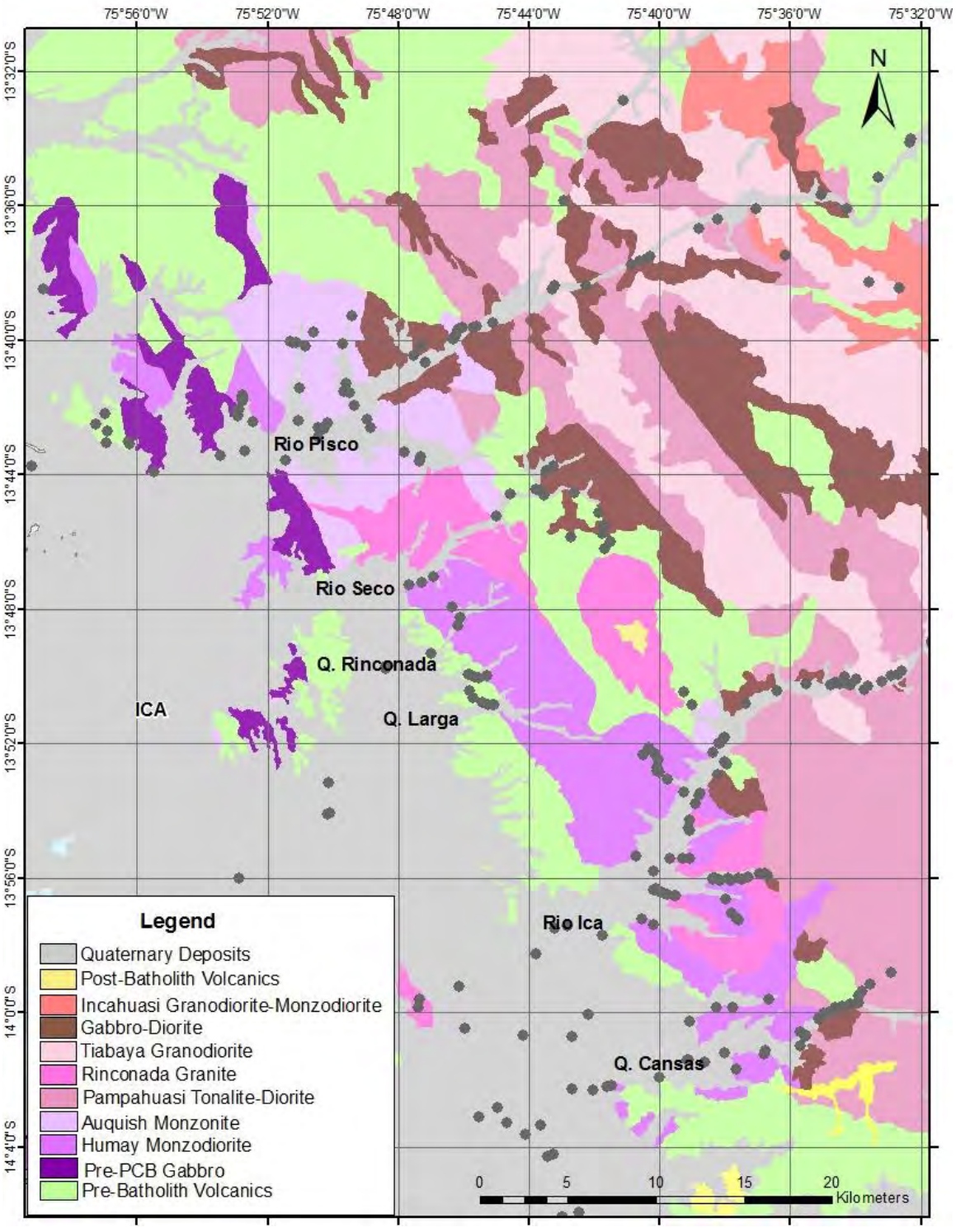

Figure 75. Simplified geologic map of the Ica-Pisco plutons in the Arequipa segment, showing the field stops. Modified from Davila (1993).

Field data and samples were collected from each rock unit of the Ica-Pisco plutons in the research area including contact zones, mingling zones, and pluton roof zone. Limitations during the field work and sampling were mainly associated with poor exposure or difficult access and uncertainty in determining the nature and origin of small enclaves. Finally, igneous complexes were defined based on the geochronological data and complemented with the field, petrographic, and geochemical data.

References

Agar, R. (1978) The Peruvian Coastal Batholith: Its monzonitic rocks and their related mineralization. The geology of the rio Pisco, a sector of the Arequipa segment of the Coastal Batholith. Geology, Doctor of Philosophy, p. 293. University of Liverpool, Liverpool.

Atherton, and Petford. (1996) Plutonism and the growth of Andean Crust at 9'S from 100 to 3 Ma. Journal of South American Earth Sciences, 9, 1-9.

Barbarin, B. (2005) Mafic magmatic enclaves and mafic rocks associated with some granitoids of the central Sierra Nevada batholith, California: nature, origin, and relations with the hosts. Lithos, 80(1-4), 155-177.

Barbarin, B., and Didier, J. (1992) Genesis and evolution of mafic microgranular enclaves through various types of interaction between coexisting felsic and mafic magmas. Earth and Environmental Science Transactions of the Royal Society of Edinburgh, 83(1-2), 145-153.

Bates, R.L., and Jackson, J.A. (1980) Glossary of Geology. American Geological Institute, Falls Church, Virginia.

Beckinsale, R.D., Sanchez-Fernandez, A.W., Brook, M., Cobbing, E.J., Taylor, W.P., and Moore, N.D. (1985) Rb-Sr whole-rock isochrons and K-Ar age determinations for the Coastal Batholith of Peru. Blackie, Glasgow.

Boily, M., Brooks, C., and Ludden, J.N. (1989) Chemical and isotopic evolution of the Coastal Batholith of southern Peru. Journal of Geophysical Research, 94(89), 12483-12489.

Chappell, B.W. (1996) Magma mixing and the production of compositional variation within granite suites: evidence from the granites of southeastern Australia. Journal of Petrology, 37(3), 449-470.

Clarke, D.B. (2007) Assimilation of xenocrysts in granitic magmas: principles, processes, proxies, and problems. The Canadian Mineralogist, 45(1), 5-30.

Cobbing, E.J., and Pitcher, W.S. (1972) The Coastal Batholith of central Peru. Journal of the Geological Society, 128(5), 421-454.

Davila, M.F. (1993) Geología de los cuadrángulos de Pisco, Guadalupe, Punta Grande, Ica y Córdova. Instituto Geológico Minero y Metalúrgico del Perú "INGEMMET", 47, 78.

Didier, J. (1973) Granites and their enclaves: The Bearing of Enclaves on the Origin of Granites. Development in Petrology Elsevier, Amsterdam.

Haederle, M., and Atherton, M.P. (2002) Shape and intrusion style of the Coastal Batholith, Peru. Tectonophysics, 345, 17-28.

Kocak, K., Zedef, V., and Kansun, G. (2011) Magma mixing/mingling in the Eocene Horoz (Nigde) granitoids, Central southern Turkey: evidence from mafic microgranular enclaves. Mineralogy and Petrology, 103(1-4), 149-167.

Larsen, E.S. (1948) Batholith and associated rocks of Corona, Elsinore, and San Luis Rey Quadrangles, Southern California. Geological Society of America Memoirs, 29, 182.

Memeti, V., Paterson, S.R., Matzel, J.E.P., Mundil, R., and Okaya, D. (2010) Magmatic lobes as "snapshots" of magma chamber growth and evolution in large, composite batholiths: An example from the Tuolumne intrusion, Sierra Nevada, California. Geological Society of America, 122, 1912-1931.

Mukasa, S.B. (1986) Zircon U-Pb ages of super-units in the Coastal batholith, Peru: Implications for magmatic and tectonic processes. Geological Society of America Bulletin, 97(2), 241.

Paterson, S.R., Okaya, D., Memeti, V., Economos, R., and Miller, R.B. (2011) Magma addition and flux calculations of incrementally constructed magma chambers in continental margin arcs: Combined field, geochronologic, and thermal modeling studies. Geosphere, 7(6), 1439-1468.

Paterson, Scott, Vali Memeti, Roland Mundil, Jiri Žák, 2016 Implications of repeated, multiscale, magmatic erosion and recycling in a mid-crustal pluton. American Mineralogy, in press, http://dx.doi.org/10.2138/am-2016-5718.

Petford, N., and Atherton, M. (1996) Na-rich Partial Melts from Newly Underplated Basaltic Crust: the Cordillera Blanca Batholith, Peru. Journal of Petrology, 37(6), 1491-1521.

Pitcher, W.S., Atherton, M.P., Cobbing, E.J., and Beckinsale, R.D. (1985) Magmatism at a plate edge: the Peruvian Andes. Wiley.

Putirka, K.D., Canchola, J., McNaughton, M., Smith, O., Torrez, G., Paterson, S.R., and Ducea, M. (2014) Day 1: Guadalupe Igneous Complex. Field Guides, 34, 1-15.

Vernon, R.H. (2004) A practical guide to rock microstructure. 594 p. Cambridge University Press, New York.

Vernon, R.H., Etheridge, M.A., and Wall, V.J. (1988) Shape and microstructure of microgranitoid enclaves: indicators of magma mingling and flow. Lithos, 22, 1-11.

Walker, B.A., Bergantz, G.W., Otamendi, J.E., Ducea, M.N., and Cristofolini, E.A. (2015) A MASH Zone Revealed: the Mafic Complex of the Sierra Valle Fértil. Journal of Petrology, 56(9), 1863-1896.

APPENDIX B

PETROGRAPHY DATA

Petrographic analyses of 124 thin sections were done on samples collected in the Ica-Pisco plutons of the Arequipa segment in the PCB. The thin sections also include samples of the volcanic envelope, gabbro-diorite bodies, some mafic enclaves, and hybrid rocks. Thin sections were examined in order to classify the rocks in terms of texture and composition and to look for features indicative of magma chamber processes. Modal analyses were performed using the point counting method with 300 points evaluated in each thin section. A full list of thin sections from the research area with the respective location, W-E distance based on trigonometry calculations, and the petrography data is presented here. The W-E distance was determined northeast of a line drawn along the base of the Andean foothills on a geologic map of the research area (Figure 76). The coordinates of the two end points used for the trigonometry calculations are listed in the table. The tables in this appendix list: (1) sample location, (2) mineral percentages, (3) modal classifications, (4) textural descriptions, (5) presence of zoning types, and (6) quantification of the plagioclase zoning.

The scheme followed for naming samples includes: the first two digits for year collected, third digit for month collected, fourth and fifth digit for day collected, stop number for each GPS collection location in a day indicated using capital letter(s) in alphabetical order of the day's location where samples were collected, rock type for each location with a lower case letter indicating different rock types collected at each GPS location, and for enclave samples a lower case "e" is used at the end of the sample name.

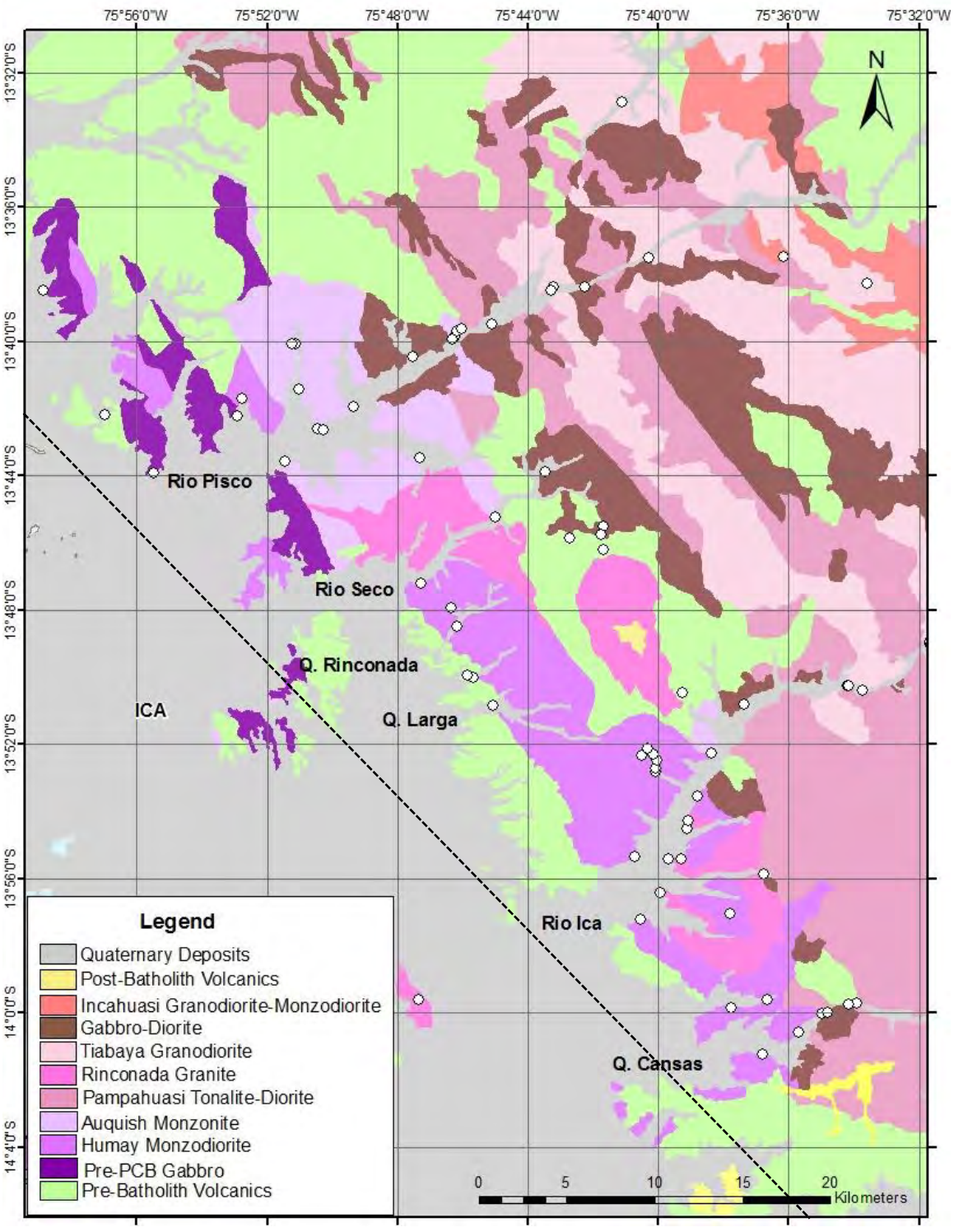

Figure 76. Simplified geologic map of the Arequipa segment, near Ica, showing the location of the thin sections of the Ica-Pisco area in the northern Arequipa segment, pre- and post-batholith rocks, and the line used to calculate E-W distance. Modified from INGEMMET (2002).

Table 9. Sample list of the Ica-Pisco samples and locations. Coordinates used to calculate W-E distance are: (-13.73 S, -75.93 W) and (-14.21 S, -75.42 W).

Sample	Coordinates		W-E Distance (Km)
	South	West	
10714H	13.95362	75.67537	1.26
10714J	13.92279	75.67860	3.44
10714K	13.87099	75.63913	10.42
10714P	13.83987	75.56205	18.55
10715B	13.73208	75.92461	0.24
10715C	13.71041	75.84041	8.16
10715F	13.63994	75.72009	22.59
10715L	13.61453	75.42432	46.44
10715M	13.60759	75.34368	52.95
10715Me	13.60759	75.34368	52.95
10719CC	14.10574	75.70329	-12.73
10719N	14.20803	75.42407	-0.15
10719R	14.17340	75.36102	7.22
10719Z	14.06247	75.42757	11.01
10720U	13.75882	75.48713	30.45
10720V	13.75105	75.48374	31.32
10721D	13.84141	75.65395	11.65
10721K	13.78687	75.78779	6.04
10721M	13.75416	75.74976	11.42
11823B	13.84676	75.62241	13.56
11823G	13.81709	75.52772	22.88
11823H	13.81559	75.52737	23.02
11824A	14.42753	75.84119	-48.09
11825A	13.83774	75.56987	18.14
11825B	13.83774	75.56913	18.20
11825G	13.74009	75.47334	32.95
11826E	13.90717	75.34074	29.61
11828A	14.42044	75.17647	1.47
11828B	14.39454	75.16142	4.61
11828E	14.26018	75.11012	18.91
11828I	14.07509	75.02568	39.66
11828J	14.07877	75.02854	39.16

Table 9. Continued

Sample	Coordinates		W-E Distance (Km)
	South	West	
11829C	13.75874	75.69473	15.13
11829D	13.76292	75.69561	14.73
11829E	13.77023	75.69466	14.23
11830C	13.87320	75.30364	35.01
11830D	13.84498	75.30433	37.18
11830E	13.82603	75.27928	40.52
11830I	13.79977	75.28555	42.12
11830K	13.80459	75.27317	42.65
11831EE	13.67616	75.32376	49.02
12715A	13.92374	75.66132	4.64
12715C	13.90900	75.65157	6.52
12716F	14.17889	75.36224	6.70
12716K	14.02594	75.16042	33.58
12717B	13.66439	75.77063	16.93
12717Be	13.66439	75.77063	16.93
12717C	13.65796	75.75182	18.83
12717D	13.64153	75.72137	22.37
12717E	13.63967	75.70375	23.82
12717H	13.62511	75.67106	27.38
12718B	13.62482	75.60254	32.46
12718D	13.63802	75.55963	34.60
12719B	13.61499	75.42549	46.32
12719D	13.59757	75.49350	42.67
12719H	13.47854	75.47002	53.77
12719I	13.48695	75.47243	52.93
12719J	13.53151	75.50472	47.04
12719K	13.60741	75.34363	52.96
12720C	13.99534	75.56479	6.15
12720D	14.00059	75.58290	4.40
12722E	14.08006	75.44305	8.49
12722J	14.01851	75.36042	19.41
12722K	14.02896	75.36022	18.61

Table 9. Continued

Sample	Coordinates		W-E Distance (Km)
	South	West	
12722L	14.04010	75.35352	18.23
12722T	13.96205	75.23788	32.89
12722V	13.91656	75.19213	39.84
12722X	13.88745	75.18649	42.54
12722Y	13.87002	75.18557	43.98
12723B	13.83760	75.22997	43.25
12723C	13.83105	75.23584	43.33
12723D	13.82891	75.25006	42.45
12723E	13.82604	75.25659	42.19
12723I	13.78803	75.37070	36.76
12723L	13.79288	75.34314	38.41
12723M	13.80357	75.31348	39.76
12723N	13.80181	75.28550	41.96
12723O	13.80322	75.27238	42.82
12723X	13.72714	75.19234	54.71
12723Z	13.73895	75.23905	50.34
12724D	13.99737	75.62933	1.22
12724E	13.99354	75.61067	2.90
12724G	14.02071	75.61295	0.60
12724H	14.00952	75.59451	2.84
12725D	13.73155	75.72396	15.10
12725F	13.79896	75.77251	6.22
12725H	13.80825	75.76949	5.72
13820E	13.69522	75.87918	6.49
13820M	13.70372	75.88187	5.62
13821C	13.69032	75.84991	9.04
13821F	13.66807	75.85175	10.65
13821H	13.66809	75.85394	10.48
13822A	13.72635	75.85740	5.65
13822C	13.72490	75.78855	10.85
13823A	13.64165	75.98121	3.15
13823E	13.47549	76.02810	12.75

Table 9. Continued

Sample	Coordinates		W-E Distance (Km)
	South	West	
13823I	13.44192	75.97067	19.64
13825D	13.70340	75.94952	0.65
13826A	13.69934	75.82201	10.39
13827A	13.67415	75.79195	14.59
13827D	13.66600	75.77174	16.72
13827F	13.66164	75.76949	17.23
13828A	13.71057	75.83787	8.33
13828D	13.66037	75.76727	17.50
13828H	13.54816	75.68507	32.40
13829B	13.76472	75.71165	13.41
13830B	13.99355	75.78896	-10.26
13830D	13.94038	75.66553	3.02
13830J	13.95086	75.62944	4.87
13901A	13.92372	75.65455	5.14
13901G	13.89267	75.64651	8.17
13901I	13.90470	75.65128	6.88
13902M	13.93131	75.61225	7.67
13903B	13.84782	75.75092	3.98
13903J	13.83401	75.76089	4.33
13903K	13.83264	75.76382	4.22
13904D	13.99982	75.57954	4.71
13904F	13.99593	75.56921	5.78
13905C	13.88067	75.66746	7.57
13905E	13.87881	75.66772	7.69
13905F	13.87463	75.66699	8.08
13906A	13.87219	75.67489	7.68
13906B	13.87158	75.66898	8.17
13906C	13.86881	75.67166	8.19

Table 10. Mineral percentages of the Ica-Pisco plutons. Qz-quartz, Pl-plagioclase, Or-orthoclase, Bt-biotite, Hbl-hornblende, Cpx-clinopyroxene, Opx-orthopyroxene, Op-opaques, and Tr-trace amounts.

Sample	Mineral (%)							
	Qz	Pl	Or	Bt	Hb	Cpx	Opx	Op
10714H	13.1	44.0	8.3	17.3	15.5	Tr		1.2
10714J	31.3	27.3	24.0	7.3	8.0	0.7		0.7
10714K	5.4	47.7	9.9	1.8	24.3	3.6		6.3
10714P	16.9	41.9	2.3	11.6	23.3	1.2		2.3
10715B	3.0	47.6	1.1	3.3	4.4	2.2	27.5	4.4
10715C	14.9	23.7	41.2	0.9				1.7
10715F	29.0	54.0	2.7	12.6				1.8
10715L	11.2	41.1	19.7	7.5	14.0	0.9	3.7	1.9
10715M	10.5	42.1	28.9	9.2	6.6	1.3		1.3
10715Me	1.3	52.0	4.0	18.4	15.8	5.3		1.3
10719CC	2.4	51.6	0.8	5.6	26.2	7.1		2.4
10719N	15.6	51.2		4.2	18.8			Tr
10719R	15.6	47.9	9.4	9.4	16.7	1.0		Tr
10719Z	21.0	45.0	5.4	11.6	16.3	Tr	Tr	0.8
10720U	18.3	40.8	13.3	12.5	10.8			2.5
10720V	25.9	44.1	9.1	3.5	7.0			4.2
10721D	13.4	40.3	17.9	11.2	14.2			1.5
10721K	17.8	22.3	35.7	3.8	12.1			1.9
10721M	8.6	38.6	13.6	0.7	17.9			5.7
11823B	22.0	38.5	8.7	14.4	11.5		2.5	1.9
11823G	32.0	33.1	22.2	5.5	5.5			1.7
11823H	19.0	50.3	21.8	2.8	5.6		0.5	
11824A	21.0	36.0	31.0	8.6	1.7			1.7
11825A	13.5	69.8		11.7	3.9			1.1
11825B	0.5	64.9		10.8	5.4	2.2	11.4	4.9
11825G	23.0	44.0	28.7	3.8				0.5
11826E	25.9	43.1	19.4	4.2	6.5			0.9
11828A	30.7	42.5	1.1	17.9	7.2			0.6
11828B	21.9	47.9		15.3	13.5			1.4
11828E	20.5	51.2	12.7	2.0	11.6			2.0
11828I	12.3	45.1	6.8	13.0	7.4	0.6	14.8	
11828J	13.1	48.4	1.6	14.8	20.5			1.6

Table 10. Continued

Sample	Mineral (%)							
	Qz	Pl	Or	Bt	Hb	Cpx	Opx	Op
11829C	0.9	68.4			25.2			5.5
11829D	2.0	63.0					29.4	5.6
11829E	25.1	55.3	1.0	1.0	17.1			0.5
11830C	17.0	34.3	29.8	9.7	6.0	1.2		2.0
11830D	12.5	44.7	22.6	8.2	10.1	0.5		1.4
11830E	15.4	45.8	15.8	8.7	11.5		1.2	1.6
11830I	17.1	39.4	19.9	13.4	8.3			1.9
11830K	18.4	47.3	10.9	10.4	12.0			1.0
11831EE	15.8	41.2	15.8	13.2	11.8		1.0	1.2
12715A	21.0	39.0	15.3	1.7	14.0	5.0	1.3	2.0
12715C	19.1	45.5	9.7	4.3	12.0	7.4	0.3	1.0
12716F	19.3	36.9	21.6	11.3	5.6	2.7	1.7	0.7
12716K	15.0	44.7	17.7	14.7	6.3	1.3		0.3
12717B	13.3	67.4	6.0		3.3	7.3	1.3	0.3
12717Be	1.7	63.3		6.3	8.3	13.3		7.0
12717C	2.3	58.0	0.3	1.0		10.7	25.3	2.0
12717D	33.3	60.3		6.0				
12717E	10.3	50.0		21.7	7.3	5.3	4.3	1.3
12717H	31.6	42.9	13.6	4.3	6.3			1.0
12718B	20.7	47.3	20.0	4.7	6.7			0.7
12718D	37.3	32.0	26.0	3.0	0.7			0.7
12719B	9.3	56.7	8.0	8.3	12.7	0.7	1.7	2.3
12719D	18.0	53.0		10.7	16.0			2.0
12719H	25.7	39.3	22.7	6.7	4.0		0.3	1.0
12719I	25.0	38.0	29.3	4.3	3.0			0.3
12719J	14.3	54.3	2.7	8.0	16.7	0.3	0.3	3.3
12719K	22.3	38.3	18.3	13.7	5.3	0.3	0.7	1.0
12720C	20.7	38.3	29.3	4.7	7.0			
12720D	0.3	64.3		0.7	1.0	15.3	15.0	3.3
12722E	20.7	45.7	9.3	11.7	11.3	0.3		1.0
12722J	2.7	72.0	0.3	6.0	16.3	2.3		0.3
12722K	0.3	61.3		1.0	2.7	19.7	10.0	5.0

Table 10. Continued

Sample	Mineral (%)							
	Qz	Pl	Or	Bt	Hb	Cpx	Opx	Op
12722L	19.7	51.7	6.7	11.0	9.7	0.3		1.0
12722T	20.3	43.7	19.7	4.3	8.7	2.0		1.3
12722V	17.7	42.7	18.3	14.0	3.0	3.0		1.3
12722X	12.7	63.3	3.3	5.3	10.3	2.7		1.7
12722Y	8.0	51.5	5.0	14.0	13.6	5.3		2.3
12723B	12.0	50.0	17.7	7.7	6.0	2.0	1.7	3.0
12723C	9.3	54.7	10.3	9.7	9.0	4.7	1.0	1.3
12723D	11.0	44.3	22.0	9.0	6.3	5.3	1.3	0.7
12723E	15.3	44.3	20.7	5.7	12.3	0.7		1.0
12723I	19.3	44.7	25.7	5.3	3.0	0.7		0.7
12723L	11.7	55.7	14.0	6.0	11.0	0.3		1.0
12723M	14.0	48.3	20.7	5.7	6.0	3.7		1.7
12723N	8.3	52.3	15.3	8.0	13.0	1.0	0.3	1.3
12723O	26.0	43.0	18.7	6.0	5.7			0.7
12723X	23.7	48.0	17.3	6.7	2.7			1.7
12723Z	17.7	45.3	26.7	5.7	2.7	0.3		1.7
12724D	23.0	54.0	11.0		10.7			1.3
12724E	21.7	47.7	17.0		10.7	1.3	0.3	1.3
12724G	11.7	65.0	0.7	0.3	13.3	6.3	1.3	1.3
12724H	0.3	64.3		0.3	15.7	14.3	2.3	0.7
12725D	20.7	36.3	18.3	11.3	10.3	1.0		2.0
12725F	14.0	56.3	16.0		7.3	4.0		1.3
12725H	2.7	68.0	0.3			28.0		
13820E	17.7	44.0	29.7	1.7	1.0	2.7		3.3
13820M	3.3	41.7	6.7	6.3	17.7	22.3	0.3	1.3
13821C	12.0	36.7	23.0	5.0	13.0	8.3	0.3	1.7
13821F	26.3	48.7	12.7	6.3	2.3			3.7
13821H	20.3	31.7	33.7	4.7	7.7	0.7		1.3
13822A	20.3	47.0	17.7	4.0	7.0	1.3		2.7
13822C	20.0	42.3	18.7	0.3	7.0	9.7		2.0
13823A	9.7	62.3	2.0	5.3	2.3	11.3	0.3	5.3
13823E	16.7	51.3	11.0	6.7	6.0	4.3	1.3	2.7

Table 10. Continued

Sample	Mineral (%)							
	Qz	Pl	Or	Bt	Hb	Cpx	Opx	Op
13823I	30.3	46.7	19.0	1.0	2.0	1.0		
13825D	12.0	35.0	31.3	0.7	4.3	9.7	2.7	4.3
13826A	11.3	45.0	21.3		12.3	8.0		2.0
13827A	16.0	41.3	18.0	5.3	7.3	9.7		2.3
13827D	5.0	65.3		4.3	17.3	1.7		6.3
13827F	27.0	60.0	4.7		5.3			3.0
13828A	20.0	34.0	32.7	7.3	0.7			5.3
13828D	24.3	35.0	28.7	5.0	3.3	0.3		3.3
13828H	23.3	52.0	16.7	5.0	2.7		0.3	
13829B	14.0	64.0				21.7		0.3
13830B	21.0	51.7	6.7	5.0	4.7	4.7	0.3	6.0
13830D	30.3	27.3	35.0	4.0	1.7	0.3		1.3
13830J	16.7	47.7	9.0	10.7	9.0	6.7	0.3	
13901A	28.3	33.7	26.0	6.7	3.3	0.7		1.3
13901G	13.3	46.0	8.7	11.7	16.0	2.7		1.7
13901I	29.3	27.0	28.7	6.7	7.7			0.7
13902M	6.0	66.0		4.7	16.7	5.3		1.3
13903B	16.3	37.3	30.3		5.7	6.7		3.7
13903J	9.0	38.7	27.3		8.0	14.0		3.0
13903K	22.7	26.0	40.7		4.3	4.7		1.7
13904D	22.7	62.3		1.3	4.0	0.7		8.7
13904F	36.3	27.0		11.7	24.0	0.7		0.3
13905C	14.3	40.7	14.0	6.7	17.0	4.0		3.3
13905E	16.3	36.0	24.7	3.3	13.3	4.7		1.7
13905F	20.7	43.3	15.3	2.0	8.7	6.3	0.7	3.0
13906A	21.3	36.3	24.3	4.7	8.0	4.0		1.3
13906B	30.3	29.7	32.0	4.3	1.3			2.3
13906C	1.0	46.7				32.3	0.3	19.7

Table 11. Normalized percentages and modal classification using IUGS classification scheme (Bas and Streckeisen, 1991) for the Ica-Pisco plutons. Qz-quartz, Pl-plagioclase, Or-orthoclase.

Sample	Modal Minerals (%)			Modal Classification
	Qz	Pl	Or	
10714H	20.0	67.3	12.7	Granodiorite
10714J	37.9	33.1	29.0	Granite
10714K	8.6	75.7	15.7	Qz-monzodiorite
10714P	27.7	68.5	3.8	Tonalite
10715B	5.8	92.1	2.1	Qz-diorite
10715C	18.7	29.7	51.6	Qz-monzonite
10715F	33.8	63.0	3.2	Tonalite
10715L	15.6	57.0	27.4	Qz-monzodiorite
10715M	12.9	51.7	35.5	Qz-monzonite
10715Me	2.2	90.8	6.9	Gabbro
10719CC	4.4	94.2	1.5	Gabbro
10719N	23.1	76.9	0.0	Tonalite
10719R	21.4	65.7	12.9	Granodiorite
10719Z	29.4	63.0	7.6	Granodiorite
10720U	25.3	56.4	18.4	Granodiorite
10720V	32.7	55.8	11.5	Granodiorite
10721D	18.3	55.1	26.5	Qz-monzodiorite
10721K	23.5	29.4	47.1	Granite
10721M	14.1	63.5	22.4	Qz-monzodiorite
11823B	31.8	55.6	12.6	Granodiorite
11823G	36.7	37.9	25.4	Granite
11823H	20.9	55.2	23.9	Granodiorite
11824A	23.9	40.9	35.2	Granite
11825A	16.2	83.8		Qz-diorite
11825B	0.8	99.2		Gabbro
11825G	24.0	46.0	30.0	Granite
11826E	29.3	48.8	21.9	Granodiorite
11828A	41.3	57.2	1.5	Tonalite
11828B	31.4	68.6		Tonalite
11828E	24.3	60.7	15.0	Granodiorite
11828I	19.2	70.2	10.6	Qz-monzodiorite
11828J	20.8	76.7	2.5	Tonalite

Table 11. Continued

Sample	Modal Minerals (%)			Modal Classification
	Qz	Pl	Or	
11829C	1.3	98.7		Gabbro
11829D	3.1	96.9		Gabbro
11829E	31.0	67.9	1.1	Tonalite
11830C	21.1	42.2	36.7	Granite
11830D	15.7	56.0	28.3	Qz-monzodiorite
11830E	20.0	59.5	20.5	Granodiorite
11830I	22.4	51.6	26.0	Granodiorite
11830K	24.0	61.7	14.3	Granodiorite
11831EE	21.7	56.6	21.7	Granodiorite
12715A	27.9	51.8	20.4	Granodiorite
12715C	25.7	61.3	13.1	Granodiorite
12716F	24.8	47.4	27.8	Granite
12716K	19.4	57.8	22.8	Qz-monzodiorite
12717B	15.3	77.8	6.9	Qz-diorite
12717Be	2.6	97.4	0.0	Gabbro
12717C	3.8	95.6	0.5	Gabbro
12717D	35.6	64.4	0.0	Tonalite
12717E	17.1	82.9	0.0	Qz-diorite
12717H	35.8	48.7	15.5	Granodiorite
12718B	23.5	53.8	22.7	Granodiorite
12718D	39.2	33.6	27.3	Granite
12719B	12.6	76.6	10.8	Qz-monzodiorite
12719D	25.4	74.6	0.0	Tonalite
12719H	29.3	44.9	25.9	Granite
12719I	27.1	41.2	31.8	Granite
12719J	20.0	76.2	3.8	Tonalite
12719K	28.3	48.5	23.2	Granodiorite
12720C	23.4	43.4	33.2	Granite
12720D	0.5	99.5	0.0	Gabbro
12722E	27.3	60.4	12.3	Granodiorite
12722J	3.6	96.0	0.4	Gabbro
12722K	0.5	99.5	0.0	Gabbro

Table 11. Continued

Sample	Modal Minerals (%)			Modal Classification
	Qz	Pl	Or	
12722L	25.2	66.2	8.5	Granodiorite
12722T	24.3	52.2	23.5	Granodiorite
12722V	22.5	54.2	23.3	Granodiorite
12722X	16.0	79.8	4.2	Qz-diorite
12722Y	12.4	79.9	7.7	Qz-diorite
12723B	15.1	62.8	22.2	Qz-monzodiorite
12723C	12.6	73.5	13.9	Qz-monzodiorite
12723D	14.2	57.3	28.4	Qz-monzodiorite
12723E	19.1	55.2	25.7	Qz-monzodiorite
12723I	21.6	49.8	28.6	Granite
12723L	14.3	68.4	17.2	Qz-monzodiorite
12723M	16.9	58.2	24.9	Qz-monzodiorite
12723N	11.0	68.9	20.2	Qz-monzodiorite
12723O	29.7	49.0	21.3	Granodiorite
12723X	26.6	53.9	19.5	Granodiorite
12723Z	19.7	50.6	29.7	Qz-monzonite
12724D	26.1	61.4	12.5	Granodiorite
12724E	25.1	55.2	19.7	Granodiorite
12724G	15.1	84.1	0.9	Qz-diorite
12724H	0.5	99.5	0.0	Gabbro
12725D	27.4	48.2	24.3	Granodiorite
12725F	16.2	65.3	18.5	Qz-monzodiorite
12725H	3.8	95.8	0.5	Gabbro
13820E	19.3	48.2	32.5	Qz-monzonite
13820M	6.5	80.6	12.9	Qz-monzodiorite
13821C	16.7	51.2	32.1	Qz-monzonite
13821F	30.0	55.5	14.4	Granodiorite
13821H	23.7	37.0	39.3	Granite
13822A	23.9	55.3	20.8	Granodiorite
13822C	24.7	52.3	23.0	Granodiorite
13823A	13.1	84.2	2.7	Qz-diorite
13823E	21.1	65.0	13.9	Granodiorite

Table 11. Continued

Sample	Modal Minerals (%)			Modal Classification
	Qz	Pl	Or	
13823I	31.6	48.6	19.8	Granodiorite
13825D	15.3	44.7	40.0	Qz-monzonite
13826A	14.6	57.9	27.5	Qz-monzodiorite
13827A	21.2	54.9	23.9	Granodiorite
13827D	7.1	92.9	0.0	Qz-diorite
13827F	29.5	65.5	5.1	Tonalite
13828A	23.1	39.2	37.7	Granite
13828D	27.7	39.8	32.6	Granite
13828H	25.4	56.5	18.1	Granodiorite
13829B	17.9	82.1	0.0	Qz-diorite
13830B	26.5	65.1	8.4	Granodiorite
13830D	32.7	29.5	37.8	Granite
13830J	22.7	65.0	12.3	Granodiorite
13901A	32.2	38.3	29.5	Granite
13901G	19.6	67.6	12.7	Qz-monzodiorite
13901I	34.5	31.8	33.7	Granite
13902M	8.3	91.7	0.0	Qz-diorite
13903B	19.4	44.4	36.1	Qz-monzonite
13903J	12.0	51.6	36.4	Qz-monzonite
13903K	25.4	29.1	45.5	Granite
13904D	26.7	73.3	0.0	Tonalite
13904F	57.4	42.6	0.0	Tonalite
13905C	20.8	58.9	20.3	Granodiorite
13905E	21.2	46.8	32.0	Granite
13905F	26.1	54.6	19.3	Granodiorite
13906A	26.0	44.3	29.7	Granite
13906B	33.0	32.2	34.8	Granite
13906C	2.1	97.9	0.0	Basalt

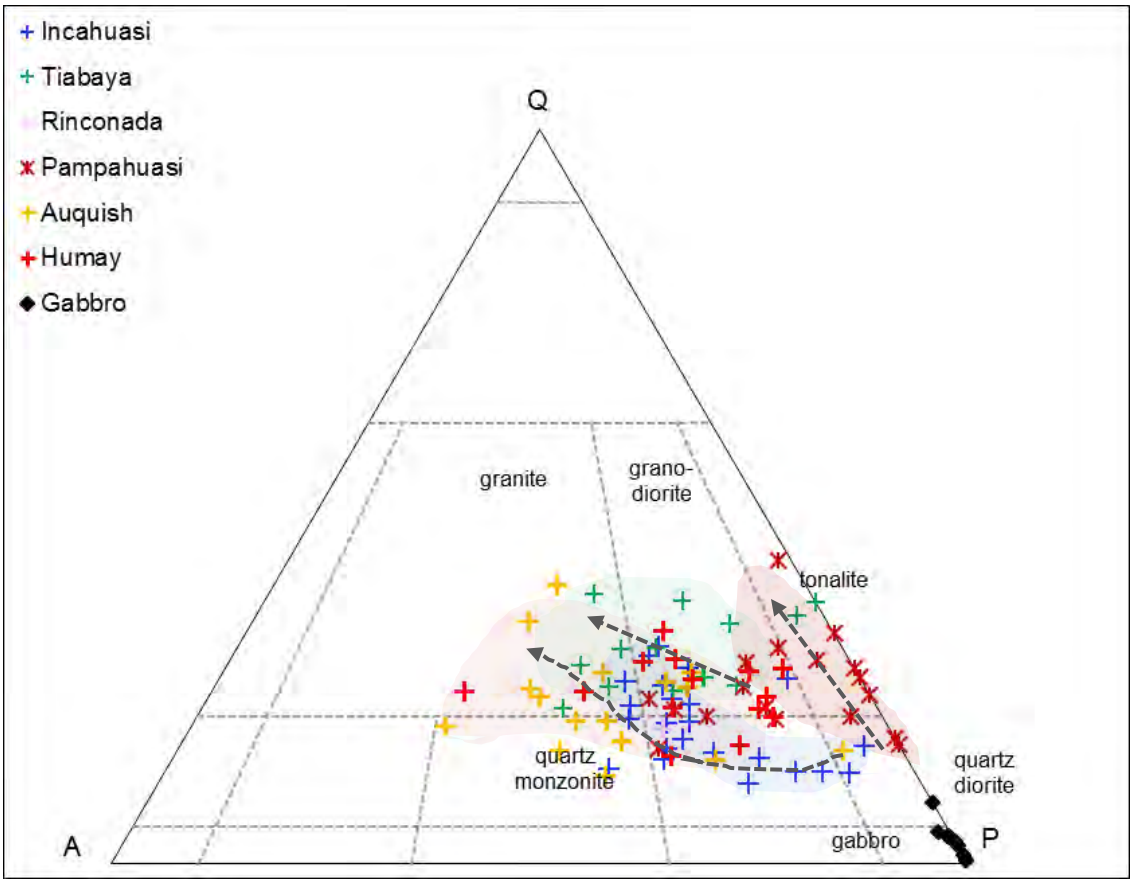

Figure 77. IUGS classification diagram (Streckeisen, 1973) based on modal analyses of samples collected from the different magmatic cycles in the Ica-Pisco area in the northern part of the Arequipa segment. Four groups can be identified based on composition and age: group 1 (yellow), group 2 (blue), group 3 (green), and group 4 (red), and gabbros (black diamonds).

Table 12. Textural description of the Ica-Pisco plutons. Ineq = inequigranular, Equi = equigranular, Pphy = porphyritic, Hp = hypidiomorphic, Sboph = subophitic, Allotr = allotriomorphic, Intgr = intergranular, C = coarse, M = medium, F = fine.

Sample	Rock Texture	Crystal Size	Crystal Texture
10714H	Ineq	M to C	Hp
10714J	Ineq	C to M	Hp
10714K	Ineq	M to C	Hp
10714P	Ineq	C to M	Hp
10715B	Ineq	M to C	Hp
10715C	Ineq	M to F	Hp
10715F	Ineq	C to M	Hp
10715L	Ineq	M to C	Hp
10715M	Ineq	C to M	Allotr
10715Me	Ineq	M to F	Hp
10719CC	Ineq	M to C	Hp
10719N	Ineq	C to M	Hp
10719R	Ineq	M to C	Hp
10719Z	Ineq	M to C	Hp
10720U	Ineq	C to M	Hp
10720V	Pphy	M to F	Allotr
10721D	Ineq	C to M	Hp
10721K	Ineq	C to M	Allotr
10721M	Ineq	M to C	Hp
11823B	Ineq	M to F	Hp
11823G	Ineq	C to M	Hp
11823H	Ineq	M to F	Hp
11824A	Ineq	C to M	Hp
11825A	Ineq	M to F	Hp
11825B	Pphy	M to F	Allotr
11825G	Ineq	C to M	Hp
11826E	Ineq	M to F	Hp
11828A	Eq	M to F	Hp
11828B	Ineq	C to M	Hp
11828E	Ineq	M to C	Hp
11828I	Ineq	C to M	Hp
11828J	Ineq	M to C	Hp

Table 12. Continued

Sample	Rock Texture	Crystal Size	Crystal Texture
11829C	Ineq	M to C	Hp
11829D	Ineq	C, M and F	Hp
11829E	Ineq to Pphy	M to F	Hp
11830C	Ineq	M to C	Hp
11830D	Ineq	C to M	Hp
11830E	Ineq	C to M	Hp
11830I	Ineq to Pphy	F to M	Hp
11830K	Ineq	C, M and F	Hp
11831EE	Ineq	C to M	Hp
12715A	Ineq	C to M	Hp
12715C	Ineq	M to C	Allotr
12716F	Ineq	C to M	Hp
12716K	Ineq	C to M	Hp
12717B	Ineq	M to F	Hp
12717Be	Ineq	M to F	Hp
12717C	Ineq	M to F	Hp
12717D	Ineq	M to F	Hp
12717E	Ineq	M to F	Hp
12717H	Ineq	C to M	Hp
12718B	Ineq	C to M	Hp
12718D	Ineq	C to M	Allotr
12719B	Ineq	C to M	Hp
12719D	Ineq	M to C	Hp
12719H	Ineq	M to F	Hp
12719I	Ineq	C to M	Hp
12719J	Eq	M>>C and F	Hp
12719K	Ineq	C to M	Hp
12720C	Ineq	C to M	Hp
12720D	Ineq	M to F	Hp, Intgr, Sboph
12722E	Ineq	M to F	Hp, Intgr
12722J	Eq	F to M	Hp, Intgr, Sboph
12722K	Ineq	M to F	Hp, Intgr

Table 12. Continued

Sample	Rock Texture	Crystal Size	Crystal Texture
12722L	Eq	M>>C and F	Hp, Intgr
12722T	Ineq	M>>C and F	Hp
12722V	Ineq	M to F	Hp
12722X	Ineq	M to F	Hp
12722Y	Eq	M to C	Hp
12723B	Ineq	M to C>>F	Hp
12723C	Ineq	M to F	Hp
12723D	Ineq	M to C>>F	Hp
12723E	Ineq	M to C>>F	Hp
12723I	Ineq	M to F	Hp
12723L	Ineq / Pphy	M to C>F	Hp
12723M	Ineq	C to M	Hp
12723N	Ineq	C to M	Hp
12723O	Ineq	M>C- F	Hp
12723X	Ineq / Pphy	M to F > C	Hp
12723Z	Ineq	C to M > F	Hp
12724D	Ineq / Pphy	M to F	Hp
12724E	Ineq / Pphy	C and F	Hp
12724G	Ineq / Pphy	C and F	Hp
12724H	Ineq	M to F >> C	Hp / Intgr
12725D	Eq	M to F >> C	Hp
12725F	Ineq	C >> M	Hp
12725H	Ineq	C > M	Hp
13820E	Ineq	M to F	Hp
13820M	Eq	M>>C and F	Hp
13821C	Ineq	C to M	Hp
13821F	Ineq	C to M	Hp
13821H	Ineq	C to M	Hp
13822A	Ineq	C to M	Hp
13822C	Eq	M>>C and F	Hp
13823A	Ineq	M to F	Allotr
13823E	Ineq	M to F	Allotr

Table 12. Continued

Sample	Rock Texture	Crystal Size	Crystal Texture
13823I	Ineq	M>>C and F	Hp
13825D	Ineq	M>>C and F	Hp
13826A	Ineq	M>>C and F	Hp
13827A	Ineq	C to M	Hp
13827D	Eq	C to M	Hp
13827F	Ineq	F to M	Hp
13828A	Ineq	C to M	Hp
13828D	Ineq	M>>C and F	Hp
13828H	Ineq	C to M	Hp
13829B	Ineq	F to M	Hp
13830B	Ineq	F to M	Hp
13830D	Eq	M>>C and F	Hp
13830J	Ineq	F to M	Hp
13901A	Ineq	M>>C and F	Hp
13901G	Ineq	M>>C and F	Hp
13901I	Ineq	M>>C and F	Hp
13902M	Ineq	C to M	Hp
13903B	Ineq	C to M	Allotr
13903J	Ineq	C to M	Allotr
13903K	Ineq	M>>C and F	Hp
13904D	Ineq	F to M	Hp
13904F	Ineq	F>>M>>C	Allotr
13905C	Ineq	M>>C and F	Hp
13905E	Ineq	M>>C and F	Hp
13905F	Ineq	F>>M>>C	Hp
13906A	Ineq	M>>C and F	Hp
13906B	Ineq	M to C	Hp
13906C	Pphy	C and F	Hp

Plagioclase Zoning

Plagioclase is the most abundant crystal in samples collected from the Ica-Pisco plutons and has a wide range of zoning microtextures. Crystal zoning reflects changes in composition and crystal structure as the crystal grows. Zoning may develop as a progressive change in composition and/or crystal structure, or it may occur abruptly from simple to complex. Progressive zoning is represented by normal zoning resulting from a gradual decrease in the anorthite, Ca-content from core to rim of the crystal. On the other hand, reverse zoning has the opposite trend from Na-rich plagioclase core to Ca-rich plagioclase rim. Step zoning refers to abrupt changes in crystal composition and oscillatory zoning is a fine-scale repetitive version of step zoning or progressive zoning. If zoning conforms to the general shape of the plagioclase crystal, it is called continuous zoning, but if it is localized at certain regions it is called sector zoning. If the sector zoning is localized in several areas of the crystal without preference, it is known as patchy zoning. Truncated/patchy zoning is characterized by major compositional hiatuses, i.e., an abrupt change at a "truncating boundary" from a relatively calcic to a more sodic plagioclase (Hibbard, 1995).

Two zoning categories are used in this study, simple and complex, and these are based on the textural complexity of zoning patterns observed in plagioclase crystals. Texturally simple zoning involves plagioclase crystals with normal zoning that goes from a Ca-rich plagioclase core to a Na-rich plagioclase rim and reverse zoning goes in the opposite trend without irregular internal zones or morphologies. Texturally complex zoning patterns refer to plagioclase crystals that contain zones alternating between oscillatory euhedral and patchy zoning, sieve textured, or irregular/wavy internal zones.

The presence of the different types of zoning was documented and quantification of the zoning types was performed by point counting method with 300 evenly spaced points taken over each thin section and the data is presented in the following tables.

Table 13. Types of plagioclase zoning in the Ica-Pisco plutons.

Sample	Classification	Type of Plagioclase Zoning			
		Normal	Reverse	Oscillatory	Patchy
10714H	Granodiorite	x	x	x	x
10714J	Granite	x	x	x	
10714K	Qz-monzodiorite	x	x	x	x
10714P	Tonalite	x	x		x
10715B	Qz-diorite		x		
10715C	Qz-monzonite				
10715F	Tonalite	x	x	x	x
10715L	Qz-monzodiorite	x		x	
10715M	Qz-monzonite	x		x	x
10715Me	Gabbro	x	x		x
10719CC	Gabbro	x		x	
10719N	Tonalite	x		x	
10719R	Granodiorite	x	x	x	x
10719Z	Granodiorite	x	x	x	
10720U	Granodiorite	x	x	x	
10720V	Granodiorite	x	x	x	x
10721D	Qz-monzodiorite	x	x	x	
10721K	Granite		x	x	
10721M	Qz-monzodiorite			x	x
11823B	Granodiorite	x			
11823G	Granite	x		x	x
11823H	Granodiorite	x	x	x	x
11824A	Granite	x		x	
11825A	Qz-diorite	x		x	
11825B	Gabbro	x	x	x	
11825G	Granite	x		x	
11826E	Granodiorite	x		x	x
11828A	Tonalite	x	x	x	
11828B	Tonalite	x	x	x	
11828E	Granodiorite	x	x	x	x

Table 13. Continued

Sample	Classification	Type of Plagioclase Zoning			
		Normal	Reverse	Oscillatory	Patchy
11828I	Qz-monzodiorite	x			
11828J	Tonalite	x			
11829C	Gabbro	x	x		
11829D	Gabbro	x			
11829E	Tonalite	x	x	x	x
11830C	Granite	x		x	x
11830D	Qz-monzodiorite	x		x	x
11830E	Granodiorite	x		x	
11830I	Granodiorite	x		x	
11830K	Granodiorite	x		x	
11831EE	Granodiorite	x		x	x
12715A	Granodiorite	x		x	x
12715C	Granodiorite	x		x	x
12716F	Granite	x		x	x
12716K	Qz-monzodiorite	x		x	x
12717B	Qz-diorite	x		x	x
12717Be	Gabbro				
12717C	Gabbro	x		x	x
12717D	Tonalite	x		x	x
12717E	Qz-diorite	x			x
12717H	Granodiorite	x		x	x
12718B	Granodiorite	x		x	x
12718D	Granite	x		x	
12719B	Qz-monzodiorite	x		x	
12719D	Tonalite	x		x	x
12719H	Granite	x		x	x
12719I	Granite	x		x	x
12719J	Tonalite	x		x	x
12719K	Granodiorite	x		x	x
12720C	Granite	x		x	x

Table 13. Continued

Sample	Classification	Type of Plagioclase Zoning			
		Normal	Reverse	Oscillatory	Patchy
12720D	Gabbro	x			
12722E	Granodiorite	x		x	x
12722J	Gabbro	x		x	x
12722K	Gabbro	x		x	
12722L	Granodiorite	x		x	x
12722T	Granodiorite	x		x	
12722V	Granodiorite	x		x	x
12722X	Qz-diorite	x		x	x
12722Y	Qz-diorite	x		x	x
12723B	Qz-monzodiorite	x			x
12723C	Qz-monzodiorite	x		x	x
12723D	Qz-monzodiorite	x		x	x
12723E	Qz-monzodiorite	x		x	x
12723I	Granite	x		x	x
12723L	Qz-monzodiorite	x		x	x
12723M	Qz-monzodiorite	x		x	x
12723N	Qz-monzodiorite	x		x	x
12723O	Granodiorite	x		x	x
12723X	Granodiorite	x			x
12723Z	Qz-monzonite	x		x	x
12724D	Granodiorite	x		x	x
12724E	Granodiorite	x		x	x
12724G	Qz-diorite	x		x	x
12724H	Gabbro	x		x	
12725D	Granodiorite	x			
12725F	Qz-monzodiorite				
12725H	Gabbro	x			
13820E	Qz-monzonite	x		x	x
13820M	Qz-monzodiorite	x		x	x
13821C	Qz-monzonite	x	x	x	x

Table 13. Continued

Sample	Classification	Type of Plagioclase Zoning			
		Normal	Reverse	Oscillatory	Patchy
13821F	Granodiorite	x		x	
13821H	Granite	x			
13822A	Granodiorite	x		x	x
13822C	Granodiorite	x		x	x
13823A	Qz-diorite	x		x	x
13823E	Granodiorite	x		x	
13823I	Granodiorite	x	x	x	x
13825D	Qz-monzonite	x			
13826A	Qz-monzodiorite	x	x	x	x
13827A	Granodiorite	x		x	x
13827D	Qz-diorite	x			
13827F	tonalite	x			
13828A	Granite	x			
13828D	Granite	x		x	
13828H	Granodiorite	x	x	x	x
13829B	Qz-diorite	x		x	
13830B	Granodiorite	x		x	
13830D	Granite	x		x	x
13830J	Granodiorite	x		x	x
13901A	Granite	x		x	x
13901G	Qz-monzodiorite	x		x	x
13901I	Granite	x		x	
13902M	Qz-diorite	x		x	x
13903B	Qz-monzonite	x	x	x	x
13903J	Qz-monzonite	x			
13903K	Granite	x		x	
13904D	Tonalite	x		x	
13904F	Tonalite	x		x	
13905C	Granodiorite	x	x	x	x
13905E	Granite	x		x	x
13905F	Granodiorite	x		x	x
13906A	Granite	x		x	x
13906B	Granite	x		x	

Table 14. Plagioclase percentage and plagioclase crystal zoning in the Ica-Pisco plutons. Simple zoning (SZ), complex zoning (CZ), and then the zoning is normalized to 100%.

Sample	Classification	Pl (%)	Zoning (%)		Zoning N (%)	
			SZ	CZ	SZ	CZ
12715A	Granodiorite	39	18	21	46	54
12715C	Granodiorite	45	27	18	59	40
12716F	Granite	37	28	9	75	24
12716K	Qz-monzodiorite	45	26	18	58	41
12717B	Qz-diorite	67	31	36	46	54
12717Be	Gabbro	63	1	62	1	98
12717C	Gabbro	58	15	43	25	74
12717D	Tonalite	60	5	55	8	92
12717E	Qz-diorite	50	10	40	19	80
12717H	Granodiorite	43	3	40	7	92
12718B	Granodiorite	47	2	44	5	94
12718D	Granite	32	1	31	3	96
12719B	Qz-monzodiorite	57	7	50	12	88
12719D	Tonalite	53	6	47	12	88
12719H	Granite	39	1	38	3	96
12719I	Granite	38	8	30	20	80
12719J	Tonalite	54	12	42	23	77
12719K	Granodiorite	38	2	36	5	94
12720C	Granite	38	1	36	3	94
12720D	Gabbro	64	16	49	24	75
12722E	Granodiorite	46	37	9	81	19
12722J	Gabbro	72	4	68	6	94
12722K	Gabbro	61	13	48	21	79
12722L	Granodiorite	52	31	21	60	41
12722T	Granodiorite	44	15	29	34	67
12722V	Granodiorite	43	3	3	40	7
12722X	Qz-diorite	63	10	53	16	84
12722Y	Qz-diorite	51	3	48	5	93

Table 14. Continued

Sample	Classification	Pl (%)	Zoning (%)		Zoning N (%)	
			SZ	CZ	SZ	CZ
12723B	Qz-monzodiorite	50	7	43	14	86
12723C	Qz-monzodiorite	55	4	51	7	93
12723D	Qz-monzodiorite	44	6	39	13	87
12723E	Qz-monzodiorite	44	14	30	31	68
12723I	Granite	45	9	36	20	81
12723L	Qz-monzodiorite	56	6	50	11	90
12723M	Qz-monzodiorite	48	5	43	11	89
12723N	Qz-monzodiorite	52	6	46	12	87
12723O	Granodiorite	43	6	37	13	87
12723X	Granodiorite	48	17	31	35	65
12723Z	Qz-monzonite	45	17	28	37	62
12724D	Granodiorite	54	16	38	30	70
12724E	Granodiorite	48	7	40	15	83
12724G	Qz-diorite	65	9	56	14	86
12724H	Gabbro	64	12	52	19	81
12725D	Granodiorite	36	8	28	22	77
12725F	Qz-monzodiorite	56	52	4	92	6
12725H	Gabbro	68	20	48	29	71
13820E	Qz-monzonite	44	27	17	61	39
13820M	Qz-monzodiorite	42	34	7	82	18
13821C	Qz-monzonite	37	7	29	20	80
13821F	Granodiorite	49	9	40	18	82
13821H	Granite	32	24	8	76	24
13822A	Granodiorite	47	19	28	41	59
13822C	Granodiorite	42	13	30	30	70
13823A	Qz-diorite	62	29	33	47	52
13823E	Granodiorite	51	28	23	55	45
13823I	Granodiorite	47	24	23	51	49

Table 14. Continued

Sample	Classification	Pl (%)	Zoning (%)		Zoning N (%)	
			SZ	CZ	SZ	CZ
13825D	Qz-monzonite	35	9	26	25	75
13826A	Qz-monzodiorite	45	17	28	38	62
13827A	Granodiorite	41	7	34	17	83
13827D	Qz-diorite	65	17	49	26	74
13827F	tonalite	60	37	23	62	38
13828A	Granite	34	9	25	27	73
13828D	Granite	35	16	19	47	53
13828H	Granodiorite	52	21	31	40	60
13829B	Qz-diorite	64	25	39	40	60
13830B	Granodiorite	52	48	4	92	8
13830D	Granite	27	4	23	16	84
13830J	Granodiorite	48	16	32	34	66
13901A	Granite	34	11	22	34	66
13901G	Qz-monzodiorite	46	15	31	33	67
13901I	Granite	27	11	16	41	59
13902M	Qz-diorite	66	15	51	23	77
13903B	Qz-monzonite	37	20	17	54	46
13903J	Qz-monzonite	39	32	6	84	16
13903K	Granite	26	8	18	31	69
13904D	Tonalite	62	16	47	25	75
13904F	Tonalite	27	21	6	77	23
13905C	Granodiorite	41	8	33	20	80
13905E	Granite	36	10	26	28	72
13905F	Granodiorite	43	16	27	37	63
13906A	Granite	36	19	18	51	49
13906B	Granite	30	21	9	70	30

References

Agar, R. (1978) The Peruvian Coastal Batholith: Its monzonitic rocks and their related mineralization. The geology of the rio Pisco, a sector of the Arequipa segment of the Coastal Batholith. Geology, Doctor of Philosophy, p. 293. University of Liverpool, Liverpool.

-. (1981) Copper mineralization and magmatic hydrothermal brines in the Rio Pisco Section of the Peruvian Coastal Batholith. Economic Geology, 76, 677-693.

Anderson, A.T. (1984) Probable relations between plagioclase zoning and magma dynamics, Fuego Volcano, Guatemala. American Mineralogist, 69, 660-676.

Appleby, S.K., Graham, C.M., Gillespie, M.R., Hinton, R.W., Oliver, G.J.H., and Eimf. (2008) A cryptic record of magma mixing in diorites revealed by high-precision SIMS oxygen isotope analysis of zircons. Earth and Planetary Science Letters, 269(1-2), 105-117.

Atherton, and Aguirre. (1992) Thermal and geotectonic setting of Cretaceous volcanic rocks near Ica, Peru, in relation to

Andean crustal thinning. Journal of South American Earth Sciences, 5(1), 47-69.

Atherton, and Petford. (1996) Plutonism and the growth of Andean Crust at 9'S from 100 to 3 Ma. Journal of South American Earth Sciences, 9, 1-9.

Bachmann, O. (2004) On the Origin of Crystal-poor Rhyolites: Extracted from Batholithic Crystal Mushes. Journal of Petrology, 45(8), 1565-1582.

Barbarin, B. (1990) Granitoids: Main petrogenetic classifications in relation to origin and tectonic setting. Geological Journal, 25(3-4), 227-238.

-. (2005) Mafic magmatic enclaves and mafic rocks associated with some granitoids of the central Sierra Nevada batholith, California: nature, origin, and relations with the hosts. Lithos, 80(1-4), 155-177.

Barbarin, B., and Didier, J. (1992) Genesis and evolution of mafic microgranular enclaves through various types of interaction between coexisting felsic and mafic magmas. Earth and Environmental Science Transactions of the Royal Society of Edinburgh, 83(1-2), 145-153.

Barbey, P., Gasquet, D., Pin, C., and Bourgeix, A.L. (2008) Igneous banding, schlieren and mafic enclaves in calc-alkaline granites: The Budduso pluton (Sardinia). Lithos, 104(1-4), 147-163.

Barnes, C.G., Petersen, S.W., Kistler, R.W., Prestvik, T., and Sundvoll, B. (1992) Tectonic implications of isotopic variation among Jurassic and Early Cretaceous

plutons, Klamath Mountains. Geological Society of America Bulletin, 104(1), 117-126.

Bas, M.J.L., and Streckeisen, A.L. (1991) The IUGS systematics of igneous rocks. Journal of the Geological Society, London, 148, 825-833.

Bates, R.L., and Jackson, J.A. (1980) Glossary of Geology. American Geological Institute, Falls Church, Virginia.

Beckinsale, R.D., Sanchez-Fernandez, A.W., Brook, M., Cobbing, E.J., Taylor, W.P., and Moore, N.D. (1985) Rb-Sr whole-rock isochrons and K-Ar age determinations for the Coastal Batholith of Peru. Blackie, Glasgow.

Boily, M., Brooks, C., and Ludden, J.N. (1989) Chemical and isotopic evolution of the Coastal Batholith of southern Peru. Journal of Geophysical Research, 94(89), 12483-12489.

Bolhar, R., Weaver, S.D., Whitehouse, M.J., Palin, J.M., Woodhead, J.D., and Cole, J.W. (2008) Sources and evolution of arc magmas inferred from coupled O and Hf isotope systematics of plutonic zircons from the Cretaceous Separation Point Suite (New Zealand). Earth and Planetary Science Letters, 268(3-4), 312-324.

Brown, G.C., and Mussett, A.E. (1993) The Innaccessible Earth. An integrated view to its structure and composition. Chapman & Hall.

Burchardt, S., Tanner, D., and Krumbholz, M. (2012) The Slaufrudalur pluton, southeast Iceland—An example of shallow magma emplacement by coupled cauldron subsidence and magmatic stoping. Geological Society of America Bulletin, 124(1-2), 213-227.

Bussell, M.A., Pitcher, W.S., and Wilson, P.A. (1976) Ring complexes of the Peruvian Coastal Batholith: a long-standing subvolcanic regime. Canadian Journal of Earth Sciences, 13(8), 1020-1030.

Carlier, G., Lorand, J.P., Liégeois, J.P., Fornari, M., Soler, P., Carlotto, V., and Cárdenas, J. (2005) Potassic-ultrapotassic mafic rocks delineate two lithospheric mantle blocks beneath the southern Peruvian Altiplano. Geology, 33(7), 601-604.

Chappell, B.W. (1996) Magma mixing and the production of compositional variation within granite suites: evidence from the granites of southeastern Australia. Journal of Petrology, 37(3), 449-470.

Chen, B., Chen, Z.C., and Jahn, B.M. (2009) Origin of mafic enclaves from the Taihang Mesozoic orogen, north China craton. Lithos, 110(1–4), 343-358.

Clarke, D.B. (2007) Assimilation of xenocrysts in granitic magmas: principles, processes, proxies, and problems. The Canadian Mineralogist, 45(1), 5-30.

Clarke, D.B., Henry, A.S., and White, M.A. (1998) Exploding xenoliths and the absence of “elephants’ graveyards” in granite batholiths. Journal of Structural Geology, 20, 1325–1343

Cobbing, E.J., Ozard, J.M., and Snelling, N.J. (1977) Reconnaissance geochronology of the crystalline basement rocks of the Coastal Cordillera of southern Peru. Geological Society of America Bulletin, 88(2), 241-246.

Cobbing, E.J., and Pitcher, W.S. (1972) The Coastal Batholith of central Peru. Journal of the Geological Society, 128(5), 421-454.

Coira, B., Davidson, J.P., Mpodozis, C., and Ramos, V. (1982) Tectonic and magmatic evolution of the Andes of northern Argentina and Chile. Earth Science Reviews, 18, 303-332.

Coldwell, B., Clemens, J., and Petford, N. (2011) Deep crustal melting in the Peruvian Andes: Felsic magma generation during delamination and uplift. Lithos, 125(1-2), 272-286.

Dallai, L., Ghezzo, C., and Sharp, Z.D. (2003) Oxygen isotope evidence for crustal assimilation and magma mixing in the Granite Harbour Intrusives, Northern Victoria Land, Antarctica. Lithos, 67(1-2), 135-151.

Daly, R.A. (1903) The mechanics of igneous intrusion. American Journal of Science, 15, 269–298.

Davila, M.F. (1993) Geología de los cuadrángulos de Pisco, Guadalupe, Punta Grande, Ica y Córdova. Instituto Geológico Minero y Metalúrgico del Perú "INGEMMET", 47, 78.

DePaolo, D.J. (1981) Trace element and isotopic effects of combined wallrock assimilation and fractional crystallization. Earth and Planetary Science Letters, 53(2), 189-202.

Didier, J. (1973) Granites and their enclaves: The Bearing of Enclaves on the Origin of Granites. Development in Petrology Elsevier, Amsterdam.

Dumond, G., Yoshinobu, A.S., and Barnes, C.G. (2005) Midcrustal emplacement of the Sausfjellet pluton, central Norway: Ductile flow, stoping, and in situ assimilation. Geological Society of America Bulletin, 117(3-4), 383-395.

Farris, D.W., and Paterson, S.R. (2007) Contamination of silicic magmas and fractal fragmentation of xenoliths in Paleocene plutons on Kodiak island, Alaska. The Canadian Mineralogist, 45(1), 107-129.

Furlong, K.P., and Myers, J.D. (1985) Thermal-mechanical modeling of the role of thermal stresses and stoping in magma contamination. Journal of Volcanology and Geothermal Research, 24(1–2), 179-191.

Gagnevin, D., Daly, J.S., and Poli, G. (2008) Insights into granite petrogenesis from quantitative assessment of the field distribution of enclaves, xenoliths and K-feldspar megacrysts in the Monte Capanne pluton, Italy. Mineralogical Magazine, 72(4), 925-940.

Gastil, G., Diamond, J., Knaack, C., Walawender, M., Marshall, M., Boyles, C., Chadwick, B., and Erskine, B. (1990) Chapter 2: The problem of the magnetite/ilmenite boundary in southern and Baja California California. Geological Society of America Memoirs, 174, 19-32.

Gehrels, G. (2011) Detrital Zircon U-Pb Geochronology: Current Methods and New Opportunities. Tectonics of Sedimentary Basins, p. 45-62. John Wiley & Sons, Ltd.

-. (2014) Detrital Zircon U-Pb Geochronology Applied to Tectonics. Annual Review of Earth and Planetary Sciences, 42(1), 127-149.

Gehrels, G., and Pecha, M. (2014) Detrital zircon U-Pb geochronology and Hf isotope geochemistry of Paleozoic and Triassic passive margin strata of western North America. Geosphere, 10(1), 49-65.

Ginibre, C., Kronz, A., and Worner, G. (2002) High-resolution quantitative imaging of plagioclase composition using accumulated backscattered electron images: new constraints on oscillatory zoning. Contributions to Mineralogy and Petrology, 142, 436-448.

Griffin, W.L., Wang, X., Jackson, S.E., Pearson, N.J., O'Reilly, S.Y., Xu, X., and Zhou, X. (2002) Zircon chemistry and magma mixing, SE China: In-situ analysis of Hf isotopes, Tonglu and Pingtan igneous complexes. Lithos, 61(3–4), 237-269.

Gromet, P., and Silver, L.T. (1987) REE Variations Across the Peninsular Ranges Batholith: Implications for Batholithic Petrogenesis and Crustal Growth in Magmatic Arcs. Journal of Petrology, 28(1), 75-125.

Haederle, M., and Atherton, M.P. (2002) Shape and intrusion style of the Coastal Batholith, Peru. Tectonophysics, 345, 17-28.

Hattori, K., and Sato, H. (1996) Magma evolution recorded in plagioclase zoning in 1991Pinatubo eruption products. American Mineralogist, 81, 982-994.

Hawkesworth, C.J., Rogers, N.W., van Calsteren, P.W.C., and Menzies, M.A. (1984) Mantle enrichment processes. Nature, 311(5984), 331-335.

Hibbard, M.J. (1995) Petrography to petrogenesis. 242-260 p. Prentice-Hall, Englewood Cliffs, New Jersey.

Hildebrand, R.S., and Whalen, J.B. (2014) Arc and slab-failure magmatism in Cordilleran batholiths II—The Cretaceous Peninsular Ranges batholith of Southern and Baja California: Paul Hoffman Volume: . Geoscience Canada, 41, 339-458.

Humphreys, M.C.S. (2009) Chemical Evolution of Intercumulus Liquid, as Recorded in Plagioclase Overgrowth Rims from the Skaergaard Intrusion. Journal of Petrology, 50(1), 127-145.

Humphreys, M.C.S., Blundy, J.D., and Sparks, R.S.J. (2006) Magma Evolution and Open-System Processes at Shiveluch Volcano: Insights from Phenocryst Zoning. Journal of Petrology, 47(12), 2303-2334.

Huppert, H.E., and Sparks, R.S.J. (1988) The Generation of Granitic Magmas by Intrusion of Basalt into Continental Crust. Journal of Petrology, 29(3), 599-624.

Johnston, S., Gehrels, G., Valencia, V., and Ruiz, J. (2009) Small-volume U–Pb zircon geochronology by laser ablation-multicollector-ICP-MS. Chemical Geology, 259(3–4), 218-229.

Kocak, K., Zedef, V., and Kansun, G. (2011) Magma mixing/mingling in the Eocene Horoz (Nigde) granitoids, Central southern Turkey: evidence from mafic microgranular enclaves. Mineralogy and Petrology, 103(1-4), 149-167.

Lackey, J.S., Valley, J.W., Chen, J.H., and Stockli, D.F. (2008) Dynamic Magma Systems, Crustal Recycling, and Alteration in the Central Sierra Nevada Batholith: the Oxygen Isotope Record. Journal of Petrology, 49(7), 1397-1426.

Lameyre, J., and Bonin, B. (1991) Granites in the main plutonic series. Elsevier.

Larsen, E.S. (1948) Batholith and associated rocks of Corona, Elsinore, and San Luis Rey Quadrangles, Southern California. Geological Society of America Memoirs, 29, 182.

Leon, W., Aleman, A., Torres, V., Rosell, W., and De La Cruz, O. (2007) Estratigrafía, sedimentología, y evolución tectónica de la cuenca de Pisco oriental. In S.E.y. Minas, Ed. serie D, Nº27. INGEMMET, Lima-Peru.

Mamani, M., Wörner, G., and Sempere, T. (2010) Geochemical variations in igneous rocks of the Central Andean orocline (13°S to 18°S): Tracing crustal thickening and magma generation through time and space. Geological Society of America Bulletin, 122(1-2), 162-182.

Marsh, B.D. (1982a) On the mechanics of igneous diapirism, stoping and zone melting. American Journal of Science, 282, 87.

Marsh, B.D. (1982b) On the mechanics of igneous diapirism, stoping, and zone melting. American Journal of Science, 282, 808-855.

Memeti, V., Paterson, S., and Mundil, R. (2014) Day 4: Magmatic evolution of the Tuolumne Intrusive Complex. Field Guides, 34, 43-74.

Memeti, V., Paterson, S.R., Matzel, J.E.P., Mundil, R., and Okaya, D. (2010) Magmatic lobes as "snapshots" of magma chamber growth and evolution in large, composite batholiths: An example from the Tuolumne intrusion, Sierra Nevada, California. Geological Society of America, 122, 1912-1931.

Miller, C.F., and Miller, J.S. (2002) Contrasting stratified plutons exposed in tilt blocks, Eldorado Mountains, Colorado River Rift, NV, USA. Lithos, 61(3–4), 209-224.

Miyashiro, A. (1974) Volcanic rock series in island arcs and active continental margins. American Journal of Science, 274, 321-355.

Moore, N.D. (1979) The Geology and Geochronology of the Arequipa Segment of the Coastal Batholith of Peru. , Doctor of Philosophy, p. 549. Liverpool, London.

-. (1984) Potassium-Argon ages from the Arequipa Segment of the Coastal Batholith of Peru and their correlation with regional tectonic events. Journal of the Geological Society, 141(3), 511-519.

Mukasa, S.B. (1984) Comparative Lead Isotope Systematics and Zircon Uranium-Lead Geochronology for the Coastal, San Nicolas and Cordillera Blanca Batholiths, Peru. Geology. University of California, Santa Barbara.

Mukasa, S.B. (1986a) Common Pb isotopic compositions of the tima, Arequipa and Toquepala segments in the Coastal batholith, Peru: Implications for magmagenesis. Geochimica Et Cosmochimica Acta, 50, 771-782.

Mukasa, S.B. (1986b) Zircon U-Pb ages of super-units in the Coastal batholith, Peru: Implications for magmatic and tectonic processes. Geological Society of America Bulletin, 97(2), 241.

Myers, J.D. (1975) Cauldron subsidence and fluidization: mechanisms of intrusion of the Coastal Batholith of Peru into its own volcanic ejecta. Geological Society of America, 86, 1209-1220.

Nixon, G.T., and Pearce, T.H. (1987) Laser-interferometry study of oscillatory zoning in plagioclase: The record of magma mixing and phenocryst recycling in calc-alkaline magma chambers, Iztaccihuatl volcano, Mexico. American Mineralogist, 72, 1144-1162.

Paterson, S.R., Memeti, V., Pignotta, G., Erdmann, S., Žák, J., Chambers, J., and Ianno, A. (2012) Formation and transfer of stoped blocks into magma chambers: The high-temperature interplay between focused porous flow, cracking, channel flow, host-rock anisotropy, and regional deformation. Geosphere, 8(2), 443-469.

Paterson, S.R., and Miller, R.B. (1998) Stoped blocks in plutons: paleo-plumb bobs, viscometers, or chronometers? Journal of Structural Geology, 20(9–10), 1261-1272.

Paterson, S.R., Okaya, D., Memeti, V., Economos, R., and Miller, R.B. (2011) Magma addition and flux calculations of incrementally constructed magma chambers in continental margin arcs: Combined field, geochronologic, and thermal modeling studies. Geosphere, 7(6), 1439-1468.

Paterson, S.R., Žák, J., and Janoušek, V. (2008) Growth of complex sheeted zones during recycling of older magmatic units into younger: Sawmill Canyon area, Tuolumne batholith, Sierra Nevada, California. Journal of Volcanology and Geothermal Research, 177(2), 457-484.

Peccerillo, A., and Taylor, S.R. (1976) Geochemistry of eocene calc-alkaline volcanic rocks from the Kastamonu area, Northern Turkey. Contributions to Mineralogy and Petrology, 58(1), 63-81.

Petford, N., and Atherton, M. (1996) Na-rich Partial Melts from Newly Underplated Basaltic Crust: the Cordillera Blanca Batholith, Peru. Journal of Petrology, 37(6), 1491-1521.

Phemister, J. (1934) Zoning in Plagioclase Feldspar.

Pignotta, G.S., and Paterson, S.R. (2007) Voluminous stoping in the Mitchell Peak Granodiorite, Sierra Nevada Batholith, Californa, USA. The Canadian Mineralogist, 35, 87-106.

Pitcher, W.S., Atherton, M.P., Cobbing, E.J., and Beckinsale, R.D. (1985) Magmatism at a plate edge: the Peruvian Andes. Wiley.

Profeta, L., Ducea, M.N., Chapman, J.B., Paterson, S.R., Henriquez, S.M., Kirsch, M., Petrescu, L., and DeCelles, P.G. (2015) Quantifying crustal thickness over time in magmatic arcs. Scientific Reports, 5(17786), 7.

Putirka, K.D., Canchola, J., McNaughton, M., Smith, O., Torrez, G., Paterson, S.R., and Ducea, M. (2014) Day 1: Guadalupe Igneous Complex. Field Guides, 34, 1-15.

Roy, S.G., Johnson, S.E., and Koons, P.O. (2012) Fractal analysis and thermal-elastic modeling of a subvolcanic magmatic breccia: The role of post-fragmentation partial melting and thermal fracture in clast size distributions. Geochemistry, Geophysics, Geosystems, 13(5), 23.

Sanchez-Fernandez, A.W. (1982) Edades Rb-Sr en los segmentos Arequipa-Toquepala del Batolito de la costa del Peru. Quinto Congreso Latinoamericano de Geologia, p. 487-504, Argentina.

Shand, S.J. (1943) The Eruptive Rocks. 444 p. John Wiley, New York.

Słaby, E., Götze, J., Wörner, G., Simon, K., Wrzalik, R., and Śmigielski, M. (2008) K-feldspar phenocrysts in microgranular magmatic enclaves: A cathodoluminescence and geochemical study of crystal growth as a marker of magma mingling dynamics. Lithos, 105(1–2), 85-97.

Soler, P., and Bonhomme, M.G. (1990) Relation of magmatic activìty to plate dynamics in central Peru from Late Cretaceous to present. Geological Society of America, 173-192.

Soler, P., and Rotach-Toulhoat, N. (1990) Sr-Nd Isotope Compositions of Cenozoic Granitoids along a Traverse of the Central Peruvian Andes. Geological Journal, 25, 351-358.

Steiger, R.H., and Jäger, E. (1977) Subcommission on geochronology: Convention on the use of decay constants in geo- and cosmochronology. Earth and Planetary Science Letters, 36(3), 359-362.

Stewart, J.W., Evernden, J.F., and Snelling, N.J. (1974) Age Determinations from Andean Peru: A Reconnaissance Survey. Geological Society of America Bulletin, 85(7), 1107-1116.

Streckeisen, A.L. (1973) Classification and nomenclature recommended by the IUGS subcommission on the systematics of igneous rocks. Geotimes, 10, 26-31.

Troll, V.R., and Schmincke, H.-U. (2002) Magma Mixing and Crustal Recycling Recorded in Ternary Feldspar from Compositionally Zoned Peralkaline Ignimbrite 'A', Gran Canaria, Canary Islands. Journal of Petrology, 43(2), 243-270.

Tulloch, A., and Kimbrough, D. (2003) Paired plutonic belts inconvergent margins and the development of high Sr/Y magmatism: Peninsular Ranges batholith of Baja-California and Median batholith of New Zealand. Geological Society of America(374), 275-295.

Turnbull, R.E. (2009) Mafic-felsic interaction in a high level magma chamber – The Halfmoon pluton, Stewart island, New Zealand: implications for understanding arc magmatism. 1-280.

Vernon, R.H. (2004) A practical guide to rock microstructure. 594 p. Cambridge University Press, New York.

Vernon, R.H., Etheridge, M.A., and Wall, V.J. (1988) Shape and microstructure of microgranitoid enclaves: indicators of magma mingling and flow. Lithos, 22, 1-11.

Walker, B.A., Bergantz, G.W., Otamendi, J.E., Ducea, M.N., and Cristofolini, E.A. (2015) A MASH Zone Revealed: the Mafic Complex of the Sierra Valle Fértil. Journal of Petrology, 56(9), 1863-1896.

Wetherill, G.W. (1956) Discordant uranium-lead ages, I. Eos, Transactions American Geophysical Union, 37(3), 320-326.

Wiebe, R.A. (1993) Basaltic injections into floored silicic magma chambers. Eos, Transactions American Geophysical Union, 74(1), 1-3.

Winter, J.D. (2010) An introduction to igneous and metamorphic petrology. 697 p. Prentice-Hall, New Jersey.

Wise, J. (2002) Examples of syntectonic emplacement instead of passive pluton emplacement in the Coastal Batholith of Peru and implications for Late Creataceous Nazca plate motions. Boletin de la Sociedad Geologica del Peru, 94, 99-106.

APPENDIX C

GEOCHEMISTRY DATA

Whole rock chemical data obtained from the Ica-Pisco plutons is presented in order to characterize the magmas and to identify processes responsible for their chemical diversification. This new geochemical data set consists of 113 whole rock analyses from the Cretaceous plutons, as well as 7 samples of Cretaceous volcanic and volcanoclastic rocks, and 4 samples of the Paleozoic and Precambrian basement. For the purpose of this research the arrangement of the samples collected from the Ica-Pisco plutons was initially based on the defined and mapped plutons by Agar (1978), Moore (1979), and Pitcher et al. (1985). The rock types were defined by modal classifications and the petrography data was presented in Appendix B.

Major and trace element concentrations of the Ica-Pisco rock samples were determined at the SGS laboratories in Canada using a Thermo Jarrell Ash Enviro II simultaneous and sequential ICP with a detection limit between 0.001 and 0.01% for major elements, 0.002 and 0.05 ppm for REE, and 0.01 to 20 ppm for other trace elements. Two instrumentation techniques were used by SGS Laboratories to get the chemical data. These are ICM90A using sodium peroxide fusion analyzed via inductively coupled plasma mass spectrometry (ICP-MS) and ICP95A using lithium metaborate fusion analyzed via inductively coupled plasma atomic emission spectroscopy (ICP-AES). The analytical major and trace element data are displayed in the following tables.

Table 15. Sample list of the Ica-Pisco samples used for chemical analyses and locations. Coordinates used to calculate W-E distance are: (-13.73 S, -75.93 W) and (-14.21 S, -75.42 W). Map units are defined using the information published by Davila (1993) and Leon et al (2007). Granite (Grt), granodiorite (Grdt), quartzdiorite (Qzdt), monzodiorite (Mzd), quartzmonzodiorite (Qzmzd), quartzmonzonite (qzmzn), monzogabbro (Mzgab), tonalite (Ton), diorite (Dt), gabbro (Gab), gneiss (Gns), dacite (Dct), trachite (Trch), andesite (And), basalt (Bas), Precambriam (Pc), Paleozoic (Pz).

Sample	Coordinates		W-E Distance (Km)	Rock Type	Map Unit
	South	West			
10714H	13.95362	75.67537	1.26	Grdt	Linga Humay
10714J	13.92279	75.67860	3.44	Grt	Linga Auquish
10714K	13.87099	75.63913	10.42	Qzmzd	Linga Humay
10714M	13.83710	75.59167	16.58	Mzd	Pampahuasi
10714P	13.83987	75.56205	18.55	Ton	Tiabaya?
10714Q	13.81248	75.51926	23.87	Grdt	Tiabaya
10715B	13.73208	75.92461	0.24	Qzdt	Linga Humay
10715C	13.71041	75.84041	8.16	Qzmzn	Linga Auquish
10715D	13.66571	75.77123	16.78	Mzd	Linga Auquish
10715E	13.66048	75.76123	17.93	Mzd	Pampahuasi
10715F	13.63994	75.72009	22.59	Ton	Tiabaya
10715I	13.59490	75.58416	36.18	Gab	Gabbro
10715L	13.61453	75.42432	46.44	Qzmzd	Incahuasi
10715M	13.60759	75.34368	52.95	Qzmzn	Incahuasi
10715O	13.55172	75.52197	44.17	Trch-And	Bella Union
10716J	14.61968	75.58145	-43.95	Pc-Gns	Precambrian
10718C	14.41117	75.64642	-32.44	Pz-Grdt	Paleozoic San Nicolas
10718H	14.67674	75.57224	-47.72	Pc-Gns	Precambrian
10718K	14.70623	75.59009	-51.34	Pc-Gns	Precambrian
10718N	14.43697	75.63412	-33.55	Dct	Guaneros
10719CC	13.97285	75.36290	22.81	Gab	Gabbro
10719N	14.20803	75.42407	-0.15	Ton	Pampahuasi
10719Q	14.18010	75.38313	5.06	Ton	Pampahuasi
10719R	14.17340	75.36102	7.22	Grdt	Pampahuasi
10719Z	14.06247	75.42757	11.01	Grdt	Pampahuasi
10720O	14.02803	75.62737	-1.04	Mzd	Linga Humay
10720T	13.78103	75.50333	27.51	Grdt	Tiabaya
10720U	13.75882	75.48713	30.45	Grdt	Tiabaya
10720V	13.75105	75.48374	31.32	Grdt	Tiabaya
10721D	13.84141	75.65395	11.65	Qzmzd	Linga Humay
10721K	13.78687	75.78779	6.04	Grt	Linga Auquish
10721M	13.75416	75.74976	11.42	Qzmzd	Linga Humay
10721N	13.74292	75.74279	12.82	Dct	Quilmana
11823G	13.81709	75.52772	22.88	Grt	Tiabaya
11823H	13.81559	75.52737	23.02	Grdt	Tiabaya

Table 15. Continued

Sample	Coordinates		W-E Distance (Km)	Rock Type	Map Unit
	South	West			
11825A	13.83774	75.56987	18.14	Qzdt	Tiabaya
11825G	13.74009	75.47334	32.95	Grt	Tiabaya
11826E	13.90717	75.34074	29.61	Grdt	Tiabaya
11828A	14.42044	75.17647	1.47	Ton	Tiabaya
11828B	14.39454	75.16142	4.61	Ton	Tiabaya
11828E	14.26018	75.11012	18.91	Grdt	Tiabaya
11829C	13.75874	75.69473	15.13	Gab	Gabbro
11829D	13.76292	75.69561	14.73	Gab	Gabbro
11830C	13.87320	75.30364	35.01	Grt	Tiabaya
11830D	13.84498	75.30433	37.18	Qzmzd	Tiabaya
11830E	13.82603	75.27928	40.52	Grdt	Tiabaya
11830I	13.79977	75.28555	42.12	Grdt	Tiabaya
11830K	13.80459	75.27317	42.65	Grdt	Tiabaya
11831EE	13.67616	75.32376	49.02	Grdt	Incahuasi
12715A	13.92374	75.66132	4.64	Grdt	Linga Humay
12715C	13.90900	75.65157	6.52	Grdt	Linga Rinconada
12716F	14.17889	75.36224	6.70	Grt	Incahuasi
12716K	14.02594	75.16042	33.58	Qzmzd	Incahuasi
12717C	13.65796	75.75182	18.83	Gab	Gabbro
12717D	13.64153	75.72137	22.37	Ton	Tiabaya
12717H	13.62511	75.67106	27.38	Grdt	Tiabaya
12718D	13.63802	75.55963	34.60	Grt	Characas
12719B	13.61499	75.42549	46.32	Grdt	Incahuasi
12719D	13.59757	75.49350	42.67	Ton	Pampahuasi
12719H	13.47854	75.47002	53.77	Grt	Tiabaya Granite
12719I	13.48695	75.47243	52.93	Grt	Tiabaya Granite
12719J	13.53151	75.50472	47.04	Ton	Pampahuasi
12719K	13.60741	75.34363	52.96	Grdt	Incahuasi
12720C	13.99534	75.56479	6.15	Grt	Linga Humay
12722E	14.08006	75.44305	8.49	Grdt	Pampahuasi
12722J	14.01851	75.36042	19.41	Gab	Gabbro
12722L	14.04010	75.35352	18.23	Grdt	Incahuasi
12722T	13.96205	75.23788	32.89	Grdt	Incahuasi
12722V	13.91656	75.19213	39.84	Grdt	Incahuasi
12722Y	13.87002	75.18557	43.98	Qzdt	Incahuasi
12723B	13.83760	75.22997	43.25	Qzmzd	Incahuasi
12723C	13.83105	75.23584	43.33	Qzmzd	Incahuasi
12723E	13.82604	75.25659	42.19	Qzmzd	Incahuasi
12723I	13.78803	75.37070	36.76	Grt	Incahuasi
12723L	13.79288	75.34314	38.41	Qzmzd	Incahuasi
12723M	13.80357	75.31348	39.76	Qzmzd	Incahuasi
12723O	13.80322	75.27238	42.82	Qzmzd	Incahuasi

Table 15. Continued

Sample	Coordinates		W-E Distance (Km)	Rock Type	Map Unit
	South	West			
12724D	13.99737	75.62933	1.22	Grdt	Linga Humay
13820E	13.69522	75.87918	6.49	Qzmzn	Linga Auquish
13820J	13.70110	75.88131	5.87	Mzgab	Linga Humay
13820M	13.70372	75.88187	5.62	Qzmzd	Linga Humay
13821C	13.69032	75.84991	9.04	Mzd	Linga Auquish
13821H	13.66809	75.85394	10.48	Qzmzn	Linga Auquish
13822A	13.72635	75.85740	5.65	Grdt	Linga Auquish
13822C	13.72490	75.78855	10.85	Grdt	Linga Auquish
13823A	13.64165	75.98121	3.15	Qzdt	Linga Humay
13823E	13.47549	76.02810	12.75	Grdt	Linga Humay
13823I	13.44192	75.97067	19.64	Grdt	Linga Humay
13825D	13.70340	75.94952	0.65	Qzmzn	Linga Auquish
13826A	13.69934	75.82201	10.39	Qzmzd	Linga Humay
13827A	13.67415	75.79195	14.59	Grdt	Linga Humay
13827G	13.66991	75.78868	15.16	Grdt	Linga Auquish
13828A	13.71057	75.83787	8.33	Grt	Linga Auquish
13828D	13.66037	75.76727	17.50	Grt	Pampahuasi
13828H	13.54816	75.68507	32.40	Grdt	Tiabaya
13829B	13.76472	75.71165	13.41	Ton	Younger Dikes
13830B	13.99355	75.78896	-10.26	Grdt	Linga Humay
13830C	13.93927	75.66932	2.83	Grt	Linga Rinconada
13830J	13.95086	75.62944	4.87	Grdt	Linga Humay
13901E	13.88234	75.63713	9.67	Grdt	Linga Humay
13901G	13.89267	75.64651	8.17	Qzmzd	Pampahuasi
13902M	13.93131	75.61225	7.67	Qzdt	Gabbro
13903B	13.84782	75.75092	3.98	Qzmzn	Linga Auquish
13903J	13.83401	75.76089	4.33	Qzmzn	Linga Auquish
13904D	13.99982	75.57954	4.71	Ton	Pampahuasi
13904J	13.98961	75.56295	6.73	Grt	Linga Rinconada
13905C	13.88067	75.66746	7.57	Grdt	Linga Humay
13905E	13.87881	75.66772	7.69	Grt	Linga Humay
13905F	13.87463	75.66699	8.08	Grdt	Linga Auquish
13906A	13.87219	75.67489	7.68	Grt	Linga Auquish
13906B	13.87158	75.66898	8.17	Grt	Linga Auquish
13910H	11.14770	77.21297	108.96	dt	Puscao
14710A	13.70844	75.95422	-0.10	Bas	Quilmana
14710C	13.62716	75.67416	26.99	Gab	Gabbro
14710G	13.61286	75.41614	47.18	Trch-And	Yura

Table 15. Continued

Sample	Coordinates		W-E Distance (Km)	Rock Type	Map Unit
	South	West			
14713C	13.73287	75.92406	0.21	Mzgab	Linga Humay
14714Ba	13.85700	75.76483	2.23	Trch-And	Quilmana
14715Aa	13.93480	75.63554	5.68	Grt	Linga Rinconada
14715D	13.93310	75.62196	6.81	Grt	Linga Rinconada
14715F	13.93172	75.61253	7.62	Gab	Gabbro
14716A	14.03909	75.69248	-6.71	Trch	Quilmana
14717C	13.94179	75.66104	3.24	Grt	Linga Rmonzonite
14724D	13.95356	75.62752	4.80	Grt	Linga Rinconada
14725Ec	13.66029	75.76186	17.90	Grdt	Pampahuasi
14727U	13.82762	75.69228	9.90	Grt	Linga Rinconada
14727Y	13.85073	75.71326	6.53	Mzd	Linga Humay

Table 16. Major elements and the elemental ratios used to calculate the alumina saturation index. The ratio ANK refers to Al2O3/ (Na2O + K2O) and the ACNK refers to Al2O3/(CaO + Na2O + K2O), both in terms of molar proportion. A=Al2O3, N=Na2O, K=K2O, and C=CaO. Fe2O3 total iron (Fe2O3T) involves the FeO and Fe2O3 concentrations.

Sample	Major Elements (wt.%)												
	SiO_2	TiO_2	Al_2O_3	$Fe_2O_3^T$	MnO	MgO	CaO	Na_2O	K_2O	$Na_2O + K_2O$	K_2O/Na_2O	ANK	ACNK
10714H	56.60	0.66	15.90	7.31	0.12	2.42	5.37	3.70	2.75	9.07	0.69	0.08	0.06
10714J	65.00	0.51	14.10	4.52	0.08	1.06	3.00	3.30	3.98	6.30	1.10	0.07	0.07
10714K	52.50	0.88	17.60	9.31	0.15	3.34	7.20	3.60	1.18	10.80	0.50	0.11	0.06
10714M	54.20	0.86	17.80	8.12	0.18	2.57	6.32	3.90	2.81	10.22	0.62	0.09	0.07
10714P	56.30	0.75	15.50	7.87	0.16	2.68	5.72	3.70	1.76	9.42	0.65	0.10	0.06
10714Q	65.30	0.48	16.00	4.20	0.08	1.51	4.13	4.00	2.84	8.13	0.97	0.07	0.05
10715B	47.80	0.56	20.40	7.95	0.13	5.96	10.40	2.90	0.17	13.30	0.28	0.05	0.03
10715C	65.10	0.44	14.50	4.10	0.06	0.74	2.35	3.10	5.34	5.45	1.32	0.06	0.07
10715D	57.40	0.85	17.70	5.05	0.09	3.13	7.00	5.90	0.47	12.90	0.84	0.11	0.05
10715E	59.30	0.72	16.20	6.90	0.13	2.15	5.20	3.90	2.99	9.10	0.75	0.09	0.06
10715F	66.10	0.25	15.90	4.06	0.12	0.80	3.34	4.50	1.97	7.84	1.35	0.05	0.03
10715I	47.80	0.76	18.20	10.90	0.22	4.65	8.43	3.30	0.61	11.73	0.39	0.08	0.05
10715L	55.50	0.81	17.90	7.60	0.13	2.90	6.20	3.80	2.52	10.00	0.61	0.09	0.06
10715M	62.80	0.69	16.60	5.46	0.10	1.77	4.04	3.90	3.82	7.94	0.97	0.09	0.07
10715O	55.00	1.05	17.30	7.40	0.13	4.20	3.74	7.20	0.83	10.94	1.93	0.23	0.07
10716J	59.30	1.29	14.80	7.66	0.12	2.65	3.63	2.60	2.41	6.23	0.72	0.21	0.15
10718C	56.90	0.99	15.00	7.59	0.12	3.42	5.49	3.00	2.78	8.49	0.55	0.12	0.08
10718H	49.20	1.61	16.10	12.00	0.20	4.24	8.59	3.80	1.04	12.39	0.44	0.17	0.10
10718K	55.80	0.75	17.70	8.23	0.19	3.45	6.46	2.60	2.20	9.06	0.40	0.09	0.06
10718N	66.30	0.56	15.90	3.35	0.03	2.01	1.14	5.70	1.30	6.84	5.00	0.23	0.06
10719CC	49.60	0.97	20.20	9.75	0.17	4.75	10.10	2.60	0.48	12.70	0.26	0.09	0.06
10719N	59.30	0.74	17.30	4.88	0.04	2.37	7.39	4.70	0.78	12.09	0.64	0.09	0.05
10719Q	55.60	0.77	16.60	8.21	0.15	2.68	6.02	3.40	2.51	9.42	0.56	0.09	0.06
10719R	58.40	0.74	16.00	6.66	0.14	2.13	5.41	3.80	2.49	9.21	0.70	0.09	0.07

Table 16. Continued

Sample	Major Elements (wt.%)												
	SiO_2	TiO_2	Al_2O_3	$Fe_2O_3^T$	MnO	MgO	CaO	Na_2O	K_2O	$Na_2O + K_2O$	K_2O/Na_2O	ANK	ACNK
10719Z	59.00	0.65	15.80	6.82	0.14	2.10	5.35	3.50	2.14	8.85	0.65	0.09	0.06
10720O	55.10	0.72	15.90	7.76	0.11	2.56	6.15	3.50	2.43	9.65	0.57	0.08	0.06
10720T	62.40	0.44	17.10	3.72	0.09	1.16	4.50	4.30	2.05	8.80	0.96	0.07	0.04
10720U	64.40	0.45	15.50	3.91	0.08	1.58	4.16	3.90	2.97	8.06	0.94	0.06	0.05
10720V	64.50	0.38	15.90	3.39	0.08	1.06	4.00	3.90	2.73	7.90	0.98	0.06	0.04
10721D	63.60	0.65	14.00	5.44	0.09	1.10	3.39	3.20	4.17	6.59	0.94	0.09	0.08
10721K	61.70	0.53	14.70	5.06	0.06	1.50	3.27	3.60	4.02	6.87	1.10	0.07	0.06
10721M	57.30	0.61	15.20	7.55	0.14	2.70	5.50	3.60	2.54	9.10	0.65	0.08	0.05
10721N	67.60	0.60	14.10	4.50	0.08	1.81	3.17	3.90	1.47	7.07	1.23	0.13	0.07
11823G	65.00	0.46	15.40	3.73	0.07	1.46	3.97	4.10	2.98	8.07	1.03	0.07	0.05
11823H	59.70	0.75	16.80	5.65	0.10	2.23	5.07	3.90	3.14	8.97	0.77	0.09	0.07
11825A	58.20	0.46	19.90	5.20	0.17	1.25	5.61	5.50	1.19	11.11	0.98	0.07	0.04
11825G	68.40	0.23	13.90	2.43	0.07	0.64	2.28	3.60	3.37	5.88	1.58	0.04	0.04
11826E	70.00	0.33	14.10	2.11	0.02	0.82	2.63	4.30	2.43	6.93	1.63	0.07	0.04
11828A	61.50	0.59	16.30	6.59	0.14	1.75	5.14	3.00	1.74	8.14	0.58	0.09	0.06
11828B	58.30	0.70	17.20	7.48	0.16	2.46	6.39	3.10	1.47	9.49	0.49	0.09	0.06
11828E	63.30	0.48	16.50	3.45	0.07	1.52	4.84	4.30	2.20	9.14	0.89	0.07	0.05
11829C	47.60	1.08	20.30	9.27	0.10	3.74	10.60	3.40	0.28	14.00	0.32	0.10	0.06
11829D	47.10	0.67	19.70	10.10	0.21	7.01	11.20	1.80	0.17	13.00	0.16	0.06	0.03
11830C	64.70	0.46	14.90	3.16	0.06	1.17	2.95	3.60	4.20	6.55	1.22	0.06	0.06
11830D	59.40	0.73	16.40	5.41	0.09	2.16	5.07	3.80	3.32	8.87	0.75	0.09	0.07
11830E	58.70	0.75	16.60	6.22	0.11	2.43	5.45	3.90	2.87	9.35	0.72	0.09	0.06
11830I	60.00	0.95	16.10	6.09	0.09	1.79	4.38	3.60	3.69	7.98	0.82	0.12	0.10
11830K	60.90	0.63	15.70	5.80	0.11	2.16	5.14	3.60	2.30	8.74	0.70	0.08	0.06

Table 16. Continued

Sample	Major Elements (wt.%)									$Na_2O + K_2O$	K_2O/Na_2O	ANK	ACNK
	SiO_2	TiO_2	Al_2O_3	$Fe_2O_3^T$	MnO	MgO	CaO	Na_2O	K_2O				
11831EE	59.60	0.79	16.00	6.22	0.10	2.34	4.86	3.20	3.55	8.06	0.66	0.09	0.08
12715A	62.90	0.97	14.40	8.08	0.15	1.38	4.90	4.00	1.96	8.90	0.82	0.14	0.09
12715C	70.70	0.34	12.00	3.49	0.05	0.48	1.55	2.70	4.75	4.25	1.74	0.05	0.07
12716F	59.30	0.77	15.70	7.29	0.12	2.68	6.15	3.30	2.20	9.45	0.54	0.09	0.06
12716K	62.10	0.83	15.60	6.86	0.11	2.21	4.81	3.30	3.17	8.11	0.69	0.10	0.08
12717C	52.10	0.63	18.90	9.11	0.17	5.16	9.89	2.90	0.42	12.79	0.29	0.06	0.04
12717D	69.20	0.22	14.70	4.10	0.11	0.68	2.90	4.10	2.04	7.00	1.41	0.04	0.03
12717H	66.00	0.44	15.30	4.29	0.08	1.59	4.26	3.80	2.33	8.06	0.89	0.07	0.05
12718D	74.80	0.16	13.60	1.91	0.06	0.42	1.49	3.98	3.84	5.47	2.67	0.03	0.03
12719B	59.30	0.82	16.10	7.33	0.13	2.62	5.60	3.50	2.68	9.10	0.63	0.10	0.07
12719D	57.10	0.64	17.00	7.16	0.15	3.17	6.99	3.30	1.31	10.29	0.47	0.08	0.05
12719H	67.90	0.38	13.30	3.58	0.04	1.07	2.65	3.20	3.89	5.85	1.21	0.06	0.05
12719I	70.00	0.37	13.90	2.93	0.05	0.87	2.51	3.50	3.73	6.01	1.39	0.06	0.05
12719J	56.20	0.83	16.80	8.88	0.16	3.21	6.63	3.30	1.71	9.93	0.50	0.10	0.06
12719K	63.30	0.62	15.00	5.40	0.09	1.75	3.79	3.30	3.80	7.09	0.87	0.08	0.07
12720C	64.30	0.81	13.70	7.20	0.11	1.74	3.99	2.70	4.30	6.69	0.68	0.10	0.10
12722E	60.30	0.66	14.90	6.82	0.13	2.18	4.99	3.20	2.32	8.19	0.64	0.09	0.06
12722J	51.40	0.56	24.10	4.35	0.06	1.70	11.10	3.00	0.63	14.10	0.27	0.05	0.04
12722L	61.40	0.74	16.30	6.08	0.12	2.28	5.23	3.90	2.40	9.13	0.75	0.10	0.06
12722T	62.40	0.64	15.40	5.52	0.09	1.86	4.08	3.40	3.63	7.48	0.83	0.08	0.07
12722V	61.10	0.73	16.20	6.32	0.12	2.47	5.43	3.20	2.99	8.63	0.59	0.09	0.07
12722Y	53.20	0.85	17.20	9.44	0.21	3.98	7.72	2.80	1.80	10.52	0.36	0.09	0.06
12723B	60.40	0.77	16.40	6.89	0.12	2.53	5.63	3.70	2.65	9.33	0.66	0.09	0.06
12723C	57.10	0.88	16.60	8.02	0.14	3.00	6.46	3.50	2.37	9.96	0.54	0.10	0.07
12723E	63.20	0.67	15.70	5.37	0.09	1.94	4.47	3.70	3.27	8.17	0.83	0.09	0.07

Table 16. Continued

Sample	Major Elements (wt.%)									$Na_2O + K_2O$	K_2O/Na_2O	ANK	ACNK
	SiO_2	TiO_2	Al_2O_3	$Fe_2O_3^T$	MnO	MgO	CaO	Na_2O	K_2O				
12723I	64.00	0.75	15.10	5.36	0.09	1.47	3.50	3.40	4.36	6.90	0.97	0.10	0.09
12723L	60.10	0.68	15.40	6.51	0.11	2.50	5.57	3.40	2.16	8.97	0.61	0.09	0.06
12723M	59.70	0.86	15.30	6.62	0.11	2.25	4.94	3.60	2.90	8.54	0.73	0.11	0.08
12723O	66.70	0.48	14.20	4.69	0.09	1.57	3.88	3.20	2.90	7.08	0.82	0.07	0.06
12724D	65.10	0.46	14.00	5.69	0.05	1.73	4.23	4.50	1.03	8.73	1.06	0.09	0.04
13820E	64.80	0.54	16.70	5.74	0.04	1.37	3.38	3.88	4.61	7.26	1.15	0.07	0.06
13820J	56.40	0.71	16.30	8.88	0.11	4.03	6.84	3.95	2.27	10.79	0.58	0.08	0.05
13820M	52.60	0.67	16.30	9.06	0.17	4.78	8.66	2.94	1.83	11.60	0.34	0.06	0.04
13821C	59.70	0.68	15.80	7.83	0.17	2.67	5.60	3.42	2.84	9.02	0.61	0.08	0.06
13821H	66.00	0.44	14.80	4.92	0.10	1.24	2.09	3.50	4.90	5.59	1.67	0.06	0.06
13822A	64.40	0.49	15.30	5.12	0.06	1.29	2.59	3.91	4.29	6.50	1.51	0.07	0.06
13822C	62.80	0.53	15.40	6.84	0.10	2.30	5.07	3.26	3.34	8.33	0.64	0.06	0.05
13823A	60.20	1.23	15.70	7.31	0.11	2.31	4.62	3.70	4.11	8.32	0.80	0.14	0.12
13823E	60.50	0.62	15.60	6.79	0.14	2.25	4.34	3.62	3.34	7.96	0.83	0.08	0.06
13823I	73.30	0.19	13.20	2.06	0.03	0.44	2.68	3.77	3.17	6.45	1.41	0.03	0.03
13825D	60.80	1.03	15.80	6.35	0.05	2.39	5.10	3.82	3.64	8.92	0.75	0.12	0.09
13826A	60.90	0.69	16.40	6.94	0.09	2.41	5.41	3.97	2.70	9.38	0.73	0.09	0.06
13827A	61.20	0.64	15.90	7.63	0.13	2.53	5.11	3.52	3.05	8.63	0.69	0.08	0.06
13827G	67.40	0.43	15.60	4.00	0.02	1.61	2.20	5.14	1.68	7.34	2.34	0.11	0.05
13828A	66.40	0.39	14.60	5.95	0.02	0.66	0.42	3.47	6.21	3.89	8.26	0.06	0.09
13828D	66.70	0.51	15.90	5.17	0.05	0.81	2.62	4.10	4.41	6.72	1.56	0.07	0.07
13828H	65.70	0.30	18.50	2.32	0.05	0.97	4.31	4.79	2.47	9.10	1.11	0.04	0.03
13829B	63.50	0.82	16.60	1.95	0.05	2.76	8.15	4.73	0.33	12.88	0.58	0.10	0.05
13830B	64.30	0.53	16.30	4.28	0.08	2.17	3.49	4.73	1.70	8.22	1.36	0.10	0.05
13830C	68.30	0.41	13.70	4.37	0.08	0.85	2.54	3.16	4.40	5.70	1.24	0.06	0.06
13830J	64.00	0.64	15.30	6.55	0.12	1.71	4.16	3.48	3.15	7.64	0.84	0.09	0.07

Table 16. Continued

Sample	Major Elements (wt.%)									$Na_2O + K_2O$	K_2O/Na_2O	ANK	ACNK
	SiO_2	TiO_2	Al_2O_3	$Fe_2O_3^T$	MnO	MgO	CaO	Na_2O	K_2O				
13901E	63.20	0.84	16.00	6.38	0.08	0.87	4.62	3.57	3.28	8.19	0.77	0.11	0.09
13901G	60.40	0.91	16.40	9.21	0.18	2.20	5.83	3.78	2.06	9.61	0.65	0.12	0.08
13902M	49.70	0.58	22.90	6.73	0.10	2.89	11.20	2.62	0.82	13.82	0.23	0.05	0.03
13903B	64.60	0.46	15.10	5.69	0.05	1.71	3.63	3.46	4.26	7.09	0.95	0.06	0.05
13903J	58.40	0.58	16.10	6.70	0.17	2.93	5.13	4.11	3.39	9.24	0.80	0.07	0.05
13904D	59.60	0.64	16.20	11.10	0.03	1.18	4.24	5.53	0.37	9.77	1.30	0.14	0.06
13904J	64.50	0.86	15.00	7.06	0.12	1.46	3.56	3.24	4.65	6.80	0.91	0.10	0.10
13905C	63.10	0.57	15.90	6.70	0.11	2.19	4.69	3.35	3.48	8.04	0.71	0.07	0.06
13905E	60.50	0.60	15.90	7.16	0.13	2.39	4.92	3.42	3.26	8.34	0.70	0.07	0.06
13905F	62.40	0.61	15.80	6.43	0.04	2.01	4.16	3.85	3.64	8.01	0.93	0.08	0.06
13906A	63.00	0.51	14.90	5.36	0.06	1.62	3.06	3.13	4.99	6.19	1.02	0.06	0.07
13906B	66.20	0.30	14.20	3.59	0.03	0.63	1.54	2.91	5.89	4.45	1.89	0.04	0.06
13910H	55.40	0.87	18.80	8.40	0.13	3.93	7.57	3.61	1.27	11.18	0.48	0.10	0.06
14710A	48.90	0.64	17.20	9.84	0.18	5.01	8.39	3.45	1.68	11.84	0.41	0.06	0.04
14710C	40.40	0.73	18.10	17.10	0.23	8.35	12.10	1.39	0.10	13.49	0.11	0.06	0.03
14710G	54.30	0.70	16.00	12.00	0.28	3.19	6.44	5.68	2.34	12.12	0.88	0.08	0.05
14713C	53.50	0.64	20.60	8.56	0.15	5.53	10.10	4.11	0.43	14.21	0.41	0.06	0.03
14714Ba	61.60	0.67	16.80	8.55	0.23	2.29	2.05	6.46	1.39	8.51	3.15	0.19	0.06
14715Aa	67.30	0.48	13.00	3.59	0.05	0.43	1.57	3.11	6.23	4.68	1.98	0.06	0.09
14715D	70.20	0.30	14.60	2.72	0.02	0.59	2.78	3.61	4.64	6.39	1.30	0.04	0.04
14715F	48.80	0.50	19.50	12.70	0.23	9.66	9.59	2.28	0.75	11.87	0.24	0.05	0.02
14716A	65.00	0.57	18.10	5.97	0.03	3.66	1.03	8.95	0.34	9.98	8.69	0.42	0.04
14717C	65.60	0.31	12.80	3.02	0.04	0.36	1.44	2.88	6.10	4.32	2.00	0.04	0.07
14724D	67.80	0.08	12.60	1.55	0.03	0.14	0.72	3.56	6.22	4.28	4.94	0.01	0.02
14725Ec	65.70	0.59	15.40	6.24	0.13	1.92	4.42	4.01	2.53	8.43	0.91	0.08	0.06
14727U	64.60	0.94	14.30	7.12	0.13	1.55	4.17	3.10	4.60	7.27	0.74	0.11	0.11
14727Y	69.50	0.48	14.30	4.99	0.03	0.84	1.45	4.07	5.93	5.52	2.81	0.07	0.08

Table 17. Trace elements data for the Ica-Pisco plutons from Cr_2O_3 to Zn.

	Cr_2O_3	P_2O_5	Rb	Cs	Sr	Ba	Th	U	Zr	Hf	Nb	Y	Cu	Zn
Method	ICP95A	ICP95A	ICM90A	ICM90A	ICM90A	ICM90A	ICM90A	ICM90A	ICM90A	ICM90A	ICM90A	ICM90A	ICM90A	ICM90A
Detection	0.01	0.01	0.2	0.1	0.1	0.5	0.1	0.05	0.5	1	1	0.5	5	5
Units	%	%	ppm	ppm	ppm	ppm	ppm	ppm	ppm	ppm	ppm	ppm	ppm	ppm
10714H	<0.01	0.14	120.00	6.80	307.00	850.00	15.40	3.98	189.00	4.00	4.00	27.10	84.00	45.00
10714J	0.02	0.09	204.00	12.50	202.00	962.00	36.40	6.92	216.00	11.00	5.00	36.20	35.00	35.00
10714K	<0.01	0.23	33.30	1.90	395.00	825.00	2.00	0.69	63.30	2.00	2.00	24.50	13.00	56.00
10714M	<0.01	0.36	131.00	8.20	469.00	1080.00	18.00	4.17	259.00	7.00	8.00	30.30	26.00	73.00
10714P	<0.01	0.16	52.70	2.70	329.00	853.00	9.90	1.83	125.00	7.00	5.00	37.20	23.00	64.00
10714Q	0.03	0.13	81.50	2.50	573.00	948.00	8.40	2.34	75.90	2.00	4.00	8.10	26.00	73.00
10715B	0.01	0.01	2.60	0.20	844.00	113.00	0.30	0.06	10.10	<1	<1	4.50	16.00	55.00
10715C	0.01	0.09	146.00	0.90	212.00	1830.00	22.20	6.24	296.00	9.00	6.00	30.10	96.00	33.00
10715D	0.02	0.01	11.40	0.50	406.00	431.00	8.10	1.93	118.00	3.00	4.00	25.10	7.00	29.00
10715E	<0.01	0.12	88.30	1.60	294.00	1170.00	14.00	4.35	267.00	7.00	5.00	25.20	38.00	25.00
10715F	0.02	0.12	43.10	2.30	416.00	1060.00	4.70	1.23	136.00	4.00	3.00	12.30	<5	55.00
10715I	<0.01	0.48	16.50	1.20	714.00	393.00	4.20	1.09	47.00	2.00	2.00	16.60	75.00	80.00
10715L	<0.01	0.16	89.00	5.90	438.00	628.00	8.40	2.44	173.00	7.00	6.00	23.60	74.00	57.00
10715M	0.02	0.14	177.00	12.90	329.00	703.00	21.30	4.63	218.00	8.00	10.00	24.60	56.00	45.00
10715O	0.02	0.45	21.50	1.00	551.00	378.00	17.60	4.37	202.00	5.00	10.00	28.00	76.00	81.00
10716J	0.02	0.29	105.00	1.00	289.00	614.00	12.80	0.82	251.00	7.00	16.00	30.90	46.00	85.00
10718C	0.02	0.16	113.00	1.90	223.00	529.00	12.00	2.76	192.00	6.00	7.00	29.20	69.00	74.00
10718H	<0.01	0.28	26.20	0.60	408.00	338.00	2.20	0.57	117.00	3.00	3.00	30.10	207.00	90.00
10718K	0.03	0.16	64.10	1.10	476.00	963.00	7.40	0.87	152.00	4.00	7.00	26.10	51.00	80.00
10718N	0.03	0.16	54.80	2.50	150.00	72.40	13.40	2.25	277.00	7.00	12.00	22.20	6.00	36.00
10719CC	0.01	0.11	11.60	1.10	538.00	254.00	2.00	0.57	57.00	1.00	2.00	13.10	13.00	61.00
10719N	0.02	0.20	21.90	0.50	464.00	397.00	10.30	1.49	170.00	4.00	3.00	26.30	6.00	9.00
10719Q	0.02	0.15	132.00	9.70	341.00	706.00	17.60	6.50	287.00	8.00	5.00	28.40	175.00	60.00
10719R	0.02	0.23	84.00	3.60	412.00	1010.00	11.00	2.73	140.00	4.00	4.00	25.00	22.00	71.00
10719Z	0.01	0.18	106.00	9.60	396.00	801.00	17.70	5.58	205.00	6.00	4.00	23.90	33.00	77.00
10720O	0.01	0.18	57.10	1.60	379.00	1010.00	11.90	2.87	148.00	4.00	5.00	29.00	6.00	21.00
10720T	0.02	0.16	53.80	3.40	659.00	927.00	3.10	1.16	86.30	2.00	4.00	7.10	113.00	39.00

Table 17. Continued

	Cr_2O_3	P_2O_5	Rb	Cs	Sr	Ba	Th	U	Zr	Hf	Nb	Y	Cu	Zn
Method	ICP95A	ICP95A	ICM90A	ICM90A	ICM90A	ICM90A	ICM90A	ICM90A	ICM90A	ICM90A	ICM90A	ICM90A	ICM90A	ICM90A
Detection	0.01	0.01	0.2	0.1	0.1	0.5	0.1	0.05	0.5	1	1	0.5	5	5
Units	%	%	ppm	ppm	ppm	ppm	ppm	ppm	ppm	ppm	ppm	ppm	ppm	ppm
10720U	0.02	0.13	83.70	3.70	565.00	920.00	8.40	2.53	72.70	2.00	3.00	6.60	41.00	45.00
10720V	0.02	0.14	53.30	1.60	585.00	910.00	5.20	1.50	77.90	2.00	4.00	7.80	62.00	91.00
10721D	0.01	0.15	228.00	12.50	206.00	1110.00	36.00	6.28	336.00	9.00	6.00	43.70	42.00	39.00
10721K	0.01	0.11	147.00	2.70	181.00	1280.00	24.40	7.21	393.00	10.00	8.00	40.60	63.00	18.00
10721M	0.02	0.12	73.50	1.80	301.00	1020.00	13.60	3.42	187.00	5.00	5.00	31.60	70.00	57.00
10721N	0.02	0.14	42.10	0.80	250.00	635.00	11.30	3.39	274.00	7.00	6.00	35.10	8.00	48.00
11823G	<0.01	0.12	91.20	2.80	502.00	897.00	9.70	3.26	78.10	3.00	5.00	7.80	16.00	31.00
11823H	<0.01	0.16	118.00	3.90	498.00	991.00	11.60	3.10	134.00	4.00	8.00	19.10	77.00	48.00
11825A	<0.01	0.16	40.40	1.80	543.00	884.00	2.80	1.13	289.00	7.00	3.00	6.60	10.00	66.00
11825G	<0.01	0.06	96.50	3.00	243.00	871.00	15.00	2.83	90.60	3.00	5.00	8.90	<5	25.00
11826E	<0.01	0.06	35.70	1.10	225.00	603.00	10.60	2.56	113.00	4.00	5.00	17.90	5.00	<5
11828A	<0.01	0.16	64.00	2.50	276.00	624.00	7.10	1.00	159.00	5.00	7.00	22.90	9.00	66.00
11828B	<0.01	0.16	53.20	2.90	340.00	554.00	6.20	1.33	135.00	4.00	5.00	24.90	17.00	67.00
11828E	<0.01	0.13	64.40	1.50	582.00	625.00	5.50	2.41	99.30	3.00	5.00	7.80	27.00	21.00
11829C	<0.01	0.11	10.40	0.70	483.00	179.00	1.50	0.40	40.20	1.00	<1	13.80	73.00	18.00
11829D	<0.01	0.02	8.40	1.00	440.00	116.00	0.20	0.07	3.00	<1	<1	5.50	8.00	62.00
11830C	<0.01	0.16	186.00	4.90	389.00	1070.00	18.10	5.93	163.00	5.00	7.00	14.20	45.00	23.00
11830D	<0.01	0.23	130.00	4.50	515.00	910.00	12.40	3.25	187.00	6.00	7.00	16.00	59.00	41.00
11830E	<0.01	0.25	143.00	7.20	515.00	807.00	13.70	4.26	162.00	5.00	8.00	20.90	70.00	55.00
11830I	<0.01	0.20	231.00	8.30	356.00	854.00	35.10	5.56	439.00	13.00	10.00	22.00	97.00	45.00
11830K	<0.01	0.20	93.40	5.70	325.00	647.00	9.80	2.47	85.50	4.00	5.00	24.70	31.00	36.00
11831EE	<0.01	0.21	192.00	10.80	302.00	601.00	17.30	5.18	197.00	9.00	9.00	27.70	73.00	39.00
12715A	<0.01	0.34	92.20	9.70	299.00	788.00	9.80	2.96	143.00	5.00	6.00	43.60	212.00	79.00
12715C	<0.01	0.05	318.00	13.30	108.00	831.00	65.80	18.90	306.00	10.00	6.00	40.80	73.00	23.00
12716F	<0.01	0.16	88.80	3.50	446.00	915.00	14.20	1.84	97.00	3.00	5.00	12.00	22.00	50.00
12716K	<0.01	0.18	180.00	14.50	305.00	682.00	26.40	5.26	290.00	8.00	11.00	31.00	44.00	60.00
12717C	<0.01	0.05	5.30	0.20	458.00	302.00	0.90	0.14	24.40	<1	<1	10.10	72.00	75.00
12717D	<0.01	0.11	45.40	3.30	370.00	1180.00	5.20	1.23	98.60	3.00	2.00	11.30	6.00	57.00

Table 17. Continued

	Cr_2O_3	P_2O_5	Rb	Cs	Sr	Ba	Th	U	Zr	Hf	Nb	Y	Cu	Zn
Method	ICP95A	ICP95A	ICM90A	ICM90A	ICM90A	ICM90A	ICM90A	ICM90A	ICM90A	ICM90A	ICM90A	ICM90A	ICM90A	ICM90A
Detection	0.01	0.01	0.2	0.1	0.1	0.5	0.1	0.05	0.5	1	1	0.5	5	5
Units	%	%	ppm	ppm	ppm	ppm	ppm	ppm	ppm	ppm	ppm	ppm	ppm	ppm
12717H	<0.01	0.11	70.60	3.10	471.00	847.00	8.80	1.68	92.50	3.00	4.00	9.40	18.00	51.00
12718D	<0.01	0.09	113.00	2.80	200.00	1110.00	14.10	3.32	95.20	3.00	6.00	11.00	20.00	9.00
12719B	<0.01	0.18	112.00	6.80	375.00	718.00	14.70	3.00	224.00	6.00	8.00	23.20	71.00	69.00
12719D	<0.01	0.16	32.10	2.00	501.00	543.00	4.80	1.15	93.70	3.00	3.00	16.80	40.00	79.00
12719H	<0.01	0.09	175.00	6.10	311.00	720.00	21.30	3.76	147.00	5.00	9.00	15.70	6.00	22.00
12719I	<0.01	0.09	154.00	5.40	293.00	816.00	14.30	4.57	167.00	5.00	11.00	17.20	8.00	30.00
12719J	<0.01	0.17	58.90	5.50	425.00	559.00	7.20	1.67	87.80	3.00	4.00	21.50	48.00	94.00
12719K	<0.01	0.14	196.00	12.90	300.00	755.00	21.80	5.22	238.00	7.00	9.00	27.20	55.00	62.00
12720C	<0.01	0.20	290.00	18.40	217.00	900.00	45.00	6.52	341.00	10.00	9.00	54.90	114.00	63.00
12722E	<0.01	0.16	128.00	10.80	309.00	843.00	22.40	5.74	214.00	7.00	5.00	27.50	66.00	74.00
12722J	<0.01	0.19	14.30	0.90	842.00	291.00	1.80	0.35	71.20	2.00	3.00	8.90	55.00	50.00
12722L	<0.01	0.20	96.90	7.40	489.00	769.00	9.40	2.84	142.00	4.00	5.00	17.90	39.00	71.00
12722T	<0.01	0.15	163.00	5.30	406.00	965.00	18.60	5.40	269.00	8.00	8.00	19.60	83.00	43.00
12722V	<0.01	0.21	136.00	7.60	408.00	857.00	14.90	4.00	216.00	6.00	10.00	25.10	34.00	71.00
12722Y	<0.01	0.23	64.50	6.80	580.00	719.00	6.60	1.71	86.30	3.00	5.00	19.30	67.00	79.00
12723B	<0.01	0.20	129.00	8.90	505.00	745.00	15.10	4.37	221.00	6.00	7.00	21.30	79.00	77.00
12723C	<0.01	0.23	113.00	7.80	498.00	706.00	13.40	3.99	175.00	5.00	6.00	21.20	97.00	85.00
12723E	<0.01	0.16	163.00	10.80	457.00	796.00	19.50	4.87	272.00	8.00	7.00	16.90	64.00	55.00
12723I	<0.01	0.18	212.00	7.40	388.00	959.00	18.20	5.79	281.00	8.00	10.00	24.30	296.00	48.00
12723L	<0.01	0.20	105.00	7.00	569.00	655.00	12.10	3.10	132.00	4.00	5.00	16.90	76.00	71.00
12723M	<0.01	0.24	156.00	10.40	495.00	717.00	16.10	3.97	218.00	7.00	10.00	22.20	135.00	80.00
12723O	<0.01	0.10	99.30	4.40	280.00	844.00	12.80	2.45	113.00	4.00	4.00	18.60	14.00	36.00
12724D	<0.01	0.09	21.40	1.90	276.00	668.00	24.90	5.22	282.00	8.00	7.00	35.70	9.00	22.00
13820E	<0.01	0.20	115.00	1.60	300.00	2100.00	19.80	5.64	274.00	8.00	6.00	38.90	20.00	14.00
13820J	<0.01	0.10	61.60	0.70	360.00	990.00	10.10	3.09	116.00	4.00	3.00	29.10	60.00	40.00
13820M	<0.01	0.07	70.70	2.10	350.00	660.00	6.90	1.85	100.00	3.00	2.00	21.70	140.00	66.00
13821C	<0.01	0.21	100.00	1.10	290.00	1000.00	15.00	3.79	240.00	7.00	4.00	32.50	70.00	48.00

Table 17. Continued

Method	Cr_2O_3 ICP95A	P_2O_5 ICP95A	Rb ICM90A	Cs ICM90A	Sr ICM90A	Ba ICM90A	Th ICM90A	U ICM90A	Zr ICM90A	Hf ICM90A	Nb ICM90A	Y ICM90A	Cu ICM90A	Zn ICM90A
Detection	0.01	0.01	0.2	0.1	0.1	0.5	0.1	0.05	0.5	1	1	0.5	5	5
Units	%	%	ppm	ppm	ppm	ppm	ppm	ppm	ppm	ppm	ppm	ppm	ppm	ppm
13821H	<0.01	0.10	145.00	1.10	190.00	1630.00	25.50	7.59	281.00	9.00	5.00	29.70	140.00	28.00
13822A	<0.01	0.11	129.00	2.30	230.00	1190.00	20.50	4.25	238.00	7.00	4.00	29.10	20.00	16.00
13822C	<0.01	0.13	111.00	2.40	280.00	1060.00	18.40	5.58	225.00	7.00	5.00	32.70	20.00	33.00
13823A	0.01	0.60	161.00	8.30	350.00	780.00	42.40	11.00	434.00	13.00	13.00	39.90	300.00	62.00
13823E	<0.01	0.16	116.00	2.70	150.00	860.00	15.40	4.20	206.00	6.00	5.00	30.80	60.00	60.00
13823I	<0.01	<0.01	75.10	1.30	210.00	1190.00	18.30	4.58	114.00	3.00	2.00	17.70	10.00	6.00
13825D	<0.01	0.41	57.90	1.20	490.00	950.00	28.40	4.90	323.00	10.00	9.00	35.80	80.00	<5
13826A	<0.01	0.20	50.90	1.00	330.00	1160.00	13.50	3.70	164.00	5.00	3.00	30.10	30.00	24.00
13827A	<0.01	0.15	108.00	3.30	250.00	1040.00	15.90	2.55	242.00	7.00	4.00	35.20	80.00	43.00
13827G	<0.01	0.08	77.20	1.40	220.00	630.00	10.50	4.17	239.00	7.00	5.00	33.30	30.00	<5
13828A	<0.01	0.06	154.00	1.50	60.00	1820.00	24.80	9.22	327.00	10.00	5.00	31.70	90.00	7.00
13828D	<0.01	0.10	126.00	2.60	240.00	1720.00	20.70	6.28	365.00	11.00	8.00	34.90	<10	15.00
13828H	<0.01	0.09	55.80	1.40	880.00	1190.00	4.90	1.39	103.00	3.00	1.00	4.10	10.00	12.00
13829B	<0.01	0.03	11.60	4.10	390.00	260.00	9.90	2.42	210.00	7.00	3.00	37.50	<10	<5
13830B	<0.01	0.19	46.70	0.90	290.00	350.00	5.80	1.74	164.00	4.00	6.00	15.40	20.00	53.00
13830C	<0.01	0.04	214.00	8.60	190.00	1070.00	40.70	6.76	240.00	8.00	4.00	39.00	20.00	28.00
13830J	<0.01	0.18	161.00	10.40	270.00	1010.00	25.30	8.83	246.00	8.00	4.00	38.70	60.00	41.00
13901E	<0.01	0.38	109.00	3.70	270.00	1040.00	24.20	4.13	59.40	3.00	5.00	50.60	150.00	38.00
13901G	<0.01	0.34	80.60	6.50	330.00	750.00	15.50	3.58	172.00	6.00	4.00	37.30	160.00	87.00
13902M	<0.01	0.03	56.70	3.80	580.00	360.00	6.20	1.76	33.50	1.00	<1	9.60	30.00	38.00
13903B	<0.01	0.06	99.80	2.80	240.00	1410.00	21.00	6.87	397.00	12.00	6.00	36.00	30.00	<5
13903J	<0.01	0.14	89.40	0.80	320.00	1190.00	18.30	4.66	255.00	7.00	4.00	30.10	50.00	24.00
13904D	<0.01	0.35	14.60	0.90	480.00	410.00	15.10	2.68	286.00	8.00	4.00	15.50	10.00	<5
13904J	<0.01	0.21	245.00	15.50	220.00	1240.00	30.20	6.39	367.00	12.00	8.00	47.10	160.00	60.00
13905C	<0.01	0.15	145.00	6.00	270.00	960.00	23.00	5.20	203.00	7.00	5.00	28.30	60.00	45.00
13905E	<0.01	0.13	141.00	5.50	290.00	910.00	21.20	5.77	207.00	7.00	4.00	27.80	50.00	51.00
13905F	<0.01	0.11	86.20	2.30	290.00	1140.00	26.80	7.70	187.00	6.00	5.00	33.80	40.00	17.00
13906A	<0.01	0.09	193.00	4.50	220.00	1430.00	30.10	6.03	480.00	14.00	6.00	32.00	40.00	17.00

Table 17. Continued

	Cr_2O_3	P_2O_5	Rb	Cs	Sr	Ba	Th	U	Zr	Hf	Nb	Y	Cu	Zn
Method	ICP95A	ICP95A	ICM90A	ICM90A	ICM90A	ICM90A	ICM90A	ICM90A	ICM90A	ICM90A	ICM90A	ICM90A	ICM90A	ICM90A
Detection	0.01	0.01	0.2	0.1	0.1	0.5	0.1	0.05	0.5	1	1	0.5	5	5
Units	%	%	ppm	ppm	ppm	ppm	ppm	ppm	ppm	ppm	ppm	ppm	ppm	ppm
13906B	<0.01	0.05	167.00	2.20	210.00	1790.00	36.80	7.87	268.00	8.00	5.00	25.40	40.00	16.00
13910H	<0.01	0.21	39.80	3.50	540.00	630.00	3.10	0.94	90.10	3.00	3.00	16.20	60.00	55.00
14710A	<0.01	0.25	30.90	2.60	980.00	680.00	7.10	1.81	95.80	3.00	2.00	16.60	60.00	100.00
14710C	<0.01	0.03	1.20	0.20	560.00	170.00	<0.1	0.21	4.10	<1	<1	4.30	20.00	111.00
14710G	<0.01	0.45	69.00	4.10	420.00	1410.00	8.90	1.96	117.00	3.00	3.00	22.80	830.00	110.00
14713C	0.01	0.24	2.40	0.10	790.00	210.00	0.20	0.07	9.10	<1	<1	10.70	<10	85.00
14714Ba	<0.01	0.29	32.70	4.20	210.00	680.00	5.70	2.09	141.00	4.00	3.00	32.80	10.00	88.00
14715Aa	<0.01	0.08	272.00	7.40	120.00	1130.00	48.00	11.70	438.00	13.00	6.00	35.90	20.00	35.00
14715D	<0.01	0.05	117.00	2.50	280.00	1780.00	25.80	5.54	154.00	5.00	4.00	24.20	20.00	24.00
14715F	<0.01	0.07	30.30	6.70	480.00	270.00	1.50	0.50	21.30	<1	<1	8.50	120.00	110.00
14716A	<0.01	0.14	5.80	0.20	70.00	20.00	5.10	1.23	104.00	3.00	3.00	8.80	<10	37.00
14717C	<0.01	0.02	335.00	13.00	110.00	810.00	111.00	31.40	284.00	10.00	3.00	35.90	10.00	29.00
14724D	<0.01	<0.01	221.00	3.30	100.00	680.00	49.30	9.18	77.60	4.00	3.00	20.30	10.00	26.00
14725Ec	<0.01	0.13	73.90	2.50	280.00	990.00	9.60	2.43	233.00	7.00	4.00	27.20	70.00	54.00
14727U	<0.01	0.27	168.00	12.90	230.00	1280.00	25.70	4.90	352.00	10.00	5.00	49.90	290.00	76.00
14727Y	<0.01	0.14	126.00	0.60	130.00	1940.00	33.30	9.46	328.00	9.00	6.00	31.60	120.00	24.00

Table 18. Trace elements data for the Ica-Pisco plutons from Li to Ni and LOI data.

	Li	Cd	Ga	Ge	Mo	Sb	Sn	W	Ta	Pb	Co	Ni	LOI
Method	ICM90A	ICM90A	ICM90A	ICM90A	ICM90A	ICM90A	ICM90A	ICM90A	ICM90A	ICM90A	ICM90A	ICM90A	ICP95A
Detection	10	0.2	1	1	2	0.1	1	1	0.5	5	0.5	5	0.01
Units	ppm	ppm	ppm	ppm	ppm	ppm	ppm	ppm	ppm	ppm	ppm	ppm	%
10714H	20.00	0.80	19.00	2.00	4.00	1.90	3.00	3.00	<0.5	20.00	19.40	6.00	0.55
10714J	10.00	0.30	17.00	2.00	4.00	3.00	4.00	2.00	<0.5	15.00	9.10	<5	0.53
10714K	<10	0.80	21.00	2.00	<2	0.60	2.00	1.00	<0.5	7.00	22.10	<5	1.42
10714M	<10	0.40	21.00	2.00	2.00	0.40	3.00	2.00	<0.5	12.00	16.70	<5	0.59
10714P	10.00	0.30	20.00	2.00	<2	0.70	2.00	1.00	<0.5	11.00	17.60	<5	0.51
10714Q	10.00	<0.2	19.00	2.00	6.00	0.60	1.00	2.00	<0.5	12.00	10.50	9.00	0.63
10715B	<10	0.20	23.00	1.00	<2	0.20	<1	1.00	<0.5	10.00	30.80	27.00	0.58
10715C	<10	0.40	18.00	2.00	4.00	1.30	1.00	2.00	<0.5	9.00	9.40	<5	1.92
10715D	<10	0.30	20.00	2.00	<2	0.90	4.00	1.00	<0.5	8.00	8.50	<5	1.23
10715E	10.00	<0.2	19.00	2.00	4.00	0.70	3.00	1.00	<0.5	7.00	15.70	5.00	0.48
10715F	20.00	0.30	19.00	2.00	4.00	0.30	2.00	2.00	<0.5	20.00	4.50	<5	0.63
10715I	10.00	<0.2	22.00	2.00	6.00	0.30	<1	2.00	<0.5	11.00	27.30	9.00	0.71
10715L	20.00	<0.2	21.00	2.00	4.00	1.10	3.00	2.00	<0.5	13.00	19.60	10.00	0.45
10715M	20.00	<0.2	19.00	2.00	3.00	1.80	3.00	5.00	0.50	45.00	12.60	7.00	0.41
10715O	30.00	<0.2	15.00	2.00	3.00	1.60	2.00	2.00	<0.5	19.00	13.20	12.00	1.78
10716J	<10	<0.2	20.00	2.00	<2	0.30	2.00	1.00	0.60	13.00	23.30	41.00	1.32
10718C	<10	0.50	17.00	2.00	3.00	1.10	2.00	2.00	<0.5	16.00	23.00	28.00	1.44
10718H	10.00	0.50	21.00	2.00	<2	0.60	2.00	1.00	<0.5	10.00	31.30	17.00	1.90
10718K	10.00	<0.2	20.00	2.00	<2	1.00	1.00	<1	<0.5	17.00	23.80	10.00	1.95
10718N	90.00	<0.2	17.00	1.00	3.00	1.30	3.00	8.00	0.50	6.00	5.80	10.00	3.28
10719CC	<10	<0.2	20.00	2.00	<2	0.40	<1	<1	<0.5	5.00	28.10	13.00	1.05
10719N	10.00	0.60	18.00	2.00	<2	2.40	3.00	1.00	<0.5	12.00	5.90	5.00	1.02
10719Q	20.00	0.40	19.00	2.00	4.00	2.90	3.00	2.00	<0.5	14.00	20.20	<5	0.21
10719R	20.00	<0.2	20.00	2.00	<2	0.40	3.00	<1	<0.5	11.00	13.90	<5	0.58
10719Z	20.00	<0.2	18.00	2.00	5.00	1.20	3.00	1.00	<0.5	13.00	14.50	6.00	0.72
10720O	<10	<0.2	19.00	2.00	<2	0.90	<1	<1	<0.5	12.00	17.50	6.00	0.95
10720T	<10	0.20	22.00	1.00	<2	0.40	1.00	8.00	<0.5	11.00	6.30	5.00	0.75

Table 18. Continued

	Li	Cd	Ga	Ge	Mo	Sb	Sn	W	Ta	Pb	Co	Ni	LOI
Method	ICM90A	ICM90A	ICM90A	ICM90A	ICM90A	ICM90A	ICM90A	ICM90A	ICM90A	ICM90A	ICM90A	ICM90A	ICP95A
Detection	10	0.2	1	1	2	0.1	1	1	0.5	5	0.5	5	0.01
Units	ppm	ppm	ppm	ppm	ppm	ppm	ppm	ppm	ppm	ppm	ppm	ppm	%
10720U	10.00	<0.2	20.00	1.00	3.00	0.40	<1	<1	<0.5	13.00	10.10	9.00	0.56
10720V	<10	0.20	20.00	2.00	5.00	0.40	<1	<1	<0.5	29.00	6.50	<5	0.85
10721D	<10	<0.2	18.00	2.00	3.00	1.70	4.00	2.00	<0.5	14.00	9.00	<5	0.49
10721K	<10	0.50	18.00	2.00	3.00	1.00	3.00	1.00	<0.5	7.00	9.90	<5	1.08
10721M	<10	0.30	20.00	2.00	<2	1.70	2.00	1.00	<0.5	11.00	18.10	8.00	1.12
10721N	<10	0.20	19.00	1.00	3.00	1.90	3.00	<1	<0.5	7.00	6.20	<5	0.69
11823G	20.00	<0.2	18.00	1.00	2.00	0.30	<1	<1	<0.5	13.00	8.70	14.00	0.58
11823H	<10	0.20	20.00	1.00	3.00	0.40	2.00	1.00	<0.5	13.00	13.70	14.00	0.58
11825A	<10	<0.2	21.00	1.00	<2	0.30	<1	<1	<0.5	9.00	6.60	8.00	0.56
11825G	<10	<0.2	16.00	2.00	<2	0.30	<1	<1	<0.5	19.00	3.70	9.00	0.82
11826E	<10	<0.2	16.00	2.00	<2	0.20	2.00	<1	<0.5	8.00	2.20	12.00	1.00
11828A	20.00	<0.2	21.00	2.00	<2	0.40	<1	<1	<0.5	11.00	10.10	12.00	0.92
11828B	20.00	<0.2	21.00	2.00	<2	0.70	1.00	<1	<0.5	13.00	14.60	8.00	0.73
11828E	<10	0.30	21.00	2.00	<2	0.20	1.00	2.00	<0.5	12.00	7.30	18.00	0.76
11829C	<10	0.20	23.00	1.00	<2	0.80	2.00	<1	<0.5	11.00	17.70	10.00	0.82
11829D	<10	<0.2	20.00	2.00	<2	0.80	<1	<1	<0.5	11.00	33.00	22.00	0.34
11830C	20.00	<0.2	20.00	1.00	3.00	0.60	2.00	2.00	<0.5	13.00	6.80	12.00	0.74
11830D	20.00	<0.2	22.00	1.00	<2	0.50	1.00	<1	<0.5	11.00	14.80	12.00	0.47
11830E	20.00	<0.2	23.00	2.00	<2	0.60	2.00	1.00	<0.5	16.00	17.30	15.00	0.62
11830I	20.00	<0.2	22.00	1.00	2.00	0.40	2.00	2.00	<0.5	23.00	13.80	13.00	0.50
11830K	20.00	<0.2	19.00	2.00	<2	0.40	1.00	<1	<0.5	11.00	13.40	10.00	0.69
11831EE	10.00	<0.2	20.00	2.00	2.00	0.80	3.00	2.00	0.60	14.00	16.10	12.00	0.84
12715A	<10	0.40	20.00	2.00	3.00	3.00	3.00	1.00	<0.5	13.00	13.90	8.00	1.02
12715C	10.00	0.20	15.00	1.00	3.00	1.60	4.00	1.00	<0.5	16.00	4.90	9.00	0.38
12716F	10.00	<0.2	18.00	1.00	<2	0.50	1.00	<1	<0.5	5.00	15.90	9.00	0.70
12716K	20.00	<0.2	19.00	1.00	4.00	1.30	4.00	2.00	0.80	17.00	16.10	15.00	0.46
12717C	<10	<0.2	19.00	2.00	<2	<0.1	<1	<1	<0.5	<5	36.20	20.00	0.17
12717D	20.00	<0.2	16.00	1.00	<2	0.10	1.00	<1	<0.5	12.00	4.50	7.00	0.73

Table 18. Continued

	Li	Cd	Ga	Ge	Mo	Sb	Sn	W	Ta	Pb	Co	Ni	LOI
Method	ICM90A	ICM90A	ICM90A	ICM90A	ICM90A	ICM90A	ICM90A	ICM90A	ICM90A	ICM90A	ICM90A	ICM90A	ICP95A
Detection	10	0.2	1	1	2	0.1	1	1	0.5	5	0.5	5	0.01
Units	ppm	ppm	ppm	ppm	ppm	ppm	ppm	ppm	ppm	ppm	ppm	ppm	%
12717H	20.00	<0.2	17.00	1.00	<2	0.30	<1	<1	<0.5	9.00	11.70	12.00	0.94
12718D	<10	<0.2	15.00	2.00	6.00	0.50	3.00	<1	0.70	17.00	2.70	9.00	0.52
12719B	20.00	<0.2	18.00	1.00	<2	1.00	2.00	1.00	0.60	13.00	19.50	15.00	0.66
12719D	20.00	<0.2	19.00	1.00	<2	5.20	<1	<1	<0.5	6.00	21.90	14.00	1.38
12719H	20.00	<0.2	16.00	1.00	<2	0.50	2.00	<1	0.90	10.00	7.60	13.00	0.81
12719I	30.00	<0.2	16.00	1.00	<2	0.20	2.00	<1	1.10	14.00	6.20	14.00	0.69
12719J	10.00	<0.2	18.00	1.00	3.00	<0.1	2.00	<1	<0.5	12.00	24.00	11.00	1.21
12719K	20.00	0.20	17.00	1.00	<2	1.40	2.00	4.00	0.60	20.00	13.40	14.00	0.68
12720C	10.00	<0.2	16.00	1.00	6.00	1.70	7.00	5.00	0.80	16.00	15.90	12.00	0.40
12722E	20.00	0.20	18.00	1.00	4.00	2.30	3.00	2.00	<0.5	15.00	16.80	10.00	0.75
12722J	10.00	0.60	25.00	<1	<2	0.10	<1	<1	<0.5	6.00	12.50	15.00	0.79
12722L	20.00	<0.2	20.00	1.00	5.00	0.70	2.00	11.00	<0.5	12.00	15.40	14.00	0.61
12722T	10.00	<0.2	19.00	<1	2.00	0.40	2.00	6.00	0.60	8.00	13.40	12.00	1.21
12722V	20.00	0.20	19.00	1.00	5.00	0.60	3.00	2.00	0.70	19.00	16.20	13.00	0.83
12722Y	30.00	0.20	20.00	1.00	2.00	1.90	1.00	1.00	<0.5	14.00	29.90	19.00	1.34
12723B	20.00	0.20	20.00	1.00	4.00	1.20	2.00	2.00	<0.5	13.00	19.30	14.00	0.55
12723C	20.00	<0.2	21.00	1.00	4.00	1.20	2.00	1.00	<0.5	12.00	22.30	20.00	0.70
12723E	20.00	<0.2	20.00	1.00	4.00	0.90	2.00	4.00	<0.5	12.00	14.80	14.00	0.62
12723I	<10	<0.2	20.00	1.00	<2	0.40	3.00	<1	0.70	12.00	11.60	11.00	0.71
12723L	20.00	<0.2	19.00	1.00	<2	0.60	2.00	<1	<0.5	9.00	20.30	14.00	0.61
12723M	20.00	<0.2	21.00	1.00	2.00	1.30	3.00	2.00	0.60	14.00	17.50	15.00	0.49
12723O	20.00	<0.2	15.00	1.00	3.00	0.30	1.00	<1	<0.5	8.00	11.50	10.00	0.70
12724D	<10	0.50	17.00	1.00	<2	0.70	4.00	<1	<0.5	<5	6.20	8.00	0.98
13820E	<10	0.20	20.00	2.00	8.00	0.90	2.00	<1	<0.5	5.00	7.90	10.00	0.50
13820J	<10	0.30	19.00	2.00	5.00	1.50	1.00	<1	<0.5	8.00	22.60	16.00	1.57
13820M	20.00	0.20	18.00	2.00	6.00	1.80	2.00	<1	<0.5	10.00	29.00	20.00	1.91
13821C	<10	0.40	18.00	2.00	6.00	0.90	2.00	<1	<0.5	8.00	18.90	13.00	0.97

Table 18. Continued

	Li	Cd	Ga	Ge	Mo	Sb	Sn	W	Ta	Pb	Co	Ni	LOI
Method	ICM90A	ICM90A	ICM90A	ICM90A	ICM90A	ICM90A	ICM90A	ICM90A	ICM90A	ICM90A	ICM90A	ICM90A	ICP95A
Detection	10	0.2	1	1	2	0.1	1	1	0.5	5	0.5	5	0.01
Units	ppm	ppm	ppm	ppm	ppm	ppm	ppm	ppm	ppm	ppm	ppm	ppm	%
13821H	<10	0.20	18.00	1.00	5.00	1.10	2.00	<1	<0.5	8.00	8.90	10.00	1.20
13822A	<10	0.40	20.00	2.00	5.00	1.10	2.00	1.00	<0.5	7.00	9.20	11.00	1.57
13822C	<10	0.30	18.00	2.00	7.00	1.50	2.00	<1	<0.5	9.00	16.50	12.00	0.93
13823A	<10	0.30	21.00	1.00	9.00	2.10	4.00	2.00	<0.5	17.00	17.20	16.00	0.28
13823E	10.00	0.30	19.00	2.00	6.00	1.20	2.00	1.00	<0.5	15.00	16.70	10.00	1.96
13823I	<10	<0.2	15.00	2.00	5.00	1.10	<1	<1	<0.5	8.00	2.50	10.00	0.49
13825D	<10	0.60	22.00	2.00	5.00	1.30	<1	<1	<0.5	7.00	12.20	26.00	0.74
13826A	<10	0.50	20.00	2.00	5.00	1.20	1.00	<1	<0.5	10.00	20.00	13.00	0.86
13827A	<10	<0.2	19.00	2.00	5.00	1.30	3.00	<1	<0.5	9.00	16.50	13.00	0.92
13827G	<10	<0.2	17.00	<1	6.00	0.90	3.00	<1	<0.5	<5	11.30	10.00	0.70
13828A	<10	0.40	18.00	2.00	8.00	1.40	6.00	<1	<0.5	<5	11.90	9.00	0.89
13828D	<10	<0.2	19.00	2.00	5.00	0.60	1.00	<1	<0.5	8.00	7.10	10.00	0.36
13828H	10.00	<0.2	23.00	1.00	4.00	0.70	<1	<1	<0.5	11.00	6.10	14.00	0.45
13829B	<10	<0.2	19.00	2.00	4.00	1.30	2.00	<1	<0.5	6.00	3.70	10.00	1.21
13830B	30.00	1.30	19.00	1.00	5.00	0.70	1.00	<1	<0.5	9.00	10.80	21.00	2.29
13830C	20.00	<0.2	16.00	2.00	5.00	1.80	3.00	<1	<0.5	14.00	7.80	11.00	0.30
13830J	20.00	<0.2	19.00	2.00	11.00	2.80	3.00	1.00	<0.5	11.00	13.50	10.00	0.39
13901E	<10	<0.2	21.00	2.00	7.00	2.00	3.00	<1	<0.5	16.00	10.90	8.00	0.15
13901G	10.00	<0.2	21.00	2.00	6.00	6.10	3.00	4.00	<0.5	27.00	17.70	8.00	0.45
13902M	20.00	0.20	22.00	1.00	4.00	1.20	1.00	<1	<0.5	8.00	20.70	16.00	1.09
13903B	<10	0.70	18.00	2.00	4.00	0.90	3.00	<1	<0.5	5.00	10.10	16.00	1.01
13903J	<10	0.70	18.00	2.00	4.00	4.10	2.00	<1	<0.5	6.00	19.90	14.00	1.33
13904D	<10	<0.2	22.00	1.00	5.00	0.70	<1	<1	<0.5	<5	21.20	12.00	0.57
13904J	10.00	<0.2	19.00	2.00	7.00	3.00	13.00	3.00	<0.5	21.00	12.60	9.00	0.40
13905C	10.00	0.40	18.00	2.00	5.00	1.30	2.00	<1	<0.5	20.00	16.90	11.00	0.52
13905E	<10	0.40	19.00	2.00	5.00	2.20	3.00	1.00	<0.5	12.00	18.20	11.00	0.78
13905F	<10	0.20	18.00	2.00	8.00	1.20	6.00	<1	<0.5	7.00	7.80	10.00	0.84
13906A	<10	0.30	17.00	2.00	5.00	1.60	3.00	<1	<0.5	9.00	12.80	12.00	1.24

Table 18. Continued

	Li	Cd	Ga	Ge	Mo	Sb	Sn	W	Ta	Pb	Co	Ni	LOI
Method	ICM90A	ICM90A	ICM90A	ICM90A	ICM90A	ICM90A	ICM90A	ICM90A	ICM90A	ICM90A	ICM90A	ICM90A	ICP95A
Detection	10	0.2	1	1	2	0.1	1	1	0.5	5	0.5	5	0.01
Units	ppm	ppm	ppm	ppm	ppm	ppm	ppm	ppm	ppm	ppm	ppm	ppm	%
13906B	<10	0.20	17.00	2.00	5.00	1.20	2.00	<1	<0.5	10.00	5.60	13.00	0.78
13910H	20.00	0.30	20.00	1.00	4.00	0.70	1.00	<1	<0.5	8.00	22.20	15.00	1.42
14710A	10.00	0.20	20.00	1.00	3.00	0.40	1.00	<1	<0.5	5.00	29.80	21.00	1.04
14710C	<10	0.80	17.00	1.00	7.00	4.60	<1	<1	<0.5	16.00	51.90	<5	0.30
14710G	20.00	<0.2	19.00	2.00	3.00	1.50	1.00	<1	<0.5	18.00	32.60	<5	0.49
14713C	<10	<0.2	22.00	1.00	9.00	8.00	<1	<1	<0.5	5.00	27.00	23.00	0.20
14714Ba	20.00	3.80	20.00	1.00	4.00	0.70	1.00	<1	<0.5	<5	8.10	<5	3.91
14715Aa	<10	0.50	14.00	1.00	10.00	9.00	3.00	<1	<0.5	15.00	4.50	<5	0.25
14715D	<10	<0.2	15.00	1.00	3.00	0.70	2.00	<1	<0.5	7.00	3.00	<5	0.51
14715F	<10	<0.2	15.00	1.00	6.00	4.30	<1	<1	<0.5	11.00	54.00	44.00	1.37
14716A	<10	0.20	17.00	<1	2.00	1.50	<1	<1	<0.5	<5	10.90	20.00	2.85
14717C	20.00	<0.2	14.00	1.00	9.00	7.60	2.00	<1	<0.5	16.00	3.90	<5	0.27
14724D	<10	0.20	12.00	1.00	3.00	1.60	<1	<1	<0.5	13.00	2.40	<5	0.66
14725Ec	<10	0.20	17.00	1.00	8.00	5.30	1.00	<1	<0.5	10.00	13.70	<5	0.71
14727U	10.00	<0.2	17.00	1.00	4.00	3.40	4.00	<1	<0.5	15.00	11.50	<5	0.66
14727Y	<10	0.30	16.00	1.00	9.00	5.30	1.00	2.00	<0.5	<5	2.50	<5	1.15

Table 19. Rare earth elements data for the Ica-Pisco plutons.

	La	Ce	Pr	Nd	Sm	Sc	Eu	Gd	Tb	Dy	Ho	Er	Tm	Yb	Lu
Method	ICM90A	ICM90A	ICM90A	ICM90A	ICM90A	ICM90A	ICM90A	ICM90A	ICM90A	ICM90A	ICM90A	ICM90A	ICM90A	ICM90A	ICM90A
Detection	0.10	0.10	0.05	0.10	0.10	5.00	0.05	0.05	0.05	0.05	0.05	0.05	0.05	0.10	0.05
Units	ppm	ppm	ppm	ppm	ppm	ppm	ppm	ppm	ppm	ppm	ppm	ppm	ppm	ppm	ppm
10714H	22.30	47.10	6.13	25.20	5.10	20.00	1.01	4.70	0.81	4.50	0.93	2.73	0.43	2.70	0.46
10714J	28.70	59.90	7.75	31.00	6.30	11.00	0.81	5.89	0.99	5.87	1.27	3.71	0.55	3.80	0.58
10714K	14.70	31.10	4.33	19.00	4.40	26.00	1.21	4.16	0.70	4.11	0.86	2.47	0.36	2.40	0.38
10714M	37.80	78.10	10.00	41.70	8.10	14.00	1.70	6.51	1.05	5.63	1.17	3.21	0.46	3.10	0.49
10714P	27.90	56.60	7.32	29.50	6.60	24.00	1.30	6.21	1.01	6.16	1.32	4.01	0.60	3.90	0.62
10714Q	19.80	37.10	4.21	15.00	2.30	<5	0.59	1.76	0.25	1.48	0.28	0.77	0.12	0.80	0.13
10715B	3.40	5.90	0.90	4.00	0.90	20.00	0.72	0.95	0.14	0.93	0.17	0.51	0.07	0.50	0.10
10715C	40.30	69.70	7.97	28.90	5.40	8.00	0.76	4.88	0.85	4.81	1.04	3.14	0.49	3.20	0.52
10715D	16.30	45.00	6.54	26.50	5.50	25.00	1.57	4.74	0.73	4.17	0.94	2.56	0.41	2.70	0.42
10715E	24.40	47.50	5.92	23.60	4.80	17.00	1.02	4.29	0.71	4.05	0.91	2.65	0.40	2.90	0.41
10715F	20.10	37.00	4.58	16.90	2.80	<5	0.93	2.28	0.38	1.94	0.40	1.29	0.19	1.30	0.23
10715I	27.60	53.70	6.39	25.70	4.70	16.00	1.18	3.76	0.55	3.02	0.65	1.74	0.23	1.50	0.24
10715L	21.70	44.40	5.59	22.20	4.70	18.00	1.19	4.09	0.67	4.05	0.86	2.58	0.37	2.40	0.39
10715M	26.80	54.40	6.60	25.50	4.90	12.00	0.97	4.11	0.67	3.78	0.85	2.57	0.37	2.50	0.39
10715O	40.40	80.70	10.60	43.40	9.00	25.00	2.16	6.45	0.90	4.77	0.96	2.61	0.38	2.30	0.41
10716J	47.60	98.70	11.70	45.50	8.50	15.00	2.12	7.13	1.11	5.65	1.15	3.16	0.41	2.50	0.46
10718C	20.80	43.00	5.08	19.90	4.30	21.00	0.94	4.71	0.76	4.62	1.04	3.05	0.44	2.70	0.46
10718H	13.10	28.80	4.12	19.80	4.80	37.00	1.56	5.29	0.86	5.33	1.12	3.14	0.48	3.00	0.50
10718K	32.60	63.40	7.69	29.40	5.80	23.00	1.33	5.09	0.79	4.34	0.93	2.59	0.41	2.40	0.42
10718N	24.20	53.80	6.27	22.50	4.10	8.00	0.65	3.76	0.64	3.85	0.81	2.46	0.37	2.50	0.40
10719CC	10.00	20.10	2.62	11.20	2.70	20.00	0.91	2.41	0.41	2.41	0.47	1.31	0.20	1.30	0.20
10719N	8.90	21.00	3.48	16.60	4.30	19.00	1.47	4.63	0.71	4.73	0.94	2.72	0.40	2.70	0.41
10719Q	24.20	50.10	6.37	26.30	5.50	21.00	1.04	5.08	0.81	4.88	1.03	2.96	0.44	2.90	0.50
10719R	24.40	49.40	6.41	26.00	5.40	15.00	1.25	4.80	0.77	4.15	0.90	2.55	0.40	2.50	0.43
10719Z	20.50	42.80	5.55	21.80	4.60	15.00	1.04	3.97	0.67	4.34	0.86	2.49	0.36	2.40	0.40
10720O	19.00	45.10	6.15	26.90	5.70	22.00	0.98	5.01	0.84	5.02	1.03	2.93	0.45	2.80	0.46
10720T	16.50	31.90	3.83	14.50	2.60	<5	0.74	1.81	0.24	1.36	0.22	0.71	0.12	0.70	0.17

Table 19. Continued

	La	Ce	Pr	Nd	Sm	Sc	Eu	Gd	Tb	Dy	Ho	Er	Tm	Yb	Lu
Method	ICM90A	ICM90A	ICM90A	ICM90A	ICM90A	ICM90A	ICM90A	ICM90A	ICM90A	ICM90A	ICM90A	ICM90A	ICM90A	ICM90A	ICM90A
Detection	0.10	0.10	0.05	0.10	0.10	5.00	0.05	0.05	0.05	0.05	0.05	0.05	0.05	0.10	0.05
Units	ppm	ppm	ppm	ppm	ppm	ppm	ppm	ppm	ppm	ppm	ppm	ppm	ppm	ppm	ppm
10720U	17.30	29.00	3.17	11.70	2.10	5.00	0.62	1.65	0.24	1.21	0.23	0.66	0.11	0.70	0.17
10720V	19.00	33.60	3.74	13.90	2.60	<5	0.65	1.86	0.26	1.52	0.25	0.71	0.11	0.80	0.17
10721D	39.10	80.60	10.20	39.00	8.60	12.00	1.11	7.16	1.20	7.00	1.48	4.56	0.66	4.40	0.67
10721K	36.70	78.20	9.79	37.60	7.70	13.00	0.82	6.47	1.06	6.65	1.44	4.26	0.66	4.30	0.72
10721M	26.00	51.30	6.70	26.80	5.70	21.00	1.18	5.41	0.90	5.27	1.12	3.34	0.50	3.10	0.53
10721N	28.90	59.20	7.80	31.50	6.80	13.00	1.22	5.94	1.02	6.08	1.23	3.55	0.59	3.90	0.60
11823G	20.10	35.90	4.26	15.40	2.60	<5	0.72	1.93	0.27	1.42	0.27	0.85	0.12	0.80	0.11
11823H	25.80	54.80	7.59	30.00	6.00	8.00	1.12	4.94	0.69	3.49	0.67	2.04	0.30	1.90	0.27
11825A	19.10	30.80	3.70	13.40	2.20	<5	1.58	1.66	0.22	1.09	0.19	0.76	0.11	0.90	0.10
11825G	24.60	41.00	4.53	15.80	2.40	<5	0.58	1.98	0.28	1.53	0.30	0.89	0.13	0.90	0.12
11826E	14.80	35.00	4.56	17.10	3.30	<5	0.80	3.18	0.49	2.68	0.56	1.94	0.30	2.10	0.27
11828A	20.50	41.00	5.42	21.40	4.70	10.00	1.27	4.35	0.70	3.92	0.81	2.53	0.41	2.50	0.37
11828B	21.70	43.80	5.94	24.70	5.40	14.00	1.31	5.05	0.74	4.14	0.84	2.69	0.42	2.70	0.38
11828E	17.00	31.90	4.05	15.00	2.80	<5	0.81	2.22	0.27	1.29	0.26	0.76	0.10	0.80	0.10
11829C	8.00	15.40	2.17	9.60	2.30	27.00	1.10	2.59	0.40	2.24	0.49	1.53	0.22	1.40	0.21
11829D	2.70	5.10	0.73	3.40	0.90	30.00	0.69	0.91	0.18	0.98	0.22	0.66	0.11	0.80	0.11
11830C	36.60	64.30	7.71	26.50	4.40	<5	0.77	3.30	0.47	2.46	0.49	1.46	0.21	1.50	0.20
11830D	23.10	46.70	6.23	24.00	4.50	9.00	1.03	3.73	0.54	2.61	0.52	1.71	0.22	1.60	0.20
11830E	26.70	54.10	7.29	28.30	5.60	10.00	1.09	4.61	0.69	3.35	0.70	2.13	0.32	2.10	0.28
11830I	39.00	75.90	9.72	36.40	6.80	10.00	1.14	5.21	0.77	3.76	0.74	2.20	0.33	2.10	0.31
11830K	33.30	57.40	6.73	24.10	4.70	14.00	1.05	4.45	0.71	3.73	0.82	2.53	0.38	2.60	0.35
11831EE	25.40	50.10	6.64	26.00	5.60	15.00	1.01	5.30	0.82	4.49	0.93	2.90	0.41	2.70	0.38
12715A	26.20	56.30	7.83	33.80	8.60	24.00	2.13	8.61	1.34	8.19	1.59	4.40	0.72	4.40	0.70
12715C	37.60	76.90	9.97	35.50	7.60	6.00	0.73	7.04	1.13	7.22	1.37	4.30	0.73	4.40	0.70
12716F	17.60	34.40	4.27	15.50	3.10	16.00	1.25	2.83	0.38	2.25	0.39	1.30	0.22	1.40	0.22
12716K	34.50	72.00	9.09	33.80	7.30	16.00	1.27	6.33	1.03	5.91	1.12	3.28	0.56	3.20	0.50
12717C	5.50	11.00	1.55	6.80	1.60	31.00	0.90	1.91	0.33	1.96	0.39	1.04	0.19	1.10	0.18

Table 19. Continued

	La	Ce	Pr	Nd	Sm	Sc	Eu	Gd	Tb	Dy	Ho	Er	Tm	Yb	Lu
Method	ICM90A	ICM90A	ICM90A	ICM90A	ICM90A	ICM90A	ICM90A	ICM90A	ICM90A	ICM90A	ICM90A	ICM90A	ICM90A	ICM90A	ICM90A
Detection	0.10	0.10	0.05	0.10	0.10	5.00	0.05	0.05	0.05	0.05	0.05	0.05	0.05	0.10	0.05
Units	ppm	ppm	ppm	ppm	ppm	ppm	ppm	ppm	ppm	ppm	ppm	ppm	ppm	ppm	ppm
12717D	20.90	40.00	4.91	18.10	3.30	<5	1.00	2.65	0.35	2.05	0.38	1.08	0.17	1.20	0.20
12717H	19.60	34.50	3.98	14.20	2.50	7.00	0.79	1.99	0.27	1.74	0.29	0.88	0.15	0.90	0.15
12718D	23.70	41.00	4.54	14.20	2.40	<5	0.60	1.94	0.29	1.83	0.36	1.11	0.19	1.30	0.17
12719B	22.30	46.90	6.08	23.00	5.40	17.00	1.21	4.87	0.73	4.39	0.84	2.54	0.42	2.60	0.40
12719D	16.70	32.90	4.24	16.70	3.40	14.00	1.12	3.45	0.53	3.15	0.56	1.71	0.29	1.70	0.28
12719H	50.20	90.20	9.61	29.10	4.70	6.00	0.72	3.34	0.50	3.00	0.54	1.48	0.23	1.50	0.25
12719I	23.40	44.90	5.42	18.80	3.90	5.00	0.74	3.25	0.49	3.07	0.55	1.64	0.27	1.80	0.27
12719J	15.60	33.10	4.37	17.60	4.40	19.00	1.20	4.36	0.65	3.94	0.77	2.33	0.37	2.30	0.36
12719K	20.80	47.30	6.56	24.70	5.50	13.00	1.02	5.39	0.84	5.11	0.96	2.76	0.44	2.80	0.44
12720C	49.00	109.00	14.60	55.60	12.40	18.00	1.25	11.50	1.73	10.60	1.92	5.60	0.91	5.60	0.86
12722E	24.90	51.30	6.73	25.80	5.70	18.00	1.18	5.46	0.82	5.06	0.96	2.91	0.48	3.00	0.49
12722J	10.90	22.40	3.07	12.50	2.70	7.00	0.92	2.21	0.32	1.86	0.31	0.91	0.14	0.80	0.13
12722L	19.10	43.70	5.97	22.00	4.50	13.00	1.12	3.97	0.56	3.27	0.64	1.81	0.29	2.00	0.30
12722T	28.50	58.70	7.44	27.10	5.20	10.00	1.04	4.33	0.64	3.76	0.68	1.97	0.34	2.00	0.32
12722V	30.90	63.20	8.10	29.60	6.10	15.00	1.29	5.48	0.83	4.66	0.85	2.50	0.43	2.60	0.42
12722Y	21.20	42.90	5.62	22.20	4.90	20.00	1.43	4.46	0.67	3.84	0.73	1.95	0.32	2.00	0.34
12723B	26.20	54.80	7.09	27.60	5.50	13.00	1.21	4.51	0.68	4.13	0.73	2.03	0.37	2.10	0.36
12723C	23.90	51.50	6.95	26.80	5.50	17.00	1.28	4.69	0.69	4.10	0.78	2.23	0.37	2.20	0.35
12723E	23.00	48.90	6.20	23.60	4.60	9.00	0.95	3.92	0.57	3.25	0.62	1.74	0.27	1.90	0.29
12723I	36.40	76.30	9.79	35.20	6.90	9.00	1.11	5.56	0.83	4.71	0.87	2.40	0.42	2.60	0.42
12723L	22.80	47.80	6.30	23.70	4.90	12.00	1.09	3.69	0.53	3.39	0.58	1.72	0.22	1.60	0.27
12723M	28.90	62.20	8.22	30.60	6.20	12.00	1.19	5.26	0.78	4.17	0.80	2.20	0.37	2.30	0.36
12723O	19.30	37.70	4.67	17.70	3.90	11.00	0.90	3.55	0.57	3.43	0.62	1.91	0.33	2.10	0.32
12724D	18.30	48.50	7.32	28.80	6.80	14.00	1.16	6.13	0.98	6.31	1.23	3.61	0.65	3.90	0.64
13820E	24.40	53.20	7.68	31.20	7.80	14.00	1.58	7.29	1.16	6.72	1.38	4.43	0.65	4.20	0.62
13820J	22.40	45.30	6.21	24.50	5.90	29.00	1.22	5.55	0.84	5.03	1.02	3.18	0.48	3.20	0.48
13820M	14.30	32.20	4.62	18.00	4.50	30.00	1.09	4.30	0.66	3.92	0.77	2.46	0.33	2.20	0.31

Table 19. Continued

	La	Ce	Pr	Nd	Sm	Sc	Eu	Gd	Tb	Dy	Ho	Er	Tm	Yb	Lu
Method	ICM90A	ICM90A	ICM90A	ICM90A	ICM90A	ICM90A	ICM90A	ICM90A	ICM90A	ICM90A	ICM90A	ICM90A	ICM90A	ICM90A	ICM90A
Detection	0.10	0.10	0.05	0.10	0.10	5.00	0.05	0.05	0.05	0.05	0.05	0.05	0.05	0.10	0.05
Units	ppm	ppm	ppm	ppm	ppm	ppm	ppm	ppm	ppm	ppm	ppm	ppm	ppm	ppm	ppm
13821C	27.80	58.80	7.95	30.50	6.70	21.00	1.38	6.13	0.97	5.54	1.14	3.58	0.54	3.50	0.51
13821H	43.20	76.90	9.26	32.00	6.10	12.00	1.20	5.51	0.85	5.04	1.04	3.27	0.51	3.30	0.51
13822A	26.50	55.50	7.11	26.20	5.70	12.00	1.19	5.36	0.84	4.87	1.01	3.15	0.49	3.20	0.45
13822C	30.80	62.00	8.09	30.20	6.70	18.00	1.19	6.33	0.94	5.69	1.17	3.50	0.54	3.60	0.53
13823A	57.60	125.00	16.40	61.90	12.60	17.00	2.14	10.30	1.43	7.81	1.41	3.97	0.59	3.80	0.56
13823E	29.00	58.60	7.69	28.60	6.30	20.00	1.35	5.94	0.91	5.22	1.09	3.36	0.50	3.30	0.51
13823I	23.40	39.60	4.40	14.40	2.80	<5	0.74	2.61	0.44	2.66	0.57	1.97	0.31	2.20	0.30
13825D	32.60	69.00	9.48	38.90	9.10	17.00	1.68	8.43	1.18	6.35	1.23	3.58	0.53	3.30	0.51
13826A	22.30	49.00	6.75	26.10	5.90	21.00	1.36	5.69	0.86	4.92	1.02	3.19	0.48	3.10	0.46
13827A	31.40	65.70	8.68	32.70	7.20	20.00	1.35	6.67	1.01	6.00	1.20	3.70	0.59	3.60	0.55
13827G	37.50	68.70	8.49	29.20	6.30	11.00	0.95	5.41	0.83	5.33	1.14	3.90	0.64	4.30	0.65
13828A	41.00	87.50	9.50	32.30	6.50	9.00	1.06	5.82	0.92	5.39	1.12	3.54	0.55	3.70	0.54
13828D	38.20	74.90	9.63	34.60	7.20	10.00	1.50	6.49	0.97	5.67	1.21	3.81	0.59	3.90	0.58
13828H	14.40	27.00	3.28	11.50	2.00	<5	0.89	1.45	0.18	0.90	0.14	0.40	0.05	0.40	<0.05
13829B	18.60	50.80	7.61	30.90	7.30	32.00	2.12	7.23	1.16	6.62	1.36	4.13	0.60	3.80	0.60
13830B	20.40	40.80	4.92	17.40	3.60	8.00	1.01	3.24	0.48	2.80	0.53	1.48	0.23	1.50	0.18
13830C	28.10	61.10	8.41	31.80	7.20	10.00	1.00	6.72	1.09	6.39	1.33	4.02	0.62	4.00	0.61
13830J	28.80	62.50	8.62	32.80	7.50	17.00	1.35	7.02	1.12	6.45	1.31	4.12	0.62	4.10	0.59
13901E	38.20	85.00	11.90	46.60	10.70	16.00	1.77	10.30	1.56	8.95	1.76	5.14	0.77	4.50	0.72
13901G	26.10	54.80	7.58	29.90	7.10	26.00	1.59	7.03	1.09	6.38	1.32	4.12	0.61	4.10	0.60
13902M	7.50	15.20	1.94	7.40	1.70	23.00	0.71	1.71	0.26	1.56	0.34	1.04	0.16	0.90	0.16
13903B	23.10	49.40	7.08	27.10	6.30	15.00	1.13	5.81	0.95	5.73	1.24	3.86	0.63	4.10	0.63
13903J	19.40	46.40	6.66	25.90	5.70	21.00	1.15	5.16	0.83	4.85	1.02	3.14	0.50	3.10	0.49
13904D	17.00	31.80	4.07	16.00	3.30	11.00	1.29	3.08	0.42	2.35	0.51	1.49	0.24	1.50	0.23
13904J	38.30	82.20	11.40	43.40	9.80	17.00	1.52	9.15	1.43	8.30	1.66	4.99	0.73	4.70	0.71
13905C	26.10	54.00	7.12	25.90	5.70	18.00	1.07	5.20	0.84	4.75	0.98	3.12	0.45	3.00	0.44
13905E	25.60	52.20	6.64	25.20	5.60	20.00	1.11	5.15	0.79	4.53	0.98	2.92	0.46	3.00	0.43

Table 19. Continued

	La	Ce	Pr	Nd	Sm	Sc	Eu	Gd	Tb	Dy	Ho	Er	Tm	Yb	Lu
Method	ICM90A	ICM90A	ICM90A	ICM90A	ICM90A	ICM90A	ICM90A	ICM90A	ICM90A	ICM90A	ICM90A	ICM90A	ICM90A	ICM90A	ICM90A
Detection	0.10	0.10	0.05	0.10	0.10	5.00	0.05	0.05	0.05	0.05	0.05	0.05	0.05	0.10	0.05
Units	ppm	ppm	ppm	ppm	ppm	ppm	ppm	ppm	ppm	ppm	ppm	ppm	ppm	ppm	ppm
13905F	29.40	66.70	9.17	32.90	7.10	19.00	1.34	6.11	0.98	5.59	1.15	3.68	0.54	3.60	0.54
13906A	27.30	56.00	7.30	26.20	5.90	15.00	1.00	5.22	0.83	4.99	1.08	3.38	0.53	3.60	0.53
13906B	17.40	31.40	3.98	15.00	3.80	8.00	0.92	3.92	0.63	3.82	0.84	2.69	0.41	2.90	0.37
13910H	11.10	24.30	3.42	13.80	3.30	23.00	1.03	3.29	0.51	2.88	0.60	1.67	0.25	1.60	<0.05
14710A	38.30	80.60	9.69	42.10	8.40	26.00	2.12	5.96	0.68	3.55	0.64	1.75	0.23	1.50	0.21
14710C	1.80	3.70	0.51	2.70	0.80	28.00	0.52	0.88	0.14	0.85	0.17	0.47	0.07	0.50	0.06
14710G	28.70	61.50	7.68	33.20	7.00	17.00	1.88	5.80	0.73	4.52	0.86	2.51	0.35	2.40	0.35
14713C	8.90	18.90	2.45	11.50	2.80	26.00	1.27	2.70	0.34	2.13	0.40	1.14	0.16	1.00	0.16
14714Ba	27.00	53.40	6.99	31.00	7.00	17.00	1.91	6.45	0.95	6.11	1.22	3.77	0.53	3.70	0.54
14715Aa	39.30	78.60	9.01	35.20	7.10	8.00	0.83	6.15	0.97	6.26	1.28	4.07	0.59	4.00	0.60
14715D	24.20	46.50	5.20	20.80	4.40	8.00	0.86	4.08	0.63	4.11	0.85	2.62	0.39	2.90	0.42
14715F	4.60	9.60	1.23	5.90	1.40	22.00	0.61	1.59	0.22	1.52	0.30	0.93	0.13	0.90	0.12
14716A	13.80	27.50	3.10	13.20	2.40	12.00	0.63	2.05	0.26	1.65	0.33	1.12	0.17	1.30	0.17
14717C	47.80	95.90	10.80	41.10	7.70	7.00	0.73	6.68	1.01	6.32	1.26	3.79	0.54	3.70	0.52
14724D	37.20	72.80	7.54	26.70	4.80	<5	0.40	3.83	0.52	3.15	0.62	2.05	0.31	2.30	0.31
14725Ec	20.00	43.60	5.45	23.60	5.10	17.00	1.00	4.87	0.71	4.61	0.96	3.01	0.43	3.10	0.43
14727U	36.70	81.40	10.30	43.90	10.00	20.00	1.36	9.33	1.43	9.13	1.82	5.44	0.75	5.20	0.74
14727Y	41.50	89.20	9.21	35.50	7.00	10.00	1.10	6.23	0.91	5.86	1.10	3.18	0.44	3.10	0.44

Table 20. Elemental ratios used for geochemical plots.

Sample	REE Ratios		
	La/Sm	Gd/Yb	Sr/Y
10714H	4.37	1.74	11.33
10714J	4.56	1.55	5.58
10714K	3.34	1.73	16.12
10714M	4.67	2.10	15.48
10714P	4.23	1.59	8.84
10714Q	8.61	2.20	70.74
10715B	3.78	1.90	187.56
10715C	7.46	1.53	7.04
10715D	2.96	1.76	16.18
10715E	5.08	1.48	11.67
10715F	7.18	1.75	33.82
10715I	5.87	2.51	43.01
10715L	4.62	1.70	18.56
10715M	5.47	1.64	13.37
10715O	4.49	2.80	19.68
10716J	5.60	2.85	9.35
10718C	4.84	1.74	7.64
10718H	2.73	1.76	13.55
10718K	5.62	2.12	18.24
10718N	5.90	1.50	6.76
10719CC	3.70	1.85	41.07
10719N	2.07	1.71	17.64
10719Q	4.40	1.75	12.01
10719R	4.52	1.92	16.48
10719Z	4.46	1.65	16.57
10720O	3.33	1.79	13.07
10720T	6.35	2.59	92.82
10720U	8.24	2.36	85.61
10720V	7.31	2.33	75.00
10721D	4.55	1.63	4.71
10721K	4.77	1.50	4.46
10721M	4.56	1.75	9.53
10721N	4.25	1.52	7.12
11823G	7.73	2.41	64.36
11823H	4.30	2.60	26.07
11825A	8.68	1.84	82.27
11825G	10.25	2.20	27.30
11826E	4.48	1.51	12.57
11828A	4.36	1.74	12.05
11828B	4.02	1.87	13.65
11828E	6.07	2.78	74.62
11829C	3.48	1.85	35.00

Table 20. Continued

Sample	REE Ratios		
	La/Sm	Gd/Yb	Sr/Y
11829D	3.00	1.14	80.00
11830C	8.32	2.20	27.39
11830D	5.13	2.33	32.19
11830E	4.77	2.20	24.64
11830I	5.74	2.48	16.18
11830K	7.09	1.71	13.16
11831EE	4.54	1.96	10.90
12715A	3.05	1.96	6.86
12715C	4.95	1.60	2.65
12716F	5.68	2.02	37.17
12716K	4.73	1.98	9.84
12717C	3.44	1.74	45.35
12717D	6.33	2.21	32.74
12717H	7.84	2.21	50.11
12718D	9.88	1.49	18.18
12719B	4.13	1.87	16.16
12719D	4.91	2.03	29.82
12719H	10.68	2.23	19.81
12719I	6.00	1.81	17.03
12719J	3.55	1.90	19.77
12719K	3.78	1.93	11.03
12720C	3.95	2.05	3.95
12722E	4.37	1.82	11.24
12722J	4.04	2.76	94.61
12722L	4.24	1.99	27.32
12722T	5.48	2.17	20.71
12722V	5.07	2.11	16.25
12722Y	4.33	2.23	30.05
12723B	4.76	2.15	23.71
12723C	4.35	2.13	23.49
12723E	5.00	2.06	27.04
12723I	5.28	2.14	15.97
12723L	4.65	2.31	33.67
12723M	4.66	2.29	22.30
12723O	4.95	1.69	15.05
12724D	2.69	1.57	7.73
13820E	3.13	1.74	7.71
13820J	3.80	1.73	12.37
13820M	3.18	1.95	16.13
13821C	4.15	1.75	8.92
13821H	7.08	1.67	6.40
13822A	4.65	1.68	7.90

Table 20. Continued

Sample	REE Ratios		
	La/Sm	Gd/Yb	Sr/Y
13822C	4.60	1.76	8.56
13823A	4.57	2.71	8.77
13823E	4.60	1.80	4.87
13823I	8.36	1.19	11.86
13825D	3.58	2.55	13.69
13826A	3.78	1.84	10.96
13827A	4.36	1.85	7.10
13827G	5.95	1.26	6.61
13828A	6.31	1.57	1.89
13828D	5.31	1.66	6.88
13828H	7.20	3.63	214.63
13829B	2.55	1.90	10.40
13830B	5.67	2.16	18.83
13830C	3.90	1.68	4.87
13830J	3.84	1.71	6.98
13901E	3.57	2.29	5.34
13901G	3.68	1.71	8.85
13902M	4.41	1.90	60.42
13903B	3.67	1.42	6.67
13903J	3.40	1.66	10.63
13904D	5.15	2.05	30.97
13904J	3.91	1.95	4.67
13905C	4.58	1.73	9.54
13905E	4.57	1.72	10.43
13905F	4.14	1.70	8.58
13906A	4.63	1.45	6.88
13906B	4.58	1.35	8.27
13910H	3.36	2.06	33.33
14710A	4.56	3.97	59.04
14710C	2.25	1.76	130.23
14710G	4.10	2.42	18.42
14713C	3.18	2.70	73.83
14714Ba	3.86	1.74	6.40
14715Aa	5.54	1.54	3.34
14715D	5.50	1.41	11.57
14715F	3.29	1.77	56.47
14716A	5.75	1.58	7.95
14717C	6.21	1.81	3.06
14724D	7.75	1.67	4.93
14725Ec	3.92	1.57	10.29
14727U	3.67	1.79	4.61
14727Y	5.93	2.01	4.11

APPENDIX D

ISOTOPE DATA

Isotopic analyses for 40 selected samples are presented for Rb-Sr, Sm-Nd, and U-Th-Pb. Radiogenic isotopes were measured at the Geochronology and Thermochronology Lab of the University of Arizona via multicollector ICP-MS. Analyses of oxygen isotopes were conducted for 9 samples at the Stable Isotope Laboratory of the California State University of Long Beach (CSULB) to constrain the relative contributions of mantle and crust and magma mixing in the Ica-Pisco plutons. Oxygen isotope values were obtained for several single minerals, including: quartz, plagioclase, feldspar, biotite, hornblende, and magnetite.

The assigned ages used to calculate initial $^{87}Sr/^{86}Sr$ of the Ica-Pisco plutonic rocks are from new U-Pb zircon ages for Auquish, Rinconada, Pampahuasi, Tiabaya, and Incahuasi. The ages used for Precambrian, Cretaceous Quilmana volcaniclastic, Gabbro, and Humay rocks are from previous published ages. All the ages used are reported in this appendix and the details of the geochronological data are presented in the appendix E.

Table 21. Location of the Ica-Pisco samples used for isotope analysis. Coordinates used to calculate W-E distance are: (-13.73 S, -75.93 W) and (-14.21 S, -75.42 W).

Sample	Rock Type	Unit	Age (Ma)	Coordinates		W-E Distance (Km)
				South	West	
10714H	Grdt	Linga Humay	105	13.95362	75.67537	1.26
10714M	Mzd	Pampahuasi	98	13.83710	75.59167	16.58
10715E	Mzd	Pampahuasi	98	13.66048	75.76123	17.93
10715F	Ton	Tiabaya	90	13.63994	75.72009	22.59
10715M	Qzmzn	Incahuasi	66	13.60759	75.34368	52.95
10718C	Pz-Grdt	Paleozoic	300	14.41117	75.64642	-32.44
10718K	Pc-Gns	Precambrian	1500	14.70623	75.59009	-51.34
10719N	Ton	Pampahuasi	98	14.20803	75.42407	-0.15
10720O	Mzd	Linga Humay	105	14.02803	75.62737	-1.04
10721M	Qzmzd	Linga Humay	105	13.75416	75.74976	11.42
10721N	Dac	Quilmana Gp	110	13.74292	75.74279	12.82
11825G	Grt	Tiabaya	90	13.74009	75.47334	32.95
11828B	Ton	Tiabaya	90	14.39454	75.16142	4.61
11829C	Gab	Gabbros	100	13.75874	75.69473	15.13
11829D	Gab	Gabbros	100	13.76292	75.69561	14.73
11830D	Qzmzd	Tiabaya	90	13.84498	75.30433	37.18
12715C	Grdt	Linga Rinconada	95	13.90900	75.65157	6.52
12716K	Qzmzd	Incahuasi	66	14.02594	75.16042	33.58
12717H	Grdt	Tiabaya	90	13.62511	75.67106	27.38
12718D	Grt	Characas	78	13.63802	75.55963	34.60
12719B	Grdt	Incahuasi	66	13.61499	75.42549	46.32
12719I	Grdt	Tiabaya	90	13.48695	75.47243	52.93
12722E	Grdt	Pampahuasi	98	14.08006	75.44305	8.49
12722L	Grdt	Incahuasi	66	14.04010	75.35352	18.23
12722T	Grdt	Incahuasi	66	13.96205	75.23788	32.89
12723E	Qzmzd	Incahuasi	66	13.82604	75.25659	42.19
13820E	Qzmzn	Linga Auquish	103	13.69522	75.87918	6.49
13820J	Mzgab	Linga Humay	105	13.70110	75.88131	5.87
13820M	Qzmzd	Linga Humay	105	13.70372	75.88187	5.62
13822C	Grdt	Linga Auquish	103	13.72490	75.78855	10.85
13823E	Grdt	Linga Humay	105	13.47549	76.02810	12.75
13825D	Qzmzn	Linga Humay	105	13.70340	75.94952	0.65
13826A	Qzmzd	Linga Humay	105	13.69934	75.82201	10.39
13827A	Grdt	Linga Humay	105	13.67415	75.79195	14.59
13828A	Grt	Linga Auquish	103	13.71057	75.83787	8.33
13830B	Grdt	Linga Humay	105	13.99355	75.78896	-10.26
13830C	Grt	Linga Rinconada	95	13.93927	75.66932	2.83
13902M	Qzdt	Gabbros	100	13.93131	75.61225	7.67
13905F	Grdt	Linga Humay	105	13.87463	75.66699	8.08
13910H	dt	Puscao	58	11.14770	77.21297	108.96

Table 22. Whole-rock Rb-Sr isotopic compositions of the Ica-Pisco plutons.

Sample	Rock Type	Unit	Age (Ma)	Rb (ppm)	Sr (ppm)	$^{87}Rb/^{86}Sr$	$^{87}Sr/^{86}Sr$	Sr_i
10714H	Grdt	Linga Humay	105	117.63	296.65	1.15	0.7060	0.7043
10714M	Mzd	Pampahuasi	98	128.62	466.41	0.80	0.7055	0.7044
10715E	Mzd	Pampahuasi	98	84.20	280.28	0.87	0.7056	0.7044
10715F	Ton	Tiabaya	90	42.42	408.93	0.30	0.7049	0.7045
10715M	Qzmzn	Incahuasi	66	174.86	333.84	1.51	0.7064	0.7050
10718C	Pz-Grdt	Paleozoic	300	107.30	209.20	1.48	0.7112	0.7049
10718K	Pc-Gns	Precambrian	1500	58.71	461.32	0.37	0.7118	0.7087
10719N	Ton	Pampahuasi	98	20.65	462.64	0.13	0.7053	0.7051
10720O	Mzd	Linga Humay	105	52.58	361.63	0.42	0.7054	0.7048
10721M	Qzmzd	Linga Humay	105	67.91	292.23	0.67	0.7053	0.7043
10721N	Dac	Quilmana Gp	110	38.83	236.40	0.48	0.7065	0.7058
11825G	Grt	Tiabaya	90	81.63	261.03	0.90	0.7057	0.7045
11828B	Ton	Tiabaya	90	42.18	370.93	1.09	0.7060	0.7046
11829C	Gab	Gabbros	100	8.56	527.89	0.05	0.7043	0.7043
11829D	Gab	Gabbros	100	3.05	464.42	0.02	0.7043	0.7042
11830D	Qzmzd	Tiabaya	90	104.64	534.94	0.57	0.7051	0.7043
12715C	Grdt	Linga Rinconada	95	278.75	106.28	7.59	0.7150	0.7048
12716K	Qzmzd	Incahuasi	66	157.17	311.96	1.46	0.7067	0.7053
12717H	Grdt	Tiabaya	90	60.79	483.77	0.36	0.7047	0.7043
12718D	Grt	Characas	78	98.57	185.85	1.53	0.7060	0.7043
12719B	Grdt	Incahuasi	66	99.87	396.00	0.73	0.7054	0.7047
12719I	Grdt	Tiabaya	90	129.48	300.75	1.25	0.7056	0.7040
12722E	Grdt	Pampahuasi	98	109.26	327.18	0.97	0.7059	0.7045
12722L	Grdt	Incahuasi	66	53.32	505.69	0.30	0.7049	0.7046
12722T	Grdt	Incahuasi	66	143.03	430.63	0.96	0.7067	0.7058
12723E	Qzmzd	Incahuasi	66	127.30	480.10	0.77	0.7070	0.7063
13820E	Qzmzn	Linga Auquish	103	97.07	267.15	1.05	0.7060	0.7045
13820J	Mzgab	Linga Humay	105	53.07	346.21	0.44	0.7053	0.7046
13820M	Qzmzd	Linga Humay	105	62.52	334.03	0.54	0.7050	0.7042
13822C	Grdt	Linga Auquish	103	97.80	259.55	1.09	0.7058	0.7042
13823E	Grdt	Linga Humay	105	102.50	275.79	1.07	0.7057	0.7041
13825D	Qzmzn	Linga Humay	105	49.75	465.38	0.31	0.7045	0.7040
13826A	Qzmzd	Linga Humay	105	40.40	309.19	0.38	0.7051	0.7045
13827A	Grdt	Linga Humay	105	94.67	230.14	1.19	0.7058	0.7041
13828A	Grt	Linga Auquish	103	139.74	49.34	8.20	0.7167	0.7047
13830B	Grdt	Linga Humay	105	41.17	266.52	0.45	0.7054	0.7047
13830C	Grt	Linga Rinconada	95	214.00	190.00	3.26	0.7087	0.7043
13902M	Qzdt	Gabbros	100	47.67	562.09	0.25	0.7046	0.7043
13905F	Grdt	Linga Humay	105	77.69	278.69	0.81	0.7057	0.7045
13910H	dt	Puscao	58	36.14	494.84	0.21	0.7043	0.7041

Table 23. Whole-rock Sm-Nd isotopic compositions of the Ica-Pisco plutons.

Sample	Rock Type	Unit	Age (Ma)	Sm (ppm)	Nd (ppm)	$^{143}Nd/^{144}Nd$	$^{147}Sm/^{144}Nd$	εNd
10714H	Grdt	Linga Humay	105	7.70	26.62	0.5127	0.1749	1.0144
10714M	Mzd	Pampahuasi	98	5.91	40.82	0.5126	0.0875	-0.3121
10715E	Mzd	Pampahuasi	98	6.72	24.28	0.5127	0.1672	0.6632
10715F	Ton	Tiabaya	90	4.11	19.95	0.5127	0.1246	1.8727
10715M	Qzmzn	Incahuasi	66	5.38	26.58	0.5127	0.1224	0.3706
10718C	Pz-Grdt	Paleozoic	300	4.51	21.45	0.5124	0.1269	-3.7843
10718K	Pc-Gns	Precambrian	1500	5.65	28.48	0.5119	0.1199	-13.9865
10719N	Ton	Pampahuasi	98	4.52	16.28	0.5127	0.1678	1.1314
10720O	Mzd	Linga Humay	105	5.83	26.71	0.5127	0.1320	1.1509
10721M	Qzmzd	Linga Humay	105	5.86	27.15	0.5127	0.1305	1.1119
10721N	Dac	Quilmana Gp	110	6.45	29.80	0.5127	0.1309	2.1458
11825G	Grt	Tiabaya	90	2.25	12.84	0.5127	0.1060	0.9949
11828B	Ton	Tiabaya	90	5.19	23.78	0.5125	0.1371	-2.4189
11829C	Gab	Gabbros	100	2.10	8.26	0.5127	0.1538	1.2875
11829D	Gab	Gabbros	100	0.81	3.08	0.5127	0.1589	1.3265
11830D	Qzmzd	Tiabaya	90	4.49	23.16	0.5127	0.1171	0.8583
12715C	Grdt	Linga Rinconada	95	7.22	34.72	0.5127	0.1257	1.3655
12716K	Qzmzd	Incahuasi	66	6.62	31.97	0.5126	0.1251	-0.3901
12717H	Grdt	Tiabaya	90	2.39	13.96	0.5127	0.1035	1.3460
12718D	Grt	Characas	78	1.98	11.77	0.5127	0.1015	1.6776
12719B	Grdt	Incahuasi	66	5.35	23.33	0.5127	0.1385	0.5072
12719I	Grdt	Tiabaya	90	5.15	22.89	0.5127	0.1361	0.3706
12722E	Grdt	Pampahuasi	98	5.77	26.93	0.5127	0.1295	0.6827
12722L	Grdt	Incahuasi	66	7.07	22.25	0.5127	0.1921	0.4096
12722T	Grdt	Incahuasi	66	3.96	26.93	0.5126	0.0888	0.1756
12723E	Qzmzd	Incahuasi	66	4.04	23.34	0.5127	0.1046	1.1119
13820E	Qzmzn	Linga Auquish	103	5.88	25.02	0.5127	0.1420	1.2680
13820J	Mzgab	Linga Humay	105	4.83	20.94	0.5127	0.1393	1.2094
13820M	Qzmzd	Linga Humay	105	3.80	16.55	0.5127	0.1387	1.1509
13822C	Grdt	Linga Auquish	103	5.63	26.66	0.5127	0.1277	0.8973
13823E	Grdt	Linga Humay	105	5.23	24.92	0.5127	0.1269	1.2289
13825D	Qzmzn	Linga Humay	105	8.00	35.20	0.5128	0.1374	3.9209
13826A	Qzmzd	Linga Humay	105	5.09	23.58	0.5127	0.1305	1.0144
13827A	Grdt	Linga Humay	105	6.06	29.34	0.5127	0.1249	1.1314
13828A	Grt	Linga Auquish	103	5.65	29.21	0.5127	0.1168	1.6386
13830B	Grdt	Linga Humay	105	3.14	16.04	0.5128	0.1181	2.5749
13830C	Grt	Linga Rinconada	95	6.39	28.96	0.5127	0.1333	1.2289
13902M	Qzdt	Gabbros	100	1.49	6.90	0.5127	0.1304	0.9558
13905F	Grdt	Linga Humay	105	6.32	31.17	0.5127	0.1225	0.9558
13910H	dt	Puscao	58	2.83	12.48	0.5128	0.1371	2.4384

Table 24. Whole-rock U-Th-Pb isotopic compositions of the Ica-Pisco plutons.

Sample	Rock Type	Age (Ma)	U (ppm)	Th (ppm)	Pb (ppm)	WR Present-Day ratios						WR Age-Corrected Pb ratios		
						$^{206}Pb/^{204}Pb$	$^{207}Pb/^{204}Pb$	$^{208}Pb/^{204}Pb$	$^{238}U/^{204}Pb$	$^{235}U/^{204}Pb$	$^{232}Th/^{204}Pb$	$(^{206}Pb/^{204}Pb)_i$	$(^{207}Pb/^{204}Pb)_i$	$(^{208}Pb/^{204}Pb)_i$
10714H	Grdt	105	3.98	15.40	20.00	18.97310	15.61190	38.80640	12.80609	0.09293	51.20215	18.79304	15.60329	38.57774
10714M	Mzd	98	4.17	18.00	12.00	19.09302	15.66275	39.14793	22.51646	0.16339	100.43165	18.77644	15.64761	38.69941
10715E	Mzd	98	4.35	14.00	7.00	19.64754	15.69120	39.61990	40.83158	0.29630	135.79040	19.07344	15.66375	39.01348
10715F	Ton	90	1.23	4.70	20.00	18.80760	15.65090	38.69010	3.94479	0.02863	15.57582	18.75214	15.64825	38.62054
10715M	Qzmzn	66	4.63	21.30	45.00	18.78820	15.58430	38.70390	6.59317	0.04784	31.34203	18.78820	15.58430	38.70390
10718C	Pz-Grdt	300	2.76	12.00	16.00	18.62611	15.64770	38.98990	11.08215	0.08042	49.78863	18.09820	15.62010	38.24486
10718K	Pc-Gns	1500	0.87	7.40	17.00	18.08911	15.62075	39.01264	3.26400	0.02369	28.68779	17.77070	15.60167	38.14765
10719N	Ton	98	1.49	10.30	12.00	19.33519	15.67980	39.69699	8.13225	0.05901	58.08926	19.22085	15.67433	39.43757
10720O	Mzd	105	2.87	11.90	12.00	19.22650	15.67450	39.00970	15.49812	0.11246	66.40156	19.00859	15.66408	38.71316
10721M	Qzmzd	105	3.42	13.60	11.00	19.12627	15.66075	39.06237	20.13080	0.14608	82.71949	18.84323	15.64721	38.69295
10721N	Dac	110	3.39	11.30	7.00	19.44807	15.68348	39.36887	31.62879	0.22952	108.94202	18.92864	15.65848	38.80104
11825G	Grt	90	2.83	15.00	19.00	18.70478	15.63652	38.71623	9.54229	0.06925	52.26265	18.57061	15.63010	38.48283
11828B	Ton	90	1.33	6.20	13.00	18.75194	15.64994	38.75095	6.56274	0.04762	31.61255	18.65967	15.64553	38.60977
11829C	Gab	100	0.40	1.50	11.00	18.72759	15.67746	38.67124	2.33022	0.01691	9.02945	18.69115	15.67571	38.62643
11829D	Gab	100	0.07	0.20	11.00	18.67941	15.65012	38.55132	0.40671	0.00295	1.20075	18.67369	15.64985	38.54596
11830D	Qzmzd	90	3.25	12.40	11.00	18.78585	15.63872	38.82570	18.97744	0.13771	74.81869	18.51902	15.62596	38.49157
12715C	Grdt	95	18.90	65.80	16.00	19.83344	15.69611	39.82023	78.01414	0.56612	280.65418	18.66287	15.63999	38.48311
12716K	Qzmzd	66	5.26	26.40	17.00	18.82711	15.63999	38.94574	19.91746	0.14453	103.29663	18.82711	15.63999	38.94574
12717H	Grdt	90	1.68	8.80	9.00	18.78457	15.63229	38.74920	11.97622	0.08691	64.82270	18.61618	15.62424	38.45971
12718D	Grt	78	3.32	14.10	17.00	18.79248	15.62967	38.71364	12.52460	0.09089	54.96409	18.64001	15.62242	38.50097

Table 24. Continued

Sample	Rock Type	Age (Ma)	U (ppm)	Th (ppm)	Pb (ppm)	WR Present-Day ratios						WR Age-Corrected Pb ratios		
						$^{206}Pb/^{204}Pb$	$^{207}Pb/^{204}Pb$	$^{208}Pb/^{204}Pb$	$^{238}U/^{204}Pb$	$^{235}U/^{204}Pb$	$^{232}Th/^{204}Pb$	$(^{206}Pb/^{204}Pb)_i$	$(^{207}Pb/^{204}Pb)_i$	$(^{208}Pb/^{204}Pb)_i$
12719B	Grdt	66	3.00	14.70	13.00	18.78084	15.63343	38.77006	14.80943	0.10747	74.98397	18.78084	15.63343	38.77006
12719I	Grdt	90	4.57	14.30	14.00	18.94660	15.64490	38.90140	21.03521	0.15265	68.01437	18.65084	15.63076	38.59766
12722E	Grdt	98	5.74	22.40	15.00	18.92830	15.64820	38.93130	24.66422	0.17898	99.45751	18.58152	15.63162	38.48713
12722L	Grdt	66	2.84	9.40	12.00	19.12320	15.73760	39.51350	15.43150	0.11198	52.77785	19.12320	15.73760	39.51350
12722T	Grdt	66	5.40	18.60	8.00	19.03080	15.68010	39.18710	43.73402	0.31736	155.65843	19.03080	15.68010	39.18710
12723E	Qzmzd	66	4.87	19.50	12.00	18.88880	15.63330	38.90950	26.13070	0.18962	108.11621	18.88880	15.63330	38.90950
13820E	Qzmzn	103	5.64	19.80	5.00	19.77730	15.69504	39.78789	74.41022	0.53997	269.93101	18.66082	15.64151	38.50185
13820J	Mzgab	105	3.09	10.10	8.00	19.02102	15.65542	38.94568	24.93318	0.18093	84.21214	18.64691	15.63749	38.54447
13820M	Qzmzd	105	1.85	6.90	10.00	18.84975	15.64655	38.76114	11.88385	0.08624	45.80033	18.67144	15.63800	38.54293
13822C	Grdt	103	5.58	18.40	9.00	19.30211	15.66882	39.17776	40.30392	0.29247	137.32987	18.69737	15.63983	38.52348
13823E	Grdt	105	4.20	15.40	15.00	18.84352	15.63729	38.81082	17.99469	0.13058	68.17887	18.57352	15.62435	38.48599
13825D	Qzmzn	105	4.90	28.40	7.00	19.55253	15.68141	40.20190	46.28450	0.33587	277.19914	18.66287	15.63999	38.48311
13826A	Qzmzd	105	3.70	13.50	10.00	19.33213	15.69625	39.26402	24.09837	0.17487	90.85603	18.97055	15.67891	38.83115
13827A	Grdt	105	2.55	15.90	9.00	19.22930	15.66741	39.22060	18.41092	0.13360	118.62234	18.95305	15.65417	38.65545
13828A	Grt	103	9.22	24.80	3.00	21.34848	15.77126	40.72876	209.59663	1.52097	582.55796	18.20359	15.62048	37.95327
13830B	Grdt	105	1.74	5.80	9.00	18.73769	15.62396	38.69738	12.38607	0.08988	42.66249	18.55185	15.61505	38.49412
13830C	Grt	95	6.76	40.70	14.00	19.47258	15.67049	39.46779	31.58165	0.22918	196.47921	18.99871	15.64777	38.53170
13902M	Qzdt	100	1.76	6.20	8.00	18.80303	15.63888	38.77744	14.12496	0.10250	51.41625	18.58664	15.62849	38.52736
13905F	Grdt	105	7.70	26.80	7.00	20.13483	15.71128	39.99016	73.10950	0.53053	262.93716	19.03786	15.65869	38.73744
13910H	dt	58	0.94	3.10	8.00	18.85153	15.67584	38.84047	7.55910	0.05485	25.75954	18.78321	15.67261	38.76639

Table 25. Oxygen isotope ratios of quartz, plagioclase, K-spar, biotite, hornblende, and magnetite of the Ica-Pisco plutons. Equivalent samples were collected at the same location during previous years. Average values for the respective unit are indicated (*).

Sample	Equivalent	Unit	Age (Ma)	Coordinates		W-E Distance (Km)	SiO_2 (wt%)	Sri	$\delta^{18}O$ (Qtz)	$\delta^{18}O$ (Pl)	$\delta^{18}O$ (Ksp)	$\delta^{18}O$ (Bt)	$\delta^{18}O$ (Hb)	$\delta^{18}O$ (Mg)	Alteration
				South	West										
14710G		Yura	>130	13.61286	75.41614	47.18	54.30			2.607		0.1			Yes
14710A	10721N	Quilmana	>130	13.70844	75.95422	-0.10	48.90	0.70576		7.582					No
14710C	11829C	Pre-PCB Gabbro	>105	13.62716	75.67416	26.99	40.40	0.70425		7.411					No
14713C	13820J	Humay	>105	13.73287	75.92406	0.21	53.50	0.70462		7.524				1.633	No
14721Ac		Auquish	105	13.70707	75.83489	8.83	64.4*		5.064		5.109			0.727	Yes
14727U	12715C	Rinconada	98	13.82762	75.69228	9.90	64.60	0.70478	9.15	5.814	7.423	4.601	5.814	1.474	No
14715G		Pampahuasi	98	13.93126	75.61616	7.38	59.3*	0.70527*	9.084			5.398	5.432		No
10714P	11828B	Pampahuasi	92	13.83987	75.56205	18.55	56.30	0.70460	9.837	7.914	8.171	5.706	5.976		No
14710F		Incahuasi	68	13.61448	75.42439	46.44	61.32*	0.70592*	9.205	7.45	8.234	3.896	6.158		No

APPENDIX E

GEOCHRONOLOGY DATA

U-Pb zircon ages are crucial to unraveling the chronology of magmatic events and better understanding the relations of the recycling processes observed in the Ica-Pisco plutons. Thus, U-Pb zircon ages from seven samples using multiple single zircon crystals per sample were performed at the LaserChron Center of the University of Arizona using laser ablation inductively coupled plasma mass spectrometry (LA-ICPMS).

LA-ICPMS methodology is performed by standard-sample bracketing to determine fractionation and the analyses are conducted on a polished crystal surface. LA-ICPMS uses a laser beam to excavate (ablate) material (typically hundreds of nanograms) from a polished sample surface and then conducts isotope analyses with a mass spectrometer. This method also yields ageswith a precision and accuracy of 1–2% (2-sigma) and it has a rapid analysis rate of approximately one analysis per minute. LA-ICP-MS achieves the same precision and accuracy as an ion probe but is considerably more efficient and cost effective (Gehrels, 2014).

The U-Pb system is used for igneous and detrital zircon geochronology data and this system is particularly powerful for geochronology because (1) there are two decay systems ($^{238}U \rightarrow ^{206}Pb$ and $^{235}U \rightarrow ^{207}Pb$), (2) half lives for the two systems are appropriate for use through all but the most recent portion of Earth time, (3) the two decay systems are linked because $^{238}U/^{235}U$ is constant in nearly all crustal rocks, and (4) there is a non-radiogenic isotope of Pb (^{204}Pb) that can be used to account for Pb present in the crystal at the time of formation. (Steiger and Jäger, 1977).To transform the U-Pb isotope data to

geologic ages a convenient means to display the two U-Pb chronometers is using a concordia diagram (Wetherill, 1956). The previous introduction to the U-Pb system and the applied methodology for dating the Ica-Pisco rocks is a very general description and for more informacion of the entire methodology used for these analyses, the construction of the concordia diagram, and the uncertainties for the U-Pb ages using LA-ICPMS the following papers should be consulted: Johnston et al. (2009), Gehrels (2011), Gehrels (2014), and Gehrels and Pecha (2014).

The purpose of this section is to summarize the present geochronological data of the Ica-Pisco plutons including nine new ages from this research. The details of the zircon crystals analyzed, the chemical data from the analyses of the individual zircon crystals, and the summary of the new ages are presented in the following tables.

Table 26. Sample list of the Ica-Pisco samples used for geochronological analysis including location, pluton, number of zircons and spots, shape and zoning of the zircon crystals. Coordinates used to calculate W-E distance are: (-13.73 S, -75.93 W) and (-14.21 S, -75.42 W). Samples are listed from west to east distance.

Sample	Coordinates		W-E Distance (Km)	Pluton/Unit	# Zircons	# Spots	Shape	Zoning
	South	West						
15826D	13.48350	75.46854	53.49	Incahuasi	300	68	subhedral and euhedral stubby	oscillatory and sector
14710F	13.61448	75.42439	46.44	Incahuasi	20	25	euhedral stubby	oscillatory
15826Fa	13.51878	75.64406	37.74	Tiabaya	14	11	subhedral	oscillatory and sector
15826Ca	13.59497	75.58428	36.16	Tiabaya	10	35	subhedral and euhedral	oscillatory
10714P	13.83987	75.56205	18.55	Pampahuasi	21	25	subhedral and euhedral	oscillatory
14727U	13.82762	75.69228	9.90	Rinconada	32	35	subhedral	oscillatory
14721Ac	13.70707	75.83489	8.83	Auquish	60	15	subhedral	oscillatory
14715G	13.93126	75.61616	7.38	Pampahuasi	19	19	euhedral stubby	oscillatory
15826Aa	13.73187	75.92377	0.31	Gabbro	7	23	subhedral	oscillatory and sector
14713C	13.73287	75.92406	0.21	Humay	2	10	subhedral	oscillatory and sector
14710A	13.70844	75.95422	-0.10	Quilmana	3	6	subhedral	oscillatory

Table 27. U-Pb geochronological analyses for sample 10714P. Note that "C" and "R" stand for core and rim respectively.

		Isotope ratios									Apparent ages (Ma)							
Analysis	U (ppm)	$^{206}Pb/^{204}Pb$	U/Th	$^{206}Pb/^{207}Pb$	± (%)	$^{207}Pb/^{235}U$	± (%)	$^{206}Pb/^{238}U$	± (%)	error corr.	$^{206}Pb/^{238}U$	± (Ma)	$^{207}Pb/^{235}U$	± (Ma)	$^{206}Pb/^{207}Pb$	± (Ma)	Best age (Ma)	± (Ma)
14P-1C	253	11876	1.5	24.7515	21.6	0.0797	21.8	0.0143	2.7	0.12	91.6	2.5	77.8	16.3	-325.2	561.2	89.9	5.6
14P-1R	233	18350	1.4	21.8049	26.6	0.0919	27.0	0.0145	4.1	0.15	93.0	3.8	89.3	23.0	-9.7	653.4	89.9	11.3
14P-2C	166	6685	1.3	20.3003	22.8	0.0969	23.4	0.0143	5.2	0.22	91.3	4.7	93.9	21.0	160.3	538.8	89.9	3.8
14P-2R	179	7879	2.2	21.0169	30.5	0.0986	31.9	0.0150	9.1	0.28	96.2	8.7	95.5	29.0	78.4	740.4	90.2	3.3
14P-3C	176	4619	1.4	20.5021	37.7	0.0961	38.0	0.0143	5.2	0.14	91.4	4.7	93.1	33.8	137.1	913.6	90.2	5.8
14P-3R	180	5012	1.8	29.1939	41.2	0.0671	41.3	0.0142	2.9	0.07	91.0	2.6	65.9	26.4	-769.0	1203.7	90.3	2.1
14P-4C	147	7100	1.8	20.5048	22.9	0.0968	23.4	0.0144	4.7	0.20	92.1	4.3	93.8	21.0	136.7	545.3	90.4	3.3
14P-5C	293	18400	1.6	21.8505	11.4	0.0909	11.9	0.0144	3.1	0.26	92.2	2.9	88.3	10.0	-14.7	277.4	90.5	4.7
14P-6C	175	8284	1.4	20.3912	24.9	0.0963	25.1	0.0142	3.0	0.12	91.1	2.7	93.3	22.4	149.8	592.6	91.0	2.6
14P-7C	172	7032	1.6	19.2935	31.1	0.1003	31.7	0.0140	6.2	0.20	89.9	5.6	97.1	29.4	278.0	727.7	91.1	2.7
14P-8C	186	7751	1.4	21.1608	14.4	0.0915	15.0	0.0140	4.3	0.28	89.9	3.8	88.9	12.8	62.2	344.9	91.3	4.7
14P-9C	259	14062	1.5	21.0296	20.9	0.0924	21.2	0.0141	3.6	0.17	90.2	3.3	89.7	18.2	77.0	501.4	91.4	4.7
14P-10C	118	7437	1.8	23.1168	38.7	0.0860	38.9	0.0144	4.0	0.10	92.2	3.6	83.7	31.3	-152.7	992.8	91.5	4.0

Table 27. Continued

		Isotope ratios									Apparent ages (Ma)							
Analysis	U (ppm)	$^{206}Pb/^{204}Pb$	U/Th	$^{206}Pb/^{207}Pb$	± (%)	$^{207}Pb/^{235}U$	± (%)	$^{206}Pb/^{238}U$	± (%)	error corr.	$^{206}Pb/^{238}U$	± (Ma)	$^{207}Pb/^{235}U$	± (Ma)	$^{206}Pb/^{207}Pb$	± (Ma)	Best age (Ma)	± (Ma)
14P-11C	127	4406	1.6	19.4878	30.1	0.1020	30.3	0.0144	3.9	0.13	92.2	3.5	98.6	28.5	255.0	705.9	91.6	2.5
14P-12C	152	7603	1.5	25.0649	45.1	0.0775	45.6	0.0141	6.5	0.14	90.2	5.8	75.8	33.3	-357.6	1220.4	91.8	4.4
14P-12R	263	15888	2.8	21.3762	26.7	0.0922	27.1	0.0143	4.4	0.16	91.5	4.0	89.6	23.2	38.0	649.3	91.9	6.6
14P-13C	276	11559	1.6	23.4276	22.4	0.0857	22.6	0.0146	3.1	0.14	93.2	2.9	83.5	18.1	-185.9	565.5	92.0	2.5
14P-14C	273	7757	1.5	23.0972	33.4	0.0858	33.5	0.0144	2.7	0.08	92.0	2.5	83.6	26.9	-150.6	849.4	92.1	4.3
14P-15C	146	4781	1.5	20.6725	23.1	0.0937	26.3	0.0140	12.7	0.48	89.9	11.3	90.9	22.9	117.6	549.9	92.2	2.9
14P-16C	146	9101	1.7	16.4845	21.0	0.1200	21.6	0.0143	4.8	0.22	91.8	4.4	115.1	23.5	627.3	457.3	92.2	3.5
14P-17C	208	3352	1.4	17.8832	34.6	0.1107	35.4	0.0144	7.2	0.20	91.9	6.6	106.6	35.8	449.1	790.9	92.2	3.6
14P-18C	261	16543	1.5	24.2805	24.9	0.0802	25.2	0.0141	3.7	0.15	90.4	3.3	78.3	19.0	-276.1	642.3	93.0	3.8
14P-19C	227	16036	1.4	18.7927	22.5	0.1035	22.7	0.0141	2.3	0.10	90.3	2.1	100.0	21.6	337.8	516.6	93.2	2.9
14P-20C	172	10721	1.4	29.5155	46.0	0.0660	46.3	0.0141	5.2	0.11	90.5	4.7	64.9	29.1	-799.9	1364.6	95.0	6.3
14P-21C	255	21701	1.5	23.0359	33.4	0.0888	34.1	0.0148	6.7	0.20	95.0	6.3	86.4	28.2	-144.0	847.8	96.2	8.7

Table 28. U-Pb geochronological analyses for sample 14710F. Note that "C" and "R" stand for core and rim respectively.

		Isotope ratios									Apparent ages (Ma)							
Analysis	U (ppm)	$^{206}Pb/^{204}Pb$	U/Th	$^{206}Pb/^{207}Pb$	± (%)	$^{207}Pb/^{235}U$	± (%)	$^{206}Pb/^{238}U$	± (%)	error corr.	$^{206}Pb/^{238}U$	± (Ma)	$^{207}Pb/^{235}U$	± (Ma)	$^{206}Pb/^{207}Pb$	± (Ma)	Best age (Ma)	± (Ma)
10F-8C	144	4188	1.5	21.9624	19.6	0.0629	21.6	0.0100	9.2	0.43	64.3	5.9	62.0	13.0	-27.1	478.0	64.3	5.9
10F4R	255	12383	1.2	21.5337	30.5	0.0661	30.7	0.0103	3.9	0.13	66.2	2.6	65.0	19.3	20.5	746.6	66.2	2.6
10F-17C	317	12697	1.1	19.1561	19.6	0.0745	19.9	0.0104	3.9	0.20	66.4	2.6	73.0	14.0	294.3	450.1	66.4	2.6
10F-11C	162	5941	1.7	16.6339	46.5	0.0860	48.4	0.0104	13.3	0.28	66.5	8.8	83.7	38.9	607.8	1062.8	66.5	8.8
10F-2R	211	8185	1.2	23.7891	36.5	0.0603	36.9	0.0104	4.9	0.13	66.7	3.3	59.4	21.3	-224.4	946.7	66.7	3.3
10F-20C	162	9718	1.5	23.0625	45.0	0.0624	45.4	0.0104	5.5	0.12	66.9	3.7	61.4	27.0	-146.8	1168.7	66.9	3.7
10F-2C	166	9429	1.3	27.8949	60.5	0.0517	60.9	0.0105	7.0	0.11	67.1	4.7	51.2	30.4	-642.4	1811.4	67.1	4.7
10F-19C	484	10805	1.2	21.0305	20.9	0.0687	21.3	0.0105	4.3	0.20	67.2	2.9	67.4	13.9	76.9	500.3	67.2	2.9
10F-5C	172	4379	1.6	18.5188	34.9	0.0781	35.7	0.0105	7.5	0.21	67.2	5.0	76.3	26.3	371.0	809.5	67.2	5.0
10F-18C	325	29621	1.1	26.7370	30.7	0.0541	31.1	0.0105	4.9	0.16	67.3	3.3	53.5	16.2	-527.5	839.0	67.3	3.3
10F-4C	280	6247	1.1	24.1936	33.6	0.0600	33.9	0.0105	4.5	0.13	67.5	3.0	59.1	19.5	-267.0	873.7	67.5	3.0
10F-9R	1515	81390	1.7	20.7445	4.4	0.0701	6.3	0.0105	4.6	0.72	67.6	3.1	68.8	4.2	109.3	103.1	67.6	3.1

Table 28. Continued

				Isotope ratios							Apparent ages (Ma)							
Analysis	U (ppm)	$^{206}Pb/^{204}Pb$	U/Th	$^{206}Pb/^{207}Pb$	± (%)	$^{207}Pb/^{235}U$	± (%)	$^{206}Pb/^{238}U$	± (%)	error corr.	$^{206}Pb/^{238}U$	± (Ma)	$^{207}Pb/^{235}U$	± (Ma)	$^{206}Pb/^{207}Pb$	± (Ma)	Best age (Ma)	± (Ma)
10F-12C	815	23895	1.2	20.9518	9.4	0.0697	9.5	0.0106	1.6	0.17	67.9	1.1	68.4	6.3	85.9	223.4	67.9	1.1
10F-6R	233	8091	1.2	26.2482	42.7	0.0557	42.8	0.0106	2.7	0.06	67.9	1.8	55.0	22.9	-478.4	1178.4	67.9	1.8
10F-14C	496	24425	1.3	19.9821	11.0	0.0732	11.9	0.0106	4.7	0.40	68.0	3.2	71.7	8.3	197.1	255.4	68.0	3.2
10F-7C	234	6590	1.1	23.2622	20.7	0.0629	21.3	0.0106	5.2	0.25	68.1	3.5	61.9	12.8	-168.3	519.2	68.1	3.5
10F-16C	527	15914	1.2	19.7044	10.0	0.0744	11.1	0.0106	4.9	0.44	68.1	3.3	72.8	7.8	229.5	231.2	68.1	3.3
10F-3C	179	6423	1.6	16.5463	31.5	0.0887	31.9	0.0106	4.8	0.15	68.2	3.3	86.2	26.4	619.2	696.0	68.2	3.3
10F-9C	1574	54488	1.7	21.2633	6.6	0.0691	6.8	0.0106	1.5	0.22	68.3	1.0	67.8	4.5	50.7	158.3	68.3	1.0
10F-1C	191	4951	1.6	28.2185	52.7	0.0521	53.0	0.0107	5.8	0.11	68.4	4.0	51.6	26.7	-674.2	1549.2	68.4	4.0
10F-15C	771	27293	1.4	22.2758	12.0	0.0663	12.3	0.0107	2.4	0.20	68.7	1.7	65.2	7.7	-61.5	293.7	68.7	1.7
10F-1R	282	10300	1.8	21.5598	20.8	0.0687	21.0	0.0107	2.7	0.13	68.8	1.9	67.4	13.7	17.5	503.7	68.8	1.9
10F-13C	406	10690	1.2	24.6630	19.9	0.0602	20.1	0.0108	3.0	0.15	69.0	2.0	59.3	11.6	-316.0	514.6	69.0	2.0
10F-10R	362	18204	1.6	23.5135	15.4	0.0632	15.6	0.0108	2.7	0.17	69.1	1.8	62.2	9.4	-195.1	386.6	69.1	1.8
10F-10C	314	14785	1.1	21.3733	21.7	0.0698	24.3	0.0108	10.9	0.45	69.4	7.5	68.5	16.1	38.4	524.6	69.4	7.5

Table 29. U-Pb geochronological analyses for sample 14713C.

		Isotope ratios									Apparent ages (Ma)							
Analysis	U (ppm)	$^{206}Pb/^{204}Pb$	U/Th	$^{206}Pb/^{207}Pb$	± (%)	$^{207}Pb/^{235}U$	± (%)	$^{206}Pb/^{238}U$	± (%)	error corr.	$^{206}Pb/^{238}U$	± (Ma)	$^{207}Pb/^{235}U$	± (Ma)	$^{206}Pb/^{207}Pb$	± (Ma)	Best age (Ma)	± (Ma)
13C-2C	53	1382	1.3	19.6101	2.3	0.4244	4.2	0.0604	3.5	0.84	377.8	13.0	359.2	12.7	240.6	52.2	377.8	13.0
13C-2D	63	2592	1.4	18.5613	2.8	0.4485	3.2	0.0604	1.6	0.49	377.9	5.8	376.2	10.1	365.8	63.1	377.9	5.8
13C-1G	130	4533	1.6	17.4184	2.5	0.5110	5.8	0.0646	5.2	0.90	403.3	20.5	419.1	20.0	507.3	54.9	403.3	20.5
13C-1C	167	5421	1.2	17.5724	0.8	0.5806	2.7	0.0740	2.6	0.96	460.2	11.6	464.8	10.2	487.9	17.2	460.2	11.6
13C-1I	297	10522	3.0	17.5098	0.6	0.6100	4.9	0.0775	4.9	0.99	481.0	22.6	483.6	18.9	495.8	12.9	481.0	22.6
13C-1J	477	20989	2.7	17.3427	0.8	0.6343	2.3	0.0798	2.1	0.94	494.8	10.1	498.8	8.9	516.9	17.1	494.8	10.1
13C-1H	184	7044	1.8	17.4597	0.6	0.6385	2.5	0.0809	2.4	0.97	501.2	11.8	501.4	10.0	502.1	13.4	501.2	11.8
13C-1D	113	3763	1.3	17.7732	1.1	0.6459	2.8	0.0833	2.6	0.92	515.6	12.8	506.0	11.2	462.8	24.3	515.6	12.8
13C-1F	139	5222	1.6	17.6198	1.1	0.6675	2.4	0.0853	2.1	0.89	527.6	10.7	519.2	9.7	482.0	24.1	527.6	10.7
13C-1E	98	3923	1.8	17.6230	1.0	0.6816	1.2	0.0871	0.7	0.57	538.5	3.5	527.7	4.9	481.6	21.6	538.5	3.5

Table 30. U-Pb geochronological analyses for sample 14715G.

	Isotope ratios										Apparent ages (Ma)							
Analysis	U (ppm)	$^{206}Pb/^{204}Pb$	U/Th	$^{206}Pb/^{207}Pb$	± (%)	$^{207}Pb/^{235}U$	± (%)	$^{206}Pb/^{238}U$	± (%)	error corr.	$^{206}Pb/^{238}U$	± (Ma)	$^{207}Pb/^{235}U$	± (Ma)	$^{206}Pb/^{207}Pb$	± (Ma)	Best age (Ma)	± (Ma)
15G-1	798	15253	2.6	20.8924	4.9	0.1018	5.0	0.0154	1.2	0.25	98.7	1.2	98.4	4.7	92.6	115.1	94.0	2.5
15G-2C	374	10221	1.2	19.2741	10.3	0.1152	11.1	0.0161	4.2	0.38	103.0	4.3	110.7	11.7	280.3	236.4	96.6	1.0
15G-4C	481	10976	0.9	21.0436	4.8	0.0997	5.1	0.0152	1.7	0.33	97.3	1.6	96.5	4.7	75.4	114.1	96.8	1.1
15G-5C	563	16269	0.9	20.6086	5.6	0.1039	6.1	0.0155	2.4	0.39	99.4	2.3	100.4	5.9	124.8	133.0	97.1	1.5
15G-6C	719	33652	0.8	21.0930	7.0	0.0987	7.1	0.0151	1.0	0.14	96.6	1.0	95.6	6.4	69.9	166.5	97.3	1.6
15G-7C	430	32803	1.0	20.5643	7.7	0.1021	7.9	0.0152	1.9	0.25	97.4	1.9	98.7	7.4	129.9	180.2	97.4	3.2
15G-8C	561	21689	1.0	21.3130	3.1	0.0982	3.4	0.0152	1.6	0.46	97.1	1.5	95.1	3.1	45.1	73.3	97.4	1.9
15G-9C	477	13888	1.0	20.2339	6.8	0.1031	6.9	0.0151	1.2	0.17	96.8	1.1	99.6	6.6	167.9	160.1	97.5	2.9
15G-10C	335	9778	1.0	20.9776	7.7	0.1034	8.4	0.0157	3.2	0.39	100.6	3.2	99.9	8.0	82.9	183.7	97.7	2.2
15G-11C	495	9690	1.0	20.5255	7.1	0.1032	7.3	0.0154	1.6	0.22	98.3	1.6	99.8	7.0	134.4	168.1	97.7	0.9
15G-12C	531	12144	1.0	21.8195	4.6	0.0984	5.9	0.0156	3.7	0.63	99.6	3.7	95.3	5.4	-11.3	111.2	98.0	1.5
15G-13C	320	4481	0.9	18.6362	6.5	0.1126	7.3	0.0152	3.3	0.46	97.4	3.2	108.4	7.5	356.7	147.4	98.3	1.6
15G-14C	603	22783	1.0	20.5989	5.4	0.1022	5.5	0.0153	0.9	0.17	97.7	0.9	98.8	5.2	126.0	127.2	98.6	1.3
15G-15C	426	14680	0.9	21.5568	5.2	0.0977	5.7	0.0153	2.3	0.40	97.7	2.2	94.6	5.2	17.9	125.9	98.7	0.9
15G-16C	579	17661	1.4	21.8015	3.9	0.0969	4.2	0.0153	1.5	0.36	98.0	1.5	93.9	3.8	-9.3	95.3	98.7	1.2
15G-17C	390	853	1.7	16.4003	29.1	0.1235	29.2	0.0147	2.7	0.09	94.0	2.5	118.2	32.6	638.4	637.8	99.4	2.3
15G-18C	481	16321	1.0	20.9883	10.3	0.1012	10.4	0.0154	1.3	0.13	98.6	1.3	97.9	9.7	81.7	245.2	99.6	3.7
15G-19C	419	9136	1.0	21.9787	8.4	0.0967	8.4	0.0154	0.9	0.10	98.7	0.9	93.8	7.6	-28.9	203.8	100.6	3.2
15G-20C	383	16036	0.9	19.1860	15.8	0.1095	16.0	0.0152	3.0	0.18	97.5	2.9	105.5	16.1	290.7	362.0	103.0	4.3

Table 31. U-Pb geochronological analyses for sample 14721Ac. Note that "C" and "R" stand for core and rim respectively.

		Isotope ratios									Apparent ages (Ma)							
Analysis	U (ppm)	$^{206}Pb/^{204}Pb$	U/Th	$^{206}Pb/^{207}Pb$	± (%)	$^{207}Pb/^{235}U$	± (%)	$^{206}Pb/^{238}U$	± (%)	error corr.	$^{206}Pb/^{238}U$	± (Ma)	$^{207}Pb/^{235}U$	± (Ma)	$^{206}Pb/^{207}Pb$	± (Ma)	Best age (Ma)	± (Ma)
21Ac-1C	3023	60008	0.5	20.7607	1.3	0.1075	1.4	0.0162	0.6	0.41	103.5	0.6	103.7	1.4	107.5	30.6	103.1	0.6
21Ac-2C	2831	48276	0.6	20.7773	1.5	0.1087	1.8	0.0164	0.8	0.48	104.8	0.9	104.8	1.7	105.6	36.4	103.5	0.6
21Ac-3C	2970	64139	0.6	20.3633	1.4	0.1098	1.6	0.0162	0.8	0.51	103.7	0.8	105.8	1.6	153.0	32.6	103.7	0.8
21Ac-4C	1469	28939	1.0	20.8157	3.1	0.1092	3.1	0.0165	0.7	0.22	105.4	0.7	105.2	3.1	101.3	72.5	104.1	0.8
21Ac-5C	778	15781	1.2	20.8038	4.0	0.1100	4.1	0.0166	0.7	0.17	106.1	0.7	105.9	4.1	102.6	94.9	104.4	0.7
21Ac-6C	3813	13880	0.4	20.1678	2.1	0.1122	2.6	0.0164	1.5	0.58	105.0	1.6	108.0	2.6	175.5	48.8	104.8	0.9
21Ac-7C	1888	42709	0.8	20.6212	1.5	0.1089	1.6	0.0163	0.7	0.45	104.1	0.8	104.9	1.6	123.4	34.6	104.9	1.2
21Ac-8C	2519	75069	0.6	20.6929	1.2	0.1093	1.6	0.0164	1.1	0.70	104.9	1.2	105.3	1.6	115.3	27.2	105.0	1.6
21Ac-9CR	1323	61481	0.8	20.5631	3.9	0.1104	4.5	0.0165	2.2	0.50	105.3	2.3	106.3	4.5	130.1	90.6	105.3	2.3
21Ac-10IR	1173	32082	0.9	20.9248	3.2	0.1088	3.2	0.0165	0.6	0.17	105.6	0.6	104.9	3.2	88.9	74.8	105.4	0.7
21Ac-11C	1546	5459	1.1	19.0314	5.7	0.1198	6.3	0.0165	2.5	0.39	105.7	2.6	114.9	6.8	309.2	130.9	105.6	0.6
21Ac-12C	2714	97407	0.6	20.7798	1.3	0.1099	1.5	0.0166	0.7	0.46	105.9	0.7	105.8	1.5	105.3	31.0	105.7	2.6
21Ac-13C	2763	40882	0.6	20.7153	0.8	0.1087	1.0	0.0163	0.6	0.63	104.4	0.7	104.8	1.0	112.7	19.0	105.8	0.5
21Ac-14C	2403	47973	0.5	20.8590	1.8	0.1066	1.9	0.0161	0.6	0.32	103.1	0.6	102.8	1.9	96.4	43.6	105.9	0.7
21Ac-15C	1125	13771	1.0	20.9734	2.6	0.1087	2.7	0.0165	0.5	0.18	105.8	0.5	104.8	2.6	83.4	62.1	106.1	0.7

Table 32. U-Pb geochronologic analyses for sample 14727U. Note that "C" and "R" stand for core and rim respectively.

		Isotope ratios									Apparent ages (Ma)							
Analysis	U (ppm)	$^{206}Pb/^{204}Pb$	U/Th	$^{206}Pb/^{207}Pb$	± (%)	$^{207}Pb/^{235}U$	± (%)	$^{206}Pb/^{238}U$	± (%)	error corr.	$^{206}Pb/^{238}U$	± (Ma)	$^{207}Pb/^{235}U$	± (Ma)	$^{206}Pb/^{207}Pb$	± (Ma)	Best age (Ma)	± (Ma)
27U-8	673	10812	1.5	20.7103	1.0	0.0984	3.6	0.0148	3.4	0.96	94.6	3.2	95.3	3.3	113.3	23.0	94.6	3.2
27U-13	686	7732	1.3	20.7392	1.0	0.0983	1.8	0.0148	1.5	0.84	94.6	1.4	95.2	1.7	110.0	23.4	94.6	1.4
27U-28	402	5585	1.4	20.3957	1.2	0.1001	5.3	0.0148	5.2	0.97	94.8	4.9	96.9	4.9	149.3	28.7	94.8	4.9
27U-12	413	3864	1.4	20.8540	1.4	0.0982	2.8	0.0148	2.4	0.86	95.0	2.3	95.1	2.5	96.9	33.1	95.0	2.3
27U-14	358	3569	1.6	21.2097	2.2	0.0966	2.7	0.0149	1.6	0.59	95.1	1.5	93.7	2.4	56.7	52.2	95.1	1.5
27U-15	446	3898	1.7	20.9102	1.6	0.0987	3.8	0.0150	3.4	0.91	95.8	3.3	95.6	3.4	90.6	36.9	95.8	3.3
27U-9	486	6411	1.3	20.5606	5.1	0.1012	5.4	0.0151	1.7	0.31	96.6	1.6	97.9	5.0	130.4	120.0	96.6	1.6
27U-19	607	4972	3.2	20.6983	1.9	0.1013	2.8	0.0152	2.0	0.72	97.3	1.9	98.0	2.6	114.6	45.2	97.3	1.9
27U-11	407	3782	1.3	19.4407	3.4	0.1081	3.6	0.0152	1.0	0.29	97.5	1.0	104.2	3.5	260.5	78.2	97.5	1.0
27U-24	608	9170	1.2	20.2006	6.7	0.1040	6.8	0.0152	1.5	0.22	97.5	1.4	100.5	6.5	171.7	155.5	97.5	1.4
27U-18	394	3676	1.6	21.3750	1.0	0.0984	2.1	0.0153	1.9	0.89	97.6	1.8	95.3	1.9	38.2	23.6	97.6	1.8
27U-33	1241	13746	4.9	20.5825	0.9	0.1023	1.1	0.0153	0.5	0.49	97.7	0.5	98.9	1.0	127.9	21.9	97.7	0.5
27U-23	481	8661	1.4	20.9492	1.1	0.1009	1.9	0.0153	1.6	0.83	98.1	1.5	97.6	1.7	86.2	24.9	98.1	1.5
27U-10	352	3495	1.8	21.4959	1.2	0.0983	1.7	0.0153	1.2	0.72	98.1	1.2	95.2	1.5	24.7	27.8	98.1	1.2
27U-17	484	5681	2.2	20.8496	0.6	0.1015	1.6	0.0153	1.5	0.92	98.2	1.4	98.1	1.5	97.4	14.6	98.2	1.4
27U-6	547	10846	1.3	20.7653	1.0	0.1023	1.4	0.0154	0.9	0.67	98.6	0.9	98.9	1.3	107.0	24.8	98.6	0.9
27U-21	404	4023	4.5	20.2795	3.5	0.1048	3.6	0.0154	0.8	0.21	98.6	0.8	101.2	3.4	162.6	81.6	98.6	0.8

Table 32. Continued

		Isotope ratios									Apparent ages (Ma)							
Analysis	U (ppm)	$^{206}Pb/^{204}Pb$	U/Th	$^{206}Pb/^{207}Pb$	± (%)	$^{207}Pb/^{235}U$	± (%)	$^{206}Pb/^{238}U$	± (%)	error corr.	$^{206}Pb/^{238}U$	± (Ma)	$^{207}Pb/^{235}U$	± (Ma)	$^{206}Pb/^{207}Pb$	± (Ma)	Best age (Ma)	± (Ma)
27U-3C	991	19345	1.1	20.7518	0.9	0.1024	1.1	0.0154	0.7	0.60	98.6	0.7	99.0	1.1	108.6	21.3	98.6	0.7
27U-20	419	4181	1.5	21.0397	1.0	0.1019	3.1	0.0155	2.9	0.95	99.4	2.9	98.5	2.9	75.9	23.0	99.4	2.9
27U-2C	281	4235	1.3	20.9285	1.2	0.1029	1.4	0.0156	0.7	0.49	99.9	0.7	99.5	1.4	88.5	29.5	99.9	0.7
27U-32	446	4488	1.8	21.2076	0.9	0.1016	2.6	0.0156	2.4	0.93	99.9	2.4	98.2	2.5	57.0	22.5	99.9	2.4
27U-3R	729	12268	1.3	20.3914	1.1	0.1056	1.9	0.0156	1.6	0.81	99.9	1.5	102.0	1.9	149.8	26.7	99.9	1.5
27U-7	1758	18482	25.6	20.5629	0.6	0.1052	2.3	0.0157	2.3	0.96	100.4	2.2	101.6	2.3	130.1	15.0	100.4	2.2
27U-29	571	11552	1.9	20.7415	1.1	0.1046	2.2	0.0157	1.9	0.86	100.7	1.9	101.1	2.1	109.7	25.8	100.7	1.9
27U-26	217	2861	1.9	21.3239	1.7	0.1018	2.2	0.0157	1.4	0.64	100.7	1.4	98.4	2.1	43.9	40.9	100.7	1.4
27U-30	400	3632	2.0	20.7047	2.0	0.1057	2.4	0.0159	1.4	0.58	101.5	1.4	102.0	2.3	113.9	46.1	101.5	1.4
27U-31	526	7947	1.4	20.9244	1.7	0.1048	1.8	0.0159	0.6	0.36	101.7	0.7	101.2	1.7	89.0	39.4	101.7	0.7
27U-25C	1129	12357	2.3	20.6627	0.9	0.1064	2.2	0.0159	2.0	0.91	102.0	2.0	102.6	2.1	118.7	21.6	102.0	2.0
27U-5R	359	7626	2.7	20.6641	1.1	0.1067	1.6	0.0160	1.1	0.68	102.3	1.1	103.0	1.5	118.5	26.9	102.3	1.1
27U-1R	339	4429	2.1	21.0742	1.2	0.1047	1.6	0.0160	1.0	0.65	102.3	1.0	101.1	1.5	72.0	28.3	102.3	1.0
27U-1C	242	3397	1.9	20.7559	2.1	0.1064	2.3	0.0160	1.0	0.43	102.4	1.0	102.6	2.2	108.1	48.5	102.4	1.0
27U-27	572	6591	2.2	20.9886	2.0	0.1055	2.5	0.0161	1.5	0.58	102.7	1.5	101.8	2.4	81.7	48.3	102.7	1.5
27U-16	305	3603	1.9	20.8914	1.8	0.1063	2.3	0.0161	1.4	0.62	103.0	1.4	102.6	2.2	92.7	42.5	103.0	1.4
27U-2R	751	9250	9.1	20.7339	1.2	0.1089	2.0	0.0164	1.5	0.78	104.7	1.6	104.9	2.0	110.6	29.2	104.7	1.6
27U-4	626	12662	1.3	20.6106	0.8	0.1119	1.9	0.0167	1.7	0.90	106.9	1.8	107.7	1.9	124.6	19.0	106.9	1.8

Table 33. U-Pb geochronological analyses for sample 15826Aa.

		Isotope ratios									Apparent ages (Ma)							
Analysis	U (ppm)	$^{206}Pb/^{204}Pb$	U/Th	$^{206}Pb/^{207}Pb$	± (%)	$^{207}Pb/^{235}U$	± (%)	$^{206}Pb/^{238}U$	± (%)	error corr.	$^{206}Pb/^{238}U$	± (Ma)	$^{207}Pb/^{235}U$	± (Ma)	$^{206}Pb/^{207}Pb$	± (Ma)	Best age (Ma)	± (Ma)
Spot 4	424	176896	1.3	19.3780	0.9	0.1415	2.3	0.0199	2.1	0.91	127.0	2.6	134.4	2.8	267.9	21.8	127.0	2.6
Spot 8	424	55245	1.4	19.8075	1.1	0.1403	2.3	0.0202	2.0	0.87	128.7	2.6	133.3	2.9	217.4	25.7	128.7	2.6
Spot 15	605	28023	1.0	20.6136	0.8	0.1353	1.9	0.0202	1.7	0.90	129.1	2.2	128.8	2.3	124.3	19.9	129.1	2.2
Spot 10	965	36686	1.1	20.5671	0.7	0.1358	1.9	0.0203	1.7	0.92	129.3	2.2	129.3	2.3	129.6	17.4	129.3	2.2
Spot 14	818	18650	1.1	20.3766	0.7	0.1373	1.5	0.0203	1.4	0.89	129.5	1.7	130.6	1.9	151.4	16.0	129.5	1.7
Spot 7	506	9070	1.3	20.5601	1.0	0.1366	1.8	0.0204	1.6	0.86	130.0	2.0	130.0	2.2	130.4	22.4	130.0	2.0
Spot 25	620	53213	1.4	20.3823	0.9	0.1379	2.0	0.0204	1.8	0.89	130.1	2.3	131.1	2.5	150.8	22.1	130.1	2.3
Spot 16	460	26584	1.1	19.7775	0.9	0.1423	2.0	0.0204	1.8	0.88	130.2	2.3	135.1	2.6	220.9	21.9	130.2	2.3
Spot 31	480	14812	1.1	20.3378	1.1	0.1386	1.9	0.0204	1.5	0.81	130.5	2.0	131.8	2.3	155.9	26.0	130.5	2.0
Spot 9	430	44397	1.3	20.0542	0.8	0.1406	1.9	0.0204	1.7	0.89	130.5	2.2	133.6	2.3	188.7	19.5	130.5	2.2
Spot 21	514	32546	1.3	20.4912	0.9	0.1376	2.1	0.0205	1.9	0.90	130.5	2.5	130.9	2.6	138.3	21.4	130.5	2.5
Spot 13	545	24592	1.3	20.1374	0.9	0.1403	1.8	0.0205	1.5	0.85	130.7	1.9	133.3	2.2	179.0	21.4	130.7	1.9
Spot 5	713	14950	1.3	20.6822	1.1	0.1367	2.0	0.0205	1.7	0.85	130.9	2.3	130.1	2.5	116.5	25.2	130.9	2.3
Spot 22	507	5541	1.1	21.5181	0.8	0.1320	1.7	0.0206	1.5	0.88	131.5	1.9	125.9	2.0	22.2	19.2	131.5	1.9
Spot 19	565	10043	1.4	20.7460	1.4	0.1371	2.1	0.0206	1.6	0.74	131.6	2.1	130.5	2.6	109.2	34.1	131.6	2.1
Spot 11	915	19786	1.1	20.6155	0.9	0.1381	1.8	0.0207	1.5	0.86	131.8	2.0	131.4	2.2	124.1	21.5	131.8	2.0
Spot 6	595	9994	1.3	21.0340	0.8	0.1357	1.7	0.0207	1.5	0.89	132.1	2.0	129.2	2.1	76.5	18.5	132.1	2.0
Spot 12	636	34127	1.3	20.4981	0.8	0.1397	1.5	0.0208	1.3	0.86	132.5	1.7	132.8	1.9	137.5	18.2	132.5	1.7
Spot 1	276	4055	1.3	21.2813	1.8	0.1347	2.5	0.0208	1.8	0.71	132.6	2.3	128.3	3.0	48.7	42.4	132.6	2.3
Spot 2	227	108147	1.3	20.4754	1.3	0.1409	2.5	0.0209	2.1	0.84	133.5	2.8	133.9	3.1	140.1	31.6	133.5	2.8
Spot 17	493	13623	1.2	20.3827	0.9	0.1419	2.4	0.0210	2.2	0.92	133.9	2.9	134.8	3.0	150.8	21.9	133.9	2.9
Spot 18	462	16254	1.0	17.1481	1.3	0.1695	2.6	0.0211	2.2	0.85	134.5	2.9	159.0	3.8	541.7	29.5	134.5	2.9
Spot 3	400	15939	1.3	20.2500	1.1	0.1438	2.3	0.0211	2.0	0.87	134.7	2.6	136.4	2.9	166.0	26.8	134.7	2.6

Table 34. U-Pb geochronologic analyses for sample 15826Ca.

		Isotope ratios									Apparent ages (Ma)							
Analysis	U (ppm)	$^{206}Pb/^{204}Pb$	U/Th	$^{206}Pb/^{207}Pb$	± (%)	$^{207}Pb/^{235}U$	± (%)	$^{206}Pb/^{238}U$	± (%)	error corr.	$^{206}Pb/^{238}U$	± (Ma)	$^{207}Pb/^{235}U$	± (Ma)	$^{206}Pb/^{207}Pb$	± (Ma)	Best age (Ma)	± (Ma)
Spot 47	315	3743	1.9	21.9444	1.5	0.0811	2.7	0.0129	2.3	0.84	82.6	1.9	79.2	2.1	25.1	36.2	82.6	1.9
Spot 41	392	20734	2.1	20.7325	1.3	0.0858	2.5	0.0129	2.1	0.85	82.7	1.7	83.6	2.0	110.8	30.8	82.7	1.7
Spot 43	346	5360	1.9	20.8058	1.4	0.0856	2.2	0.0129	1.8	0.80	82.8	1.5	83.4	1.8	102.4	32.0	82.8	1.5
Spot 42	519	10148	1.9	21.0143	1.5	0.0853	2.4	0.0130	1.9	0.79	83.2	1.6	83.1	1.9	78.8	35.4	83.2	1.6
Spot 37	340	7613	2.2	20.9258	1.8	0.0856	2.5	0.0130	1.7	0.70	83.3	1.4	83.4	2.0	88.8	41.8	83.3	1.4
Spot 55	356	5619	2.0	21.6511	1.6	0.0829	2.8	0.0130	2.3	0.82	83.4	1.9	80.9	2.2	7.4	38.9	83.4	1.9
Spot 56	323	2378	1.7	22.5014	2.9	0.0801	3.4	0.0131	1.8	0.52	83.7	1.5	78.2	2.6	86.1	72.1	83.7	1.5
Spot 62	294	6372	2.1	21.7727	1.7	0.0829	2.8	0.0131	2.2	0.78	83.8	1.8	80.8	2.2	6.1	42.1	83.8	1.8
Spot 66	232	14328	1.9	20.5449	1.4	0.0881	2.5	0.0131	2.0	0.82	84.1	1.7	85.7	2.0	132.1	33.5	84.1	1.7
Spot 70	431	13774	1.8	20.5573	1.5	0.0883	2.1	0.0132	1.5	0.70	84.3	1.2	85.9	1.7	130.7	35.5	84.3	1.2
Spot 44	308	8162	1.9	21.4766	1.4	0.0847	2.2	0.0132	1.7	0.78	84.5	1.5	82.6	1.8	26.8	33.8	84.5	1.5
Spot 67	212	2092	1.5	23.8265	1.9	0.0764	2.7	0.0132	1.9	0.69	84.5	1.6	74.7	1.9	228.3	49.0	84.5	1.6
Spot 45	303	13568	1.4	21.0826	1.6	0.0865	2.7	0.0132	2.1	0.79	84.7	1.8	84.3	2.2	71.1	39.2	84.7	1.8

Table 34. Continued

		Isotope ratios									Apparent ages (Ma)							
Analysis	U (ppm)	$^{206}Pb/^{204}Pb$	U/Th	$^{206}Pb/^{207}Pb$	± (%)	$^{207}Pb/^{235}U$	± (%)	$^{206}Pb/^{238}U$	± (%)	error corr.	$^{206}Pb/^{238}U$	± (Ma)	$^{207}Pb/^{235}U$	± (Ma)	$^{206}Pb/^{207}Pb$	± (Ma)	Best age (Ma)	± (Ma)
Spot 65	228	39626	2.0	20.6623	1.3	0.0883	2.2	0.0132	1.8	0.81	84.8	1.5	85.9	1.8	118.7	31.1	84.8	1.5
Spot 52	315	11521	2.1	21.3713	1.5	0.0854	2.7	0.0132	2.2	0.82	84.8	1.8	83.2	2.1	38.6	36.5	84.8	1.8
Spot 58	305	27063	1.4	20.5102	1.5	0.0896	2.3	0.0133	1.8	0.77	85.4	1.5	87.1	2.0	136.1	35.0	85.4	1.5
Spot 68	286	10803	2.1	21.1948	1.8	0.0867	2.5	0.0133	1.7	0.70	85.4	1.5	84.5	2.0	58.4	41.9	85.4	1.5
Spot 63	272	2237	1.5	24.3986	2.0	0.0756	3.0	0.0134	2.3	0.75	85.6	1.9	74.0	2.1	288.4	50.7	85.6	1.9
Spot 60	415	29593	2.4	20.7736	1.1	0.0895	2.1	0.0135	1.8	0.85	86.3	1.5	87.0	1.7	106.0	25.6	86.3	1.5
Spot 64	259	19133	1.6	20.7572	1.5	0.0904	2.3	0.0136	1.8	0.77	87.1	1.6	87.8	2.0	107.9	34.8	87.1	1.6
Spot 38	270	15353	1.2	20.4250	1.4	0.0976	2.5	0.0145	2.1	0.82	92.6	1.9	94.6	2.3	145.9	33.2	92.6	1.9
Spot 51	181	18269	1.3	20.5504	1.6	0.0979	2.3	0.0146	1.7	0.74	93.4	1.6	94.8	2.1	131.5	37.0	93.4	1.6
Spot 36	135	3415	1.2	22.2390	2.0	0.0911	3.2	0.0147	2.5	0.78	94.0	2.3	88.5	2.7	57.5	48.7	94.0	2.3
Spot 39	191	3278	3.2	22.0710	2.4	0.0919	3.5	0.0147	2.5	0.71	94.1	2.3	89.2	3.0	39.0	59.2	94.1	2.3
Spot 69	130	5000	1.2	21.8485	3.8	0.0936	4.3	0.0148	2.0	0.47	94.9	1.9	90.8	3.7	14.5	91.1	94.9	1.9
Spot 54	14	344	0.1	2.6192	2.0	1.1712	9.0	0.0222	8.7	0.97	141.9	12.2	787.2	49.1	3838.9	30.4	141.9	12.2

Table 35. U-Pb geochronological analyses for sample 15826D.

		Isotope ratios									Apparent ages (Ma)							
Analysis	U (ppm)	$^{206}Pb/^{204}Pb$	U/Th	$^{206}Pb/^{207}Pb$	± (%)	$^{207}Pb/^{235}U$	± (%)	$^{206}Pb/^{238}U$	± (%)	error corr.	$^{206}Pb/^{238}U$	± (Ma)	$^{207}Pb/^{235}U$	± (Ma)	$^{206}Pb/^{207}Pb$	± (Ma)	Best age (Ma)	± (Ma)
Spot 22	214	7391	1.0	21.5709	2.2	0.0564	3.2	0.0088	2.3	0.73	56.6	1.3	55.7	1.7	16.3	52.0	56.6	1.3
Spot 59	412	5026	0.8	21.4254	3.5	0.0573	4.1	0.0089	2.1	0.52	57.1	1.2	56.6	2.2	32.6	83.8	57.1	1.2
Spot 23	201	1465	1.5	26.3254	3.5	0.0466	3.9	0.0089	1.8	0.47	57.1	1.0	46.3	1.8	486.2	92.8	57.1	1.0
Spot 30	121	2336	1.7	23.6339	3.1	0.0520	4.0	0.0089	2.5	0.63	57.2	1.4	51.4	2.0	207.9	77.2	57.2	1.4
Spot 31	113	952	1.6	29.4410	14.6	0.0418	14.8	0.0089	2.2	0.15	57.3	1.3	41.6	6.0	792.8	415.1	57.3	1.3
Spot 9	157	753	1.5	32.7978	2.6	0.0376	3.3	0.0089	2.0	0.62	57.4	1.2	37.5	1.2	1109.4	77.9	57.4	1.2
Spot 24	467	108071	0.8	20.5881	1.1	0.0600	2.2	0.0090	1.9	0.87	57.5	1.1	59.1	1.2	127.2	24.9	57.5	1.1
Spot 17	149	3574	1.4	22.0654	2.1	0.0561	3.2	0.0090	2.5	0.77	57.7	1.4	55.5	1.8	38.4	50.5	57.7	1.4
Spot 26	140	3213	1.0	21.1964	3.0	0.0586	3.9	0.0090	2.5	0.64	57.8	1.4	57.8	2.2	58.2	72.0	57.8	1.4
Spot 34	168	12086	1.4	20.9573	1.9	0.0593	2.9	0.0090	2.2	0.77	57.9	1.3	58.5	1.6	85.2	44.0	57.9	1.3
Spot47	134	1859	1.3	23.2490	6.6	0.0535	7.0	0.0090	2.4	0.33	57.9	1.4	53.0	3.6	166.9	165.4	57.9	1.4
Spot 10	174	1100	1.2	29.4110	5.1	0.0423	5.4	0.0090	1.9	0.36	57.9	1.1	42.1	2.2	789.9	144.0	57.9	1.1
Spot 66	150	1408	1.4	25.8837	7.9	0.0481	8.1	0.0090	1.7	0.21	58.0	1.0	47.7	3.8	441.5	208.8	58.0	1.0
Spot 18	283	7488	1.3	21.2371	1.7	0.0587	2.8	0.0090	2.2	0.79	58.0	1.3	57.9	1.6	53.7	40.3	58.0	1.3
Spot 30	287	2278	0.8	23.6807	2.8	0.0527	3.2	0.0090	1.6	0.48	58.1	0.9	52.1	1.6	212.9	70.9	58.1	0.9
Spot 1	138	2119	1.0	23.4808	3.3	0.0531	4.0	0.0090	2.3	0.57	58.1	1.3	52.6	2.1	191.6	83.1	58.1	1.3
Spot 65	117	786	1.4	35.2433	16.4	0.0354	16.5	0.0091	2.0	0.12	58.1	1.1	35.3	5.7	1333.5	526.7	58.1	1.1
Spot 67	190	9054	1.3	21.4449	1.9	0.0584	3.0	0.0091	2.3	0.77	58.3	1.4	57.6	1.7	30.4	46.1	58.3	1.4
Spot 32	116	4076	1.6	22.2484	2.7	0.0564	3.5	0.0091	2.2	0.63	58.4	1.3	55.7	1.9	58.5	67.0	58.4	1.3
Spot58	108	1325	1.5	26.0328	6.7	0.0482	7.1	0.0091	2.2	0.31	58.4	1.3	47.8	3.3	456.6	178.2	58.4	1.3
Spot 27	153	11492	1.4	20.7829	2.3	0.0604	2.9	0.0091	1.8	0.61	58.4	1.0	59.6	1.7	105.0	55.0	58.4	1.0
Spot 26	149	2322	1.7	22.7265	2.5	0.0553	3.4	0.0091	2.3	0.67	58.4	1.3	54.6	1.8	110.6	62.4	58.4	1.3
Spot 69	189	2359	1.4	22.1317	7.3	0.0569	7.7	0.0091	2.2	0.29	58.6	1.3	56.2	4.2	45.7	178.5	58.6	1.3
Spot 28	213	4796	1.0	21.8528	2.3	0.0576	3.4	0.0091	2.5	0.73	58.6	1.5	56.9	1.9	14.9	56.5	58.6	1.5
Spot34	248	11437	1.5	21.6705	2.3	0.0581	3.3	0.0091	2.4	0.72	58.6	1.4	57.4	1.8	5.2	55.0	58.6	1.4

Table 35. Continued

					Isotope ratios						Apparent ages (Ma)							
Analysis	U (ppm)	$^{206}Pb/^{204}Pb$	U/Th	$^{206}Pb/^{207}Pb$	± (%)	$^{207}Pb/^{235}U$	± (%)	$^{206}Pb/^{238}U$	± (%)	error corr.	$^{206}Pb/^{238}U$	± (Ma)	$^{207}Pb/^{235}U$	± (Ma)	$^{206}Pb/^{207}Pb$	± (Ma)	Best age (Ma)	± (Ma)
Spot 52	99	2993	1.3	23.8023	2.7	0.0530	3.4	0.0091	2.2	0.63	58.7	1.3	52.4	1.8	225.7	66.9	58.7	1.3
Spot 21	131	2806	1.4	22.9115	2.8	0.0550	4.0	0.0091	2.9	0.72	58.7	1.7	54.4	2.1	130.6	69.5	58.7	1.7
Spot 57	173	1781	1.7	23.6416	3.6	0.0533	4.0	0.0091	1.7	0.43	58.7	1.0	52.8	2.0	208.7	90.0	58.7	1.0
Spot 16	149	1363	1.7	26.6110	8.5	0.0474	8.8	0.0092	2.3	0.26	58.7	1.4	47.0	4.1	514.9	228.3	58.7	1.4
Spot 54	95	1713	1.7	25.7513	4.1	0.0490	4.9	0.0092	2.7	0.55	58.7	1.6	48.6	2.3	428.0	106.9	58.7	1.6
Spot 4	160	2349	1.1	22.3049	2.4	0.0566	3.3	0.0092	2.2	0.67	58.8	1.3	55.9	1.8	64.7	59.7	58.8	1.3
Spot 60	183	7009	1.5	22.1049	2.3	0.0572	3.5	0.0092	2.6	0.76	58.8	1.5	56.5	1.9	42.7	55.2	58.8	1.5
Spot 27	120	1361	1.5	25.0513	6.0	0.0506	6.4	0.0092	2.1	0.33	58.9	1.2	50.1	3.1	356.2	155.1	58.9	1.2
Spot 33	121	1375	1.8	26.2173	2.8	0.0483	4.1	0.0092	3.0	0.73	59.0	1.8	47.9	1.9	475.3	74.9	59.0	1.8
Spot 11	115	12280	1.6	21.6711	2.7	0.0586	4.0	0.0092	3.0	0.74	59.1	1.8	57.8	2.3	5.2	65.1	59.1	1.8
Spot 25	194	11822	1.4	21.4800	2.6	0.0591	3.4	0.0092	2.2	0.65	59.1	1.3	58.3	2.0	26.4	63.0	59.1	1.3
Spot 19	224	3269	0.8	22.5143	2.3	0.0564	2.8	0.0092	1.5	0.55	59.1	0.9	55.7	1.5	87.5	56.7	59.1	0.9
Spot 15	108	2929	1.6	23.6243	2.2	0.0537	3.2	0.0092	2.3	0.71	59.1	1.3	53.2	1.6	206.9	55.9	59.1	1.3
Spot 49	424	29136	1.1	19.0799	2.8	0.0666	3.3	0.0092	1.8	0.54	59.1	1.1	65.4	2.1	303.4	63.9	59.1	1.1
Spot 48	71	2803	1.7	22.1566	3.7	0.0573	4.8	0.0092	3.2	0.65	59.1	1.9	56.6	2.7	48.4	89.0	59.1	1.9
Spot 5	172	1485	1.0	25.7459	13.1	0.0494	13.3	0.0092	2.2	0.16	59.1	1.3	48.9	6.4	427.4	345.8	59.1	1.3
Spot 14	111	7384	1.1	22.6277	2.7	0.0562	4.0	0.0092	3.0	0.74	59.2	1.7	55.5	2.2	99.9	66.0	59.2	1.7
Spot 35	169	1784	1.1	22.9169	3.8	0.0555	4.5	0.0092	2.4	0.54	59.2	1.4	54.9	2.4	131.2	93.6	59.2	1.4
Spot 8	133	24527	1.2	21.1572	1.9	0.0602	2.4	0.0092	1.6	0.64	59.3	0.9	59.4	1.4	62.7	44.7	59.3	0.9
Spot 63	407	5650	1.0	22.0244	1.3	0.0579	2.0	0.0093	1.5	0.75	59.4	0.9	57.2	1.1	33.9	32.3	59.4	0.9
Spot 7	526	4439	0.6	21.2218	1.7	0.0602	2.2	0.0093	1.5	0.66	59.5	0.9	59.4	1.3	55.4	40.2	59.5	0.9
Spot 70	288	11731	1.2	21.1741	1.6	0.0604	2.6	0.0093	2.0	0.77	59.5	1.2	59.5	1.5	60.7	39.1	59.5	1.2
Spot 64	200	4269	1.5	22.7841	2.3	0.0561	3.2	0.0093	2.2	0.68	59.5	1.3	55.5	1.7	116.8	57.5	59.5	1.3
Spot 56	128	42829	1.2	19.5385	2.4	0.0655	3.9	0.0093	3.0	0.77	59.5	1.8	64.4	2.4	249.0	56.2	59.5	1.8
Spot 23	199	5636	1.0	22.1658	3.4	0.0577	3.9	0.0093	1.8	0.46	59.5	1.1	57.0	2.1	49.4	83.6	59.5	1.1

Table 35. Continued

		Isotope ratios									Apparent ages (Ma)							
Analysis	U (ppm)	$^{206}Pb/^{204}Pb$	U/Th	$^{206}Pb/^{207}Pb$	± (%)	$^{207}Pb/^{235}U$	± (%)	$^{206}Pb/^{238}U$	± (%)	error corr.	$^{206}Pb/^{238}U$	± (Ma)	$^{207}Pb/^{235}U$	± (Ma)	$^{206}Pb/^{207}Pb$	± (Ma)	Best age (Ma)	± (Ma)
Spot 28	83	2539	1.9	22.8480	3.4	0.0560	4.1	0.0093	2.4	0.58	59.6	1.4	55.4	2.2	123.7	83.3	59.6	1.4
Spot 32	207	34589	1.5	21.1555	2.1	0.0605	2.9	0.0093	2.0	0.68	59.6	1.2	59.7	1.7	62.8	50.9	59.6	1.2
Spot 3	279	9357	1.1	21.5728	1.9	0.0597	2.8	0.0093	2.1	0.74	59.9	1.3	58.8	1.6	16.1	46.2	59.9	1.3
Spot 61	80	713	1.5	33.0803	13.1	0.0390	13.5	0.0094	3.5	0.26	60.0	2.1	38.8	5.1	1135.5	400.2	60.0	2.1
Spot 20	130	11399	1.4	21.1839	2.6	0.0609	3.6	0.0094	2.5	0.68	60.0	1.5	60.0	2.1	59.7	62.7	60.0	1.5
Spot 62	169	8019	1.3	21.0837	2.5	0.0613	3.0	0.0094	1.7	0.55	60.2	1.0	60.4	1.8	70.9	60.0	60.2	1.0
Spot 35	271	1888	1.1	24.3719	4.2	0.0531	4.6	0.0094	1.9	0.41	60.3	1.1	52.6	2.3	285.7	106.0	60.3	1.1
Spot 13	154	17964	1.5	22.0619	1.5	0.0587	2.9	0.0094	2.5	0.85	60.3	1.5	57.9	1.6	38.0	37.1	60.3	1.5
Spot 50	153	11673	1.8	20.6279	2.3	0.0629	3.2	0.0094	2.3	0.69	60.3	1.4	61.9	1.9	122.6	54.9	60.3	1.4
Spot 29	178	3780	1.3	22.7677	2.5	0.0572	3.7	0.0095	2.7	0.73	60.6	1.6	56.5	2.0	115.0	62.1	60.6	1.6
Spot 12	191	20295	1.3	21.0112	2.0	0.0620	2.8	0.0095	2.0	0.69	60.6	1.2	61.1	1.7	79.1	48.7	60.6	1.2
Spot 2	198	2629	1.0	23.4898	2.3	0.0558	3.3	0.0095	2.3	0.70	61.0	1.4	55.1	1.8	192.6	58.5	61.0	1.4
Spot 6	232	27542	1.5	21.2210	1.9	0.0618	3.0	0.0095	2.3	0.76	61.1	1.4	60.9	1.8	55.4	45.8	61.1	1.4
Spot 33	203	1931	1.3	20.0409	3.8	0.0661	4.6	0.0096	2.6	0.57	61.6	1.6	65.0	2.9	190.3	87.9	61.6	1.6
Spot 68	251	983	1.0	10.3491	12.3	0.1283	14.8	0.0096	8.2	0.56	61.8	5.1	122.6	17.1	1560.0	231.3	61.8	5.1
Spot 29	82	2621	1.5	18.4318	5.7	0.0724	6.3	0.0097	2.7	0.43	62.1	1.7	71.0	4.3	381.6	128.7	62.1	1.7
Spot 51	105	2583	1.6	22.7994	3.2	0.0603	4.6	0.0100	3.2	0.71	64.0	2.0	59.5	2.6	118.5	79.5	64.0	2.0
Spot 53	152	37050	1.2	15.4674	3.7	0.0891	4.7	0.0100	2.9	0.62	64.1	1.9	86.7	3.9	763.0	78.4	64.1	1.9

Table 36. U-Pb geochronological analyses for sample 15826Fa.

		Isotope ratios									Apparent ages (Ma)							
Analysis	U (ppm)	$^{206}Pb/^{204}Pb$	U/Th	$^{206}Pb/^{207}Pb$	± (%)	$^{207}Pb/^{235}U$	± (%)	$^{206}Pb/^{238}U$	± (%)	error corr.	$^{206}Pb/^{238}U$	± (Ma)	$^{207}Pb/^{235}U$	± (Ma)	$^{206}Pb/^{207}Pb$	± (Ma)	Best age (Ma)	± (Ma)
Spot 41	1535	11557	1.0	20.9656	0.9	0.0834	1.5	0.0127	1.2	0.81	81.2	0.9	81.3	1.1	84.3	20.3	81.2	0.9
Spot 38	945	25721	1.2	20.2379	0.9	0.0875	1.7	0.0128	1.4	0.85	82.3	1.1	85.2	1.3	167.4	20.6	82.3	1.1
Spot 37	631	16016	1.5	20.6400	1.2	0.0860	1.9	0.0129	1.5	0.80	82.5	1.3	83.8	1.6	121.3	27.3	82.5	1.3
Spot 36	613	14082	1.6	20.3921	1.2	0.0872	2.0	0.0129	1.6	0.81	82.6	1.3	84.9	1.6	149.7	27.7	82.6	1.3
Spot 42	581	5938	1.4	21.2660	1.1	0.0839	2.0	0.0129	1.7	0.84	82.9	1.4	81.8	1.6	50.4	25.7	82.9	1.4
Spot 46	580	18057	1.3	21.2280	1.0	0.0856	2.0	0.0132	1.8	0.88	84.4	1.5	83.4	1.6	54.7	23.4	84.4	1.5
Spot 39	369	3399	1.6	21.4790	1.6	0.0846	2.2	0.0132	1.5	0.71	84.4	1.3	82.5	1.7	26.6	37.2	84.4	1.3
Spot 40	217	2245	1.7	22.1967	2.3	0.0844	3.0	0.0136	1.9	0.62	87.0	1.6	82.3	2.3	52.8	56.3	87.0	1.6
Spot 45	209	2291	1.1	16.8896	2.3	0.1146	2.9	0.0140	1.8	0.61	89.9	1.6	110.2	3.0	574.8	49.7	89.9	1.6
Spot 43	989	33297	1.0	19.9714	0.8	0.0993	1.6	0.0144	1.4	0.85	92.1	1.2	96.2	1.5	198.3	19.2	92.1	1.2
Spot 44	623	548	2.0	6.0086	4.0	0.3413	4.8	0.0149	2.6	0.55	95.2	2.5	298.2	12.3	2522.0	66.8	95.2	2.5

Table 37. U-Pb geochronological analyses for sample 14710A.

		Isotope ratios									Apparent ages (Ma)							
Analysis	U (ppm)	$^{206}Pb/^{204}Pb$	U/Th	$^{206}Pb/^{207}Pb$	± (%)	$^{207}Pb/^{235}U$	± (%)	$^{206}Pb/^{238}U$	± (%)	error corr.	$^{206}Pb/^{238}U$	± (Ma)	$^{207}Pb/^{235}U$	± (Ma)	$^{206}Pb/^{207}Pb$	± (Ma)	Best age (Ma)	± (Ma)
14710A-3R	582	63097	3.4	17.1910	0.7	0.7043	1.3	0.0878	1.1	0.83	542.6	5.5	541.3	5.3	536.2	15.5	542.6	5.5
14710A-3C	79	38930	2.1	5.8843	0.8	11.8828	1.6	0.5071	1.4	0.87	2644.3	30.1	2595.2	14.9	2557.1	13.1	2557.1	13.1
14710A-3R	91	81168	2.3	5.8650	0.7	11.3314	2.9	0.4820	2.8	0.97	2536.0	59.7	2550.8	27.4	2562.6	12.0	2562.6	12.0
14710A-1	75	50270	2.2	5.8252	0.7	11.9024	1.5	0.5029	1.3	0.87	2626.1	28.1	2596.8	14.1	2574.0	12.5	2574.0	12.5
14710A-4R	218	19764	1.7	5.4984	0.6	10.2141	2.2	0.4073	2.1	0.96	2202.7	39.0	2454.4	20.2	2670.0	10.7	2670.0	10.7
14710A-2C	1432	1114	0.6	4.1445	2.9	2.8335	4.1	0.0852	2.9	0.70	526.9	14.6	1364.4	30.8	3128.5	46.5	3128.5	46.5

Table 38. Summary of the new ages for the Ica-Pisco plutons. The sample 14713C has inherited zircons with ages possibly associated with the Paleozoic basement rocks in this area. Samples listed in order from oldest to youngest.

Sample	Pluton	Rock Type	# Zircons	# Spots	Th-U ratio	Apparent Age $^{206}Pb/^{238}U$	Weighted Mean $^{206}Pb/^{238}U$ Age
15826D	Incahuasi	Granodiorite	300	68	0.6-1.8	57-64	58.9±0.6
14710F	Incahuasi	Granodiorite	20	25	1.1-1.8	64-69	68.0±0.9
15826Ca	Tiabaya	Gabbro	10	35	0.1-3.2	81.8-94.9	85.3±1.3
15826Fa	Tiabaya	Granodiorite	14	11	1.0-2.0	81-95	84.4±2.7
10714P	Pampahuasi	Tonalite	21	25	13-2.8	90-96	91.4±1.4
14715G	Pampahuasi	Qz-Diorite	19	19	0.8-2.6	94-103	97.8±0.7
14727U	Linga Rinconada	Granite	32	35	1.1-4.9	95-107	98.3±1.9
14721Ac	Linga Auquish	Monzonite	60	15	0.4-1.2	103-106	104.8±0.4
15826Aa	Pre-PCB Gabbro	Gabbro	7	23	1.0-1.4	127-135	131.0±1.5
14713C	Pre-PCB Gabbro	Gabbro	2	10	1.2-3.0	378-538	No concordia
14710A	Quilmana	Basaltic andesite	3	6	1.7-3.4	542-2670	No concordia

REFERENCES

Gehrels, G. (2011) Detrital Zircon U-Pb Geochronology: Current Methods and New Opportunities. Tectonics of Sedimentary Basins, p. 45-62. John Wiley & Sons, Ltd.

-. (2014) Detrital Zircon U-Pb Geochronology Applied to Tectonics. Annual Review of Earth and Planetary Sciences, 42(1), 127-149.

Gehrels, G., and Pecha, M. (2014) Detrital zircon U-Pb geochronology and Hf isotope geochemistry of Paleozoic and Triassic passive margin strata of western North America. Geosphere, 10(1), 49-65.

Johnston, S., Gehrels, G., Valencia, V., and Ruiz, J. (2009) Small-volume U–Pb zircon geochronology by laser ablation-multicollector-ICP-MS. Chemical Geology, 259(3–4), 218-229.

Steiger, R.H., and Jäger, E. (1977) Subcommission on geochronology: Convention on the use of decay constants in geo- and cosmochronology. Earth and Planetary Science Letters, 36(3), 359-362.

Wetherill, G.W. (1956) Discordant uranium-lead ages, I. Eos, Transactions American Geophysical Union, 37(3), 320-326.

APPENDIX F

REFERENCES FOR ZIRCON DATA FROM DEFINED ARC SECTORS

The data analysis for the Cordilleran margin is divided into 8 arc sectors, including from north (British Columbia) to south (Patagonia): (A) the Coast Ranges, (B) the Sierra Nevada, (C) the Peninsular Ranges to Mojave, (D) southeastern Mexico and Central America, (E) the northern Andes, (F) the Peruvian Andes, (G) the south-central Andes, and (H) the southern Andes. The zircon data used are from bedrock and detrital zircon ages and the age compilation is complemented with whole rock geochemical data. The references for the age compilations and geochemical data for each arc sector are presented in the following paragraphs.

Bedrock Ages

(A) Alldrick et al. (2001); Andronicos et al. (2003); Butler et al. (2002, 2006); Crawford et al. (1999, 2009); Diakow (2006); Friedman and Mortensen (2002); Friedman et al. (2001); Gareau (1991a,b); Gareau et al. (1997); Gehrels (2000, 2001); Gehrels and Boghossian (2000); Gehrels et al. (1991, 2006, 2009); Haggart et al. (2006a,b); Klepeis et al. (1998); Klepeis and Crawford (1999); Mahoney et al. (2007a,b,c,d,e, 2009); Ray et al. (1998); Rusmore et al. (2000, 2001, 2005); Saleeby (2000); van der Heyden (1989, 2004)

(B) Paterson (unpublished)

(C) A. Iriondo (pers. comm., 2011, in Arvizu, 2012); A. Velázquez-Santelis (pers. comm., 2011, in Arvizu, 2012); Anderson and Silver (1979); Anderson et al. (1980, 2005); Arvizu (2012); Arvizu et al. (2009); Barth and Wooden (2006); Barth et al. (1990); Castineiras (pers. comm. in Izaguirre, 2009); Damon et al. (1983); Fackler-

Adams et al. (1997); Gilbert (2012); González-León et al. (2008); Haxel et al. (2005); Henry et al. (2003); Iriondo (2001); Iriondo and McDowell (2011); Iriondo et al. (2005); Izaguirre (2009); Johnson et al. (1999a,b, 2003); Kimbrough and Moore (2003); Kimbrough et al. (2001); Lawton et al. (2012); Leggett (2008); M. Enríquez (pers. comm., 2011, in Arvizu, 2012); Mauel et al. (2011); McDowell et al. (2001); Miller et al. (1995); Ortega-Rivera et al. (1997); Peña-Alonso et al. (2012); Pérez-Segura et al. (2009, 2013); Peryam et al. (2011); Poole et al. (1991); Premo and Morton (2014); Premo et al. (2014a,b); Ramos-Velázquez et al. (2008); Riggs et al. (1993); Schmidt and Paterson (2002); Snow et al. (1991); Spencer et al. (2011); Valencia et al. (2006); Vega-Granillo et al. (2008, 2011, 2012, 2013)

(D) Alaniz-Álvarez et al. (1996); Barboza-Gudiño et al. (2004, 2008); Bissig et al. (2008); Campa Uranga et al. (2004,2012); Campa-Uranga and Iriondo (2004); Centeno-García et al. (2011); Ducea et al. (2004); Elías-Herrera and Ortega-Gutiérrez (2002); Elías-Herrera et al. (2000, 2005, 2007, 2011); Fastowsky et al. (2005); Ferrari et al. (2014); Garza-Gonzales (2007); Godinez-Urban et al. (2011); Hernández-Pineda et al. (2011); Jones et al. (1995); Keppie et al. (2004); Kirsch et al. (2012, 2014); Lawton and Molina-Garza (2014); Martens et al. (2012); Martini et al. (2009, 2011); Martiny et al. (2000); Mortensen et al. (2008); Murillo-Muñeton (1994); Ortega-Obregón et al. (2009, 2012, 2014); Ramos-Arias and Keppie (2011); Ratschbacher et al. (2009); Solari et al. (2001, 2007, 2010, 2011); Torres de León et al. (2012); Valencia et al. (2009, 2013); Weber et al. (2005, 2007); Yañez et al. (1991); Zavala-Monsivais et al. (2009, 2012)

(E) Aspden et al. (1995); Bustamante et al. (2010); Cardona et al. (2010a,b); Chew et al. (2008); Chiariadia et al. (2009); Cochrane (2013); Cochrane et al. (2014);

Litherland et al. (1994); Mantilla Figueroa et al. (2013); Martínez (2007); Montes et al. (2010); Restrepo et al. (2011); Riel et al. (2013); Schütte et al. (2010); Vallejo et al. (2006); van der Lelij (2013); Villagomez et al. (2011); Vinasco et al. (2006); Viscarret et al. (2009); Weber et al. (2010); Winter (2008)

(F) Boekhout et al. (2012, 2013); Cardona (2006); Cardona et al. (2009); Chew et al. (2007); Dalmayrac et al. (1980); de Haller et al. (2006); Demouy et al. (2012); Lancelot (1978); Lipa (2005); Marocco (1978); Mišković et al. (2009, in press); Mukasa (1984, 1986a,b); Mukasa & Tilton (1985a,b); Polliand et al. (2005); Romero et al. (2013); Schaltegger et al. (2008); Sillitoe & Mortensen (2010); Vidal et al. (1995); Witt et al. (2013)

(G) Aguirre-Urreta et al. (2008); Alasino et al. (2012); Alessandretti et al. (2013); Álvarez et al. (2011); Barredo et al. (2012); Coloma et al. (2012); Dahlquist and Alasino (2012); Dahlquist et al. (2006, 2013); Damm et al. (1986); Deckart et al. (2014); Grosse et al. (2009); Gulbranson et al. (2010); Hervé et al. (2013, 2014); Jara and Charrier (2014); Maksaev (1990); Maksaev et al. (2006, 2009, 2010, 2014); Mancuso et al. (2010); Martin et al. (1999); Martina et al. (2011); Masterman (2003); Munizaga et al. (2008); Pankhurst et al. (1996, 2006); Parada et al. (2005); Pineda and Calderón (2008); Poma et al. (2014); Rocha-Campos et al. (2011); Rossel et al. (2013); Salazar et al. (2009); Schiuma and Llambías (2008); Söllner et al. (2007); Tornos et al. (2010); Vásquez Illanes (2008); Vennari et al. (2014); Willner et al. (2008)

(H) Aragón et al. (2011); Barbeau et al. (2009a,b); Benedini and Gregori (2013); Bruce et al. (1991); Calderón et al. (2007); Castro et al. (2011); Césari et al. (2011); Chernicoff et al. (2013); Cúneo et al. (2013); Deckart et al. (2014); Hervé et al. (2007,

2013); Kohn et al. (1995); Martin et al. (2001); Pankhurst et al. (1999, 2006); Parada et al. (1997); Rapela et al. (2005); Rolando et al. (2004); Suárez et al. (2009, 2010, 2014); Varela et al. (2005, 2012)

Detrital Zircon Ages

(A) Dumitru et al. (2013); Fuentes et al. (2011); Laskowski et al. (2013); Leier and Gehrels (2011); Paterson (unpublished); Raines et al. (2013); Surpless and Beverly (2013)

(B) Barbeau et al. (2005); Dickinson and Gehrels (2008); Dumitru et al. (2013); Gehrels and Pecha (2014); Grove (pers. comm. to Paterson); Laskowski et al. (2013); Lawton and Bradford (2011); Lawton et al. (2010); Morgan et al. (2005); Paterson (unpublished); Riggs et al. (2012, 2013); Sharman et al. (2013, 2014)

(C) Alsleben et al. (2012); Fletcher et al. (2007); Gehrels (pers. comm. to Paterson); Gehrels and Pecha (2014); Gehrels and Stewart (1998); Gonzáles-León et al. (2005, 2009, 2011); Jacobson et al. (2011); Kimbrough et al. (2001); Mauel et al. (2011); Peryam et al. (2011); Pompa-Mera et al. (2013); Premo and Morton (2014); Sharman et al. (2014); Spencer et al. (2011)

(D) Barboza-Gudiño (2012); Barboza-Gudiño et al. (2010, 2012); Campos-Madrigal et al. (2013); Centeno-García et al. (2011); Escalona-Alcázar et al. (2009); Gillis et al. (2005); Godínez-Urban et al. (2011); Grodzicki et al. (2008); Helbig et al. (2012); Hinojosa-Prieto et al. (2008); Keppie et al. (2008); Kirsch et al. (2012); Lawton and Molina-Garza (2014); Lawton et al. (2009); Martini et al. (2009, 2011); Mendoza-Rosales et al. (2010); Morales-Gámez et al. (2008); Ocampo-Díaz et al. (2014); Ortega-

Flores et al. (2014); Ortega-Obregón et al. (2009); Palacios-García and Martini (2014); Pérez-Gutiérrez et al. (2009); Ramos-Arias and Keppie (2011); Rubio-Cisneros and Lawton (2011); Silva-Romo et al. (2015); Solari et al. (2010); Talavera-Mendoza et al. (2007, 2013); Torres de León et al. (2012); Valencia et al. (2013); Venegas-Rodríguez et al. (2009); Witt et al. (2012)

(E) Ayala et al. (2009, 2012); Bande et al. (2012); Cardona et al. (2010a,b, 2012); Chew et al. (2007); Cochrane (2013); Horton et al. (2010a,b); Mantilla Figueroa et al. (2013); Nie et al. (2010, 2012); Saylor et al. (2011, 2012); Weber et al. (2010); Xie et al. (2010); Zapata et al. (2009)

(F) Boekhout et al. (2013); Cardona et al. (2009); Decou et al. (2013); Leier et al. (2010); Michalak (2013); Reimann et al. (2010); Reitsma (2012)

(G) Álvarez et al. (2011); Augustsson (2015); Bahlburg et al. (2009); Di Giulio et al. (2012); Encinas et al. (2014); Hervé et al (2013); Naipauer et al. (2012, 2014); Oliveros et al. (2012); Sagripanti et al. (2011); Tunik et al. (2010); Willner et al. (2008)

(H) Augustsson et al. (2006); Barbeau et al. (2009a,b); Calderón et al. (2007); Chernicoff et al. (2013); Fildani et al. (2003); Hervé et al. (2003); Sepúlveda et al. (2010).

Geochemistry

(B) Barth et al. (2011); Bateman and Chappell (1979); Bateman et al. (1988); Burgess (2006); Chen and Moore (1982); Chen and Tilton (1991); Coleman et al. (2012); Economos et al. (2008, 2010); Frost (1988); Frost et al. (1988); Gray (2008); Kistler et al. (1986); Kistler and Ross (1990); Kylander-Clark et al. (2005); Loetterle (2008); Memeti

(2009); Peck et al. (1983); Ratajeski et al. (2001); Reid et al. (1983); Saleeby et al. (1988, 1990, 2007); Solgadi and Sawyer (2008); Stern et al. (1982); Zak et al. (2009)

(C) Allen, C.M. (1989); Allen, E.F. (2007); Anderson and Rowley (1982); B. John, T. Cameron, and J. Lawford Anderson (unpublished); Barth (1989, 1990); Barth et al. (1990); Beckerman et al. (1982); Beckerman (1982); Brand (1985); Davis and Wooden (1989); DePaolo (1981); Farber (thesis); Fox et al. (1989); Fox and Miller (1990); Frizzell et al. (1986); Glazner et al. (2008); Hayes (1992); Herzig (1991); Hill (1986); Ianno (unpublished); Ianno and Hartman (unpublished); Ianno and Paterson (unpublished); J. Brand and Lawford Anderson (unpublished); J. Morrison and D. Miller (unpublished); Kistler (1983, 2014); Kistler and Lee (1989); J.L. Anderson (unpublished); Lee (1984); Mayo (dissertation); Miller (1977); Miller and Glazner (1995); Miller and Young; Miller et al. (1990, 1995) ; Morton (2014); Ramo et al. (2002); Wooden and Barth (unpublished data); Young (1990); Young et al. (1992)

(D) Centeno-García (1994); Centeno-García and Silva-Romo (1997); Centeno-García et al. (1993); Elías-Herrera (2003); Elías-Herrera et al. (2005); Freydier et al. (1996a,b); Galaz et al. (2013); Garza-González (2007); Grajales-Nishimura et al. (1999); Helbig et al. (2012); Helbig, unpublished; Kirsch et al. (2012, 2014); Lapierre et al. (1992); Martiny (2008); Ortega-Obregón et al. (2010); Rosales-Lagarde et al. (2005); Schaaf et al. (2002); Solari et al. (2010); Talavera-Mendoza (2000); Tardy et al. (1994); Torres et al. (1999); Valencia-Moreno et al. (2001); Yañez et al. (1991).

REFERENCES

References for Bedrock Zircon Ages

Aguirre-Urreta, M.B., Pazos, P.J., Lazo, D.G., Fanning, C.M., Litvak, V.D., 2008. First U-Pb SHRIMP age of the Hauterivian stage, Neuquén Basin, Argentina: Journal of South American Earth Sciences, v. 26, p. 91–99.

Alaniz-Álvarez, S.A., van der Heyden, P., Samaniego, A.F.N., and Ortega-Gutiérrez, F., 1996, Radiometric and kinematic evidence for Middle Jurassic strike-slip faulting in southern Mexico related to the opening of the Gulf of Mexico: Geology, v. 24, p. 443–446, doi: 10.1130/0091-7613(1996)024<0443.

Alasino, P.H., Dahlquist, J.A., Pankhurst, R.J., Galindo, C., Casquet, C., Rapela, C.W., Larrovere, M.A., and Fanning, C.M., 2012, Early Carboniferous sub- to mid-alkaline magmatism in the Eastern Sierras Pampeanas, NW Argentina: A record of crustal growth by the incorporation of mantle-derived material in an extensional setting: Gondwana Research, v. 22, p. 992–1008, doi: 10.1016/j.gr.2011.12.011.

Alessandretti, L., Philipp, R.P., Chemale, F., Jr, Brückmann, M.P., Zvirtes, G., Matté, V., and Ramos, V.A., 2013, Provenance, volcanic record, and tectonic setting of the Paleozoic Ventania Fold Belt and the Claromecó Foreland Basin: Implications on sedimentation and volcanism along the southwestern Gondwana margin: Journal of South American Earth Sciences, v. 47, p. 12–31, doi: 10.1016/j.jsames.2013.05.006.

Alldrick, D.J., 2001, Geology and mineral deposits of the Ecstall belt, northwest British Columbia, in Geological Fieldwork 1999, Paper 2000-1, B.C. Ministry of Energy and Mines, p. 279–306.

Álvarez, J., Mpodozis, C., Arriagada, C., Astini, R., Morata, D., Salazar, E., Valencia, V.A., and Vervoort, J.D., 2011, Detrital zircons from late Paleozoic accretionary complexes in north-central Chile (28°–32°S): Possible fingerprints of the Chilenia terrane: Journal of South American Earth Sciences, v. 32, p. 460–476, doi: 10.1016/j.jsames.2011.06.002.

Anderson, T. H., and Silver, L. T., 1979, The role of the Mojave-Sonora megashear in the tectonic evolution of northern Sonora, in Anderson, T. H., and Roldan-Quintana, J., eds., Geology of Northern Sonora: Field Trip Guidebook for the 1979 Annual Meeting in San Diego, Geological Society of America, Boulder, Colorado, p. 59–68.

Anderson, T. H., L. T. Silver, and G. A. Salas, 1980, Distribution and U-Pb isotope ages of some lineated plutons, northwestern Mexico, in Crittenden, Sr., Coney, P.J., and Davis, G.H., eds., Cordilleran metamorphic core complexes: Geological Society of America Memoir, v. 153, p. 269–283.

Anderson, T.H., Rodríguez-Castañeda, J.L., and Silver, L.T., 2005, Jurassic rocks in Sonora, Mexico: Relations to the Mojave-Sonora megashear and its inferred northwestward extension, in Anderson, T.H., Nourse, J.A., McKee, J.W., and Steiner, M.B., eds., The Mojave-Sonora Megashear Hypothesis: Development, Assessment, and Alternatives: Geological Society of America Special Papers, v. 393, p. 51–95.

Andronicos, C.L., Chardon, D.H., Hollister, L.S., Gehrels, G.E., and Woodsworth, G.J., 2003, Strain partitioning in an obliquely convergent orogen, plutonism, and synorogenic collapse: Coast Mountains Batholith, British Columbia, Canada: Tectonics, v. 22, p. 1012, doi: 10.1029/2001TC001312.

Aragón, E., Castro, A., Díaz-Alvarado, J., and Liu, D.Y., 2011, The North Patagonian batholith at Paso Puyehue (Argentina-Chile). SHRIMP ages and compositional features: Journal of South American Earth Sciences, v. 32, p. 547–554, doi: 10.1016/j.jsames.2011.02.005.

Arvizu, H.E., 2012, Magmatismo permo-triásico en el NW de Sonora, México: Inicio de la subducción y maduración de un margen continental activo [M.Sc. thesis]: Universidad Nacional Autónoma de México, Centro de Geociencias, Querétaro, Mexico, 250 p.

Arvizu, H.E., Iriondo, A., Izaguirre, A., Chávez-Cabello, G., Kamenov, G.D., Solís-Pichardo, G., Foster, D.A., and Cruz, R.L.-S., 2009, Rocas graníticas pérmicas en la Sierra Pinta, NW de Sonora, México: Magmatismo de subducción asociado al inicio del margen continental activo del SW de Norteamérica: Revista Mexicana de Ciencias Geológicas, v. 26, p. 709–728.

Aspden, J. A., Bonilla, W., and Duque, P., 1995, The El Oro metamorphic complex Ecuador: Geology and economic mineral deposits: Overseas Geology and Mineral Resources, v. 67, 63 p.

Barbeau, D.L., Jr., Gombosi, D.J., Zahid, K.M., Bizimis, M., Swanson-Hysell, N., Valencia, V., and Gehrels, G.E., 2009, U-Pb zircon constraints on the age and provenance of the Rocas Verdes basin fill, Tierra del Fuego, Argentina: Geochemistry, Geophysics, Geosystems, v. 10, Q12001, doi:10.1029/2009GC002749.

Barbeau, D.L., Jr., Olivero, E.B., Swanson-Hysell, N.L., Zahid, K.M., Murray, K.E., and Gehrels, G.E., 2009, Detrital-zircon geochronology of the eastern Magallanes foreland basin: Implications for Eocene kinematics of the northern Scotia Arc and Drake Passage: Earth and Planetary Science Letters, v. 284, p. 489–503, doi: 10.1016/j.epsl.2009.05.014.

Barboza-Gudiño, J.R., Hoppe, M., Gómez-Anguiano, M., and Martínez-Macías, P.R., 2004, Aportaciones para la interpretación estratigráfica y estructural de la porción noroccidental de la Sierra de Catorce, San Luis Potosí, México: Revista Mexicana de Ciencias Geológicas, v. 21, p. 299–319.

Barboza-Gudiño, J.R., Orozco-Esquivel, M.T., Gómez-Anguiano, M., and Zavala-Monsiváis, A., 2008, The Early Mesozoic volcanic arc of western North America in northeastern Mexico: Journal of South American Earth Sciences, v. 25, p. 49–63.

Barredo, S., Chemale, F., Marsicano, C., Ávila, J.N., Ottone, E.G., and Ramos, V.A., 2012, Tectono-sequence stratigraphy and U–Pb zircon ages of the Rincón Blanco Depocenter, northern Cuyo Rift, Argentina: Gondwana Research, v. 21, p. 624–636, doi: 10.1016/j.gr.2011.05.016.

Barth, A.P., and Wooden, J.L., 2006, Timing of magmatism following initial convergence at a passive margin, southwestern U.S. Cordillera, and ages of lower crustal magma sources: Journal of Geology, v. 114, p. 231–245.

Barth, A.P., Tosdal, R.M., and Wooden, J.L., 1990, A petrologic comparison of Triassic plutonism in the San Gabriel and Mule Mountains, Southern California: Journal of Geophysical Research, v. 95, p. 20075–20096.

Benedini, L., and Gregori, D., 2013, Significance of the Early Jurassic Garamilla formation in the western Nordpatagonian Massif: Journal of South American Earth Sciences, v. 45, p. 259–277, doi: 10.1016/j.jsames.2013.03.016.

Bissig, T., Mortensen, J.K., Tosdal, R.M., and Hall, B.V., 2008, The rhyolite-hosted volcanogenic massive sulfide District of Cuale, Guerrero terrane, West-Central Mexico: silver-rich, base metal mineralization emplaced in a shallow marine continental margin setting: Economic Geology, v. 103, p. 141–159.

Boekhout, F., Spikings, R., Sempere, T., Chiaradia, M., Ulianov, A., and Schaltegger, U., 2012, Mesozoic arc magmatism along the southern Peruvian margin during Gondwana breakup and dispersal: Lithos, v. 146-147, p. 48–64, doi: 10.1016/j.lithos.2012.04.015.

Boekhout, F., Sempere, T., Spikings, R., and Schaltegger, U., 2013, Late Paleozoic to Jurassic chronostratigraphy of coastal southern Peru: Temporal evolution of sedimentation along an active margin: Journal of South American Earth Sciences, v. 47, p. 179–200, doi: 10.1016/j.jsames.2013.07.003.

Bruce, R.M., Nelson, E.P., Weaver, S.G., and Lux, D.R., 1991, Temporal and spatial variations in the southern Patagonian batholith; Constraints on magmatic arc development: Geological Society of America Special Papers, v. 265, p. 1–12.

Bustamante, C., Cardona, A., Bayona, G., Mora, A., Valencia, V., Gehrels, G., and Vervoort, J., 2010, U-Pb LA-ICP-MS geochronology and regional correlation of Middle Jurassic intrusive rocks from the Garzon Massif, Upper Magdalena Valley and Central Cordillera, southern Colombia: Boletín de Geología, v. 32, p. 1–17.

Butler, R.F., Gehrels, G.E., Baldwin, S.L., and Davidson, C., 2002, Paleomagnetism and geochronology of the Ecstall pluton in the Coast Mountains of British Columbia:

Evidence for local deformation rather than large-scale transport: Journal of Geophysical Research: Solid Earth, v. 107, p. EPM 3–1–EPM 3–13, doi: 10.1029/2001JB000270.

Butler, R.F., Gehrels, G.E., Hart, W., Davidson, C., and Crawford, M.L., 2006, Paleomagnetism of Late Jurassic to mid-Cretaceous plutons near Prince Rupert, British Columbia, in Haggart, J.W., Enkin, R.J., and Monger, J.W.H., eds., Paleogeography of the North American Cordillera: Evidence For and Against Large- Scale Displacements: Geological Association of Canada Special Paper 46, p. 171–200.

Calderón, M., Fildani, A., Hervé, F., Fanning, C.M., Weislogel, A., and Cordani, U., 2007, Late Jurassic bimodal magmatism in the northern sea-floor remnant of the Rocas Verdes basin, southern Patagonian Andes: Journal of the Geological Society, London, v. 164, p. 1011–1022.

Campa-Uranga, M.F., and Iriondo, A., 2004, Significado de dataciones Cretácicas de los arcos volcánicos de Taxco, Taxco Viejo y Chapolapa, en la evolución de la plataforma Guerrero-Morelos: GEOS Unión Geofísica Mexicana, v. 24, p. 173.

Campa-Uranga, M.F., García Díaz, J.L., and Iriondo, A., 2004, El arco sedimentario del Jurásico Medio (Grupo Tecocoyunca y Las Lluvias) de Olinalá: GEOS Unión Geofísica Mexicana, v. 24, p. 174.

Campa-Uranga, M.F., Torres de León, R., Iriondo, A., and Premo, W.R., 2012, Caracterización geológica de los ensambles metamórficos de Taxco y Taxco el Viejo, Guerrero, México: Boletín de la Sociedad Geológica Mexicana, v. 64, p. 369–385.

Cardona, A., Cordani, U.G., and MacDonald, W.D., 2006, Tectonic correlations of pre-Mesozoic crust from the northern termination of the Colombian Andes, Caribbean region: Journal of South American Earth Sciences, v. 21, p. 337–354.

Cardona, A., Cordani, U.G., Ruiz, J., Valencia, V.A., Armstrong, R., CHEW, D., Nutman, A., and Sánchez, A.W., 2009, U-Pb Zircon Geochronology and Nd Isotopic Signatures of the Pre-Mesozoic Metamorphic Basement of the Eastern Peruvian Andes: Growth and Provenance of a Late Neoproterozoic to Carboniferous Accretionary Orogen on the Northwest Margin of Gondwana: The Journal of Geology, v. 117, p. 285–305, doi: 10.1086/597472.

Cardona, A., Valencia, V.A., Bayona, G., Duque, J., Ducea, M., Gehrels, G., Jaramillo, C., Montes, C., Ojeda, G., and Ruiz, J., 2010, Early-subduction-related orogeny in the northern Andes: Turonian to Eocene magmatic and provenance record in the Santa Marta Massif and Rancheria Basin, northern Colombia: Terra Nova, v. 23, p. 26–34, doi: 10.1111/j.1365-3121.2010.00979.x.

Cardona, A., Valencia, V., Garzón, A., Montes, C., Ojeda, G., Ruiz, J., Weber, M., 2010. Permian to Triassic I to S-type magmatic switch in the northeast Sierra Nevada de

Santa Marta and adjacent regions, Colombian Caribbean: tectonic setting and implications within Pangea paleogeography. Journal of South American Earth Sciences, v. 29, p. 772–783.

Castro, A., Moreno-Ventas, I., Fernàndez, C., Vujovich, G., Gallastegui, G., Heredia, N., Martino, R.D., Becchio, R., Corretgé, L.G., Díaz-Alvarado, J., Such, P., García-Arias, M., and Liu, D.Y., 2011, Petrology and SHRIMP U–Pb zircon geochronology of Cordilleran granitoids of the Bariloche area, Argentina: Journal of South American Earth Sciences, v. 32, p. 508–530, doi: 10.1016/j.jsames.2011.03.011.

Centeno-García, E., Busby, C., Busby, M., and Gehrels, G., 2011, Evolution of the Guerrero composite terrane along the Mexican margin, from extensional fringing arc to contractional continental arc: Geological Society of America Bulletin, v. 123, p. 1776–1797, doi: 10.1130/B30057.1.

Césari, S.N., Limarino, C.O., Llorens, M., Passalia, M.G., Loinaze, V.P., and Vera, E.I., 2011, Journal of South American Earth Sciences: Journal of South American Earth Sciences, v. 31, p. 426–431, doi: 10.1016/j.jsames.2011.03.012.

Chernicoff, C.J., Zappettini, E.O., Santos, J.O., McNaughton, N.J., and Belousova, E., 2013, Combined U-Pb SHRIMP and Hf isotope study of the Late Paleozoic Yaminué Complex, Rio Negro Province, Argentina: Implications for the origin and evolution of the Patagonia composite terrane: Geoscience Frontiers, v. 4, p. 37–56, doi: 10.1016/j.gsf.2012.06.003.

Chew, D.M., Schaltegger, U., Košler, J., Whitehouse, M.J., Gutjahr, M., Spikings, R.A., and Miscovic, A., 2007, U-Pb geochronologic evidence for the evolution of the Gondwanan margin of the north-central Andes: Geological Society of America Bulletin, v. 119, p. 697–711, doi: 10.1130/B26080.1.

Chew, D.M., Magna, T., Kirkland, C.L., Mišković, A., Cardona, A., Spikings, R., and Schaltegger, U., 2008, Detrital zircon fingerprint of the Proto-Andes: Evidence for a Neoproterozoic active margin?: Precambrian Research, v. 167, p. 186–200, doi: 10.1016/j.precamres.2008.08.002.

Chiaradia, M., Vallance, J., Fontboté, L., Stein, H., Schaltegger, U., Coder, J., Richards, J., Villeneuve, M., Gendall, I., 2009. U-Pb, Re-Os and 40Ar/39Ar geochronology of the Nambija Au-skarn and Pangui porphyry Cu deposits, Ecuador: implications for the Jurassic metallogenic belt of the northern Andes. Mineralium Deposita, v. 44, p. 371–387.

Cochrane, R., 2013, U-Pb thermochronology, geochronology and geochemistry of NW South America: Rift to drift transition, active margin dynamics and implications for the volume balance of continents [Ph.D. thesis]: Université de Genève, 209 p.

Cochrane, R., Spikings, R., Gerdes, A., Ulianov, A., Mora, A., Villagómez, D., Putlitz, B., and Chiaradia, M., 2014, Permo-Triassic anatexis, continental rifting and the

disassembly of western Pangaea: Lithos, v. 190-191, p. 383–402, doi: 10.1016/j.lithos.2013.12.020.

Coloma, F., Salazar, E. and Creixell, C., 2012. Nuevos antecedentes acerca de la construcción de los plutones Pérmicos y Permo-Triásicos en el valle del río Tránsito, Región de Atacama, Chile. XIII Congreso Geológico Chileno, Antofagasta, p. 330–332.

Crawford, M.L.L., Klepeis, K.A.A., Gehrels, G., and Isachsen, C., 1999, Batholith emplacement at mid-crustal levels and its exhumation within an obliquely convergent margin: the influence of granite emplacement on tectonics: Tectonophysics, v. 312, p. 57–78.

Crawford, M.L., Klepeis, K.A., Gehrels, G.E., and Lindline, J., 2009, Mid-Cretaceous–Recent crustal evolution in the central Coast orogen, British Columbia and southeastern Alaska, in Miller, R.B., and Snoke, A.W., eds., Crustal Cross-Sections from the Western North American Cordillera and Elsewhere: Implications for Tectonic and Petrologic Processes: Geological Society of America Special Paper 456, p. 97–124.

Cúneo, R., Ramezani, J., Scasso, R., Pol, D., Escapa, I., Zavattieri, A.M., and Bowring, S.A., 2013, High-precision U–Pb geochronology and a new chronostratigraphy for the Cañadón Asfalto Basin, Chubut, central Patagonia: Implications for terrestrial faunal and floral evolution in Jurassic: Gondwana Research, v. 24, p. 1267–1275, doi: 10.1016/j.gr.2013.01.010.

Dahlquist, J.A., and Alasino, P.H., 2012, Primera edad U-Pb en circon usando LA-ICP-MS de un dique traquiandesítico emplazado en el granito tipo a Los Árboles, Sierras Pampeanas Orientales: Revista de la Asociación Geológica Argentina, v. 69, p. 296–299.

Dahlquist, J.A., Pankhurst, R.J., Rapela, C.W., Casquet, C., Fanning, C.M., Alasino, P., and Baez, M., 2006, The San Blas Pluton: An example of Carboniferous plutonism in the Sierras Pampeanas, Argentina: Journal of South American Earth Sciences, v. 20, p. 341–350, doi: 10.1016/j.jsames.2005.08.006

Dahlquist, J.A., Alasino, P.H., and Bello, C., 2013, Devonian F-rich peraluminous A-type magmatism in the proto-Andean foreland (Sierras Pampeanas, Argentina): geochemical constraints and petrogenesis from the western-central region of the Achala batholith: Mineralogy and Petrology, v. 108, p. 391–417, doi: 10.1007/s00710-013-0308-0..

Dalmayrac, B., Laubacher, G., and Marocco, R., 1980, Géologie des Andes Péruviennes—Caractères généraux de l'évolution géologique des Andes Peruviennes: Traveaux et documents de l'office de la recherche scientifique et téchique Outre-Mer, Paris, v. 122, 507 p.

Damm, W., Pichowiak, S., and Todt, W., 1986, Geochemie, Petrologie und

Geochronologie der Plutonite und des metamorphen Grundgebirges in Nordchile: Berliner geowissenschaftliche Abhandlungen, v. A 66, p. 73–146.

Damon, P.E., Shafiqullah, M., and Clark, K.F., 1983, Geochronology of the porphyry copper deposits and related mineralization of Mexico: Canadian Journal of Earth Sciences, v. 20, no. 6, p. 1052–1071.

De Haller, A., Corfu, F., Fontboté, L., Schaltegger, U., Barra, F., Chiaradia, M., Frank, M., and Alvarado, J.Z., 2006, Geology, geochronology, and Hf and Pb isotope data of the Raúl-Condestable iron oxide-copper-gold deposit, central coast of Peru: Economic Geology, v. 101, p. 281–310.

Deckart, K., Hervé, F., Fanning, C.M., Ramírez, V., Calderón, M., and Godoy, E., 2014, U-Pb Geochronology and Hf-O Isotopes of zircons from the Pennsylvanian Coastal Batholith, South-Central Chile: Andean Geology, v. 41, p. 49–82, doi: 10.5027/andgeoV41n1-a03.

Demouy, S., Paquette, J.-L., de Saint Blanquat, M., Benoit, M., Belousova, E.A., O'Reilly, S.Y., García, F., Tejada, L.C., Gallegos, R., and Sempere, T., 2012, Spatial and temporal evolution of Liassic to Paleocene arc activity in southern Peru unraveled by zircon U–Pb and Hf in-situ data on plutonic rocks: Lithos, v. 155, p. 183–200, doi: 10.1016/j.lithos.2012.09.001.

Diakow, L.J., 2006, Geology of the Tahtsa Ranges between Eutsuk Lake and Morice Lake, Whitesail Lake Map Area, West-Central British Columbia: British Columbia Geological Survey Geoscience Map 2006–5, scale 1:150,000.

Ducea, M.N., Gehrels, G.E., Shoemaker, S., Ruiz, J., and Valencia, V.A., 2004, Geologic evolution of the Xolapa Complex, southern Mexico: Evidence from U-Pb zircon geochronology: Geological Society of America Bulletin, v. 116, p. 1016–1025.

Elías-Herrera, M., and Ortega-Gutiérrez, F., 2002, Caltepec fault zone: An Early Permian dextral transpressional boundary between the Proterozoic Oaxacan and Paleozoic Acatlán complexes, southern Mexico, and regional tectonic implications: Tectonics, v. 21, p. 1–19.

Elías-Herrera, M., Sánchez-Zavala, J.L., and Macías-Romo, C., 2000, Geologic and geochronologic data from the Guerrero terrane in the Tejupilco area, southern Mexico: new constraints on its tectonic interpretation: Journal of South American Earth Sciences, v. 13, p. 355–375.

Elías-Herrera, M., Ortega-Gutiérrez, F., Sánchez-Zavala, J.L., Macías-Romo, C., Ortega-Rivera, A., and Iriondo, A., 2005, La falla de Caltepec: raíces expuestas de una frontera tectónica de larga vida entre dos terrenos continentales del sur de México: Boletín de la Sociedad Geológica Mexicana, v. 57, p. 83–109.

Elías-Herrera, M., Sánchez-Zavala, J.L., Ortega-Gutiérrez, F., Iriondo, A., Macías-Romo, C., and Ángeles-Moreno, E., 2007, El margen septentrional del Complejo Xolapa

en el área de Zenzontepec, Oaxaca: restricciones geológicas y geocronológicas para la evolución tectónica del sur de México, in Simposio GeoChortis: La Conexión Chortis-Sur de México en el Tiempo y en el Espacio, abstract GC2007-06P.

Elías-Herrera, M., Ortega-Gutiérrez, F., Macías-Romo, C., Sánchez-Zavala, J.L., and Solari, L.A., 2011, Colisión oblicua del Cisuraliano-Guadalupiano entre bloques continentales en el sur de México: evidencias estratigráfico- estructurales y geocronológicas, in Simposio en Honor del Dr. Zoltan de Cserna, Libro de resúmenes, Mexico D.F., Instituto de Geología, UNAM, p. 159–164.

Fackler-Adams, B.N., Busby, C.J., and Mattinson, J.M., 1997, Jurassic magmatism and sedimentation in the Palen Mountains, southeastern California: Implications for regional tectonic controls on the Mesozoic continental arc: Geological Society of America Bulletin, v. 109, p. 1464–1484.

Fastovsky, D.E., Hermes, O.D., Strater, N.H., Bowring, S.A., Clark, J.M., Montellano, M., and Rene, H.R., 2005, Pre–Late Jurassic, fossil-bearing volcanic and sedimentary red beds of Huizachal Canyon, Tamaulipas, Mexico, in Anderson, T.H., Nourse, J.A., McKee, J.W., and Steiner, M.B. eds., The Mojave-Sonora Megashear hypothesis: development, assessment, and alternatives, Geological Society of America Special Paper 393, p. 401–426.

Ferrari, L., Bergomi, M., Martini, M., Tunesi, A., Orozco-Esquivel, T., and López-Martínez, M., 2014, Late Cretaceous - Oligocene magmatic record in southern Mexico: The case for a temporal slab window along the evolving Caribbean-North America-Farallon triple boundary: Tectonics, v. 33, p. 1738–1765, doi:10.1002/2014TC003525.

Friedman, R.M., and Mortensen, J.K., 2002, U-Pb zircon and titanite dating in support of British Columbia Geological Survey regional mapping studies, in Geological Fieldwork 2001: British Columbia Ministry of Energy and Mines Paper 2002–1, p. 135–149.

Friedman, R.M., Gareau, S.A., and Woodsworth, G.J., 2001, U-Pb dates from the Scotia-Quaal metamorphic belt, Coast Plutonic Complex, central-western British Columbia: Geological Survey of Canada Current Research 2001–F9 14, 7 p.

Gareau, S.A., 1991a, Geology of the Scotia-Quaal Metamorphic Belt, Coast Plutonic Complex, British Columbia [Ph.D. thesis]: Ottawa, Canada, Carleton University, 390 p.

Gareau, S.A., 1991b, The Scotia-Quaal metamorphic belt: A distinct assemblage with pre–early Late Cretaceous deformational and metamorphic history, Coast Plutonic Complex, British Columbia: Canadian Journal of Earth Sciences, v. 28, p. 870–880.

Gareau, S.A., Friedman, R.M., Woodsworth, G.J., and Childe, F., 1997, U-Pb ages from

the northeastern quadrant of Terrace map area, west-central British Columbia: Geological Survey of Canada Current Research 1997-A, p. 31–40.

Garza-González, E.C., 2007, Metalogenia del porfido de cobre de Tiámaro, Estado de Michoacán [Ph.D. thesis]: Universidad Nacional Autónoma de México, Mexico, 279 p.

Gehrels, G., Rusmore, M., Woodsworth, G., Crawford, M., Andronicos, C., Hollister, L., Patchett, J., Ducea, M., Butler, R., Klepeis, K., Davidson, C., Friedman, R., Haggart, J., Mahoney, B., et al., 2009, U-Th-Pb geochronology of the Coast Mountains batholith in north-coastal British Columbia: Constraints on age and tectonic evolution: Geological Society of America Bulletin, v. 121, p. 1341–1361, doi: 10.1130/B26404.1.

Gehrels, G.E., 2000, Reconnaissance geology and U-Pb geochronology of the west flank of the Coast Mountains between Juneau and Skagway, southeastern Alaska: Geological Society of America Special Papers 343, p. 213–233.

Gehrels, G.E., 2001, Geology of the Chatham Sound region, southeast Alaska and coastal British Columbia: Canadian Journal of Earth Sciences, v. 38, p. 1579–1599, doi: 10.1139/cjes-38-11-1579.

Gehrels, G.E., and Boghossian, N.D., 2000, Reconnaissance geology and U-Pb geochronology of the west flank of the Coast Mountains between Bella Coola and Prince Rupert, coastal British Columbia: Geological Society of America Special Papers 343, p. 61–75.

Gehrels, G.E., McClelland, W.C., Samson, S.D., Patchett, P.J., and Brew, D.A., 1991, U–Pb geochronology of Late Cretaceous and early Tertiary plutons in the northern Coast Mountains batholith: Canadian Journal of Earth Sciences, v. 28, p. 899–911, doi: 10.1139/e91-082.

Gehrels, G., Valencia, V., and Pullen, A., 2006, Detrital zircon geochronology by laser ablation multicollector ICPMS at the Arizona LaserChron Center, in Olszewski, T. ed., Geochronology: emerging opportunities, The Paleontological Society Short Course v. 12, p. 67–76.

Gehrels, G., Rusmore, M., Woodsworth, G., Crawford, M., Andronicos, C., Hollister, L., Patchett, J., Ducea, M., Butler, R., Klepeis, K., Davidson, C., Friedman, R., Haggart, J., Mahoney, B., et al., 2009, U-Th-Pb geochronology of the Coast Mountains batholith in north-coastal British Columbia: Constraints on age and tectonic evolution: Geological Society of America Bulletin, v. 121, p. 1341–1361, doi: 10.1130/B26404.1.

Gilbert, J.C., 2012, Age and Provenance of the Glance Conglomerate, Morita Formation, and Equivalent Strata from U-Pb Geochronology, Southeastern Arizona and Southwestern New Mexico [M.S. thesis]: Las Cruces, New Mexico, New Mexico State University, 181 p.

Godínez-Urban, A., Lawton, T.F., Molina-Garza, R.S., Iriondo, A., Weber, B., and López-Martínez, M., 2011, Jurassic volcanic and sedimentary rocks of the La Silla and Todos Santos Formations, Chiapas: Record of Nazas arc magmatism and rift-basin formation prior to opening of the Gulf of Mexico: Geosphere, v. 7, p. 121–144.

González-León, C.M., Scott, R.W., Löser, H., Lawton, T.F., Robert, E., and Valencia, V.A., 2008, Upper Aptian-Lower Albian Mural Formation: stratigraphy, biostratigraphy and depositional cycles on the Sonoran shelf, northern México: Cretaceous Research, v. 29, p. 249–266, doi: 10.1016/j.cretres.2007.06.001.

Grosse, P., Söllner, F., Baéz, M.A., Toselli, A.J., Rossi, J.N., de la Rosa, J.D., 2009, Lower Carboniferous post-orogenic granites in central-eastern Sierra de Velasco, Sierras Pampeanas, Argentina: U–Pb monazite geochronology and Sr–Nd isotopes: International Journal of Earth Sciences, v. 98, p. 1001–1025.

Gulbranson, E.L., Montanez, I.P., Schmitz, M.D., Limarino, C.O., Isbell, J.L., Marenssi, S.A., and Crowley, J.L., 2010, High-precision U-Pb calibration of Carboniferous glaciation and climate history, Paganzo Group, NW Argentina: Geological Society of America Bulletin, v. 122, p. 1480–1498, doi: 10.1130/B30025.1.

Haggart, J.W., Diakow, L.J., Mahoney, J.B., Woodsworth, G.J., Struik, L.S., Gordee, S.M., and Rusmore, M., 2006a, Geology, Bella Coola region (NTS 93D/01, /07, /08, /10, /15, and parts of 93D/02, /03, /06, /09, /11, /14, /16, and 92M/15 and /16), British Columbia: Geological Survey of Canada Open-File 5385, and British Columbia Geological Survey Geoscience Map 2006–7, 3 sheets, scale 1:100,000.

Haggart, J.W., Woodsworth, G.J., and McNicoll, V.J., 2006b, Uranium-lead geochronology of two intrusions in the Southern Bowser Basin, British Columbia: Geological Survey of Canada Current Research, v. F2, p. 1–6.

Haxel, G.B., Wright, J.E., Riggs, N.R., Tosdal, R.M., and May, D.J., 2005, Middle Jurassic Topawa Group, Baboquivari Mountains, south-central Arizona: Volcanic and sedimentary record of deep basins within the Jurassic magmatic arc, in Anderson, T.H., Nourse, J.A., McKee, J.W., and Steiner, M.B., eds., The Mojave-Sonora megashear hypothesis: Development, Assessment, and Alternatives: Geological Society of America Special Paper, v. 393, p. 329–357.

Henry, C.D., McDowell, F.W., and Silver, L.T., 2003, Geology and geochronology of granitic batholith complex, Sinaloa, México: Implications for Cordilleran magmatism and tectonics, in Johnson, S.E., Paterson, S.R., Fletcher, J.M., Girty, G.H., Kimbrough, D.L., and Martín-Barajas, A, eds., Tectonic evolution of northwestern Mexico and the Southwestern USA: Geological Society of America Special Papers 374, p. 237–273.

Hernandez-Pineda, G.A., Solari, L.A., Gómez-Tuena, A., Mendez-Cardenas, D.L., and Perez-Arvizu, O., 2011, Petrogenesis and thermobarometry of the 50 Ma Rapakivi granite-syenite Acapulco intrusive: Implications for post-Laramide

magmatism in southern Mexico: Geosphere, v. 7, p. 1419–1438, doi: 10.1130/GES00744.1..

Hervé, F., Pankhurst, R.J., Fanning, C.M., Calderón, M., and Yaxley, G.M., 2007, The South Patagonian batholith: 150 my of granite magmatism on a plate margin: Lithos, v. 97, p. 373–394, doi: 10.1016/j.lithos.2007.01.007.

Hervé, F., Calderón, M., Fanning, C.M., Pankhurst, R.J., and Godoy, E., 2013, Provenance variations in the Late Paleozoic accretionary complex of central Chile as indicated by detrital zircons: Gondwana Research, v. 23, p. 1122–1135, doi: 10.1016/j.gr.2012.06.016.

Hervé, F., Fanning, C. M., Calderón, M., and Mpodozis, C., 2014, Early Permian to Late Triassic batholiths of the Chilean Frontal Cordillera (28°-31°S): SHRIMP U-Pb zircon ages and Lu-Hf and O isotope systematics: Lithos, v. 184-187, p. 436-446.

Iriondo, A., 2001, Proterozoic basements and their Laramide juxtaposition in NW Sonora, Mexico: Tectonic constraints on the SW margin of Laurentia [Ph.D. thesis]: University of Colorado, Boulder, Colorado, 222 p.

Iriondo, A., McDowell, F.W., 2011, New middle Jurassic U-Pb zircon age for felsic gnimbrite intercalated with the clastic Plomosas formation in Chihuahua, northern Mexico, in Alcayde, M., Gómez-Caballero, J.A., (eds.), Simposio Dr. Zoltán de Cserna: sesenta años geologizando en México. Libro de resúmenes, México D.F., 14–15 junio 2011: México, Universidad Nacional Autónoma de México, Instituto de Geología, p. 99–100.

Iriondo, A., Martínez-Torres, L.M., Kunk, M.J., Atkinson, W.W., Jr., Premo, W.R., McIntosh, W.C., 2005, Northward Laramide thrusting in the Quitovac region, northwestern Sonora, Mexico: Implications for the juxtaposition of Paleoproterozoic basement blocks and the Mojave-Sonora megashear hypothesis, in Anderson, T.H., Nourse, J.A., McKee, J.W., Steiner, M.B., eds., The Mojave-Sonora megashear hypothesis: Development, assessment, and alternatives: Geological Society of America Special Paper 393, 631–669.

Izaguirre, A., 2009, El basamento paleoproterozoico (~1.71–1.68 Ga) Yavapai en el área Mina La Herradura en el NW de Sonora: Sus implicaciones para el desarrollo del arco magmático continental Mesozoico-Cenozoico del NW de México [M.Sc. thesis]: Universidad Nacional Autónoma de México, Centro de Geociencias, Querétaro, 202 p.

Jara, P., and Charrier, R., 2014, Nuevos antecedentes estratigráficos y geocronológicos para el Meso-Cenozoico de la Cordillera Principal de Chile entre 32° y 32°30'S: Implicancias estructurales y paleogeográficas: Andean Geology, v. 41, p. 174–209, doi: 10.5027/andgeoV410n12-a0?7.

Johnson, S.E., Paterson, S.R., and Tate, M.C., 1999a, Structure and emplacement history of a multiple-center, cone-sheet–bearing ring complex: The Zarza Intrusive

Complex, Baja California, Mexico: Geological Society of America Bulletin, v. 111, p. 607–619.

Johnson, S.E., Tate, M.C., and Fanning, C.M., 1999b, New geologic mapping and SHRIMP U–Pb zircon data in the Peninsular Ranges batholith, Baja California, Mexico: evidence for a suture?: Geology, v. 27, p. 743–746.

Johnson, S.E., Fletcher, J.M., Fanning, C.M., Vernon, R.H., Paterson, S.R., and Tate, M.C., 2003, Structure, emplacement and lateral expansion of the San José tonalite pluton, Peninsular Ranges batholith, Baja California, México: Journal of Structural Geology, v. 25, p. 1933–1957, doi: 10.1016/S0191-8141(03)00015-4.

Jones, N.W., Lopez, R., and Cameron, K.L., 1995, Linda Vista pluton and latest Permian-Late Triassic orogeny, Las Delicias area, Coahuila, México: Geological Society of America Abstracts with Programs, v. 27, p. 388.

Keppie, J.D., Nance, R.D., Dostal, J., Ortega-Rivera, A., Miller, B.V., Fox, D., Powell, J.T., Mumma, S.A., and Lee, J.K.W., 2004, Mid-Jurassic tectonothermal event superposed on a Paleozoic geological record in the Acatlán Complex of southern Mexico: hotspot activity during the breakup of Pangea: Gondwana Research, v. 7, p. 239–260.

Kimbrough, D.L., and Moore, T.E., 2003, Ophiolite and volcanic arc assemblages on the Vizcaino Peninsula and Cedros Island, Baja California Sur, México: Mesozoic forearc lithosphere of the Cordilleran magmatic arc, in Johnson, S.E., Paterson, S.R., Fletcher, J.M., Girty, G.H., Kimbrough, D.L., and Martín-Barajas, A, eds., Tectonic evolution of northwestern Mexico and the Southwestern USA: Geological Society of America Special Papers 374, p. 43–71.

Kimbrough, D.L., Smith, D.P., Mahoney, J.B., Moore, T.E., Grove, M., Gastil, R.G., Ortega-Rivera, A., and Fanning, C.M., 2001, Forearc-basin sedimentary response to rapid Late Cretaceous batholith emplacement in the Peninsular Ranges of southern and Baja California: Geology, v. 29, p. 491–494.

Kirsch, M., Keppie, J.D., Murphy, J.B., and Solari, L.A., 2012, Permian–Carboniferous arc magmatism and basin evolution along the western margin of Pangea: geochemical and geochronological evidence from the eastern Acatlán Complex, southern Mexico: Geological Society of America Bulletin, v. 124, p. 1607–1628.

Kirsch, M., Helbig, M., Keppie, J.D., Murphy, J.B., Lee, J.K.W., and Solari, L.A., 2014, A Late Triassic tectonothermal event in the eastern Acatlan Complex, southern Mexico, synchronous with a magmatic arc hiatus: The result of flat-slab subduction?: Lithosphere, v. 6, p. 63–79, doi: 10.1130/L349.1.

Klepeis, K.A., and Crawford, M.L., 1999, High-temperature arc-parallel normal faulting and transtension at the roots of an obliquely convergent orogen: Geology, v. 27, p. 7–10, doi: 10.1130/0091-7613(1999)027<0007:HTAPNF>2.3.CO;2.

Klepeis, K.A., Crawford, M.L., and Gehrels, G.E., 1998, Structural history of the crustal-scale Coast shear zone north of Portland Canal, southeast Alaska and British Columbia: Journal of Structural Geology, v. 20, p. 883–904, doi: 10.1016/S0191-8141(98)00020-0.

Kohn, M.J., Spear, F.S., Harrison, T.M., and Dalziel, I.W.D., 1995, 40Ar/39Ar geochronology and P-Tf paths from the Cordillera Darwin metamorphic complex, Tierra del Fuego, Chile: Journal of Metamorphic Geology, v. 13, p. 251–270.

Lancelot, J.R., Laubacher, G., Marocco, R., and Renaud, U., 1978, U/Pb radiochronology of two granitic plutons from the Eastern Cordillera (Peru): extent of Permian magmatic activity and consequences: Geologische Rundschau, v. 67, p. 236–243.

Lawton, T.F., and Molina Garza, R.S., 2014, U-Pb geochronology of the type Nazas Formation and superjacent strata, northeastern Durango, Mexico: Implications of a Jurassic age for continental-arc magmatism in north-central Mexico: Geological Society of America Bulletin, B30827.1, doi: 10.1130/B30827.1.

Lawton, T.F., Gilbert, J.C., and Amato, J.M., 2012, Age of the Jurassic arc system in southern Arizona: Geological Society of America Abstract with Programs, v. 44, p. 23.

Leggett, W.J., 2009, Stratigraphy, Sedimentology and Geochronology of Lower and Middle Jurassic Rocks Near Rancho San Martin del Rincon, North-Central Sonora, Mexico [M.S. thesis]: Las Cruces, New Mexico, New Mexico State University, 203 p.

Lipa, V., 2005, Análise estructural do Plutón Abancay e sua importância na evolução tectônica da porção sul de Abancay-Perú [M.Sc. thesis]: UNICAMP, Brasil.

Litherland, M., Aspden, J.A., Jemielita, R.A., 1994. The metamorphic belts of Ecuador. Overseas Memoir of the British Geological Survey, Nottingham, UK, v. 11, p. 147.

Mahoney, J.B., Haggart, J.W., Woodsworth, G.J., Hooper, R.L., and Snyder, L.S., 2007a, Geology, Kitlope Lake (east part) (93E/04), British Columbia: Geological Survey of Canada Open-File 5588, and Geoscience British Columbia Map 2007–11–4, 1 sheet, scale 1:50,000.

Mahoney, J.B., Haggart, J.W., Hooper, R.L., Snyder, L.S., and Woodsworth, G.J., 2007b, Geology, Tsaytis River (93E/05), British Columbia: Geological Survey of Canada Open-File 5587, and Geoscience British Columbia Map 2007–11–3, 1 sheet, scale 1:50,000.

Mahoney, J.B., Haggart, J.W., Hooper, R.L., Snyder, L.S., and Woodsworth, G.J., 2007c, Geology, parts of Chikamin Mountain and Troitsa Lake (93E/06, 11), British Columbia: Geological Survey of Canada Open- File 5586, and Geoscience British Columbia Map 2007–11–2, 1 sheet, scale 1:50,000.

Mahoney, J.B., Haggart, J.W., Hooper, R.L., Snyder, L.S., and Woodsworth, G.J., 2007d, Geology, Tahtsa Peak (93E/12), British Columbia: Geological Survey of Canada Open-File 5585, and Geoscience British Columbia Map 2007–11–1, 1 sheet, scale 1:50,000.

Mahoney, J.B., Hooper, R.L., Gordee, S.M., and Haggart, J.W., 2007e, Geology, Foresight Mountain (93E/03), British Columbia: Geological Survey of Canada Open- File 5386 (revised), and Geoscience British Columbia Map 2006–2, 1 sheet, scale 1:50,000.

Mahoney, J.B., Gordee, S.M., Haggart, J.W., Friedman, R.M., Diakow, L.J., and Woodsworth, G.J., 2009, Magmatic evolution of the eastern Coast Plutonic Complex, Bella Coola region, west-central British Columbia: Geological Society of America Bulletin, v. 121, no. 9–10, p. 1362–1380, doi:10.1130/B26325.1

Maksaev, V., 1990, Metallogeny, geological evolution and thermochronology of the Chilean Andes between latitudes 21° and 26° south, and the origin of the major porphyry copper deposits [Ph.D. thesis]: Dalhousie, Dalhousie University, 554 p.

Maksaev, V., Munizaga, F., Fanning, M., Palacios, C., and Tapia, J., 2006, SHRIMP U–Pb dating of the Antucoya porphyry copper deposit: new evidence for an Early Cretaceous porphyry-related metallogenic epoch in the Coastal Cordillera of northern Chile: Mineralium Deposita, v. 41, p. 637–644, doi: 10.1007/s00126-006-0091-5.

Maksaev, V., Munizaga, F., Valencia, V., and Barra, F., 2009, LA-ICP-MS zircon U-Pb geochronology to constrain the age of post-Neocomian continental deposits of the Cerrillos Formation, Atacama Region, northern Chile: tectonic and metallogenic implications: Andean Geology, v. 36, p. 264–287.

Maksaev, V., Almonacid, T.A., Munizaga, F., Valencia, V., McWilliams, M., and Barra, F., 2010, Geochronological and thermochronological constraints on porphyry copper mineralization in the Domeyko alteration zone, northern Chile: Andean Geology, v. 37, p. 144–176.

Maksaev, V., Munizaga, F., and Tassinari, C., 2014, Timing of the magmatism of the paleo-Pacific border of Gondwana: U-Pb geochronology of Late Paleozoic to Early Mesozoic igneous rocks of the north Chilean Andes between 20° and 31°S: Andean Geology, v. 41, no. 3, p. 447–506, doi: 10.5027/andgeoV41n3-a01.

Mancuso, A.C., Chemale, F., Barredo, S.P., Ávila, J., Ottone, E.G., and Marsicano, C., 2010. Age constraints fort he northernmost outcrops of the Triassic Cuyania Basin, Argentina: Journal of South American Earth Sciences, v. 30, no. 2, p. 97–103. doi:10.1016/j.jsames.2010.03.001.

Mantilla Figueroa, L.C., Bissig, T., Valencia, V., and Hart, C.J.R., 2013, The magmatic history of the Vetas-California mining district, Santander Massif, Eastern

Cordillera, Colombia: Journal of South American Earth Sciences, v. 45, p. 235–249, doi: 10.1016/j.jsames.2013.03.006.

Marocco R., 1978, Un segment E-W de la chaîne des Andes peruviennes: la déflexion d'Abancay.- Etude géologique de la Cordillère orientale et des hauts plateaux entre Cuzco et San Miguel, sud de Pérou (12°30'S à 14°00 S): Géologie des Andes péruviennes, Travaux et documents de L'O.R.S.T.O.M., v. 94, 195 p.

Martens, U.C., Brueckner, H.K., Mattinson, C.G., Liou, J.G., and Wooden, J.L., 2012, Timing of eclogite-facies metamorphism of the Chuacús complex, Central Guatemala: Record of Late Cretaceous continental subduction of North America's sialic basement: Lithos, v. 146–147, p. 1–10, doi: 10.1016/j.lithos.2012.04.021.

Martin, M. W., Clavero, J., and Mpodozis, C., 1999, Late Palaeozoic to Early Jurassic tectonic development of the high Andean Principal Cordillera, El Indio region, Chile (29°–30°S): Journal of South American Earth Sciences, v. 12, p. 33–49.

Martin, M., Pankhurst, R.J., Fanning, C.M., Thomson, S.N., Calderón, M., and Hervé, F., 2001, Age distribution of plutons across the southern Patagonian batholith: New U-Pb data on zircons: Third South American Symposium of Isotope Geology, Pucón, Chile, CD-ROM, SERNAGEOMIN, p. 580–585.

Martina, F., Viramonte, J.M., Astini, R.A., Pimentel, M.M., and Dantas, E., 2011, Mississippian volcanism in the south-central Andes: New U–Pb SHRIMP zircon geochronology and whole-rock geochemistry: Gondwana Research, v. 19, p. 524–534, doi: 10.1016/j.gr.2010.07.004.

Martínez, A.M.C., 2007. Petrogenesis and evolution of Aburra Ophiolite, Colombian Andes, Central Range [Ph.D. thesis], University of Brasilia, 178 p.

Martini, M., Ferrari, L., López-Martínez, M., Cerca-Martínez, M., Valencia, V.A., and Serrano-Durán, L., 2009, Cretaceous–Eocene magmatism and Laramide deformation in southwestern Mexico: No role for terrane accretion, in Kay, S.M., Ramos, V.A., and Dickinson, W.R., eds., Backbone of the Americas: Shallow subduction, plateau uplift, and ridge and terrane collision, Geological Society of America Memoir 204, p. 151–182.

Martini, M., Mori, L., Solari, L., and Centeno-García, E., 2011, Sandstone provenance of the Arperos Basin (Sierra de Guanajuato, central Mexico): Late Jurassic–Early Cretaceous back-Arc spreading as the foundation of the Guerrero Terrane: The Journal of Geology, v. 119, p. 597–617, doi: 10.1086/661989.

Martiny, B., Martínez-Serrano, R.G., Morán-Zenteno, D.J., Macías-Romo, C., and Ayuso, R.A., 2000, Stratigraphy, geochemistry and tectonic significance of the Oligocene magmatic rocks of western Oaxaca, southern Mexico: Tectonophysics, v. 318, p. 71–98.

Masterman, G.L., 2003. Structural and geochemical evolution of the Rosario Copper - molybdenum porphyry deposit and related copper veins, Collahuasi District, Northern Chile [Ph.D. thesis]: University of Tasmania, Australia, 253 p.

Mauel, D.J., Lawton, T.F., González-León, C., Iriondo, A., and Amato, J.M., 2011, Stratigraphy and age of Upper Jurassic strata in north-central Sonora, Mexico: Southwestern Laurentian record of crustal extension and tectonic transition: Geosphere, v. 7, p. 390–414, doi: 10.1130/GES00600.1.

McDowell, F.W., Roldán-Quintana, J., and Connelly, J.N., 2001, Duration of Late Cretaceous–early Tertiary magmatism in east-central Sonora, Mexico: Geological Society of America Bulletin, v. 113, p. 521–531.

Miller, J.S., Glazner, A.F., Walker, J.D., and Martin, M.W., 1995, Geochronologic and isotopic evidence for Triassic-Jurassic emplacement of the eugeoclinal allochton in the Mojave Desert region, California: Geological Society of America Bulletin, v. 107, p. 1441–1457.

Mišković, A., Spikings, R.A., Chew, D.M., Košler, J., Ulianov, A., and Schaltegger, U., 2009, Tectonomagmatic evolution of Western Amazonia: Geochemical characterization and zircon U-Pb geochronologic constraints from the Peruvian Eastern Cordilleran granitoids: Geological Society of America Bulletin, v. 121, p. 1298–1324, doi: 10.1130/B26488.1.

Montes, C., Guzmán, G., Bayona, G., Cardona, A., Valencia, V., and Jaramillo, C., 2010, Clockwise rotation of the Santa Marta massif and simultaneous Paleogene to Neogene deformation of the Plato-San Jorge and Cesar-Ranchería basins: Journal of South American Earth Sciences, v. 29, p. 832–848.

Mortensen, J.K., Hall, B.V., Bissig, T., Friedman, R.M., Danielson, T., Oliver, J., Rhys, D.A., Ross, K.V., and Gabites, J.E., 2008, Age and paleotectonic setting of volcanogenic massive sulfide deposits in the Guerrero Terrane of central Mexico: Constraints from U-Pb age and Pb isotope studies: Economic Geology, v. 103, p. 117–140.

Mukasa, S.B., 1984, Comparative Pb isotope systematics and zircon U-Pb geochronology for the Coastal, San Nicolás and Cordillera Bltnca batholiths, Peru [Ph.D. thesis]: Santa Barbara, University of California, 362 p.

Mukasa, S.B., 1986a, Lead isotopic compositions of the Lima and Arequipa segments in the Coastal batholith, Peru: implications for magmagenesis: Geochimica et Cosmochimica Acta, v. 50, p. 771–782.

Mukasa, S.B., 1986b, Zircon U-Pb ages of super-units in the Coastal batholith, Peru: Implications for magmatic and tectonic processes: Geological Society of America Bulletin, v. 97, p. 241–254, doi: 10.1130/0016-7606(1986)97<241:ZUAOSI>2.0.CO;2.

Mukasa, S.B., and Tilton, G.R., 1985a, Zircon U-Pb ages of super-units in the Coastal batholith, Peru, in Pitcher, W.S., Atherton, M.P., Cobbing, E.J., and Beckingsale, R.D., eds., Magmatism at the plate edge: The Peruvian Andes: Glasgow, UK, Blackie, p. 203–207.

Mukasa, S.B., and Tilton, G.R., 1985b, Pb isotope systematics as a guide to crustal involvement in the generation of the Coastal batholith, Peru, in Pitcher, W.S., Atherton, M.P., Cobbing, E.J., and Beckingsale, R.D., eds., Magmatism at the plate edge: The Peruvian Andes: Glasgow, UK, Blackie, p. 235–238.

Munizaga, F., Maksaev, V., Fanning, C.M., Giglio, S., Yaxley, G., and Tassinari, C.C.G., 2008, Late Paleozoic–Early Triassic magmatism on the western margin of Gondwana: Collahuasi area, Northern Chile: Gondwana Research, v. 13, p. 407–427, doi: 10.1016/j.gr.2007.12.005.

Murillo-Muñeton, G., 1994, Petrologic and geochronologic study of Grenville-age granulites and post-granulite plutons from the La Mixtequita area, state of Oaxaca in southern Mexico, and their tectonic significance [M.Sc. thesis]: University of Southern California, 326 p.

Ortega-Obregón, C., Keppie, J.D., Murphy, J.B., Lee, J.K.W., and Ortega-Rivera, A., 2009, Geology and geochronology of Paleozoic rocks in western Acatlan Complex, southern Mexico: Evidence for contiguity across an extruded high-pressure belt and constraints on Paleozoic reconstructions: Geological Society of America Bulletin, v. 121, p. 1678–1694.

Ortega-Obregón, C., Solari, L.A., Ortega-Gutiérrez, F., and Elías-Herrera, M., 2012, Arc-related intrusions in the Oaxacan Complex: evidence for Early to Late Permian Pacific plate subduction beneath the west central margin of Gondwana: Geological Society of America Abstracts with Programs, v. 44, p. 18.

Ortega-Obregón, C., Solari, L., Gómez-Tuena, A., Elías-Herrera, M., Ortega-Gutiérrez, F., and Macías-Romo, C., 2014, Permian–Carboniferous arc magmatism in southern Mexico: U–Pb dating, trace element and Hf isotopic evidence on zircons of earliest subduction beneath the western margin of Gondwana: International Journal of Earth Sciences, v. 103, p. 1287–1300.

Ortega-Rivera, A., Farrar, E., Hanes, J.A., Archibald, D.A., Gastil, R.G., Kimbrough, D.L., Zentilli, M., López-Martínez, M., Feraud, G., and Ruffet, G., 1997, Chronological constraints on the thermal and tilting history of the Sierra San Pedro Mártir pluton, Baja California, México, from U/Pb, 40Ar/39Ar, and fission-track geochronology: Geological Society of America Bulletin, v. 109, p. 728–745, doi: 10.1130/0016-7606(1997)109<0728:CCOTTA>2.3.CO;2.

Pankhurst, R.J., Millar, I.L., and Hervé, F., 1996, A Permo-Carboniferous U-Pb age for part of the Guanta Unit of the Elqui-Limarí Batholith at Río del Tránsito, Northern Chile: Revista geológica de Chile, v. 23, p. 35–42.

Pankhurst, R.J., Weaver, S.D., Hervé, F., and Larrondo, P., 1999, Mesozoic-Cenozoic evolution of the North Patagonian batholith in Aysen, southern Chile: Journal of the Geological Society, London, v. 156, p. 673–694.

Pankhurst, R.J., Rapela, C.W., Fanning, C.M., and Márquez, M., 2006, Gondwanide continental collision and the origin of Patagonia: Earth-Science Reviews, v. 76, p. 235–257, doi: 10.1016/j.earscirev.2006.02.001.

Parada, M.A., Feraud, G., Fuentes, F., Aguirre, L., Morata, D., and Larrondo, P., 2005, Ages and cooling history of the Early Cretaceous Caleu pluton: testimony of a switch from a rifted to a compressional continental margin in central Chile: Journal of the Geological Society, London, v. 162, p. 273–287.

Parada, M.A., Palacios, C., and Lahsen, A., 1997, Jurassic extensional tectono-magmatism and associated mineralization of the El Faldeo polymetallic district, Chilean Patagonia: geochemical and isotopic evidence of crustal contribution: Mineralium Deposita, v. 32, p. 547–554.

Peña-Alonso, T.A., Delgado-Argote, L.A., Weber, B., Velasco-Tapia, F., and Valencia, J.R., 2012, Geology and emplacement history of the Nuevo Rosarito plutonic suite in the southern Peninsular Ranges batholith, Baja California, México: Revista Mexicana de Ciencias Geológicas, v. 29, p. 1–23.

Pérez-Segura, E., González-Partida, E., and Valencia, V.A., 2009, Late Cretaceous adakitic magmatism in east-central Sonora, Mexico, and its relation to Cu-Zn-Ni-Co skarns: Revista Mexicana de Ciencias Geológicas, v. 26, p. 411–427.

Pérez-Segura, E., González-Partida, E., and Roldán-Quintana, J., 2013, Genetic implications of new Sr and Nd isotopic data of the intrusive rocks from the Laramide Arc in Northern Sonora, Mexico.: Journal of Iberian Geology, v. 39, doi: 10.5209/rev_JIGE.2013.v39.n1.41755.

Peryam, T.C., Lawton, T.F., Amato, J.M., González-León, C.M., and Mauel, D.J., 2011, Lower Cretaceous strata of the Sonora Bisbee Basin: A record of the tectonomagmatic evolution of northwestern Mexico: Geological Society of America Bulletin, v. 124, p. 532–548.

Pineda, G. and Calderón, M., 2008. Geología del área Monte Patria-El Maqui, Región de Coquimbo. Servicio Nacional de Geología y Minería, Carta Geológica de Chile, Serie de Geología Básica, 1:100.000, N° 116, 44 p.

Polliand, M., Schaltegger, U., Frank, M., and Fontboté, L., 2005, Formation of intra-arc volcanosedimentary basins in the western flank of the central Peruvian Andes during Late Cretaceous oblique subduction: field evidence and constraints from U-Pb ages and Hf isotopes: International Journal of Earth Sciences, v. 94, p. 231–242, doi: 10.1007/s00531-005-0464-5.

Poma, S., Zappettini, E.O., Quenardelle, S., Santos, J.O., Koukharsky, M., Belousova, E.,

and McNaughton, N.J., 2014, Geochemistry, U-Pb SHRIMP zircon dating and Hf isotopes of the Gondwanan magmatism in NW Argentina: petrogenesis and geodynamic implications: Andean Geology, v. 41, p. 267–292, doi: 10.5027/andgeoV41n2-a01.

Poole, F.G., William, J.P., Jr, Madrid, R.J., and Amaya-Martínez, R., 2005, Tectonic synthesis of the Ouachita-Marathon-Sonora orogenic margin of southern Laurentia, in Anderson, T.H., Nourse, J.A., McKee, J.W., and Steiner, M.B., eds., The Mojave-Sonora Megashear Hypothesis: Development, Assessment, and Alternatives: Geological Society of America Special Papers, v. 393, p. 543–596.

Premo, W.R. and Morton, D.M, 2014, SHRIMP-RG U-Pb ages of provenance and metamorphism from detrital zircon populations and Pb-Sr-Nd signatures of pre-batholiothic metasedimentary rocks at Searl Ridge, north-central Peninsular Ranges batholith, southern California: Implications for their age, origin, and tectonic setting, in Morton, D.M. and Miller F., eds., Contributions to the Geology of the Peninsular Ranges Batholith, southern California. Geological Society of America Memoir 211, p. 449–498.

Premo, W.R., Morton, D.M., and Fanning, C.M., 2014a, U-Pb zircon geochronology of Cretaceous tonalitic plutons in the northern Peninsular Ranges batholith, southern California: Implications for the timing of Late Cretaceous tectonic evolution of the southern California-Baja region, in Morton, D.M. and Miller F., eds., Contributions to the Geology of the Peninsular Ranges Batholith, southern California. Geological Society of America Memoir 211, p. 145–180.

Premo, W.R. Morton, D.M, and Kistler, R.L., 2014b, Age and isotopic systematics of late Cretaceous samples from the greater Los Angeles region: Implications for the types of crust that underlie Los Angeles and their distribution along late Cenozoic fault systems, in Morton, D.M. and Miller F., eds., Contributions to the Geology of the Peninsular Ranges Batholith, southern California. Geological Society of America Memoir 211, p. 21–59.

Ramos-Arias, M.A., and Keppie, J.D., 2011, U-Pb Neoproterozoic–Ordovician protolith age constraints for high- to medium-pressure rocks thrust over low-grade metamorphic rocks in the Ixcamilpa area, Acatlán Complex, southern Mexico: Canadian Journal of Earth Sciences, v. 48, p. 45–61.

Ramos-Velázquez, E., Calmus, T., Valencia, V., Iriondo, A., Valencia-Moreno, M., and Bellon, H., 2008, U-Pb and 40Ar/39Ar geochronology of the coastal Sonora batholith: New insights on Laramide continental arc magmatism: Revista Mexicana de Ciencias Geológicas, v. 25, p. 314–333.

Rapela, C.W., Pankhurst, R.J., Fanning, C.M., and Hervé, F., 2005, Pacific subduction coeval with the Karoo mantle plume: the Early Jurasssic Subcordilleran belt of northwestern Patagonia, in Vaughan, A.P.M., and Pankhurst, R.J., eds., Terrane Processes at the Margins of Gondwana: Geological Society, London, Special

Publications, v. 246, p. 217–239, doi: 10.1144/GSL.SP.2005.246.01.07.

Ratschbacher, L., Franz, L., Min, M., Bachmann, R., Martens, U., Stanek, K., Stübner, K., Nelson, B.K., Herrmann, U., Weber, B., López-Martínez, M., Jonckheere, R., Sperner, B., Tichomirowa, M., et al., 2009, The North American-Caribbean plate boundary in Mexico-Guatemala-Honduras, in James, K.H., Lorente, M.A., and Pindell, J.L., eds., The Origin and Evolution of the Caribbean Plate, London, Geological Society of London, v. 328, p. 219–293.

Ray, G.E., Brown, J.A., Friedman, R.M. and Cornelius, S.B., 1998, Geology of the Nifty Zn-Pb-Ba prospect, Bella Coola district, British Columbia: B.C. Ministry of energy, Mines and Petroleum Resources, Geological Fieldwork 1997, Paper 1998-1, p. 20–28.

Restrepo, J.J., Ordóñez-Carmona, O., Armstrong, R., and Pimentel, M.M., 2011, Triassic metamorphism in the northern part of the Tahamí Terrane of the central cordillera of Colombia: Journal of South American Earth Sciences, v. 32, p. 497–507, doi: 10.1016/j.jsames.2011.04.009.

Riel, N., Guillot, S., Jaillard, E., Martelat, J.E., Paquette, J.L., Schwartz, S., Goncalves, P., Duclaux, G., Thebaud, N., Lanari, P., Janots, E., and Yuquilema, J., 2013, Metamorphic and geochronogical study of the Triassic El Oro metamorphic complex, Ecuador: Implications for high-temperature metamorphism in a forearc zone: Lithos, v. 156-159, p. 41–68, doi: 10.1016/j.lithos.2012.10.005.

Riggs, N.R., Mattinson, J.M., and Busby, C.J., 1993, Correlation of Jurassic eolian strata between the magmatic arc and the Colorado Plateau: New U-Pb geochronologic data from southern Arizona: Geological Society of America Bulletin, v. 105, p. 1231–1246, doi: 10.1130/0016-7606(1993)105<1231.

Rocha-Campos, A.C., Basei, M.A., Nutman, A.P., Kleiman, L.E., Varela, R., Llambias, E., Canile, F.M., and da Rosa, O. de C.R., 2011, 30 million years of Permian volcanism recorded in the Choiyoi igneous province (W Argentina) and their source for younger ash fall deposits in the Paraná Basin: SHRIMP U–Pb zircon geochronology evidence: Gondwana Research, v. 19, p. 509–523, doi: 10.1016/j.gr.2010.07.003.

Rolando, A.P., Hartmann, L.A., Santos, J.O., Fernandez, R.R., Etcheverry, R.O., Schalamuk, I.A., and McNaughton, N.J., 2004, SHRIMP U-Pb zircon dates from igneous rocks from the Fontana Lake region, Patagonia: Implications for the age of magmatism, Mesozoic geological evolution and age of basement: Revista de la Asociación Geológica Argentina, v. 59, p. 671–684.

Romero, D., Valencia, K., Alarcón, P., Peña, D., and Ramos, V.A., 2013, The offshore basement of Perú: Evidence for different igneous and metamorphic domains in the forearc: Journal of South American Earth Sciences, v. 42, p. 47–60, doi: 10.1016/j.jsames.2012.11.003.

Rossel, P., Oliveros, V., Ducea, M.N., Charrier, R., Scaillet, S., Retamal, L., and Figueroa, O., 2013, The Early Andean subduction system as an analog to island arcs: Evidence from across-arc geochemical variations in northern Chile: Lithos, v. 179, p. 211–230, doi: 10.1016/j.lithos.2013.08.014.

Rusmore, M.E., Woodsworth, G.J., and Gehrels, G.E., 2000, Structural history of the Sheemahant shear zone, southwest of Bella Coola, British Columbia, and implications for the Late Cretaceous evolution of the Coast orogen, in Stowell, H.H., and McClelland, W.C., eds., Tectonics of the Coast Mountains, SE Alaska and Coastal British Columbia: Geological Society of America Special Paper 343, p. 89–106.

Rusmore, M.E., Gehrels, G.E., and Woodsworth, G.J., 2001, Southern continuation of the Coast shear zone and Paleocene strain partitioning in British Columbia–southeast Alaska: Geological Society of America Bulletin, v. 113, p. 961–975, doi: 10.1130/ 0016-7606(2001)113<0961:SCOTCS>2.0.CO;2.

Rusmore, M.E., Woodsworth, G.J., and Gehrels, G.E., 2005, Two-stage exhumation of midcrustal arc rocks, Coast Mountains, British Columbia: Tectonics, v. 24, TC5013, doi: 10.1029/2004TC001750.

Salazar, E., Arriagada, C., Mpodozis, M., Martínez, F., Peña, M., and Álvarez, J., 2009, Análisis estructural del Oroclino de Vallenar: primeros resultados. XII Congreso Geológico Chileno, Santiago, Chile, v. 3, p. S9-026.

Saleeby, J.B., 2000, Geochronologic investigations along the Alexander-Taku terrane boundary, southern Revillagigedo Island to Cape Fox areas, southeast Alaska, in Stowell, H.H., and McClelland, W.C., eds., Tectonics of the Coast Mountains in SE Alaska and Coastal British Columbia: Geological Society of America Special Paper 343, p. 107–143.

Schaltegger, U., Guex, J., Bartolini, A., Schoene, B., and Ovtcharova, M., 2008, Precise U-Pb age constraints for end-Triassic mass extinc- tion, its correlation to volcanism and Hettangian post-extinction recovery: Earth and Planetary Science Letters, v. 267, p. 266–275, doi: 10.1016/j.epsl.2007.11.031.

Schiuma, M., and Llambías, E.J., 2008, New ages and chemical analysis on Lower Jurassic volcanism close to the Huincul High, Neuquén. Revista de la Asociación Geológica Argentina. Simposio Jurásico de América del Sur, v. 63, p. 644–652.

Schmidt, K.L., and Paterson, S.R., 2002, A doubly vergent fan structure in the Peninsular Ranges batholith: Transpression or local complex flow around a continental margin buttress?: Tectonics, v. 21, p. 1050, doi: 10.1029/2001TC001353.

Schütte, P., Chiaradia, M., and Beate, B., 2010, Geodynamic controls on Tertiary arc magmatism in Ecuador: Constraints from U–Pb zircon geochronology of Oligocene–Miocene intrusions and regional age distribution trends: Tectonophysics, v. 489, p. 159–176, doi: 10.1016/j.tecto.2010.04.015.

Sillitoe, R.H., and Mortensen, J.K., 2010, Longevity of porphyry copper formation at Quellaveco, Peru: Economic Geology, v. 105, p. 1157–1162.

Snow, J.K., Asmeron, Y., and Lux, D.R., 1991, Permian-Triassic plutonism and tectonics, Death Valley region, California and Nevada: Geology, v. 19, p. 629–632.

Solari, L.A., Dostal, J., Ortega-Gutiérrez, F., and Keppie, J.D., 2001, The 275 Ma arc-related La Carbonera stock in the northern Oaxacan Complex of southern Mexico: U-Pb geochronology and geochemistry: Revista Mexicana de Ciencias Geológicas, v. 18, p. 149–161.

Solari, L.A., Torres de León, R., Hernández Pineda, G., Solé, J., Solís-Pichardo, G., and Hernández-Treviño, T., 2007, Tectonic significance of Cretaceous–Tertiary magmatic and structural evolution of the northern margin of the Xolapa Complex, Tierra Colorada area, southern Mexico: Geological Society of America Bulletin, v. 119, p. 1265–1279.

Solari, L.A., Gómez-Tuena, A., Ortega-Gutiérrez, F., and Ortega-Obregón, C., 2011, The Chuacús Metamorphic Complex, central Guatemala: geochronological and geochemical constraints on its Paleozoic–Mesozoic evolution: Geologica Acta, v. 9, p. 1–21.

Solari, L.A., Ortega-Gutiérrez, F., Elías-Herrera, M., Gómez-Tuena, A., and Schaaf, P., 2010, Refining the age of magmatism in the Altos Cuchumatanes, western Guatemala, by LA–ICPMS, and tectonic implications: International Geology Review, v. 52, p. 977–998.

Söllner, F., Gerdes, A., Grosse, P., and Toselli, A.J., 2007, U-Pb age determinations by LA-ICP-MS on zircons of the Huaco granite, Sierra Velasco (NW-Argentina): A long-therm history of melt activity within an igneous body: 20. Colloquium on Latin American Earth Sciences Abstract Volume, Kiel, Germany, p. 57.

Spencer, J.E., Richard, S.M., Gehrels, G.E., Gleason, J.D., and Dickinson, W.R., 2011, Age and tectonic setting of the Mesozoic McCoy Mountains Formation in western Arizona, USA: Geological Society of America Bulletin, v. 123, p. 1258–1274, doi: 10.1130/B30206.1.

Suárez, M., Demant, A., La Cruz, De, R., and Fanning, C.M., 2009, Relationship between volcanism and marine sedimentation in northern Austral (Aisén) Basin, central Patagonia: Stratigraphic, U–Pb SHRIMP and paleontologic evidence: Journal of South American Earth Sciences, v. 27, p. 309–325, doi: 10.1016/j.jsames.2008.11.009.

Suárez, M., La Cruz, De, R., Aguirre-Urreta, B., and Fanning, M., 2010, 40Ar/39Ar and U–Pb SHRIMP dating of Aptian tuff cones in the Aisén Basin, Central Patagonian Cordillera: Journal of South American Earth Sciences, v. 29, p. 731–737, doi:10.1016/j.jsames.2009.11.003.

Suárez, M., Márquez, M., La Cruz, De, R., Navarrete, C., and Fanning, M., 2014, Cenomanian-? early Turonian minimum age of the Chubut Group, Argentina: SHRIMP U–Pb geochronology: Journal of South American Earth Sciences, v. 50, p. 67–74, doi:10.1016/j.jsames.2013.10.008.

Tornos, F., Velasco, F., Barra, F., and Morata, D., 2010, The Tropezón Cu–Mo–(Au) deposit, Northern Chile: the missing link between IOCG and porphyry copper systems?: Mineralium Deposita, v. 45, p. 313–321, doi: 10.1007/s00126-010-0277-8.

Torres-de León, R., Solari, L.A., Ortega-Gutiérrez, F., and Martens, U., 2012, The Chortis Block–southwestern Mexico connections: U-Pb zircon geochronology constraints: American Journal of Science, v. 312, p. 288–313, doi: 10.2475/03.2012.02.

Valencia, V.A., Barra, F., Weber, B., Ruiz, J., Gehrels, G., Chesley, J., and López-Martínez, M., 2006, Re–Os and U–Pb geochronology of the El Arco porphyry copper deposit, Baja California Mexico: Implications for the Jurassic tectonic setting: Journal of South American Earth Sciences, v. 22, p. 39–51, doi: 10.1016/j.jsames.2006.08.005.

Valencia, V.A., Ducea, M., Talavera-Mendoza, O., Gehrels, G.E., Ruiz, J., and Shoemaker, S., 2009, U-Pb geochronology of granitoids in the north-western boundary of the Xolapa Terrane: Revista Mexicana de Ciencias Geológicas, v. 26, p. 189–200.

Valencia, V.A., Righter, K., Rosas-Elguera, J., López-Martínez, M., and Grove, M., 2013, The age and composition of the pre-Cenozoic basement of the Jalisco Block: implications for and relation to the Guerrero composite terrane: Contributions to Mineralogy and Petrology, v. 166, p. 801–824, doi: 10.1007/s00410-013-0908-z.

Vallejo, C., Spikings, R.A., Luzieux, L., Winkler, W., Chew, D., Page, L., 2006. The early interaction between the Caribbean Plateau and the NW South American Plate. Terra Nova, v. 18, p. 264–269.

van der Heyden, P., 1989, U-Pb and K-Ar Geochronometry of the Coast Plutonic Complex, 53°N to 54°N, British Columbia, and Implications for the Insular-Intermontane Superterrane Boundary [Ph.D. dissertation]: Vancouver, University of British Columbia, 392 p.

van der Heyden, P., 2004, Uranium-Lead and Potassium- Argon Ages from Eastern Bella Coola and Adjacent Parts of Anahim Lake and Mount Waddington Map Areas, West-Central British Columbia: Geological Survey of Canada Current Research 2004–A2, 14 p.

Van der Lelij, R., 2013. Reconstructing North-Western Gondwana with implications for the evolution of the Iapetus and Rheic oceans: A geochronological,

thermochronological and geochemical study [Ph.D. thesis]: University of Geneva, Switzerland, no. Sc. 4581, 221 p.

Varela, R., Basei, M.A.S., Cingolani, C.A., Siga, O., Jr, and Passarelli, C.R., 2005, El basamento cristalino de los Andes norpatagónicos en Argentina: geocronología e interpretación tectónica: Revista geológica de Chile, v. 32, p. 167–187, doi: 10.4067/S0716-02082005000200001.

Varela, A.N., Poiré, D.G., Martin, T., Gerdes, A., Goin, F.J., Gelfo, J.N., and Hoffmann, S., 2012, U-Pb zircon constraints on the age of the Cretaceous Mata Amarilla Formation, Southern Patagonia, Argentina: its relationship with the evolution of the Austral Basin: Andean Geology, v. 39, doi: 10.5027/andgeoV39n3-a01.

Vásquez Illanes, P.S., 2008, Late Triassic to Early Jurassic Plutonism in south Chile (34°-37°S): Its significance for the geodynamic evolution in the transition from Gondwana to Andean orogeny [Ph.D. thesis]: Technische Universität Berlin, 160 p.

Vega-Granillo, R., Salgado-Souto, S., Herrera-Urbina, S., Valencia, V., Ruiz, J., Meza-Figueroa, D., and Talavera-Mendoza, O., 2008, U–Pb detrital zircon data of the Rio Fuerte Formation (NW Mexico): Its peri-Gondwanan provenance and exotic nature in relation to southwestern North America: Journal of South American Earth Sciences, v. 26, p. 343–354, doi: 10.1016/j.jsames.2008.08.011.

Vega-Granillo, R., Salgado-Souto, S., Herrera-Urbina, S., Valencia, V., and Vidal-Solano, J.R., 2011, Metamorphism and deformation in the El Fuerte region: their role in the tectonic evolution of NW Mexico: Revista Mexicana de Ciencias Geológicas, v. 28, p. 10–23.

Vega-Granillo, R., Vidal-Solano, J.R., and Herrera-Urbina, S., 2012, Island arc tholeiites of Early Silurian, Late Jurassic and Late Cretaceous ages in the El Fuerte region, northwestern Mexico: Revista Mexicana de Ciencias Geológicas, v. 29, p. 492–513.

Vega-Granillo, R., Vidal-Solano, J.R., Solari, L., López-Martínez, M., Gómez-Juárez, O.S., and Herrera-Urbina, S., 2013, Geochemical and geochronological constraints on the geologic evolution of the western Sonobari Complex, northwestern Mexico: Geologica Acta, v. 11, p. 443–463, doi: 10.1344/105.000002059.

Vennari, V.V., Lescano, M., Naipauer, M., Aguirre-Urreta, B., Concheyro, A., Schaltegger, U., Armstrong, R., Pimentel, M., and Ramos, V.A., 2014, New constraints on the Jurassic–Cretaceous boundary in the High Andes using high-precision U–Pb data: Gondwana Research, v. 26, p. 374–385.

Vidal, C., Paredes, J., Macfarlane, A., and Tosdal, R., 1995, Geología y metalogenía del distrito minero Parcoy, provincia aurífera de Pataz, La Libertad, in Volumen jubilar Alberto Benavides, Sociedad Geológica del Perú, p. 351–377.

Villagómez, D., Spikings, R., Magna, T., Kammer, A., Winkler, W., and Beltrán, A., 2011, Geochronology, geochemistry and tectonic evolution of the Western and Central cordilleras of Colombia: Lithos, v. 125, p. 875–896, doi: 10.1016/j.lithos.2011.05.003.

Vinasco, C.J., Cordani, U.G., González, H., Weber, M., and Pelaez, C., 2006, Geochronological, isotopic, and geochemical data from Permo-Triassic granitic gneisses and granitoids of the Colombian Central Andes: Journal of South American Earth Sciences, v. 21, p. 355–371.

Viscarret, P., Wright, J., and Urbani, F., 2009, New U-Pb zircon ages of El Baúl Massif, Cojedes State, Venezuela: Revisita Técnica de la Facultad de Ingenieria Universidad del Zulia, v. 32, p. 210–221.

Weber, B., Cameron, K.L., Osorio, M., and Schaaf, P., 2005, A Late Permian tectonothermal event in Grenville crust of the southern Maya Terrane: U-Pb zircon ages from the Chiapas Massif, southeastern Mexico: International Geology Review, v. 47, p. 509–529.

Weber, B., Iriondo, A., Premo, W.R., Hecht, L., and Schaaf, P., 2007, New insights into the history and origin of the southern Maya block, SE México: U-Pb-SHRIMP zircon geochronology from metamorphic rocks of the Chiapas massif: International Journal of Earth Sciences, v. 96, p. 253–269.

Weber, M., Cardona, A., Valencia, V., García-Casco, A., Tobón, M., and Zapata, S., 2010, U/Pb detrital zircon provenance from late cretaceous metamorphic units of the Guajira Peninsula, Colombia: Tectonic implications on the collision between the Caribbean arc and the South American margin: Journal of South American Earth Sciences, v. 29, p. 805–816.

Willner, A.P., Gerdes, A., and Massonne, H.-J., 2008, History of crustal growth and recycling at the Pacific convergent margin of South America at latitudes 29°–36° S revealed by a U–Pb and Lu–Hf isotope study of detrital zircon from late Paleozoic accretionary systems: Chemical Geology, v. 253, p. 114–129, doi: 10.1016/j.chemgeo.2008.04.016.

Winter, L.S., 2008, The genesis of ‘giant’ copper-zinc-gold-silver volcanogenic massive sulphide deposits at Tambogrande, Perú: age, tectonic setting, paleomorphology, lithogeochemistry and radiogenic isotopes [Ph.D. thesis]: University of British Columbia, Vancouver, 274 p.

Witt, W.K., Hagemann, S.G., Villanes, C., and Zeng, Q., 2013, New geochronological results and structural evolution of the Pataz gold mining district: Implications for the timing and origin of the batholith-hosted veins: Ore Geology Reviews, v. 50, p. 143–170.

Yañez, P., Patchett, P.J., Ortega-Gutiérrez, F., and Gehrels, G.E., 1991, Isotopic studies of the Acatlán Complex, southern Mexico: Implications for Paleozoic North

American Tectonics: Geological Society of America Bulletin, v. 103, p. 817–828.

Zavala-Monsiváis, A., Barboza-Gudiño, J.R., Valencia, V.A., Rodríguez-Hernández, S.E., and García-Arreola, M.E., 2009, Las sucesiónes volcánicas pre-Cretácicas en el noreste de México: GEOS Unión Geofísica Mexicana, v. 29, p. 53.

Zavala-Monsiváis, A., Barboza-Gudiño, J.R., Velasco-Tapia, F., and García-Arreola, M.E., 2012, Sucesión volcánica Jurásica en el área de Charcas, San Luis Potosí: Contribución al entendimiento del Arco Nazas en el noreste de México: Boletín de la Sociedad Geológica Mexicana, v. 64, p. 277–293.

References for Detrital Zircon Ages

Alsleben, H., Wetmore, P.H., Gehrels, G.E., and Paterson, S.R., 2012, Detrital zircon ages in Palaeozoic and Mesozoic basement assemblages of the Peninsular Ranges batholith, Baja California, Mexico: constraints for depositional ages and provenance: International Geology Review, v. 54, p. 93–110.

Álvarez, J., Mpodozis, C., Arriagada, C., Astini, R., Morata, D., Salazar, E., Valencia, V.A., and Vervoort, J.D., 2011, Journal of South American Earth Sciences: Journal of South American Earth Sciences, v. 32, p. 460–476, doi: 10.1016/j.jsames.2011.06.002.

Augustsson, C., Münker, C., Bahlburg, H., and Fanning, C.M., 2006, Provenance of late Palaeozoic metasediments of the SW South American Gondwana margin: a combined U–Pb and Hf-isotope study of single detrital zircons: Journal of the Geological Society, v. 163, p. 983–995.

Augustsson, C., Rüsing, T., Niemeyer, H., Kooijman, E., Berndt, J., Bahlburg, H., and Zimmermann, U., 2015, 0.3 byr of drainage stability along the Palaeozoic palaeo-Pacific Gondwana margin; a detrital zircon study: Journal of the Geological Society, v. 172, p. 186–200.

Ayala, R.C., Bayona, G.A., Ojeda-Marulanda, C., Cardona, A., Valencia, V., Padrón, C.E., Yoris, F., Mesa-Salamanca, J., and García, A., 2009, Estratigrafia y procedencia de las unidades comprendidas entre el Campaniano y el Paleogeno en la subcuenca de Cesar: aportes a la evolución tectónica del área: Geología Colombiana, v. 34, p. 3–34.

Ayala, R.C., Bayona, G., Cardona, A., Ojeda, C., Montenegro, O.C., Montes, C., Valencia, V., and Jaramillo, C., 2012, The paleogene synorogenic succession in the northwestern Maracaibo block: Tracking intraplate uplifts and changes in sediment delivery systems: Journal of South American Earth Sciences, v. 39, p. 93–111, doi: 10.1016/j.jsames.2012.04.005.

Bahlburg, H., Vervoort, J.D., Frane, Du, S.A., Bock, B., Augustsson, C., and Reimann,

C., 2009, Timing of crust formation and recycling in accretionary orogens: Insights learned from the western margin of South America: Earth-Science Reviews, v. 97, p. 215–241, doi: 10.1016/j.earscirev.2009.10.006.

Bande, A., Horton, B.K., Ramirez, J.C., Mora, A., Parra, M., and Stockli, D.F., 2012, Clastic deposition, provenance, and sequence of Andean thrusting in the frontal Eastern Cordillera and Llanos foreland basin of Colombia: Geological Society of America Bulletin, v. 124, p. 59–76, doi: 10.1130/B30412.1.

Barbeau, D.L., Jr., Ducea, M.N., Gehrels, G.E., Kidder, S., Wetmore, P.H., and Saleeby, J.B., 2005, U-Pb detrital-zircon geochronology of northern Salinian basement and cover rocks: Geological Society of America Bulletin, v. 117, p. 466–481, doi: 10.1130/B25496.1.

Barbeau, D.L., Jr., Gombosi, D.J., Zahid, K.M., Bizimis, M., Swanson-Hysell, N., Valencia, V., and Gehrels, G.E., 2009a, U-Pb zircon constraints on the age and provenance of the Rocas Verdes basin fill, Tierra del Fuego, Argentina: Geochemistry, Geophysics, Geosystems, v. 10, Q12001, doi: 10.1029/2009GC002749.

Barbeau, D.L., Jr., Olivero, E.B., Swanson-Hysell, N.L., Zahid, K.M., Murray, K.E., and Gehrels, G.E., 2009b, Detrital-zircon geochronology of the eastern Magallanes foreland basin: Implications for Eocene kinematics of the northern Scotia Arc and Drake Passage: Earth and Planetary Science Letters, v. 284, p. 489–503, doi: 10.1016/j.epsl.2009.05.014.

Barboza-Gudiño, J.R., Zavala-Monsiváis, A., Venegas-Rodríguez, G., and Barajas-Nigoche, L.D., 2010, Late Triassic stratigraphy and facies from northeastern Mexico: Tectonic setting and provenance: Geosphere, v. 6, p. 621–640.

Barboza-Gudiño, J.R., Molina-Garza, R.S., and Lawton, T.F., 2012, Sierra de Catorce: Remnants of the ancient western equatorial margin of Pangea in central Mexico, in Aranda-Gómez, J.J., Tolson, G., and Molina-Garza, R.S., eds., The Southern Cordillera and beyond: Geological Society of America Field Guide 25, p. 1–18.

Boekhout, F., Sempere, T., Spikings, R., and Schaltegger, U., 2013, Late Paleozoic to Jurassic chronostratigraphy of coastal southern Peru: Temporal evolution of sedimentation along an active margin: Journal of South American Earth Sciences, v. 47, p. 179–200, doi: 10.1016/j.jsames.2013.07.003.

Calderón, M., Fildani, A., Hervé, F., Fanning, C.M., Weislogel, A., and Cordani, U., 2007, Late Jurassic bimodal magmatism in the northern sea-floor remnant of the Rocas Verdes basin, southern Patagonian Andes: Journal of the Geological Society, London, v. 164, p. 1011–1022.

Campos-Madrigal, E., Centeno-García, E., Mendoza-Rosales, C., and Silva-Romo, G., 2013, Sedimentología, reconstrucción paleoambiental y significado tectónico de las sucesiones clásticas del Jurásico Medio en el área de Texcalapa, Puebla -

Huajuapan de León, Oaxaca: Revisión de las formaciones Ayuquila y Tecomazúchil: Revista Mexicana de Ciencias Geológicas, v. 30, p. 24–50.

Cardona, A., Cordani, U.G., Ruiz, J., Valencia, V.A., Armstrong, R., Chew, D., Nutman, A., and Sánchez, A.W., 2009, U-Pb Zircon Geochronology and Nd Isotopic Signatures of the Pre-Mesozoic Metamorphic Basement of the Eastern Peruvian Andes: Growth and Provenance of a Late Neoproterozoic to Carboniferous Accretionary Orogen on the Northwest Margin of Gondwana: The Journal of Geology, v. 117, p. 285–305, doi: 10.1086/597472.

Cardona, A., Valencia, V., Bustamante, C., García-Casco, A., Ojeda, G., Ruiz, J., Saldarriaga, M., and Weber, M., 2010a, Permian to Triassic I to S-type magmatic switch in the northeast Sierra Nevada de Santa Marta and adjacent regions, Colombian Caribbean: Tectonic setting and implications within Pangea paleogeography: Journal of South American Earth Sciences, v. 29, p. 784–804, doi: 10.1016/j.jsames.2009.08.012.

Cardona, A., Valencia, V.A., Bayona, G., Duque, J., Ducea, M., Gehrels, G., Jaramillo, C., Montes, C., Ojeda, G., and Ruiz, J., 2010b, Early-subduction-related orogeny in the northern Andes: Turonian to Eocene magmatic and provenance record in the Santa Marta Massif and Rancheria Basin, northern Colombia: Terra Nova, v. 23, p. 26–34, doi: 10.1111/j.1365-3121.2010.00979.x.

Cardona, A., Montes, C., Ayala, C., Bustamante, C., Hoyos, N., Montenegro, O., Ojeda, C., Niño, H., Ramírez, V., Valencia, V., Rincón, D., Vervoort, J., and Zapata, S., 2012, From arc-continent collision to continuous convergence, clues from Paleogene conglomerates along the southern Caribbean–South America plate boundary: Tectonophysics, v. 580, p. 58–87, doi: 10.1016/j.tecto.2012.08.039.

Centeno-García, E., Busby, C., Busby, M., and Gehrels, G., 2011, Evolution of the Guerrero composite terrane along the Mexican margin, from extensional fringing arc to contractional continental arc: Geological Society of America Bulletin, v. 123, p. 1776–1797, doi: 10.1130/B30057.1.

Chernicoff, C.J., Zappettini, E.O., Santos, J.O., McNaughton, N.J., and Belousova, E., 2013, Combined U-Pb SHRIMP and Hf isotope study of the Late Paleozoic Yaminué Complex, Rio Negro Province, Argentina: Implications for the origin and evolution of the Patagonia composite terrane: Geoscience Frontiers, v. 4, p. 37–56, doi: 10.1016/j.gsf.2012.06.003.

Chew, D.M., Schaltegger, U., Košler, J., Whitehouse, M.J., Gutjahr, M., Spikings, R.A., and Miskovíc, A., 2007, U-Pb geochronologic evidence for the evolution of the Gondwanan margin of the north-central Andes: Geological Society of America Bulletin, v. 119, p. 697–711, doi: 10.1130/B26080.1.

Cochrane, R., 2013, U-Pb thermochronology, geochronology and geochemistry of NW South America: Rift to drift transition, active margin dynamics and implications

for the volume balance of continents [Ph.D. thesis]: Geneva, Université de Genève, 209 p.

Decou, A., Eynatten, von, H., Dunkl, I., Frei, D., and Wörner, G., 2013, Late Eocene to Early Miocene Andean uplift inferred from detrital zircon fission track and U–Pb dating of Cenozoic forearc sediments (15–18°S): Journal of South American Earth Sciences, v. 45, p. 6–23, doi: 10.1016/j.jsames.2013.02.003.

Di Giulio, A., Ronchi, A., Sanfilippo, A., Tiepolo, M., Pimentel, M., and Ramos, V.A., 2012, Detrital zircon provenance from the Neuquen Basin (south-central Andes): Cretaceous geodynamic evolution and sedimentary response in a retroarc-foreland basin: Geology, doi: 10.1130/G33052.1.

Dickinson, W.R., and Gehrels, G.E., 2008, Sediment delivery to the Cordilleran foreland basin: Insights from U-Pb ages of detrital zircons in Upper Jurassic and Cretaceous strata of the Colorado Plateau: American Journal of Science, v. 308, p. 1041–1082.

Dumitru, T.A., Ernst, W.G., Wright, J.E., Wooden, J.L., Wells, R.E., Farmer, L.P., Kent, A.J., and Graham, S.A., 2013, Eocene extension in Idaho generated massive sediment floods into the Franciscan trench and into the Tyee, Great Valley, and Green River basins: Geology, v. 41, p. 187–190, doi: 10.2475/02.2012.03.

Encinas, A., Stinnesbeck, W., and Valencia, V.A., 2014, First radiometric age (U-Pb, LA-ICP-MS, on detrital zircons) from the Punta Topocalma Formation: insights on Late Cretaceous marine deposition in central Chile: Andean Geology, v. 41, p. 436–445, doi: 10.5027/andgeoV410n2-a0?8.

Escalona-Alcázar, F.D.J., Delgado-Argote, L.A., Weber, B., Núñez-Peña, E.P., Valencia, V.A., and Ortiz-Acevedo, O., 2009, Kinematics and U-Pb dating of detrital zircons from the Sierra de Zacatecas, Mexico: Revista Mexicana de Ciencias Geológicas, v. 26, p. 48–64.

Fildani, A., Cope, T.D., Graham, S.A., and Wooden, J.L., 2003, Initiation of the Magallanes foreland basin: Timing of the southernmost Patagonian Andes orogeny revised by detrital zircon provenance analysis: Geology, v. 31, p. 1081–1084.

Fletcher, J.M., Grove, M., Kimbrough, D., Lovera, O., and Gehrels, G.E., 2007, Ridge-trench interactions and the Neogene tectonic evolution of the Magdalena shelf and southern Gulf of California: Insights from detrital zircon U-Pb ages from the Magdalena fan and adjacent areas: Geological Society of America Bulletin, v. 119, p. 1313–1336, doi: 10.1130/B26067.1.

Fuentes, F., DeCelles, P.G., Constenius, K.N., and Gehrels, G.E., 2011, Evolution of the Cordilleran foreland basin system in northwestern Montana, U.S.A.: Geological Society of America Bulletin, v. 123, p. 507–533, doi: 10.1130/B30204.1.

Gehrels, G., and Pecha, M., 2014, Detrital zircon U-Pb geochronology and Hf isotope geochemistry of Paleozoic and Triassic passive margin strata of western North America: Geosphere, v. 10, p. 49–65, doi: 10.1130/GES00889.S3.

Gehrels, G.E., and Stewart, J.H., 1998, Detrital zircon U-Pb geochronology of Cambrian to Triassic miogeoclinal and eugeoclinal strata of Sonora, Mexico: Journal of Geophysical Research, v. 103, p. 2471–2487.

Gillis, R.J., Gehrels, G.E., Ruiz, J., and Gonzalez, L.A.F. de D., 2005, Detrital zircon provenance of Cambrian-Ordovician and Carboniferous strata of the Oaxaca terrane, southern Mexico: Sedimentary Geology, v. 182, p. 87–100.

Godínez-Urban, A., Lawton, T.F., Molina-Garza, R.S., Iriondo, A., Weber, B., and López-Martínez, M., 2011, Jurassic volcanic and sedimentary rocks of the La Silla and Todos Santos Formations, Chiapas: Record of Nazas arc magmatism and rift-basin formation prior to opening of the Gulf of Mexico: Geosphere, v. 7, p. 121–144.

González-León, C.M., Stanley, G.D.J., Gehrels, G.E., and Centeno-García, E., 2005, New data on the lithostratigraphy, detrital zircon and Nd isotope provenance, and paleogeographic setting of the El Antimonio Group, Sonora, Mexico, in Anderson, T.H., Nourse, J.A., McKee, J.W., and Steiner, M.B., eds., The Mojave-Sonora Megashear Hypothesis: Development, Assessment, and Alternatives, Geological Society of America Special Paper 393, p. 259–282.

González-León, C.M., Valencia, V.A., Lawton, T.F., Amato, J.M., Gehrels, G.E., Leggett, W.J., Montijo-Contreras, O., and Fernández, M.A., 2009, The lower Mesozoic record of detrital zircon U-Pb geochronology of Sonora, México, and its paleogeographic implications: Revista Mexicana de Ciencias Geológicas, v. 26, p. 301–314.

González-León, C.M., Solari, L., Solé, J., Ducea, M.N., Lawton, T.F., Bernal, J.P., Becuar, E.G., Gray, F., Martínez, M.L., and Santacruz, R.L., 2011, Stratigraphy, geochronology, and geochemistry of the Laramide magmatic arc in north-central Sonora, Mexico: Geosphere, v. 7, p. 1392–1418, doi: 10.1130/GES00679.S5.

Grodzicki, K.R., Nance, R.D., Keppie, J.D., Dostal, J., and Murphy, J.B., 2008, Structural, geochemical and geochronological analysis of metasedimentary and metavolcanic rocks of the Coatlaco area, Acatlán Complex, southern Mexico: Tectonophysics, v. 461, p. 311–323.

Helbig, M., Keppie, J.D., Murphy, J.B., and Solari, L.A., 2012, U-Pb geochronological constraints on the Triassic–Jurassic Ayú Complex, southern Mexico: Derivation from the western margin of Pangea-A: Gondwana Research, v. 22, p. 910–927.

Hervé, F., Fanning, C.M., and Pankhurst, R.J., 2003, Detrital zircon age patterns and provenance of the metamorphic complexes of southern Chile: Journal of South American Earth Sciences, v. 16, p. 107–123, doi: 10.1016/S0895-9811(03)00022-

1.

Hervé, F., Calderón, M., Fanning, C.M., Pankhurst, R.J., and Godoy, E., 2013, Provenance variations in the Late Paleozoic accretionary complex of central Chile as indicated by detrital zircons: Gondwana Research, v. 23, p. 1122–1135, doi: 10.1016/j.gr.2012.06.016.

Hinojosa-Prieto, H.R., Nance, R.D., Keppie, J.D., Dostal, J.V., Ortega-Rivera, A., and Lee, J.K.W., 2008, Ordovician and Late Paleozoic–Early Mesozoic tectonothermal history of the La Noria area, northern Acatlán Complex, southern Mexico: Record of convergence in the Rheic and paleo-Pacific Oceans: Tectonophysics, v. 461, p. 324–342, doi: 10.1016/j.tecto.2008.06.002.

Horton, B., Parra, M., Saylor, J., Nie, J., Mora, A., Torres, V., Stockli, D., and Strecker, M., 2010a, Resolving uplift of the northern Andes using detrital zircon age signatures: GSA Today, v. 20, no. 7, p. 4–10, doi: 10.1130/GSATG76A.1.

Horton, B.K., Saylor, J.E., Nie, J., Mora, A., Parra, M., Reyes-Harker, A., and Stockli, D.F., 2010b, Linking sedimentation in the northern Andes to basement configuration, Mesozoic extension, and Cenozoic shortening: Evidence from detrital zircon U-Pb ages, Eastern Cordillera, Colombia: Geological Society of America Bulletin, v. 122, p. 1423–1442, doi: 10.1130/B30118.1.

Jacobson, C.E., Grove, M., Pedrick, J.N., Barth, A.P., Marsaglia, K.M., Gehrels, G.E., and Nourse, J.A., 2011, Late Cretaceous–early Cenozoic tectonic evolution of the southern California margin inferred from provenance of trench and forearc sediments: Geological Society of America Bulletin, v. 123, p. 485–506, doi: 10.1130/B30238.1.

Keppie, J.D., Dostal, J., Miller, B.V., Ramos-Arias, M.A., Morales-Gámez, M., Nance, R.D., Murphy, J.B., Ortega-Rivera, A., Lee, J.K.W., Housh, T., and Cooper, P., 2008, Ordovician-earliest Silurian rift tholeiites in the Acatlán Complex, southern Mexico: Evidence of rifting on the southern margin of the Rheic Ocean: Tectonophysics, v. 461, p. 130–156.

Kimbrough, D.L., Smith, D.P., Mahoney, J.B., Moore, T.E., Grove, M., Gastil, R.G., Ortega-Rivera, A., and Fanning, C.M., 2001, Forearc-basin sedimentary response to rapid Late Cretaceous batholith emplacement in the Peninsular Ranges of southern and Baja California: Geology, v. 29, p. 491–494.

Kirsch, M., Keppie, J.D., Murphy, J.B., and Solari, L.A., 2012, Permian–Carboniferous arc magmatism and basin evolution along the western margin of Pangea: geochemical and geochronological evidence from the eastern Acatlán Complex, southern Mexico: Geological Society of America Bulletin, v. 124, p. 1607–1628.

Laskowski, A.K., DeCelles, P.G., and Gehrels, G.E., 2013, Detrital zircon geochronology of Cordilleran retroarc foreland basin strata, western North America: Tectonics, v. 32, p. 1027–1048, doi: 10.1002/tect.20065.

Lawton, T.F., and Bradford, B.A., 2011, Correlation and provenance of Upper Cretaceous (Campanian) fluvial strata, Utah, USA, from zircon U-Pb geochronology and petrography: Journal of Sedimentary Research, v. 81, p. 495–512, doi: 10.2110/jsr.2011.45.

Lawton, T.F., and Molina Garza, R.S., 2014, U-Pb geochronology of the type Nazas Formation and superjacent strata, northeastern Durango, Mexico: Implications of a Jurassic age for continental-arc magmatism in north-central Mexico: Geological Society of America Bulletin, B30827.1, doi: 10.1130/B30827.1.

Lawton, T.F., Bradford, I.A., Vega, F.J., Gehrels, G.E., and Amato, J.M., 2009, Provenance of Upper Cretaceous-Paleogene sandstones in the foreland basin system of the Sierra Madre Oriental, northeastern Mexico, and its bearing on fluvial dispersal systems of the Mexican Laramide Province: Geological Society of America Bulletin, v. 121, p. 820–836, doi: 10.1130/B26450.1.

Lawton, T.F., Barboza-Gudiño, J.R., González-León, C.M., Gray, G.G., Iriondo, A., Leggett, W.J., Peryam, T.C., and Rubio-Cisneros, I.I., 2010, Latest Triassic-Middle Jurassic age of Cordilleran-Nazas arc in Mexico indicated by U-Pb detrital zircon and volcanic-rock ages: Geological Society of America Abstracts with Programs, v. 42, p. 345.

Leier, A.L., and Gehrels, G.E., 2011, Continental-scale detrital zircon provenance signatures in Lower Cretaceous strata, western North America: Geology, v. 39, p. 399–402, doi: 10.1130/G31762.1.

Leier, A.L., McQuarrie, N., Horton, B.K., and Gehrels, G.E., 2010, Upper Oligocene Conglomerates of the Altiplano, Central Andes: The Record of Deposition and Deformation Along the Margin of a Hinterland Basin: Journal of Sedimentary Research, v. 80, p. 750–762, doi: 10.2110/jsr.2010.064.

Mantilla Figueroa, L.C., Bissig, T., Valencia, V., and Hart, C.J.R., 2013, The magmatic history of the Vetas-California mining district, Santander Massif, Eastern Cordillera, Colombia: Journal of South American Earth Sciences, v. 45, p. 235–249, doi: 10.1016/j.jsames.2013.03.006.

Martini, M., Ferrari, L., López-Martínez, M., Cerca-Martínez, M., Valencia, V.A., and Serrano-Durán, L., 2009, Cretaceous–Eocene magmatism and Laramide deformation in southwestern Mexico: No role for terrane accretion, in Kay, S.M., Ramos, V.A., and Dickinson, W.R., eds., Backbone of the Americas: Shallow subduction, plateau uplift, and ridge and terrane collision, Geological Society of America Memoir 204, p. 151–182.

Martini, M., Mori, L., Solari, L., and Centeno-García, E., 2011, Sandstone provenance of the Arperos Basin (Sierra de Guanajuato, central Mexico): Late Jurassic–Early Cretaceous back-Arc spreading as the foundation of the Guerrero Terrane: The Journal of Geology, v. 119, p. 597–617, doi: 10.1086/661989.

Mauel, D.J., Lawton, T.F., González-León, C., Iriondo, A., and Amato, J.M., 2011, Stratigraphy and age of Upper Jurassic strata in north-central Sonora, Mexico: Southwestern Laurentian record of crustal extension and tectonic transition: Geosphere, v. 7, p. 390–414, doi: 10.1130/GES00600.1.

Mendoza-Rosales, C.C., Centeno-García, E., Silva-Romo, G., Campos-Madrigal, E., and Bernal, J.P., 2010, Barremian rift-related turbidites and alkaline volcanism in southern Mexico and their role in the opening of the Gulf of Mexico: Earth and Planetary Science Letters, v. 295, p. 419–434.

Michalak, M.J., 2013, Exhumation of the Peruvian Andes—insights from mineral chronometers [Ph.D. thesis]: Los Angeles, University of California, 176 p.

Morales-Gámez, M., Keppie, J.D., and Norman, M.D., 2008, Ordovician-Silurian rift-passive margin on the Mexican margin of the Rheic Ocean overlain by Carboniferous-Permian periarc rocks: Evidence from the eastern Acatlán Complex, southern Mexico: Tectonophysics, v. 461, p. 291–310.

Morgan, J.R., Kimbrough, D.L., and Grove, M., 2005, Detrital U/Pb zircon ages from the Peninsular Ranges Mesozoic flysch belt of southern and Baja California, in Gonzalez-Yajimovich, O.E., ed., VII International Meeting on the Geology of the Baja California Peninsula: Ensenada, Baja California, Mexico, Abstracts with Programs, p. 4.

Naipauer, M., Morabito, E.G., Marques, J.C., Tunik, M., Vera, E.A.R., Vujovich, G.I., Pimentel, M.P., and Ramos, V.A., 2012, Intraplate Late Jurassic deformation and exhumation in western central Argentina: Constraints from surface data and U–Pb detrital zircon ages: Tectonophysics, v. 524-525, p. 59–75, doi: 10.1016/j.tecto.2011.12.017.

Naipauer, M., Tunik, M., Marques, J.C., Rojas Vera, E.A., Vujovich, G.I., Pimentel, M.M., and Ramos, V.A., 2014, U-Pb detrital zircon ages of Upper Jurassic continental successions: implications for the provenance and absolute age of the Jurassic-Cretaceous boundary in the Neuquen Basin, in Sepúlveda, S. A., Giambiagi, L. B., Moreiras, S. M., Pinto, L., Tunik, M., Hoke, G. D., and Farías, M., eds., Geodynamic Processes in the Andes of Central Chile and Argentina: Geological Society, London, Special Publications 399, doi: 10.1144/SP399.1.

Nie, J., Horton, B.K., Mora, A., Saylor, J.E., Housh, T.B., Rubiano, J., and Naranjo, J., 2010, Tracking exhumation of Andean ranges bounding the Middle Magdalena Valley Basin, Colombia: Geology, v. 38, p. 451–454, doi: 10.1130/G30775.1.

Nie, J., Horton, B.K., Saylor, J.E., Mora, A., Mange, M., Garzione, C.N., Basu, A., Moreno, C.J., Caballero, V., and Parra, M., 2012, Integrated provenance analysis of a convergent retroarc foreland system: U–Pb ages, heavy minerals, Nd isotopes, and sandstone compositions of the Middle Magdalena Valley basin, northern Andes, Colombia: Earth-Science Reviews, v. 110, p. 111–126, doi: 10.1016/j.earscirev.2011.11.002.

Ocampo-Díaz, Y.Z.E., Talavera-Mendoza, O., Jenchen, U., Valencia, V.A., Medina-Ferrusquia, H.C., and Guerrero-Suastegui, M., 2014, Procedencia de la Formación La Casita y la Arcosa Patula: implicaciones para la evolución tectono-magmática del NE de México entreel Carbonífero y el Jurásico: Revista Mexicana de Ciencias Geológicas, v. 31, p. 45–63.

Oliveros, V., Labbé, M., Rossel, P., Charrier, R., and Encinas, A., 2012, Late Jurassic paleogeographic evolution of the Andean back-arc basin: New constrains from the Lagunillas Formation, northern Chile (27°30'–28°30'S): Journal of South American Earth Sciences, v. 37, p. 25–40, doi: 10.1016/j.jsames.2011.12.005.

Ortega-Flores, B., Solari, L., Lawton, T.F., and Ortega-Obregón, C., 2014, Detrital-zircon record of major Middle Triassic–Early Cretaceous provenance shift, central Mexico: demise of Gondwanan continental fluvial systems and onset of back-arc volcanism and sedimentation: International Geology Review, v. 56, p. 237–261, doi: 10.1080/00206814.2013.844313.

Ortega-Obregón, C., Keppie, J.D., Murphy, J.B., Lee, J.K.W., and Ortega-Rivera, A., 2009, Geology and geochronology of Paleozoic rocks in western Acatlán Complex, southern Mexico: Evidence for contiguity across an extruded high-pressure belt and constraints on Paleozoic reconstructions: Geological Society of America Bulletin, v. 121, p. 1678–1694.

Palacios-García, N.B., and Martini, M., 2014, From back-arc rifting to arc accretion: the Late Jurassic–Early Cretaceous evolution of the Guerrero terrane recorded by a major provenance change in sandstones from the Sierra de los Cuarzos area, central Mexico: International Geology Review, v. 56, p. 1377–1394, doi: 10.1080/00206814.2014.938367.

Pérez-Gutiérrez, R., Solari, L.A., Gómez-Tuena, A., and Valencia, V.A., 2009, El terreno Cuicateco: ¿cuenca oceánica con influencia de subducción del Cretácico Superior en el sur de México? Nuevos datos estructurales, geoquímicos y geocronológicos: Revista Mexicana de Ciencias Geológicas, v. 26, p. 222–242.

Peryam, T.C., Lawton, T.F., Amato, J.M., González-León, C.M., and Mauel, D.J., 2011, Lower Cretaceous strata of the Sonora Bisbee Basin: A record of the tectonomagmatic evolution of northwestern Mexico: Geological Society of America Bulletin, v. 124, p. 532–548.

Pompa-Mera, V., Schaaf, P., Hernández-Treviño, T., Weber, B., Solís-Pichardo, G., Villanueva-Lascurain, D., and Layer, P., 2013, Geology, geochronology, and geochemistry of Isla María Madre, Nayarit, Mexico: Revista Mexicana de Ciencias Geológicas, v. 30, p. 1–23.

Premo, W.R., and Morton, D.M, 2014, SHRIMP-RG U-Pb ages of provenance and metamorphism from detrital zircon populations and Pb-Sr-Nd signatures of pre-batholiothic metasedimentary rocks at Searl Ridge, north-central Peninsular Ranges batholith, southern California: Implications for their age, origin, and

tectonic setting, in Morton, D.M., and Miller F., eds., Contributions to the Geology of the Peninsular Ranges Batholith, southern California: Geological Society of America Memoir 211, p. 449-498.

Raines, M. K., S. M. Hubbard, R. B. Kukulski, A. L. Leier, and G. E. Gehrels, 2013, Sediment dispersal in an evolving foreland: Detrital zircon geochronology from Upper Jurassic and lowermost Cretaceous strata, Alberta Basin, Canada: Geological Society of America Bulletin, v. 125, B30671.1, doi:10.1130/B30671.1.

Ramos-Arias, M.A., and Keppie, J.D., 2011, U-Pb Neoproterozoic–Ordovician protolith age constraints for high- to medium-pressure rocks thrust over low-grade metamorphic rocks in the Ixcamilpa area, Acatlán Complex, southern Mexico: Canadian Journal of Earth Sciences, v. 48, p. 45–61.

Reimann, C.R., Bahlburg, H., Kooijman, E., Berndt, J., Gerdes, A., Carlotto, V., and López, S., 2010, Geodynamic evolution of the early Paleozoic Western Gondwana margin 14°–17°S reflected by the detritus of the Devonian and Ordovician basins of southern Peru and northern Bolivia: Gondwana Research, v. 18, p. 370–384, doi: 10.1016/j.gr.2010.02.002.

Reitsma, M.J., 2012, Reconstructing the Late Paleozoic - Early Mesozoic plutonic and sedimentary record of south-east Peru: Orphaned back-arcs along the western margin of Gondwana [Ph.D. thesis]: Geneva, Université de Genève, 246 p.

Riggs, N.R., Barth, A.P., González-León, C.M., Jacobson, C.E., Wooden, J.L., Howell, E.R., and Walker, J.D., 2012, Provenance of Upper Triassic strata in south-western North America as suggested by isotopic analysis and chemistry of zircon crystals, in Rasbury, E.T., Hemming, S.R., and Riggs, N.R., eds., Mineralogical and Geochemical Approaches to Provenance: Geological Society of America Special Paper 487, p. 13–36, doi:10.1130/2012.2487(02).

Riggs, N.R., Reynolds, S.J., Lindner, P.J., Howell, E.R., Barth, A.P., Parker, W.G., and Walker, J.D., 2013, The Early Mesozoic Cordilleran arc and Late Triassic paleotopography: The detrital record in Upper Triassic sedimentary successions on and off the Colorado Plateau: Geosphere, v. 9, p. 602–613, doi: 10.1016/j.crte.2013.03.004.

Rubio-Cisneros, I.I., and Lawton, T.F., 2011, Detrital zircon U-Pb ages of sandstones in continental red beds at Valle de Huizachal, Tamaulipas, NE Mexico: Record of Early-Middle Jurassic arc volcanism and transition to crustal extension: Geosphere, v. 7, p. 159–170.

Sagripanti, L., Bottesi, G., Naipauer, M., Folguera, A., and Ramos, V.A., 2011, U/Pb ages on detrital zircons in the southern central Andes Neogene foreland (36°–37°S): Constraints on Andean exhumation: Journal of South American Earth Sciences, v. 32, p. 555–566, doi: 10.1016/j.jsames.2011.03.010.

Saylor, J.E., Horton, B.K., Nie, J., Corredor, J., and Mora, A., 2011, Evaluating foreland basin partitioning in the northern Andes using Cenozoic fill of the Floresta basin, Eastern Cordillera, Colombia: Basin Research, v. 23, p. 377–402, doi: 10.1111/j.1365-2117.2010.00493.x.

Saylor, J.E., Stockli, D.F., Horton, B.K., Nie, J., and Mora, A., 2012, Discriminating rapid exhumation from syndepositional volcanism using detrital zircon double dating: Implications for the tectonic history of the Eastern Cordillera, Colombia: Geological Society of America Bulletin, v. 124, p. 762–779, doi: 10.1130/B30534.1.

Sepúlveda, F.A., Palma-Heldt, S., Hervé, F., and Fanning, C.M., 2010, Permian depositional age of metaturbidites of the Duque de York Complex, southern Chile: U-Pb SHRIMP data and palynology: Andean Geology, v. 37, p. 375–397.

Sharman, G.R., Graham, S.A., Grove, M., and Hourigan, J.K., 2013, A reappraisal of the early slip history of the San Andreas fault, central California, USA: Geology, v. 41, p. 727–730, doi: 10.1130/G34214.1.

Sharman, G.R., Graham, S.A., Grove, M., Kimbrough, D.L., and Wright, J.E., 2014, Detrital zircon provenance of the Late Cretaceous-Eocene California forearc: Influence of Laramide low-angle subduction on sediment dispersal and paleogeography: Geological Society of America Bulletin, B31065.1, doi: 10.1130/B31065.1.

Silva-Romo, G., Mendoza-Rosales, C.C., Campos-Madrigal, E., Centeno-García, E., and Peralta-Salazar, R., 2015, Early Mesozoic Southern Mexico–Amazonian connection based on U–Pb ages from detrital zircons: The La Mora Paleo-River in the Mixteca Terrane and its paleogeographic and tectonic implications: Gondwana Research, v. 28, no. 2, p. 689–701, doi: 10.1016/j.gr.2014.06.005.

Solari, L.A., Ortega-Gutiérrez, F., Elías-Herrera, M., Gómez-Tuena, A., and Schaaf, P., 2010, Refining the age of magmatism in the Altos Cuchumatanes, western Guatemala, by LA–ICPMS, and tectonic implications: International Geology Review, v. 52, p. 977–998.

Spencer, J.E., Richard, S.M., Gehrels, G.E., Gleason, J.D., and Dickinson, W.R., 2011, Age and tectonic setting of the Mesozoic McCoy Mountains Formation in western Arizona, USA: Geological Society of America Bulletin, v. 123, p. 1258–1274, doi: 10.1130/B30206.1.

Surpless, K.D., and Beverly, E.J., 2013, Understanding a critical basinal link in Cretaceous Cordilleran paleogeography: Detailed provenance of the Hornbrook Formation, Oregon and California: Geological Society of America Bulletin, v. 125, p. 709–727, doi: 10.1130/B30690.1.

Talavera-Mendoza, O., Ruiz, J., Gehrels, G.E., Valencia, V.A., and Centeno-García, E., 2007, Detrital zircon U/Pb geochronology of southern Guerrero and western

Mixteca arc successions (southern Mexico): New insights for the tectonic evolution of southwestern North America during the late Mesozoic: Geological Society of America Bulletin, v. 119, p. 1052–1065.

Talavera-Mendoza, O., Ruiz, J., Corona-Chavez, P., Gehrels, G.E., Sarmiento-Villagrana, A., García-Díaz, J.L., and Salgado-Souto, S.A., 2013, Origin and provenance of basement metasedimentary rocks from the Xolapa Complex: New constraints on the Chortis–southern Mexico connection: Earth and Planetary Science Letters, v. 369–370, p. 188–199.

Torres-de León, R., Solari, L.A., Ortega-Gutiérrez, F., and Martens, U., 2012, The Chortis Block--southwestern Mexico connections: U-Pb zircon geochronology constraints: American Journal of Science, v. 312, p. 288–313, doi: 10.2475/03.2012.02.

Tunik, M., Folguera, A., Naipauer, M., Pimentel, M. M., and Ramos, V. A., 2010, Early uplift and orogenic deformation in the Neuquén Basin: constraints on the Andean uplift from U–Pb and Hf isotopic data of detrital zircons: Tectonophysics, v. 489, p. 258–273.

Valencia, V.A., Righter, K., Rosas-Elguera, J., López-Martínez, M., and Grove, M., 2013, The age and composition of the pre-Cenozoic basement of the Jalisco Block: implications for and relation to the Guerrero composite terrane: Contributions to Mineralogy and Petrology, v. 166, p. 801–824, doi: 10.1007/s00410-013-0908-z.

Venegas-Rodríguez, G., Barboza-Gudiño, J.R., and López-Doncel, R.A., 2009, Geocronología de circones detríticos en capas del Jurásico Inferior de las áreas de la Sierra de Catorce y El Alamito en el estado de San Luis Potosí: Revista Mexicana de Ciencias Geológicas, v. 26, p. 466–481.

Weber, M., Cardona, A., Valencia, V., García-Casco, A., Tobón, M., and Zapata, S., 2010, U/Pb detrital zircon provenance from late cretaceous metamorphic units of the Guajira Peninsula, Colombia: Tectonic implications on the collision between the Caribbean arc and the South American margin: Journal of South American Earth Sciences, v. 29, p. 805–816.

Willner, A.P., Gerdes, A., and Massonne, H.-J., 2008, History of crustal growth and recycling at the Pacific convergent margin of South America at latitudes 29°–36° S revealed by a U–Pb and Lu–Hf isotope study of detrital zircon from late Paleozoic accretionary systems: Chemical Geology, v. 253, p. 114–129, doi: 10.1016/j.chemgeo.2008.04.016.

Witt, C., Brichau, S., and Carter, A., 2012, New constraints on the origin of the Sierra Madre de Chiapas (south Mexico) from sediment provenance and apatite thermochronometry: Tectonics, v. 31, TC6001, doi: 10.1029/2012TC003141.

Xie, X., Mann, P., and Escalona, A., 2010, Regional provenance study of Eocene clastic

sedimentary rocks within the South America–Caribbean plate boundary zone using detrital zircon geochronology: Earth and Planetary Science Letters, v. 291, p. 159–171, doi: 10.1016/j.epsl.2010.01.009.

Zapata, S., Weber, M., Cardona, A., Valencia, V., Guzmán, G., and Tobón, M., 2010, Provenance of Oligocene conglomerates and associated sandstones from the Siamaná Formation, Serranía de Jarara, Guajira, Colombia: implications for Oligocene Caribbean-South American tectonics: Geologia Colombiana, v. 27, p. 7–24.

References for Geochemistry Data

Allen, C.M., 1989, Petrogenesis of the reversely zoned Turtle pluton, southeastern California [Ph.D. thesis]: Virginia Polytechnic Institute and State University, Blacksburg, Virginia, 374 p.

Allen, E.F., 2007, Crustal contamination effects in central San Bernardino Mountains intrusives, CA [M.Sc. thesis]: Loma Linda University, 131 p.

Anderson, J.L., and M.C. Rowley, 1981, Synkinematic intrusion of peraluminous and associated metaluminous granitic magmas, Whipple Mountains, California: Canadian Mineralogist, v. 19, p. 83–101.

Barth, A.P., 1989, Mesozoic rock units in the upper plate of the Vincent Thrust Fault, San Gabriel Mountains, Southern California [Ph.D. thesis]: University of Southern California, 379 p.

Barth, A.P., 1990, Mid-crustal emplacement of Mesozoic plutons, San Gabriel Mountains, California, and implications for geologic history of the San Gabriel terrane, in Anderson, J.L., ed., The nature and origin of Cordilleran magmatism: Geological Society of America Memoir 174, p. 33–45.

Barth, A.P., Tosdal, R.M., and Wooden, J.L., 1990, A petrologic comparison of Triassic plutonism in the San Gabriel and Mule Mountains, Southern California: Journal of Geophysical Research, v. 95, p. 20075–20096.

Barth, A.P., Wooden, J.L., Howard, K.A., and Richards, J.L., 2008, Late Jurassic plutonism in the southwest U.S. Cordillera, in Wright, J.E., and Shervais, J.W., eds., Ophiolites, Arcs, and Batholiths: A Tribute to Cliff Hopson: Geological Society of America Special Paper 438, p. 379–396, doi: 10.1130/2008.2438(13).

Bateman, P.C., and Chappell, B.W., 1979, Crystallization, fractionation, and solidification of the Tuolumne Intrusive Series, Yosemite National Park, California: Geological Society of America Bulletin, v. 90, p. 465–482, doi: 10.1130/0016-7606(1979)90<465.

Bateman, P.C., Chappell, B.W., Kistler, R.W., Peck, D.L., and Busacca, A.J., 1988, Tuolumne Meadows Quadrangle, California; analytic data: U.S. Geological Survey Bulletin, 1819, 43 p.

Beckerman, G.M., 1982, Petrology of the southern portion of the Teutonia Batholith: A large intrusive complex of Jurassic and Cretaceous age in the eastern Mojave Desert [M.Sc. thesis], University of Southern California, 223 p.

Beckerman, G.M., Robinson, J.P., and Anderson, J.L., 1982, The Teutonia batholith: A large intrusive complex of Jurassic and Cretaceous age in the eastern Mojave Desert, California, in Frost, E.G., and Martin, D.L., eds., Mesozoic-Cenozoic tectonic evolution of the Colorado River region, California, Arizona, and Nevada: San Diego, California, Cordilleran Publishers, p. 205–220.

Brand, J.H., 1985, Mesozoic alkalic quartz monzonite and peraluminous ponzogranites of the northern portion of the Joshua Tree National Monument, southern California [M.Sc. thesis], University of Southern California, 187 p.

Burgess, S.D., 2006, Field, geochemical, and geochronologic study of the inner Tuolumne Intrusive Series [M.Sc. thesis], San Jose State University, Paper 2871, 157 p.

Centeno-García, E., 1994, Tectonic evolution of the Guerrero terrane, western Mexico [Ph.D. thesis]: Tucson, University of Arizona, 224 p.

Centeno-García, E., and Silva-Romo, G., 1997, Petrogenesis and tectonic evolution of central Mexico during Triassic-Jurassic time: Revista Mexicana de Ciencias Geológicas, v. 14, p. 244–260.

Centeno-García, E., Ruiz, J., Coney, P.J., Patchett, P.J., and Ortega-Gutiérrez, F., 1993, Guerrero terrane of Mexico: Its role in the Southern, Cordillera from new geochemical data: Geology, v. 21, p. 419–422.

Chen, J. H., and Moore, J. G., 1982, Uranium-lead isotopic ages from the Sierra Nevada batholith, California: Journal of Geophysical Research, v. 87, p. 4761–4784.

Chen, J. H., and Tilton, G. R., 1991, Applications of lead and strontium isotopic relationships to the petrogene- sis of granitoid rocks, central Sierra Nevada batholith, California: Geological Society of America Bulletin, v. 103, p. 439–447.

Coleman, D.S., Bartley, J.M., Glazner, A.F., and Pardue, M.J., 2012, Is chemical zonation in plutonic rocks driven by changes in source magma composition or shallow-crustal differentiation?: Geosphere, v. 8, p. 1568–1587, doi: 10.1130/GES00798.1.

DePaolo, D.J., 1981, A neodymium and strontium isotopic study of the Mesozoic calc-alkaline granitic batholiths of the Sierra Nevada and Peninsular Ranges, California: Journal of Geophysical Research, v. 86, no. B11, p. 10470-10488.

Economos, R.C., Hanzl, P., Hrdlicková, K., Buriánek, D., Said, L.-O., Gerdes, A., and Peterson, S.R., 2008, Geochemical and structural constraints on the magmatic history of the Chandman Massif of the eastern Mongolian Altay Range, SW Mongolia: Journal of Geosciences, v. 53, p. 33–352.

Economos, R.C., Memeti, V., Paterson, S.R., Miller, J.S., Erdmann, S., and Zak, J., 2010, Causes of compositional diversity in a lobe of the Half Dome granodiorite, Tuolumne Batholith, Central Sierra Nevada, California: Earth and Environmental Science Transactions of the Royal Society of Edinburgh, v. 100, p. 173–183, doi: 10.1017/S1755691009016065.

Elías-Herrera, M., 2003, The real Guerrero Terrane, southern Mexico: new insights from recent studies: Geological Society of America Abstract with Programs, paper no. 27-5.

Elías-Herrera, M., Ortega-Gutiérrez, F., Sánchez-Zavala, J.L., Macías-Romo, C., Ortega-Rivera, A., and Iriondo, A., 2005, La falla de Caltepec: raíces expuestas de una frontera tectónica de larga vida entre dos terrenos continentales del sur de México: Boletín de la Sociedad Geológica Mexicana, v. 57, p. 83–109.

Fox, L.K., and Miller, D.M., 1990, Jurassic granitoids and related rocks of the southern Bristol Mountains, southern Providence Mountains, and Colton Hills, Mojave Desert, California, in Anderson, J.L., ed., The nature and origin of Cordilleran magmatism: Geological Society of America Memoir 174, p. 111–132.

Freydier, C., Lapierre, H., Briqueu, L., Tardy, M., Coulon, C., and Martinez-Reyes, J., 1996a, Volcaniclastic sequences with continental affinities within the Late Jurassic–Early Cretaceous Guerrero intra-oceanic arc (western Mexico): Journal of Geology, v. 105, p. 483–502.

Freydier, C., Martinez, J.R., Lapierre, H., Tardy, M., and Coulon, C., 1996b, The Early Cretaceous Arperos oceanic basin (western Mexico). Geochemical evidence for an aseismic ridge formed near a spreading center: Tectonophysics, v. 259, p. 343–367.

Frizzell, V.A., Mattinson, J.M., and Matti, J.C., 1986, Distinctive Triassic megaporphyritic monzogranite: Evidence for only 160 km offset along the San Andreas Fault, southern California: Journal of Geophysical Research: Solid Earth, v. 91, p. 14080–14088, doi: 10.1029/JB091iB14p14080.

Frost, T.P., 1986, The Lamarck Granodiorite, Sierra Nevada, California: Fractionation and Interaction of Mafic and Felsic Magmas [Ph.D. thesis]: Stanford University, 426 p.

Glazner, A. F., et al. (2008). Chemical variability and the composite nature of dikes from the Jurassic Independence dike swarm, eastern California. IN: Ophiolites, arcs, and batholiths: a tribute to Cliff Hopson. J. E. Wright and J. W. Shervais, eds. GSA Special Paper438: 455-480.

Herzig, C. T. (1991). Petrogenetic and tectonic development of the Santiago Peak Volcanics, northern Santa Ana Mountains, California. PhD thesis: Riverside, University of California: 376p.

Hill, R. I., et al. (1988). "San Jacinto intrusive complex: 2. geochemistry." Journal of Geophysical Research 93(B9): 10349-10372.

Hill, R. I. and L. T. Silver (1988). "San Jacinto intrusive complex: 3. constraints on crustal magma chamber processes from strontium isotope heterogeneity." Journal of Geophysical Research 93(B9): 10373-10388.

Kistler, R. W. and D. E. Lee (1989). Rubidium, strontium, and strontium isotopic data for a suite of granitoid rocks from the Basin and Range province, Arizona, California, Nevada, and Utah. USGS Open-File Report 89-199.

Kistler, R. W., et al. (2014). Pb-Sr-Nd-O isotopic characterization of Mesozoic rocks throughout the northern end of the Peninsular Ranges batholith: Isotopic evidence for the magmatic evolution of oceanic arc-continental margin accretion during the Late Cretaceous of southern California. IN: Peninsular Ranges batholith, Baja California and southern California. D. M. Morton and F. K. Miller, eds. GSA Memoir 211: 263-316.

Miller, C. F. (1977). "Early alkalic plutonism in the calc-alkalic batholithic belt of California." Geology 5: 685-688.

Miller, J. S. and A. F. Glazner (1995). "Jurassic plutonism and crustal evolution in the central Mojave Desert, California." Contributions to Mineralogy and Petrology 118: 379-395.

Miller, D. M. and C. J. Busby, eds. (1995). Jurassic magmatism and tectonics of the North American cordillera. Geological Society of America Special Paper 299.

Morton, D. M. and F. K. Miller, eds. (2014). Peninsular Ranges batholith, Baja California and southern California. Geological Society of America Memoir 211.

Rämö, O. T., et al. (2002). "Geochemistry of Mesozoic plutons, southern Death Valley region, California: Insights into the origin of Cordilleran interior magmatism." Contributions to Mineralogy and Petrology 143: 416-437.

Young, E. D., et al. (1992). "Geochemical evolution of Jurassic diorites from the Bristol Lake region, California, USA, and the role of assimilation." Contributions to Mineralogy and Petrology 110: 68-86.